Edited by
Christoph Leyens and Manfred Peters

WILEY-VCH

Titanium and Titanium Alloys

Fundamentals and Applications

DGM

Titanium and Titanium Alloys

Edited by
C. Leyens and M. Peters

Related Titles from Wiley-VCH

H.-P. Degischer, B. Kriszt (Eds.)

Handbook of Cellular Metals

2002
ISBN 3-527-30339-1

G. Kostorz

Phase Transformations in Materials

2001
ISBN 3-527-30256-5

K. U. Kainer (Ed.)

Magnesium Alloys and Technology

2003
ISBN 3-527-30570-X

Titanium and Titanium Alloys

Fundamentals and Applications

Edited by
C. Leyens and M. Peters

WILEY-VCH

WILEY-VCH GmbH & Co. KGaA

Edited by

Dr. Christoph Leyens
Dr. Manfred Peters
DLR – German Aerospace Center
Institute of Materials Research
51170 Köln
Germany

Foreword

In 1791 the British reverend, mineralogist and chemist, William Gregor, was the first to discover titanium. Four years later, Martin Klaproth, a Berlin chemist, independently isolated titanium oxide. The story of the Greek mythological children of Uranos and Gaia, the Titans, provided him the inspiration for naming it titanium. The Titans, utterly hated by their father, were held in captivity in the earth's crust, similar to the hard to extract ore. It took more than 100 years to isolate the metal. The first alloys, including today's most popular Ti-6Al-4V, were developed in the late 1940s in the United States. Today a large number of titanium alloys have paved the way for light metals to vastly expand into many industrial applications.

Titanium and its alloys stand out primarily due to their high specific strength and excellent corrosion resistance, at just half the weight of steels and Ni-based superalloys. This explains their early success in the aerospace and the chemical industries. But other markets such as architecture, chemical processing, medicine, power generation, marine and offshore, sports and leisure, and transportation are seeing increased application of titanium.

This book is intended for students, materials scientists, engineers, and technicians from research, development, production, and design departments who want to become familiar with titanium and its alloys. Introductory chapters covering the metallurgical background, mechanical properties, oxidation behavior, and oxidation protection are followed by chapters on production and processing, and introductions to various traditional and new fields of application. Besides titanium and its conventional alloys, insight is also provided on titanium aluminides and titanium matrix composites. The variety of applications of titanium and its alloys in aerospace and non-aerospace markets are documented in detail. Extensive references allow further expansion on each individual subject.

Cologne, June 2003   C. Leyens and M. Peters

Contents

List of Contributors

Dr. rer. nat. habil. F. Appel
GKSS Research Center
Institute for Materials Research
Max-Planck-Straße 1
D-21502 Geesthacht
Germany
email: fritz.appel@gkss.de

Dipl.-Ing. W. Beck
FormTech GmbH
Mittelwendung 35
D-8844 Weyhe-Dreye
Germany
email: werner.beck@formtech.de

Priv.-Doz. Dr. V. Biehl
Stryker Leibinger GmbH & Co. KG
Bötzinger Straße 41
D-79111 Freiburg
Germany
email: volker.biehl@leibinger.com

Prof. Dr.-Ing. J. K. Bigoney
Springfield Metallurgical Services Inc.
127 Main Street
Springfield, VT 05156-0826
USA
email: info@smslab.net

Prof. Dr.-Ing. J. Breme
Lehrstuhl für Metallische Werkstoffe
Universität des Saarlandes
D-66041 Saarbrücken
Germany
email: j.breme@mx.uni-saarland.de

Prof. Dr. H. Clemens
The University of Leoben
Department of Physical Metallurgie
and Materials Testing
A-8700 Leoben
Austria
email:
Helmut.Clemens@unileoben.ac.at

Dr. E. Eisenbarth
Lehrstuhl für Metallische Werkstoffe
Universität des Saarlandes
D-66041 Saarbrücken
Germany
email: e.eisenbarth@mx.
uni-saarland.de

Dr.-Ing. F. Fischer
Otto Fuchs Metallwerke
D-58528 Meinerzhagen
Germany
email: quality@otto-fuchs.com

Dr.-Ing. J. Hausmann
DLR-German Aerospace Center
Institute of Materials Research
D-51170 Köln
Germany
email: joachim.hausmann@dlr.de

Dr.-Ing. J. Hemptenmacher
DLR-German Aerospace Center
Institute of Materials Research
D-51170 Köln
Germany
email: joerg.hemptenmacher@dlr.de

Dr.-Ing. H. Kestler
Plansee AG
Technology Center
A-6600 Reutte
Austria
email: heinrich.kestler@plansee.at

Dr.-Ing. J. Kumpfert
Airbus Industrie
1 Rond Point Maurice Bellonte
F-31707 Blagnac
France
email: joerg.kumpfert@airbus.fr

Dr.-Ing. C. Leyens
DLR-German Aerospace Center
Institute of Materials Research
D-51170 Köln
Germany
email: christoph.leyens@dlr.de

Dr.-Ing. C. Liesner
Titan-Aluminium-Feinguß GmbH
Kapellenstr. 44
D-59909 Bestwig
Germany
email: christian.liesner@tital.de

Dr.-Ing. J. Lindigkeit
Dentaurum
J. P. Winkelstroeter KG
Turnstraße 31
D-75228 Ispringen
Germany
email: juergen.lindigkeit@
dentaurum.de

Dr. L. Lunde
Institute for Energy Technology
N-2027 Kjeller
Norway
email: liv.lunde@ife.no

H.-P. Nicolai
Titan-Aluminium-Feinguß GmbH
Kapellenstr. 44
D-59909 Bestwig
Germany
email: hans-peter.nicolai@tital.de

Dr. rer. nat. M. Oehring
GKSS Research Center
Institute for Materials Research
Max-Planck-Straße 1
D-21502 Geesthacht
Germany
email: michael.oehring@gkss.de

Dr.-Ing. M. Peters
DLR-German Aerospace Center
Institute of Materials Research
D-51170 Köln
Germany
email: manfred.peters@dlr.de

Dr.-Ing. O. Schauerte
Volkswagen AG
Brieffach 1504
D-38436 Wolfsburg
Germany
email: oliver.schauerte@volkswagen.de

Dr. M. Seiersten
Institute for Energy Technology
N-2027 Kjeller
Norway
email: marion.seiersten@ife.no

Dr.-Ing. H. Sibum
DTG-Deutsche Titan GmbH
D-45143 Essen
Germany
email: sibum@dtg.kts.krupp.com

Dr.-Ing. G. Terlinde
Otto Fuchs Metallwerke
D-58528 Meinerzhagen
Germany
email: terlinde.gr@otto-fuchs.com

Prof. Dr.-Ing. L. WAGNER
Institut für Werkstoffkunde
und Werkstofftechnik
TU Clausthal
Agricolastraße 6
D-38678 Clausthal-Zellerfeld
Germany
email: lothar.wagner@tu-clausthal.de

CHARLES H. WARD, PhD
European Office of Aerospace Research
and Development
223/231 Old Marylebone Road
London NW1 5TH
UK
email: charles.ward@london.af.mil

Dr.-Ing. T. WITULSKI
Otto Fuchs Metallwerke
D-58528 Meinerzhagen
Germany
email: witulski.th@otto-fuchs.com

1
Structure and Properties of Titanium and Titanium Alloys

M. Peters, J. Hemptenmacher, J. Kumpfert* and C. Leyens
DLR – German Aerospace Center, Cologne, Germany
* Airbus Industrie, Blagnac, France

1.1
Introduction

In 1791 William Gregor the British reverend, mineralogist, and chemist discovered titanium. He examined the magnetic sand from the local river, Helford, in the Menachan Valley in Cornwall, England, and isolated "black sand", now known as "ilmenite". By removing the iron with a magnet and treating the sand with hydrochloric acid he produced the impure oxide of a new element. He named it "mechanite", after the location. Four years later, the Berlin chemist Martin Heinrich Klaproth independently isolated titanium oxide from a Hungarian mineral, now known as "rutile". Greek mythology provided him a new name from the children of Uranos and Gaia, the titans. The titans were utterly hated by their father and so detained in captivity by him in the earth's crust, similar to the hard to extract ore – hence he named it Titanium.

It took more than 100 years before Matthew Albert Hunter from Rensselaer Polytechnic Institute in Troy, N.Y., was able to isolate the metal in 1910 by heating titanium tetrachloride ($TiCl_4$) with sodium in a steel bomb. Finally, Wilhelm Justin Kroll from Luxembourg is recognized as father of the titanium industry. In 1932 he produced significant quantities of titanium by combining $TiCl_4$ with calcium. At the beginning of World War II he fled to the United States. At the U.S. Bureau of Mines he demonstrated that titanium could be extracted commercially by reducing $TiCl_4$ by changing the reducing agent from calcium to magnesium. Today this is still the most widely used method and is known as the "Kroll process". After the Second World War, titanium-based alloys were soon considered key materials for aircraft engines. In 1948 the DuPont Company was the first to produce titanium commercially. Today aerospace is still the prime consumer of titanium and its alloys, but other markets such as architecture, chemical processing, medicine, power generation, marine and offshore, sports and leisure, and transportation are gaining increased acceptance.

Titanium is not actually a rare substance as it ranks as the ninth most plentiful element and the fourth most abundant structural metal in the Earth's crust exceeded only by aluminum, iron, and magnesium. Unfortunately, it is seldom found in high concentrations and never found in a pure state. Thus, the difficulty

Tab. 1.1 Physical properties of high-purity polycrystalline α titanium (>99.9%) at 25 °C.

Structure prototype	Mg
Pearson symbol	hP2
Space group	P6₃/mmc (194)
β-transus temperature	882 °C
Lattice parameters	a = 0.295 nm
	c = 0.468 nm
	c/a = 1.587
Thermal expansion coefficient [10^{-6}K^{-1}]	8.36
Thermal conductivity [W/mK]	14.99
Specific heat capacity [J/kgK]	523
Electrical resistance [10^{-9} Ωm]	564.9
Elastic modulus [GPa]	115
Shear modulus [GPa]	44
Poisson's ratio	0.33

in processing the metal makes it expensive. Even today it is produced only in a batch process, and no continuous process exists as for other structural metals. Titanium usually occurs in mineral sands containing ilmenite ($FeTiO_3$), found in the Ilmen mountains of Russia, or rutile (TiO_2), from the beach sands in Australia, India, and Mexico. Titanium dioxide is a very versatile white pigment used in paint, paper, and plastic, and consumes most of world production. Besides Russia, Australia, India, and Mexico, workable mineral deposits include sites in the United States, Canada, South Africa, Sierra Leone, Ukraine, Norway, and Malaysia.

Of all the 112 chemical elements in the periodic system known today, about 85% are metals or metalloids. There are various ways to classify the metals, such as ferrous or nonferrous metals, ingot or sintered metals, light or heavy metals. Titanium is classified as a nonferrous and light metal.

The properties of metals are essentially based on the metallic bonding of the atoms in the crystal lattice. This means that the free, mobile valence electrons in the lattice result in classic "metallic" properties such as electrical conductivity, plastic deformation by atomic slip in crystal lattices, and alloying by incorporation of impurity atoms into the crystal lattice with the consequence of increased hardness and strength as well as reduced ductility. Tab. 1.1 shows a selection of important physical properties of highly pure polycrystalline α titanium.

Metals vary substantially in weight. At 0.5 g cm^{-3} Lithium has the lowest density while Osmium and Iridium are the heaviest metals with a density of 22.5 g cm^{-3}. The separation point between light and heavy metals is 5 g cm^{-3}. Therefore, Titanium with a density of 4.51 g cm^{-3} is the heaviest light metal. Although twice as heavy as the classic light metal – aluminum – it has only about half the specific weight of iron or nickel (Fig. 1.1).

Titanium alloys primarily stand out due to two properties: high specific strength and excellent corrosion resistance. This also explains their preferential use in the aerospace sector, the chemical industry, medical engineering, and the
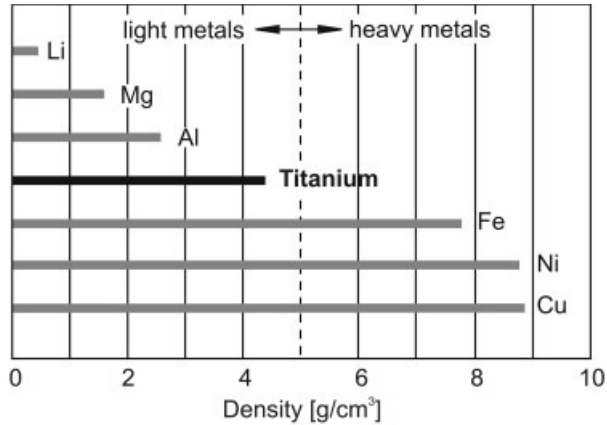
Fig. 1.1 Density of selected metals.
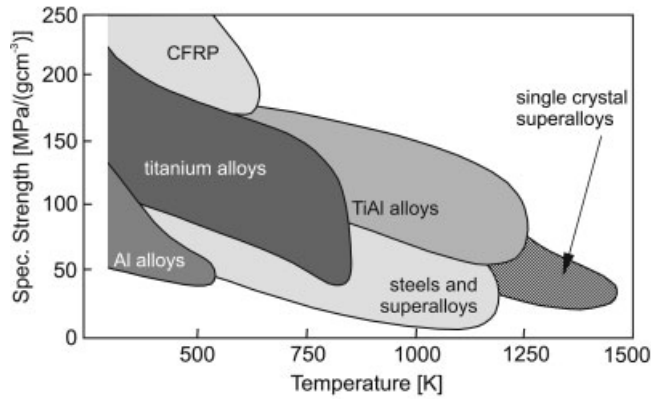
Fig. 1.2 Specific strength versus use temperature of selected structural materials compared with titanium alloys and aluminides.

leisure sector. Only at temperatures below 300 °C do carbon fiber reinforced plastics have a higher specific strength than titanium alloys (Fig. 1.2). At higher temperatures the specific strength of titanium alloys is particularly attractive. However, the maximum application temperature is limited by their oxidation behavior. Since titanium aluminides partly overcome this disadvantage, they have become the subject of intense alloy development efforts. While conventional elevated temperature titanium alloys are used only up to temperatures slightly above 500 °C, TiAl-based alloys directly compete with well-established high temperature steels and Ni-base superalloys (Fig. 1.2).

1.2
The Metallurgy of Titanium

1.2.1
Crystal Structure

Like a number of other metals – e.g. Ca, Fe, Co, Zr, Sn, Ce, and Hf – titanium can crystallize in various crystal structures. However, each modification is only stable within particular temperature ranges. The complete transformation from one into another crystal structure is called allotropic transformation; the respective transformation temperature is called the transus temperature.

Pure titanium, as well as the majority of titanium alloys, crystallizes at low temperatures in a modified ideally hexagonal close packed structure, called α titanium. At high temperatures, however, the body-centered cubic structure is stable and is referred to as β titanium. The β-transus temperature for pure titanium is 882±2 °C. The atomic unit cells of the hexagonal close packed (hcp) α titanium and the body-centered cubic (bcc) β titanium are schematically shown in Fig. 1.3 with their most densely packed planes and directions highlighted.

The existence of the two different crystal structures and the corresponding allotropic transformation temperature is of central importance since they are the basis for the large variety of properties achieved by titanium alloys.

Both plastic deformation and diffusion rate are closely connected with the respective crystal structure. In addition, the hexagonal crystal lattice causes a distinctive anisotropy of mechanical behavior for the α titanium. The elastic anisotropy is particularly pronounced. The Young's modulus of titanium single crystals consistently varies between 145 GPa for a load vertical to the basal plane and only 100 GPa parallel to this plane.
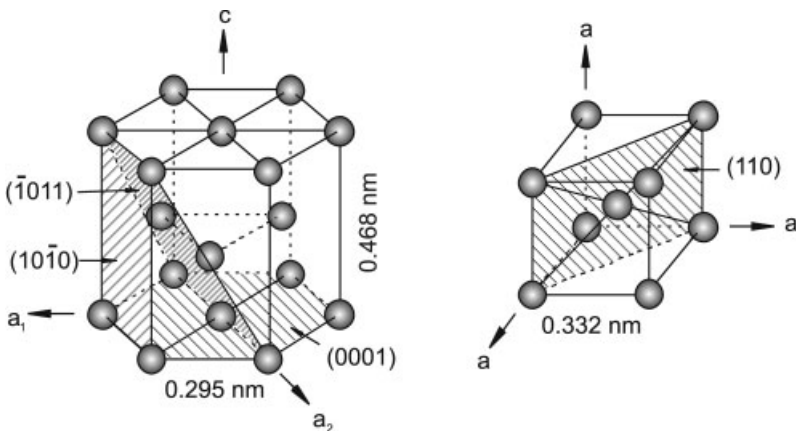
Fig. 1.3 Crystal structure of hcp α and bcc β phase.

1.2.2
Plastic Deformation

The essential features of the three crystal structures pertinent to metals are summarized in Tab. 1.2. The ease of plastic deformation increases from the hexagonal close packed (hcp) lattice to the body-centered cubic (bcc) to the face-centered cubic (fcc) lattice. This phenomenon also explains the limited plastic deformability of the hcp α titanium compared to the bcc β titanium. Generally the number of slip systems – which is equivalent to the number of dislocation glide opportunities in a crystal lattice – is only 3 for the hcp structure while it is 12 for the bcc lattice. The number of slip systems is determined by the number of slip planes multiplied by the number of slip directions. These planes and directions of highly dense packed atoms are energetically most favorable for plastic deformation.

The denser slip planes are packed with atoms, the easier dislocations can glide. Therefore, a slip plane in the hcp lattice with a packing density of 91% should be superior to a slip plane in the bcc lattice with a packing density of only 83%. However, the energy needed for plastic deformation is also directly dependent on the length of the minimal slip path. For hcp lattice structures this minimum slip path corresponds to $b_{min} = 1 \cdot a$, while for bcc structures $b_{min} = 0.87 \cdot a$, with a being the lattice parameter of the respective unit cell. This in turn favors the plastic deformation of the bcc over the hcp structure.

In α titanium the lattice parameters of the hexagonal close packed crystal structure are a = 0.295 nm and c = 0.468 nm, giving a c/a ratio of 1.587. For an ideally close packed hexagonal lattice the c/a ratio is 1.633. The insertion of interstitially dissolved atoms in the hcp lattice, e.g. C, N, or O, or the incorporation of substitutional atoms with smaller atomic radii than titanium, e.g. Al, slightly increases the c/a ratio of the α titanium. The lattice parameter of bcc β titanium at 900 °C is a = 0.332 nm.

Tab. 1.2 Characteristic parameters of metallic structure types.

Structure type	N	CN	P	Slip planes Slip directions		Slip system per unit cell	Atom density of slip plane	b_{min}/a
				indices	*numbers*			
hcp (c/a = 1,633)	6	12	74%	{0001} $\langle 11\bar{2}0 \rangle$	1 3	1 × 3 = 3	≈ 91%	1
bcc	2	8	68%	{110} $\langle 111 \rangle$	6 2	6 × 2 = 12	≈ 83%	1/2 $\sqrt{3}$ ≈ 0,87
fcc	4	12	74%	{111} $\langle 110 \rangle$	4 3	4 × 3 = 12	≈ 91%	1/2 $\sqrt{2}$ ≈ 0,71

N   Number of atoms per unit cell
CN   Coordination number
P   Packing density
b_{min}/a Minimal slip component
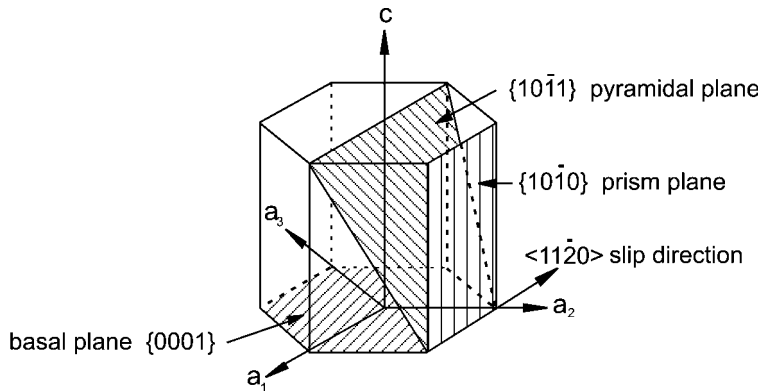
Fig. 1.4 Slip systems of hexagonal crystal lattices.

Compared to an ideally packed hexagonal crystal structure the reduced c/a ratio of α titanium leads to a larger spacing between prism planes. This causes the packing density of the prism planes to increase relative to the basal plane and thus favoring slip on prism planes rather than on basal planes.

Prism and basal planes have three slip systems each. However, only two are independent of each other, resulting in only four independent slip systems. Slip on pyramidal planes does not increase the number further since this glide is composed of a prism and a basal component and therefore cannot be considered an independent slip system. However, according to the von-Mises criterion at least five independent slip systems are required for homogeneous plastic deformation of metals. In fact, polycrystalline hexagonal α titanium is extremely difficult to deform. The limited ductility that is observed is the result of additional deformation on secondary slip systems as well as possible mechanical twinning. The three active slip systems in α titanium are depicted in Fig. 1.4.

1.2.3
β/α-Transformation

Upon cooling from the β phase field of titanium the most densely packed planes of the bcc β phase {110} transform to the basal planes {0001} of the hexagonal α phase. The distance between the basal planes in α is slightly larger than the corresponding distance between the {110} planes in β (see also Tab. 1.2: b_{min}/a). Therefore, the β/α transformation causes a slight atomic distortion (Fig. 1.5). This leads to a slight contraction of the c-axis relative to the a-axis in the hcp α and reduces the c/a-ratio below the value of ideally close packed hexagonal atomic structures. A slight increase in volume is observed macroscopically during cooling through the β/α transformation temperature.

Fig. 1.5 β/α transformation according to Burgers relationship.
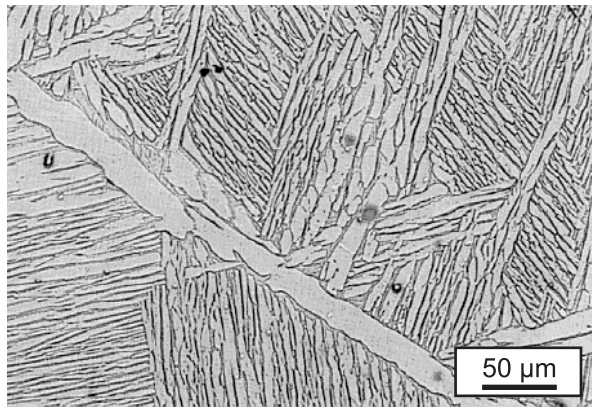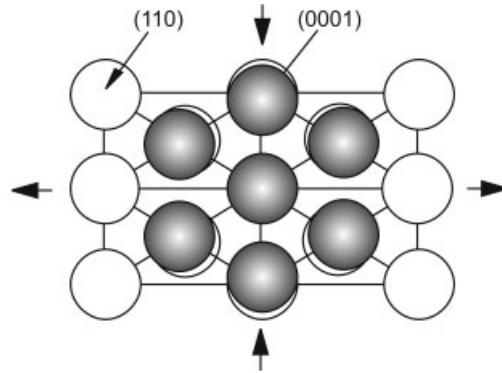
Fig. 1.6 Lamellar microstructure of Ti-6Al-4V (basket-weave).

The corresponding transformation of the slip planes of the bcc β titanium into the basal planes of the hcp α titanium and the respective orientations of the slip directions is given by the following orientation relationship:

$$\{0001\}_\alpha//\{110\}_\beta$$
$$\langle 1120\rangle_\alpha//\langle 111\rangle_\beta$$

Since the Burgers vectors can also describe the slip directions, the above orientation relationship is referred to as a Burgers relationship. The six slip planes and the two slip directions of the β titanium unit cell give a maximum of 12 variants of orientation to the α. This variety of orientations is also reflected in the metallographic microstructure. Within the prior β grains, which can be as large as several millimeters, individual α lamellar packets nucleate and grow according to the previously mentioned 12 orientation relationships, with the individual lamellar packets having a common orientation within them. The large – but limited to 12 – number of pos-

sible orientations results in multiple repetitions of the orientation of the lamellar packets. Consequently, this results in a very characteristic microstructure similar in appearance to the weave pattern of a basket and are therefore referred to as basket-weave structures (Fig. 1.6).

1.2.4
Diffusion

Because of the densely packed atoms in hcp α titanium, diffusion is considerably lower than in bcc β titanium: the diffusion coefficient of α titanium is orders of magnitude smaller than that of β titanium. The following coefficients are given for self-diffusion of titanium at 500 °C and 1000 °C. The resulting diffusion paths, d, after 50 h at 500 °C and 1 h at 1000 °C illustrate these differences.

500 °C: $D_{\alpha\text{-Ti}} \approx 10^{-19} \, \text{m}^2/\text{s}$ after 50 h: $d \approx 0.8 \, \mu\text{m}$
         $D_{\beta\text{-Ti}} \approx 10^{-18} \, \text{m}^2/\text{s}$ $d \approx 0.9 \, \mu\text{m}$

1000 °C: $D_{\alpha\text{-Ti}} \approx 10^{-15} \, \text{m}^2/\text{s}$ after 1 h: $d \approx 4 \, \mu\text{m}$
          $D_{\beta\text{-Ti}} \approx 10^{-13} \, \text{m}^2/\text{s}$ $d \approx 40 \, \mu\text{m}$

The different diffusion coefficients of α and β titanium are influenced by the microstructure and thus influence the mechanical behavior of the two phases, e.g. creep performance, hot workability, and superplasticity. The limited volume diffusion in α titanium translates into a superior creep performance of α titanium and α containing Ti alloys compared to β titanium.

Below the β-transus temperature, time- and temperature-dependent diffusion processes are substantially slower. Therefore, fast cooling leads to a very fine lamellar structure whereas upon slow cooling a coarse lamellar structure is obtained. The radial spread of the α lamellae is parallel to the {110} planes of the β phase. If sufficient cooling rate is provided, the individual lamellae not only nucleate at grain boundaries but also on the growth front of individual lamellar packets.

At high cooling rates from temperatures above the martensite start temperature, the bcc β transforms completely into the hcp α by a diffusionless transformation process, leaving behind a metastable fine plate-like, or acicular, martensitic microstructure.

The martensitic transformation does not lead to embrittlement; however, strength is slightly increased compared to α titanium. The martensite can be further split into hexagonal α′ martensite and orthorhombic α″ martensite, the latter being observed on quenching from temperatures below about 900 °C. The orthorhombic α″ martensite is characterized by good deformability. The hexagonal α′ martensite has a similar orientation relationship to β as that of α. The martensitic microstructure is therefore also characterized by a very fine basket-weave structure with needle-like character due to its diffusionless nucleation process.
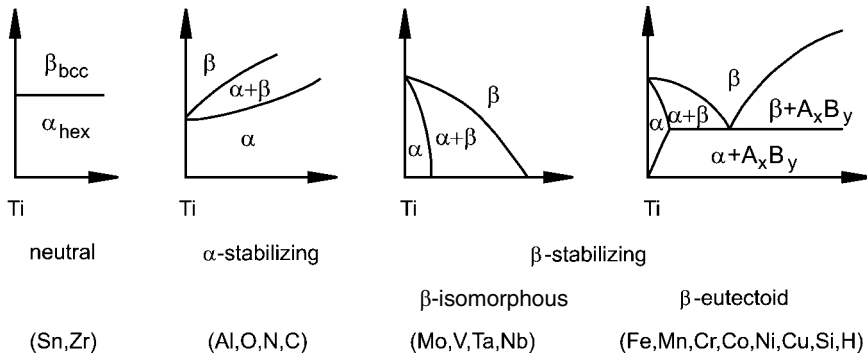
Fig. 1.7 Influence of alloying elements on phase diagrams of Ti alloys (schematically).

1.3
The Classification of Titanium Alloys

Depending on their influence on the β-transus temperature, the alloying elements of titanium are classified as neutral, α-stabilizers, or β-stabilizers (Fig. 1.7). The α-stabilizing elements extend the α phase field to higher temperatures, while β-stabilizing elements shift the β phase field to lower temperatures. Neutral elements have only minor influence on the β-transus temperature. Apart from the regular alloying elements, there are also primarily nonmetallic elements on the order of few 100 ppm present as impurities.

Among the α-stabilizers, aluminum is by far the most important alloying element of titanium. The interstitial elements oxygen, nitrogen, and carbon also belong to this category. In addition to extending the α phase field to higher temperatures, the α-stabilizers develop a two-phase α+β field. α-stabilizing elements are subdivided into β-isomorphous and β-eutectic elements. Of these, the β-isomorphous elements, e.g. Mo, V, and Ta, are by far more important due to their much higher solubility in titanium. On the other hand, even very low volume fractions of β-eutectic elements, e.g. Fe, Mn, Cr, Co, Ni, Cu, Si, and H, can lead to the formation of intermetallic compounds. Sn and Zr are considered neutral elements since they have (nearly) no influence on the α/β phase boundary. As far as strength is concerned, they are not neutral since they primarily strengthen the α phase.

Usually titanium alloys are classified as α, α+β, and β alloys, with further subdivision into near-α and metastable β alloys. This is schematically outlined in a three-dimensional phase diagram, which is composed of two phase diagrams with an α- and a β-stabilizing element respectively (Fig. 1.8). According to this scheme, the α alloys comprise commercially pure (cp) titanium and alloys exclusively alloyed with α-stabilizing and/or neutral elements. If minor fractions of β-stabilizing elements are added, they are referred to as near-α alloys. The α+β alloys, the most widely used alloy group, follow this class; at room temperature these alloys have a β volume fraction ranging from about 5 to 40%. If the proportion of β-stabilizing elements is further increased to a level where β no longer transforms to martensite upon fast
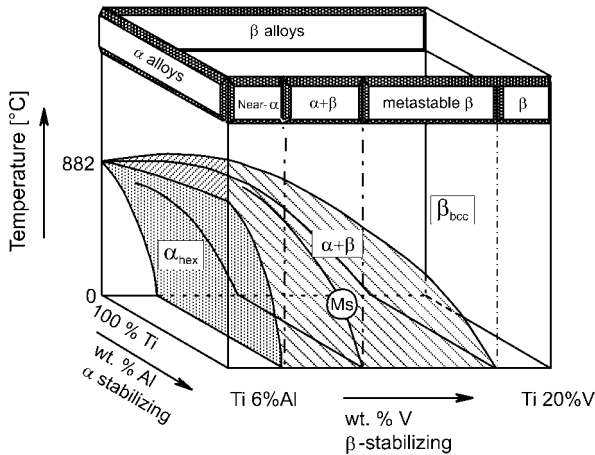
Fig. 1.8 Three-dimensional phase diagram to classify Ti alloys (schematically).
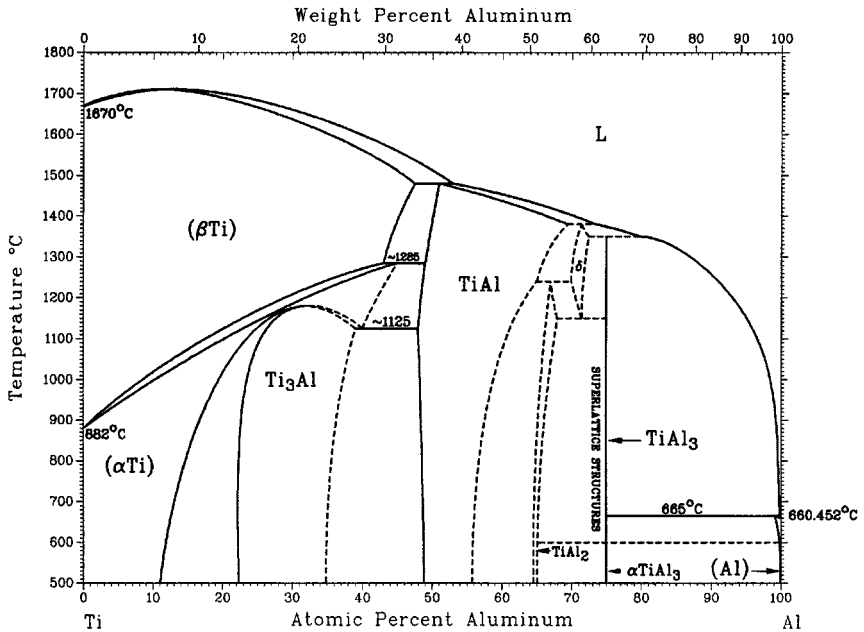
Fig. 1.9 The Ti-Al phase diagram (T.B. Massalski, 1990).

quenching, the alloys are still in the two-phase field and the class of metastable β alloys is reached. It should be noted that these alloys can still reveal an equilibrium α volume fraction of more than 50%. Finally, the single-phase β alloys mark the end of the alloying scale of the conventional titanium alloys.

The most important and by far most intensively investigated titanium phase diagram is the system Ti-Al (Fig. 1.9). Apart from the α and β phases, which are of central importance for the conventional titanium alloys, several intermetallic phases are present, such as α_2-Ti$_3$Al, γ-TiAl, TiAl$_2$ and TiAl$_3$. Of these only the α_2-Ti$_3$Al and γ-TiAl are of technical relevance today, since TiAl$_2$ and the stoichiometric compound TiAl$_3$ (a line compound) are extremely brittle. Titanium aluminide alloys of technical interest are found in the range of the two-phase field $\alpha+\alpha_2$ and of γ-TiAl. With the exception of model alloys, the latter alloys are usually also two-phase $\alpha_2+\gamma$ or multi-phase alloys depending on the alloying elements. Due to its steadily increasing importance in particular for high-temperature applications, two separate chapters of this book deal exclusively with γ-titanium aluminides (Chapter 4 and Chapter 14). If these aluminides are alloyed with Nb another intermetallic phase – Ti$_2$AlNb – appears, which is the basis for the class of orthorhombic titanium aluminides (Chapter 3). A further intermetallic phase with some technical relevance is the τ phase, which belongs to the cubic L1$_2$ family. This phase is present when elements like V, Cr, Mn, Fe, Co, Ni, Cu, or Zn substitute for about 10% of the aluminum in high Al-containing TiAl$_3$-base alloys.

1.4
Metallographic Preparation of the Microstructure

As described in the following sections, the mechanical properties of titanium alloys are predominantly determined by the chemical composition as well as the corresponding microstructure. The metallographic preparation and the subsequent microstructural investigations are therefore of great interest.

Cutting of titanium specimens should be done with water cooling to prevent a local overheating caused by its relatively low thermal conductivity in comparison to other metals. Furthermore, the velocity of the cutting blade and the feed rate should be reduced. The material may be characterized from ductile to tough; therefore, in addition to SiC cutting blades, diamond cutting blades are also effective. A relatively weak diamond bonding, e.g. in epoxy, is recommended. High cutting performance is achieved as blunt diamonds break loose to uncover new ones.

Titanium tends to create deformation surface layers, which may exhibit pseudo microstructures. One sophisticated solution to this problem is electrolytic polishing. However, this is only recommended for polishing very pure titanium, which is otherwise extremely difficult to polish mechanically. The handling of the electrolyte, generally containing perchloric acid, needs particular safety measures. Specifications of current, voltage, time, and etching area must be precisely followed to achieve reproducible results.

Mechanical polishing is the leading method to prepare the microsection for all Ti alloys. The primary stage is precise water cooled grinding on SiC-paper up to grit 1200, the final paper can be waxed. The first polishing uses a strong synthetic or cotton cloth with diamonds of grit 6 µm or even 3 µm, which accordingly requires a longer polishing time. Pressure on the disk should be moderate. The fi-

nal polishing may be successfully achieved with colloidal silicon dioxide of fine grit, i.e. 0.04 µm, on a synthetic leather cloth. This suspension is basic and has a pH value of approximately 9.8, acting as a weak etchant. Alternatively, a fine-grained Al_2O_3 suspension with an additive of cold saturated hydrous oxalic acid can be used for final polishing on a short fiber velvet cloth. Liquid soap is an approved addition for both suspensions. The final polishing will in general be repeated in short steps several times, followed by etching of the microsection and verification of the microstructure under the optical microscope.

A universal etchant is a hydrous solution, consisting of 3 ml HF (40% conc.) and 5 ml HNO_3 (65% conc.) in 100 ml H_2O. Immediately before etching a small amount of H_2O_2 can be added. After only a few seconds the etchant effect is seen, which should be precisely time controlled through close microsection observation. At first, a spurious layer or a strain-induced microstructure is often to be seen. However, each etching or polishing step reduces these artifacts. In general, the microstructure is well developed after 3 etching/polishing steps.

Images of very fine precipitates or transformation products in Ti-alloys can only be made with the aid of the transmission electron microscope. A special preparation is necessary for the thin foil specimens required here. First, the 3 mm diameter specimens are mechanically thinned down to 100-150 µm thickness. Further preparation is often achieved by electrolytic etching using the double injection method at about –30 °C temperature and about 20 V voltage. A common electrolyte is a solution of 59.7% methanol, 35.5% butanol and 4.8% perchloric acid. In some Ti-alloys this method may cause artifacts due to hydrogen penetration. In this case, ion thinning is well a proven alternative. An angle of incidence smaller than 12° is recommended to prepare areas large enough for transmission.

1.5
The Microstructure of Titanium Alloys

As previously mentioned, the microstructure has a substantial influence on the properties of titanium alloys. The microstructure of conventional titanium alloys

Tab. 1.3 Influence of microstructure on selected properties of titanium alloys.

fine	coarse	Property	lamellar	equiaxed
○	○	Elastic modulus	○	+/– (texture)
+	–	Strength	–	+
+	–	Ductility	–	+
–	+	Fracture toughness	+	–
+	–	Fatigue crack initiation	–	+
–	+	Fatigue crack propagation	+	–
–	+	Creep strength	+	–
+	–	Superplasticity	–	+
+	–	Oxidation behavior	+	–
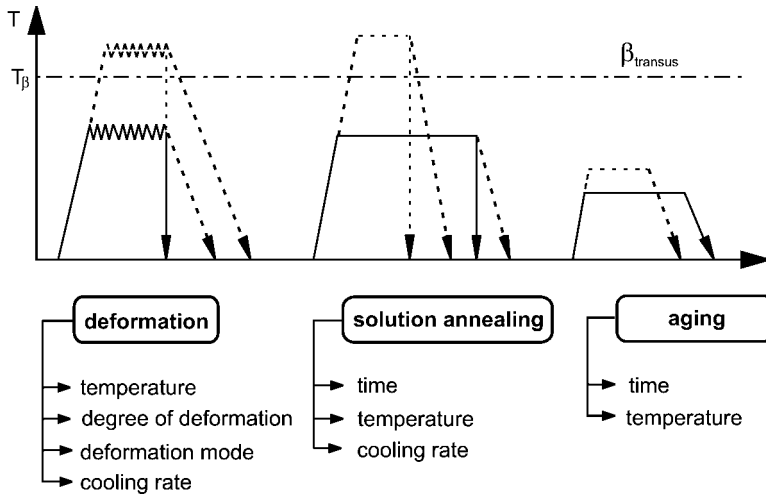
Fig. 1.10 Thermomechanical treatment of titanium alloys.

is primarily described by the size and arrangement of the two phases α and β. The two extreme cases of phase arrangements are the lamellar microstructure, which is generated upon cooling from the β phase field, and the equiaxed microstructure, which is a result of a recrystallization process. Both types of microstructure can have a fine as well as a coarse arrangement of their two phases. The influence of the various microstructures on the mechanical behavior of titanium alloys has been the subject of numerous investigations, thus some general statements can be made. Tab. 1.3 shows qualitatively how the size of the phases (comparison of fine and coarse microstructures) on the one hand, and the arrangement of the phases (comparison between lamellar and equiaxed microstructures) on the other, have an effect on some important selected mechanical properties.

Generally, the different microstructures are generated by thermomechanical treatments. These are considered as a complex sequence of solution heat treatment, deformation, recrystallization, aging, and annealing for stress relief as schematically outlined in Fig. 1.10.

A central point for thermomechanical treatment is the β-transus temperature, T_β, since it separates the single β phase field from the two-phase α+β field. Lamellar microstructures are a result of simple cooling from temperatures above the β-transus temperature. Once the temperature falls below the transus temperature α nucleates at grain boundaries and then grows as lamellae into the (prior) β grain. An example of this structure is shown for the Ti-6Al-4V alloy in a high temperature microscopy sequence (Fig. 1.11).

Depending on the cooling rate, the lamellae are either fine or coarse. Slow cooling from the β phase field results in pure lamellar microstructures (Fig. 1.12 a), with the lamellae becoming coarser with reduced cooling rate. Rapid quenching leads to a martensitic transformation of β, resulting in a very fine needle-like microstructure (Fig. 1.12 b). Unlike the martensite known in steels, which leads to
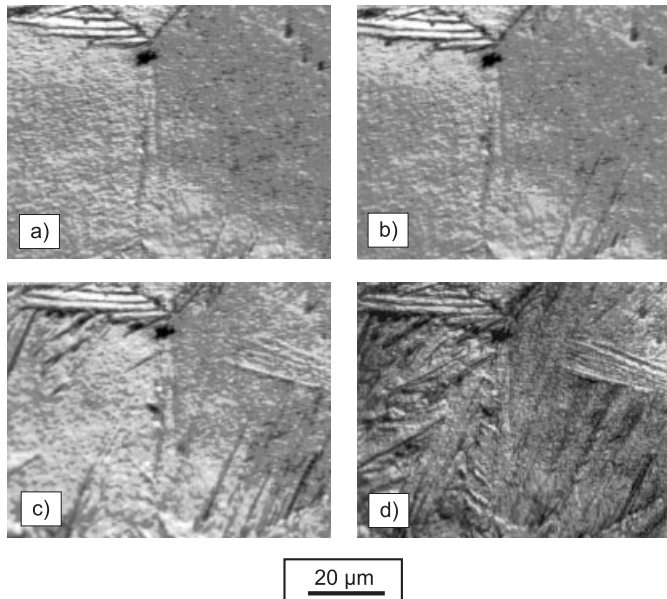
Fig. 1.11 Cooling from the β phase field of Ti-6Al-4V (high-temperature microscopy).

strong distortion of the crystal lattice with accompanying marked increase in hardness and strength, the hardening effect observed for titanium alloys on martensitic transformation is only moderate.

The chemical compositions of the α and β phases change in the two-phase field with decreasing temperature under equilibrium conditions. Vanadium strongly enriches β and thus stabilizes this phase at lower temperatures. The metallographic figures of all slowly cooled specimens show β as a small seam around the coarse and light colored α lamellae (Figs 12 a, c, d). With high cooling rates from temperatures above the martensitic start temperature (MS) and through the two-phase field, β transforms into martensite (Fig. 1.12 d). The martensitic start temperature varies depending on the starting structure and the homogeneity of the microstructure. At lower temperatures, the β volume fraction further decreases and no longer transforms to martensite at temperatures below MS (Fig. 1.12 f).

Unlike lamellar microstructures, equiaxed microstructures are the result of a recrystallization process. Therefore, the alloy first has to be highly deformed in the α+β field to introduce enough cold work into the material. Upon subsequent solution heat treatment at temperatures in the two-phase field, a recrystallized and equiaxed microstructure is generated (Fig. 1.13 a). Extended annealing coarsens the equiaxed microstructure (Fig. 1.13 b). The solution heat treatment temperature itself determines the volume fraction of the primary α. Solution heat treatment just below the β-transus temperature results in bimodal microstructures that consist partly of equiaxed (primary) α in a lamellar α+β matrix (Fig. 1.13 c, d). Bimod-
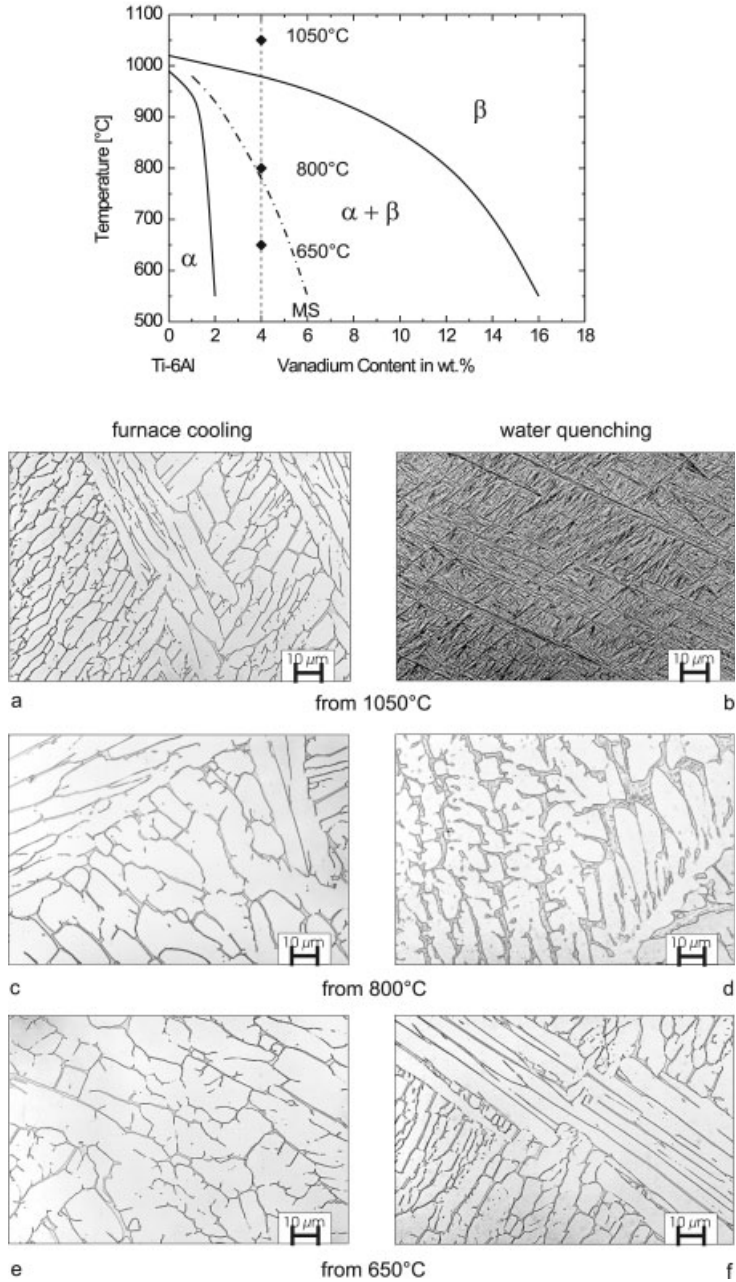
Fig. 1.12 Schematic ternary phase diagram Ti-6Al-V (MS: martensite start temperature); microstructure of Ti-6Al-4V after slow cooling (50 °C/h) and water quenching from 1050 °C, 800 °C, and 650 °C.
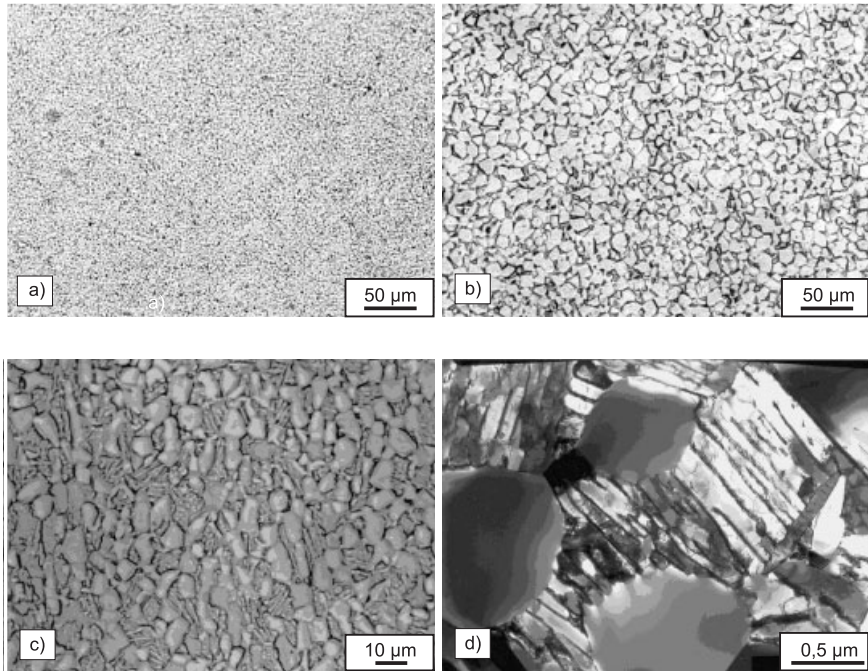
Fig. 1.13 Equiaxed microstructures of Ti-6Al-4V via recrystallization: a) fine equiaxed; b) coarse equiaxed; c, d) bimodal (OM, TEM).

al microstructures can be considered to be a combination of lamellar and equiaxed microstructure.

The various microstructures have a strong influence on the mechanical behavior of the titanium alloys. Fine-scale microstructures increase the strength as well as the ductility. Furthermore, they retard crack nucleation and are a prerequisite for superplastic deformation. Coarse microstructures, on the other hand, are more resistant to creep and fatigue crack growth. Equiaxed microstructures often have high ductility as well as fatigue strength and are preferred for superplastic deformation, while lamellar structures have high fracture toughness and show superior resistance to creep and fatigue crack growth. Since bimodal microstructures combine the advantages of lamellar and equiaxed structures, they exhibit a well-balanced property profile.

1.6
Property Profiles of the Titanium Alloy Classes

This section will briefly characterize and categorize the properties of the different titanium alloy classes. How one can directly influence some important properties of titanium alloys is outlined by example at the end of Chapter 1. Furthermore, there are other chapters in the book that will provide more depth on this subject.

Tab. 1.4 Properties of α, α+β and β Ti alloys.

	α	α+β	β
Density	+	+	−
Strength	−	+	++
Ductility	−/+	+	+/−
Fracture toughness	+	−/+	+/−
Creep strength	+	+/−	−
Corrosion behavior	++	+	+/−
Oxidation behavior	++	+/−	−
Weldability	+	+/−	−
Cold formability	− −	−	−/+

The properties of titanium alloys are primarily determined by the arrangement, volume fraction, and individual properties of the two phases α and β. Compared with the body-centered cubic β, the hexagonal α is more densely packed and has an anisotropic crystal structure. Compared with β, α is characterized by the following properties:

- higher resistance to plastic deformation
- reduced ductility
- anisotropic mechanical and physical properties
- a diffusion rate which is at least two orders of magnitude lower
- higher creep resistance.

In Tab. 1.4, the essential differences between the three alloy classes – α, α+β and β – are outlined on the basis of physical, mechanical, and technological properties.

Since the most important α-stabilizing element, aluminum, has only half the specific weight of titanium, α alloys have a lower *density* than β alloys, even more so since the latter are often extensively alloyed with heavy elements such as Mo or V.

Usually α alloys, which are single phase, show only moderate *strength*. However, the two-phase α+β alloys and the metastable β alloys can be hardened to high and very high strength levels respectively.

The very high strength levels of the metastable β alloys have to be paid for with a low *ductility*. If not age-hardened, they show relatively good ductility similar to that of α and α+β alloys. Moreover, the ductility is strongly related to the microstructure.

Since the *fracture toughness* of titanium alloys is strongly dependent on the microstructure and the aging condition, there is no firm correlation between the different alloy classes. In particular, coarse and lamellar microstructures show higher fracture toughness values than fine and equiaxed ones. The high toughness of lamellar microstructures can be explained by the ability of this structure to deflect propagating cracks along differently oriented lamella packets. This causes a rough crack front profile that consumes extra energy for crack propagation.

The relatively limited ability for atoms to diffuse and crystals to deform in hexagonal lattices are the major reason for the superior *creep* behavior of α. With increasing

volume fraction of β the creep behavior of Ti-alloys deteriorates. High creep resistance is also observed for two-phase microstructures with a discontinuous distribution of β. This is mostly the case for lamellar and partly also for bimodal structures.

The high affinity of titanium for oxygen means that even in air at room temperature a very thin, dense oxide layer (TiO_2) forms on the metal surface, and is the reason for the excellent *corrosion* behavior of titanium alloys. Among the alloy classes, α is more stable than β.

The maximum operating temperature of titanium alloys is not primarily limited by insufficient strength, but by their relatively poor *oxidation* behavior. Here, β is more susceptible than α. The oxidation behavior of titanium alloys and titanium aluminides is described in more detail in Chapter 7.

High reactivity with oxygen and hydrogen from the ambient environment – a drawback for titanium alloys – can cause the alloy to embrittle. Therefore, *welding* of titanium alloys has to be performed either in vacuum or an inert gas atmosphere. α and α+β alloys are easier to weld than β alloys, particularly when the latter are aged to high strength levels.

The more limited deformation capability and the stronger work hardening ability of the α phase implies that α and α+β alloys can only be *deformed* at high temperatures. The deformation temperature decreases with increasing β volume fraction; some metastable β alloys can even be deformed at room temperature. Superplastic deformation requires a fine equiaxed microstructure embedded in a continuous β phase (see Chapters 8 and 10).

1.7
The Alloying Elements of Titanium

The properties of titanium alloys are essentially determined by two factors: the chemical composition and the microstructure.

The chemical composition of the titanium alloys primarily determines the properties and volume fraction of the phases, α and β. Due to the limited deformation capability of hexagonal dense packed crystal structures, α is less ductile compared with the body-centered cubic β. As already described in paragraph 1.2.4, the diffusion coefficient of α is more than two orders of magnitude lower than that of β. Therefore, the resistance to creep and oxidation increases with increasing aluminum content, while simultaneously the ductility and the deformation capability deteriorate. Therefore, care had to be taken when new alloys were developed so as to not exceed 9 wt. % of the so-called aluminum-equivalent

$$Al\ eq. = wt.\ \%Al + 1/3\ wt.\ \%Sn + 1/6\ wt.\ \%Zr + 10\ wt.\ \%O < 9\ wt.\ \%$$

for otherwise the alloy-embrittling intermetallic compound Ti_3Al precipitated. For this reason the aluminum content of conventional titanium alloys was limited to a maximum of 6 wt. % for a long time. Today, however, this borderline is intentionally crossed, as demonstrated by the large activities on titanium aluminides. Scientists and engineers have learned to take advantage of the extraordinary prop-

erties of intermetallic compounds on the basis of Ti_3Al (α_2) and, in particular, of TiAl (γ) as outlined in more detail in Chapters 4 and 14.

Si, Sn, Zr, and interstitial oxygen strengthen α. Si atoms tend to segregate to dislocations and thus effectively prevent dislocation climb, which improves creep behavior. Zr tends to homogenize fine silicide precipitates. Mo, V, and Nb are moderate solid solution strengtheners of β. In metastable β alloys the β phase can be effectively strengthened by fine omega precipitates (see Chapter 2). Unfortunately, these high strength levels are usually accompanied by falls in ductility. Nb is known to improve the oxidation behavior of titanium alloys, while small additions of Pd substantially improve their corrosion resistance.

1.8
The Conventional Titanium Alloys

Today more than 100 titanium alloys are known, of which, however, only 20 to 30 have reached commercial status. Of these, the classic alloy Ti-6Al-4V covers more than 50% of usage. Another 20 to 30% are unalloyed titanium. Categorized by alloy classes, Tab. 1.5 lists currently used titanium alloys and their most important mechanical properties. The chemical composition, frequently used short or trade names, the β-transus temperature, the developing company, and the year of introduction of the individual alloys are also noted. Not listed are alloys of the CIS states, since their usage in western countries is still limited.

1.8.1
α Alloys

α alloys are primarily used in the chemical and process engineering industry. Here excellent corrosion behavior and deformability are of prime concern while high (specific) strength only ranks second. The various commercially pure (cp) titanium grades differ primarily in oxygen content. As an interstitial alloying element, oxygen drastically increases strength with a simultaneous reduction in ductility. To reach the required strength levels of cp titanium grades, only oxygen is intentionally alloyed; while elements like carbon and iron are considered impurities brought into the alloy via the manufacturing process.

The four cp titanium Grades 1 to 4 (Tab. 1.5) cover a room temperature tensile strength level of 240 to 740 MPa. Of these, Grade 1 has the lowest strength level and excellent cold formability. Therefore, it is used for deep drawing applications, as cladding alloy for steel reactors, as well as sheet metal for explosive claddings – generally speaking for parts which require excellent corrosion resistance but only low strength. Grade 2, with tensile strength levels between 390 and 540 MPa, is the most popular cp titanium grade. Higher strength Grade 3 is nearly exclusively used for pressure vessel applications. This still moderately cold-formable higher strength grade allows for designs with reduced wall thickness and is therefore used where weight is a concern. Grade 4 has the highest strength of up to

Tab. 1.5 Mechanical properties of selected titanium alloys.

Alloy	Chemical Composition [wt. %]	T_β [°C]	Developer	Year	Hardness [HV]	E [GPa]	YS [MPa]	TS [MPa]	%El	K_{Ic} [MPa m$^{1/2}$]
α Titanium Alloys										
high purity Ti	99.98 Ti	882			100	100–145	140	235	50	
Grade 1	(cp-Ti: 0.2Fe, 0.18O)	890	miscellaneous		120		170–310	>240	24	
Grade 4	(cp-Ti: 0.5Fe-0.40O)	950	miscellaneous		260	100–120	480–655	>550	15	
Grade 6	(Ti-5Al-2.5Sn)	1040	miscellaneous	1953	300	109	827	861	15	70
Near-α Titanium Alloys										
Ti-6-2-4-2-S	Ti-6Al-2Sn-4Zr-2Mo-0.1Si	995	RMI, USA	1970	340	114	990	1010	13	70
TIMETAL 1100	Ti-6Al-2.7Sn-4Zr-0.4Mo-0.4Si	1010	Timet, USA	1988		112	900–950	1010–1050	10–16	60–75
TIMETAL 685	Ti-6Al-5Zr-0.5Mo-0.25Si	1020	IMI, UK	1969		120	850–910	990–1020	6–11	68
TIMETAL 834	Ti-5.8Al-4Sn-3.5Zr-0.5Mo-0.7Nb-0.35Si-0.06C	1045	IMI, UK	1984	350	120	910	1030	6–12	45
α+β Titanium Alloys										
Ti-6-4	Ti-6Al-4V	995	miscellaneous	1954	300–400	110–140	800–1100	900–1200	13–16	33–110
Ti-6-6-2	Ti-6Al-6V-2Sn	945	miscellaneous		300–400	110–117	950–1050	1000–1100	10–19	30–70
Ti-6-2-2-2	Ti-6Al-2Sn-2Zr-2Mo-2Cr-0.25Si					110–120	1000–1200	1100–1300	8–15	65–110
Ti-6-2-4-6	Ti-6Al-2Sn-4Zr-6Mo	940	Pratt & Whitney, USA		330–400	114	1000–1100	1100–1200	13–16	30–60
Ti-17	Ti-5Al-2Sn-2Zr-4Mo-4Cr	890	GE, USA	1968	400	112	1050	1100–1250	8–15	30–80

Tab. 1.5 (continued)

Alloy	Chemical Composition [wt. %]	T_β [°C]	Developer	Year	Hardness [HV]	E [GPa]	YS [MPa]	TS [MPa]	%El	K_{Ic} [MPa m$^{1/2}$]
Metastable β Titanium Alloys										
SP 700	Ti-4.5Al-3V-2Mo-2Fe	900	NKK, J	1989	300–500	110	900	960	8–20	60–90
Beta III	Ti-11.5Mo-6Zr-4.5Sn	760	Colt/Crucible, USA	1960	250–450	83–103	800–1200	900–1300	8–20	50–100
Beta C	Ti-3Al-8V-6Cr-4Mo-4Zr	795	RMI, USA	1969	300–450	86–115	800–1200	900–1300	6–16	50–90
Ti-10-2-3	Ti-10V-2Fe-3Al	800	Timet, USA	1976	300–470	110	1000–1200	1000–1400	6–16	30–100
Ti-15-3	Ti-15V-3Cr-3Al-3Sn	760	Timet, USA	1981	300–450	80–100	800–1000	800–1100	10–20	40–100

740 MPa and is preferentially used for mountings and fittings. However, complex parts have to be shaped at temperatures around 300 °C.

For the highest corrosion protection requirements, the Pd-containing alloy Grade 7 was developed. However, due to its high price the nearly equivalent alloy Grade 12 is often preferred. If higher strength levels are required, Ti-5Al-2.5Sn is a good choice. As one of the oldest titanium alloys, it gained acceptance decades ago for low-temperature applications as a material for hydrogen tanks and pressure vessels. Like the other α alloys, Ti-5Al-2.5Sn cannot be age hardened and is thus easy to weld.

1.8.2
Near-α Alloys

Near-α titanium alloys are the classic high-temperature alloys. This alloy class is ideal for high temperatures since it combines the excellent creep behavior of α alloys with the high strength of α+β alloys. Today their upper operating temperature is limited to about 500 to 550 °C.

Ti-8-1-1 was the first titanium alloy particularly developed for high temperatures. The high Al content led, however, to stress corrosion problems; therefore, all conventional titanium alloys in use today are limited in aluminum content to a maximum of 6%. The follow-up alloy, Ti-6-2-4-2, developed by Timet, also has this lower Al content. In the 1970s investigations by RMI were of central importance to the further success of elevated temperature titanium alloys: research discovered that small additions of only up to 0.1 wt. % Si would substantially improve the creep behavior of Ti-6-2-4-2. The alloy was named Ti-6-2-4-2-S. It was argued that Si would precipitate at high temperatures on dislocations, thus effectively hindering their climb and likewise deformation. Since then all new high temperature titanium alloys have been alloyed with up to 0.5% of Si.

The first commercial Si-containing titanium alloy was developed by IMI in the United Kingdom: IMI 679. The follow-up alloy, IMI 685, was the first alloy to be used in the β-annealed condition due to the superior creep performance of this microstructure. One of the most advanced conventional high temperature titanium alloys today is the American TIMETAL 834, originally developed in the UK. Its maximum service temperature is aimed close to 600 °C, assuming sufficient long-term stability and oxidation protection can be provided.

1.8.3
α+β Alloys

Among the α+β alloys, Ti-6Al-4V is by far the most popular titanium alloy. More than 50% of all alloys in use today are of this composition. The alloy was developed in the early 1950s in the United States at the Illinois Institute of Technology and is therefore one of the very first titanium alloys to be made. There are two reasons for the success of Ti-6Al-4V. First, the good balance of its properties, as can be seen from Tabs 1.4 and 1.5. Second, it is the by far the most intensively developed and tested titanium alloy, which is a major advantage – especially in the aerospace industry, the largest user of Ti-6Al-4V.

Other α+β alloys like Ti-6-6-2 and IMI 550 were primarily developed for high strength. High strength and high toughness is realized with Ti-6-2-4-6. Alloys Ti-6-2-2-2-2, Ti-55-24-S or Ti-17 were primarily developed for elevated temperature applications in gas turbine engines up to about 400 °C.

1.8.4
Metastable β Alloys

Over the last few decades the importance of metastable β alloys has steadily increased. These alloys can be hardened to extremely high strength levels of more than 1400 MPa. The complex microstructure enables the designer to optimize for both high strength and high toughness. This is true for TIMETAL 10-2-3 and Beta C. Other β alloys like TIMETAL 15-3 can be deformed at room temperature down to thin foils. In particular, TIMETAL 21S was specially developed as an oxidation resistant foil alloy to be used as the matrix for long fiber reinforced titanium alloys. TIMETAL LCB is a price-sensitive β alloy (LCB=low-cost beta) particularly aimed at applications beyond the aerospace sector, e.g. for the automotive industry (see Chapter 18). Beta-CEZ was developed in France for application at moderate temperatures in gas turbine engines. Due to its very fine grained bimodal microstructure, the Japanese alloy SP 700 features excellent superplastic behavior even at temperatures as low as 700 °C. Wide spread application of β alloys is, however, limited by its relatively high specific weight, modest weldability, poor oxidation behavior, and complex microstructure. Chapter 2 particularly addresses β alloys.

1.9
Textures in Titanium Alloys

Unlike aluminum and steel alloys, titanium alloys can have a pronounced anisotropy of properties, which can be directly related to the inherent anisotropy of the hexagonal crystal structure of α. These crystallographic textures develop upon deformation (deformation texture) and can be further pronounced by a subsequent recrystallization annealing (recrystallization texture). Generally basal and transverse textures are distinguishable. Essentially, they describe the orientation of the (0002) planes of the hexagonal α relative to the deformation plane and deformation direction. For the two basic texture types, the (0002) planes are either parallel or perpendicular to the deformation plane, as schematically outlined in Fig. 1.14.

Crystallographic textures generally depend on the degree, the mode, and the temperature of deformation as well as on the subsequent recrystallization annealing. Usually the intensity of the texture increases with increasing deformation degree. In Fig. 1.15 the influence of deformation mode and temperature is schematically shown on (0002) pole figures. Two basic deformation modes are considered: axial material flow, for example, with uniaxial rolling, and radial deformation as is the case in upset forging or multidirectional rolling. For the α+β alloy Ti-6Al-4V four temperature regions can be distinguished. At temperatures below 900 °C, where
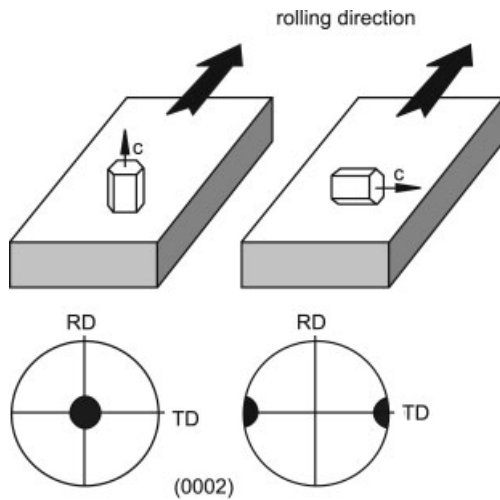
Fig. 1.14 Basal and transverse textures of titanium alloys (schematic, (0002) pole figures).
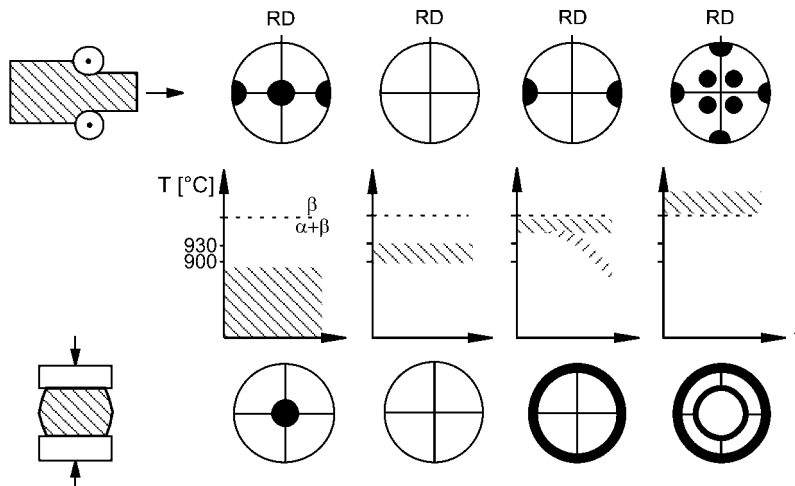
Fig. 1.15 Influence of deformation temperature and mode on texture of Ti-6Al-4V (schematic, (0002) pole figures).

the hcp is mainly present, primarily basal-type textures form. They may reveal an extra transverse part, when uniaxially deformed. At temperatures between 900 and 930 °C, almost no textures are observed independent of deformation mode. Here, a substantial volume fraction of the bcc β is present. It is worth mentioning that this temperature window is also preferentially used to achieve maximum deformation for superplastic forming. At deformation temperatures just below the transus temperature, the basal component of the texture disappears. Here the (0002) pole figures are just left with a transverse pole, which is radial after multidirectional deformation. Above the β-transus temperature a classic cube texture is observed.
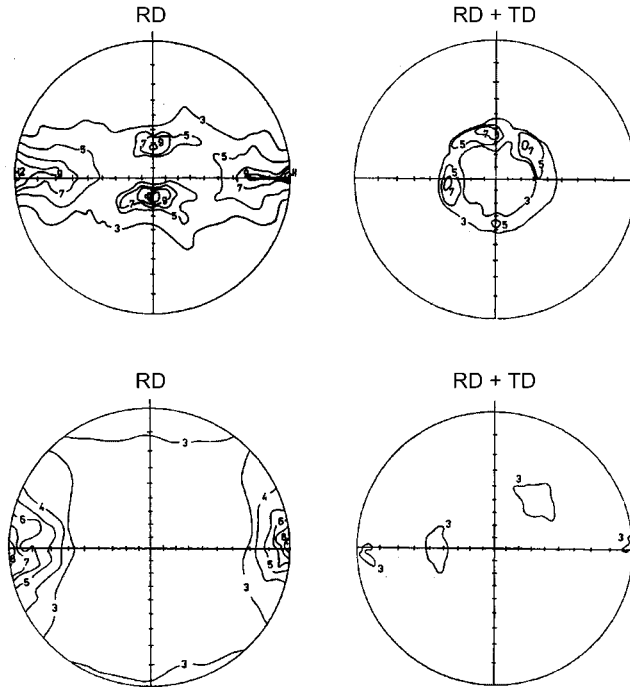
Fig. 1.16 (0002) pole figures of equiaxed Ti-6Al-4V for different defor-
mation modes and temperatures (schematic).

Since the crystallographic textures are principally determined by the mode of
deformation, the crystallographic textures of the equiaxed and bimodal microstruc-
tures can be varied independently of each other. This occurs primarily through
the subsequent recrystallization annealing temperature – sufficiently high defor-
mation degrees provided. As an example, Fig. 1.16 shows four (0002) pole figures
for the alloy Ti-6Al-4V that were generated by varying only the deformation tem-
perature and deformation mode. For all conditions the microstructures were
equiaxed. It is obvious that crystallographic textures may offer an extra opportu-
nity to purposely design the properties of titanium alloys.

1.10
Mechanical Properties of Titanium Alloys

To generally improve the properties of materials, and titanium alloys in particular,
there are essentially two ways to proceed: alloying and processing. Recently a third
option has gained importance: the production of composite materials (Fig. 1.17).

Alloying lays the basis for an increase in strength (e.g. solid-solution strengthen-
ing, age hardening), allows the generation of ordered structures (e.g. intermetallic

```
┌─────────────────┐        ┌─────────────────┐        ┌─────────────────┐
│    alloying     │◄─────► │   processing    │◄─────► │   composites    │
│   (chemistry)   │        │ (microstructure)│        │     (MMC)       │
└─────────────────┘        └─────────────────┘        └─────────────────┘
```

– density	– hardening	– density
– precipitation hardening	– thermo-mech. treatment	– stiffness
– solid solution hardening	– stress corrosion cracking	– strength
– ordered structure	– SPF (grain size)	– wear
– stiffness	– rapid solidification	– fatigue
– thermal expansion	– mechanical alloying	– thermal expansion
– corrosion behavior	– consolidation	– corrosion protection
– oxidation behavior	– HIP (PM, casting)	– oxidation protection

Fig. 1.17 Ways to modify the properties of titanium alloys.

compounds of titanium aluminides), determines most of the physical properties (e.g. density, elastic modulus, coefficient of thermal expansion), and largely controls the chemical resistance of the material (corrosion, oxidation).

Processing allows the careful balancing of the property profile of materials. Depending on the specific property profile required for the final application, different microstructures can be generated for titanium alloys by means of thermomechanical treatment to optimize for strength (solid solution strengthening, dispersion strengthening, grain boundary strengthening, texture hardening), ductility, toughness, superplasticity, stress corrosion, creep resistance, etc. The processing techniques of rapid solidification and mechanical alloying extend the spectrum of potential alloy compositions. Hot-isostatic pressing minimizes defects in cast or powder metallurgy based components.

The third option is beyond the limits of metallurgy alone. Here different materials are combined to create a *composite* with superior behavior. The properties of the new compound often follow a simple rule-of-mixtures of the individual component properties. In this case titanium alloys and aluminides are strengthened with particles or fibers to become metal-matrix composites (MMCs). Apart from the nature, volume fraction, and orientation of the strengthening component, and also the matrix material itself, the boundaries between matrix and reinforcement have a major influence on the mechanical behavior of the composite. In Chapter 12 one prospective composite – SiC long fiber reinforced titanium alloys – is described in more detail.

In the final part of this chapter some examples will be given to demonstrate how individual properties of titanium alloys can be selectively improved by either alloying, processing, or by use of composites. Although in each case only one single property aspect will be stressed, the authors are aware that the optimization of a real component always concerns many properties.

1.10.1
Strength

Of all metallic materials, only the highest strength steels have a higher specific strength than titanium alloys. The yield strength values of conventional titanium alloys range between about 800 and 1200 MPa, with metastable β alloys showing the highest values. For special applications – e.g. bolt or screw fasteners – the highest tensile and fatigue strengths are required. To increase the strength of titanium alloys, all three measures can be taken: alloying, processing and composites.

Alloying additions alone are not typically used to increase strength in Ti alloys. The β alloy TIMETAL 125 (Ti-6V-6Mo-6Fe-3Al) was, however, specially developed for high strength fastener applications. A double aging treatment leads to very fine precipitates in the β matrix. Compared to Ti-6Al-4V in Fig. 1.18, this alloy can be age hardened to exceptionally high yield and tensile strength levels of 1590 MPa and 1620 MPa, respectively, and still has an acceptable elongation to fracture of 6%.

Increased strength by processing is shown for the intermetallic Ti_3Al-base alloy "Super-Alpha-2" (Ti-25Al-10Nb-3V-1Mo (at. %)). In a specific thermomechanical treatment, i.e. via optimization of deformation, solution heat treatment and aging, it is possible to increase tensile strength from about 1100 MPa in the as-received condition to nearly 1800 MPa (Fig. 1.18). First the alloy was deformed by swaging at temperatures below 1000 °C, which transformed the as-received microstructure into a fine equiaxed microstructure with about 60% primary α_2 phase. Subsequent solution heat treatment close below the β-transus temperature followed by water quenching led to fine primary α_2 in a matrix of ordered cubic B2 phase. The very high strength was a result of the final aging treatment at 700 °C since very fine orthorhombic O phase precipitated from the strongly supersaturated B2 phase. The strength levels achieved are among the highest ever reported for conventionally processed titanium alloys.

These ultra-high strength values are only outperformed by titanium matrix composites. As an example, SiC fiber-reinforced Ti-6Al-4V with a fiber volume fraction of 35% can easily reveal tensile strength values beyond 2000 MPa along the fiber direction (Fig. 1.18). In the transverse direction, values are presently below the matrix strength level, due to weak bonding between fiber and matrix. For the introduction of these composites in a high performance component it is therefore essential that the design guarantees a more or less uniaxial loading. From Fig. 1.18 it is, however, also obvious that a strength increase – either by alloying, processing or via composites, is nearly always accompanied by a decrease in ductility. More details on long fiber-reinforced composites are given in Chapter 12.

1.10.2
Stiffness

The Young's modulus represents a measure for the stiffness of a material. Its value is directly related to the atomic bonding in the crystal lattice and thus increases with its degree of ordering. On alloying with aluminum, the elastic modu-
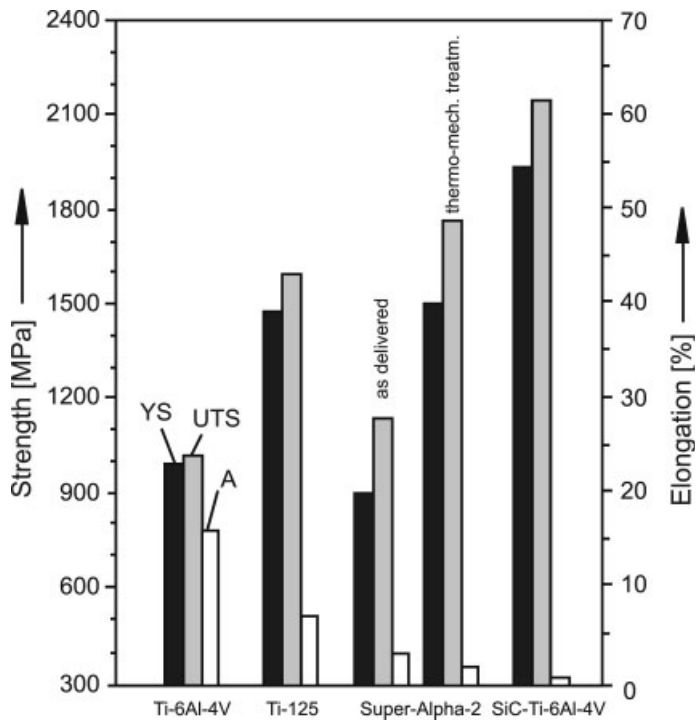
Fig. 1.18 Strength increase of titanium alloys by alloying (TIMETAL 125), thermomechanical treatment (Super-Alpha-2) and fiber reinforcement (SiC-Ti-6Al-4V) compared to Ti-6Al-4V.

lus strongly increases as a result of the accompanying changes in crystal structure, as shown in Fig. 1.19. The alloy composed of the two solid solution phases α and β, Ti-6Al-4V, has the lowest modulus. As one of the two phases becomes ordered stiffness increases, as in the Ti_3Al phase of the $\alpha_2+\beta$ alloy Ti-25Al-10Nb-3V-1Mo. The highest Young's moduli are measured for the TiAl alloy Ti-48Al-2Cr-2Nb, where the two main phases, α_2 and γ are both ordered intermetallics.

Processing can also influence the stiffness of titanium alloys. Because of the pronounced anisotropic character of the hexagonal crystal structure of α, the elastic modulus of strongly textured structures can substantially vary with load direction. Fig. 1.20 depicts how a transverse texture produced in Ti-6Al-4V by careful choice of deformation parameters can exhibit quite an anisotropy in stiffness for an otherwise homogenous microstructure. In the transverse direction, i.e. parallel to the c-axis of the hexagonal crystal structure of α, the Young's modulus is higher than in the rolling direction. Usually a pronounced anisotropy of properties is not desired. However, it is imaginable that the texture can be deliberately used as a stiffness-increasing measure, similar to directionally solidified or single crystal Ni-base superalloys. For these alloys, designers have learned to live with and benefit from anisotropic properties.
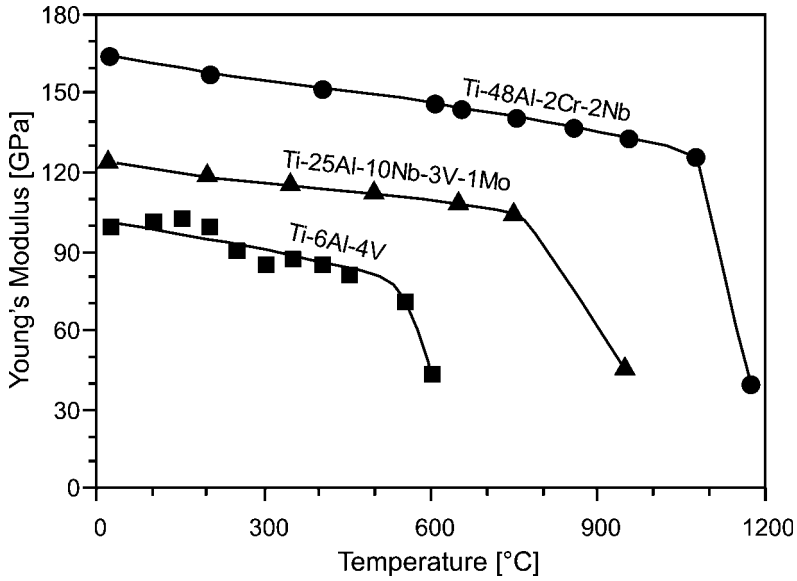
Fig. 1.19 Influence of temperature on the elastic modulus of α+β, α$_2$+B2/O and α$_2$ alloys.
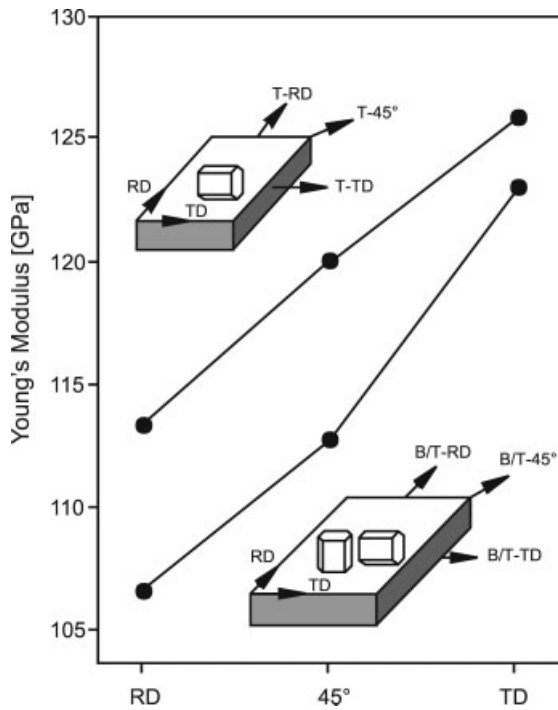
Fig. 1.20 Influence of texture on the Young's modulus of Ti-6Al-4V.

Increased stiffness is a prime aim in the development of particle-reinforced titanium composites. SiC, B_4C, TiB_2, BN, and TiC particles are the strengthening components usually incorporated into the material by powder-metallurgical processing. The XD process (**ex**othermic **d**ispersion) represents an exception. Here the strengthening component is incorporated into the titanium matrix by precipitation from the liquid melt.

The stiffness increase of long-fiber reinforced titanium alloys usually follows the rule-of-mixtures. Since the elastic modulus of SiC fibers is more than three times higher than that of the titanium alloy matrix, a fiber volume fraction of only 30–35% doubles the stiffness of the composite compared to the non-reinforced titanium matrix.

1.10.3
Elevated Temperature Strength

By far most research and development activity on titanium alloys is directed towards increased elevated temperature capability. Essentially three different methods have been adopted: further development of the conventional near-α alloys, development of dispersion strengthened titanium alloys, and development of titanium aluminide alloys based on the intermetallic compounds Ti_3Al and TiAl.

For improvement of high temperature behavior of conventional titanium alloys, investigations by Seagle, Hall, and Bomberger in the 1970s were of major importance. They showed that the addition of only 0.1% Si would substantially improve the creep behavior of the alloy Ti-6-2-4-2 (Fig. 1.21). One possible explanation is that at high temperatures Si precipitates as silicides on dislocations, thus hindering dislocation climb, a key deformation mechanism for creep. Although not finally clarified, the positive influence of silicon on the creep behavior is unquestioned.
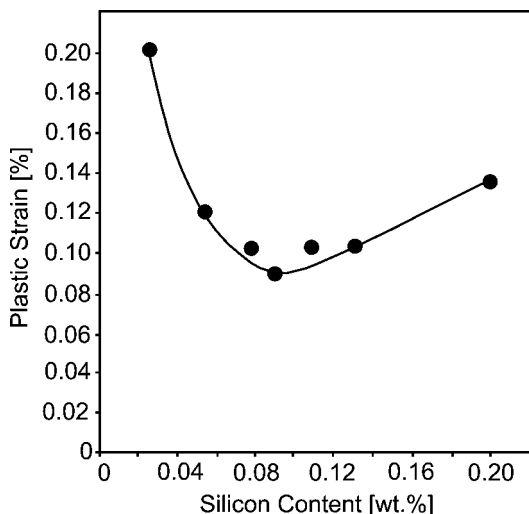
Fig. 1.21 Influence of Si on the creep behavior of Ti-6242 (S. Seagle, J.A. Hall, and H. Bomberger).
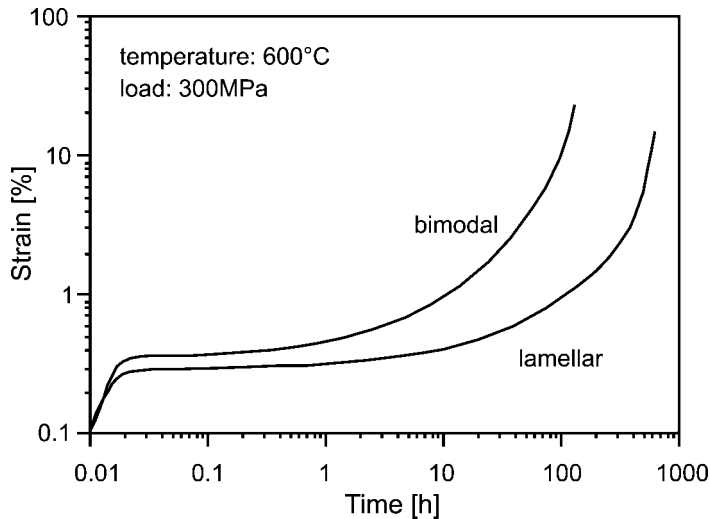
Fig. 1.22 Influence of microstructures on creep of TIMETAL 1100.

Yet not only silicon determines the mechanical behavior of the elevated temperature near-α titanium alloys, the microstructure also has a strong influence. Here the size and arrangement of the hexagonal α and the body-centered cubic β are of prime importance. Lamellar microstructures, originating from cooling out of the β phase field, and equiaxed microstructures, as a result of a recrystallization process, can either individually have a fine or coarse distribution or can both be present in a bimodal microstructure. Compared with equiaxed microstructures, lamellar structures usually show superior creep behavior due to their coarser structure meaning a lower volume fraction of phase boundaries (as shown in Fig. 1.22). On the other hand, equiaxed and bimodal microstructures show superior fatigue properties due to their fine microstructures. Therefore, for primarily creep limited titanium components used in the compressor of gas turbine engines lamellar microstructures (e.g. TIMETAL 685 or 829) are used, whereas bimodal microstructures (e.g. TIMETAL 834) are chosen for primarily low-cycle fatigue limited parts. Selection depends on the area of application and on the design philosophy of the engine manufacturer (Fig. 1.23).

Another way to improve creep properties makes use of rapid solidification processing. Upon fast quenching very finely distributed, high temperature stable dispersoids based on metalloids or rare-earth metals (Er_2O_3, TiB, Y_2O_3) are incorporated into the titanium alloy. However, high solidification rates are required to yield the effective homogeneous distribution and nanometer-size of dispersoids (Fig. 1.24). Like in other dispersion-strengthened materials, the coarsening of the dispersoids plays a major role since increasing particle size and simultaneously decreasing particle distance reduce the effectiveness of high temperature strengthening.

bimodal

lamellar

Fig. 1.23 Typical microstructure of elevated temperature titanium alloys: bimodal (TIMETAL 834) and lamellar (TIMETAL 1100).

Fig. 1.24 Dispersion strengthened rapid solidified Ti-25V-2Er-0.02B.

While rapid solidification techniques only play a minor role in increasing the operating temperatures of titanium alloys, by far the most activities are concentrated on the development of titanium aluminides. These materials based on the intermetallic compounds Ti_3Al (α_2) and TiAl (γ) have the potential to raise the application temperature of titanium-based alloys to about 650 °C and 800 °C, respectively. Their excellent creep behavior is due to their ordered structure, which is, unfortunately, also the cause for aluminides to be quite brittle and accordingly hard to deform. Alloying with β-stabilizing elements like Nb, V, or Mo has been effective at increasing the ductility of Ti_3Al-base alloys. γ aluminides, which are even less ductile, are alloyed with Cr, Nb, V, or Mn for similar reasons, however to a lesser extent. Slightly substoichiometric they show a two-phase $\alpha_2+\gamma$ microstructure. Since Ti_3Al alloys have only moderate long-term stability they presently play only a minor role while today the main focus of research and development on titanium aluminides is directed to TiAl-base alloys (see Chapters 2, 3, and 14).

1.10.4
Damage Tolerance and Fatigue

In the aerospace industry fail-safe design following damage tolerance criteria plays a major role, since only the knowledge of the interconnection between damage and critical material condition allows assessment of the lifetime of a component. The damage tolerance of a material describes its behavior in the presence of loads and defects such as cracks. It is characterized as fracture toughness. Since in titanium alloys fracture toughness values only reach about half those for steels, an increase is more than desirable. The influence of alloying elements on fracture toughness is relatively small. Normally the metastable β alloys are superior to α+β alloys. However, processing, i.e. microstructural modification, has a larger influence on fracture toughness. Here lamellar microstructures demonstrate higher values than equiaxed structures, as shown for Ti-6Al-4V by J-integral measurements on two extreme microstructural conditions, coarse lamellar and fine equiaxed (Fig. 1.25).

The fatigue behavior of a material is characterized under cyclic loading conditions. The accumulation of damage is usually subdivided into fatigue crack initiation and fatigue crack propagation phases. The behavior of a titanium alloy is influenced by a number of parameters including alloy chemistry, microstructure, environment, test temperature, as well as loading conditions like load amplitude, load frequency, load sequence, or mean stress.

As a first order approximation, a cyclic fatigue test can serve as a measure for fatigue crack initiation. Smooth specimens are cycled until fracture at constant stress amplitude and mean stress. The results are documented in terms of Wöhler diagrams. The quotient of static yield strength and fatigue strength can be considered a rough estimate for fatigue crack initiation. Generally, the resistance to
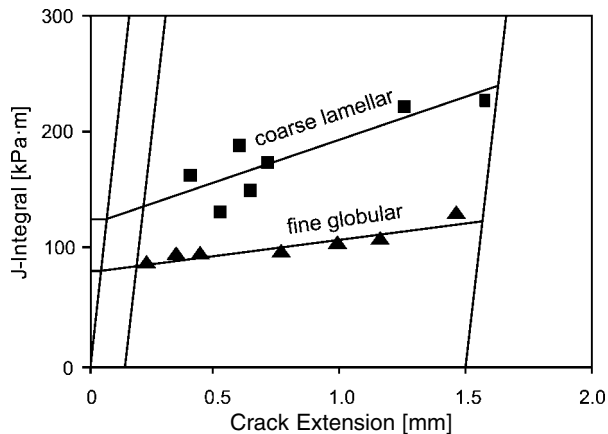
Fig. 1.25 Influence of microstructures on fracture toughness of Ti-6Al-4V (J-integral measurements).
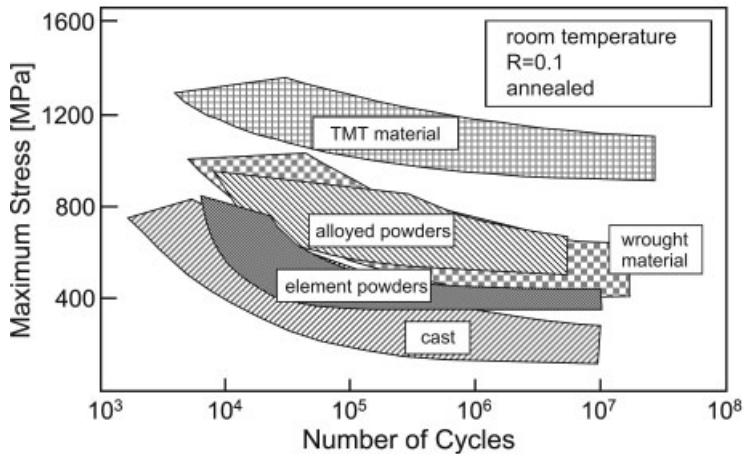
Fig. 1.26 High-cycle fatigue of Ti-6Al-4V at room temperature for different alloy conditions.

fatigue crack initiation for titanium alloys decreases with coarsening of the microstructure, i.e. fine equiaxed microstructures have higher fatigue strength than coarse lamellar microstructures. Fig. 1.26 shows Wöhler diagrams of differently processed Ti-6Al-4V specimens. The highest fatigue strength values are measured in very fine equiaxed microstructures produced by thermomechanical treatment, while the coarse cast lamellar structures show the lowest values (see Chapter 5).

The second stage of fatigue damage, after crack initiation and before final fracture, is the growth of fatigue cracks. This is normally investigated on pre-cracked compact tension specimens, and the fatigue crack growth rate (da/dN) is plotted versus the amplitude of the stress intensity at the crack tip (ΔK). As shown in Fig. 1.27, da/dN-ΔK-curves are substantially influenced by the microstructure. For constant amplitude and R-ratio (minimum to maximum load) the lamellar microstructure of Ti-6Al-4V shows a more favorable fatigue crack growth behavior than the equiaxed structure. A look at the fracture surfaces points out substantial differences between the two microstructures with regard to roughness, fractured area per mm crack growth, and local crack plane orientation relative to the loading direction – observations that are able to explain the influence of microstructure on the fatigue crack growth behavior (see also Chapter 5).

It is generally experienced that in microstructures with inherently high resistance to fatigue crack initiation the cracks tend to propagate faster, and vice versa. Obviously these two properties cannot easily be optimized at the same time – similar to the balance between strength and ductility.
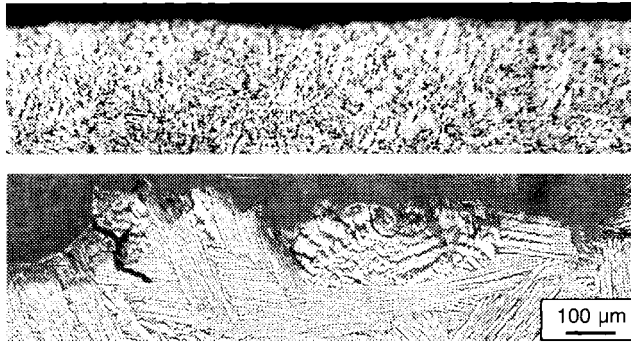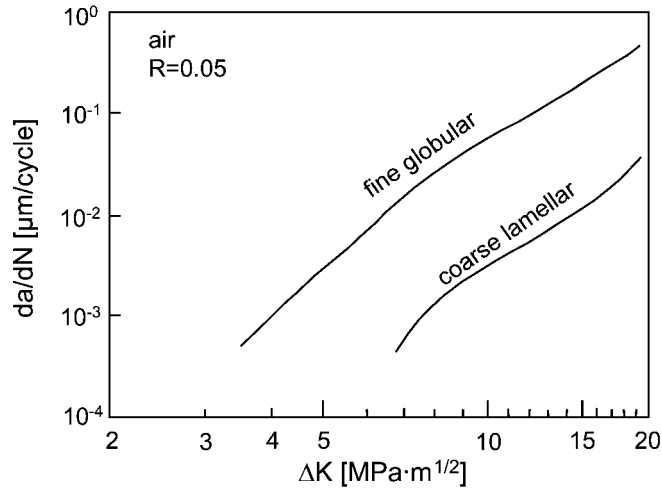
Fig. 1.27 Fatigue crack growth behavior of two extreme microstructures of Ti-6Al-4V and respective fracture contours of fine equiaxed and coarse lamellar microstructures.

1.11
Referenced Literature and Further Reading

1 S. ABKOWITZ (ed.): The Emergence of the Titanium Industry and the Development of the Ti-6Al-4V Alloy, TMS, Warrendale, PA, USA (2000)

2 J. ALBRECHT, G. LÜTJERING, Microstructure and Mechanical Properties of Titanium Alloys, in: Titanium '99, Science and Technology, Vol. I, 363–374, CRISM, "Prometey", St. Petersburg, Russia (2000)

3 P. J. BANIA, A. J. HUNT, R. E. ADAMS, Ultra High Strength Titanium Alloy for Fasteners, in: Titanium '92: Science and Technology, 2899–2906, TMS, Warrendale, PA, USA (1993)

4 T. R. BIELER, M. G. GLAVICIC, S. L. SEMIATIN, Using OIM to Investigate the Microstructural Evolution of Ti-6Al-4V, JOM, 54, (2002) 31–36

5 R. R. BOYER, Titanium for Aerospace: Rationale and Applications, Advanced Performance Materials **2** (1995) 349–368

6 R. R. BOYER, G. WELSCH, E. W. COLLINGS (eds.): Materials Properties Handbook: Titanium Alloys, ASM International, Metals Park, OH (1994)

7 R. R. BOYER, D. EYLON, G. LÜTJERING (eds.): Fatigue Behavior of Titanium Alloys, TMS, Warrendale, Pa, USA (1999)

8 L. CHRISTODOULOU, J. M. BRUPBACHER, Metal Matrix Composites – XD^{TM} Materials for Aerospace Applications, Materials Edge, Nov. 1990, 29–33

9 J. M. DONACHIE: Titanium, A Technical Guide, ASM International, Metals Park, OH (1988)

10 H. M. FLOWER, Microstructural development in relation to hot working of titanium alloys, Materials Science and Technology, 6 (1990) 1082–1092

11 K. GREGORY, Fatigue Crack Propagation in Titanium Alloys, in: Handbook of Fatigue Crack Propagation in Metallic Structures, A. Carpinteri (eds.), Vol. I, S. 281–322, Elsevier Science B.V. (1994)

12 M. HANSEN: Constitution of Binary Alloys, McGraw-Hill, New York, Toronto, London (1958)

13 HEMKER, D. M. DIMIDUK, (eds.): Structural Intermetallics, TMS, Warrendale, PA, USA (2001)

14 Y.-W. KIM, D. M. DIMIDUK, M. H. LORETTO (eds.): Gamma Titanium Aluminides, TMS, Warrendale, PA, USA (1999)

15 H. A. LIPSITT, Titanium Aluminides – An Overview, in: High-Temperature Ordered Intermetallic Alloys, 351–364, MRS, Pittsburgh, PA, USA (1985)

16 G. LÜTJERING (ed.): Proc. 10th World Conference on Titanium, Hamburg, Germany, 2003, Wiley-VCH, Weinheim, Germany (2004)

17 G. LÜTJERING, J. ALBRECHT, A. GYSLER, Mechanical Properties of Titanium Alloys, in: Titanium '92: Science and Technology, 1635–1646, TMS, Warrendale, PA, USA, (1993)

18 G. LÜTJERING, A. GYSLER, L. WAGNER, Crack Propagation in Ti-Alloys, in: 6th World Conf. on Titanium, 71-80, Les Editions de Physique, Les Ulis Cedex, France, 1989

19 G. LÜTJERING, J. C. WILLIAMS: Titanium Alloys, Springer (2003)

21 G. MARCI, Comparison of Fatigue Crack Propagation Threshold of two Ti-Turbine-Disk Materials, Int. Journal of Fatigue, Vol. 16 (1994), S. 409–412

22 M. PETERS, G. LÜTJERING, G. ZIEGLER, Control of Microstructures of α+β Titanium Alloys, Zeitschrift für Metallkunde **74** (1983) 274–282

23 M. PETERS, K. WELPMANN, H. DÖKER, Fatigue Crack Growth Behaviour of Two Extreme Microstructures of Ti-6Al-4V, in: Titanium Science and Technology, G. LÜTJERING, U. ZWICKER, W. BUNK (eds.), S. 2267–2274, DGM, Oberursel (1985)

24 M. PETERS, P.-J. WINKLER, Leichtmetalle in der Luft- und Raumfahrt: I. Stand der Werkstoffentwicklung, METALL **46** (1992) 1226–1234

25 M. PETERS, H. BUHL, Titanium Alloys, in: Advanced Aerospace Materials, Springer, 58-72, Berlin/Heidelberg/New York/London/Paris/Tokyo/Hong Kong (1992)

26 M. PETERS, W.A. KAYSSER, Composites – New Developments and Applications, in: PTM '93, 727–738, DGM, Oberursel (1993)

27 M. PETERS, C. LEYENS, W.A. KAYSSER (eds.): IMI 834 und TIMETAL 1100, 1–76, DLR, Köln (1994)

28 I. J. POLMEAR: Light Alloys, Metallurgy of the Light Metals, Butterworth-Heinemann, Oxford, UK (1995)

29 S. R. SEAGLE, G. S. HALL, H. B. BOMBERGER, High Temperature Properties of Ti-6Al-2Sn-4Zr-2Mo-0.09Si, Metals Engineering Quarterly, February 1975, pp. 48–54

30 G. TERLINDE, Beta Titanium Alloys, in: Titanium '95: Science and Technology, Vol. III, pp. 2177–2194, The Institute of Materials, London (1996)

31 U. ZWICKER: Titan und Titanlegierungen, Springer, Berlin/Heidelberg/New York (1974)

2
Beta Titanium Alloys
G. Terlinde and G. Fischer, *OTTO FUCHS Metallwerke, Meinerzhagen, Germany*

2.1
Introduction

Beta titanium alloys are the most versatile class of titanium alloys. They offer the highest strength to weight ratios and very attractive combinations of strength, toughness, and fatigue resistance at large cross sections. Some of the disadvantages compared to α+β alloys are increased density, a rather small processing window, and higher cost (Tab. 2.1). The development and use of beta alloys since the 1950's has been well described in the literature [1, 2], the alloys are summarized in Tab. 2.2 [1].

In the past Ti-13V-11Cr-3Al had been applied to a larger extent (SR-71 Project). Currently five alloys are mainly used: Ti-10-2-3, Beta C, Ti-15-3, TIMETAL 21S, and BT 22 [3] for structural components, and Ti 17 for gas turbine engine compressor discs. Among these alloys, Ti-10-2-3 offers, when properly processed, the best combinations of strength, toughness, and high cycle fatigue strength of any

Tab. 2.1 Advantages and disadvantages of beta titanium alloys [3].

Advantages	*Disadvantages*
– high strength-to-density ratio	– high density
– low modulus	– low modulus
– high strength/high toughness	– poor low and high temperature properties
– high fatigue strength	– small processing window (some alloys)
– good deep hardenability	– high formulation cost
– low forging temperature	– segregation problems
– strip producible – low-cost TMP* (some alloys)	– high springback
– cold formable (some alloys)	– microstructural instabilities
– easy to heat treat	– poor corrosion resistance (some alloys)
– excellent corrosion resistance (some alloys)	– interstitial pick up
– excellent combustion resistance (some alloys)	

* TMP: thermomechanical processing

Tab. 2.2 Composition, category, applications, source and year of introduction of major beta titanium alloys [2].

Alloy composition	Commercial name	Category	Mo-Eq u.	Actual and potential applications	Introduction Year-by
Ti-35V-15Cr	Alloy C	beta	47	burn-resistant alloy	90-P & W
Ti-40Mo		beta	40	corrosion resistance	52-RemCru
Ti-30Mo		beta	30	corrosion resistance	52-RemCru
Ti-6V-6Mo-5.7Fe-2.7Al	TIMETAL 125	metastable	24	high-strength fasteners	90-TIMET
Ti-13V-11Cr-3Al	B 120 VCA	metastable	23	airframe, landing gear, springs	52-RemCu
Ti-1Al-8V-5Fe	1-8-5	metastable	19	fasteners	57-RMI
Ti-12Mo-6Zr-2Fe	TMZF	metastable	18	orthopedic implants	92-Howmedica
Ti-4.5Fe-6.8Mo-1.5Al	TIMETAL LCB	metastable	18	low cost, high strength alloy	90-TIMET
Ti-15V-3Cr-1Mo-0.5Nb-3Al-3Sn-0.5Zr	VT 35	metastable	16	high strength airframe castings	na*-Russia
Ti-3Al-8V-6Cr-4Mo-4Zr	Beta C	metastable	16	oil fields, springs, fasteners	69-RMI
Ti-15Mo	IMI 205	metastable	15	corrosion resistance	58-IMI
Ti-8V-8Mo-2Fe-3Al	8-8-2-3	metastable	15	high strength forgings	69-TIMET
Ti-15Mo-2.6Nb-3Al-0.2Si	TIMETAL 21S	metastable	13	oxidation/corrosion resistant, TMCs	89-TIMET
Ti-15V-3Cr-3Sn-3Al	15-3	metastable	12	sheet, plate, airframe castings	78-USAF
Ti-11.5Mo-6Zr-4.5Sn	Beta III	metastable	12	high strength	69-Crucible
Ti-10V-2Fe-3Al	10-2-3	metastable	9.5	high strength forgings	71-TIMET
Ti-5V-5Mo-1Cr-1Fe-5Al	VT 22	metastable	8.0	high strength forgings	na*-Russia
Ti-5Al-2Sn-2Zr-4Mo-4Cr	Ti-17	beta-rich	5.4	high strength, medium temperature	68-GEAE
Ti-4.5Al-3V-2Mo-2Fe	SP 700	beta-rich	5.3	high strength, SPF	89-NKK
Ti-5Al-2Sn-2Cr-4Mo-4Zr-1Fe	Beta-CEZ	beta-rich	5.1	high strength, medium temperature	90-CEZUs
Ti-13Nb-13Zr		beta-rich	3.6	orthopedic implants	92-Smith & N.

* na: not announced

titanium alloy. Recently some new alloys like Beta-CEZ, LCB, and SP 700 have been developed and are now being introduced. More information about the particular use of these alloys will be given later.

One of the keys for successful application of beta alloys is the development of appropriate processing conditions. Systematic correlations between processing, microstructure, and properties must be derived in order to find a technically reasonable and safe processing window. Questions beyond these issues, in particular concerning the corrosion behavior, alloy development, applications, etc., are described in more detail elsewhere [1, 2].

Subsequently, a brief introduction to the metallurgy and processing of beta titanium alloys will be given. Then, an attempt will be made to describe the effects of deformation and heat treatment on microstructure and on the main properties like tensile values, toughness, high cycle fatigue (HCF), and fatigue crack propagation (FCP).

2.2
Metallurgy and Processing

A beta alloy is defined here as a titanium alloy with sufficient β-stabilizer content to suppress the martensitic transformation during quenching to room temperature. This means that 100% beta phase is retained (Fig. 2.1). The beta stability can
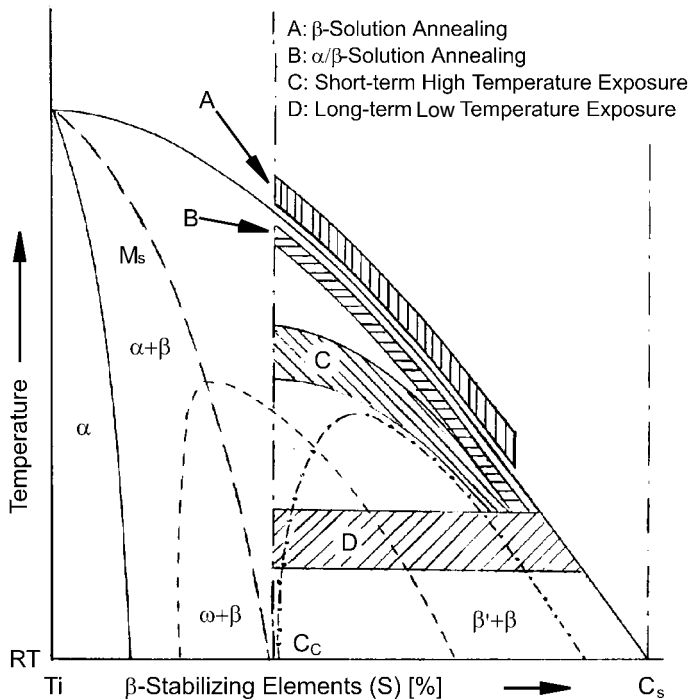
Fig. 2.1 Schematic phase diagram of metastable beta alloy [9].

be described by the molybdenum equivalent, which combines the effects of the various β-stabilizing elements like Mo, V, Fe, Cr, Nb, etc. [3]. A minimum value of about 10% is necessary to stabilize the beta phase during quenching (see Mo equivalent in Tab. 2.2). Beyond a β-stabilizer concentration of c_s, stable β alloys exist (Fig. 2.1). Between the minimum concentration, c_c, and c_s alloys are metastable; most commercial β alloys fall into this range (Tab. 2.2).

With the help of Fig. 2.1 and a qualitative TTT-diagram of Ti-10-2-3 in Fig. 2.2 [4, 5], the development of the basic microstructures will be explained briefly; more comprehensive descriptions are given in [6, 7].

Processing of β alloys usually consists of a hot working operation followed by a heat treatment. The final hot working step is normally performed in the α+β field for the leaner beta alloys, and preferentially in the β field for the richer beta alloys. The heat treatment consists of a solution treatment followed by quenching and a subsequent aging treatment. A solution heat treatment above the β-transus temperature results in coarse β grains (Fig. 2.3 a). Solution treating slightly below the β transus leads to the precipitation of primary α (α_p) (Fig. 2.3 b and c). The heat treatment temperature controls the α_p volume fraction, while forging and rolling deformation influences the α_p shape. Without working a needle-like α_p shape develops; an increased amount of hot working leads to a globular α_p shape.
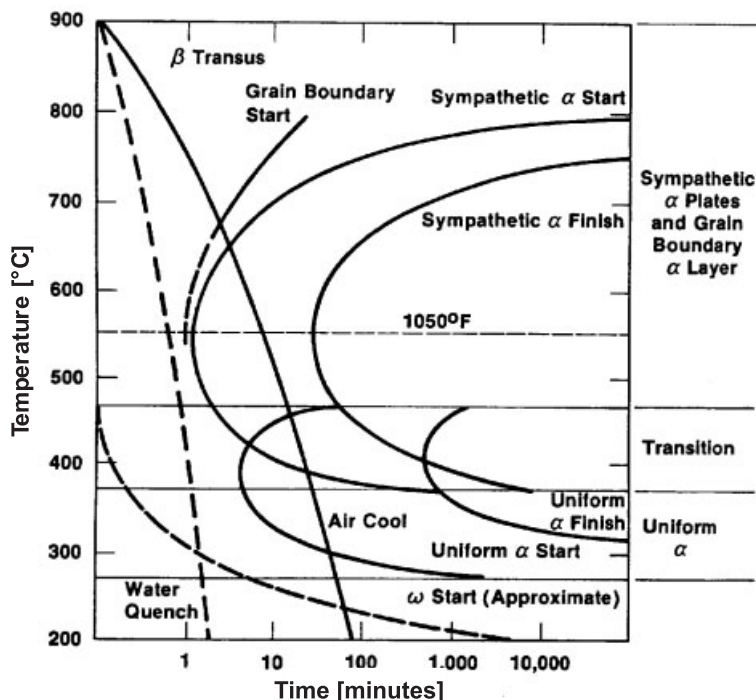
Fig. 2.2 Qualitative TTT-diagram for Ti-10-2-3 (β-ST) [4, 5].
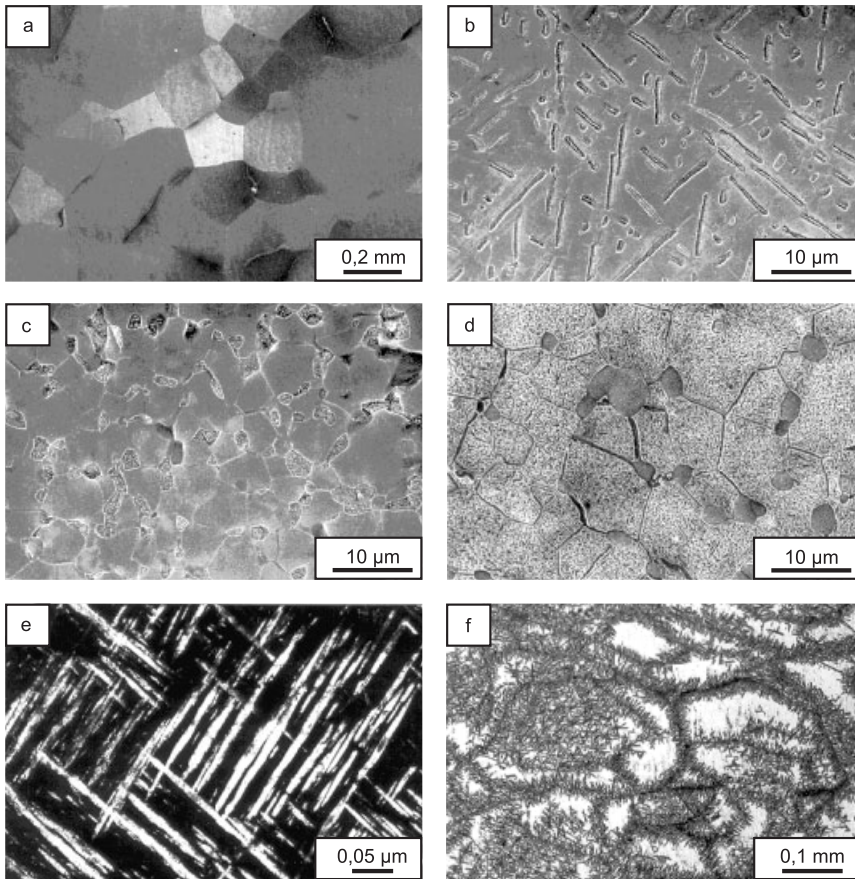
Fig. 2.3 Different microstructures of beta alloys; (a)–(e): Ti-10-2-3; f: Beta C); (a) β-ST and aged; (b) 10% elongated α_p; (c)10% globular p; (d) 10% α_p (recrystallized) with GB-α; (e) secondary α (TEM); (f) inhomogeneous precipitation of secondary α.

The β grain size and size distribution are controlled by a proper selection of temperatures and deformation starting from ingot breakdown [8]. Several cycles of deformation and recrystallization are possible if small grain sizes are required.

Grain boundaries are preferred sites for a film-like α precipitation during forging, cooling from β-forging, and heat treatment. The precipitation of detrimental grain boundary α can be suppressed by rapid cooling from the β phase field. Since this is impossible to realize as, for example, in the case of large cross sections, subsequent α/β-processing can break up the grain boundary film (Figs. 2.2 and 2.3 d).

At lower temperatures, typically 400 °C to 600 °C, the secondary α (α_s) precipitates in a fine distribution (Fig. 2.3 e and 2.3 f). It has a significant strengthening effect depending on its volume fraction and size, which in turn are controlled by

aging temperature and time as well as by the solution treatment temperature [6]. The precipitation of α_s can be homogeneous as it is found in lean beta alloys like Ti-10-2-3, or inhomogeneous in richer beta alloys, like Beta C or Ti-15-3. In the latter case, precipitation starts from grain boundaries and later in the grain leaving some local areas unaged (Fig. 2.3f). Cold work generally enhances the aging response and can lead to a more homogenous distribution of the α_s [9]. The uniformity of the α_s can also be influenced by step aging procedures as will be discussed later. In lean alloys coherent ω phase can precipitate at low temperatures (Fig. 2.2). It will not be discussed further since it is not used due to its embrittling effect [4]. Alloys with a high amount of β-stabilizer can form intermetallic compounds. Their possible effect on properties is discussed in [6, 7].

In summary, the following microstructural constituents are important for property control of beta titanium alloys:

- β grain size
- α_p and α_s including their shape, size, and volume fraction
- grain boundary α.

2.3
Mechanical Properties

2.3.1
Tensile Properties

Through aging, a wide range of yield stresses (typically 900 to 1400 MPa) can be reached in beta titanium alloys. With increased aging, however, all β alloys show a significant reduction in ductility. This is illustrated for Ti-10-2-3 in Fig. 2.4 where the elongation to fracture is plotted versus the yield strength. This observation has been explained as an increased strain localization in the aged matrix and by a higher yield stress difference between the soft primary α and the aged β matrix, which leads to early crack nucleation (Fig. 2.5) [10]. In more highly β-stabilized alloys like Ti-15-3 or Beta C, with an inhomogeneous α_s precipitation, duplex aging procedures have been developed. They consist of "high/low"- or "low/high" aging sequences. Duplex aging allows, for example, higher strength in shorter time than single-step aging [9, 11, 12]. Some authors also claim an improvement in ductility [11], while others do not find an effect on ductility [12, 13]. Duplex aging was mainly developed for an improvement of toughness and fatigue resistance and will be further discussed in that context.

Besides the dominating effect of aging, primary α (α_p) can also influence ductility. As described in section 2.2, processing influences both the shape and size of α_p. A coarsening of the α_p as well as a change from globular to acicular α_p leads to a reduction in ductility in Ti-10-2-3, as shown in Fig. 2.4 [10, 14]. The reason for both observations is the increased "effective" size or slip length of the soft α_p favoring early crack nucleation [10, 15]. An increase in the volume fraction of α_p
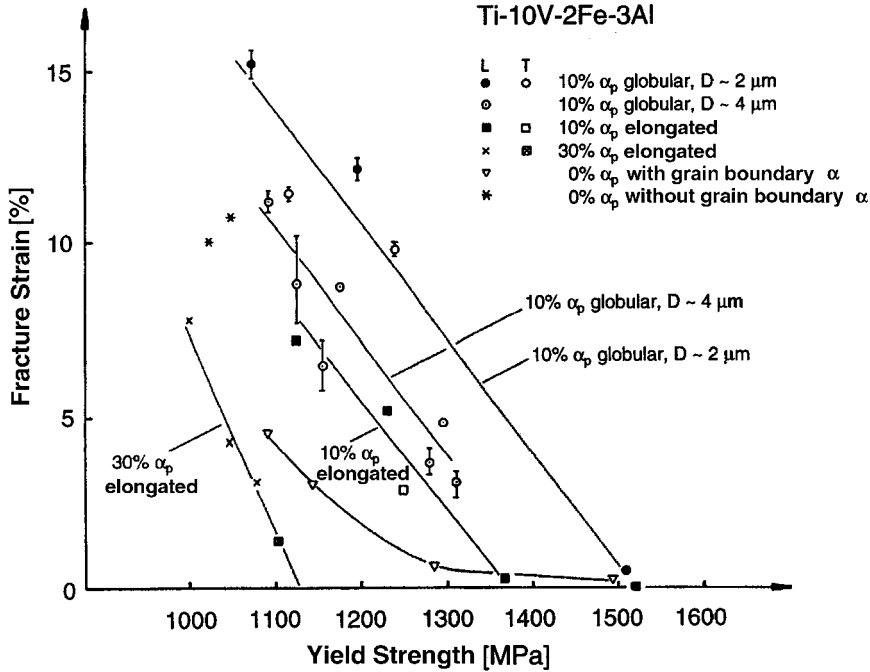
Fig. 2.4 Elongation to fracture versus yield strength for different microstructures in Ti-10-2-3.

(lower solution heat treatment temperatures) leads to a reduced ductility at constant macroscopic yield strength (Fig. 2.4, 10% α_p versus 30% α_p). In order to achieve a comparable yield stress, the β of the microstructure with a higher volume fraction of soft α_p must be aged higher, which in turn favors crack nucleation [10, 15]. At a constant aging treatment an increase in the α_p volume fraction reduces yield strength and increases ductility, as shown in Tab. 2.3 [4, 10, 16].

The effects of grain size and grain boundary are interrelated. These parameters do not affect strength [17], but can have a pronounced effect on ductility. The presence of grain boundary α, especially as a continuous film, lowers ductility since the strain is localized in the soft α film leading to crack nucleation and fracture at grain boundaries (Fig. 2.4, 2.5 c and d) [6, 10, 16, 17, 18]. For alloys Ti-10-2-3, Ti-15-3, and Beta C, a grain refinement has been shown to improve ductility (Fig. 2.6) [17, 19, 20, 21]. In cases where crack nucleation occurs at grain boundary α, this observation can be explained by a reduced slip length in the soft film resulting in delayed crack nucleation. If crack nucleation is intergranular, there is no conclusive explanation for a grain size effect on ductility. A summary of the effects of the various microstructural parameters on tensile properties is given in Tab. 2.4.
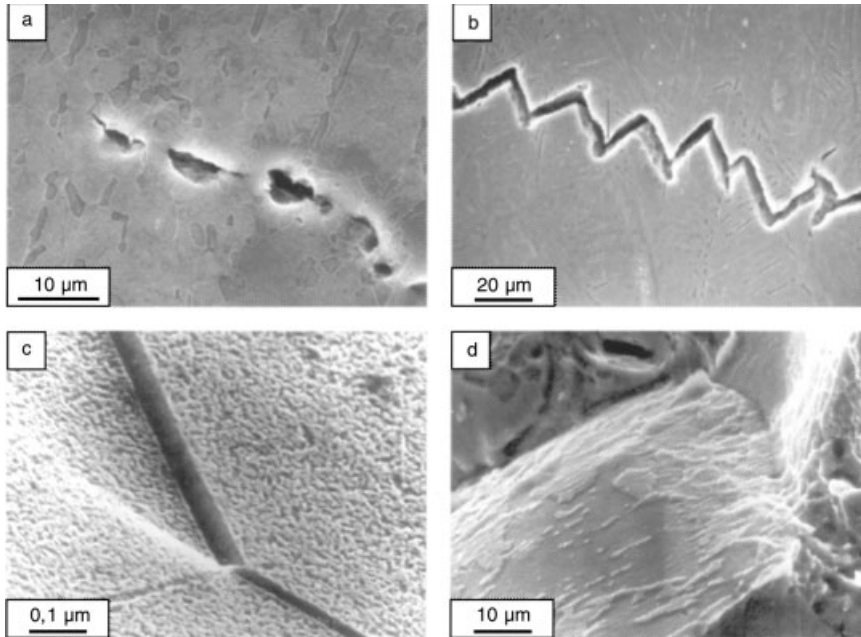
Fig. 2.5 (a), (b): Increased matrix aging leading to localization of slip [15]; (a) YS=1100 MPa; (b) YS=1400 MPa;

(c), (d): Preferential plastic deformation in grain boundary α; (c) [10] leading to grain boundary fracture (d).

Tab. 2.3 Yield strength, K_{Ic}, and true fracture strain for two volume fractions of α_P at constant aging treatment for Ti-10-2-3 [15].

α_p volume fraction [%]	Yield Strength [MPa]	K_{Ic} [MPa]	F
10	1402	20	0
30	1101	34	0.04

2.3.2
Fracture Toughness

Increased aging significantly reduces fracture toughness. This has been shown for various beta alloys [13, 15, 20, 22, 23], an example is given for Ti-10-2-3 in Fig. 2.7. Fractography has revealed that as for ductility, an increased strain localization and increased strength difference between the soft α_p and the aged matrix is the reason for this trend [15]. Therefore, because of the same micromechanisms of fracture both properties show the same trend. Duplex aging has been tried in order to increase the strength and toughness compared to single-step aging [12, 13, 23, 24]. The results indicate that a low/high aging combination improves the
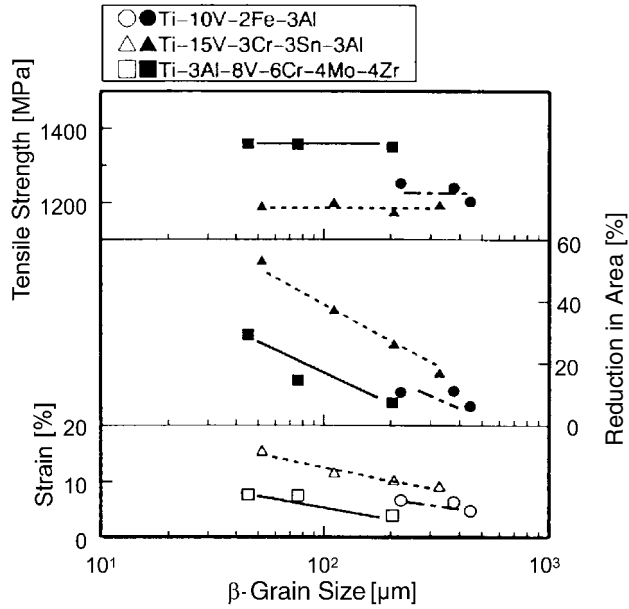
Fig. 2.6 Effect of β grain size on tensile properties of three commercial beta alloys aged at 500 °C for 8 hrs [17].

Tab. 2.4 Effect of microstructure parameters on properties of Ti-10-2-3.

Microstructure	El (RA)	K_{Ic}	HCF	FCP (threshold region)
Secondary α(α_s)				
– increasing volume fraction YS ↑	–	–	+	○ (–)
decreasing size YS ↑	–	–	+	○ (–)
– inhomogeneous distribution (e.g. preferential formation at grain boundaries)			–	○
Primary α(α_p)				
– volume fraction: increasing (10% → 30%) YS = constant	–	–		○
aging treatment constant (YS ↓)	+	+		
– morphology: (globular → elongated)	–	+		○ (+)
– size: (e.g. 2 μm → 4 μm)	–	○		○
Grain boundary α(GBα)	–	○ (–)	–	○
β grain size: (large → small)	+			○
transgranular fracture		○		
intergranular fracture	○ (+)	+/–	+	

El (RA): Elongation to fracture (reduction in area); K_{Ic}: Fracture toughness; HCF: High cycle fatigue; FCP: Fatigue crack propagation; +: improvement; –: deterioration; ○: no effect

toughness of Ti-10V-1Fe-1Cr-3Al [12], but has no effect on the toughness of Beta C [13, 24]. For Ti-15-3, a high/low combination appears to be more successful on improving the toughness [23]. The toughness increase, from about 43 MPa m$^{1/2}$ to 66 MPa m$^{1/2}$, when using duplex aging instead of single aging on Ti-15-3 is considerable. The investigation showed that a mixture of coarse, long primary α ("high aging") and fine secondary α ("low aging") was able to cause a more tortuous crack path increasing the toughness by this geometrical effect.

The role of primary α ($α_p$) on toughness has been studied in numerous investigations [8, 14, 15, 20, 21, 25]. For example, if the $α_p$ shape changes from elongated to globular toughness will decrease (Fig. 2.7) [14, 15]. Fractographic examination has shown that elongated $α_p$ leads to a more pronounced crack deviation [15]. An increase of the $α_p$ volume fraction has been shown to drastically reduce toughness when comparing at constant yield strength (Fig. 2.7). The same reason largely applies for this effect as for ductility, namely an increased degree of matrix aging is compensating for the higher amount of soft $α_p$ [15]. When comparing at constant aging, an increase in the $α_p$ volume fraction leads to an increase in toughness (Tab. 2.3).

Several authors have studied the role of grain size and grain boundary α [15, 17, 19, 20, 22, 26, 27]. A beta grain refinement has been found to reduce the frac-
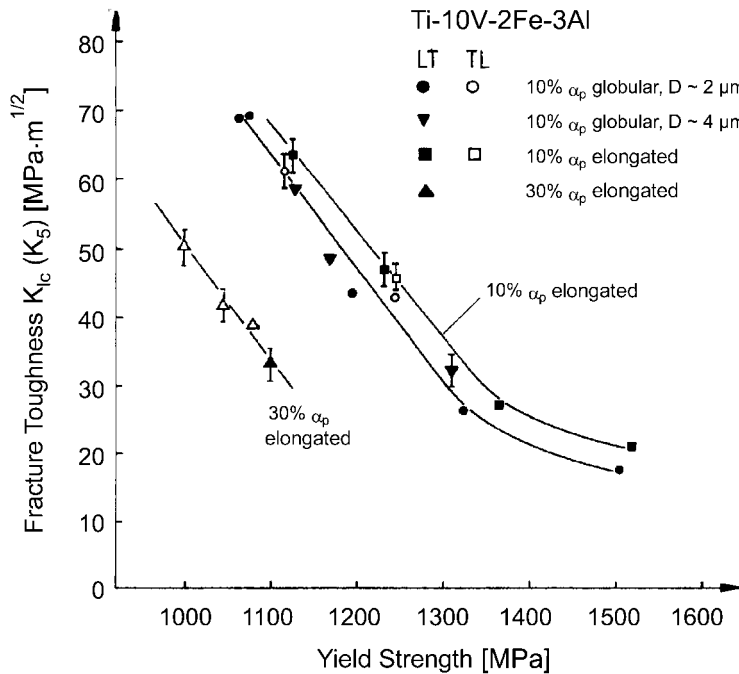
Fig. 2.7 Fracture toughness versus yield strength for different microstructures with primary α phase in Ti-10-2-3 [15].

ture toughness of Ti-15-3 [17, 28]; while for Beta C and Ti-10-2-3 no effect was found (Fig. 2.8) [17, 19].

Grain boundary α has been claimed to decrease [15, 27] or increase [29] fracture toughness or not to effect it [15]. Examples are shown in Fig. 2.9 where fracture toughness is plotted versus yield strength. Comparing two microstructures with and without primary α (β-ST, DA), and with a grain size of 300 μm, there is no influence of grain boundary α on toughness. For a microstructure with primary α and very small, recrystallized grains that are decorated with grain boundary α (Fig. 2.3 d), then the fracture toughness drops drastically compared to the microstructure with large grains (β-ST).

In order to explain observations that appear contradictory, it is necessary to take into account the degree of aging, plastic zone size, and stress state in addition to grain size and grain boundary α (Fig. 2.10) [15, 20]. The subsequent conclusions can be seen as a further development of an earlier model by Williams et al. [25] that treats the grain boundary α as a low energy fracture path by plastic zone confinement to this soft film.

(1) If the plastic zone is much smaller than the grain size (high strength, large grain) the fracture will start from the transgranular pre-fatigue crack [15]. For this fracture mode grain boundary α will not affect fracture toughness as has been shown on Ti-10-2-3 [15, 20], since the intrinsic toughness of the aged matrix is measured (Fig. 2.9, compare β-ST and DA).
(2) If the plastic zone size is much larger than the beta grain size (small grain, low strength), cracks can initiate and proceed in the soft grain boundary α
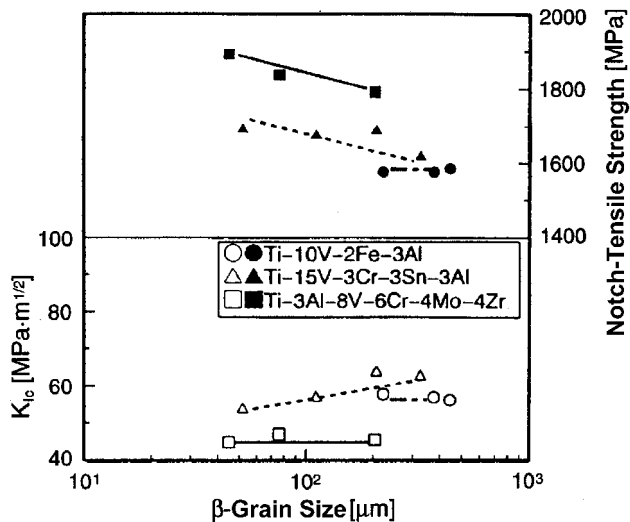
Fig. 2.8 Effect of β grain size on notched tensile strength and fracture toughness of three commercial beta alloys aged at 500 °C after ref. [17].
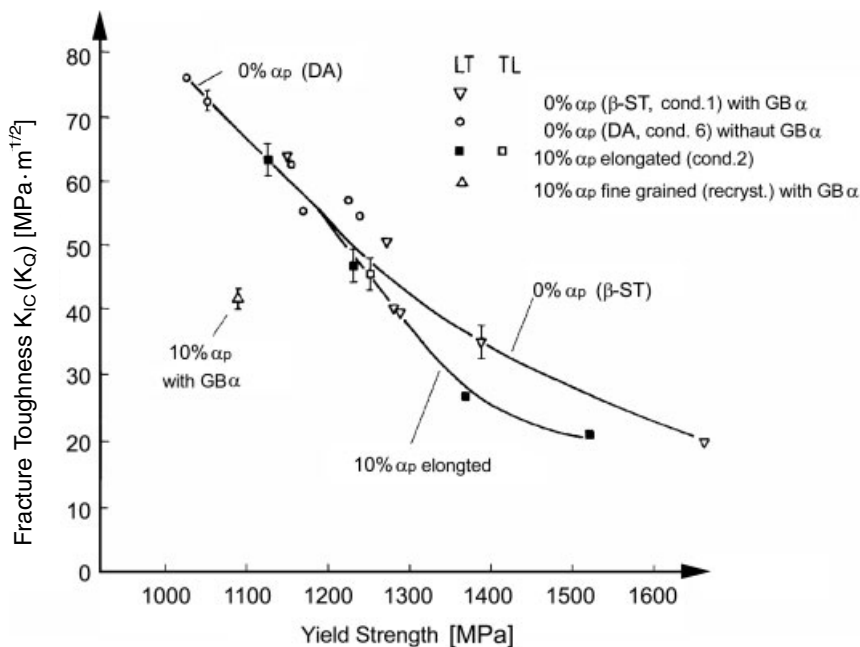
Fig. 2.9 Fracture toughness versus yield strength in Ti-10-2-3, influence of grain boundary α phase and grain size [15].

which can be regarded as a low energy path [15, 22, 25]. At constant yield stress, fracture toughness will be smaller than for the transgranular fracture [15] (Fig. 2.9, compare β-ST and 10% α_p with grain boundary α). As long as the grain boundary fracture mechanism is active, an increasing grain size should increase toughness since more tortuosity of the crack path is created which, as a geometrical effect, increases toughness. This mechanism has been used in an improved manner for the development of alloy Beta-CEZ. Instead of a continuous grain boundary α film, a broken up grain boundary α ('necklace') has been produced, which still deflects the crack but is a higher energy path and does not reduce ductility [27, 29]. In addition, in the case of intergranular fracture, an increase in matrix aging will lead to a stronger confinement of the plastic zone to the soft grain boundary α film thus leading to a lower toughness [25]. In the case of stretched grains, for example by forging, intergranular fracture and the crack deviation effect can lead to a pronounced anisotropy in fracture toughness.

(3) If no grain boundary α is present, toughness should be independent of beta grain size, since fracture will advance transgranularly.

In summary, using this approach it is possible to explain seemingly contradictory results (Tab. 2.4, Fig. 2.10). An optimum toughness is given by a combination of a

I)

a)   b)

Effect of secondary α-phase:

inhomogenous slip distibution
combined with high degtee of hardening

II)

c)   d) Pore Formation

Pore Formation   Plastic Zone

plastische
Zone

Effect of primary α-phase:

transcystalline crack path with resistance
against crack propagation by crack
deflection for elanated rimary α-phase

III)

Pore Formation

e)   f) Plastic Zone   g) Plastic Zone

Plastic Zone   Pore Formation

Pore Formation

Effect of grain size and
grain boundary α-phase:

recrystallized microstructure

Plastic zone < grain size

high resistance against crack
propagation, little crade deflection

Plastic zone > grain size

low resistance against crack propagation
with grain boundary α-phase, crack
deflection depends on grain size

Fig. 2.10 Schematic illustration of crack initiation and growth in beta alloys.

high energy crack path and maximum crack deviation. One such combination is an aged matrix with acicular α_p (example Ti-10-2-3), another possibility is a broken up grain boundary α with a large grain size (example Beta-CEZ).

2.3.3
Fatigue (HCF)

The good fatigue potential of beta alloys has been known for quite some time [30]. A high cycle fatigue strength (HCF) around 700 MPa (R=−1, K_t=1) can be achieved in Ti-10-2-3 for large cross sections (≥100 mm); this is not possible for any other titanium alloy. New fatigue critical applications in the aerospace industry [31] have triggered some recent research efforts to understand and optimize the fatigue behavior. Boyer and Hall [22] as well as Jha and Ravichandran [32] have reviewed the effects of various thermomechanical treatments on fatigue along with the corresponding microstructures. Subsequently, their discussions will be briefly summarized, and some recent results will be added and discussed.

An increase in aging, or 0.2% yield strength, can increase HCF strength. This effect has been observed for example in Ti-10-2-3 [5, 33, 34], Beta C [35], Ti-15-3

[28, 36], and SP 700 [37]. Fig. 2.11 shows the HCF strength for various beta alloys as a function of yield strength at R = 0.1. Similar results have been obtained for R = −1. From the data it appears that the richer beta alloys like Beta C or Ti-15-3 have a lower fatigue strength level than the leaner alloys such as Ti-10-2-3 or SP 700. One possible reason may be the trend for an inhomogeneous precipitation of α_s in the richer alloys. Gregory et al. have shown that for Beta C crack nucleation occurs in the transgranular precipitate-free regions [35]. Using a duplex aging procedure a more homogeneous α_s precipitation resulting in a 50 MPa increase in fatigue strength was achieved (Tab. 2.5).

From this work (Fig. 2.11, Tab. 2.5) it also appears that an upper limit exists for HCF strength that cannot be exceeded by further aging. It can be concluded that the soft regions, like grain boundary α, precipitate-free zones, or primary α, where fatigue cracks initiate become more and more dominant at higher strength since the strength differential between these zones and the aged matrix becomes greater. In addition, the trend to localized slip in an aged matrix that has been observed at high strength in Ti-10-2-3 [8] may contribute to an upper limit in fatigue strength.

A grain size reduction has been shown to increase the fatigue strength of Beta C [19], Ti-10-2-3 [38], and Ti-8-8-2-3 [39]. This is illustrated in Tab. 2.6 for Beta C. Grain boundary α has been discussed as a crack nucleation site. As has been shown for static properties [15, 20], the grain size reduces the slip length of grain boundary α leading to delayed crack nucleation. The detrimental role of grain boundary α on fatigue was also shown for Ti-10-2-3 [34]. The effect of α/β defor-
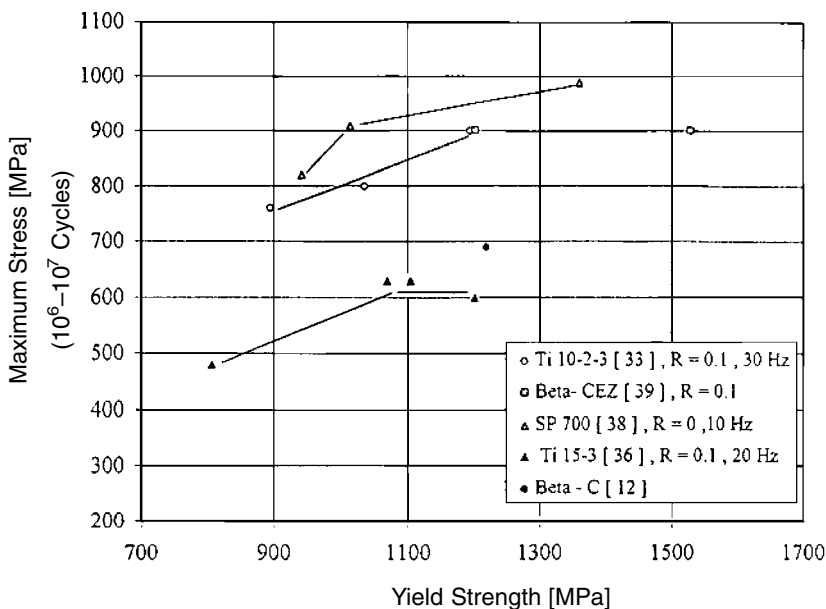
Fig. 2.11 HCF strength versus yield strength for different beta alloys.

Tab. 2.5 Effect of aging degree and duplex aging on HCF strength in Beta C [35].

Heat treatment	YS [MPa]	HCF-Strength σ_a [MPa] at 10^7 cycles; $R=-1$, $K_t=1$
927 °C, AC	850	390
927 °C, AC + 16 h/540 °C	1085	575
927 °C, AC + 4 h/440 °C + 16 h/560 °C	1085	625
927 °C, AC + 72 h/440 °C + 16 h/500 °C	1325	625

Tab. 2.6 Effect of grain size on HCF strength in Beta C bar, $R=0,1$, $K_t=1$ [19].

Grain size [µm]	YS [MPa]	HCF-Properties (10^6 cycles)	
		HCF Strength [MPa]	HCF Strength / YS
40	1255	815	0,65
34	1188	800	0,67
75	1220	690	0,57
122	1344	670	0,50

mation after β-forging was investigated and it was found that the purely β-forged condition showed a higher ratio of HCF strength to yield strength than the β + α/β-forged material with ≥30% α/β deformation (Fig. 2.12). While considerable amounts of grain boundary were observed in the purely β-processed condition, they were effectively removed by an α/β-deformation of ≥30%. This also explains why more than 30% α/β deformation does not further improve fatigue strength. Campagnac et al. have also observed the interdependence of HCF strength on α/β deformation in the range between 0.35 and 1.0 true strain [40]. If grain boundary α is suppressed and cracks initiate in the aged matrix, a grain size effect on HCF strength should not be expected. A summary of microstructural effects on fatigue is given in Tab. 2.4.

Although there are numerous open questions regarding the understanding and optimization of fatigue (role of primary α, notched fatigue results, etc.) the existing results already give some indications how to improve fatigue resistance: aging to an optimum level, small grain size, reduction/suppression of grain boundary α, and homogeneous distribution of secondary α.
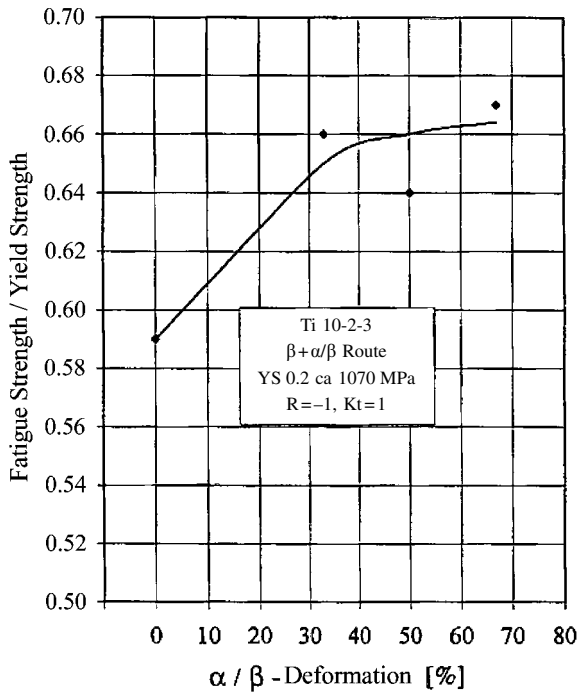
Fig. 2.12 HCF strength versus α/β forging deformation for Ti-10-2-3 [34]

2.3.4
Fatigue Crack Propagation (FCP)

In contrast to other mechanical properties, fatigue crack propagation resistance is much less sensitive to processing and microstructure and even to chemical composition of alloys [41, 42]. Fig. 2.13 shows a da/dN-ΔK plot with results on Ti-10-2-3, Ti-15-3, TIMETAL 21S, Beta C, and Beta-CEZ that are taken from several references [39, 41-45]. This figure updates an earlier comparison [42] by including new data for TIMETAL 21S and Beta-CEZ. Although quite different products and processing conditions were taken, the curves fall in a narrow band especially at intermediate da/dN values (Paris-region). Compared to mill-annealed Ti-6-4, the fatigue crack propagation rates are slightly higher at low da/dN values [42].

The influence of processing and the resulting microstructures has been particularly investigated for Ti-10-2-3 [41, 42, 46, 47], and to a lesser extent for Beta C [13], Ti-15-3 [39, 48], TIMETAL 21S [43], and Beta-CEZ [27]. Increased aging does not significantly change behavior in the threshold and Paris region for Ti-10-2-3 [42, 46], TIMETAL 21S [43], and Ti-15-3 [48]. A slightly higher fatigue crack growth rate (factor of about 2) has been found at higher strength for Beta-CEZ [27]. For Ti-10-2-3 a variety of eleven forging and heat treatment conditions has

Fig. 2.13 Fatigue crack growth for different beta alloys in comparison to mill-annealed Ti-6-4.
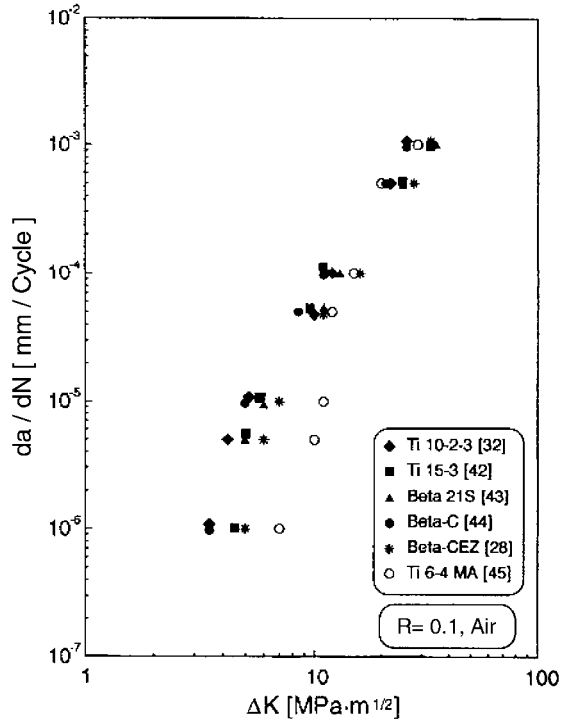
been investigated at a nominal yield strength of 1240 MPa [41, 47]. For all the α-aged conditions very little effect of microstructure on FCP was observed (Fig. 2.14). Only one ω-aged condition, which is commercially irrelevant, showed a significantly higher threshold value. This effect is due to a change in slip distribution caused by the coherent, shearable ω particles and the resultant roughness of the crack front profile [41]. An investigation of the Russian BT 22 alloy has shown that compared to globular primary α, lamellar α increases the fatigue crack growth rate by a factor of 5 [26]. Fractographic analysis has generally shown macroscopically and microscopically rather flat and transgranular fracture surfaces [41, 42, 46]. Crack closure measurements as a function of yield stress [46] resulted in relatively small crack closures (about 1 MPa m$^{1/2}$), which are not consistently varying with yield stress.

A discussion of results must consider that the volume affected in a FCP test is very small. For example, the plastic zone size at $\Delta K = 5$ MPa m$^{1/2}$ and yield strength = 1100 MPa is on the order of 1–2 μm. Therefore, it encompasses only a few α_s particles and the crack will grow by a local decohesion of α_s/β interfaces. The α_s precipitates as a dominating parameter probably do not vary sufficiently in size, shape, and volume fraction to achieve major differences in FCP. This is in contrast to $\alpha + \beta$ Ti alloys like Ti-6-4, which can be considerably influenced in fatigue crack growth. On the other hand, beta alloys are hardly inferior in fatigue
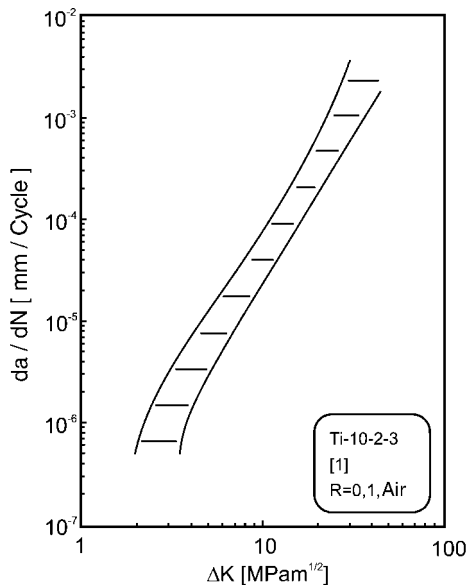
Fig. 2.14 Fatigue crack growth for eleven different microstructures in Ti-10-2-3; YS = 1240 MPa [41].

The figure shows a plot of da/dN [mm/Cycle] on the vertical axis (ranging from 10^{-7} to 10^{-2}) versus ΔK [MPam$^{1/2}$] on the horizontal axis (ranging from 1 to 100).

Ti-10-2-3
[1]
R = 0,1, Air

crack growth resistance. The insensitivity of FCP to microstructure gives the chance to optimize other mechanical properties without damaging FCP.

2.4
Applications

Despite the obvious potential of beta alloys, their share of the titanium market is still small (1% of the US market) [3]. However, their use is continuously increasing, especially in aerospace [31]. This is through increased use of existing alloys like Ti-10-2-3. Most of the landing gear of the Boeing 777 airplane, for example, is produced from Ti-10-2-3 forgings, including the large truck beam (see Chapter 13). In addition, Fig. 2.15 shows the rotor head of the Westland Super Lynx helicopter, which is also produced from Ti-10-2-3 instead of Ti-6-4. Ti-10-2-3 is also currently used in other helicopter programs. The driving force for selection of Ti-10-2-3 in the latter case was increased fatigue properties of the beta alloy. There are numerous other applications for beta alloys, including BT22 as a competitor to Ti-10-2-3, Ti-15-3 (sheet and castings), and TIMETAL 21S with its good high temperature properties [31].

Outside aerospace, beta alloys can be used for downhole service (deep oil and gas wells) where Beta C is a particularly appropriate candidate because of its good combination of mechanical and corrosion properties [49]. New alloys under development are: TIMETAL LCB (LCB – low cost beta) with its first application in automotive springs [3], SP 700 as a high strength alloy with improved cold and superplastic formability [37], and TMZF (Ti-12Mo-6Zr-2Fe) as a surgical implant alloy with low modulus, good strength, and corrosion resistance [51].
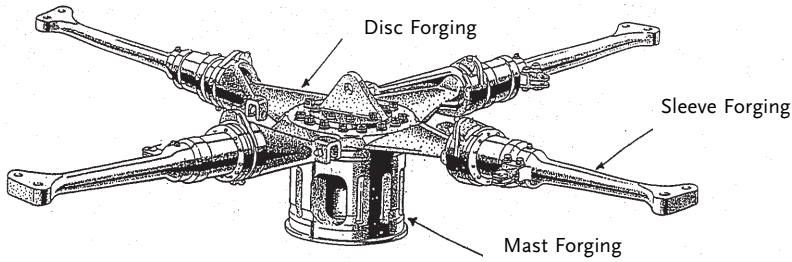
Courtesy of Westland Helicopters

Fig. 2.15   Super Lynx helicopter main bolted rotor head made from Ti-10-2-3.

The description of applications is by far not complete and the reader is referred to the referenced literature. But it shows that beta alloys have an excellent property potential for a wide field of applications. One particular challenge for the introduction of this alloy family is the necessity for strict process control, since some properties are very sensitive to process variations. Uniformity of properties is a major issue particularly for large parts with complex shapes since the variations in local deformation have to be controlled. The improved understanding of the relationships between processing and microstructures/properties is the necessary basis for a successful introduction of beta alloys into further applications.

2.5
Referenced Literature and Further Reading

1 D. Eylon, R. R. Boyer, D. A. Voss (eds.): Beta Titanium Alloys in the 1990's, TMS, Warrendale, PA, USA (1993)

2 A. Vassel, D. Eylon, Y. Combers (eds.): Beta Titanium Alloys, Editions de la Revue de Metallurgie, No. d serie 8 (1993)

3 P. Bania: Beta Titanium Alloys and Their Role in the Titanium Industry, in: Beta Titanium Alloys in the 1990's, D. Eylon et al. (eds.), TMS, Warrendale, PA, USA (1993) 6

4 T. W. Duerig, G. T. Terlinde, J. C. Williams: Phase Transformations and Tensile Properties of Ti-10V-2Fe-3Al, Met. Trans. 11A (1980) 1987

5 G. W. Kuhlman: Alcoa Green Letter No. 224: Alcoa Titanium Alloy Ti10V2Fe3Al Forgings (1987)

6 T. W. Duerig, J. C. Williams: Overview: Microstructure and Properties of Beta Titanium Alloys, in: Beta Titanium Alloys of the 1980's, R. R. Boyer et al. (eds.), TMS, Warrendale, PA, USA (1984) 19

7 A. Vassel: Microstructural Instabilities in Beta Titanium Alloys, in: Beta Titanium Aloys of 1990's, R. R. Boyer et al. (eds.), TMS, Warrendale, PA, USA (1993) 173

8 F. Froes, H. B. Bomberger: The Beta Titanium Alloys, J. of Metals, July (1985) 28.

9 S. Ankem, S. Seagle: Heat Treatment of Metastable Beta Titanium Alloys, in: Beta Titanium Alloys, in: Beta Titanium Alloys of the 1980's, R. R. Boyer et al. (eds.), TMS, Warrendale, PA, USA (1984) 107

10 G. T. TERLINDE, T. W. DUERIG, J. C. WILLIAMS: Microstructure, Tensile Deformation and Fracture in Aged Ti-10V-2Fe-3Al, Met. Trans. 14A (1983) 2101

11 N. NIWA, H. TAKATORI: Effect of Duplex Aging after Cold Working on the Mechanical Properties of Ti-10V-3Cr-3Sn-3Al, in: Titanium '92, Science and Technologie, F.H. FROES, et al. (eds.), TMS, Warrendale, PA, USA (1993) 1883

12 J. WANG, X. DUAN: A Study of the Duplex Aging of Ti-10V-1Fe-1Cr-3Al Near Beta Alloy, 6th World Conference on Titanium, France (1988) 1607

13 D. BUTTINELLI, F. FELLI, G. D. FESTA, A. J. QUERALES: Effect of Heat Treatments on on the Fatigue Behavior of the Beta-C Titanium Alloy, in: Titanium '92, Science and Technology, F.H. FROES et al. (eds.), TMS, Warrendale, PA, USA (1993) 505

14 R. R. BOYER, G. W. KUHLMAN: Processing Properties Relationships of Ti-10V-2Fe-3Al, Met. Trans. 18A (1987) 2095

15 G. T. TERLINDE, H. J. RATHJEN, K. H. SCHWALBE: Microstructure and Fracture Toughness of the Aged β-Ti Alloy Ti10V-2Fe-3Al, Met. Trans. (1988) 1037

16 A. BHATTACHARJEE, V. A. JOSHI, A. K. GOGIA: Effect of heat treatment on tensile behaviour of a Ti-10V-2Fe-3Al alloy, in: Titanium '99, CRISM Prometey, St. Petersburg, Russia (2000) 529-536

17 Y. KAWABE, S. MUNEKI: Strengthening Capability of Beta Titanium Alloys, in: Beta Titanium Alloys of the 1990's, D. EYLON et al. (eds.), TMS, Warrendale, PA, USA (1993) 187

18 J. C. CHESNUTT, F. H. FROES: Effect of α Phase Morphology and Distribution on the Tensile Ductility of a Metastable Beta Titanium Alloy, Met. Trans. 8A (1977) 1013

19 J. G. FERRERO, J. R. WOOD, P. A. RUSSO: Microstructure/Property Relationships in Bar Products of Beta-C^{TM}, in: Beta Titanium Alloys of the 1990's, D. EYLON et al. (eds.), TMS, Warrendale, PA, USA (1993) 211

20 G. T. TERLINDE, K. H. SCHWALBE: The Role of α Phase in the Fracture Toughness and Tensile Fracture of an Aged Metastable β-Ti Alloy, in: Microstructure, Fracture Toughness and Fatigue Crack Growth Rate in Titanium Alloys, A.K. CHAKRABARTI et al. (eds.), TMS, Warrendale, PA, USA (1987) 97

21 R. R. BOYER et al.: Microstructure/Property Relationships in Ti-15V-3Cr-3Al-3Sn High Strength Castings, in Microstructure/Property Relationships in Ti-Aluminides and Alloys, TMS, Warrendale, PA, USA (1991) 511

22 R. R. BOYER, J. A. HALL: Microstructure/Property Relationship in Titanium Alloys, in: Titanium '92, Science and Technology, F.H. FROES et al. (eds.), TMS, Warrendale, Pa, USA (1993) 77

23 N. NIWA, H. TAKATORI: Effect of Step Aging on the Fracture Toughness of Ti-15V-3Cr-3Sn-3Al Alloy, in: Beta Titanium Alloys in the 1990's, D. EYLON et al. (eds.), TMS Warrendale, PA, USA (1993) 237

24 L. WAGNER, J. K. GREGORY: Improvement of Mechanical Behavior in Ti-3Al-8V-6Cr-4Mo-4Zr by Duplex Aging, ibid, 199

25 J. C. WILLIAMS et al.: ASTM STP 651, Philadelphia, USA (1978) 64

26 I. S. POLKIN et al.: Structure and Mechanical Properties of VT22 (α+β) High Strength Titanium Alloy Semiproducts, Titanium '92, Science and Technology, F. H. FROES et al. (eds.), TMS, Warrendale, PA, USA (1993) 1569

27 D. GRANDEMANGE, Y. COMBRES, D. EYLON: Effect of the Morphology of the Primary α Phase on the Mechanical Properties of Beta CEZ Alloy, in: Beta Titanium Alloys in the 1990's, D. EYLON ET. AL. (eds.), TMS, Warrendale, PA, USA (1993) 227

28 E. BRESLAUER, A. ROSEN: Relationship Between Microstructure and Mechanical Properties in Metastable β-Titanium 15-3 Alloy, Mat. Science and Technology, Mai (1991) 441

29 WURZWALLNER, G. LÜTJERING, H. PUSCHNIK, R. R. BOYER: Microstructure and Mechanical Properties of β-CEZ, in Beta Titanium Alloys, Editions de la Revue de Metallurgie, No. de serie: 8 (1994) 135

30 R. R. BOYER: Design Properties of a High Strength Titanium Alloy, Ti-10V-2Fe-3Al, Journal of Metals 32 (1980) 61

31 R. R. BOYER: Applications of Beta Titanium Alloys in Airframes, in: Beta Tita-

nium Alloys of the 1990's, D. EYLON et al. (eds.), TMS, Warrendale, PA, USA (1993) 335

32 S. K. JHA, K. S. RAVICHANDRAN: High-Cycle Fatigue Resistance in Beta-Titanium Alloys, Journal of Metals 52 (2000) 30–35

33 G. W. KUHLMAN, A. K. CHAKRABARTI, T. L. YU, R. PISHKO, G. T. TERLINDE: LCF, Fracture Toughness, and Fatigue/Fatigue Crack Propagation Resistance Optimisation in Ti-10V-2Fe-3Al Alloy Through Microstructural Modification, in: Microstructure, Fracture Toughness and Fatigue Crack Growth Rate in Titanium Alloys, TMS, Warrendale, PA, USA (1987) 171

34 G. TERLINDE: Otto Fuchs Internal Report, T17 (1995)

35 J. K. GREGORY, L. WAGNER: Heat Treatment and Mechanical Behavior in β-C, Proc. III Int. Meeting on Titanium, Turino, Italy (1991)

36 D. P. DAVIES: Influence of Processing Variables on the Mechanical Properties of Ti-15V-3Cr-3Al-3Sn Sheet for Helicopter Erosion Shield Applications, in: Titanium '92, Science and Technology, F. H. FROES et al. (eds.), TMS, Warrendale, PA, USA (1993) 1923

37 T. FUJITA et al.: Fatigue and Fracture Toughness Properties in the Beta Rich (α + β) Titanium Alloy SP 700, in: Beta Titanium Alloys of the 1990's, D. EYLON et al. (eds.), TMS, Warrendale, PA, USA (1993) 297

38 R. CHAIT, T. S. DE SISTO: The Influence of Grain Size on the High Cycle Fatigue Crack Initiation of a Metastable Beta Ti Alloy, Met. Trans. 8A (1977) 1017

39 P. BANIA et al.: Development and Properties of Ti-15V-3Cr-3Sn-3Al (Ti15-3), in: Beta Titanium Alloys of the 1980's, R. R. BOYER et al. (eds.), TMS, Warrendale, PA, USA (1984) 209

40 M. H. CAMPAGNAC, J. C. CHAIZE, G. ANTOINE: Introduction of Beta Titanium Alloys on Mechanical Parts Highly Stressed on Helicopter, in: Beta Titanium Alloys, Editions de la Revue de Metallurgie, No de serie: 8 (1994) 271

41 T. W. DUERIG, J. E. ALLISON, J. C. WILLIAMS: Microstructural Influences on Fatigue Crack Propagation in Ti-10V-2Fe-3Al, Met. Trans. 16A (1985) 739

42 G. W. KUHLMANN, A. K. CHAKRABARTI: Room Temperature Fatigue Crack Propagation in Beta-Titanium Alloys, in: Microstructure, Fracture Toughness and Fatigue/Fatigue Crack Growth Rate in Titanium Alloys, TMS, Warrendale, PA, USA (1987) 3

43 J. C. FANNING: Timetal 21S Property Data, in: Beta Titanium Alloys of the 1990's, D. EYLON et al. (eds.), TMS Warrendale, PA, USA (1993) 397

44 J. R. WOOD et al.: Properties of Beta-C (Ti3Al8V6Cr4Mo4Zr), in Beta Titanium Alloys of the 1990's, D. EYLON et al. (eds.), TMS Warrendale, PA, USA (1993) 463

45 M. J. DONACHIE, Jr. (ed.): Titanium, A Technical Guide, ASM Intern. (1988) 180

46 B. DOGAN, G. TERLINDE, K. H. SCHWALBE: Effect of Yield Stress and Environment on Fatigue Crack Propagation of Aged Ti-10V-2Fe-3Al, in: 6th World Titanium Conf., France (1988) 181

47 S. K. JHA et al., Effect of Mean Stress and Aging on Fatigue Crack Growth in a metastable Titanium Alloy, Ti-10V-2Fe-3Al, Metall. Trans. 31A (2000) 703

48 R. D. BRIGGS et al.: Crack Growth Studies in the Ti-15-3 Beta Titanium Alloy, ibid, 65

49 D. C. DUNLOP, R. W. SCHULZ: Utilisation of Beta-C. Titanium Components in Downhole Service: in: Beta Titanium in the 1990's, D. EYLON et al. (eds.), TMS Warrendale, PA, USA (1993) 347

3

Orthorhombic Titanium Aluminides:
Intermetallics with Improved Damage Tolerance

J. Kumpfert, *Airbus Industrie, Blagnac, France*
C. Leyens, *DLR-German Aerospace Center, Cologne, Germany*

3.1
Introduction

Titanium aluminides represent an important class of alloys, providing a unique set of physical and mechanical properties that can lead to substantial payoffs in future aircraft engines. TiAl-base materials exhibit the highest potential for near-term applications in rotating parts of commercial aircraft engines. The most recent alloy family within the group of titanium aluminides is the orthorhombic titanium aluminides, based on the intermetallic compound Ti_2AlNb. For demanding elevated temperature applications, e.g. jet engines, this new class of alloys competes with conventional near-α titanium alloys, the almost mature γ TiAl alloys and, as all high temperature titanium base alloys, nickel-based materials [1, 2].

It is important to note that it took more than 25 years of very intensive research around the globe to obtain a maturity level of intermetallic γ-TiAl base alloys that is sufficient to consider this material seriously for low risk rotating components in commercial jet engines. If this enterprise will finally prove to be technically and economically successful, new generations of intermetallic alloys will appear less exotic to designers. However, since mainly high-risk components are left over for new material developments, the barrier for implementation is increasing. In the U.S., orthorhombic titanium aluminides were considered earlier for lower risk parts, such as compressor casings and other static parts [1]. Due to the progress made in development, many such components appear to be feasible with TiAl alloys today. Thus, orthorhombic alloys need to fulfil the requirements of other components, where especially high fracture toughness and high strength is a requirement for application at temperatures above 500 °C. In this regime nickel-based alloys are often employed, for example, in large jet engine disks. Replacement of the nickel-based disks remains, however, one of the biggest challenges in the design of new high performance lightweight compressors. A sophisticated approach to designing a lightweight alternative to conventional disks or blisks (bladed disk) is the bladed-ring (bling) concept. Long-fiber reinforced high temperature titanium matrix composites (TMCs) capable of long-term service above 500 °C generate further demand for a new high temperature titanium-based material [2, 3] (see Chapter 12). Orthorhombic titanium aluminides appear to be quite

promising for this application, but will only find increased attention if they offer a unique set of properties not provided by competing alloys.

Today conventional titanium-based alloys represent one third of the weight of modern aircraft engines and, are the second most used engine material following Ni-based superalloys. Modern high-pressure compressors employ near-α titanium alloys in the front, and Ni-based superalloys in stages exceeding $\sim 500\,°$C. The improved thrust-to-weight ratio of today's jet engines is in part a result of a higher stage pressure ratio of modern compressors in conjunction with higher mechanical loads, as well as significant weight reductions by replacing Ni-based alloys by last generation near-α titanium alloys. This alloy class derives its creep resistance from the close-packed hcp α phase, and its strength from microstructures with a high density of α/β interfaces, as well as solid solution strengthening of the individual phases. With respect to mechanical properties, conventional near-α titanium alloys have a temperature capability up to $550\,°$C–$600\,°$C. It seems, after 40 years of alloy development, that this defines an upper limit of this class of material. However, the main reason for employing heavy Ni-based alloys down to service temperatures of $500\,°$C is the severe environmental embrittlement of conventional titanium alloys due to oxidation [4, 5]. Development of oxidation resistant coatings may further increase the temperature limit for these alloys [6].

Tab. 3.1 compares some important properties of nickel-based alloys with conventional near-α titanium and γ TiAl-based alloys in a qualitative manner to highlight the differences between the individual property profiles in a clear arrangement. While near-α titanium alloys exhibit high fracture toughness, high strength, lower density, and easy formability, they suffer from low oxidation resistance combined with high temperature embrittlement and limited creep resistance compared to nickel-based alloys. On the other hand, TiAl-based alloys exhibit an improved creep resistance, relatively good oxidation resistance, low density, and a very high specific Young's modulus. In addition, it appears that the limited strength capability of "conventional" TiAl-based alloys can be overcome by increased niobium content in the regime between 5–10 at.% [7, 8]. Thus, TiAl-based materials exhibit the highest potential for near-term application in rotating parts of commercial aircraft engines. However, damage tolerance remains an issue for designing components with TiAl. Their limited fracture toughness and low crack growth resistance make current TiAl-based alloys an unlikely candidate for components with high damage tolerance requirements, e.g. compressor disks. Since higher niobium content (5–10 at.%) in TiAl-based alloys primarily supports the formation of finer microstructures and increases the α_2 phase volume fraction, it is most likely that the previous statement can be extended to these new derivatives of γ titanium aluminides. In conclusion, no lightweight, damage tolerant material has the requisite maturity today to replace nickel-based alloys above $500\,°$C. Such a material could allow a significant performance boost through introduction of new lightweight compressors no longer dependent on the use of large quantities of heavy nickel-based alloys.

The orthorhombic titanium aluminides emerged in the early 1990's based on extensive investigation of Alpha-2 alloys in the 1980's (Tab. 3.2) [9–13]. In the late

Tab. 3.1 Property profiles of advanced high temperature alloys for jet engines.

	Near-α Ti	*Ni Base*	*γ TiAl*
Density	+	−	++
Specific tensile strength	+	−	+/−
HT spec. Young's modulus	+/−	+	++
RT ductility	+	+	−
Formability	+	+	−
Creep	−	++	++
RT fracture toughness	+	++	−
RT crack growth	+	+	−
Specific fatigue strength	+	−	+/−
Oxidation	−	++	++
HT embrittlement	−	+	+/−

1970's niobium was identified to be the most effective alloying element at improving the room temperature ductility of Alpha-2 alloys based on the brittle intermetallic Ti_3Al [14]. The first generation of Ti_3Al-based alloys, the near-α_2 alloys exhibited a Nb-equivalent in the range of 10–12 at.%. Further research clearly indicated that an increased Nb-equivalent (13–20 at.%) has a beneficial effect on the balance of room and high temperature properties [15]. In the fairly extensively characterized Ti_3Al alloy Ti-25Al-10Nb-3V-1Mo (Super-Alpha 2[TM]), vanadium was intended to be a cheap replacement of niobium, while molybdenum improved the high temperature strength, creep resistance, and Young's modulus. However, vanadium additions are also known to reduce the oxidation resistance [16].

Beyond the simple ternary orthorhombic titanium aluminides, more complex alloys contain Mo and Ta as β-stabilizing elements, as well as Si to further improve the high temperature capability. In general, Ti-Al-Nb alloys with relatively high niobium contents possess improved combinations of strength, toughness, and

Tab. 3.2 Alloy categories of Ti-Al-Nb alloys with 22–25 at.% aluminum.

Group		*Phases*	*Nb-equivalent [at.%]*	*Composition [at.%]*	*Source*
Ti_3Al	Near-α_2	$\alpha_2 + \beta/\beta_0$	10–12	Ti-24Al-10Nb	Blackburn & Smith (1978)
				Ti-25Al-8Nb-2Mo-2Ta	Marquardt (1989)
	$(\alpha_2 + O)$	$\alpha_2 + O + \beta_0$	13–20	Ti-25Al-10Nb-3V-1Mo	Blackburn & Smith (1982)
				Ti-25Al-17Nb-1Mo	Blackburn & Smith (1989)
Ti_2AlNb	Ortho-rhombic	$O + \beta_0$	21–27	Ti-22Al-27Nb	Rowe (1991)
				Ti-22Al-24Nb-Mo-Ta-Si	Rhodes (1997)

creep resistance than near-α_2 alloys. Ti_3Al-based alloys are also known for a very severe environmentally-induced embrittlement effect at temperatures as low as 550 °C [17, 18]. Predominantly due to these phenomena, work on Ti_3Al-base alloys has been discontinued in favor of the orthorhombic titanium alloys based on the intermetallic phase Ti_2AlNb. In addition, orthorhombic titanium aluminides are currently the best choice for development of high temperature titanium matrix composites (TMCs) [2, 3]. Due to their excellent compatibility with the SiC fiber and their room temperature ductility, well beyond 3%, orthorhombic alloys outperform other titanium aluminides as a matrix material. Therefore, orthorhombic TMCs currently represent the highest performance lightweight material with respect to elevated temperature stiffness and strength.

This chapter gives an overview of monolithic orthorhombic titanium aluminides, with special emphasis on microstructure evolution, the composition-microstructure-property relationships, and addresses the issue of environmental embrittlement for this new class of material. The property profile of orthorhombic titanium aluminides will be described in relation to γ TiAl titanium aluminides and conventional near-α titanium alloys.

3.2
Physical Metallurgy: Crystal Structures, Phase Equilibria, and Alloy Chemistry

Depending on chemistry and thermomechanical history, orthorhombic titanium aluminides contain different volumes of the ordered phases β_0 (Strukturbericht: B2, space group: $Pm\overline{3}m$, Pearson symbol: cP2), α_2 Ti_3Al (Strukturbericht: DO_{19}, space group: $P6_3/mmc$, Pearson symbol: hP8), and the ordered orthorhombic O Ti_2AlNb phase (Strukturbericht: A_2BC, space group: CmCm, Pearson symbol: oC16). A schematic representation of the individual lattices is shown in Fig. 3.1. The orthorhombic Ti_2AlNb phase can be considered as a structure with ternary ordering on the hcp α_2 lattice. The structural model of the O phase was first suggested by Banerjee et al. [10] and was later confirmed and refined by neutron diffraction [19]. The phase compositions in the ternary orthorhombic alloy Ti-22Al-25Nb are shown in Tab. 3.3. In a near equilibrium three-phase microstructure, the niobium content of the orthorhombic Ti_2AlNb phase is in between the niobium-rich β_0 phase and the aluminum-rich Ti_3Al phase. The fundamental benefit of orthorhombic alloys is based on the unique property profile of the O phase, i.e. the remarkable balance between good room temperature ductility and high creep resistance as compared to the α_2 phase.

The partial isothermal section of the Ti-Al-Nb system at 700 °C is shown in Fig. 3.2a [20]. The compositional range of Ti_3Al- and Ti_2AlNb-based alloys are indicated at a time. It is obvious that at a constant Nb content of 25 at.% the β_0 phase volume fraction is strongly influenced by the Al content in near-equilibrium microstructures. Approaching values of about 25 at.% leads to single phase alloys with little benefit for practical applications. Lower Al content also lowers the oxidation resistance. Reducing the Nb content below approximately 20 at.% at
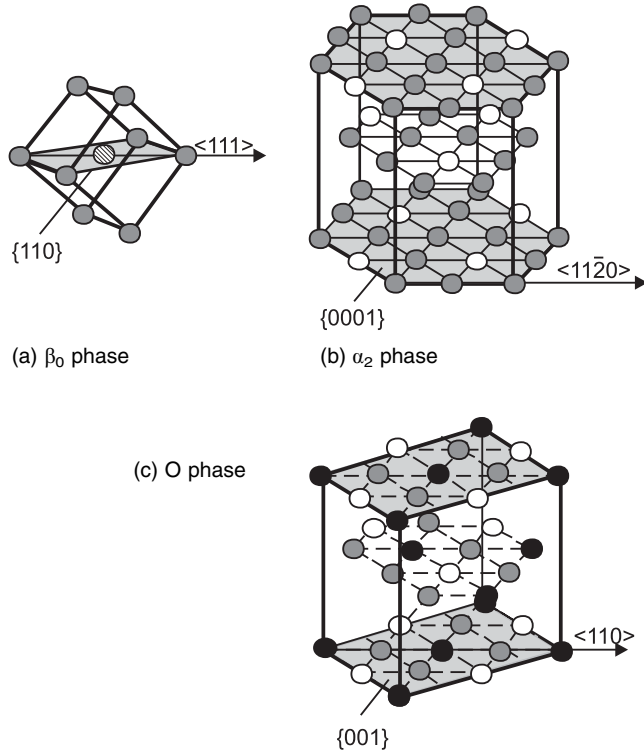
Fig. 3.1 Lattice representation of the (a) cubic β_0 phase, (b) α_2 Ti$_3$Al phase, and (c) the ordered orthorhombic O Ti$_2$AlNb phase.

Tab. 3.3 Phase compositions in Ti-22Al-25Nb in at.%.

Microstructure	β_0			α_2			O		
	Al	Nb	Ti	Al	Nb	Ti	Al	Nb	Ti
Single phase*	22.0	25.5	Bal	–	–	–	–	–	–
Two phase*	22.1	25.5	Bal	25.8	16.9	Bal	–	–	–
Three phase+	15.5	30.5	Bal	25.2	16.9	Bal	24.6	21.4	Bal

* Metastable structure, + near-equilibrium structure.

a constant Al level stabilizes the brittle α_2 Ti$_3$Al phase, while higher Nb content increases the density and is known to decrease the oxidation resistance [21]. Therefore, the best balance of properties for ternary orthorhombic aluminides can be expected in the range Ti-(22–23)Al-(25–26)Nb (at.%).

The Ti-25Al isopleth is shown in Fig. 3.2 b [22]. The β_0 transus temperature is in the range between 1050° to 1100 °C for most orthorhombic titanium alloys. The β to β_0 ordering temperature, T$_c$, was found to be about 1100–1130 °C for alloys contain-
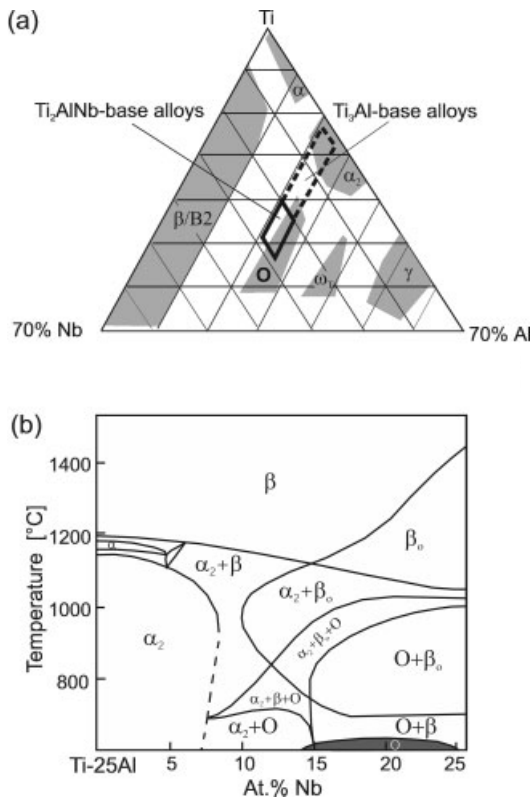
Fig. 3.2 (a) Partial isothermal section of the Ti-Al-Nb system at 700 °C [20], (b) an isopleth of the Ti-Al-Nb system at a constant 25Al at.% [22].

ing Nb in the range of 11 to 15 at.%, but appears to raise sharply for Nb concentrations above 20 at.% [19, 23–25]. For the orthorhombic alloy Ti-22Al-26Nb, the β to β_0 transition temperature has been determined to be above 1600 °C and it is thought that β_0 ordering may persist to near the melting temperature [26].

3.3
Properties of Orthorhombic Titanium Aluminides

Both the physical and mechanical properties are of interest in evaluation of the potential payoff for orthorhombic titanium aluminides in future aerospace systems. While the physical properties are predominantly determined by the chemistry, the mechanical properties are in addition strongly influenced by the microstructure.

3.3.1
Physical Properties

Due to the high amount of stabilizing β elements necessary to stabilize the O phase in orthorhombic titanium aluminides, the density is well above titanium and particularly γ TiAl alloys. However, the density of Ti-22Al-25Nb is still almost 40% below that of Ni-based alloys. Thus, the specific mechanical properties of orthorhombic titanium aluminides must outperform competing titanium-based alloys due to their higher density.

The specific Young's modulus is especially high for TiAl-based materials over a wide temperature range (Fig. 3.3a). Specific room temperature Young's moduli of orthorhombic titanium aluminides are within a narrow band including IN 718, near-α titanium alloys and Ti_3Al-based alloys. Above 500 °C, however, orthorhombic aluminides exhibit an advantage over disordered near-α titanium alloys in spite of their higher density. Investigations of the elastic properties of different titanium aluminides revealed a lower Young's and shear modulus of the O phase in comparison to the γ TiAl and $α_2$ Ti_3Al phases [27]. In combination with a Poisson's ratio of 0.3 for the O phase, it is concluded that this phase has weaker interatomic bonding and structural ordering and less directional bonding than the γ TiAl and $α_2$ Ti_3Al phases.

For high temperature structural applications in new jet engines, the coefficient of thermal expansion (CTE) is also an important parameter among the physical properties. Such properties are mainly determined by the inter-atomic bonding character and therefore by the chemistry, and to a lesser extent by microstructure, neglecting crystallographic texture. Fig. 3.3b shows the CTE values of the Ti_2AlNb-based alloy Ti-22Al-25Nb in comparison to a conventional near-α alloy (TIMETAL 834), a TiAl-based material (K5) and IN 718. Investigation of different Ti-Al-(Nb, V, Cr, Mo) alloys indicates that an increasing aluminum content causes higher CTE values, while increasing the content of high melting point elements, e.g. niobium, decreases the coefficient of thermal expansion. Therefore, orthorhombic titanium aluminides exhibit a lower coefficient of thermal expansion than conventional titanium alloys and especially γ TiAl alloys.

3.3.2
Microstructures

The microstructure of orthorhombic titanium aluminides can be varied in a wide range depending on processing methods and subsequent heat treatments [28]. For orthorhombic titanium aluminides the coarse microstructure of the as-cast ingot can be converted into a fine equiaxed microstructure by conventional high strain rate forging.

Based on a fine-grained, equiaxed microstructure resulting from recrystallization during hot working, homogeneous microstructures can be achieved by additional thermal treatments to develop the end properties of interest. Similar to conventional titanium alloys equiaxed, fine-grained lamellar (bimodal), and coarse-
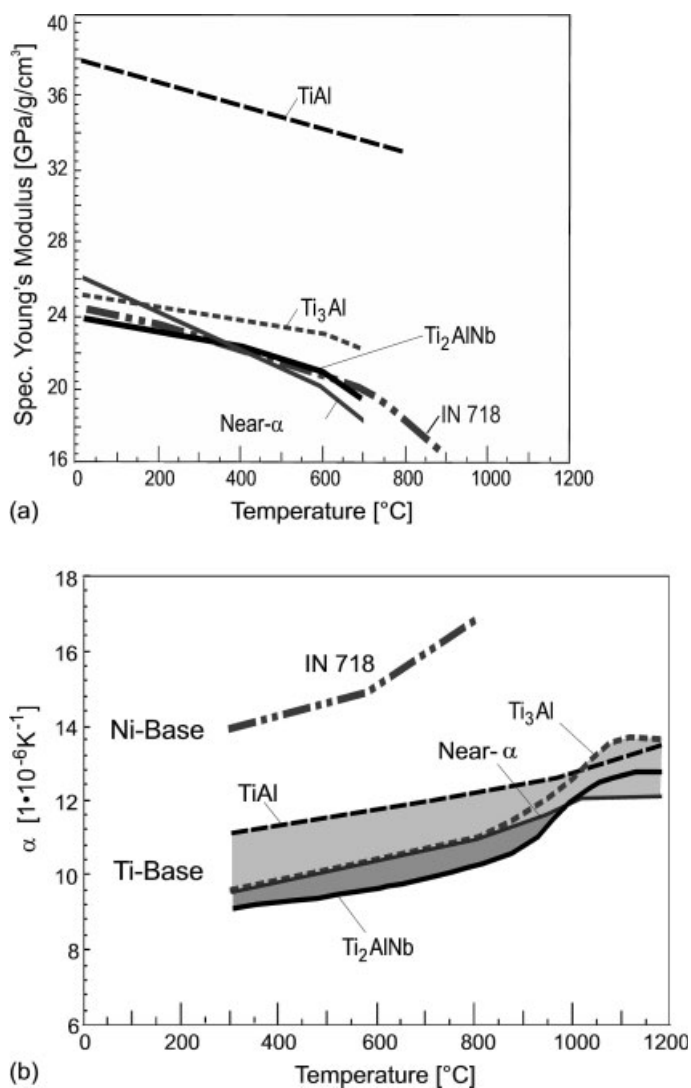
Fig. 3.3 Physical properties of a Ti_2AlNb-based alloy (Ti-22Al-25Nb), near-α titanium alloy (TIMETAL 834), TiAl-based alloy (Ti-46.5Al-3.0Nb-2.1Cr-0.2W) and nickel-based alloy (IN 718); (a) specific Young's modulus, (b) coefficient of thermal expansion (CTE).

grained lamellar microstructures can be obtained by appropriate thermomechanical processing (TMP). For practical applications at elevated temperatures of up to 700 °C, thermally stable microstructures are required. In addition, the achievable cooling rates in large components during thermal treatment are usually limited. Fig. 3.4 a–c shows three typical homogeneous microstructures of the orthorhombic alloy Ti-22Al-25Nb, which are thermally stable up to 700 °C, for long durations

(a)

(b)

(c)

(d)
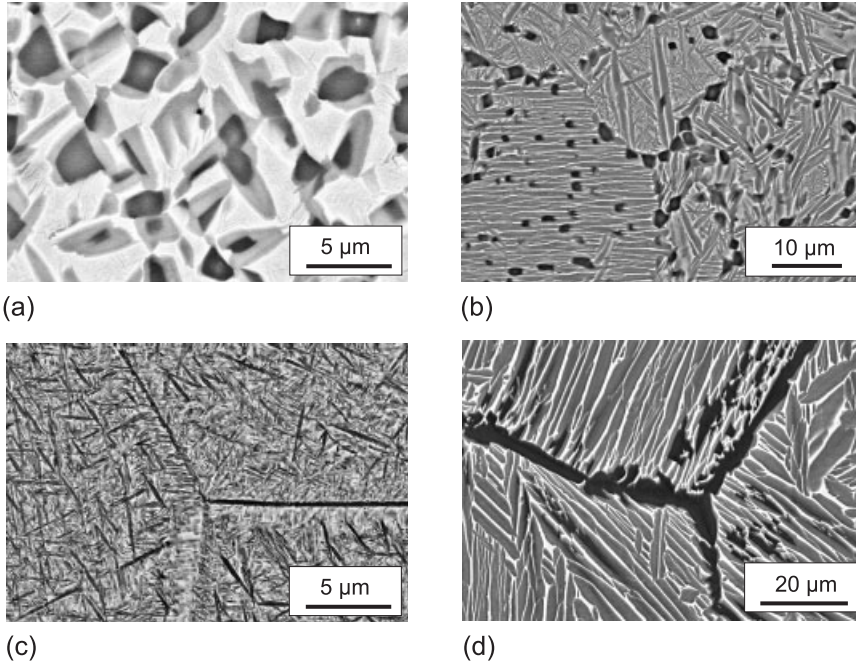
Fig. 3.4 Typical microstructures of an orthorhombic titanium aluminide alloy (Ti$_2$AlNb-based alloy Ti-22Al-25Nb, at.%) obtainable from hot-worked fully recrystallized material:

(a) equiaxed, (b) bimodal, (c) lamellar, (d) lamellar with coarse secondary O laths and thick grain-boundary α$_2$ phase.

and where the required TMP parameters appear to be transferable to large components. Due to cooling through the α$_2$ + β$_0$ phase field in conjunction with sluggish transformation kinetics described above, all microstructures shown in Fig. 3.4a–c exhibit a three-phase mixture. The average grain size of the selected microstructures ranges from 3 μm (equiaxed) to 30 μm (bimodal) up to 200 μm (coarse grained lamellar). In the case of the bimodal structure, primary α$_2$ particles hindered the grain growth of the β$_0$ phase during solution heat treatment at T$_β$-20 °C and are therefore often found along the grain boundaries. To effectively hinder β$_0$ phase grain growth near T$_β$, approximately 8 to 12 vol.-% of finely distributed α$_2$ particles are necessary. Slow cooling at a rate of 1 K/min and below from above the β transus leads to coarse secondary O laths within the former β$_0$ phase and the formation of a thick grain-boundary α$_2$ phase due to accelerated grain boundary diffusion vs. volume diffusion (Fig. 3.4d). However, this phase is known to be very detrimental to the mechanical properties of orthorhombic titanium aluminides.

3.3.3
Mechanical Properties

3.3.3.1 **Tensile Properties**

The most dominant strengthening mechanism in Ti_3Al-base alloys with a content of β-stabilizing elements in the range of 10–20% of Nb-equivalent was determined to be boundary strengthening by a Hall-Petch type of effect [18, 29, 30]. Thus, the greatest factor in strengthening of Alpha-2 alloys was determined to be the secondary α_2 lath size. The orthorhombic titanium aluminides with a Nb-equivalent between 21 and 27% (Tab. 3.2) represent the most versatile class of titanium aluminide alloys, similar to the class of conventional β titanium alloys containing relatively high amounts of β-stabilizing elements. Depending on microstructure, orthorhombic titanium aluminides offer a wide range of tensile properties. In the case of the simple ternary orthorhombic alloy Ti-22Al-25Nb, room temperature fracture elongation can be varied between 0 and 16%, while the yield strength can be as high 1600 MPa or reduced to 650 MPa (Fig. 3.5). This is a much wider range than can be obtained with γ TiAl or near-α titanium alloys. In contrast to these alloy classes, orthorhombic aluminides offer the possibility to produce very fine secondary laths with a width of 50 nm and below [31]. The high Nb content in orthorhombic alloys decelerates diffusion processes in the bulk material and leads to sluggish phase transformations. Thus, even relatively low cooling rates of only 10 K/min are sufficient to fully retain the high temperature β_0 phase. Subsequent low temperature aging can produce very fine secondary orthorhombic laths since the formation of the O phase from the supersaturated β_0 phase does not require long-range diffusion. However, such microstructures are not thermally stable at elevated temperatures. Microstructures which are thermally stable to 700 °C typically lead to room temperature yield strengths of up to 1100 MPa in Ti-22Al-25Nb (Fig. 3.4c). Other thermally stable microstructures such as fine-grained equiaxed or coarse-grained lamellar microstructures exhibit lower yield strengths in the range of 700 to 950 MPa (Fig. 3.4b, d).

With respect to fracture elongation, orthorhombic alloys show a special characteristic not found in any other titanium aluminide alloy. Only orthorhombic alloys enable a high room temperature ductility on the order of 13% with a coarse-grained lamellar microstructure. This clearly demonstrates the inherently higher ductility of the O phase in comparison to the α_2 phase. An important presumption, however, is a low strength within the transformed β/β_0 grains, i.e. coarse secondary orthorhombic lath size. Increasing the strength in a coarse-grained lamellar material by decreasing the lath size eventually leads to low-energy intergranular fracture, which is promoted by grain boundary precipitation of the α_2 phase (Fig. 3.4d). Thermomechanical treatments that reduce the grain boundary α_2 phase enable a concurrent increase in strength and ductility in orthorhombic alloys with a lamellar microstructure [31]. Other parameters essential for controlling ductility in orthorhombic alloys are the oxygen content and the amount of β_0 phase. Oxygen is a strong stabilizer of the brittle α_2 phase and thus significantly reduces elongation to failure for different microstructures if its content exceeds
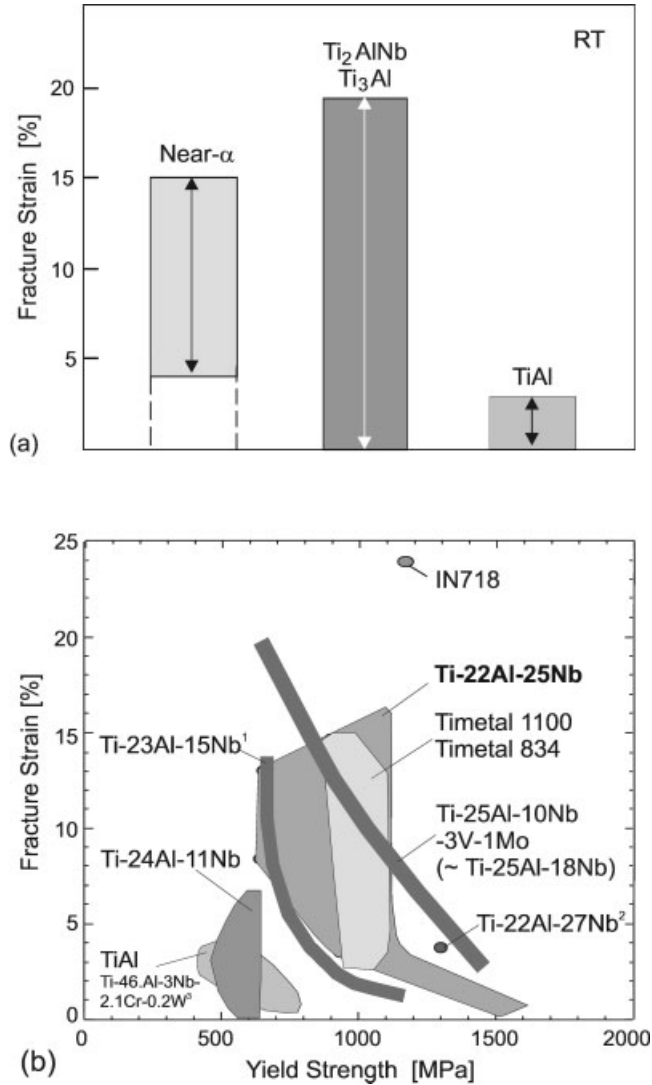
Fig. 3.5 Room temperature tensile properties of orthorhombic titanium aluminides (Ti$_2$AlNb) in comparison to near-α titanium, Ti$_3$Al-based, and TiAl-based alloys, (a) typical range of ductility for different microstructures, (b) fracture elongation vs. yield strength for different compositions and microstructures.

approximately 1000 ppm. A sufficient amount of ductile β$_0$ phase on the order of 15 volume percent is important to reduce stress concentration effects at interfaces. Crack initiation at O/O grain boundaries at low strain levels was obtained if the β$_0$ phase was not present at such locations having high strain incompatibilities [32]. The volume fraction of β$_0$ phase is controlled by processing and chemis-

try, predominantly by aluminum content. Thus, for thermally stable, near-equilibrium microstructures having adequate ductility, the aluminum content needs to remain below 25 at.%. In addition, data available today on tensile properties of ternary (Ti$_3$Al+Nb)- and Ti$_2$AlNb-based alloys also clearly indicate that fracture elongation and yield strength can be increased simultaneously by increasing Nb content between 11 and 27 at.% (Fig. 3.5 b). Finally, the product of fracture elongation and yield strength can be used as a measure of the quality of a specific material, since unfavorable microstructural features as described above or chemical inhomogeneities leading to brittle precipitates usually reduce fracture elongation and/or tensile strength. High strength and high fracture elongation at the same time require homogeneous microstructures, which significantly delay crack initiation during tensile testing. The best balance of room temperature tensile properties can be obtained with a bimodal microstructure in the orthorhombic alloy Ti-22Al-25Nb (Fig. 3.4 b). With such a microstructure yield strength values of 1100 MPa with a ductility of 4% can be obtained.

Results on the specific elevated temperature tensile strength of the orthorhombic alloy Ti-22Al-25Nb are shown in Fig. 3.6. In spite of its higher density, the simple ternary alloy Ti-22Al-25Nb reaches higher values in comparison to latest generation near-α titanium alloys. However, as mentioned above, the thermal stability of the microstructures need to be considered for long-term service at ele-
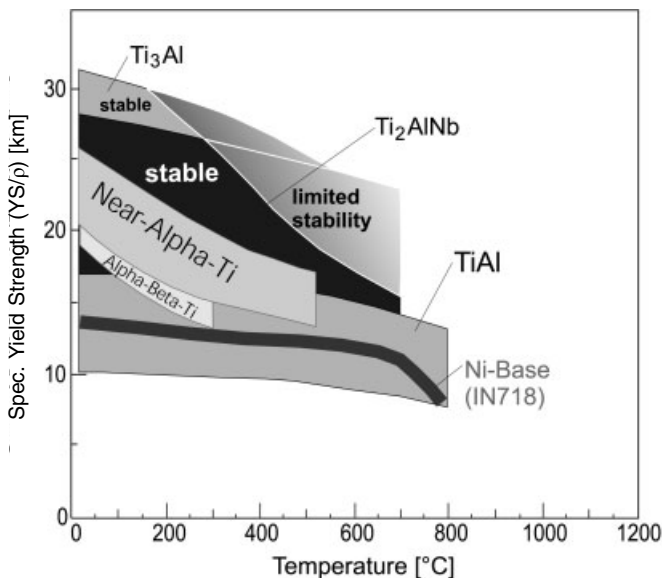
Fig. 3.6 Specific yield strength ranges as a function of temperature and microstructure for an orthorhombic titanium aluminide alloy (Ti$_2$AlNb, Ti-22Al-25Nb) in comparison to near-α titanium alloys (TIMETAL 834/1100), a Ti$_3$Al-based alloy (Ti-25Al-10Nb-3V-1Mo), a TiAl-based alloy (Ti-46.5Al-3.0Nb-2.1Cr-0.2W), and a nickel-based alloy (IN718).

vated temperatures. Allowing only thermally stable microstructures, as shown in Fig. 3.6, the Ti-22Al-25Nb alloy only achieves values a little above a third generation TiAl-base alloy (e.g. Ti-46.5Al-3.0Nb-2.1Cr-0.2W) on a density corrected basis [33, 34]. In addition, the maximum service temperature of orthorhombic alloys remains approximately 70–90 °C below the γ TiAl alloys. This is mainly due to environmental influences, which will be addressed in detail later.

3.3.3.2 Creep Behavior

Creep behavior of the orthorhombic titanium aluminides is strongly influenced by microstructure, where the basic trends are known from titanium alloys and other titanium aluminides. Extensive investigations have been performed on parameters influencing minimum creep rate, while the primary creep regime is less explored.

In the case of the Ti-22Al-25Nb alloy a fine-grained equiaxed microstructure leads to a high creep rate, while a coarse-grained lamellar microstructure reduces the minimum creep rate by two orders of magnitude (Fig. 3.7a). Based on the calculated apparent activation energies and creep exponents, grain boundary sliding was determined to be the dominant creep mechanism for the duplex material at 650 °C, while dislocation climb mechanisms control the creep deformation of lamellar Ti-22Al-25Nb between 200 and 400 MPa [35]. Studies on different orthorhombic alloys in comparison to Ti_3Al and conventional titanium base alloys showed that orthorhombic alloys exhibited the highest activation energies for grain-boundary diffusion and lattice self-diffusion, respectively [32]. Therefore, O alloys exhibit a lower minimum creep rate than conventional titanium alloys, independent of microstructure (Fig. 3.7b) [36]. In comparison to Ti_3Al-based alloys, Ti_2AlNb alloys still show an advantage as long as crystallographic texture hardening can be neglected and a high volume fraction of the O phase is present at testing temperature [35, 37]. At higher stress levels, where dislocation-controlled creep is dominant, the volume fraction of the O phase becomes important. With increasing volume fraction of O phase in the microstructure, higher creep resistance can be obtained [38]. In the low to intermediate stress regime, which is usually most important for practical applications, grain size appears to be more influential on minimum creep rate than phase composition, volume fraction, or morphology. Thus, when designing creep-limited applications with orthorhombic alloys, grain size needs special attention. However, the inherent ductility of the orthorhombic phase eases achievement of an adequate balance between room temperature ductility and creep resistance for Ti_2AlNb alloys in comparison to TiAl-based alloys. In addition, the minimum creep rate of Ti_2AlNb alloys can be improved significantly by partially substituting niobium with molybdenum [39].

However, it is important to note that the design of rotating components in engines often limits creep strains to below 0.4%. Such strains are typically attained within the primary creep regime of orthorhombic alloys, especially at higher stress levels [39]. In Ti_3Al-based alloys, and also in ($α_2$+O)-based alloys, the lamellar microstructure shows lower primary creep strains than equiaxed structures [18]. The same trend could also be obtained for the orthorhombic alloy Ti-22Al-25Nb. No dependence
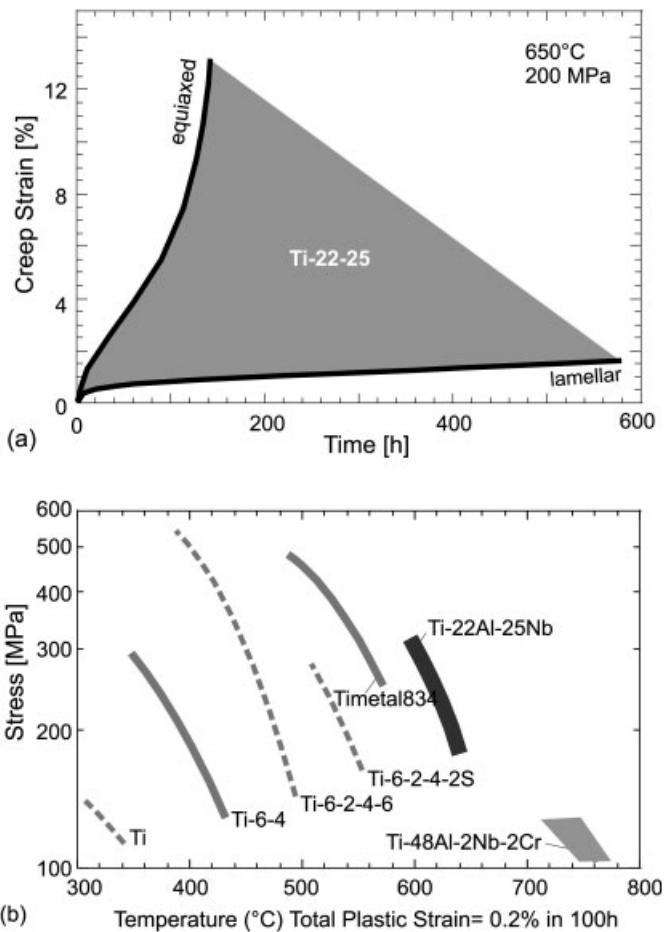
Fig. 3.7 Creep performance of the ternary orthorhombic alloy Ti-22Al-25Nb, (a) influence of microstructure on creep resistance, (b) temperature for total creep strain to 0.2% in 100 h in comparison to titanium base alloys [61] and the TiAl-based alloy Ti-48Al-2Nb-2Cr [62].

of primary creep strain on lath dimensions was observed in β heat-treated structures of Ti$_3$Al-base alloys [18, 40]. However, a beneficial effect on primary creep was obtained by adding a quaternary element, e.g. tungsten, to a Ti$_2$AlNb-based alloy [41].

3.3.3.3 Fatigue Strength, Crack Growth Behavior, and Fracture Toughness

The highest payoff for new high temperature titanium based materials in aviation can be expected in rotating components of jet engines, especially if the new material is able to replace the heavy nickel-based alloys in the hot section of the compressor. However, such components are fracture critical, i.e. failure of the compo-

nent must be guaranteed not to occur during the lifetime under extreme cyclic loading conditions. Therefore, high-cycle fatigue (HCF), low-cycle fatigue (LCF), crack growth, and fracture toughness need special attention in comparison to the well characterized materials used today.

HCF strength is determined by the material's resistance to crack nucleation, which again is associated with first dislocation movements. An increase in yield strength generally results in an increase in HCF strength as long as internal defects in the material can be kept small so as not to act as crack initiation sites. In this case the HCF strength of orthorhombic, near-α titanium, and TiAl-base alloys are expected to follow the respective yield strength. Comparing the relative yield strengths of these alloy classes in Fig. 3.6 with their respective HCF strengths in Fig. 3.8a supports this assertion. Internal defects, which can lead to early crack initiation during cyclic loading, and thus to lower HCF strength, are found to be the grain-boundary α_2 phase in lamellar microstructures and interfaces between α_2 particles in equiaxed microstructures [42]. Strain incompatibilities between the β phase and the α_2 phase cause local stress peaks and thus early crack initiation sites. Therefore, it is necessary to reduce or avoid primary α_2 conglomerates and continuous grain-boundary α_2 phase in order to increase the HCF strength of orthorhombic titanium aluminides. Thus, the optimum microstructure for HCF strength in orthorhombic alloys is a fine-grained bimodal material with a homogeneous distribution of primary α_2 and a minimum of grain boundary α_2 phase. Through these findings it is also obvious that a high chemical homogeneity of orthorhombic ingots is an important prerequisite to obtain reliably high HCF strength. Due to the slow diffusion rate of niobium, this requirement needs special attention during the manufacturing of Ti$_2$AlNb-based alloys [31].

Ordered alloys are known to work-harden much faster than their disordered counterparts [43]. This phenomenon can contribute quite significantly to the HCF strength of titanium aluminides. Fig. 3.8b provides the fatigue strength values shown in Fig. 3.8a normalized by the individual yield strengths of the different materials. TiAl-based alloys reach HCF strength values on the order of 100% of their yield strength below the brittle to ductile transition temperature, which is attributed to a pronounced cyclic hardening effect [33]. Disordered conventional near-α titanium alloys typically achieve a ratio of room temperature HCF strength to yield strength at 10^7 cycles of about 0.56–0.66. The respective ratio of the orthorhombic titanium aluminide alloy Ti-22Al-23Nb, however, is about 0.7–0.8 depending on microstructure [42], and thus bridges the gap between disordered titanium and TiAl-based alloys. The stronger directional atomic bonding in TiAl-based alloys gives the material a limited plastic deformability, but also causes the phenomenon of an essentially constant fatigue strength up to 600 °C [33]. In the case of the orthorhombic alloy Ti-22Al-23Nb, however, the high temperature HCF strength at 540 °C is decreased by 15–20%, depending on microstructure [42].

During low cycle fatigue (LCF), crack propagation becomes an important issue in addition to crack initiation. The ranges of room temperature fatigue crack propagation rates for different microstructures are shown in Fig. 3.9a for two orthorhombic alloys, a near-α titanium alloy, and a TiAl-based alloy. The crack growth
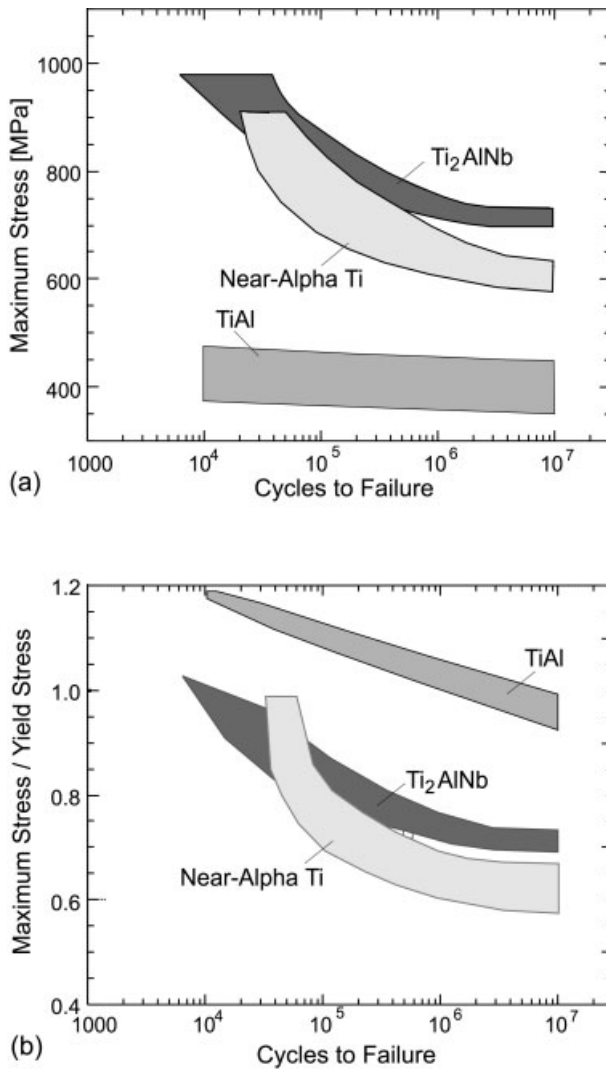
Fig. 3.8 Constant-load-controlled fatigue behavior of Ti-22Al-23Nb
(Ti_2AlNb, [42]), Ti-46.5Al-3.0Nb-2.1Cr-0.2W (TiAl, [44]), and TIME-
TAL 834 (near-α titanium [50, 63]) at room temperature (R=0.1),
(a) maximum stress vs. cycles, (b) maximum stress normalized by
the yield stress of the individual alloy vs. cycles.

rates of the orthorhombic alloys are in between the TiAl-based alloy and the con-
ventional near-α titanium alloy. The lower crack-growth resistance of the orthor-
hombic alloys in comparison to the near-α titanium alloy may contribute to the
decreasing difference with respect to fatigue strength in the LCF regime between
the orthorhombic alloy Ti-22Al-23Nb and the near-α titanium alloy (Fig. 3.8a).
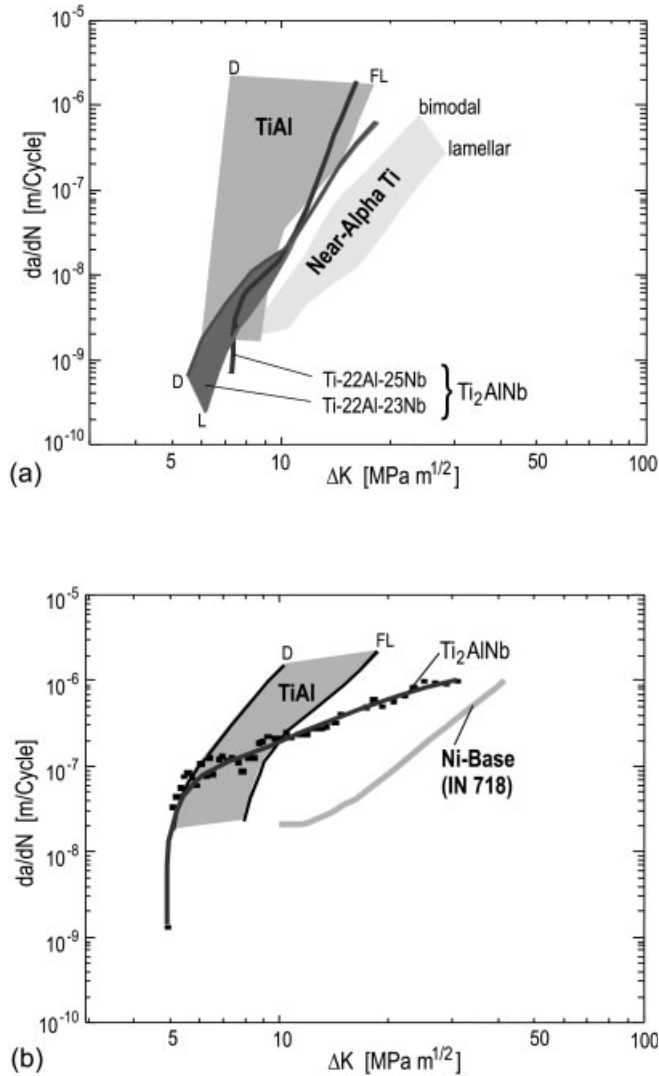
Fig. 3.9 Fatigue crack growth behavior of the Ti_2AlNb-base alloys Ti-22Al-25Nb and Ti-22Al-23Nb [42]), Ti-46.5Al-3.0Nb-2.1Cr-0.2W (TiAl, [44]), and TIMETAL 834 (near-α titanium [63]), (a) room temperature, (b) 650 °C (IN 718 [64]).

The orthorhombic alloys with a lamellar microstructure show lower crack growth rates in the near-threshold region than with an equiaxed microstructure tested at room temperature in air. However, in the high growth rate regime, no significant influence of microstructure was found. This general trend is also confirmed if crack closure effects are considered [42]. Increasing the temperature to 650 °C significantly increases the crack growth resistance of the orthorhombic al-

loy Ti-22Al-25Nb in comparison to the TiAl-based alloy (Fig. 3.9b). The increased ductility of the orthorhombic alloy at 650 °C reduces stress peaks at the crack tip, which improves the crack growth resistance. However, 650 °C is below the brittle-to-ductile transition temperature of the TiAl-based alloy, providing an explanation why the fatigue crack growth behavior does not change significantly in this temperature regime [44]. Therefore, in the intermediate temperature regime of 500–700 °C, orthorhombic alloys exhibit a good fatigue crack growth resistance when tested at higher frequencies. At lower frequencies (e.g. 1 Hz), however, environmentally-assisted crack growth appears to degrade the cyclic properties of the orthorhombic alloy [45]. It is also important to consider at this point that the fatigue crack growth behavior of a material has a strong influence on the life-prediction methods required. The relatively poor crack-growth resistance of TiAl-based alloys most probably requires new design approaches if high-risk components in jet engines are to be realized with this class of material [46]. Whether orthorhombic alloys, however, will enable use of conventional design approaches based on its crack growth behavior will therefore very much depend on the loading condition, and especially on the extent of environmental impact on the cyclic properties. Since the environmentally-assisted degradation of the mechanical properties, and especially LCF strength, is a key concern for all high temperature titanium base materials, this issue will be addressed in a separate chapter.

The influence of microstructure on room temperature fracture toughness is shown in Fig. 3.10a for the orthorhombic alloy Ti-22Al-25Nb. Depending on microstructure, toughness values vary between 10 and 30 MPa $m^{1/2}$. The lowest fracture toughness values result from equiaxed microstructures, while coarse-grained lamellar microstructures can lead to low or high fracture toughness values depending on colony size within the transformed β_0 phase, e.g. the size of the secondary O laths. Fractography revealed that coarse secondary O laths lead to a rough and tortuous crack path. The same trend can be obtained for bimodal microstructures with fine or coarse secondary O laths. Thus, it appears that the interfaces in the transformed β_0 phase, rather than grain size, predominantly control fracture toughness in orthorhombic alloys. It can be assumed that this behavior is a result of crack deflection between differently oriented orthorhombic colonies, i.e. large aligned packets with an O/β_0 lath structure. Such a behavior has been shown for Ti_3Al-based and near-α titanium alloys [47–49].

The room temperature fracture toughness versus yield strength for different microstructures of the orthorhombic alloy Ti-22Al-25Nb are shown in Fig. 3.10b in comparison to a TiAl-base, Ti_3Al-based, and a near-α titanium alloy. It is important to note, that only microstructures resulting in a room temperature ductility above 1% were considered. This is an important limitation since for Ti_3Al- and TiAl-based alloys a ductility-toughness inverse relationship exists at lower temperatures [34, 47]. Microstructural features leading to high strength, i.e. fine grain or fine secondary lath size, yield improved tensile properties but low fracture toughness. In the Ti_3Al-based alloy Ti-25Al-10Nb-3V-1Mo fracture toughness values up to 50 MPa $m^{1/2}$ can be obtained with a microstructure resulting in zero room temperature ductility during tensile testing. Since a minimum ductility is necessary
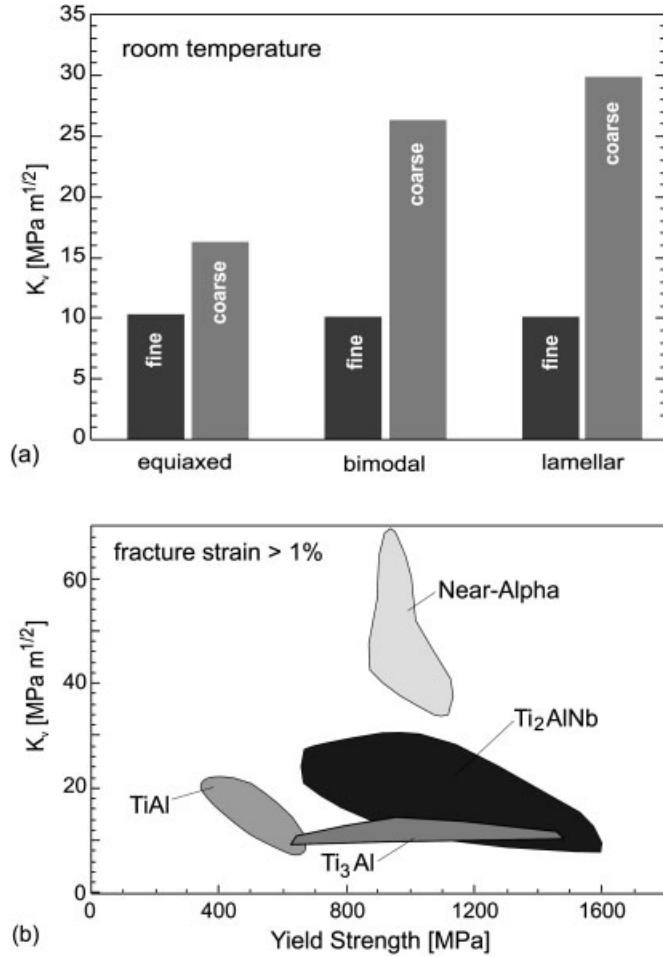
Fig. 3.10 (a) Variation of fracture toughness (K_v, Chevron specimens) of the Ti_2AlNb-based alloy Ti-22Al-25Nb with microstructure at room temperature, (b) K_v vs. yield strength for Ti-22Al-25Nb (Ti_2AlNb), Ti-25Al-10Nb-3V-1Mo (Ti_3Al), Ti-46.5Al-3.0Nb-2.1Cr-0.2W (γ TiAl, [34]), and TIMETAL 1100 (near-α alloy). Note that only microstructures of the individual materials are considered, which lead to more than 1% fracture elongation at room temperature.

for most applications, Fig. 3.10b gives a ranking of the strength-toughness capabilities of the different titanium-based alloy classes. Therefore, a simple orthorhombic alloy like Ti-22Al-25Nb does not achieve the same fracture toughness level as conventional near-α titanium alloys, but clearly demonstrates the highest room temperature strength-toughness-ductility combination of all titanium aluminides.

3.4
Oxidation and Environmental Embrittlement

Environmental degradation of the mechanical loading capabilities of high temperature titanium alloys is primarily a result of oxidation or subsurface embrittlement by dissolution of interstitials from the atmosphere. The second mechanism is usually named "environmental embrittlement". Oxidation and environmental embrittlement can become life limiting for many titanium-based alloys significantly below a maximum temperature where the mechanical properties still meet specific component requirements. The maximum service temperature of the latest generation near-α alloys in jet engines is about 520 °C, although their mechanical loading capabilities for such applications would be sufficient up to 600 °C [50]. A detailed description of the oxidation behavior and ways to improve the oxidation resistance of titanium alloys and titanium aluminides are given in Chapter 6. In the following, the specific characteristics of oxidation and embrittlement of orthorhombic titanium aluminides will be addressed and related to that of other titanium-based materials.

Since the impact of environment on mechanical properties increases with temperature, this issue is especially important for titanium aluminides designed for service temperatures between 500 °C and 800 °C. Severe environmental degradation of mechanical properties at temperature as low as 550 °C presented one major barrier for implementation of Ti_3Al-base alloys [1, 17, 18]. Thus, orthorhombic titanium aluminides will only be considered for practical high temperature applications if they succeed to demonstrate to be less susceptible to environmental influences than Ti_3Al and near-α titanium base alloys between 500 and 700 °C. Obviously, the availability of protective coatings would require a reassessment of the service temperature potential of the different alloy classes [6].

As described in more detail in Chapter 6, like for all titanium-based alloys, aluminum is the primary element controlling oxidation of orthorhombic alloys. Increasing the aluminum content from about 10 at.% in conventional near-α alloys to about 46 at.% in TiAl-based alloys increases the volume fraction of the protective alumina (Al_2O_3) in the oxide scale and thus leads to reduced oxidation rates. Fig. 3.11 shows typical isothermal oxidation mass gain vs. time curves for near-α, Ti_3Al, and TiAl-based alloys tested at 800 °C. Notably, the γ TiAl alloy tested was a second generation material whose oxidation resistance is far lower than that of latest generation γ titanium aluminides. In this comparison, after short-term exposure at 800 °C, orthorhombic alloys fall in the range of $α_2$ Ti_3Al for Ti-20Al-25Nb [51], in the range of γ TiAl alloys for Ti-22Al-25Nb [52] and even below that for more complex alloys such as Ti-22Al-21Nb-2Ta-0.5Si [51].

Adding niobium to Ti_3Al not only improves the mechanical properties but also the oxidation resistance [14]. However, a maximum in the oxidation resistance of ternary Ti_3Al+Nb alloys is obtained at about 11 at.% [21]. This observation contributed to the definition of the well known Ti_3Al-base alloy Ti-24Al-11Nb, which was the first alloy of this class showing a more balanced profile between room and elevated temperature properties. Increasing the niobium content further decreases
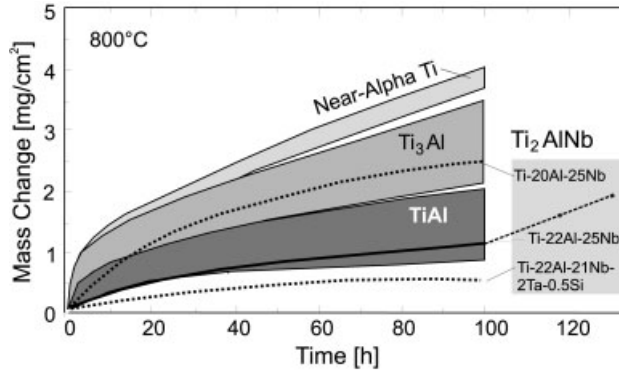
Fig. 3.11 Isothermal oxidation resistance of different Ti$_2$AlNb-based alloys relative to TiAl, Ti$_3$Al, and near-α titanium alloys [21, 34, 51, 52, 54].

the oxidation resistance; however, it still remains higher than for binary Ti$_3$Al [21]. In the orthorhombic regime of ternary Ti-Al-Nb alloys, the alloy Ti-25Al-21Nb was found to exhibit the highest oxidation resistance [51]. Additions of Ta, Mo, and Si to Ti-22Al-21Nb were also found to improve oxidation. However, there is no general agreement on the beneficial effect of Mo and Si. While Ta appears to reduce the oxidation rate of orthorhombic titanium aluminides, Mo and Si have no effect on the scale growth rate [53]. Obviously, the optimum chemistry for maximum oxidation resistance of orthorhombic titanium aluminides has yet to be explored.

Moreover, long-term oxidation resistance of orthorhombic alloys has not yet been investigated in great detail. For example, Ti-22Al-25Nb undergoes breakaway oxidation after 100 h exposure to air at 800 °C, which leads to unacceptably high oxidation rates [21, 54] such that the maximum service temperature of this alloy is below 650 °C [21]. The major issue for simple ternary orthorhombic alloys [54] and even more complex chemistries [53] is their inability to form stable protective alumina scales. The high Nb content in the alloy leads to formation of non-protective, Nb-rich oxides such as AlNbO$_4$. Even though alumina forms along with titania, usually no continuous alumina scale is found on these alloys [54]. While more complex orthorhombic alloys such as Ti-22Al-20Nb-Ta-1Mo do not show such a transition up to 500 h [55], the useful service temperature range of simple ternary orthorhombic alloys seems to be limited to below 700 °C. Protective coatings might expand the temperature limit substantially [56, 57].

In contrast to the results for isothermal oxidation experiments described above, thermal cyclic testing provides results more relevant to practical use of the alloys (Fig. 3.12). Under thermal cyclic conditions, the orthorhombic alloy Ti-22Al-25Nb exhibits similar behavior to the conventional near-α alloy TIMETAL 834. While mass change curves are in the same range during the first few hundred hours of exposure, adhesion of the oxide scale is obviously better for Ti-22Al-25Nb than

TIMETAL 834; on the latter, the oxide scale started to spall off after roughly 300 h of exposure. On Ti-22Al-25Nb spallation occurred after approximately 700 thermal cycles, characterized by rapid loss of major parts of the oxide scale. Unlike the orthorhombic and conventional alloys, mass gain of second and third generation γ TiAl alloys (Ti-48Al-2Cr-2Nb and Ti-45Al-8Nb) is low and adhesion of the oxide scale is excellent up to 1000 cycles with no sign of scale spallation. Obviously, the oxidation rate alone is not sufficient to select a material for high temperature use. However, for the orthorhombic titanium aluminides, rapid oxidation especially on thermal cycling requires careful consideration at temperatures exceeding approximately 650 °C for this class of alloys. Furthermore, environmental embrittlement plays a major role with regard to the mechanical properties of the material. Similar to Ti$_3$Al-based alloys, orthorhombic Ti$_2$AlNb alloys suffer from large hardening of the subsurface zone, while for γ TiAl alloys this phenomenon is observed at a much smaller extent [58].

For near-α, Ti$_3$Al-based, and TiAl-based alloys it is known that the fatigue and fatigue crack growth crack growth behavior is very sensitive to environmental embrittlement. In all these alloy classes, embrittlement has been shown to become a significant problem for higher strain range applications at temperatures as low as 100–200 °C below the temperature level where oxidation behavior becomes a limiting factor [45, 51, 55, 59]. This kind of embrittlement can also be found in orthorhombic alloys and can be monitored by using microhardness profiling methods [52, 54, 55]. Fig. 3.13 shows such a profile for the alloy Ti-22Al-25Nb after aging at 900 °C for 500 h. The subsurface zone beneath the oxide scale shows higher microhardness values and exhibits a brittle fracture morphology, while the fracture
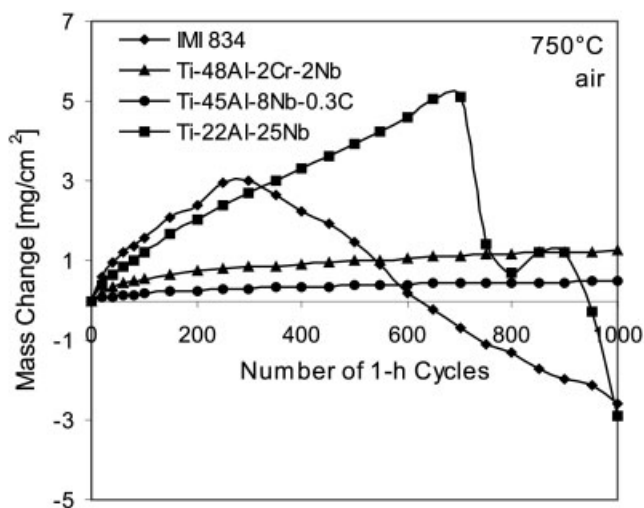
Fig. 3.12 Cyclic oxidation behavior of orthorhombic alloy Ti-22Al-25Nb compared to near-α alloy TIMETAL 834 as well as γ TiAl alloys Ti-48Al-2Cr-2Nb (2nd generation) and Ti-45Al-8Nb (3rd generation).

surface of the unaffected material indicates a ductile failure mode. The depth of embrittlement was found to be two times higher in a near-α titanium alloy in comparison to the orthorhombic alloy Ti-22Al-25Nb after aging at 650 °C for 500 h, indicating that diffusion is slowed in the ordered alloy [52]. The main sources of embrittlement of the subsurface zone after long-term aging were determined to be oxygen and nitrogen penetration, which can be dissolved interstitially or form brittle phases [54, 55]. However, the mechanism of dynamic embrittlement where a zone ahead of an advancing crack is embrittled within a very short period of time appears to be a result of hydrogen sweeping into the slip planes of titanium phases [17, 59]. In this case the hydrogen is released by dissociation processes of moisture in the environment near freshly formed active metal surfaces.

In this context it is important to note that there is no simple correlation between oxidation rate and environmental embrittlement for titanium aluminides [55]. Extensive investigations of different orthorhombic alloys revealed constant embrittlement rates in spite of very different oxidation rates [51]. Therefore, the impact of static and dynamic environmental embrittlement is a major issue for evaluating the high temperature capabilities of orthorhombic alloys. Fatigue studies, especially in the high strain range regime (LCF), can be expected to be very sensitive to environmental embrittlement [50].

Fig. 3.14 shows the impact of environmental embrittlement on the fatigue behavior for the orthorhombic alloy Ti-22Al-25Nb (Fig. 3.14a) in comparison to the conventional high-temperature titanium alloy TIMETAL 834 (Fig. 3.14b). Polished specimens were aged at 600 °C between 10 and 1000 h and tested afterwards at room temperature by total strain control ($R_e = \varepsilon_{min}/\varepsilon_{max} = 0$). The aging treatment after 600 °C/1000 h led to an embrittled subsurface zone with a thickness of 50 µm and 15–20 µm for TIMETAL 834 and Ti-22Al-25Nb, respectively. The reference curve was determined with polished specimens without any further treatment. Both materials were tested with a bimodal microstructure, which did not change during aging. In both cases it is obvious that the impact of the brittle subsurface zone increases with strain amplitude. Therefore, a minimum or critical
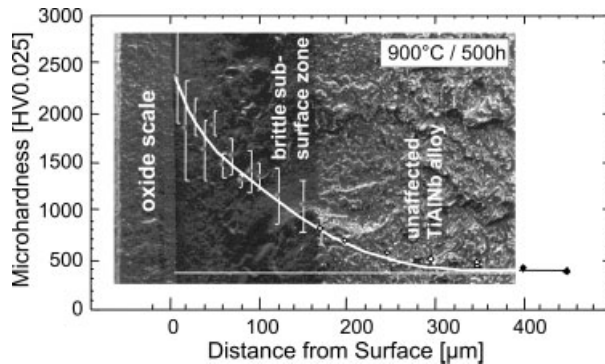
Fig. 3.13 Microhardness profile of Ti-22Al-25Nb after 500 h exposure to air and corresponding fracture surface.
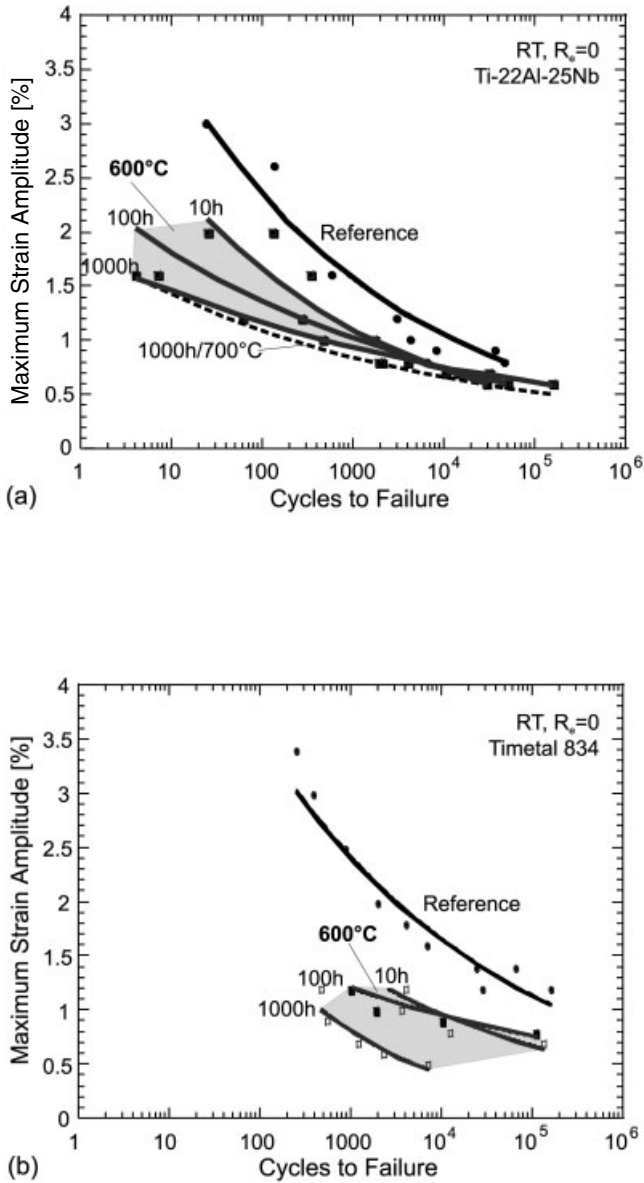
Fig. 3.14 Effect of environmental embrittlement during exposure at 600 °C in air on low-cycle fatigue strength of (a) Ti-22Al-25Nb (Ti$_2$AlNb) and (b) TIMETAL 834 (near-α alloy) (constant-load-controlled fatigue tests with R$_e$=0, f=0.33 Hz).
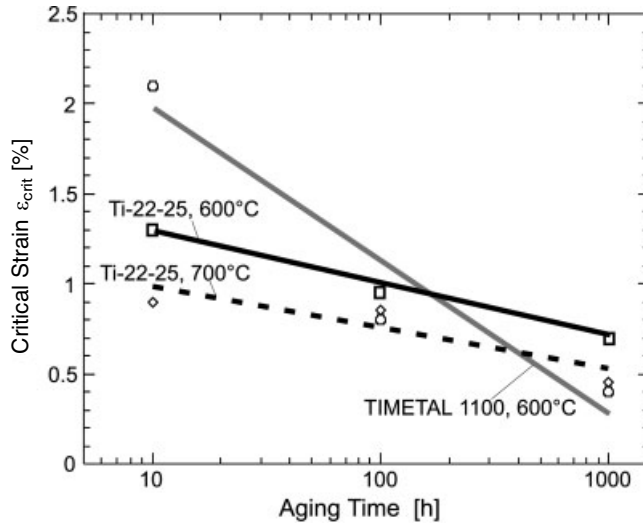
Fig. 3.15 Critical strain to crack initiation (ε_{crit}) at the surface after exposure at 600 °C up to 1000 h for Ti-22Al-25Nb (Ti$_2$AlNb) and TIME-TAL 1100 (near-α alloy).

strain exists to initiate a surface crack and finally degrade the fatigue properties. This critical stress was determined with stepped tensile tests with polished specimens, which were observed *in situ* with a microscope. Fig. 3.15 shows that the critical strain for initiating surface cracks decreases from 1.3% to 0.7% for Ti-22Al-25Nb for aging times between 10 and 1000 h at 600 °C. The critical strain to crack initiation appears to follow a parabolic law, indicating that a diffusion-controlled mechanism determines the depth of the embrittled zone and thus the strain to crack initiation. Increasing the temperature to 700 °C shifts ε_{crit} to lower values. The corresponding line of the near-α titanium alloy is much steeper and ε_{crit} decreases from 2.1% to 0.4% after aging at 600 °C. The more rapid growth rate of the brittle subsurface zone in the disordered near-α titanium alloy coincides with the more pronounced embrittlement effect after long-term aging in comparison to the orthorhombic titanium aluminide alloy Ti-22Al-25Nb. Even after aging at 700 °C for 1000 h, the orthorhombic alloy did not fail up to strain amplitudes of 0.5% and 10^5 cycles (Fig. 3.14 a). This is a significant improvement in comparison to the latest generation near-α titanium alloy, where cracks initiate during the first cycle at a maximum strain amplitude of only 0.4% after aging at 600 °C for 1000 h. Also, the impact of environmental embrittlement on low-cycle fatigue behavior of a TiAl alloy appears to be at least comparable to the orthorhombic material [60]. Compared to tests in vacuum, constant strain rate low cycle fatigue tests (R = 0.1) in air of the γ TiAl alloy Ti-47Al-2Nb2Mn + 0.8 vol.% TiB$_2$ resulted in a 95% reduction in the maximum number of cycles to failure at temperatures as low as 600 °C.

Tab. 3.4 Properties of orthorhombic titanium aluminides vs. advanced high temperature titanium alloys and Ni-base alloys.

	Near-α Ti (e.g. TIMETAL 834)	Orthorhombic Ti$_2$AlNb	γ TiAl	Ni-based (e.g. IN 718)
Density	+	+/−	++	−
HT spec. Young's modulus	+/−	+	++	+
Coefficient of thermal expansion	+/−	+	−	−
RT ductility	++	++	−	+
Formability	+	+	−	+
Specific HT tensile strength	−	+	+/−	−
Creep resistance	−	+	+	++
Specific RT-HCF strength	+	+	−	+/−
RT crack growth	+	+/−	−	+
RT crack growth threshold	+	+/−	+/−	+/−
RT fracture toughness	+	+/−	−	++
Oxidation resistance	−	+	+	++
HT embrittlement (Thickness of brittle subsurface zone)	−	+/−	+	
Embrittlement & RT fatigue	−	+/−	+	+

However, further investigation is necessary to quantify the high temperature capability of orthorhombic alloys considering the issue of environmental embrittlement. In addition, dynamic environmental embrittlement needs more attention during crack growth experiments in different environments in order to give more detailed understanding of the embrittlement effect in ordered and disordered high temperature titanium-based alloys.

3.5
Concluding Remarks

Orthorhombic titanium aluminides based on the intermetallic compound Ti$_2$AlNb emerged in the early 1990's out of the group of titanium aluminides. Despite its less mature development in comparison to other high temperature titanium-based materials, existing orthorhombic alloys offer a balanced set of room and elevated temperature properties. Thus, Ti$_2$AlNb-based alloys show high room temperature ductility as well as good formability, high specific elevated temperature tensile and fatigue strength, reasonable room temperature fracture toughness and crack growth behavior, good creep, and moderate oxidation resistance combined with a low coefficient of thermal expansion. From Tab. 3.3 it is obvious that orthorhombic titanium aluminides show a well-balanced property profile without significant drawbacks. With the development of more complex orthorhombic alloys, more improvements can be expected.

With respect to elevated temperature application, embrittlement rather than oxidation is the most important environmental concern for orthorhombic titanium aluminides. However, the impact of environmental effects on high strain range fatigue properties (LCF) is less pronounced than in conventional near-α titanium alloys and at least comparable to γ TiAl-based alloys. The maximum service temperature of orthorhombic alloys is expected to be 50–90 °C below γ based alloys, mainly due to a less pronounced strength retention capability with increasing temperature. When considering orthorhombic titanium aluminides for potential applications, their attractive properties are counterbalanced with higher material (Nb) and machining costs. However, in order to develop a damage tolerant, lightweight, high-temperature material, the orthorhombic titanium aluminides provide progress in the right direction.

3.6
Referenced Literature and Further Reading

1   J. C. Williams: Intermetallics for Structural Applications: Potential, Reality and the Road Ahead, in ISSI – Structural Intermetallics, TMS, Warrendale, PA. (1997).

2   J. Kumpfert, M. Peters, U. Schulz and W. A. Kaysser: Advanced Material and Coatings for Future Gas Turbine Technology, in Gas Turbine Operation and Technology for Land, Sea and Air Propulsion and Power Systems, Canada Communication Group Inc., St. Joseph Corporation Company, Canada (1999).

3   J. Kumpfert, R. Leucht, J. Hemptenmacher and H. J. Dudek: Effects of Matrix Properties on TMC Properties, in ECCM-7, The Institute of Materials, London, UK (1996).

4   C. Leyens, M. Peters, D. Weinem and W. A. Kaysser: Influence of Long-Term Annealing on Tensile Properties and Fracture of Near-α Titanium Alloy Ti-6Al-2.75Sn-4Zr-0.40Mo-0.45Si, Metallurgical and Materials Transactions, **27A**, (1996) 1709–1717.

5   C. Leyens, K.-H. Trautmann, M. Peters and W. A. Kaysser: Influence of Intermetallic Ti-Al Coatings on the Fatigue Properties of TIMETAL 1100, Scripta Materialia, **36**(11) (1997) 1309–1314.

6   C. Leyens, M. Peters and W. A. Kaysser: Oxidation-resistant coatings for application on high-temperature titanium alloys in aeroengines, Advanced Engineering Materials, **2**(5) (2000) 265-269.

7   F. Appel, U. Brossmann, U. Christoph, S. Eggert, P. Janschek, U. Lorenz, J. Müllauer, M. Oehring and J. D. H. Paul: Recent Progress in the Development of Gamma Titanium Aluminide Alloys, Advanced Engineering Materials, **2**(11), (2000) 699-720.

8   Y.-W. Kim: Gamma Titanium Aluminides: Their Status and Future, JOM, **47**(7) (1995) 39-41.

9   D. Banerjee, A. K. Gogia, T. K. Nandy and K. Muraleedharan: The physical metallurgy of Ti₃Al based alloys, in ISSI-Structural Intermetallics, TMS, Warrendale, PA, USA (1993).

10 D. Banerjee, A. K. Gogia, T. K. Nandy and V. A. Joshi: A new ordered orthorhombic phase in a Ti₃Al-Nb alloy, Acta Metallurgica et Materialia, **36**(4) (1988) 871-882.

11 D. Banerjee, R. G. Rowe and E. L. Hall: Deformation of the Orthorhombic Phase in Ti-Al-Nb Alloys, in High Temperature Ordered Intermetallic Alloys IV, MRS, Pittsburgh, PA, USA (1991).

12 R. G. Rowe: Recent Developments in Ti-Al-Nb Titanium Aluminide Alloys, in High Temperature Aluminides & Intermetallics, TMS, Warrendale, PA, USA (1990)

13 R. G. Rowe, D. G. Konitzer, A. P. Wood-field and J. C. Chesnutt: Tensile and Creep Behavior of Ordered Orthorhombic Ti$_2$AlNb-Based Alloys, in High-Temperature Ordered Intermetallic Alloys IV, MRS, Pittsburgh, PA, USA (1991).

14 M. J. Blackburn, D. L. Ruckle and C. E. Bevan: Research to Conduct an Exploratory Experimental and Analytical Investigation of Alloys, AFWAL, Wright-Patterson AFB, OH, USA (1978).

15 M. J. Blackburn and M. P. Smith: R&D on Composition and Processing of Titanium Aluminide Alloys for Turbine Engines, AFWAL, Wright-Patterson AFB, OH, USA (1982).

16 J. Kumpfert and C. H. Ward: Titanium Aluminides, in Advanced Aerospace Materials, H. Buhl (ed), Springer Verlag, Berlin (1992) 73–83.

17 C. H. Ward, J. C. Williams and A. W. Thompson: Dynamic Environmental Embrittlement of an α$_2$ Titanium Aluminide, Scripta Metallurgica et Materialia, **28** (1993) 1017–1021.

18 J. Kumpfert: Gefügemodellierung, Textur und mechanische Eigenschaften von Ti3Al-Basislegierungen, Vol. Reihe 5, Nr. 400, VDI Verlag GmbH, Düsseldorf, (1995) 187.

19 H. T. Kestner-Weykamp, C. H. Ward, T. F. Broderick and M. J. Kaufman: Microstructure and phase relationships in the Ti$_3$Al+Nb system, Scripta Metallurgica et Materialia, **23** (1989) 1697–1702.

20 L. A. Bendersky: Ternary intermetallic phases in Ti-Al-Nb system and microstructure of the Ti-30Al-20Nb (at%) alloy based on their coexistence, in 3rd International SAMPE Metals Conference, SAMPE, Covina, CA, USA (1993).

21 C. Leyens and H. Gedanitz: Long-term Oxidation of Orthorhombic Alloy Ti-22Al-25Nb in Air Between 650 and 800 °C, Scripta Materialia, **41**(8) (1999) 901–906.

22 P. K. Sagar and Y. V. R. K. Prasad: Hot Deformation and Microstructural Evolution in an α$_2$/O Titanium Aluminide Alloy Ti-25Al-15Nb, Z. Metallkd., **89** (1998) 433–441.

23 K. Muraleedharan, T. K. Nandy, D. Banerjee and S. Lele: Transformations in a Ti-24Al-15Nb Alloy: Part II, A Composition Invariant β$_0$/O Transformation. Metallurgical Transactions A, **23A** (1992) 417–431.

24 R. Strychor, J. C. Williams and W. A. Soffa: Phase Transformations and Modulated Microstructures in Ti-Al-Nb Alloys, Metallurgical Transactions A, **19A** (1988) 225–234.

25 L. A. Bendersky and W. J. Boettinger: Phase Transformations in the (Ti, Al)$_3$ Nb Section of the Ti-Al-Nb System-II, Experimental TEM Study of Microstructures, Acta Metallurgica et Materialia, **42**(7) (1994) 2337–2352.

26 V. K. Vasudevan, J. Yang and A. P. Woodfield: On the β to B2 Ordering Temperature in a Ti-22Al-26Nb Orthorhombic Titanium Aluminide, Scripta Materialia, **15**(9) (1996) 1033–1039.

27 F. Chu, T. E. Mitchell, B. Majumdar, D. Miracle, T. K. Nandy and D. Banerjee: Elastic properties of the O phase in Ti-Al-Nb alloys, Intermetallics, **5** (1997) 147–156.

28 J. Kumpfert, H. Assler, D. B. Miracle, J. E. Spowart: Transverse Properties of Titanium Matrix Composites, in Materials Week 2000, Munich.

29 J. Kumpfert, C. H. Ward, Y. T. Lee and M. Peters: Improvement of Ductility and Strength of Ti-25Al-10Nb-3V-1Mo by TMT, in Proc. Titanium '92, TMS, Warrendale, PA, USA (1994).

30 C. H. Ward: Microstructure Evolution and its Effect on Tensile and Fracture Behavior of Ti-Al-Nb α$_2$ Intermetallics, International Materials Reviews, **38**(2) (1993) 79–101.

31 J. Kumpfert and W. A. Kaysser: Orthorhombic titanium aluminides – phases, phase transformation and microstructure evolution, Zeitschrift für Metallkunde, **92**(2) (2001) 128–134.

32 C. J. Boehlert: Microstructure, creep, and tensile behavior of a Ti-12Al-38Nb (at.%) beta plus orthorhombic alloy, Materials Science & Engineering A, **267**(1) (1999) 82–98.

33 J. Kumpfert, Y. W. Kim and D. M. Dimiduk: Effect of microstructure on fatigue and tensile properties of the gamma TiAl alloy Ti-46.5Al-3.0Nb-2.1Cr-0.2W, Materi-

als Science and Engineering, **A192/193** (1995) 465–473.

34 Y.-W. KIM and D. M. DIMIDUK: Designing Gamma TiAl Alloys: Fundamentals, Strategy and Production, in ISSI – Structural Intermetallics, TMS, Warrendale, PA (1997).

35 J. KUMPFERT: Orthorhombische Titanaluminide am Beispiel der Legierung Ti-22Al-25Nb, in Werkstoffwoche 1998 – Werkstoffe für die Verkehrstechnik, Wiley-VCH, Weinheim, Germany (1998).

36 D. BANERJEE: Ti$_3$Al and its Alloys, in Intermetallic Compounds, J. H. WESTBROOK and R. L. FLEISCHER (eds.), John Wiley & Sons, Chichester, UK (1995) 91–131.

37 R. G. ROWE and M. LARSON: The Effect of Microstructure and Composition on the Creep Behavior of O Phase Titanium Aluminide Alloys, in Titanium '95, The Institute of Materials, London, UK (1995).

38 P. R. SMITH and W. J. PORTER: The effect of heat treatment on the tensile and creep behavior of "neat" matrix Ti-22Al-23Nb, Journal of Materials Science, **32**(23) (1997) 6215–6220.

39 P. R. SMITH and J. A. GRAVES: Tensile and Creep Properties of High Temperature Titanium Alloys, in Recent Advances in Titanium Metal Matrix Composites, TMS, Warrendale, PA, USA (1995).

40 R. S. MISHRA, D. BANERJEE and A. K. MUKHERJEE: Primary Creep in a Ti-25Al-11Nb alloy, Materials Science and Engineering 3, **A192/A19** (1995) 756–762.

41 F. TANG, S. NAKAZAWA and M. HAGIWARA: Creep Behavior of Tungsten-Modified Orthorhombic Ti-22Al-20Nb-2W Alloy, Scripta Mater., **43**(12) (2000) 1065–1070.

42 S. LÜTJERING: The Effect of Microstructure on the Tensile and Fatigue Behavior of Ti-22Al-23Nb in Air and Vacuum, University of Dayton, OH, USA (1998) 185.

43 G. SAUTHOFF: Plastic Deformation, in Intermetallic Compounds – Principles and Practice, J. H. Westbrook and R. L. Fleischer (eds.), John Wiley & Sons, Chichester, UK (1995) 911–934.

44 J. M. LARSEN, B. D. WORTH, S. J. BALSONE and J. W. JONES: An Overview of the Structural Capability of Available Gamma Titanium Aluminide Alloys, in Gamma Titanium Aluminides, TMS, Warrendale, PA, USA (1995).

45 S. J. BALSONE, D. C. MAXWELL and T. F. BRODERICK: Fatigue Crack Growth Behavior of Titanium Aluminide Ti-25Al-25Nb, in 23rd Symposium on Fracture Mechanics, ASTM, Philadelphia, PA, USA (1993).

46 D. M. DIMIDUK: Gamma Titanium Aluminides – An Emerging Materials Technology, in Gamma Titanium Aluminides, TMS, Warrendale, PA, USA (1995).

47 J. KUMPFERT: Titanaluminide – eine neue Legierungsklasse für Hochtemperaturanwendungen, in Titan und Titanlegierungen, M. PETERS, C. LEYENS, and J. KUMPFERT (eds.), DGM Informationsgesellschaft, Oberursel, (1996) 71–106.

48 J. KUMPFERT, D. WEINEM, M. PETERS and W. A. KAYSSER: Processing Window and Mechanical Behavior for Fine Grained Beta-Structure of the Near-Alpha-Titanium Alloy TIMETAL 1100, in Microstructure and Mechanical Properties of High-Temperature Materials, H. MUGHRABI, et al. (eds.), Wiley-VCH, Weinheim (1998) 79–94.

49 K. S. CHAN: Influence of Microstructure on Intrinsic and Extrinsic Toughening in an Alpha-Two Titanium Aluminide Alloy, Met. Trans. A, **23A** (1991) 183–199.

50 D. HELM: Application of Ti-Alloys as Compressor Disks and Blades, in Fatigue Behavior of Titanium Alloys, TMS, Warrendale, PA, USA (1998).

51 W. J. BRINDLEY, J. L. SMIALEK, J. W. SMITH and M. P. BRADY: Environmental Effects on Orthorhombic Ti-Matrix Materials, in Proceedings of the 1994 Orthorhombic Titanium Matrix Composite Workshop, WL-TR-95-4068, Air Force Wright Laboratory, Wright-Patterson AFB, OH (1994).

52 J. KUMPFERT and C. LEYENS: Microstructure Evolution, Phase Transformations and Oxidation of an Orthorhombic Titanium Aluminide Alloy, in International Symposium on Structural Intermetallics, TMS, Warrendale, PA (1997).

53 A. RALISON, F. DETTENWANGER and M. SCHÜTZE: Oxidation of orthorhombic Ti$_2$AlNb alloys at 800 °C in air, Materials and Corrosion, **51** (2000) 317–328.

54 C. LEYENS: Environmental Effects on Orthorhombic Alloy Ti-22Al-25Nb in Air Between 650 and 1000 °C, Oxidation of Metals, **52**(5/6) (2000) 474–503.

55 M. P. BRADY, W. J. BRINDLEY, J. L. SMIALEK and I. E. LOCCI: Oxidation and Protection of Gamma Titanium Aluminides, JOM, **48**(11) (1996) 46–50.

56 S. G. WARRIER, S. KRISHNAMURTHY and P. R. SMITH: Oxidation Protection of Ti-Aluminide Orthorhombic Alloys: An Engineered Multilayer Approach, Metallurgical and Materials Transactions, **29A** (1998) 1279–1288.

57 J. R. DOBBS, M. F. X. GIGLIOTTI and M. J. KAUFMAN: Effect of exposure on the microstructure of coated and uncoated orthorhombic Ti-aluminides, in Surface Performance of Titanium, (1997) 139–153.

58 M. P. BRADY, B. A. PINT, P. F. TORTORELLI, I. G. WRIGHT and R. J. HANRAHAN: High-temperature oxidation and corrosion of intermetallics, in Corrosion and Environmental Degradation of Materials, M. Schütze (ed.), Wiley-VCH, Weinheim, Germany (2000).

59 O. SCHAUERTE, A. GYSLER and G. LÜTJERING: Effect of Environment on High-Temperature Fatigue of IMI 834, in Fatigue Behavior of Titanium Alloys, TMS, Warrendale, PA, USA (1999).

60 F. O. R. FISCHER, H. J. MAIER and H.-J. CHRIST: Influence of Environment, Mean Stress and Temperature on the Low-Cycle Fatigue Behavior of a Near-Gamma Titanium Aluminide, in Titanium '99, Central Research Institute of Structural Materials (CRISM) "Prometey", Russia (1999).

61 R. BOYER, G. WELSCH and E. W. COLLINGS: Titanium Alloys, in Materials Properties Handbook, S. Lampmann (ed.), Vol. 1, ASM International, Materials Park, OH, USA (1994).

62 M. M. KELLER, P. E. JONES, W. J. PORTER III and D. EYLON: Effects of Processing Variables on the Creep Behavior of Investment Cast Ti-48Al-2Nb-2Cr, in Gamma Titanium Aluminides, TMS, Warrendale, PA, USA (1995).

63 F. TORSTER: Einfluß von Mikrostruktur und Textur auf die Schwingfestigkeit der Titanlegierung IMI834, TU Hamburg Harburg, Hamburg (1995) 1-91.

64 J. N. VINCENT and L. REMY: High Temperature Fatigue of Superalloys for Cast Turbine Wheel, in High Temperature Alloys for Gas Turbines 1982, D. Reidel Publishing Company, Dordrecht, Holland (1982)

4

γ-Titanium Aluminide Alloys: Alloy Design and Properties

F. Appel and M. Oehring, *GKSS Research Center Geesthacht GmbH, Geesthacht, Germany*

4.1
Introduction

There are ever increasing demands for the development of energy conversion systems with improved efficiency and ecological compatibility. Advanced design concepts are based on higher service temperatures, lighter weight, and higher operation speeds. The conventional metallic systems currently in use have been developed over the last 50 years to near the limits of their capability. If further advances are to be made, new classes of materials will be required. Titanium aluminide alloys based on the intermetallic phases $\gamma(TiAl)$ and $\alpha_2(Ti_3Al)$ are widely recognized as having the potential to meet the design requirements mentioned above [1–6]. The outstanding thermo-physical properties of these materials rely mainly on the strongly ordered nature and the directional bonding of the compounds. These involve

- high melting point of 1460 °C
- low density of 3.9–4.2 g cm^{-3}
- high elastic moduli
- low diffusion coefficient
- good structural stability
- good resistance against oxidation and corrosion
- high ignition resistance when compared with conventional titanium alloys.

Based largely on these properties, TiAl alloys could ultimately find use in a wide range of components in the automotive industry, power plant turbines and gas turbine engines. The intention in these applications is to substitute the heavier nickel- or iron-based superalloys in certain ranges of stress and temperature. The industrial implementation of a new material depends, apart from the improved performance and possible innovations, also on availability of suitable processing routes for the production of components. These requirements have initiated worldwide research and development during the past decade, including alloy design, characterization and processing. In Germany, long-term development was supported by government projects, which involved research institutes and industrial laboratories. The state of development achieved will be included in this article.

The paper is organized so that the current knowledge concerning the composition, constitution and microstructure of alloys will be reviewed first, which is relevant for engineering applications. Afterwards, the most important mechanical properties will be described including strength, ductility, creep resistance, fracture toughness, and fatigue. Optimization of these properties often leads to conflicting alloy design concepts. The desired balance of properties can only be met if the relevant failure mechanisms are known. Thus, the third point of the discussion concerns micromechanisms of deformation and fracture and the resulting structure/property relationships. In the final section of the paper, the processing routes and metallurgical techniques that are utilized for the production of semi-finished products and components are described. Metallurgical research in this field is mainly driven by the requirements of industry; and, currently, a major need is for quantitative, physically-based models that can be applied to metal-forming processes so as to control, improve and optimize the microstructure and texture. The discussion will be illustrated by results that have been obtained in our research on titanium aluminide alloys at the GKSS-Research Center Geesthacht. The paper is also oriented on recent conference proceedings [4, 7–9], in which the current status of the research is documented; the reader is referred to these volumes for more details and references.

4.2
Constitution of γ-Titanium Aluminide Alloys

The binary Ti–Al phase diagram (Fig. 4.1) contains several intermetallic phases, which represent superlattices of the terminal solid solutions, and have been long recognized to be attractive bases for lightweight high-temperature materials [13]. Besides their reduced density compared to Ti alloys, these intermetallic compounds promised high strength at elevated temperatures due to their high ordering temperatures. Further, their high Al contents indicated appreciable corrosion resistance in comparison with Ti alloys. In the past two decades of research, however, structural materials have emerged only from alloys based on the $\alpha_2(Ti_3Al)$ phase with hexagonal DO_{19} structure or the $\gamma(TiAl)$ phase with tetragonal $L1_0$ structure (Fig. 4.2). Among these compounds, the interest is strongly focused on γ titanium aluminide alloys, which for engineering applications always contain minor fractions of the $\alpha_2(Ti_3Al)$ phase. Here, the ternary intermetallic phase Ti_2AlNb with an orthorhombic structure should also be mentioned [14, 15], it shows some remarkable properties and is therefore currently being explored as an engineering material (see chapter 3).

Despite intensive research, the binary Ti–Al phase diagram presently remains a matter of debate, which is predominantly caused by the high sensitivity of phase equilibria to non-metallic impurities like oxygen [16, 17]. However, recent phase diagram calculations have shown [12, 16–18] that the phase diagram (Fig. 4.1) suggested by McCullough et al. [10] reasonably reflects the phase equilibria in a concentration range of 40–55 at% Al, disregarding small deviations of the solubility lines.
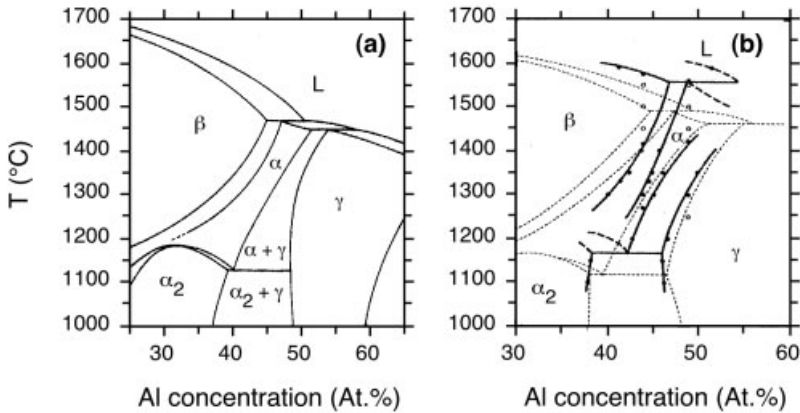
Fig. 4.1 Constitution of Ti-Al-alloys. (a) Binary Ti-Al-phase diagram as proposed by McCullough et al. [10]. (b) Quasi-binary section of the ternary Ti-Al-Nb diagram for a Nb concentration of 8 at% as determined by Zhang et al. [11] in comparison to the binary phase diagram calculated by Okamoto [12].
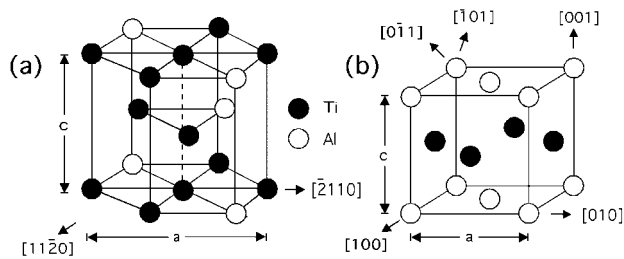
Fig. 4.2 Crystal structures of binary titanium aluminide phases. (a) Hexagonal $\alpha_2(Ti_3Al)$ phase (Strukturbericht designation DO_{19}, prototype Ni_3Sn, Pearson symbol hP8, space group $P6_3/mmc$, lattice parameters a=0.5782 nm, c=0.4629 nm), (b) tetragonal $\gamma(TiAl)$ phase (Strukturbericht designation $L1_0$, prototype AuCu, Pearson symbol tP2, space group P4/mmm, lattice parameters a=0.4005 nm, c=0.4070 nm).

Engineering alloys based on the γ(TiAl) phase usually have Al concentrations of 45–48 at% and thus solidify peritectically according to the phase diagram. Depending on processing conditions and composition, even two peritectic reactions might occur. During ingot processing or casting, the peritectic solidification often results in macroscopic columnar grains and a pronounced microsegregation of the alloying elements. Both of these features in the cast microstructure can be removed only with difficulty [19], and might be harmful to the mechanical properties. The growth of columnar grains in preferential crystallographic orientations with respect to the heat flow direction can further result in strong solidification textures. The casting textures are particularly pronounced if grains of the hexagonal α solid solution solidify, as is the case for many engineering alloys [20, 21].

Thus, the texture of cast alloy parts can be influenced by selecting different solidification paths through relatively small variations of the alloy composition, and this is used in the development of directional solidification processing [22]. In particular, complete solidification through the β phase without a peritectic reaction is possible for Al contents < 45 at%, which currently is also being investigated for the development of cast alloys [20].

After solidification, binary γ(TiAl) alloys pass through the single-phase field of the α solid solution, which decomposes on further cooling according to the reactions $\alpha \rightarrow \alpha + \gamma \rightarrow \alpha_2 + \gamma$ or $\alpha \rightarrow \alpha_2 \rightarrow \alpha_2 + \gamma$ [23, 24]. The existence of this single-phase high-temperature field is a characteristic feature of γ(TiAl) alloys in comparison to other intermetallic alloys. Similar to steels after heat treatment in the austenite region, a variety of different phase transformations can occur on cooling from the region or on subsequent heat treatments. These allow, in principle, a wide range of microstructures to be obtained [24, 25]. Thus, the mechanical properties can be adapted to some extent to the intended application by conventional metallurgical processing, and the limited damage tolerance of alloys may be controlled, as will be described in more detail.

The eutectoid transformation $\alpha \rightarrow \alpha_2 + \gamma$ on cooling should also be mentioned, which occurs in all engineering γ(TiAl) alloys. The mechanism of this reaction seems to be identical to the reaction $\alpha \rightarrow \alpha + \gamma$, proceeding via nucleation and growth of single γ lamellae. The occurrence of a discontinuous reaction, which evolves behind a moving interface, has not been observed up to now [26]. For alloy compositions that deviate from the eutectoid composition, the volume fraction of the γ phase has to increase abruptly, following thermodynamic equilibrium, if the temperature falls below that of the eutectoid transformation. This can occur by the formation of new γ lamellae, or by growth of existing ones. The typically applied cooling rates, however, often do not allow thermodynamic equilibrium to be approached, and therefore the obtained microstructures are not stable at the intended service temperatures of around 700 °C. Thus, when selecting processing conditions, an equilibration treatment or adequate cooling conditions have to be taken into consideration.

In the past decade a broad range of engineering alloys has emerged as a result of a number of alloy development programs for different processing routes and applications. The alloys can be described by the general composition

Ti-(45–48)Al-(0.1–10)X (at%),

with X designating the elements Cr, Nb, V, Ta, Mo, Zr, W, Si, C, and B [4]. Here it should be pointed out that in this article all compositions are given in at%. For the compositions mentioned above, the α_2 phase is generally present with a volume fraction of up to 20%, with the remainder being the γ phase. Considering the effect of the various alloying elements on constitution, two alloying strategies might be distinguished. Metals in most cases are added to γ(TiAl) alloys in solid solution to influence the properties of the γ phase, such as planar defect energies or the diffusion coefficient. In contrast, the alloying of non-metallic elements aims at the formation of third (or more) phases to obtain precipitation hardening or grain refinement during

casting. With respect to intrinsic properties on alloying, the solubility in the γ phase, partitioning of alloying elements to the α_2 and γ phases, and occupation of the two sublattices of the γ phase by a certain alloying element are of interest. The known ternary phase diagrams show [27–32] that most metals are only soluble up to around 2 at% in the γ phase. For higher concentrations of the listed metallic elements, either the bcc β solid solution or the B2 ordered variant predominantly occur as the third phase. However, in some systems like Ti-Al-Cr, further phases, e.g. the Laves phase Ti(Cr, Al)$_2$, have been observed [27]. The alloying elements Zr, Nb and Ta are exceptional in that they are soluble at higher contents, up to around 9 at% in the case of Nb, depending on temperature [30, 32]. In contrast to V, Cr, Mo, Ta, and W, which are enriched in the α_2 phase, Nb and Mn are distributed in equal amounts to the α_2 and γ phases, whereas Zr is concentrated in the γ phase. With respect to solid solution effects, Nb turns out to be favorable in comparison to binary alloys as it improves the intrinsic properties of the γ phase but does not change the constitution for concentrations up to 8 at% [11] (Fig. 4.1 b). For more details on the effect of certain alloying additions the reader is referred to sections 4.5.2 and 4.5.4 of this chapter.

4.3
Phase Transformations and Microstructure

As described in the previous section, engineering γ(TiAl) alloys pass the single-phase region of the α solid solution after solidification. After the temperature has fallen below the α-transus temperature, different phase transformations are possible and are dependent on the cooling rate. The α phase cannot decompose at the highest cooling rates, but orders to the α_2 phase [33]. With decreasing cooling rate the massive $\alpha \rightarrow \gamma$ transformation, the lamellar reaction (in which crystallographically oriented plates of the γ phase are precipitated from α) and, at very low cooling rates, the formation of γ grains are observed [25, 34, 35]. The lamellar reaction shows two variants at the highest cooling rates for which this reaction occurs. These are the formation of Widmannstätten colonies in lamellar colonies [25] and "feathery structures" consisting of γ lamellae with a misorientation of $2\,°–15\,°$ in comparison to the common orientation relationship described in the following [35]. Furthermore, the formation of the lamellar microstructure can be followed by a discontinuous coarsening reaction, which might significantly alter the microstructure [36]. For higher Al concentrations around 49 at%, a secondary precipitation of α_2 Widmannstätten plates from the γ phase is possible on the four close-packed {111} planes [25]. However, based on the current knowledge, the best combination of mechanical properties is achieved for lamellar microstructures that have fine lamellar spacings and small colony sizes. For this reason, alloy development is mainly focused on this type of microstructure, and lamellar microstructures are primarily considered in the following. The potential diversity of possible microstructures has, however, only rarely been investigated with respect to the resulting properties. In addition, the possible reactions might occur unintentionally and have to be taken into account during the development of alloys and processing, e.g. if the cooling rate varies locally due

to different cross-sections of a component. In this respect it has to be considered that the reaction kinetics can be sensitive to the alloy composition. For instance, alloying with low amounts of B depresses the occurrence of an undesired massive reaction even at the highest industrially possible cooling rates, thus allowing the formation of fine lamellar microstructures [37, 38].

The formation mechanism of lamellar microstructures has not been completely elucidated yet. It has been proposed by different researchers [39–41] that γ lamellae are formed from the α phase by the movement of Shockley partial dislocations, which cause the lattice transition from hcp to fcc. This lattice transformation is coupled with diffusion processes to equilibrate the composition and to obtain the chemical ordering of the γ phase. Indeed, Sun has provided direct evidence [33] that γ lamellae are formed by a shear transformation. However, the work of Aindow and collaborators shows [42] that this transformation proceeds by the diffusion-controlled movement of interface ledges along close-packed planes. The movement of Shockley partial dislocations can be involved in the motion of ledges but is not required. In any case, the transformation is of a displacive type, which leads to a crystallographic alignment between $α_2$ and γ lamellae according to the Blackburn relationship [39, 43]

$$(0001)_{α_2} || \{111\}_γ \quad \text{and} \quad \langle 11\bar{2}0 \rangle_{α_2} || \langle 1\bar{1}0]_γ \ . \qquad \text{(eqn. 4.1)}$$

The arising lamellar interfaces are atomically flat over large distances and are parallel to the basal planes of $α_2$ and the $\{111\}$ planes of γ. In the lamellar microstructure six different variants of γ lamellae can occur, which can formally be described by rotations of $60°$ around an [111] direction [3, 44–47]. Thus, besides the $α_2/γ$ interfaces, there exist different types of $γ/γ$ interfaces, among which true twin boundaries (rotation of $180°$ around $\langle 111 \rangle$) are most frequent and have the lowest interfacial energy [48]. Since the c/a ratio of the $L1_0$ structure slightly differs from unity, coherency stresses and dense networks of interface dislocations also occur at $γ/γ$ interfaces [5, 46, 47, 49]. Moreover, the anisotropy of the thermal expansion coefficients causes internal stresses at interfaces between differently oriented γ lamellae. These structural features of lamellar microstructures are demonstrated in Fig. 4.3. Under mechanical loading, stress-induced structural changes of misfitting interfaces occur, which have various implications on the deformation and fracture phenomena of lamellar titanium aluminides [50].

In addition to the described phase transformations, the microstructure can also be influenced by recrystallization during hot working. As shown in Fig. 4.4 for hot extruded material, the lamellar microstructures present in ingot material can be fully converted to equiaxed microstructures having grain sizes in the range of several microns with thermomechanical treatment in the $α_2 + γ$ or $α + γ$ regions. By subsequent heat treatment at temperatures close to the α-transus temperature, different fractions of lamellar colonies can be obtained whose colony size and lamellar spacing are dependent on the heat treatment conditions [24]. Fig. 4.4 displays a calorimeter trace of the phase transformations on heating hot worked material, together with the types of possible microstructures obtained for different heat treatment temperatures.
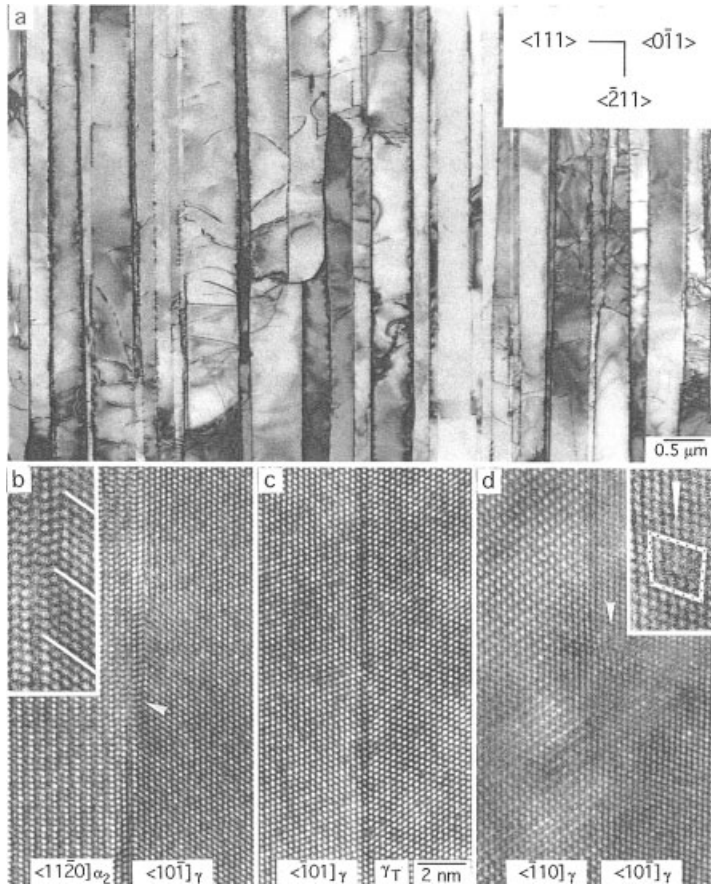
Fig. 4.3 Structure of lamellar interfaces of a two-phase alloy of composition Ti-48Al-2Cr. (a) Transmission electron micrograph showing the lamellar microstructure, with the lamellar interfaces being in edge–on orientation; foil orientation $\langle 011 \rangle_\gamma$. (b)–(d) High resolution electron micrographs in $\langle 001 \rangle$ projection showing (b) an α_2/γ interface, (c) a coherent interface between 180° rotational variants γ/γ_T with true twin orientation, (d) a semicoherent interface between 120° rotational variants γ_1/γ_2 with matrix/matrix orientation. Note the misfit dislocation (arrowed) with a Burgers vector out of the interfacial plane.

4.4
Micromechanisms of Deformation

As with many other intermetallic phases, titanium aluminides are relatively brittle materials, exhibiting little plasticity at ambient temperatures. Typical of such deformation behavior is that the gliding dislocations are either too low in density or too immobile to allow the specimen to match the superimposed strain rate. The brittle material behavior often persists up to relatively high temperatures and pro-
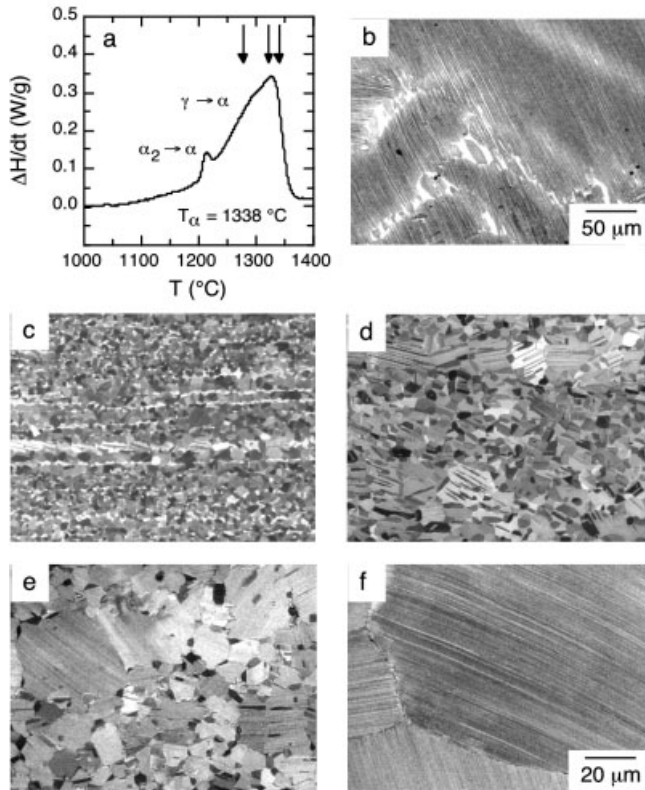
Fig. 4.4 Phase transformations in an alloy Ti-45Al-(5–10)Nb-X. (a) Differential scanning calorimetry trace as obtained on heating the alloy with a rate of 20 K min^{-1} (see Fig. 4.1 b). The arrows designate heat treatment temperatures, which have been chosen for the specimens shown in (d)–(f). (b)–(f) Scanning electron micrographs taken in the back-scattering eletron mode of different microstructures obtained in this alloy. (b) Ingot material, (c) completely recrystallized equiaxed microstructure of material extruded slightly above the eutectoid temperature, and microstructure of extruded material after a heat treatment at (d) 1280 °C, (e) 1320 °C, and (f) 1340 °C.

vides severe constraints upon hot working procedures. Furthermore, structural refinement due to recovery and recrystallization is triggered by the imparted strain energy and, thus, depends on the nature of the deformed state. At elevated temperatures titanium aluminides suffer from insufficient creep resistance and structural changes. Such behavior is often associated with dislocation climb and the operation of diffusion assisted dislocation sources. Thus, for the performance of TiAl alloys, the micromechanisms governing the multiplication and mobility of the dislocations might be important in several different ways and will now be considered.

4.4.1
Slip and Twinning Systems

In $\alpha_2(Ti_3Al) + \gamma(TiAl)$ alloys, that are of engineering significance, deformation is mainly confined to the $\gamma(TiAl)$ phase. The deformation behavior of $\gamma(TiAl)$ is closely related to the slip elements of the $L1_0$ structure that are illustrated in Fig. 4.5. Slip occurs under most conditions on $\{111\}_\gamma$ planes along the close-packed $\langle 110 \rangle$ directions [3, 5] and can be provided by ordinary dislocations with the Burgers vector $b = 1/2\langle 110]$ and superdislocations with the Burgers vectors $b = \langle 101]$ or $b = 1/2\langle 112]$. At very high temperatures, dislocations with a $\langle 100 \rangle$ Burgers vector have also been observed [51]. The parentheses used with the Miller indices follow the convention introduced by Hug [52], which denotes all distinct permutations of $\pm h$ $\pm k$. In addition, deformation can also be provided by mechanical twinning along $1/6\langle 11\overline{2}]\{111\}_\gamma$ (Fig. 4.5 b). However, unlike disordered face centered cubic materials, there is only one distinct twinning shear direction $b_3 = 1/6\langle 11\overline{2}]$ that does not alter the ordered structure of $\gamma(TiAl)$ [53–55]. Shear in the reverse direction along $-2b_3$ is the "complementary" or "anti-twinning" mode. Shear along b_1 and b_2 alters the ordering and is designated as "pseudo-twinning".

Perfect and partial dislocations are liable to adopt different core configurations, thus reducing their energy. Owing to the ordered $L1_0$ structure, different types of planar faults are involved in the dissociation reactions, such as superlattice intrinsic or extrinsic stacking faults, antiphase boundaries and complex stacking faults. Planar and nonplanar dissociations have been observed and theoretically justified for $\langle 011]$ and $1/2\langle 112]$ superdislocations [3, 52, 56, 57]; examples of planar dissociations are shown in Fig. 4.5 c. Non-planar dissociations often lead to the formation of sessile configurations [58–60]. Ordinary $1/2\langle 110]$ dislocations seem to have compact cores, which has been attributed to the high energy of the complex stacking fault that would be involved in the dissociation [58, 61]. The observations follow the plausible trend that the highest planar fault energies produce the smallest spreadings. The differences in the dissociation modes of ordinary and superdislocations have significant implications on their glide resistance and ability to cross glide or climb. The energy of planar faults has been investigated as function of alloy composition by first principles electronic structure calculations [62]. Accordingly, the formation energies for the above mentioned planar defects are significantly reduced by micro-alloying with Cr, Nb and Mn, when compared with binary alloys of stoichiometric composition. It will be demonstrated in section 4.5.3 that these trends can be used in alloy design to optimize mechanical properties.

The relative contributions of the individual dislocation mechanisms mainly depend on the aluminum concentration, the content of ternary elements and the deformation temperature. In the γ phase of two-phase alloys, glide of superdislocations is difficult and requires significantly higher stresses when compared with ordinary dislocations and order twinning [3, 5, 56]. At room temperature, deformation is mainly provided by ordinary dislocations and mechanical twinning (Fig. 4.6 a), i.e. the γ phase exhibits a significant plastic anisotropy. Thus, in terms of the von Mises criterion for a general plastic shape change of polycrystalline ma-
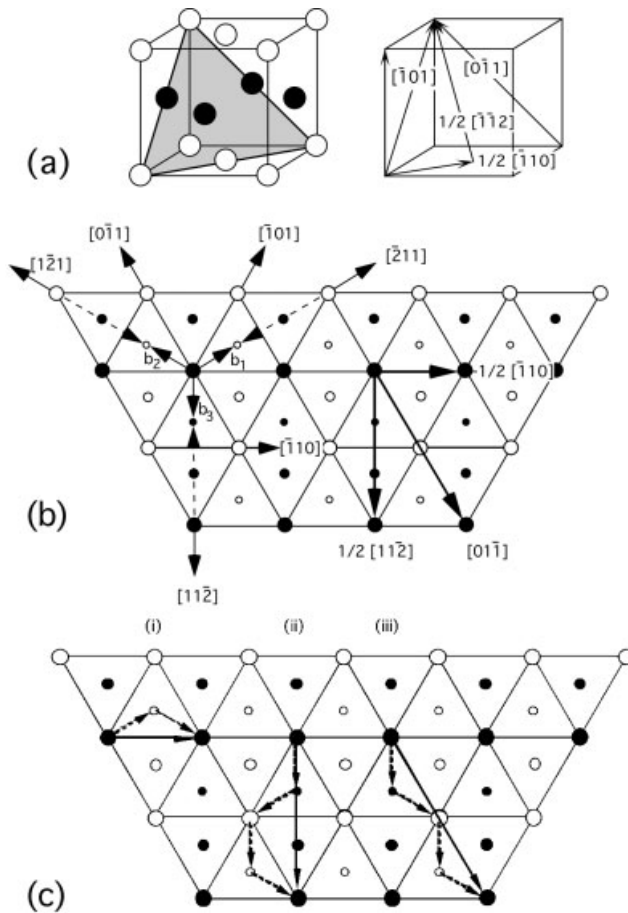
Fig. 4.5 Potential slip and twinning systems in γ(TiAl). (a) Atomic arrangement of the ordered L1$_0$ structure of γ(TiAl) with one of the four octahedral {111}$_\gamma$ planes involving the Burgers vectors 1/2[$\bar{1}$10], 1/2[$\bar{1}$ $\bar{1}$2], [0$\bar{1}$1], and [$\bar{1}$01]. (b) Schematic drawing of the three-layer sequence of atom stacking on the (111)$_\gamma$ plane shown by small, medium and large circles. The open and shaded circles denote Ti and Al atoms, respectively. b$_1$ =1/6[$\bar{2}$11],

b$_2$ =1/6[1$\bar{2}$1]and b$_3$ =1/6[11$\bar{2}$] are the Burgers vectors of partial dislocations. b$_3$ is perpendicular to the Burgers vector b=1/2[$\bar{1}$10] for ordinary slip and represents the Shockley partial dislocations for true twinning, whereas b$_1$ and b$_2$ represent pseudo-twinning. (c) Schematic drawing of planar dissociations of perfect dislocations with the Burgers vectors (i) b=1/2[$\bar{1}$10], (ii) b=1|2[11$\bar{2}$], (iii) b=[0$\bar{1}$1].

terial, there is a lack of independent slip systems that can be activated at given stress. In grains or lamellae that are unfavorably oriented for glide of ordinary dislocations or twinning, significant constraint stresses can be developed due to the shape change of deformed adjacent grains. These constraint stresses often initiate local glide of superdislocations, as demonstrated in Fig. 4.6b. The lamella γ$_2$ shown in this micrograph had an ⟨110] orientation with respect to the sample
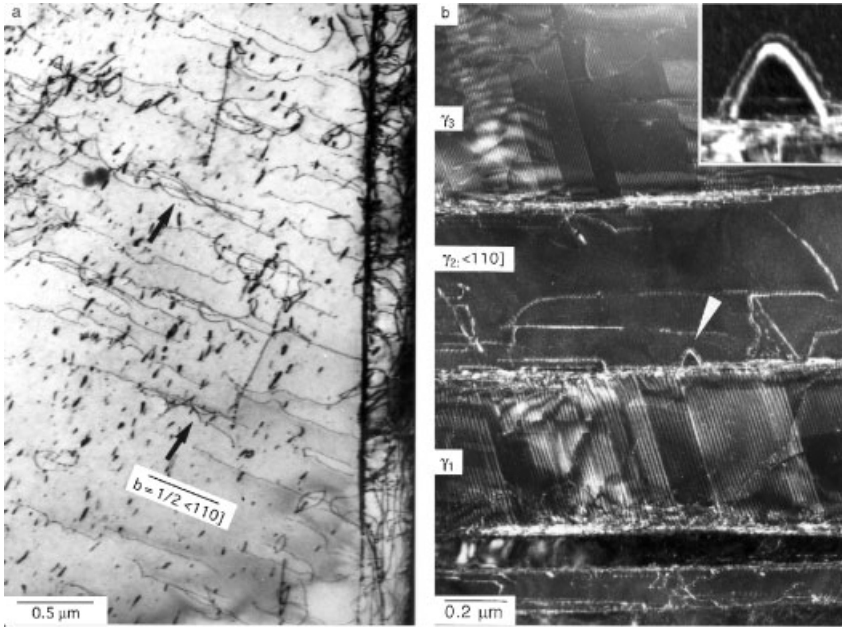
Fig. 4.6 Deformation structures in two-phase titanium aluminide alloys. Ti-48Al-2Cr with a lamellar microstructure, compression at room temperature to strain $\varepsilon = 3$ %, transmission electron micrographs with foil orientations close to $\langle 101]$. (a) Ordinary dislocations with Burgers vector $b = 1/2\langle 110]$ with mainly screw character. Note the formation of dislocation multipoles (arrowed), which probably contribute to work hardening. (b) Generation of superdislocations in front of immobilized twins. Due to its $\langle 110]$ orientation parallel to the compression axis, lamella γ_2 is unfavorably oriented for glide of $1/2\langle 110]$ dislocations and true twinning. The generation of superdislocations (mostly of type $1/2\langle 11\bar{2}]$ is probably supported by high constraint stresses exerted by the deformation twins immobilized in the adjacent lamellae γ_1 and γ_2.

axis and, thus, could not deform by ordinary dislocations or order twinning. The extensive twinning of the adjacent lamellae, γ_1 and γ_3, probably generated high constraint stresses, which led to the emission of superdislocations from the interfaces. An inability to accommodate such stresses apparently leads to premature failure. Similar arguments probably hold for the α_2 phase.

Deformation studies performed on Ti$_3$Al single crystals have shown that deformation at room temperature is restricted to prism glide on $\langle 11\bar{2}0\rangle\{10\bar{1}0\}$ systems [63]. Crystals or lamellae of the α_2 phase with an orientation of the c axis parallel to the tensile axis are extremely difficult to deform, which is a critical issue for $\alpha_2(\mathrm{Ti_3Al}) + \gamma(\mathrm{TiAl})$ alloys and certainly limits the ductility [64]. This plastic anisotropy, together with the sensitivity of the material to cleavage fracture, is probably the main reason for the low temperature failure of $\alpha_2(\mathrm{Ti_3Al}) + \gamma(\mathrm{TiAl})$ alloys (see section 4.5.6). At temperatures above 700 °C, the α_2 phase can also deform on pyramidal $\langle 11\bar{2}6\rangle\{20\bar{2}1\}$ slip systems [63]. This was also confirmed for α_2 lamellae

in two-phase alloys by electron microscopy [65]. The propensity for twinning of the γ phase strongly increases with temperature in two-phase alloys. As will be shown later, ordinary dislocations are able to climb under these conditions. Furthermore, anti-twinning operations, supported by constraint stresses, may also contribute to deformation [5, 66]. Taken together, these factors certainly reduce the plastic anisotropy of the γ and α_2 phases and make deformation of polycrystalline $\alpha_2(Ti_3Al) + \gamma(TiAl)$ much more easy.

4.4.2
Dislocation Multiplication

Ordinary dislocations with Burgers vectors $b = 1/2\langle110]$ have a compact core structure, which makes cross glide and climb relatively easy. Multiplication of these dislocations can therefore take place through the operation of dislocation sources incorporating stress driven cross-slip or climb, as has been observed in disordered metals [5, 67]. At room temperature, multiplication has been found to be closely related to jogs in screw dislocations, which were probably generated by cross-slip [5, 50, 67]. The kinematics of the processes involved is sketched in Fig. 4.7a. Since the jogs are immobile in the direction of the motion of the screw dislocations, dislocation dipoles are trailed at the jogs (Fig. 4.7a, stage ii). The anchored segments bow out under the applied stress in a fashion similar to a Frank-Read source. The adjacent dipole arms can overcome their elastic interaction and pass each other, if the applied shear stress is larger than [68]

$$\tau_d = \mu b/8\pi(1 - \nu)\,h \;. \qquad \qquad (eqn.\,4.2)$$

Where μ is the shear modulus, ν is Poisson's ratio and h the height of the jog. If the bowing process continues, the dipole arms can effectively behave independently of each other and act as single ended dislocation sources (Fig. 4.7a, stage iii). Fig. 4.7b shows a dislocation dipole trailed at a high jog, which is probably in the initial stage of this multiplication mechanism. Due to the high flow stress of the titanium aluminides, relatively narrow dipoles can probably act as dislocation sources as suggested by Eqn. 4.2. Dipoles of smaller height, which cannot multiply at the given stress, will be pinched off from the dislocation. These defects can also operate as dislocation sources when, in later stages of deformation, the flow stress increases due to work hardening (Fig. 4.7a, stage iv) [5]. The mechanisms described here confirm the early models of dipole generation and dislocation multiplication, which were proposed by Gilman and Johnston [69].

At elevated temperatures dislocation multiplication can be supported by point defect supersaturations and diffusion processes. As with disordered metals, in γ(TiAl) vacancies predominate in thermal equilibrium over interstitials because their formation energy is significantly lower than that of interstitials [70, 71]. Processing routes for titanium aluminide alloys often involve thermal treatments followed by rapid cooling (see section 4.3), which certainly leads to large vacancy supersaturations. Non-equilibrium concentrations of point defects may also occur
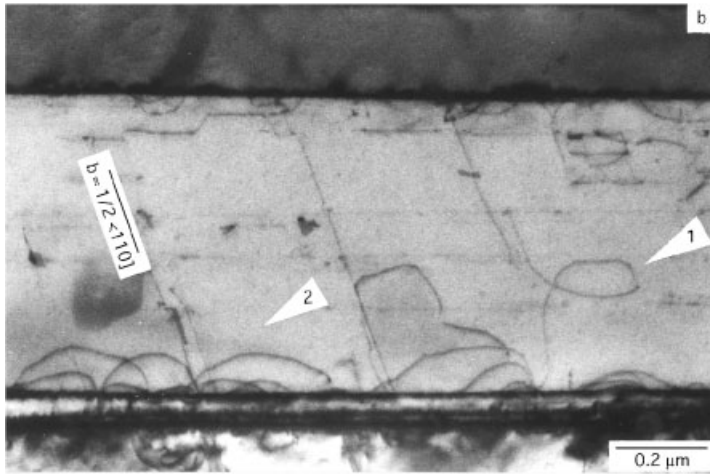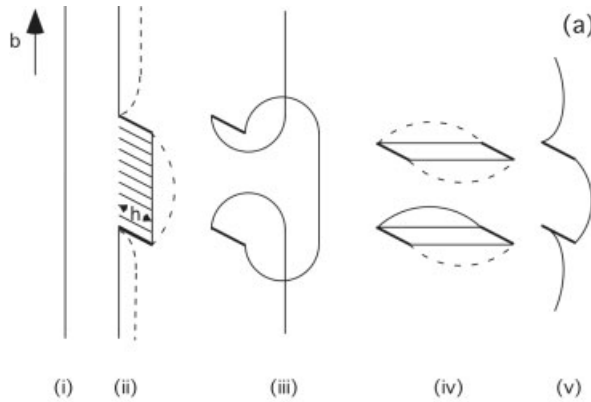
Fig. 4.7 Cross-glide and multiplication of ordinary dislocations in γ(TiAl). (a) Schematic drawing of the behavior of a jogged screw dislocation, (i) and (ii) anchoring of the dislocation at jogs of height h, (iii) operation of dipole arms as single- or double-ended dislocation sources, (iv and v) trailing and termination of dipoles at small jogs. At higher stresses, the dipole arms may overcome their elastic interaction and operate as single- or double-ended dislocation sources (dashed lines).

(b) Initial stage of multiplication of an ordinary 1/2⟨110] dislocation by cross-glide corresponding to stage (iii) in Fig. 4.7a. The dipole arms trailed at the jog (arrow 1) in the screw dislocation are widely separated so that they could pass each other and may act as single-ended source. Note the emission of the dislocation loops from the interface (arrow 2). Ti-48Al-2Cr, compression at T=300 K to strain ε=3%.

due to hot or cold working of the material. Dislocation motion in large vacancy supersaturations seems therefore to be a common situation for γ(TiAl) alloys. The resulting climb processes can apparently initiate multiplication. The details of the mechanisms can hardly be deduced from post mortem electron microscopy because of their complex kinematics.

In the present study direct information about climb processes have been deduced from in situ heating experiments. The samples were compressed at T = 300 K to strain ε = 3%, which introduced sufficient dislocations for observation and certainly a small supersaturation of intrinsic point defects due to jog dragging processes. During the in situ experiments, the dislocations moved under the combined action of thermomechanical stresses and osmotic climb forces due to the chemical potential of the excess vacancies. As described above, this defect structure is probably characteristic of the situation in industrial two-phase alloys subjected to high temperature deformation.

Fig. 4.8 demonstrates the growth of climb sources during a long period of about 350 min by using a sequence of micrographs, part of an in situ study performed at 820 K. Accordingly, dislocations were generated by the nucleation and growth of prismatic loops (arrow 1). As schematically shown in Fig. 4.8 e, the expansion of each loop is achieved by the removal of one atomic plane, thus the mechanism is exhausted after only one cycle of the source. The expanding loop designated with arrow 2 contains a jog so that climb on different atomic planes occurs. After one cycle of the source, a new dipole is generated so that the mechanism is regenerative. The climb processes often lead to the formation of spiral sources, which generate complex configurations of interconnected multiple loops [5]. Apparently, the critical vacancy concentration c^v/c_o^v required to operate the Bardeen-Herring climb sources is relatively low. The geometric situation occurring during the in situ experiments has been described in [72, 73]. For a loop expanding from a source of length L, the critical value is:

$$\ln(c^v/c_o^v) \geq [\mu b \Omega / L\, 2\pi(1-\nu)kT]\, \ln(L\alpha/1,8\,b)\,. \qquad \text{(eqn. 4.3)}$$

Where c^v is the non-equilibrium concentration of the vacancies, c_o^v the equilibrium concentration belonging to temperature T, Ω is the atomic volume, α = 4, and ν is Poisson's ratio. For the present experimental conditions, T = 820 K and L = 150–350 b, the values c/c_o = 3–1.7 were obtained [5, 74]. These supersaturations are small in comparison to those produced initially after rapid cooling, which are easily on the order of 10^3–10^4 [68, 73]. Thus, Bardeen-Herring sources can probably operate throughout the entire period during annealing out of excess vacancies. Such processes are expected to be particularly important for creep deformation, where only slow strain rates occur [75]. It may therefore be concluded that rapid quenches from high temperatures have detrimental effects on the creep resistance of the material. If these quenches are required to establish a desired microstructure, the excess vacancies should be annealed out by careful heat treatments of the sample.

It should be pointed out that the dynamic dislocation sources described here were only observed on ordinary 1/2⟨110] dislocations. As described above, superdislocations exhibit wide and complex dissociations, which restricts cross-slip and climb. Multiplication of superdislocations by the mechanisms described above is therefore considered to be difficult. In view of these results it appears plausible that the structure of deformed TiAl alloys mainly consists of ordinary dislocations.
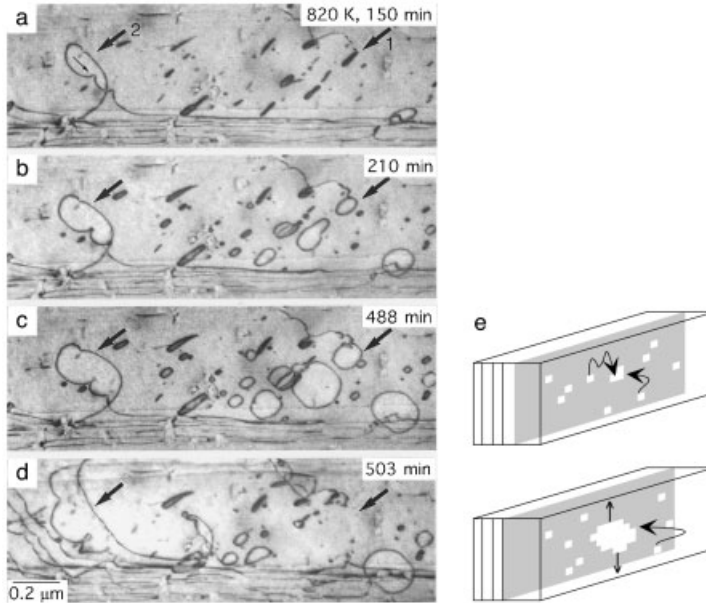
Fig. 4.8 Generation of ordinary dislocations with Burgers vector b=1/2⟨110] at elevated temperatures. (a–d) Operation of Bardeen-Herring dislocation climb sources during an in situ heating experiment inside the TEM at T=820 K. Details: (1) nucleation and growth of prismatic dislocation loops, (2) expansion of a dislocation loop containing two jogs (small arrow). After one cycle of the source a new dipole is generated so that the mechanism is regenerative. Ti-48Al-2Cr, pre-deformation at T=300 K to strain ε=3%. (e) Schematic drawing of the mechanism.

A mechanism common to both low and elevated temperatures is the emission of dislocations from the lamellar interfaces. The process was found to be closely related to mismatch structures and coherency stresses present at the semicoherent interfaces described in Section 4.3. The coherency stresses are comparable with the yield stress of the material and give rise to the formation of loop structures adjacent to the interfaces [49, 76, 77]. Dislocation segments of such a configuration are expected to be released from the interfaces when an additional shear stress is superimposed. Extended dislocation glide processes starting from the interfaces are therefore a significant feature of the deformation structure of lamellar alloys. As an example Fig. 4.9 demonstrates the dislocation structure adjacent to semicoherent α_2/γ interfaces observed after deformation at room temperature. In most cases, the dislocations have a Burgers vector b=1/2⟨110] inclined to the lamellar interfaces and, thus, contribute to shear deformation across the lamellae. Dislocation emission from the interfaces may effectively contribute to the accommodation of stress concentrations. In lamellae that are unfavorably oriented for 1/2⟨110] glide or twinning, significant constraint stresses can be developed due to the shape change of deformed adjacent lamellae. The constraint stresses are believed to assist overcoming the high Peierls stresses expected for the superdisloca-
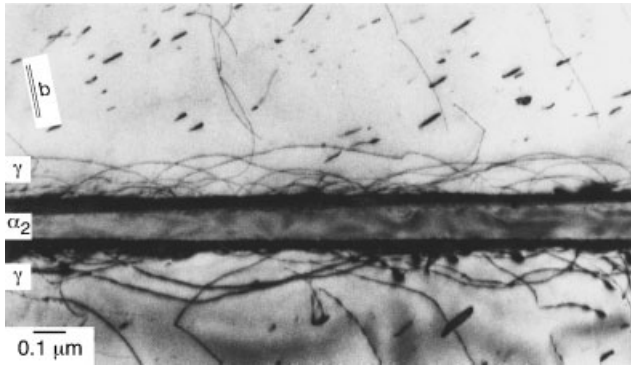
Fig. 4.9 Generation of dislocations at lamellar interfaces. Ti-48Al-2Cr, compression at $T = 300$ K to strain $\varepsilon = 3\%$. Initiation of glide processes of ordinary dislocations with Burgers vector $b = 1/2\langle 110]$ at α_2/γ interfaces. Foil orientation close to $\langle 101]$.

tions, thus glide processes of these dislocations are locally initiated, a behavior that was demonstrated in Fig. 4.6 b. The interface mechanisms support dislocation generation and are therefore beneficial for the ductility and damage tolerance of the material at ambient temperatures. The mechanisms are, on the other hand, a serious limitation for the creep resistance and structural stability of the material under long-term exposure.

4.4.3
Twin Nucleation

For γ(TiAl) several heterogeneous nucleation mechanisms have been proposed [57, 78–81], which basically are related to the dissociation of superdislocations and the coalescence of planar defects; experimental confirmation is rare, however. There is good evidence that the lamellar interfaces of two-phase alloys are the prevalent sites for twin formation [5, 82]. The nucleation occurs heterogeneously at the misfit dislocations, with Burgers vector out of the interfacial plane. Dissociation of these dislocations provides Shockley partial dislocations with a Burgers vector parallel to the twinning shear direction $\eta_1 = \langle 11\overline{2}]$, thus supporting twin nucleation. An initial stage of this mechanism is demonstrated in Fig. 4.10 by a high resolution electron micrograph. More details concerning the dislocation reaction involved are described in [82]. The view of heterogeneous nucleation is also supported by the fact that twinning in Al-rich single-phase alloys at low temperatures apparently is very difficult. This might be in part a consequence of the fact that lamellar interfaces are almost absent in these materials. Thus, like in disordered materials, in γ(TiAl) twin nucleation can easily be rationalized, whereas the pole mechanism proposed in literature does not satisfactorily account for the rapid growth of the twins [79].
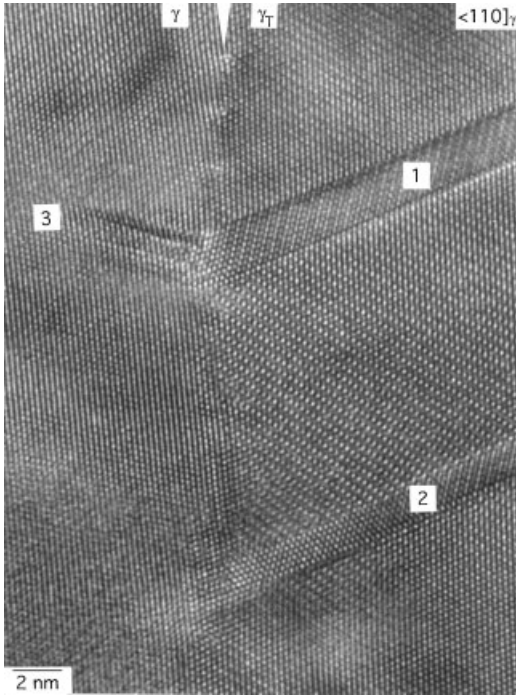
Fig. 4.10 Generation of deformation twins in two-phase titanium aluminide alloys. Heterogeneous nucleation of embryonic twins at an interface γ/γ_T between γ variants with true twin orientation. The tilt misfit of the interface is accommodated by an array of misfit dislocations (arrowed). The narrow twins (1) and (2) were nucleated from the misfit dislocations. Ti-48Al-0.37C, compression at 300 K to strain $\varepsilon = 3\%$.

4.4.4
Glide Resistance and Dislocation Mobility

As with many other materials, in γ(TiAl) the mobility of dislocations is determined by interactions with various lattice defects. The relevant processes may be described in terms of thermodynamic glide parameters. In doing so, dislocation propagation is considered as a thermally activated process, and the strain rate is described as [83, 84]

$$\dot{\varepsilon} = \dot{\varepsilon}_0 \exp(-\Delta G/kT) . \qquad (\text{eqn.}\,4.4)$$

The stress experienced by an individual dislocation results from the superposition of the applied stress, σ, with stresses, σ_μ, from internal sources. The coherency stresses existing at the lamellar interfaces of two-phase alloys represent typical examples of internal stresses. In the framework of this model the total stress, σ, is given by [5]

$$\sigma = \sigma_\mu + \sigma^* = \sigma_\mu + (f/V)(\Delta F^* + kT \ln \dot{\varepsilon}/\dot{\varepsilon}_0) . \qquad (\text{eqn.}\,4.5)$$

The other parameters involved in eqns. 4.4 and 4.5 are: ΔG – Gibbs free energy of activation, ΔF^* – free energy of activation, k – Boltzmann constant. $\dot{\varepsilon}_0$ is propor-

tional to the mobile dislocation density and considered to be constant. The Taylor factor f=3.06 was used to convert σ and ε̇ to average shear quantities. V=lbΔR is the activation volume, which contains the obstacle distance, l, the Burgers vector, b, and the activation distance, ΔR. V can be described as the number of atoms that have to be coherently thermally activated for overcoming the glide obstacles by the dislocations [83, 84]. The activation parameters defined by Eqns. 4.4 and 4.5 were related to temperature and strain rate sensitivities of the flow stress by [83, 84]

$$\Delta G = \frac{Q_e + V\sigma(T/\mu f)(\partial\mu/\partial T)}{1 - (T/\mu)(\partial\mu/\partial T)} \qquad\qquad (eqn.\,4.6)$$

with

$$V = fkT/(\Delta\sigma/\Delta\ln\dot\varepsilon)_T \quad\text{and}\quad Q_e \equiv \Delta H = -TV(\Delta\sigma/\Delta T)_{\dot\varepsilon}/f\,. \qquad (eqn.\,4.7)$$

Q_e is the experimental activation energy, which is identical to the activation enthalpy, ΔH, when the obstacle distance is independent of stress [83, 84]. Different deformation mechanisms exhibit characteristic activation volumes and energies. It is therefore expected that these parameters will undergo significant changes when there is a change of the mechanism that controls the glide resistance of the dislocations.

The activation parameters were determined in a wide temperature range for various TiAl alloys with different microstructures and compositions [5, 67, 85, 86]. For a given composition and microstructure, the parameters depend on ε, ε̇ and T. First, the values determined at the beginning of deformation at ε=1.25% will be considered. At constant temperature and strain rate, σ and 1/V are linearly related, according to Eqn. 4.5. The characteristic temperature dependence of these two quantities is demonstrated in Fig. 4.11. The behavior is almost typical of all two-phase alloys. The flow stress is nearly independent of temperature up to about 1000 K, and then decreases. In contrast, 1/V passed through a broad minimum at temperatures between 600 and 800 K, which indicates that significant changes in the micromechanisms controlling the dislocation velocity occur. Thus, separate consideration will be given to the domains I, II and III designated in Fig. 4.11. The activation parameters estimated in domain I (T=295 K) are typically [5, 67, 85, 86]:

$$V = (70 - 130)b^3,\ \Delta G = 0.7 - 0.85\,eV,\ \Delta F^* = 1.3\,eV\,.$$

V was referenced to the Burgers vector of ordinary dislocations, which in two-phase alloys mainly provide deformation of the γ phase. The small value of V and the relatively high activation energies suggest that the glide resistance of the dislocations arises from a dense arrangement of strong obstacles. These features of dislocation dynamics become evident in the dislocation structure observed after room temperature deformation. Fig. 4.12 demonstrates the strong bowing out of screw

Fig. 4.11 Deformation characteristics of titanium aluminide alloys. Dependence of the flow stress, σ, and the reciprocal activation volume, 1/V, of different alloys on the deformation temperature. The drawn lines refer to the values of a Ti-47Al-2Cr-0.2Si alloy with a near gamma microstructure. Values estimated at strain ε=1.25% and strain rate ἐ=4.16 ·10^{-4} s^{-1}.
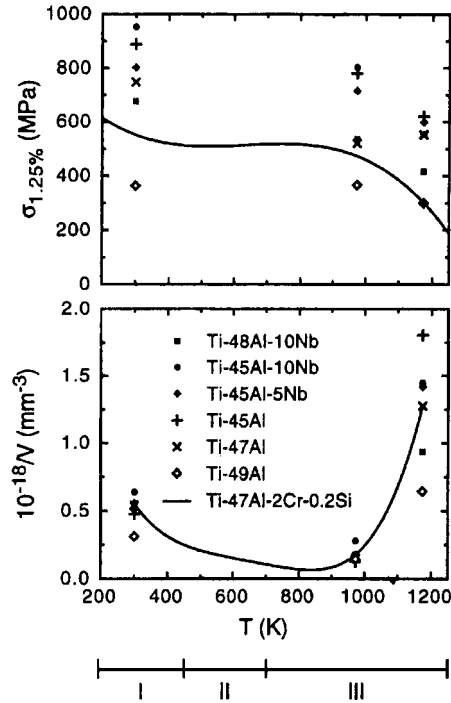
dislocations between glide obstacles, which were also observed in other studies [87, 88]. Some controversy has arisen in the TiAl literature over the nature of the glide obstacles. The ongoing discussion involves lattice friction, intrinsic mechanisms like jog dragging, and extrinsic pinning by impurity related defects. In Fig. 4.12 a large fraction of the obstacles can undoubtedly be identified as jogs because dislocation dipoles and debris are trailed from them. However, it is tempting to speculate that extrinsic glide resistance is also present. In TiAl alloys, oxygen, nitrogen and carbon are unavoidable impurity elements, which have a low solubility in the γ phase [89]. Thus, these elements can easily precipitate as oxides, nitrides and carbides, which may act as localized glide obstacles. This hypothesis was supported by Kad and Fraser [90], who observed anchoring of 1/2⟨110] dislocations at oxide particles. The presence of extrinsic glide resistance is also suggested by the observed pinning of twinning partial dislocations [5, 86, 91]. This pinning process cannot be attributed to an intrinsic mechanism, like jog dragging, because cross-glide and jog formation is impossible in partial dislocations. Additional glide resistance certainly arises from a lattice friction mechanism. Due to the directional bonding of γ(TiAl), high lattice friction is expected for all types of dislocations [92–95]. This is also suggested by the observation that the dislocations in the unloaded TEM samples are still bowed out in a smooth arc. It is therefore assumed that high lattice friction forces occur on all characters of dislocations, which impede a complete relaxation of the bowed segments into
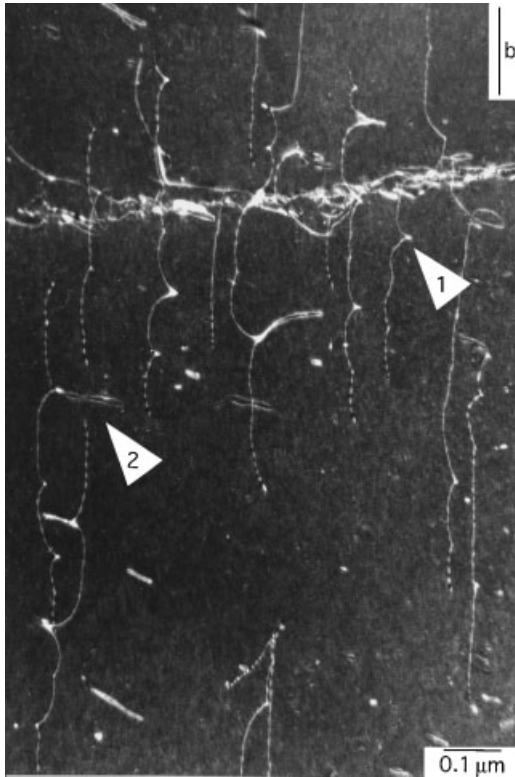
Fig. 4.12 Dislocation dynamics in domain I of the σ(T)-curve shown in Fig. 4.11. Pinning of screw dislocations with Burgers vector b = 1/2⟨110] by localized obstacles and jogs (arrow 1). Additional glide resistance arises probably from a lattice friction mechanism. This is indicated by the observation that the dislocations in the unloaded sample are still bowed out in a smooth arc. Note the dislocation dipoles and debris defects that are trailed and terminated at jogs (arrow 2). Ti-48Al-2Cr, compression at T = 300 K to strain ε = 3%.

the geometrically shortest configuration between the obstacles. This type of glide resistance probably disappears at about 600 K, which is suggested by the small value of 1/V. Nevertheless, the flow stress, σ, is practically constant in this temperature domain. It is therefore speculated that the dislocation mobility in domain II of the σ(T)-curve is impeded by another mechanism. Two-phase alloys exhibit discontinuous yielding and negative strain rate sensitivity in the intermediate temperature interval (450–650 K). These phenomena are usually associated with the Portevin-LeChatelier effect [68, 73], which arises from the dynamic interaction of diffusing defects with the dislocations. The resulting glide resistance and strain ageing effects were investigated using the classic yield-point return technique [91, 96, 97], as demonstrated in Fig. 4.13a. The observed fast kinetics (Fig. 4.13b) and low activation energy of the aging process of $Q_a = 0.6$–0.8 eV [91, 96, 97] suggest that rapid defect accumulation at the dislocations occurs at low temperatures. A wide range of alloy compositions and microstructures was investigated in order to identify the relevant defect species [98]. The strain ageing phenomena strongly depend on off-stoichiometric deviations and are particularly pronounced in Ti-rich alloys. This gives rise to the conclusion that Ti_{Al} antisite defects, i.e. Ti atoms situated on the Al sublattice, are involved in the pinning process. In TiAl alloys no

structural vacancies are formed, thus, deviation from stoichiometry is compensated by antisite defects [70, 71, 99]. Association of the Ti_{Al} antisite defects with vacancies leads to the formation of anti-structural bridges that provide paths of easy diffusion. It is tempting to speculate that defect agglomerates consisting of antisite atoms and vacancies will produce an asymmetric distortion. If such a defect interacts with the stress field of a dislocation, vacancy jumps may be initiated so that the vacancy/antisite complex is reoriented and the strain energy of the dislocation is lowered. Locking of the dislocations, therefore, occurs in a fashion that has been described for Snoek atmospheres [73]. As the test temperature is raised, the strain ageing phenomena gradually disappear because the defect atmospheres probably migrate with the dislocations and, thus, provide less glide resistance.

The observations indicate that in the intermediate temperature range $T = (0.3–0.4)T_m$ (T_m – absolute melting temperature) fast and effective locking of the dislocations occurs, analogous to the well known blue-brittleness in steels, which may be harmful for ductility and damage tolerance of the material. Support of this view is provided by recent studies of fracture toughness in γ(TiAl)-based alloys, which demonstrated the link between dislocation dynamics and the characteristics of crack propagation [100, 101]. During service the components repeatedly pass
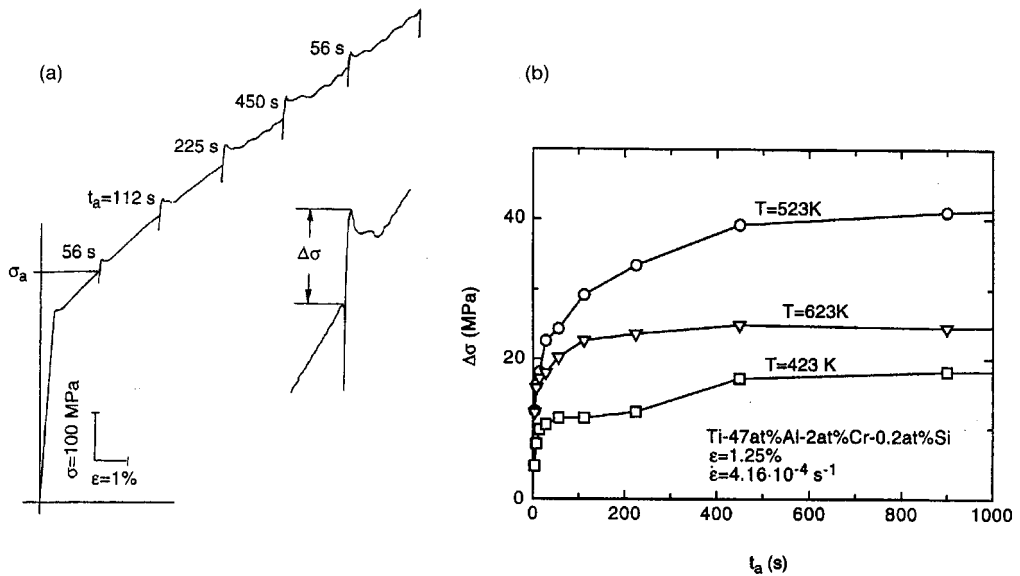
Fig. 4.13 Deformation behavior in domain II of the σ(T) curve (Fig. 4.11); Portevin-LeChatelier effect in a Ti-47Al-2Cr-0.2 Si alloy with near gamma microstructure. (a) Sequence of static strain aging experiments performed at T=523 K under a relaxing load. The stress increments were measured as the difference in stress before aging and the peak level on reloading. Different time intervals, t_a, between unloading and subsequent reloading are indicated. (b) Kinetics of strain aging under relaxing stresses and the deformation parameters indicated.

through the critical temperature range for atmosphere formation; thus, premature failure of the components may occur, which requires adequate safety factors.

Deformation at elevated temperatures (domain III) is characterized by a strong increase of $1/V$ with T. The activation parameters estimated for two-phase alloys at $T = 1100$ K are typically [85]:

$$V = (50 - 90)b^3, \ \Delta H = 2.9 - 3.2 \, \text{eV} \, .$$

For comparison, the Ti self-diffusion energy of γ(TiAl) was estimated as $Q_{sd} = 3.01$ eV [102], while recent measurements have led to $Q_{sd} = 2.6$ eV [103]. This energy is indicative of a diffusion-assisted dislocation mechanism [101]. Under these conditions, the interaction of the dislocations with vacancies leads to dislocation climb, which is manifested by the formation of helical dislocation configurations. The operation of the mechanism was confirmed by in situ TEM observations [5, 104], which are demonstrated by a series of micrographs in Fig. 4.14. Climb was preferentially observed on ordinary $1/2\langle 110]$ dislocations, which is plausible as these dislocations have a compact core structure [58, 61]. However, objection to the climb hypothesis may be raised on the grounds that the associated activation volumes are too large for climb. In the present evaluation, V was referenced to the Burgers vector of ordinary dislocations, which mainly contribute to the deformation of two-phase alloys. The values estimated at $T = 1100$ K are $(50–90)$ b^3, whereas from theory, climb is associated with $V = (1–10)$ b^3 [73, 84]. This significant difference indicates that the activation parameters determined by deformation tests and microscopic features of dislocation dynamics can be correlated in a very complex manner. There are mainly three reasons that may account for the discrepancy. First, non-planar dissociation of the dislocation core on intersecting $\{111\}_\gamma$ planes can lead to locking of the respective dislocation segments. Supporting evidence for such a mechanism is provided by the observation that the climb structure involves straight segments with $\langle 110 \rangle$ orientations (Fig. 4.14). Climb of dissociated dislocations is expected to be impeded by additional energy barriers [73]. Thus, climb may be restricted to the non-dissociated parts of the dislocations, which can give rise to a larger activation volume. Second, it is also possible that deformation is primarily accomplished by slip, but the factor controlling the amount of slip is the climb of dislocations about strong obstacles. The relative contributions of the two processes certainly depend on the deformation conditions $\dot{\varepsilon}$ and T [104, 105]. It might be expected that at a deformation temperature of 1000 K only relatively low strain rates can be realized by pure climb. At higher strain rates dislocation glide certainly significantly contributes to deformation. Thus, the total activation volume reflects the contributions of both glide and climb. Third, the activation volume was calculated according to Eqn. 4.7 assuming a Taylor factor of $f = 3.06$. However, at elevated temperatures, strain accommodation between differently oriented grains can in part be accomplished by climb of the dislocations out of their $\{111\}$ slip planes, which tend to reduce the Taylor factor and thus the values of V.

Another characteristic feature of high-temperature deformation is the strong increase in the reciprocal activation volume with strain, ε, when compared with low-
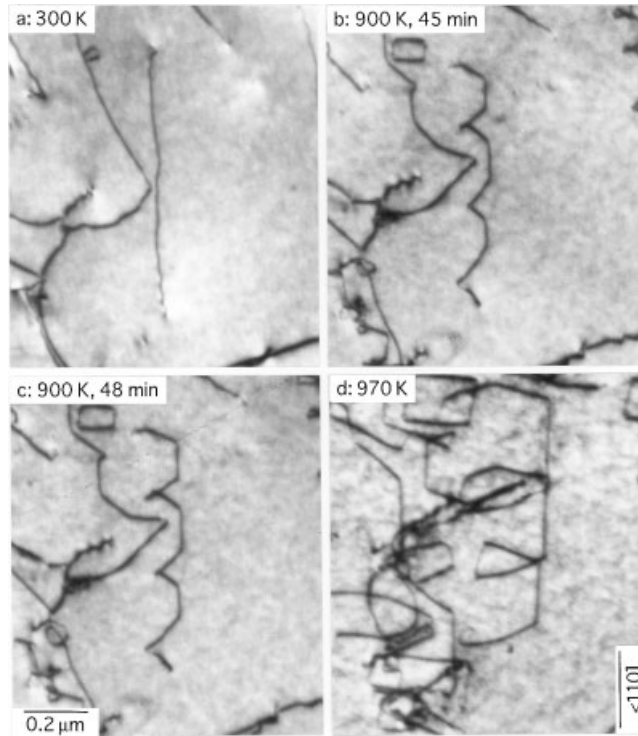
Fig. 4.14 Deformation behavior in domain III of the σ(T) curve (Fig. 4.11); climb of ordinary dislocations in a deformed sample observed during in situ heating inside the TEM. Ti-48Al-2Cr, pre-deformation at T=300 K to strain ε=3%.

er test temperatures [104]. This indicates the onset of a new thermally activated process as deformation proceeds. The behavior is demonstrated in Fig. 4.15, where the values determined at T=293, 973 and 1100 K are compared. The relatively weak increase of 1/V with ε observed at 293 K can be attributed to a work hardening mechanism due to dislocation dipoles [106, 107]. At elevated temperatures, intensive climb interactions of dislocations and point defects are expected due to enhanced diffusion. In order to realize the superimposed strain rate, a sufficient number of dislocations must be present. Initially, the dislocations are probably generated by the cross-glide mechanisms described in section 4.4.2. Absorption of vacancies leads to climb bow-out and formation of helical dislocations, as described before. Such configurations are relatively sessile with respect to glide because energy would be required in order to restore the dislocations to their original glide plane. During plastic deformation and work hardening, the density and mutual interaction of defects increase, as may the rate of climb processes. This behavior is apparently reflected in the strong increase of 1/V with ε and thus lends support to the climb hypothesis.
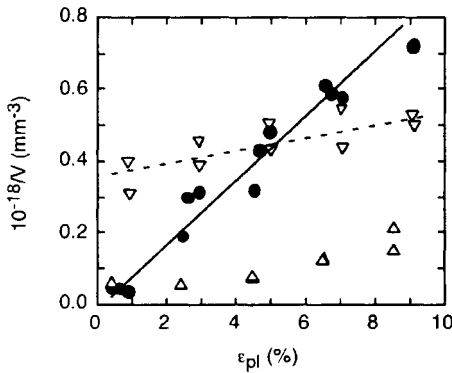
Fig. 4.15 Deformation behavior in domain III of the σ(T) curve (Fig. 4.11); dependence of the reciprocal activation volume, 1/V, on strain, ε, for the deformation temperatures T = 293 K (∇), T = 973 K (Δ), and T = 1100 K (●). Values estimated at $\dot\varepsilon = 4.16 \cdot 10^{-4}$ s^{-1}; Ti-47Al.

According to eqn. 4.5, an increase of 1/V is associated with an increase of the thermal stress part, σ*. Thus, the strain dependence of 1/V shown in Fig. 4.15 suggests that a thermal contribution to work hardening is produced by dislocation climb. This speculation is supported by the observation that the work hardening rate at high temperatures becomes strongly rate dependent.

Concerning this complex situation, it is difficult to make generalizations about the ability of dislocations to climb in TiAl. Apart from the deformation conditions T, ε and $\dot\varepsilon$, careful attention has to be paid in each case to other climb-controlling factors; these may involve alloy chemistry, constitution, microstructure, and impurity content. However, it is reasonable to assume that deformation of two-phase alloys at T ≥ 1100 K, ε ≥ 10% and $\dot\varepsilon \geq 10^{-4}$ s^{-1} is mainly determined by dislocation climb. In this context, the effects of alloy composition will be considered in Sections 4.5.2 and 4.5.3.

4.5
Mechanical Properties

For engineering applications, titanium aluminides must possess a good balance of various mechanical properties. In the following sections, the metallurgical factors will be considered that determine strength, ductility, creep, toughness, and fatigue.

4.5.1
Grain Refinement

Two-phase titanium aluminide alloys contain dense arrangements of internal boundaries due either to phase transformations or hot working. These boundaries are known to be very effective barriers for all types of perfect and twinning partial dislocations [5, 49]. As with many other metals, the stress required to transmit dislocations through the boundaries is considered to be athermal in nature and has often been described in terms of a Hall-Petch equation:

$$\sigma = \sigma_o + k_y D^{-1/2} \qquad\qquad\qquad\qquad\qquad\text{(eqn. 4.8)}$$

Where k_y is a material constant and D is a structural length parameter of the microstructure. σ_0 is a constant stress contribution, which has often been associated with other types of glide obstacles. A typical example are glide obstacles, which can be overcome with the aid of thermal activation, as described in Section 4.4.4. On the basis of this approximation, Hall-Petch relations have been revealed for several classes of two-phase alloys [108–110]. However, this is not considered to be confirmation of the specific dislocation pile-up model behind the Hall-Petch description, but may only reflect the fact that the slip distance of the dislocations correlates with the distance between phase or grain boundaries. However, the microstructures are mostly quite complex and rich in detail, encompassing different length parameters being relevant for the slip path of the dislocations and twins. This holds particularly for the analysis of duplex microstructures, where more than one length parameter is needed. These involve the grain sizes of the different phases, colony sizes and lamellar spacings. It is also often the case that coarse microstructures are investigated so that an insufficient number of grains or colonies is sampled. Thus, among the grains significant constraint stresses can be developed, which apparently lead to unrealistic yield stresses [111]. In fully lamellar alloys, the relevant structural parameter determining the yield strength in terms of the Hall-Petch equation is probably the lamellar spacing; this was shown by computer modeling of the yield behavior [112] and deformation experiments performed on PST-crystals [113–115]. The translation of shear processes through different lamellar interfaces was investigated by electron microscope observations [5, 49]. The investigations show that perfect and twinning partial dislocations are piled-up at the interfaces, which leads to stress concentrations. In response to the stress concentrations, new shear processes are initiated in the adjacent lamella, the slip systems of which depend on the orientation relationships existing between the lamellae [5].

The use of powder metallurgy is advantageous for analyzing the effects of grain refinement because fine-grained and texture-free materials with uniform microstructure and equiaxed grains can be obtained from consolidated powder. Thus, evaluation in terms of the Hall-Petch equation is straightforward. Fig. 4.16 shows the data measured at room temperature on a two-phase alloy and plotted according to eqn. 4.8 [116]. By linear regression, the Hall-Petch constants $\sigma_0 = 133$ MPa and $k_y = 0.91$ MPa m$^{1/2}$ were determined. The stress part, σ_0, which is independent of the grain size, is generally very small. k_y is at the lower limit of the values reported in the literature for polycrystalline materials [108–110]. Nevertheless, the term $k_y D^{-1/2}$ accounts for about 70% of the yield stress of TiAl alloys with globular microstructure [5, 49]. This result clearly indicates that the strength of TiAl alloys is mainly determined by the microstructure. Thus, grain refinement is an important issue for the design of alloys with improved strength properties.

Alloys with fully lamellar microstructures are beneficial for high temperature strength, fracture toughness and creep resistance, but suffer from poor ductility at low and ambient temperatures. Duplex structures are conducive for tensile ductili-
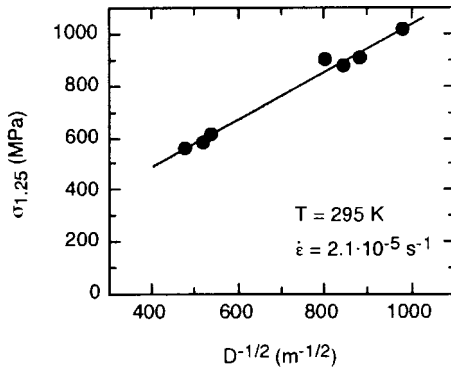
Fig. 4.16 Flow stress in dependence of the inverse square root of mean linear grain size as measured in compression at the beginning of plastic deformation ($\varepsilon = 1.25\%$) on different specimens of a PM processed Ti-47Al-3.7(Nb, Cr, Mn, Si)-0.5B alloy with equiaxed microstructure. A linear regression gives Hall-Petch constants $\sigma_0 = 133$ MPa and $k_y = 0.91$ MPa m$^{0.5}$. Values estimated at $\dot{\varepsilon} = 4.1 \cdot 10^{-5}$ s^{-1} s

ty, but are inferior when fracture toughness, high temperature strength and creep resistance are required. Thus, concerning the intended high temperature applications, lamellar alloys probably provide the best balance of mechanical properties. With this perspective in mind, process development is currently focused on techniques that provide fine-grained, fully lamellar microstructures. This concept was successfully demonstrated on an extruded two-phase alloy [117, 118]. There are detailed reviews on the correlation between microstructure and mechanical properties, the reader is referred to these articles for further details and references.

4.5.2
Effects of Alloy Composition

Extensive research performed during the last decade has demonstrated that alloy composition significantly affects the mechanical properties. Nevertheless, the role of the various alloying elements is not sufficiently clear. In the Ti-Al system the extension of the individual phase fields between α_2(Ti$_3$Al) and γ(TiAl) shown in Fig. 4.1 depends on the addition of a third element. Thus, microalloying alters the path by which microstructures evolve. This may easily mask strength variations caused by solid solution or precipitation hardening and makes an assessment of alloying effects difficult. Nevertheless, certain rules have been empirically established that may be used as guidelines in alloy design towards desired properties [119].

- In general, a reduction in aluminum content tends to increase the strength level, but reduces ductility and oxidation resistance.
- Additions of Cr, Mn and V up to a level of 2 at% for each element have been shown to enhance ductility.
- Additions of 1–2 at% Nb are required in order to achieve sufficient oxidation resistance.
- W, Mo, Si, and C up to a level of 0.2–2 at% for each element are added in order to improve the creep resistance.
- B additions of 0.2–2 at% act as grain refining coagulant and are used for stabilizing the microstructure during high temperature service.

Boron additions lead to the formation of different types of titanium borides; however, in most cases TiB_2 platelets are present. It is generally assumed that the borides affect the kinetics of the high-temperature phase transformations in that they provide nucleation sites for the α and β phases [120–123]. The degree of grain refinement and the mechanical properties that can be achieved by boron additions apparently also depend on the Al content and cooling rate that occurred in the high-temperature phase field. Several aspects of the relevant mechanisms need further investigation.

Based on these experiences, extensive alloy development has been performed with the goal of improved mechanical properties. As with conventional materials, solid solution and precipitation hardening were utilized. In the case of TiAl alloys, the challenge is to strengthen the material without compromising other desired properties, such as low temperature ductility and toughness. The complex situation in this field of metallurgy will be illustrated in the following two sections.

4.5.3
Solid Solution Effects due to Nb Additions

Recently, it has been shown that a significant strengthening effect can be achieved when 5–10 at% Nb is added to TiAl alloys [86, 119, 124]. The reader is referred to Fig. 4.11, where the yield stresses and the reciprocal activation volumes of different alloys were compared. Accordingly, TiAl alloys with 5–10 at% Nb exhibit yield stresses in excess of 800 MPa. These values are significantly higher than those of conventional two-phase alloys, which are represented in Fig. 4.11 by a Ti-47Al-2Cr-0.2Si alloy. Despite the extensive body of investigation broadly confirming these results, there is some controversy about the nature of the strengthening effect of Nb additions, i.e. whether it arises from solid solution hardening or from a structural change. Atom location by channeling enhanced microanalysis (ALCHEMI) studies have revealed that Nb solely occupies the Ti sublattice [125, 126]. Solid solution hardening would arise from a short-range interaction between the dislocations and the Nb atoms, and thus should be manifested by an additional stress part, σ*, and larger values of 1/V, according to eqn. 4.5. This is clearly not the case, as demonstrated in Fig. 4.11. Solid solution hardening of the Nb-bearing alloys would rely on the very small size misfit of Ti and Nb atoms, which is about 0.2% maximum [127]. This seems unlikely to completely explain the observed strengthening effect in Al-lean alloys. Strong solute dislocation interactions are only expected for large misfits or defects that introduce non-centrosymmetric distortions [73]. Thus, the viewpoint that the high strength of Nb bearing alloys arises from Nb solution hardening [128] should be considered with caution. Since the activation volume is practically independent of the Nb content, the strengthening effect should be attributed to an athermal mechanism that is probably associated with a structural change. This is supported by the observation that Nb-bearing alloys exhibit almost the same yield stress as binary alloys with the same Al content. Electron microscope observations have shown that the Nb additions lead to a significant structural refinement. In particular, the lamellar consti-

tuents of the microstructure exhibit very fine lamellar spacings and a high density of α_2 lamellae. This results in a dense arrangement of interfaces, which impede dislocation glide and mechanical twinning. The characteristic features of microstructure and deformation of high Nb-containing alloys are demonstrated in Fig. 4.17. In view of these findings, the high flow stress of alloys of the type Ti-45Al-(5–10)Nb can be rationalized in terms of a Hall-Petch mechanism [86].

However, in spite of the similarity in the mechanisms determining the yield strength of binary and Nb-containing alloys, several other aspects of dislocation dynamics are notable. These are associated with the dislocation core structure, the energies of planar defects and the diffusion properties. For Nb-bearing alloys, an abundant activation of twinning has been recognized and the superdislocations were found to be widely dissociated, an observation that suggests that the stacking fault energies of γ(TiAl) are lowered by the Nb additions. In many grains or lamellae, dissociated superdislocations, planar faults and twins coexist (Fig. 4.18). Thus, it is speculated that twin nucleation can occur by the superposition of extended stacking faults on alternate {111} planes [82]. The strong contribution of mechanical twinning and superdislocation glide certainly reduces the plastic anisotropy of γ(TiAl) (see section 4.4.1), which is conducive for the deformation of polycrystalline material. This might be the reason that optimized Nb-containing alloys exhibit room temperature tensile yield stresses in excess of 1000 MPa and plastic tensile elongations of 2–3% (section 4.7). The binary reference alloys exhibit only poor elongations of less than 1% under the same conditions.

Concerning high-temperature deformation and creep resistance, the important point to note is that the activation enthalpy of high Nb-containing alloys is $\Delta H = 4$–4.5 eV, which is significantly higher than that of conventional alloys [86, 129, 130] (section 4.4.4). This finding agrees with recent tracer measurements of the Nb solute diffusion, which revealed that Nb is a slow diffuser in γ(TiAl) [131]. The result implies that diffusion-assisted deformation mechanisms might be impeded in such alloys. Furthermore, climb processes of the superdislocations are difficult because of their wide dissociation. These characteristics of the dislocation dynamics are probably the reason for the high yield stress of the alloys at 700 °C. Nb is also a commonly added element because of its ability to improve oxidation resistance [132]. Thus, alloys of the type Ti-45Al-(5–10)Nb exhibit several desirable attributes that give them the potential for expanding the service range of titanium aluminides to higher temperatures [129, 130].

4.5.4
Precipitation Hardening

In TiAl alloys, appreciable improvements in strength and creep resistance can be achieved by precipitation hardening from oxides [90, 133], nitrides [134], silicides [135, 136], and carbides [91, 134, 137–139]. The strengthening effect critically depends on the size and the dispersion of the particles. In this respect, carbides, nitrides and silicides appear to be beneficial as the optimum dispersion can be achieved by homogenization and ageing procedures. Details of the hardening
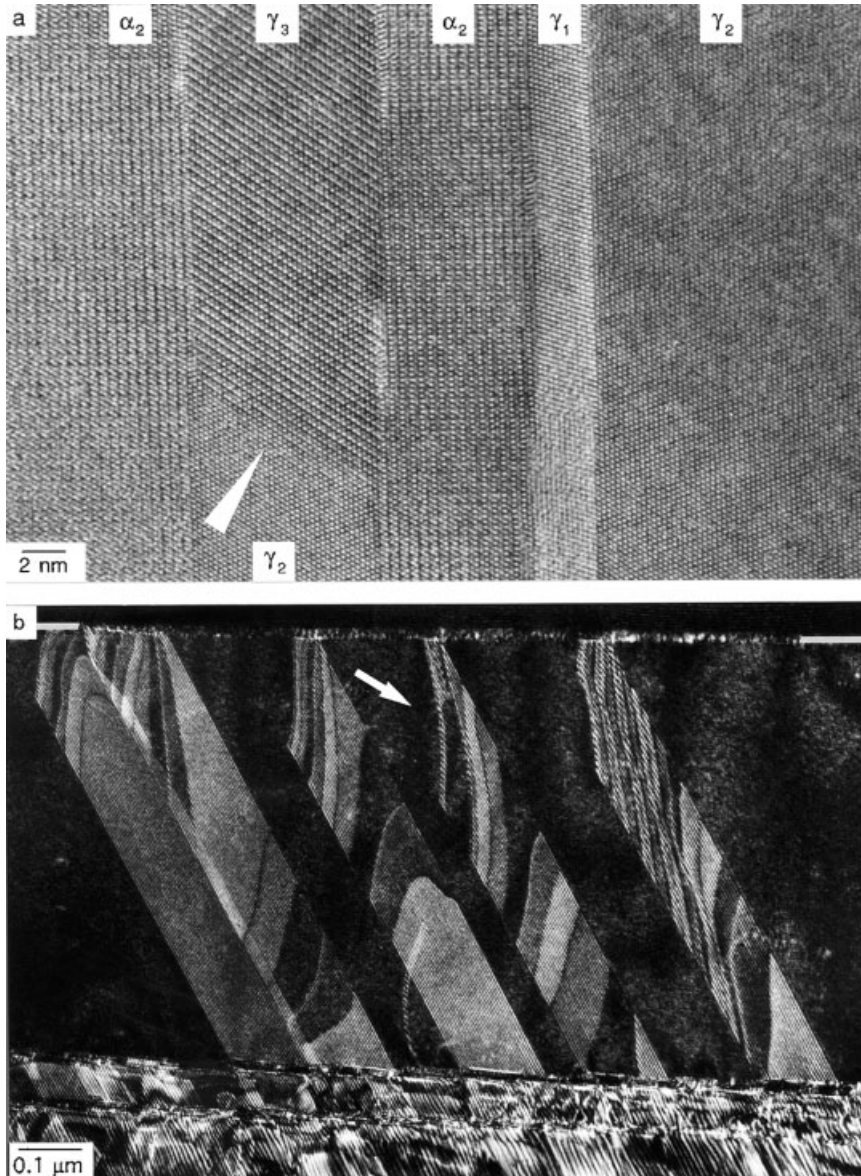
Fig. 4.17 Microstructure and deformation mechanisms in high niobium containing alloys. (a) High resolution TEM micrograph showing the lamellar microstructure of a Ti-45Al-10Nb alloy that had been extruded below the α-transus temperature. Note the small lamellar spacings, the high density of α_2 lamellae, the ledges at the interfaces, and the domain boundary in one of the γ lamellae. (b) Deformation twins generated in a Ti-45Al-5Nb alloy by compression at T=973 K to strain ε=3%. Twinning partial dislocations (arrowed) are piled up against a lamellar boundary.

Fig. 4.18 Deformation structure observed in a Ti-45Al-10Nb alloy after tensile deformation at T = 295 K to a plastic strain ε = 1% and flow stress σ = 1050 MPa. Note the widely disso-ciated superdislocations, stacking faults and deformation twins coexisting in a deformed γ grain.

mechanism were investigated for carbides and will be considered here. A systematic series of carbon-doped alloys with the baseline composition Ti-48.5Al-(0.02–0.4)C were subjected to different thermal treatments [91, 137, 138]. Annealing at 1250 °C and quenching resulted in a carbon solid solution, whereas Ti_3AlC perovskite precipitates were formed by subsequent ageing at 750 °C. Annealing at temperatures above 800 °C leads to the formation of the H-phase Ti_2AlC with a plate-like morphology [137]. Thus, the strengthening effect of the additional glide obstacles could be quantitatively assessed.

Fig. 4.19 shows the dependence of the yield strength and of the reciprocal activation volume on the carbon concentration for the deformation temperatures T = 293 and 973 K [91]. For the quenched materials, in which carbon is thought to be present as solute atoms (or tiny agglomerates), the flow stress was found to be nearly independent of carbon concentration, c (Fig. 4.19a). At room temperature, the reciprocal activation volume $1/V_i$ of these materials slightly increased with c, which indicates the density of short-range obstacles increases with c. It is therefore concluded that carbon atoms in solid solution act as weak glide obstacles that can apparently be easily overcome with the aid of thermal activation. Thus, the mechanism is manifested in the activation volume, but is rather ineffective for hardening the material.

In contrast, the flow stress increased with c when the material was aged and carbon was present as Ti_3AlC precipitates. At room temperature, the reciprocal ac-
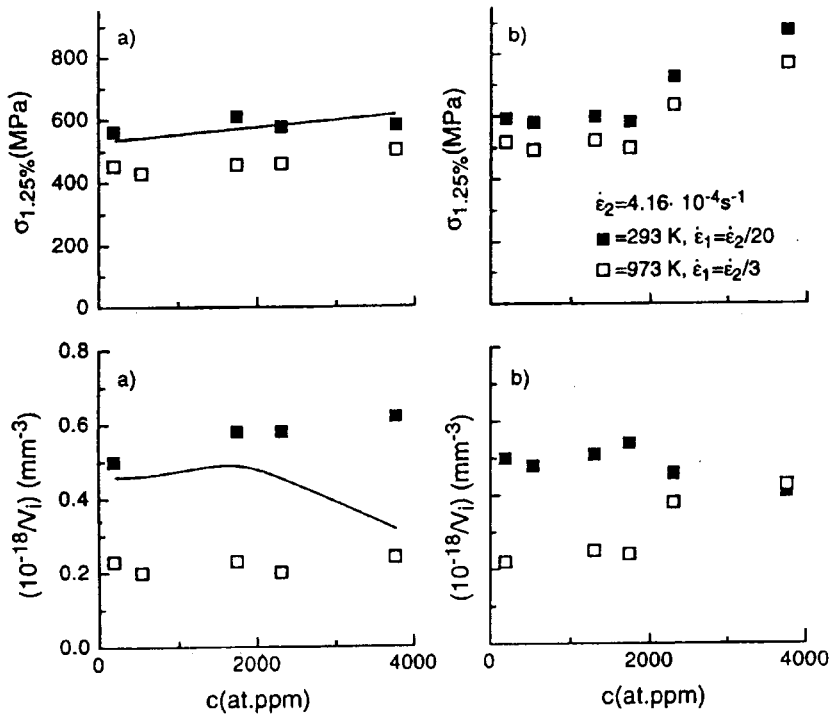
Fig. 4.19 Precipitation hardening of a two-phase titanium aluminide alloy with the base-line composition Ti-48.5Al-(0.02–0.4)C. Dependence of the flow stress, σ, and the reciprocal activation volume on the carbon concentration, c. (a) Homogenized and quenched alloys with carbon in solid solution or in form of tiny agglomerates. The drawn lines refer to the room temperature values of the materials in the as HIPed condition where carbon is present as coarse dispersion of the H-phase Ti_2AlC and the perovskite phase Ti_3AlC. (b) Quenched and aged materials that contain a fine dispersion of Ti_3AlC perovskite precipitates. Values estimated at strain $\varepsilon = 1.25\%$.

tivation volumes of these materials slightly decrease with c. A natural explanation of this behavior is that the perovskite precipitates are glide obstacles with a long-range stress field that cannot be overcome by a single activation event. This implies that the significant strengthening effect of the perovskite precipitates is athermal in nature. This view is supported by the fact that the high flow stress of the heavily doped material was maintained up to 973 K. The presence of the perovskite precipitates probably reduces the plastic anisotropy of the γ phase, which is suggested by the observation that superdislocation glide and mechanical twinning significantly contribute to deformation. The situation is similar to that observed in the high Nb-containing alloys. The glide resistance provided by the perovskite precipitates was investigated by TEM observations and specified in terms of dislocation/point obstacle interactions [5, 91]. In confirmation of the mechanical data, the perovskite precipitates were found to be strong glide obstacles for all

characters of perfect and twinning partial dislocations, as demonstrated in Fig. 4.20. The obstacle strength was characterized in terms of the parameters defined in Fig. 4.20c. The interaction with $\langle 101]$ superdislocations is characterized by obstacle distance $l_c = 50$–100 nm, angle of attack $\psi = 110°$ and line tension forces $f_m = 1.5 \cdot 10^{-8}$ N or $f_m/\mu b^2 = 0.57$. The effective shear stresses acting on the dislocation segments were determined by comparing their curvature with line tension configurations (Fig. 4.20a). This led to an average value $\tau_c = 300$ MPa. The
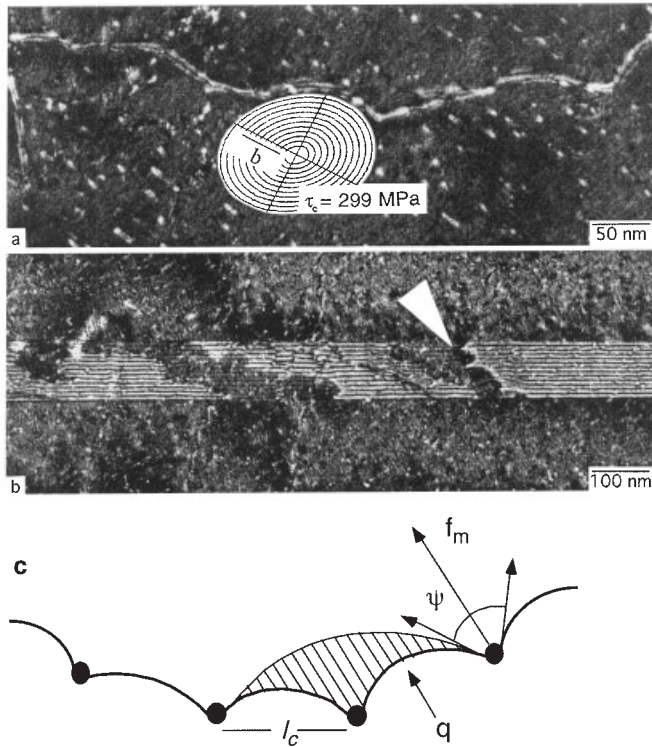
Fig. 4.20 Precipitation hardening of a two-phase titanium aluminide alloy Ti-48Al-0.37C; analysis of dislocation structures observed after room temperature compression to strain $\varepsilon = 3\%$ and stress $\sigma = 1000$ MPa. Pseudo weak beam images recorded using $g = (002)_{TiAl}$ reflection from near the [020] pole in the g/3.1g condition. Note the high density of Ti$_3$AlC-precipitates that are manifested by strain contrast. (a) Pinning of superdislocations with Burgers vector b = [011] by perovskite precipitates Ti$_3$AlC. The insert shows line tension configurations calculated for different stresses and projected into the image plane. For the segment analyzed, the length $l_c = 110$ nm, the half axis $q = 80$ nm and effective shear stress $\tau_c = 299$ MPa were determined. (b) Pinning of twinning partial dislocations (arrowed) by precipitates. Twinned and untwinned regions occur due to the immobilization of the twinning partial dislocation. (c) Assessment of the precipitation hardening in terms of dislocation/point obstacle interactions; l$_c$ obstacle distance, q major semi-axis of line tension configurations of dislocations describing the curvature of bowed-out segments, ψ angle of attack, f$_m$ interaction force.

yield stress to deform the sample to strain $\varepsilon = 3\%$ was $\sigma = 1000$ MPa. From this value the applied shear stress $\tau = \sigma/f = 330$ MPa can be determined, which agrees well with the value estimated by the line tension analysis. Thus, the hardening effect achieved by the perovskite precipitates can solely be attributed to their elastic interaction with the dislocations. Fig. 4.19 also includes the values of carbon-doped materials, which were tested after HIP followed by slow cooling. Due to this treatment, most of the perovskite precipitates were probably transformed into coarse H-phase particles Ti_2AlC [137]. In this condition, the flow stress of the materials is relatively low and almost independent of carbon concentration. The related reciprocal activation volumes decrease significantly with c, which clearly indicates that the Ti_2AlC particles are also athermal glide obstacles. The coarse dispersion of this phase seems to be less effective in strengthening the material. This observation agrees with the widely accepted view that both the size and dispersion of the particles are important for an effective precipitation strengthening. Hardening of γ(TiAl)-based alloys by fine dispersions of perovskite precipitates seems therefore to be a suitable technique for improving the high-temperature strength and creep resistance. Industrial application of the technique might be difficult because high-temperature annealing and quenching is required, which can be a problem for large components.

4.5.5
Creep Resistance

As shown in section 4.4.4, the deformation behavior of TiAl alloys becomes strongly rate dependent at homologous temperatures above $0.5T_M$. Under these conditions, creep and rupture processes of the material are primary design considerations. In many high-temperature applications, e.g. gas turbines, the operating temperature, and hence the efficiency, are limited by the creep characteristics of the material. Designs are usually made on the basis of a maximum permissible amount of creep, such as 0.1 or 1%, during the expected lifetime of a particular component. In this respect, most γ(TiAl)-based alloys are inferior to the nickel-based superalloys, even if the comparison is made on a density corrected basis. This deficit in creep resistance limits the substitution of superalloys by titanium aluminides. The problem became evident during the past five years, and has attracted many research activities [140–146]. The creep properties were found to depend on both alloy composition and microstructure, and considerable improvements have been achieved by optimizing these two factors. The data was summarized and critically assessed in recent reviews [147, 148] to which the reader is referred for more details. As with many other materials, the creep characteristics of TiAl alloys involve primary, secondary (or steady state) and tertiary regions, the extent of which depend on stress and temperature. The dependence of the steady state or minimum creep rate, $\dot{\varepsilon}$, upon the testing conditions is often described in terms of the Dorn equation

$$\dot{\varepsilon} = A\,\sigma_a^n \exp(-Q_c/RT)\,. \qquad \qquad (eqn.\,4.9)$$

Where Q_c is the activation energy, σ_a is the applied stress, A is a dimensionless material constant, and R is the universal gas constant. Analysis of the data leads to stress exponents n = 3–8 and a correspondingly wide range of activation energies Q_c = 190–700 kJ mol^{-1} [148]. This indicates that several mechanisms are involved in creep, which in certain ranges of stress and temperature are superimposed. At intermediate stresses and temperatures, which correspond to the intended service conditions, the creep rate is apparently controlled by dislocation climb, which is suggested by the estimated stress exponents of n = 3–4 and activation energies Q_c = 300–400 kJ mol^{-1}, which are reasonably close to the Ti self-diffusion energy of γ(TiAl). However, many aspects of creep are still a matter of debate and controversy. In particular, little information is available on the long-term creep behavior under modest stresses and temperatures, although these conditions are more appropriate for the anticipated engineering application. The intention of this section is to address this imbalance of information by analyzing such experiments.

The tests were performed at 700 °C and involve low stresses of σ_a = 80–140 MPa in order to achieve low creep rates [75, 149, 150]. Fig. 4.21 depicts the creep curves of different two-phase alloys determined under these conditions. As with other mechanical properties, the creep characteristics of γ(TiAl)-based alloys are sensitive to the nature and scale of the microstructure. Fully lamellar microstructures exhibit the best creep resistance [147] and, thus, will be considered here. However, depending on temperature and stress, the primary creep strain of fully lamellar materials can exceed that of duplex material. This might be a critical problem for the application of the otherwise creep resistant material. There is good evidence that the high primary creep rate of lamellar alloys is associated with the emission of dislocations from the lamellar interfaces [74, 75], as was described in Section 4.4.2. The creep behavior of two-phase alloys sensitively depends on the processing conditions and the fine details of the microstructure. This is demonstrated in Fig. 4.21 b, where the creep curves of different microstructural forms of an industrial alloy are compared. The lamellar modifications (1) and (3), distinguished significantly in the lamellar spacing, which might be the main reason for the observed difference in creep behavior. It is well documented that fine lamellar spacings are beneficial for a good creep resistance [147, 148]. Furthermore, processing of the alloy (1) involved investment casting followed by fast cooling, which probably led to a significant vacancy supersaturation. Thus, the fast creep rate may in part be attributed to the dislocation point defect interactions, which were described in sections 4.4.2 and 4.4.4.

Under creep conditions, lamellar alloys suffer from spheroidization and coarsening. Since many aspects of this structural degradation are intimately linked to defect configurations at the atomic level, standard techniques of metallography are often inadequate to provide the necessary information. Thus, imaging techniques of conventional transmission electron microscopy have been coupled with high resolution electron microscopy to characterize the relevant processes. A prominent feature in the microstructure of crept lamellar alloys is the existence of multiple-height ledges at γ/γ interfaces. An initial stage of the process is shown
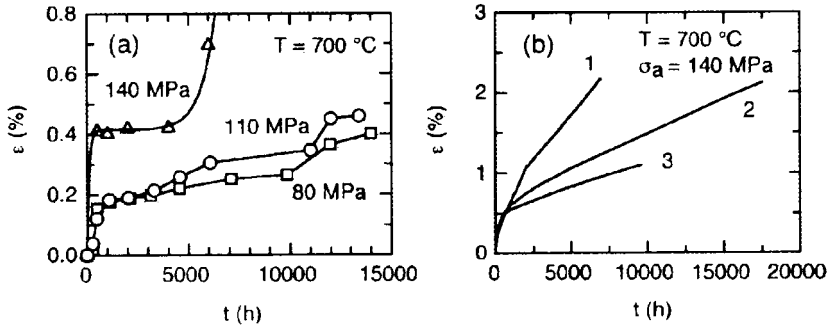
Fig. 4.21 Creep characteristics of two-phase titanium aluminides. (a) Ti-48Al-2Cr, duplex structure containing a high volume fraction of lamellar colonies. (b) Ti-47Al-3.7 (Nb, Mn, Cr, Si)-0.5B; (1) investment casting, nearly lamellar microstructure, lamellar spacings 0.1– 1.5 μm; (2) investment casting + HIP, duplex microstructure; (3) investment casting + HIP + heat treatment at $T_\alpha + \Delta T = 1380\,^\circ$C, nearly lamellar microstructure, lamellar spacings 10 nm–0.5 μm.

in Fig. 4.22. The ledges had often grown into zones, which extended over about 10 nm. The atomic arrangement in these zones is reminiscent of a faulted 9R structure. The growth of this phase can formally be rationalized by two shear processes on adjacent $(111)_\gamma$ planes along the true twinning direction $1/6[11\overline{2}]$ and one anti-twinning operation along $1/3[\overline{1}\,\overline{1}2]$ on every third $(111)_\gamma$ plane. It is speculated that these large ledges arise from one-plane steps, which moved under diffusional control along the interfaces and were piled-up at misfit dislocations (arrowed in Fig. 4.22). Once a sharp pile-up is formed, the configuration may arrange into a tilt configuration with a long-range stress field. This would cause further perfect or Shockley partial dislocations to be incorporated into the ledge. This would explain the large height of the ledges (up to 200 nm) and the observation that in all cases they were associated with misfit dislocations. The 9R structure has probably a slightly higher energy than the $L1_0$ structure of γ(TiAl) [151]. When the slabs grow further it might be energetically favorable to reconstruct the $L1_0$ structure and to nucleate a new γ grain, an earlier stage of this process is apparently demonstrated in Fig. 4.23. The high resolution micrograph shows that the grain is already completely ordered, which suggests that the ordering reaction occurs during, or immediately after nucleation.

There is a significant body of evidence in the TiAl literature indicating that dissolution of the α_2 lamellae occurs during creep [74, 75, 139, 142, 152]. The phase transformation is probably driven by a non-equilibrium constitution [150]. Since the phase boundaries of the $\alpha+\gamma$ phase field in the binary phase diagram are strongly dependent on temperature, the volume fraction of the α_2 and γ phases might be particularly sensitive to the thermal history of the material. The thermo-mechanical treatment of the alloy investigated here was carried out above the eutectoid temperature, where a relatively high volume fraction of the α phase occurs. Upon cooling, a significant excess fraction of the α_2 phase can be retained,
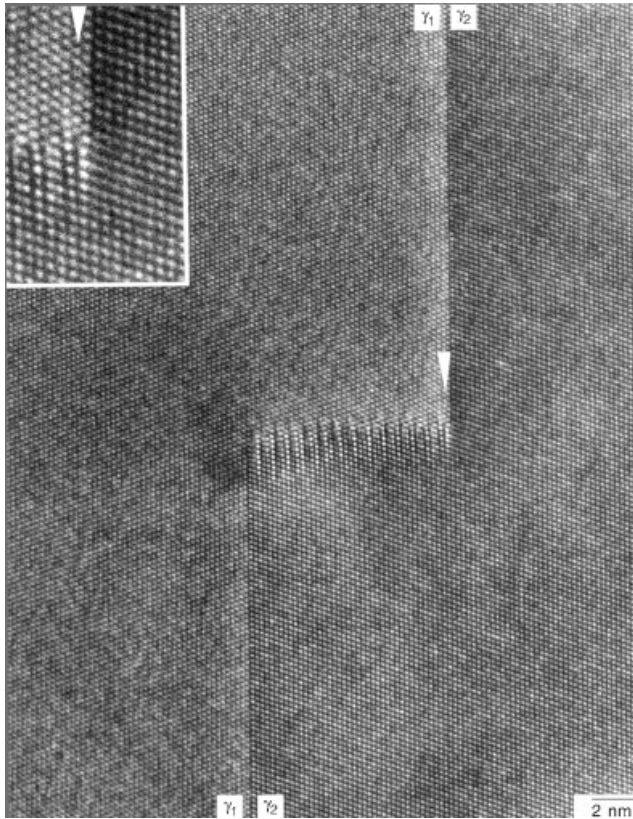
Fig. 4.22 Structural changes of lamellar γ/γ interfaces observed after long-term creep. Ti-48Al-2Cr alloy with a duplex microstructure containing a high volume fraction of lamellar colonies. Formation of a high ledge, note the misfit dislocation (arrowed) that is manifested by an additional $(111)_\gamma$ plane parallel to the interface. Creep conditions: $\sigma_a = 140$ MPa, $T = 700\,^\circ$C, $t = 5988$ h, $\varepsilon = 0.69\%$.

since the $\alpha/\alpha_2 \rightarrow \gamma$ phase transformation is sluggish. Thus, during long-term creep, dissolution of the α_2 phase is expected in order to establish the equilibrium concentration at the test temperature of 700 °C. This interpretation is supported by the high resolution micrograph shown in Fig. 4.24 a. There is clear evidence that the density of ledges in the α_2/γ interfaces is significantly higher than at the γ/γ interfaces [74, 75]. This is probably a consequence of the complex transport processes associated with the α_2/γ phase transformation. The interfacial ledges are often associated with misfit dislocations having a Burgers vector component perpendicular to the interfacial plane. Climb of these dislocations and propagation of the ledges lead to a lateral migration of the interfaces. Not only must the stacking sequence be changed during migration of the interface from the DO_{19} structure of $\alpha_2(Ti_3Al)$ to the $L1_0$ structure of $\gamma(TiAl)$, but the local chemical composition also has to be adjusted. Accommodation of the composition requires long-
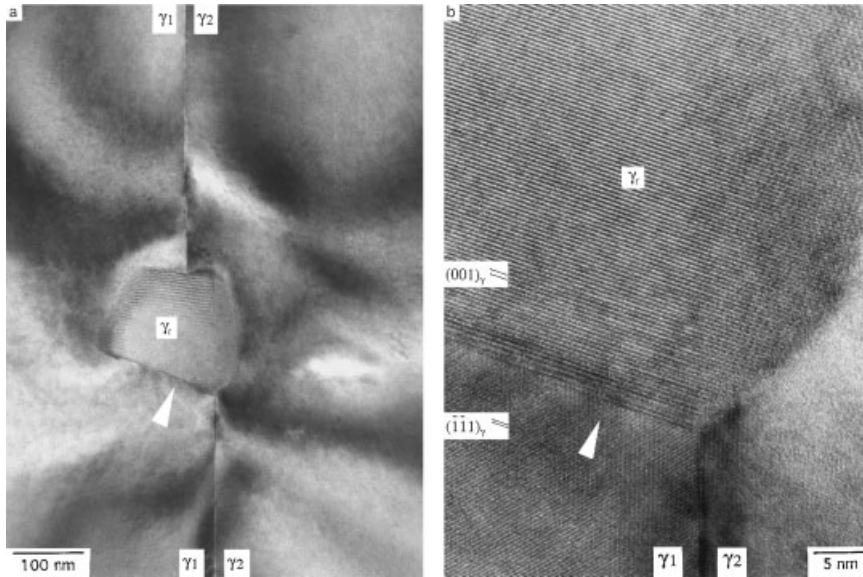
Fig. 4.23 Recrystallization processes at γ/γ interfaces observed after long-term creep of a Ti-48-Al-2Cr alloy. Creep conditions: $T = 700\,^{\circ}C$, $\sigma_a = 140$ MPa, $t = 5988$ h, $\varepsilon = 0.69\%$. (a) Recrystallized γ grain (designated as γ_r) formed at a ledge of an interface joining twin related γ variants. (b) Higher magnification of the region arrowed in Fig. 4.23 a. Note the orientation relationship $(001)\|(\overline{1}\overline{1}1)$ between the recrystallized grain γ_r and the parent γ lamella.

range diffusion, which is probably sluggish at the creep temperature of $700\,^{\circ}C$. The process is probably supported by the mismatch structures present at the interfaces. Interfacial dislocations and ledges represent regions where deviation from the ideal crystalline structure is concentrated [73]. This provides paths of easy diffusion, which can effectively support the required exchange of Ti and Al atoms. Thus, it is speculated that misfit dislocations and ledges are strongly involved in achieving the phase equilibrium during migration of the α_2/γ interfaces.

One may expect these processes to be thermally activated and supported by superimposed external stresses. The degree and fine details of the structural changes may therefore depend on the applied deformation conditions. In this respect, the coherency stresses present at the interfaces are certainly significant because they are comparable to or even higher than the shear stresses applied during creep tests and are often associated with mismatch structures. Thus, it seems reasonable that degradation of the lamellar structure has also been observed after heat treatments at moderately high temperatures without externally applied stress. The processes finally end with the formation of new γ grains and a complex conversion of the lamellar morphology to a fine spheroidized microstructure. An initial stage of this phase transformation and recrystallization process is demonstrated in Fig. 4.24 b.

The boundaries between the newly formed γ grains and the parent α_2 phase contain a high density of misfit dislocations, which gives supporting evidence for
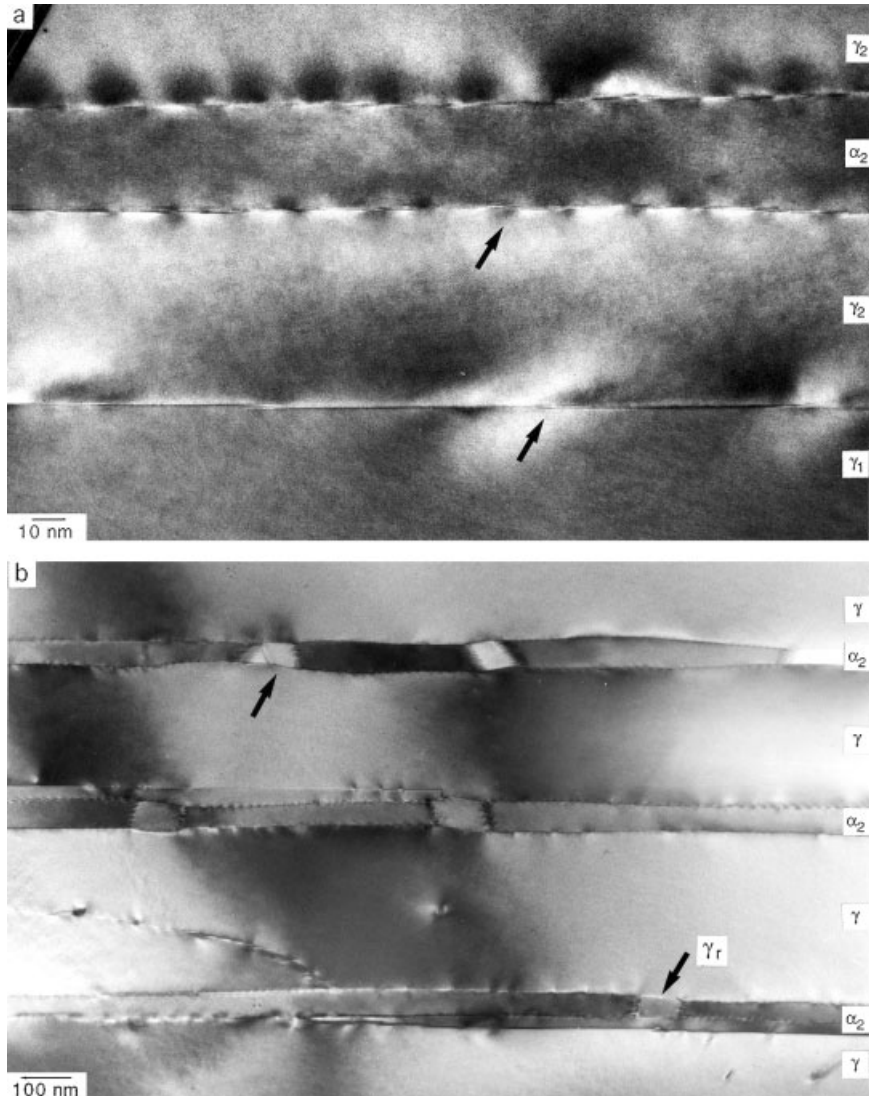
Fig. 4.24 Phase transformation and recrystallization processes observed after long-term creep on a Ti-48Al-2Cr alloy with a duplex microstructure containing a high volume fraction of lamellar colonies. Creep conditions: $\sigma_a = 110$ MPa, T = 700 °C, t = 13 400 h, $\varepsilon = 0.46\%$. (a) Low magnification image showing γ/γ and α$_2$/γ interfaces. Note the significantly higher density of ledges in the α$_2$/γ interfaces. (b) Conversion of the lamellar morphology of a Ti-48Al-2Cr alloy during long-term creep. Spheroidization of α$_2$ lamellae due to the formation of γ grains (designated as γ$_r$).
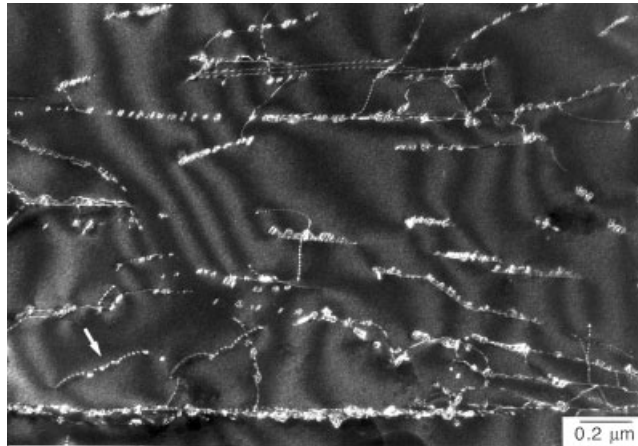
Fig. 4.25 Precipitation effects observed after long-term creep of a Ti-48Al-2Cr alloy; creep conditions: $\sigma_a = 110$ MPa, T = 700 °C, t = 13 400 h, $\varepsilon = 0.46\%$.

the mechanisms described above. The phase transformation and recrystallization processes certainly lead to a reduction of the high interface energy of the lamellar morphology, which is probably another reason for the observed degradation of the microstructure [74, 75].

The dislocation processes and structural changes described here can be effectively impeded by precipitation hardening [75, 139], as has been described in Section 4.5.4. A characteristic feature of the microstructure of crept samples is the presence of precipitates. Most, if not all precipitates are situated at isolated dislocations and the mismatch structures of sub-grain boundaries and lamellar interfaces (Fig. 4.25). Denuded zones were observed next to decorated defects, indicating that the precipitates were heterogeneously nucleated [75, 150]. The nature of the precipitates could not be identified. However, it has been established by field-ion microscopy [89] that α_2(Ti$_3$Al) preferentially scavenges oxygen, carbon and nitrogen from γ(TiAl) in the two-phase alloys. Accordingly, in α_2(Ti$_3$Al) the solubility limit for these elements is at least one order of magnitude higher than in γ(TiAl). It may thus be envisaged that the precipitation effects result from the $\alpha_2 \rightarrow \gamma$ phase transformation described in the previous section. In the newly formed γ phase, the concentration of these elements can easily exceed the solubility limit so that precipitation of oxides, nitrides or carbides occurs. The heterogeneous nucleation of the precipitates leads to a strong pinning of the dislocations and embrittlement of the material, which is certainly harmful for its damage tolerance after long-term service.

4.5.6
Crack Propagation and Fracture Toughness

Like other intermetallics, titanium aluminides suffer from brittleness at low and ambient temperatures, which makes processing, machining and handling difficult. The fracture behavior is known to be very sensitive to microstructure [153–156]. Intergranular fracture and cleavage are the dominant fracture mechanisms in duplex microstructures, while interfacial delamination, translamellar fracture and decohesion of lamellar colonies are the most important failure processes in lamellar alloys.

Fig. 4.26 shows a high resolution image of a crack that propagated in a thin foil of a lamellar alloy [157]. The crack followed the $\{111\}_\gamma$ planes, which indicates that γ(TiAl) is prone to cleavage fracture on these planes. This finding is consistent with the earlier predictions of Yoo and Fu [158], who calculated the ideal cleavage energies for different crystallographic planes of γ(TiAl). The brittleness of the material may in part also be attributed to the plastic anisotropy of the α_2(Ti$_3$Al) and γ(TiAl) phase that was described in section 4.4.1. The intrinsic brittleness of two-phase alloys persists up to about 700 °C; however, the transition to ductile behavior depends on the strain rate.

Alloys with a fully lamellar microstructure and random colony orientations exhibit a fracture toughness of $K_Q = 25$–30 MPa m$^{0.5}$ at room temperature, while the values for duplex microstructures are $K_Q = 12$–15 MPa m$^{0.5}$. The relatively high fracture toughness of lamellar alloys was attributed to the formation of shear ligaments and micro-crack shielding [154]. As demonstrated in Fig. 4.26, crack propagation across the lamellae is characterized by various interactions of the crack tip with lamellar boundaries, involving crack deflection and crack tip immobilization so that a much more tortuous crack path is traversed. Ahead the crack tip, a plastic zone is formed, which is often extended over several lamellae and consists of deformation twins and dislocations. Thus, the shape of the plastic zone is strongly determined by the crystallography of these slip elements. In Fig. 4.26, the crack tip plasticity apparently becomes evident by two dislocations, which are arranged in a dipole configuration. Stable crack growth requires the plastic zone to keep up with the cleavage crack, which is difficult if the mobility and multiplication rate of the dislocations is low. The mechanisms governing the dislocation mobility in the plastic zone at room temperature were found to be quite similar to those in bulk material [50]. Due to this high glide resistance, the dislocations may easily be outrun by the crack. In this respect, deformation twinning might be very effective as twins can rapidly propagate. Furthermore, mechanical twinning provides shear components involving the c direction of the tetragonal unit cell, which reduces the plastic anisotropy of γ(TiAl). Crack tip shielding has been recognized by electron microscope examination of crack tips [82, 159].

The variation of the fracture toughness with temperature is shown in Fig. 4.27 for two different microstructural forms of a two-phase alloy [100]. The data again indicate that resistance against unstable crack propagation can most effectively be derived from toughening mechanisms related to the lamellar morphology. However, the temperature dependence of the fracture toughness of the near gamma
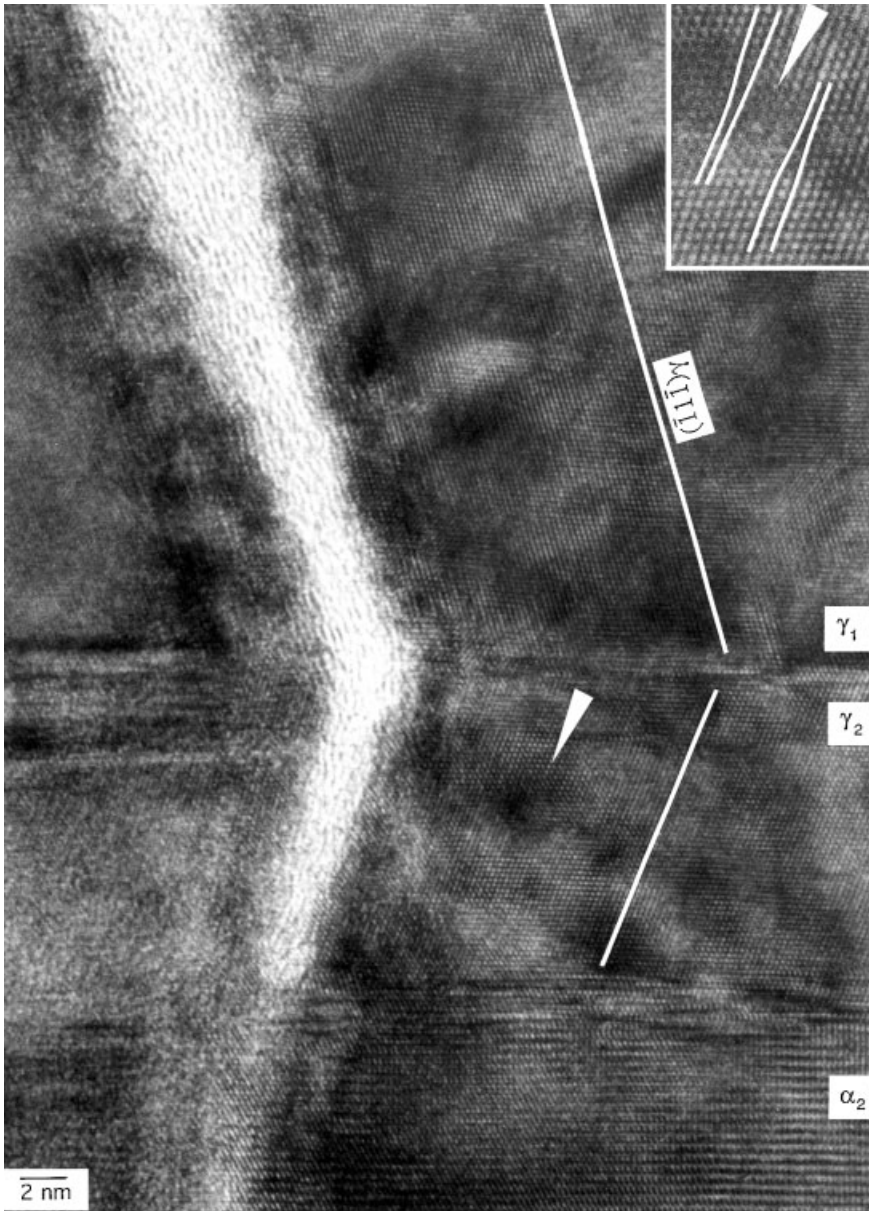
Fig. 4.26 Crack propagation in a lamellar $\alpha_2 + \gamma$ titanium aluminide alloy. Note the cleavage–like fracture on $\{111\}_\gamma$ planes, the deflection of the crack at the interface γ_1/γ_2, the generation of a dislocation dipole (insert), and the immobilization of the crack at the α_2
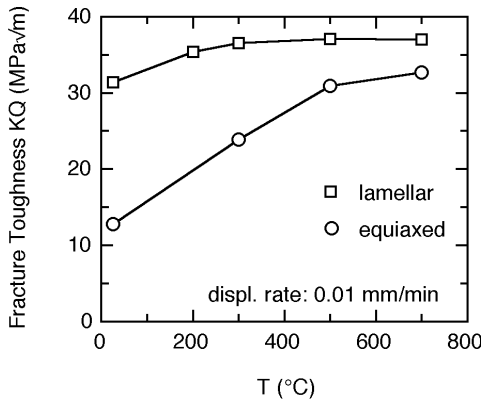
lamella.

material suggests that crack tip plasticity can also lead to appreciable toughening. From the discussion in section 4.4.4, it can be speculated that the high glide resistance of the dislocations will be drastically reduced at elevated temperatures due to thermal activation and diffusion assisted climb. Unlike the situation at room temperature, the glide processes can easily spread within the plastic zone so that the constraints due to the local crystallography and slip geometry are less restrictive. It is therefore expected that the problems associated with the lack of independent slip systems (which can simultaneously operate at a given stress) can in part be compensated so that the crack tips are effectively shielded. Thus, the fracture
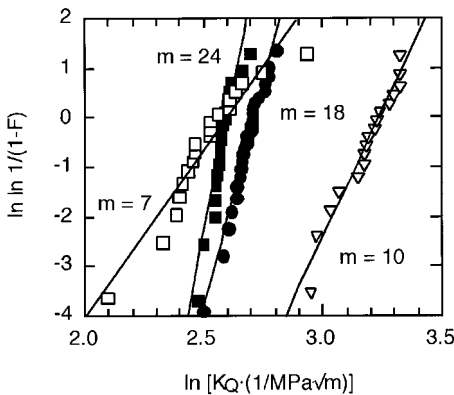
Fig. 4.27 Dependence of the fracture toughness, K_Q, on the test temperature for the lamellar and near gamma microstructural form of a Ti-47Al-2Cr-0.2Si alloy. Values measured on chevron-notched bending bars.

Fig. 4.28 Weibull–plot of the fracture toughness of different two-phase titanium aluminide alloys, (1-F) failure probability. Values measured on chevron-notched bending bars at T=25 °C and a displacement rate of v_m=0.01 mm min^{-1}. (□) Ti-48Al-2Cr, lamellar microstructure with preferred orientation of the lamellae, crack propagation parallel to

mechanism changes from cleavage at low temperatures to an energy absorbing ductile form at elevated temperatures [100].

In view of the observed cleavage fracture, it is supposed that unfavorably oriented γ grains or lamellae may provide easy crack paths. Once nucleated on $\{111\}_\gamma$ planes, the cracks are subjected to high tensile stresses and can rapidly grow to a critical length. It is speculated that large colonies with lamellar interfaces perpendicular to the loading axis have particularly detrimental effects on the tensile strength and reliability of polycrystalline material. The variation of strength within a given volume can be analyzed in terms of Weibull-statistics. Fig. 4.28 shows the data obtained on different two-phase alloys ranked in a Weibull plot [100, 157]. Fine-grained alloys typically exhibit a Weibull modulus of m = 18–24, whereas the values for coarse-grained lamellar materials are m = 7–10. For comparison, values of m = 5–15 are common for glasses and ceramics. Thus, the reliability of coarse-grained lamellar materials is a critical issue for the design of load-bearing components, which requires adequate safety factors.

4.5.7
Fatigue Behavior

By far, the most anticipated engineering applications of TiAl alloys involve components subjected to fluctuating or cyclic loading, which may result in failure by fatigue. In this respect, TiAl alloys are considered with particular caution because the material is prone to cleavage fracture. Once nucleated, cleavage cracks may grow extremely fast under repeated rapidly applied loads.

This requires that the damage tolerance of materials with respect to intrinsic or service-generated defects must be demonstrated. Understanding of fatigue and fatigue crack growth properties is therefore of major concern in the assessment of the potential of TiAl alloys. In an attempt to survey the behavior under cyclic loading, a variety of TiAl alloys in cast and wrought forms were examined in a wide temperature interval [4, 155, 156, 160–163]. Most fatigue data have been obtained under constant load amplitude test conditions using sharp cracked specimens and standard procedures. A significant body of data was determined at 25 Hz with a stress ratio of R = 0.1, where $R = \sigma_{min}/\sigma_{max}$ is the ratio of the minimum stress, σ_{min}, to the maximum stress, σ_{max}, applied over the fatigue cycle. Basic fatigue data in high-cycle fatigue are conventionally displayed on S/N plots, i.e. a plot of cyclic stress levels versus the logarithm of cyclic life. Ductile metallic systems exhibit a well defined "knee" in S/N plots at about 10^6 cycles. Beyond the knee, the curves are horizontal, and the related stress amplitude is often considered a fatigue limit. Unlike ductile metals, TiAl alloys exhibit flat S/N curves at low and intermediate temperatures, which at high cycle numbers continue to decline slowly with increasing number of cycles to failure. For such materials, it is customary to define the fatigue strength or endurance limit as the stress amplitude corresponding to a specified number of cycles, often 10^7. For duplex and lamellar TiAl alloys, the 10^7 cycle fatigue strength is 70–80% of the tensile strength. While such data may suggest a safe fatigue design at relatively high stresses, the component life-

times can vary markedly at similar stress levels because knowledge and control of the stress become extremely important.

Fractographic analysis has revealed that the propagation of fatigue cracks strongly depends on microstructure [156, 160, 162, 163]. Crack propagation in lamellar alloys is very complex because the colony orientation strongly influences the local crack growth direction [156]. Translamellar advance is observed when the crack surface is nominally perpendicular to the lamellar plates, and interlamellar failure or decohesion of the lamellae occurs if the crack plane is parallel to the interfaces. Thus, the local crack growth rates are likely to vary substantially depending on lamellar orientation and crack advance mode. While this behavior bears several similarities to the characteristics observed under monotonic loading, toughening seems to be more difficult under fatigue conditions. It is well documented that crack bridging by shear ligaments significantly contributes to the toughening of lamellar alloys under monotonic loading (Section 4.5.6). Under fatigue conditions, shear ligaments are seldom observed, and if formed, such ligaments apparently fail easily [160]. Thus, it is tempting to speculate that a significant crack resistance under fatigue conditions is only obtained when the crack is forced to propagate across the lamellae. Duplex and equiaxed microstructures fail primarily by transgranular cleavage of the gamma grains, which results in very poor fatigue crack growth resistance.

These differences in the failure modes are probably the reason why fatigue cracks in equiaxed gamma and duplex microstructures propagate significantly faster than in lamellar alloys. However, at room temperature, crack growth is generally very rapid when compared with ductile metals. Fatigue crack growth resistance curves (represented as crack growth increment per cycle, da/dN, versus the alternating stress intensity factor range, ΔK) are very steep, i.e. the crack growth rate is extremely sensitive to the applied stress intensity factor. In duplex alloys, for example, the crack growth rate spans four to six orders of magnitude for 1 MPa m$^{0.5}$ change in applied stress intensity. Crack growth data have often been generalized by the Paris law:

$$da/dN = C_P(\Delta K)^n .$$
(eqn. 4.10)

Where n is constant and C_P is an empirical parameter that depends upon material properties and frequency. The fast cyclic crack growth at room temperature translates into large exponents of the Paris law [164], which are 5–10 times higher than typical values of ductile metallic systems, depending on microstructure. This also implies that the fraction of the total fatigue life resulting from crack propagation is very small.

The influence of high test temperatures on the fatigue life is difficult to assess because it can be overshadowed by the spurious effects of oxidation and corrosion. There is good evidence, however, that the growth rates in duplex alloys at intermediate temperatures of 540–600 °C are faster than at room temperature. At temperatures above the transition from brittle to ductile material behavior, the crack growth rates tend to be lower than at room temperature. Under these conditions,

duplex alloys exhibit smooth crack surfaces, indicating a less tortuous fatigue crack path. Above 800 °C, the fatigue life seems to be limited by oxidation [4].

Environmental embrittlement seems also to be an important issue in the fatigue life of TiAl alloys. Tests performed in vacuum at room temperature lead to significantly lower crack growth rates than those performed in air [161]. These observations were discussed in terms of hydrogen embrittlement.

In view of these findings, it may be summarized that the fatigue crack growth rates for TiAl alloys will often be higher than allowed by current design requirements for moving components in high temperature applications. It should be noted, however, that the sub-critical crack growth at R=0.1 occurs at relatively high fatigue thresholds of $\Delta K_{th}=5$–10 MPa m$^{0.5}$, which are comparable to, or even slightly higher than, those of ferritic and austenitic steels. A damage tolerant design may therefore be based on the fatigue threshold value in that the stress intensity during service is kept below ΔK_{th} [4, 155]. In this context, many problems have to be solved; these involve the growth behavior of small cracks and the effect of the stress ratio on the threshold stress intensity.

4.6
Basic Aspects of Processing

For the manufacture of semifinished products and components from γ(TiAl) alloys, conventional metallurgical processing techniques are applied or are under development. However, the processing conditions have to be adjusted to the particular properties of the ordered intermetallic phase, which have been described in the previous chapters. With respect to processing, these peculiarities involve:

- the limited ductility and susceptibility to cleavage fracture require a certain microstructural condition and control of microstructural defects, and limits workability, even at high temperature
- the significant plastic anisotropy
- the low dislocation mobilities and difficulty of dislocation cross glide and climb, both of which impede recovery
- the relatively low diffusivity
- the low grain boundary mobility, which retards recrystallization.

In the following, basic problems and effects of cast and wrought processing will be reviewed. The important development of industrial processing technologies for γ(TiAl) alloys is treated in Chapter 14 [165] of this volume.

4.6.1
Manufacture of Ingots

Ingot production of γ(TiAl) alloys closely follows that for conventional titanium alloys, with some special alterations. Vacuum arc remelting (VAR) of the elements or master alloys is currently the most widely used practice. In order to ensure a

reasonable chemical homogeneity throughout ingots of 200 to 300 mm diameter, the meltstocks are usually double or triple melted. Plasma arc melting and induction skull melting are currently being developed as cost-effective technologies for clean melting and production of large-scale ingots [166–169].

Longitudinal macro-sections of the as-melted ingots are usually characterized by large columnar grains growing inwards and upwards along the direction of heat extraction. These lamellar grains have grains sizes from a few hundred µm up to a few mm and exhibit a significant texture, as already mentioned in section 4.2. The peritectic solidification leads to an unavoidable micro-segregation that, together with macro-segregation, is the most serious problem of ingot production. Fig. 4.29 shows the dendritic microstructure as observed in a 150 kg ingot of nominal compo-

the lamellar interfaces. (▽) Ti-48Al-2Cr, lamellar microstructure with preferred orientation of the lamellae, crack propagation perpendicular to the lamellar interfaces. (●) Ti-47Al-3.7(Nb, Cr, Mn, Si)-0.5B, duplex microstructure, 20% gamma grains. (■) Ti-47Al-3.7(Nb, Cr, Mn, Si)-0.5B, duplex microstructure, 80% gamma grains.
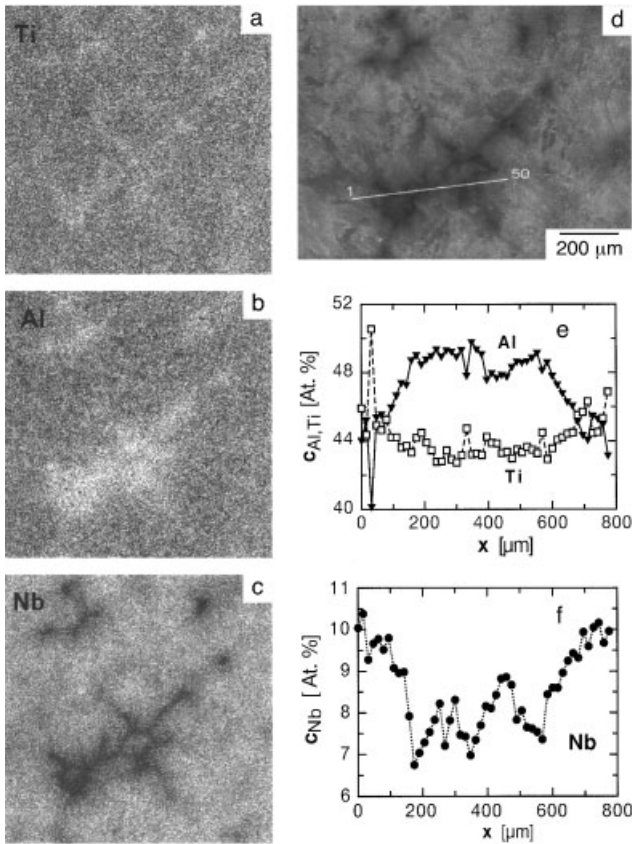
sition Ti-45Al-10Nb. Elemental EDX mapping reveals that interdendritic regions are rich in Al and depleted in Nb, whereas Nb is enriched in the dendritic cores [19]. From the corresponding concentration profile (Fig. 4.29), it is seen that interdendritic areas contain approximately 50 at% Al and are thus single-phase γ. If one regards the length scale of the concentration variations, it is apparent that such inhomogeneities pose a serious problem to the mechanical properties and that they are only eliminated with difficulty by homogenization heat treatments, particularly for heavy elements like Nb, Ta and W [166–168, 170, 171].

VAR ingots typically contain 100 to 300 ppm nitrogen and 500 to 800 ppm oxygen by weight. Ingots with oxygen levels in excess of 1200 ppm are generally unacceptable for subsequent hot working. Prior to further processing, the ingots are usually hot isostatically pressed (HIP) in the α+γ phase field at about 200 MPa for several hours in order to close casting porosity.

4.6.2
Casting

Casting of γ titanium aluminide components was explored early, and has been developed sufficiently to allow successful gas turbine engine tests of low-pressure turbine blades [172] and the commercial use of turbocharger wheels [173]. For these applications the widely used Ti-48Al-2Cr-2Nb alloy [174, 175] and a high Nb-containing alloy [176], respectively, have been utilized. As already reported, large columnar grains are often formed on solidification, which grow in the direction of heat flux. Through subsequent solid-state phase transformations, lamellar or duplex microstructures with a high fraction of lamellar colonies are obtained. Due to the size and the pronounced anisotropy of the lamellar colonies, the casting texture is of significant importance for components. For engineering alloys, the texture is often determined by the growth of columnar grains of the α phase, although it is expected from the binary phase diagram for Al contents <49 at% that primary β grains should be formed. The reason for this behavior could be that the selection of the primary phase on solidification strongly depends on the cooling rate [177]. Another explanation would be that the peritectically formed α phase determines the texture. Thus, the lamellar interfaces in most cases are parallel to the long axis of a component, and despite relatively large colony sizes of 300–400 µm, acceptable ductility and strength are attained. A significant achievement in the casting of γ titanium aluminides was the development of the "XD" alloys [178, 179], for which Ti borides are used as a grain refiner (see Section 4.5.2). By adding B, the grain size after casting can be reduced to about one third [123, 180]. Despite this progress, the current problems of casting γ(TiAl) alloys originate mainly from insufficient microstructural control over the whole component, and from casting porosity that is not satisfactorily governed. This requires postcasting HIP treatments for consolidation and a careful quality control of components.

4.6.3
Dynamic Recrystallization on Hot Working

The coarse, non-uniform, textured and segregated microstructure, as well as the poor fracture resistance of γ titanium aluminide alloys make hot working of ingot material difficult, although research in this field has made significant progress in the last several years [181–183]. The range of potential temperatures and strain rates for hot working operations of ingot material is usually evaluated through compression testing of cylinders with a volume of a few cubic centimeters. In this way workability maps can be established that define a domain where uniform and crack-free deformation is possible. Accordingly, isothermal forging can be carried out near the eutectoid temperature with strain rates up to 10^{-2} s^{-1} [184, 185]. The flow stress response observed in this domain reflects the effect of dynamic recrystallization in that the flow curves exhibit a broad peak at low strains ($\varepsilon = 10\%$), followed by flow softening to an ostensibly constant stress level (Fig. 4.30). Under these conditions, the evolution of the microstructure occurs by thermally activated deformation and recovery processes, and thus depends on temperature, strain rate and strain. Likewise, the peak stress exhibits a systematic variation with testing conditions. A detailed study of these effects was performed on a Ti-45.5Al-2.2Cr-2Nb alloy in the temperature range 1093 to 1320 °C [186]. On average, a strain rate sensitivity of m=0.28 was found, and the apparent activation energy was determined to be Q=417 kJ mol^{-1} (4.3 eV), a value that is significantly higher than the activation energy Q_d=250 kJ mol^{-1} (2.6 eV) for Ti self-diffusion [103]. The effects of strain rate and temperature are often incorporated into the Zener-Hollomon parameter, Z, which is defined as:

$$Z = \dot{\varepsilon}\exp(Q/RT) . \tag{eqn. 4.11}$$

For the range of testing conditions mentioned above, the peak stress σ_p was found to be uniquely related to Z according to:

$$\sigma_p = CZ^m . \tag{eqn. 4.11}$$
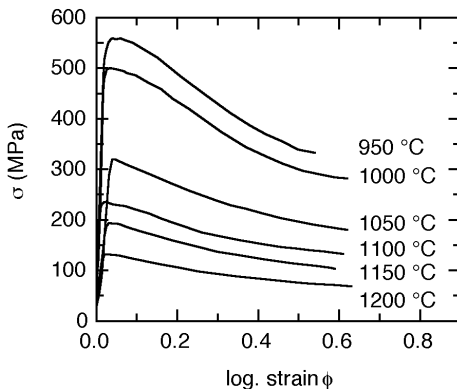
Fig. 4.29 Microsegregation in ingot material of composition Ti-45Al-10Nb. The ingot of 150 kg weight was produced by triple VAR melting. (a)–(c) Elemental mapping by energy dispersive X-ray analysis, (d) scanning electron micrograph obtained in the backscatter-
ing electron mode, (e), (f) line profiles of the alloying elements. The concentration profiles were taken along the line shown in (d) exhibiting Al enrich-

For isothermal tests, the magnitude of the coefficient is $C = 2 \cdot 10^{-2}$ MPa. The parameters so determined are almost consistent with the assumption that diffusion-assisted, non-conservative dislocation processes are strongly involved in hot working of γ-based alloys.

By hot working under the conditions mentioned above, the predominantly lamellar microstructures of ingot material are transformed to fine equiaxed microstructures by dynamic recrystallization/globularization. Although there is a vast body of literature going back more than 10 years and a collection of reviews, the exact nature of the recrystallization, globularization and phase transformation processes in γ-based alloys during hot working is not yet clear. Recrystallization of ordered structures is expected to be difficult for mainly two reasons [187]. First, the ordered state has to be restored and, second, there is a drastic reduction in grain boundary mobility compared with disordered metals. A study of recrystallization during creep showed that recrystallized grains are formed at ledges of lamellar grains. This process obviously is closely related to the mismatch structures at these interfaces [75]. After hot working, however, formation of recrystallized grains at colony boundaries [188] as well as a bulging process of recrystallization [189] were also observed.

In contrast to the fundamental mechanisms, the influences of alloy composition and initial microstructure on recrystallization have been elucidated in more detail. The kinetics of dynamic recrystallization has been systematically investigated on a series of binary and engineering alloys with Al contents ranging from 45 to 54 at% [188]. The samples were deformed in compression at T = 1000 °C to different strains between 10% and 75%, and subsequently the volume fraction of recrystallized/spheroidized grains was determined by quantitative metallography. The fraction of this microstructural constituent generally increased with strain; however, no recrystallization occurred before the flow stress peak. For higher strains there was a marked effect of the Al concentration on the recrystallization behavior (Fig. 4.31). The largest volume fractions of recrystallized grains were found in alloys with Al contents of 48–50 at% [188].

As cast, these alloys had a duplex or near-gamma microstructure with relatively small grain sizes of 50 to 100 μm. Deformation occurred by mechanical twinning and glide or climb of ordinary dislocations. Dynamic recrystallization was primarily initiated at pre-existing grain boundaries. This combination of fine as-cast grain size and deformation processes is apparently a good precondition for a homogeneous refinement of the microstructure. The reasons for the slow recrystallization kinetics on the Ti-rich side of stoichiometry are not altogether clear because the deformation mechanisms are almost the same as in the alloys with near-stoichiometric compositions. The Ti-rich alloys had a coarse-grained, lamellar structure with colony sizes up to 2000 μm. In these alloys highly localized shear bands were often observed, which apparently originated from local bending of the lamellae [188]. Investigations on specimens with a preferential orientation of lamellae of 0°, 45° and 90° to the deformation axis have further shown that shear bands were formed in specimens of the 'hard orientations' (0° and 90°), but were almost absent in those of the 'soft orientation' where slip propagated along the la-
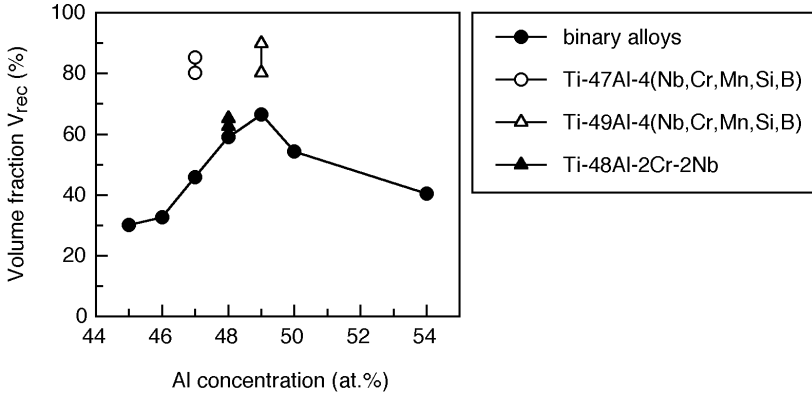
Fig. 4.30 Flow curves determined on ingot material of alloy Ti-45Al-(5–10)Nb-X. Logarithmic strain rate $\dot{\varphi} = 10^{-3}$ s^{-1}.

mellae. The shear bands consisted of very fine, equiaxed grains and often completely traversed the work piece. Subsequent deformation therefore probably was concentrated in shear bands where it preferentially occurred by grain boundary sliding. Thus, outside the shear bands, the amount of imparted strain energy was relatively low, making recrystallization sluggish (Fig. 4.32) [188]. These mechanisms not only result in an inhomogeneous microstructure, but often lead to premature failure of the work piece. Strain localization and shear band formation are therefore critical issues in hot working of γ-based alloys, in particular for engineering alloys, which have Al concentration of 45–47 at% and, thus, exhibit fully lamellar microstructures in the as-cast condition.
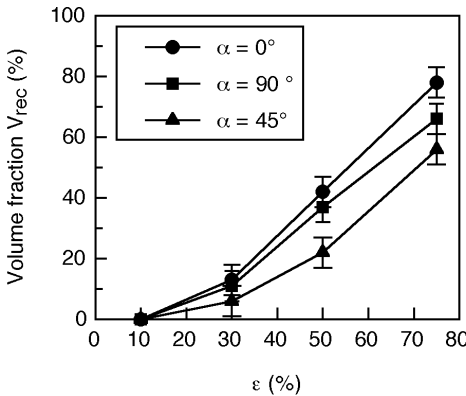
Fig. 4.31 Recrystallization kinetics of γ titanium aluminide alloys. Metallographically determined volume fraction of recrystallized/globularized grains after forging different binary and engineering alloys. Forging was performed at 1000 °C and a strain rate $\dot{\varepsilon} = 5 \cdot 10^{-4}$ s^{-1} to a strain of 75% [188].

On the Al-rich side of stoichiometry, the decrease of recrystallization probably was a consequence of the particular deformation mode of such alloys. Deformation of Al-rich alloys is mainly provided by superdislocations, while mechanical twinning is almost absent. Hot deformation of these alloys at 1000 °C exhibited a strong work hardening compared with Ti-rich alloys. This indicates that sufficient strain energy is imparted. However, the restricted ability of the superdislocations to cross-glide and climb apparently makes formation of sub-boundaries and recrystallization difficult.

The dynamic recrystallization of γ titanium aluminide alloys can be accelerated when small particles such as borides or silicides are present in the alloys, as was recognized in early work by Nobuki et al. [184]. This is demonstrated in Fig. 4.31 where B and Si containing alloys are compared with the equivalent binary alloys [188]. In contrast, alloying additions up to 2 at% of the metallic elements Cr and Nb have almost no effect on the recrystallization behavior as concluded by comparing the alloy Ti-48Al-2Cr-2Nb with its binary counterpart (Fig. 4.31). The beneficial effect of the boride particles may arise for two reasons. Boron is known to significantly refine the as-cast microstructure, which is generally a good precondition for homogeneous hot working and recrystallization. However, it might also be speculated that particle-stimulated dynamic recrystallization occurs. This is expected when dislocations are accumulated at the boride particles during deformation. At high temperatures, the dislocations may be able to overcome the particles with the aid of thermal activation without forming pile-up structures. Thus, particle-stimulated recrystallization will only occur for larger particles, lower temperatures and higher strain rates. In this case, optimization of particle sizes and hot working conditions are of major concern for ingot breakdown of boron-containing alloys.

The failure criteria and hot working limits of γ-based alloys seem to be closely related to the deformation mechanisms described in preceding sections. In TiAl, the {111} planes serve as dislocation glide planes and twin-habit planes. It is now fairly well established that the cohesion energy of these planes is relatively low [5, 50, 55], making the γ(TiAl) phase prone to cleavage fracture on {111} planes. Thus, blocked slip or twinning may lead to crack nucleation. Unfavorably oriented grains or lamellar colonies may therefore provide easy crack paths, so that the crack can rapidly grow to a critical length. As described in section 4.5.6 stable crack growth requires that the plastic zone follows the cleavage crack, which appears to be difficult given low dislocation mobility (see section 4.5.6). This combination of low dislocation mobility and susceptibility to cleavage fracture limits the ability of the material to accommodate constraint stresses and thus severely limits the working window to high temperatures and low strain rates [190].

4.6.4
Development of Hot Working Routes

As has been described in the preceding sections, lamellar microstructures with small colony sizes and lamellar spacings are currently preferred within the different possible microstructural morphologies due to their superior combination of

mechanical properties. In order to refine the colony size, rapid grain growth in the α field at temperatures above 1300 °C has to be limited since lamellar colonies are formed from prior α grains. This can be achieved in principle by applying two types of wrought processing routes. One type utilizes processing in the α field, which allows refinement of the α grain size by dynamic recrystallization [4, 117, 181]. After processing in the α field, however, subsequent hot working steps, e.g. closed-die forging, are not useful because the refined lamellar microstructures would be again broken up. For the other type of hot working routes, processing is performed below the α-transus temperature resulting in fine equiaxed or duplex microstructures, which increase the workability in any further working step. The lamellar microstructure has to then be formed by a final heat treatment. Control of the α grain size can be provided in this case by the presence of additional phases, e.g. borides. For both types of processing routes the lamellar spacing depends on the cooling rate, i.e. on the undercooling, and on the alloy composition, which influences the transformation kinetics, e.g. via the number of sites for heterogeneous nucleation, the driving force and the diffusion coefficient. In this respect, additions of B might be detrimental as borides serve as heterogeneous nucleation sites of γ lamellae [37] and, thus, cause the formation of relatively coarse lamellar spacings.

Primary ingot breakdown of γ titanium aluminide alloys can be accomplished by isothermal forging [24, 109, 191], conventional canned forging [192, 193] and extrusion [170, 194]. Typical conditions for large-scale industrial isothermal forging are T = 1000 to 1200 °C and logarithmic strain rates in the range $\dot{\phi} = 10^{-3}$ to 10^{-2} s^{-1} [129, 181, 183, 195]. Under these conditions, billets of 50 kg can be successfully forged to a strain of 80% [157]. The microstructure typically developed appears as an inhomogeneous, partially recrystallized lamellar structure. In an attempt to further improve the structural homogeneity, isothermal forging has been modified in several different ways. Canning and thermal insulation of the work piece is very effective in avoiding surface chilling and cracking [181]. This technique expands the processing window by decreasing the minimum temperature, increasing the highest strain rate, and increasing the maximum strain under which deformation occurs without observable macroscopic failure. Thus, by canned forging, a larger amount of strain energy can be imparted, which is certainly beneficial for homogeneous dynamic recrystallization. Canned forging makes it possible to obtain significant refinement of the microstructure, as demonstrated in Fig. 4.33 [157]. However, even under these conditions, recrystallization of the lamellar structure is incomplete. A more homogeneous refinement of cast microstructures can be achieved by two-step isothermal forging (Fig. 4.33), which may involve an intermediate heat treatment for static recrystallization.

Fully recrystallized microstructures can be obtained by the "α-forging" process [181]. The practice comprises billet pre-heating to a temperature high in the α+γ phase field, followed by rapid cooling to a temperature low in the α+γ field and subsequent forging. Due to the high cooling rate, the α phase is retained in a metastable condition. The technique is, however, restricted to relatively small billets in order to attain sufficient cooling rates.
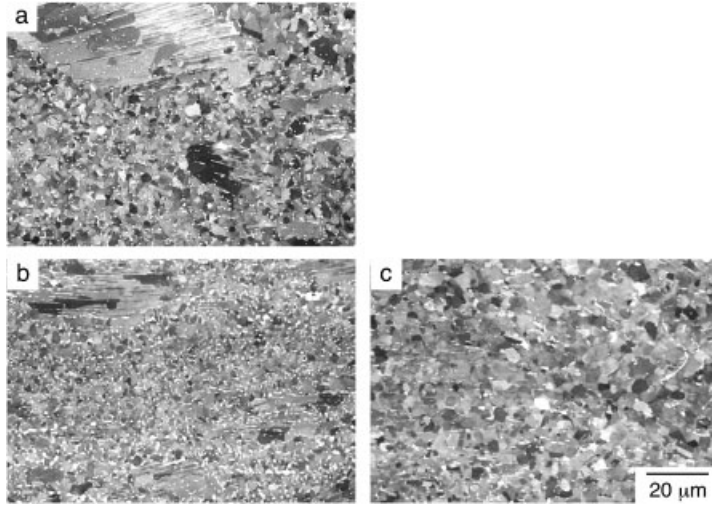
Fig. 4.32 Recrystallization behavior in dependence of the orientation of lamellae. Metallographically determined fraction of recrystallized grains as obtained after forging. The specimens of alloy Ti-48Al-2Cr had three preferential orientations of lamellae at angle α to the deformation axis. Forging was performed at $1000\,^{\circ}$C and a strain rate $\dot{\varepsilon} = 5\cdot10^{-4}\,\text{s}^{-1}$ to different strains [188].

Extrusion has turned out to be an effective primary process, which is performed at relatively high temperatures in either the $\alpha+\gamma$ or α phase fields. Under these conditions, severe oxidation and corrosion occur and, thus, the work piece has to be encapsulated. Conventional Ti alloys or steels are used as can material. At the extrusion temperature the can materials have significantly lower flow stresses than the γ(TiAl) alloy billet. This flow stress mismatch is often as high as 300 MPa and leads to inhomogeneous extrusion or even cracking. The problems can largely be overcome by a thermal insulation, which reduces the heat transfer from the work piece to the can and enables controlled dwell periods between preheating and extrusion [181]. For extrusion temperatures above $1000\,^{\circ}$C, as is generally applied for γ(TiAl) alloys, heat losses are mainly caused by radiation; however, heat losses of the billet can effectively be prevented with a can design involving radiation shields [196]. Taking advantage of these concepts, extrusion processes have been widely used for γ(TiAl) alloy ingot breakdown. The high hydrostatic pressures involved should allow for forming of virtually any composition desired. For example, 80 kg ingots of composition Ti-45Al-(5–10)Nb-X were uniformly extruded with a 10:1 reduction in cross-section into differently shaped dies, including those with rectangular geometry [157], obtaining bars with a length of 6–8 m.

After extrusion, fully recrystallized microstructures are observed for extrusion ratios > 6:1. The microstructural condition can be varied between equiaxed, duplex or fully lamellar microstructures by selecting the extrusion temperature (Fig. 4.34). The lamellar materials exhibit colony sizes < 100 µm and small lamel-
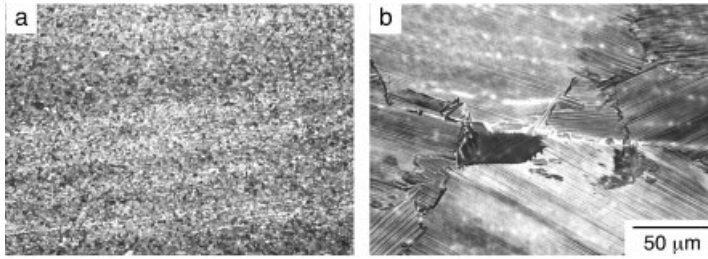
Fig. 4.33 Microstructure of ingot material after isothermal forging. Alloy Ti-45Al-10Nb. (a) Forging at 1100 °C, (b) canned isothermal forging at 1000 °C, (c) two-step forging at 1150 °C. Scanning electron micrographs taken in the backscattering electron mode. The forging direction lies vertically in the images.

lae spacings < 200 nm and have excellent mechanical properties [4, 117, 129, 157]. However, after extrusion the lamellar microstructures are still inhomogeneous, showing bands that consist of fine and coarse grains or of lamellar colonies and equiaxed grains. These inhomogeneities in the microstructure are associated with significant variations in the local chemical composition that arise due to solidification segregation (Fig. 4.35). This observation provides supporting evidence that dynamic recrystallization during hot working is strongly affected by local composition. The coarse-grained bands probably originate from prior Al-rich interdendritic regions, where no α_2 phase was present. Thus, grain growth following recrystallization is not impeded by particles of the α phase. On the contrary, fine-grained bands or bands of lamellar colonies are formed from the former Al-depleted core regions of dendrites.

In general, on hot working textures are formed that might be of particular importance for γ-based alloys since the desired lamellar microstructures exhibit strong anisotropic mechanical properties. Compared to solid solution phases, the analysis of texture evolution suffers from some peculiarities of γ-based alloys including the occurrence of ordinary and superdislocations, recrystallization of an ordered phase as well as the presence of different phases at the working temperature and the subsequent phase transformations. Up to now, only a limited number of investigations were devoted to texture development, mostly for temperatures where the γ phase strongly predominates [197, 198]. In these studies, the observed hot working textures could be mainly described as deformation textures of the γ phase. On extrusion, which is carried out at higher temperatures, a significant temperature dependence of texture formation was observed (Fig. 4.36). As shown by pole figures, on extrusion below the α-transus temperature, weak ⟨111⟩- and [001]-fiber textures are formed in the extrusion direction, whereas extrusion in the α phase field leads to ⟨112⟩ and ⟨101⟩ textures [199]. The texture components mentioned can be ascribed first to the deformation of the γ phase because for these orientations multiple symmetrical slip is possible on extrusion. The latter components might be explained by prismatic slip in the hexagonal α phase
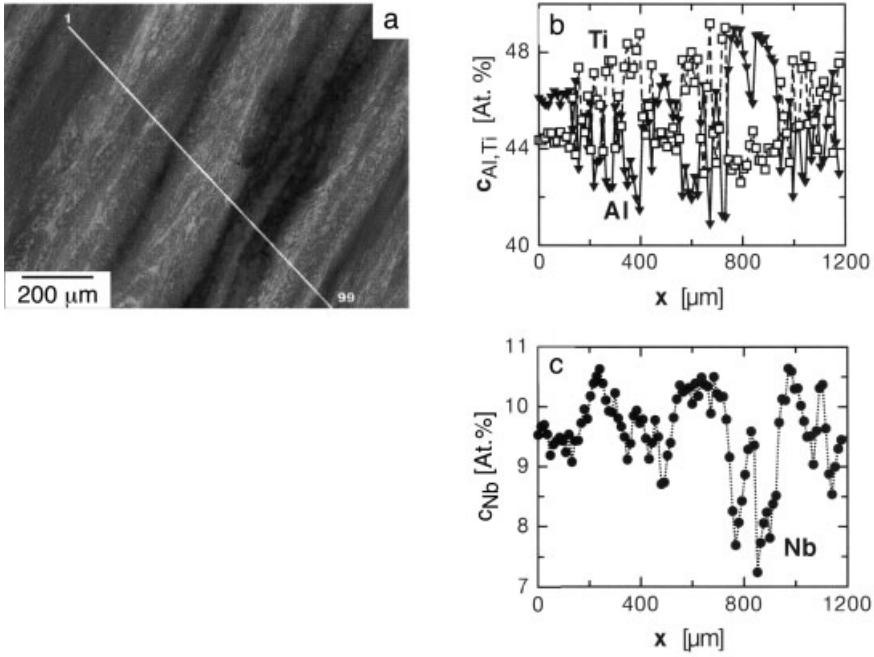
Fig. 4.34 Microstructure of extruded ingot material of alloy Ti-45Al-(5–10)Nb-X. Extrusion ratio 10:1. (a) Extrusion temperature slightly

above the eutectoid temperature, (b) extrusion temperature above the α-transus temperature. Scan-

ning electron micrographs taken in the backscattering electron mode. The extrusion direction lies horizontally in the images.
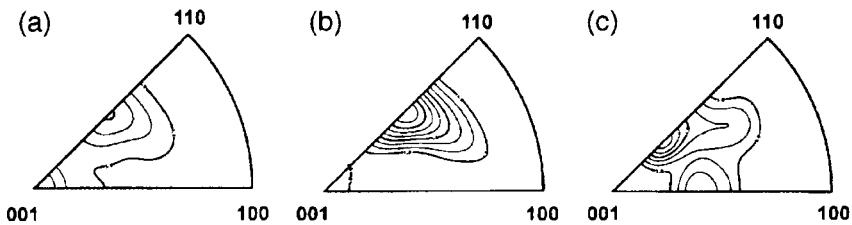
Fig. 4.35 Microanalysis of segregation after extrusion. Alloy Ti-45Al-10Nb. (a) Scanning electron micrograph taken in the backscattering electron mode. (b), (c) Concentration line profiles taken along the line shown in (a). The bands in the microstructure reflect the segregation of Nb and Al in the ingot materi-

and by the transformation to the γ phase on cooling, according to the Blackburn orientation relationship (section 4.3) [199]. Apparently, no texture components are generated by dynamic recrystallization. This could be understood in terms of a bulging mechanism of recrystallization [189, 190]. The complex processes of texture evolution, however, are far from being completely elucidated. Although the textures occurring after extrusion only show pole densities up to 2 mrd, material extruded above the α-transus temperature has a significant orientation dependence of the mechanical properties [38]. This might be attributed to the pronounced anisotropy of lamellar microstructures and has to be considered with respect to the main loading axis of a component.

As already mentioned, the refinement obtained in the microstructure after primary processing increases the workability, thus enabling secondary processes like sheet rolling [195], superplastic forming [182] and isothermal closed-die forging. Wrought processing routes involving closed-die forging are of interest for manufacturing a variety of components, in particular turbine and engine parts that have to withstand severe loading conditions. As an example, the processing route for the fabrication of high-pressure jet engine turbine blades will be presented, which has been jointly developed by Rolls-Royce Deutschland (Dahlewitz, Germany), ThyssenKrupp Turbinenkomponenten (Remscheid, Germany) and GKSS Research Center. The processing involved extrusion of ingot material, subsequent isothermal forging in several steps, and a final heat treatment. Finishing of the
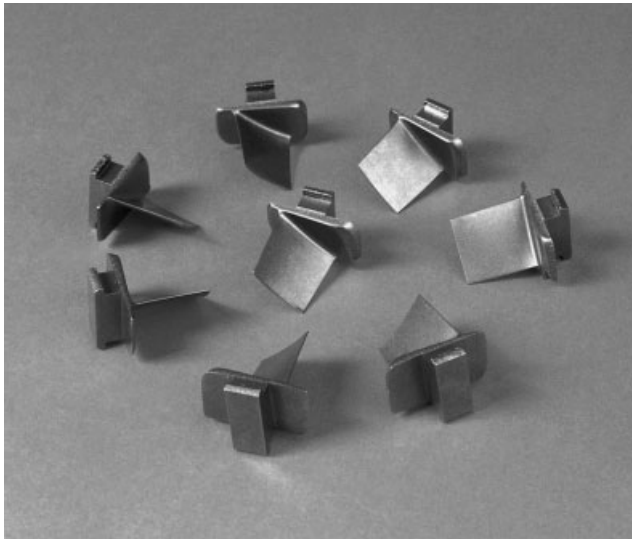
al. Bright bands contain a high fraction of α_2 whereas dark bands are single-phase γ with grain sizes up to 10 μm.

Fig 4.36 Texture formation on extrusion of an alloy Ti-47Al-3.7(Nb, Cr, Mn, Si)-0.5B. Inverse pole figures of the extrusion direction. Extrusion ration 7:1. (a) Extrusion temperature 1250 °C, (b) extrusion temperature

blades was carried out by Leistritz Turbomaschinen (Nuremberg, Germany) using electro-chemical milling [38]. For processing, a B-containing alloy of composition Ti-47Al-3.7(Nb, Cr, Mn, Si)-0.5B was used, which turned out to be quite workable. After forging, a fine-grained equiaxed microstructure with improved homogeneity was found, when compared to the extruded condition. The blades were finally heat-treated for a short duration directly at the α-transus temperature and quenched in oil. Thus, a lamellar microstructure with small colony size and lamellar spacing was formed, showing good homogeneity over the entire component. The 610 MPa yield strength, σ_{ys}, obtained probably cannot be further increased for this type of alloy by conventional metallurgical processing. In summary, it can be concluded that B-containing alloys based on Ti-47Al are well suited for wrought processing due to their fast recrystallization kinetics (section 4.6.3), as manifested in the successful production of more than 200 blades (Fig. 4.37). Demands for high strength and better oxidation resistance have initiated another project aimed at the development of hot working routes for the production of turbine blades from high Nb alloys.

4.7
Conclusions

In recent years, considerable progress has been achieved in the development of γ titanium aluminide alloys, which now exhibit significantly increased creep and corrosion resistance as well as room temperature strengths similar to high-strength titanium alloys. However, neither the toughness nor the ductility has been improved substantially, and due to the physical metallurgy of this alloy class, further improvement of these properties seems hardly possible. Recently, Dimiduk has critically assessed the currently achievable property profile of γ alloys within the competition of high-temperature structural materials [2]. One of his main conclusions may be drawn from Fig. 4.38 showing specific strength data of several high temperature alloys. As can be seen from this diagram, conventional γ alloys similar to Ti-48Al-2Cr-2Nb cannot compete with most Ti alloys and Ni-based superalloys, while more recent titanium aluminide alloys are clearly superior for temperatures up to 750 °C. Furthermore, recent generation alloys have an acceptable room temperature ductility of about 2.5% and, besides their excellent specific stiffness, exhibit specific creep strengths exceeding those of most superalloys [2]. In contrast to Fe and Ni aluminides, γ alloys are unique as a structural material in a certain temperature range. If applications are considered where the materials have to withstand severe loading conditions, wrought high-strength γ alloys are of particular interest. Due to the current state of development, prototype components of such alloys can be manufactured, but the development of a reproducible industrial processing technology and the qualification of a component is still at its beginning. Considering the complex metallurgy of γ alloys, process development on an industrial scale will require enormous efforts, as was the case for other structural materials. However, the expected innovation potential of γ al-
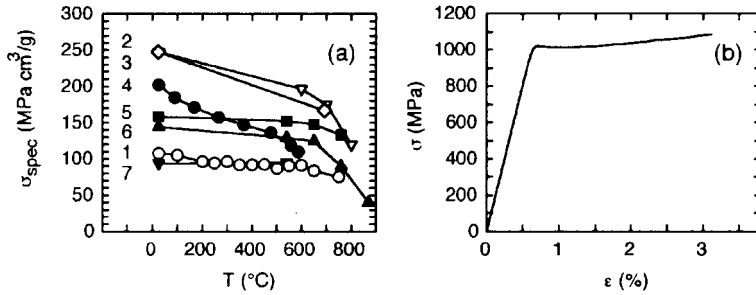
1300 °C, (c) extrusion temperature 1380 °C. The inverse pole figures show that after extrusion below the α-transus temperature weak ⟨111⟩ and ⟨001⟩ texture components of pole density 1.6 mrd (a) and 2.5 mrd (b) occur, while extrusion above the α-transus temperature leads to a ⟨112⟩ component of pole density 2.1 mrd and a very weak ⟨101⟩ component.

loys for jet engine, automotive and stationary gas turbine applications seems to be comparable to that of superalloys and Ti alloys, thus indicating an urgent need for increased development efforts. Despite first commercial applications, this also holds for casting technologies, as only cheap near net-shape casting will open the possibility to fabricate mass products like turbocharger wheels.

4.8
Acknowledgments

4.9
Referenced Literature and Further Reading

1 *Intermetallic Compounds*, eds. J. H. WESTBROOK, R. L. FLEISCHER (Wiley, Chichester, 1995).

2 D. M. DIMIDUK, Mater. Sci. Eng. A263, 281 (1999).

3 M. YAMAGUCHI, Y. UMAKOSHI, Progress in Materials Science 34, 1 (1990).

4 Y.-W. KIM, D. M DIMIDUK, in: *Structural Intermetallics 1997*, eds. M. V. NATHAL, R. DAROLIA, C. T. LIU, P. L. MARTIN, D. B. MIRACLE, R. WAGNER, M. YAMAGUCHI (TMS, Warrendale, PA, 1997), p. 531.

5 F. APPEL, R. WAGNER, Mater. Sci. Eng. R22, 187, 1998.

6 G. SAUTHOFF, *Intermetallics*, VCH Verlagsgesellschaft, Weinheim, 1995.

7 *Gamma Titanium Aluminides*, eds. Y.-W. KIM, R. WAGNER, M. YAMAGUCHI (TMS, Warrendale, PA, 1995).

8 *Gamma Titanium Aluminides 1999*, eds. Y.-W. KIM, D. M. DIMIDUK, M. H. LORETTO (TMS, Warrendale, PA, 1999).

9 *Structural Intermetallics 2001*, eds. K. J. HEMKER, D. M. DIMIDUK, H. CLEMENS, R. DAROLIA, H. INUI, J. M. LARSEN, V. K. SIKKA, M. THOMAS, J. D. WHITTENBERGER (TMS, Warrendale, PA, 2001).

10 C. McCullough, J.J. Valencia, C.G. Levi, R. Mehrabian, Acta Metall. 37, 1321 (1989).

11 G.L. Chen, W.J. Zhang, Z.C. Liu, S.J. Li, Y.-W. Kim, *Gamma Titanium Aluminides 1999,* eds. Y.-W. Kim, D.M. Dimiduk, M.H. Loretto (TMS, Warrendale, PA, 1999), p. 371.

12 H. Okamoto, J. Phase Equilibria 14, 120 (1993).

13 J.B. McAndrew, H.D. Kessler, J. Met. 8, 1348 (1956).

14 D. Banerjee, Progress in Materials Science 42, 135 (1997).

15 J. Kumpfert, Adv. Eng. Mater. 3, 851 (2001).

16 I. Ohnuma. Y. Fujita, H. Mitsui, K. Ishikawa, R. Kainuma, K. Ishida, Acta Mater. 48, 3113 (2000).

17 U.R. Kattner, J.C. Lin, Y.-A. Chang, Metall Trans. 23A, 2081 (1992).

18 F. Zhang, S.L. Chen, Y.-A. Chang, U.R. Kattner, Intermetallics 5, 471 (1997).

19 U. Brossmann, M. Oehring, F. Appel, in: *Structural Intermetallics 2001,* eds. K.J. Hemker, D.M. Dimiduk, H. Clemens, R. Darolia, H. Inui, J.M. Larsen, V.K. Sikka, M. Thomas, J.D. Whittenberger (TMS, Warrendale, PA, 2001), p. 191.

20 S. Naka, M. Thomas, C. Sanchez, T. Khan, in: *Structural Intermetallics 1997,* eds. M.V. Nathal, R. Darolia, C.T. Liu, P.L. Martin, D.B. Miracle, R. Wagner, M. Yamaguchi (TMS, Warrendale, PA, 1997), p. 313.

21 M. DeGraef, N. Biery, L. Rishel, T.M. Pollock, A. Cramb, *Gamma Titanium Aluminides 1999,* eds. Y.-W. Kim, D.M. Dimiduk, M.H. Loretto (TMS, Warrendale, PA, 1999), p. 247.

22 D.R. Johnson, H. Inui, M. Yamaguchi, Acta Mater. 44, 2523 (1996).

23 A. Denquin, S. Naka, T. Khan, in: *Titanium '92, Science and Technology,* eds. F.H. Froes, I.L. Caplan (TMS, Warrendale, PA, 1992), p. 1017.

24 Y.-W. Kim, Acta Metall. Mater. 40, 1121 (1992).

25 Y. Yamabe, M. Takeyama, M. Kikuchi, in: *Gamma Titanium Aluminides,* eds. Y.-W. Kim, R. Wagner, M. Yamaguchi (TMS, Warrendale, PA, 1995), p. 111.

26 M. Takeyama, M. Kikuchi, Intermetallics 6, 573 (1998).

27 T.J. Jewett, B. Ahrens, M. Dahms, Intermetallics 4, 542 (1996).

28 M. Palm, G. Inden, in: *Structural Intermetallics 1997,* eds. M.V. Nathal, R. Darolia, C.T. Liu, P.L. Martin, D.B. Miracle, R. Wagner, M. Yamaguchi (TMS, Warrendale, PA, 1997), p. 73.

29 A.K. Singh, D. Banerjee, Metall. Mater. Trans. 28A, 1745 (1997).

30 A. Hellwig, M. Palm, G. Inden, Intermetallics 6, 79 (1998).

31 N. Saunders, in: *Gamma Titanium Aluminides 1999,* eds. Y.-W. Kim, D.M. Dimiduk, M.H. Loretto (TMS, Warrendale, PA, 1999), p. 183.

32 R. Kainuma, Y. Fujita, H. Mitsui, I. Ohnuma, K. Ishida, Intermetallics 8, 855 (2000).

33 Y.Q. Sun, Phil. Mag. Lett. 78, 305 (1998).

34 T.T. Cheng, M.H. Loretto, Acta Mater. 13, 4801 (1998).

35 Z. Zhang, K.J. Leonard, D.M. Dimiduk, V.K. Vasudevan, in: *Structural Intermetallics 2001,* eds. K.J. Hemker, D.M. Dimiduk, H. Clemens, R. Darolia, H. Inui, J.M. Larsen, V.K. Sikka, M. Thomas, J.D. Whittenberger (TMS, Warrendale, PA, 2001), p. 515.

36 S. Mitao, L.A. Benderski, Acta Mater. 45, 4475 (1997).

37 Y.-W. Kim, D.M. Dimiduk, *Structural Intermetallics 2001,* eds. K.J. Hemker, D.M. Dimiduk, H. Clemens, R. Darolia, H. Inui, J.M. Larsen, V.K. Sikka, M. Thomas, J.D. Whittenberger (TMS, Warrendale, PA, 2001), p. 625.

38 M. Oehring, U. Lorenz, F. Appel, D. Roth-Fagaraseanu, *Structural Intermetallics 2001,* eds. K.J. Hemker, D.M. Dimiduk, H. Clemens, R. Darolia, H. Inui, J.M. Larsen, V.K. Sikka, M. Thomas, J.D. Whittenberger (TMS, Warrendale, PA, 2001), p. 157.

39 M.J. Blackburn, in: *The Science, Technology and Application of Titanium,* eds. R.I. Jaffe, N.E. Promisel (Pergamon Press, Oxford, 1970), p. 663.

40 A. Denquin, S. Naka, in: *Gamma Titanium Aluminides*, eds. Y.-W. Kim, R. Wagner, M. Yamaguchi (TMS, Warrendale, PA, 1995), p. 141.

41 A. Denquin, S. Naka, Acta Mater. 44, 343 (1996).

42 P. Shang, T.T. Cheng, M. Aindow, Phil. Mag. A 79, 2553 (1999).

43 S.M.L. Sastry, H.A. Lipsitt, Metall. Trans. 8A, 299 (1977).

44 H. Inui, M.H. Oh, A. Nakamura, M. Yamaguchi, Phil. Mag. A 66, 539 (1992).

45 G.J. Mahon, J.M. Howe, Metall. Trans. 21A, 1655 (1990).

46 B.K. Kad, P.M. Hazzledine, Phil. Mag. Lett. 66, 133 (1992).

47 W. Wunderlich, T. Kremser, G. Frommeyer, Acta Metall. Mater. 41, 1792 (1993).

48 S. Zghal, S. Naka, A. Couret, Acta Mater. 45, 3005 (1997).

49 F. Appel, P.A. Beaven, R. Wagner, Acta Metall. Mater. 41, 1721 (1993).

50 F. Appel, U. Christoph, R. Wagner, Phil. Mag. A 72, 241 (1995).

51 S.H. Whang, Y.D. Hahn, Scripta Metall. Mater. 23, 1679 (1990).

52 G. Hug, A. Loiseau, P. Veyssière, Phil. Mag. A 57, 499 (1988).

53 J.W. Christian, D.E. Laughlin, Acta Metall. 14, 1617 (1988).

54 M.H. Yoo, C.L. Fu, J.K. Lee, in: *Twinning in Advanced Materials*, eds. M.H. Yoo, M. Wuttig (TMS, Warrendale, PA, 1994), p. 97.

55 M.H. Yoo, C.L. Fu, Metall. Trans. 29A, 49 (1998).

56 V.K. Vasudevan, M.A. Stucke, S.A. Court, H.L. Fraser, Phil. Mag. Letters 59, 299 (1989).

57 G. Hug, P. Veyssière, in: *Electron Microscopy in Plasticity and Fracture Research,* Physical Research, Vol. 14, eds. U. Messerschmidt, F. Appel, J. Heydenreich, V. Schmidt, (Akademie-Verlag, Berlin, 1990), p. 451.

58 K.J. Hemker, B. Viguier, M.J. Mills, Mater. Sci. Eng. A164, 391 (1993).

59 S. Sriram, V.K. Vasudevan, D.M. Dimiduk, in: *High-Temperature Ordered Intermetallic Alloys VI,* Mat. Res. Soc. Symp. Proc., Vol. 364, eds. J.A. Horton, I. Baker, S. Hanada, R.D. Noebe, D.S.

Schwartz (MRS, Pittsburgh, PA, 1995), p. 647.

60 B.J. Inkson, C.J. Humphreys, Phil. Mag. Lett. 71, 307 (1995).

61 P.J. Simmons, M.J. Mills, S.I. Rao, in: *High-Temperature Ordered Intermetallic Alloys VI,* Mat. Res. Soc. Symp. Proc., Vol. 364, eds. J.A. Horton, I. Hanada, R.D. Noebe, D.S. Schwartz (MRS, Pittsburgh, PA, 1995), p. 137.

62 C. Woodward, J.M. MacLaren, D.M. Dimiduk, in: *High-Temperature Ordered Intermetallic Alloys V,* Mat. Res. Soc. Symp. Proc., Vol. 288, eds. I. Baker, R. Darolia, J.D. Whittenberger, M.H. Yoo, R.D. Noebe, D.S. Schwartz (MRS, Pittsburgh, PA, 1993), p. 171.

63 A. Godfrey, D. Hu, M.H. Loretto, Phil. Mag. A 77, 287 (1998).

64 J.M.K. Wiezorek, P.M. DeLuca, M.J. Mills, H.L. Fraser, Phil. Mag. Lett. 75, 271 (1997).

65 S.R. Singh, J.M. Howe, Phil. Mag. Lett. 65, 233 (1992).

66 Y. Umakoshi, T. Nakano, T. Takenaka, K. Sumimoto, T. Yamane, Acta Metall. Mater. 41, 1149 (1993).

67 F. Appel, R. Wagner, in: *Gamma Titanium Aluminides*, eds. Y.-W. Kim, R. Wagner, M. Yamaguchi (TMS, Warrendale, PA, 1995), p. 231.

68 J. Friedel, *Dislocations*, Oxford, 1964.

69 J.J. Gilman, W.G. Johnston, Solid State Phys. 13, 147 (1962).

70 Y. Shirai, M. Yamaguchi, Mater. Sci. Eng. A152, 173 (1992).

71 U. Brossmann, R. Würschum, K. Badura, H.E. Schaefer, Phys. Rev. B 49 6457 (1994).

72 R.W. Baluffi, A.V. Granato in: *Dislocation in Solids, Vol. 4,* ed. F.R.N. Nabarro (North-Holland, Amsterdam, 1979), p. 1.

73 J.P. Hirth, J. Lothe, *Theory of Dislocations,* 2nd ed., (Malabar, Krieger, 1992).

74 F. Appel, Intermetallics 9, 907 (2001).

75 F. Appel, M. Oehring, P.J. Ennis, in: *Gamma Titanium Aluminides 1999*, eds. Y.-W. Kim, D.M. Dimiduk, M.H. Loretto (TMS, Warrendale, PA, 1999), p. 603.

76 F. Appel, U. Christoph, R. Wagner, in: *Interface Control of Electrical, Chemical and Mechanical Properties*, eds. S.P. Murarka, K. Rose, T. Ohmi, T. Seidel, Ma-

ter. Res. Soc. Symp. Proc., Vol. 318 (MRS, Pittsburgh, PA, 1994), p. 691.

77 F. Appel, U. Christoph, Intermetallics 7, 1273 (1999).

78 M. H. Yoo, C. L. Fu, J. K. Klee, J. Phys. III 1, 1065 (1991).

79 J. W. Christian, S. Mahajan, Progress in Materials Science 39, 1 (1995).

80 M. H. Yoo, Scripta Mater. 39, 569 (1998).

81 E. Cerreta, S. Mahajan, Acta Mater. 49, 3803 (2001).

82 F. Appel, in: *Advances in Twinning*, eds. S. Ankem, C. S. Pande (TMS, Warrendale, PA, 1999), p. 171.

83 G. Schöck, Phys. Stat. Sol. 8, 499 (1965).

84 A. G. Evans, R. W. Rawlings, Phys. Stat. Sol. 34, 9 (1969).

85 F. Appel, U. Lorenz, M. Oehring, U. Sparka, R. Wagner, Mater. Sci. Eng. A233, 1 (1997).

86 J. D. H. Paul, F. Appel, R. Wagner, Acta Mater. 46, 1075 (1998).

87 S. Sriram, D. M. Dimiduk, P. M. Hazzledine, V. K. Vasudevan, Phil. Mag. A 76, 965 (1997).

88 S. Zghal, A. Menand, A. Couret, Acta Mater. 46, 5899 (1998).

89 A. Menand, A. Huguet, A. Nérac-Partaix, Acta Mater. 44, 4729 (1996).

90 B. K. Kad, H. L. Fraser, Phil. Mag. Lett. 70, 211 (1994).

91 U. Christoph, F. Appel, R. Wagner, Mater. Sci. Eng. A239–240, 39 (1997).

92 B. A. Greenberg, V. I. Anisimov, Yu. N. Gornostirev, G. G. Taluts, Scripta Metall. 22, 589 (1988).

93 S. A. Court, V. K. Vasudevan, H. L. Fraser, Phil. Mag. A 61, 141 (1990).

94 J. Panova, D. Farkas, in: *High-Temperature Ordered Intermetallic Alloys VI,* Mat. Res. Soc. Symp. Proc., Vol. 364, eds. J. A. Horton, I. Baker, S. Hanada, R. D. Noebe, D. S. Schwartz (MRS, Pittsburgh, PA, 1995), p. 151.

95 J. P. Simmons, S. I. Rao, D. M. Dimiduk, Phil. Mag. A 75, 1299 (1997).

96 M. A. Morris, T. Lipe, D. G. Morris, Scripta Mater. 34, 1337 (1996).

97 U. Christoph, F. Appel, R. Wagner, in: *High-Temperature Ordered Intermetallic VII*, Mater. Res. Soc. Symp. Proc., Vol. 460, eds. C. C. Koch, C. T. Liu, N. S.

Stoloff, A. Wanner (MRS, Pittsburgh, PA, 1997), p. 77.

98 U. Fröbel, F. Appel, Acta Mater. 50, 3693 (2002).

99 M. H. Yoo, C. L. Fu, Metall. Trans. 29A, 49 (1998).

100 U. Lorenz, F. Appel, R. Wagner, Mater. Sci. Eng. A 234-236, 846 (1997).

101 F. Appel, U. Lorenz, U. Sparka, R. Wagner, Intermetallics, 6, 603 (1998).

102 S. Kroll, H. Mehrer, N. Stolwijk, Chr. Herzig, R. Rosenkranz, G. Frommeyer, Z. Metallkunde 83, 8 (1992).

103 Chr. Herzig, T. Przeorski, Y. Mishin, Intermetallics 7, 389 (1999).

104 F. Appel, Mater. Sci. Eng. A 317, 115 (2001).

105 B. K. Kad, H. L. Fraser, Phil. Mag. A, 69, 689 (1994).

106 F. Appel, U. Sparka, R. Wagner, Intermetallics, 7 325 (1999).

107 J. D. H. Paul, U. Sparka, F. Appel, in: *Structural Intermetallics 2001,* eds. K. J. Hemker, D. M. Dimiduk, H. Clemens, R. Darolia, H. Inui, J. M. Larsen, V. K. Sikka, M. Thomas, J. D. Whittenberger (TMS, Warrendale, PA, 2001), p. 403.

108 V. K. Vasudevan, S. A. Court, P. Kurath, H. L. Fraser, Scripta Metall. 23, 467 (1989).

109 C. Koeppe, A. Bartels, J. Seeger, H. Mecking, Metall. Trans. 24A, 1795 (1993).

110 Y.-W. Kim, Intermetallics 6, 623 (1998).

111 B. K. Kad, R. J. Asaro, Phil. Mag. A75, 87 (1997).

112 D. M. Dimiduk, P. M. Hazzledine, T. A. Parthasarathy, S. Seshagiri, M. G. Mendiratta, Metall. Mater. Trans. 29A, 37 (1998).

113 T. Fujiwara, A. Nakamura, M. Hosomi, S. R. Nishitani, Y. Shirai, M. Yamaguchi, Phil. Mag. A 61, 591 (1990).

114 Y. Umakoshi, T. Nakano, Mater. Sci. Eng. A 152, 81 (1992).

115 Y. Umakoshi, T. Nakano, Acta Metall. Mater. 41, 1155 (1993).

116 R. Gerling, M. Oehring, F.-P. Schimansky, R. Wagner, in: *Advances in Powder Metallurgy and Particulate Materials,* Vol. 3(12), eds. M. Phillips, J. Porter (Metal Powder Industries Federation,

APMI International, Princeton NJ, 1995), p. 91.

117 C.T. Liu, P.J. Maziasz, D.R. Clemens, J.H. Schneibel, V.K. Sikka, T.G. Nieh, J. Wright, L.R. Walker, in: *Gamma Titanium Aluminides*, eds. Y.-W. Kim, R. Wagner, M. Yamaguchi (TMS, Warrendale, PA, 1995), p. 679.

118 P.J. Maziasz, C.T. Liu, Metall. Mater. Trans. 20A, 105 (1998).

119 S.C. Huang, in: *Structural Intermetallics*, eds. R. Darolia, J.J. Lewandowski, C.T. Liu, P.L. Martin, D.B. Miracle, M.V. Nathal (TMS, Warrendale, PA, 1993), p. 299.

120 M.E. Hyman, C. McCullough, C.G. Levi, R. Mehrabian, Metall. Trans. 22A, 1647 (1991).

121 B. Inkson, C.B. Boothroyd, C.J. Humphreys, Acta Metall. Mater. 43, 1429 (1995).

122 A.B. Godfrey, M.H. Loretto, Intermetallics, 4, 47 (1996).

123 J.A. Christodoulou, H.M. Flower, Adv. Eng. Mater. **2**, 631 (2000).

124 G. Chen, W. Zhang, Y. Wang, J. Wang, Z. Sun, J. Wu, L. Zhou, in: *Structural Intermetallics*, eds. R. Darolia, J.J. Lewandowski, C.T. Liu, P.L. Martin, D.B. Miracle, M.V. Nathal (TMS, Warrendale, PA, 1993), p. 319.

125 E. Mohandas, P.A. Beaven, Scripta Metall. Mater. 25, 2023 (1991).

126 C.J. Rossouw, C.T. Forwood, M.A. Gibson, P.R. Miller, Phil. Mag. A 74, 77 (1996).

127 C. Woodward, S.A. Kajihara, S.I. Rao, D.M. Dimiduk, in: *Gamma Titanium Aluminides 1999*, eds. Y.-W. Kim, D.M. Dimiduk, M.H. Loretto (TMS, Warrendale, PA, 1999), p. 49.

128 G.L. Chen, Z.C. Liu, J.P. Lin, W.J. Zhang, in: *Structural Intermetallics 2001*, eds. K.J. Hemker, D.M. Dimiduk, H. Clemens, R. Darolia, H. Inui, J.M. Larsen, V.K. Sikka, M. Thomas, J.D. Whittenberger (TMS, Warrendale, PA, 2001), p. 475.

129 F. Appel, M. Oehring, R. Wagner, Intermetallics 8, 1283 (2000).

130 F. Appel, M. Oehring, J.D.H. Paul, U. Lorenz, in: *Structural Intermetallics 2001*, eds. K.J. Hemker, D.M. Dimiduk, H.

Clemens, R. Darolia, H. Inui, J.M. Larsen, V.K. Sikka, M. Thomas, J.D. Whittenberger (TMS, Warrendale, PA, 2001), p. 63.

131 Chr. Herzig, T. Przeorski, M. Friesel, F. Hisker, S. Divinski, Intermetallics 9, 461 (2001).

132 H. Nickel, N. Zheng, A. Elschner, W. Quadakkers, Microchim. Acta 119, 846 (1995).

133 T. Kawabata, T. Abumiya, O. Izumi, Acta Metall. Mater. 40, 211 (1994).

134 W.H. Tian, M. Nemoto, in: *Gamma Titanium Aluminides*, eds. Y.-W. Kim, R. Wagner, M. Yamaguchi (TMS, Warrendale, PA, 1995), p. 689.

135 S. Tsuyama, S. Mitao, K. Minakawa, Mater. Sci. Eng. A 153, 451 (1992).

136 T. Noda, M. Okabe, S. Isobe, M. Sayashi, Mater. Sci. Eng. A192/193, 774 (1995).

137 S. Chen, P.A. Beaven, R. Wagner, Scripta Metall. Mater. 26, 1205 (1992).

138 W.H. Tian, T. Sano, M. Nemoto, Phil. Mag. A 68, 965, (1993).

139 P.-I. Gouma, K. Subramanian, Y.-W. Kim, M.J. Mills, Intermetallics 6, 689 (1998).

140 H. Oikawa, Mater. Sci. Eng. A 153, 427 (1992).

141 Y. Ishikawa, K. Maruyama, H. Oikawa, in: *Structural Intermetallics*, eds. R. Darolia, J.J. Lewandowski, C.T. Liu, P.L. Martin, D.B. Miracle, M.V. Nathal (TMS, Warrendale, PA, 1993), p. 345.

142 B.D. Worth, J.W. Jones, J. Allison, Metall. Trans. 26A, 2947 (1995).

143 R.W. Hayes, P.L. Martin, Acta Metall. Mater. 43, 2716 (1995).

144 K. Maruyama, R. Yamamoto, H. Nakauki, N. Fujisuna, Mater. Sci. Eng. A239–240, 419 (1997).

145 J.N. Wang, T.G. Nieh, Acta Mater. 46, 1887 (1998).

146 F. Herrouin, D.H. Hu, P. Bowen, I.P. Jones, Acta Mater. 46, 4963 (1998).

147 J. Beddoes, W. Wallace, L. Zhao, Intern. Mater. Review 40, 197 (1995).

148 T.A. Parthasaraty, M.G. Mendiratta, D.M. Dimiduk, Scripta Mater. 37, 315 (1997).

149 M. Oehring, P.J. Ennis, F. Appel, R. Wagner, *High-Temperature Ordered Inter-*

metallics VII, Mater. Res. Soc. Symp. Proc., Vol. 460, eds. C. C. Koch, C. T. Liu, N. S. Stoloff, A. Wanner (MRS, Pittsburgh, PA 1997), p. 257.

150 M. Oehring, F. Appel, P. J. Ennis, R. Wagner, Intermetallics 7, 335 (1999).

151 F. Ernst, M. W. Finnis, D. Hoffmann, T. Muschik, U. Schönberger, U. Wolf, Phys. Rev. Lett. 69, 620 (1992).

152 M. F. Bartholomeusz, J. A. Wert, Metall. Mater. Trans. 25A, 2371 (1994).

153 K. S. Chan, Y.-W. Kim, Metall. Trans. 23A, 1663 (1992).

154 K. S. Chan, Metall. Trans. 24A, 569 (1993).

155 D. M. Dimiduk, in: Gamma Titanium Aluminides, eds. Y.-W. Kim, R. Wagner, M. Yamaguchi (TMS, Warrendale, PA, 1995), p. 3.

156 P. Bowen, N. J. Rogers, A. W. James, in: Gamma Titanium Aluminides, eds. Y.-W. Kim, R. Wagner, M. Yamaguchi (TMS, Warrendale, PA, 1995), p. 849.

157 F. Appel, U. Brossmann, U. Christoph, S. Eggert, P. Janschek, U. Lorenz, J. Müllauer, M. Oehring, J. D. H. Paul, Adv. Eng. Mater. 2, 699 (2000).

158 M. H. Yoo, C. L. Fu, Mater. Sci. Eng. A153, 470 (1992).

159 F. Appel, in: High-Temperature Ordered Intermetallics IX, Mater. Res. Soc. Symp. Proc., Vol. 646, eds. J. H. Schneibel, K. J. Hemker, R. D. Noebe, S. Hanada, G. Sauthoff (MRS, Pittsburgh, PA, 2001), p. N.1.8.2.

160 B. D. Worth, J. M. Larsen, A. H. Rosenberger, in: Structural Intermetallics 1997, eds. M. V. Nathal, R. Darolia, C. T. Liu, P. L. Martin, D. B. Miracle, R. Wagner, M. Yamaguchi (TMS, Warrendale, PA, 1997), p. 563.

161 G. Hénaff, C. Mabru, A. Tonneau, J. Petit, in: Gamma Titanium Aluminides 1999, eds. Y.-W. Kim, D. M. Dimiduk, M. H. Loretto (TMS, Warrendale, PA, 1999), p. 549.

162 K. S. Chan, in: Gamma Titanium Aluminides 1999, eds. Y.-W. Kim, D. M. Dimiduk, M. H. Loretto (TMS, Warrendale, PA, 1999), p. 517.

163 S. J. Trail, P. Bowen, Mater. Sci. Eng. A192/193, 443 (1995).

164 P. C. Paris, F. Erdogan, J. Basic Eng. Trans. ASME Ser. D 85, 528 (1963).

165 H. Kestler, H. Clemens, this volume.

166 S Reed, in: Gamma Titanium Aluminides, eds. Y.-W. Kim, R. Wagner, M. Yamaguchi (TMS, Warrendale, PA, 1995), p. 475.

167 D. M. Dimiduk, P. L. Martin, Y.-W. Kim, Mater. Si. Eng. A243, 66 (1998).

168 P.A McQuay, R. Simkins, D. Y. Seo, T. T. Bieler, in: Gamma Titanium Aluminides 1999, eds. Y.-W. Kim, D. M. Dimiduk, M. H. Loretto (TMS, Warrendale, PA, 1999), p. 197.

169 V. Güther, A. Otto, H. Kestler, H. Clemens, Gamma Titanium Aluminides 1999, eds. Y.-W. Kim, D. M. Dimiduk, M. H. Loretto (TMS, Warrendale, PA, 1999), p. 225.

170 P. L. Martin, C. G. Rhodes, P. A. McQuay, in: Structural Intermetallics, eds. R. Darolia, J. J. Lewandowski, C. T. Liu, P. L. Martin, D. B. Miracle, M. V. Nathal (TMS, Warrendale, PA, 1993), p. 177.

171 U. Brossmann, M. Oehring, U. Lorenz, F. Appel, H. Clemens, Z. Metallkd. 92, 1009 (2001).

172 C. M. Austin, T. J. Kelly, in: Gamma Titanium Aluminides, eds. Y.-W. Kim, R. Wagner, M. Yamaguchi (TMS, Warrendale, PA, 1995), p. 21.

173 T. Tetsui, S. Ono, Intermetallics 7, 689 (1999).

174 S.-C. Huang, US Patent 4,879,092, 1989.

175 S.-C. Huang. D. W. McKee, D. S. Shih, J. C. Chesnutt, in: Intermetallic Compounds – Structure and Mechanical Properties, ed. O. Izumi, (The Japan Inst. of Metals, Japan, 1991), p. 363.

176 T. Noda, Intermetallics 6, 709 (1998).

177 D. R. Johnson, H. Inui, M. Yamaguchi, Intermetallics 6, 647 (1998).

178 A. R. C. Westbrook, Mater. Sci. Technol. 6, 958, 1990.

179 S. L. Kampe, J. A. Clarke, L. Christodoulou, MRS Bull. 194, 285 (1990).

180 R. Wagner, F. Appel, B. Dogan, P. J. Ennis, U. Lorenz, J. Müllauer, H. P. Nicolai, W. Quadakkers, L. Singheiser, W. Smarsly, W. Vaidya, K. Wurzwallner, in: Gamma Titanium Aluminides, eds. Y.-W. Kim, R. Wagner, M. Yamaguchi (TMS, Warrendale, PA, 1995), p. 387.

181 S. L. Semiatin, in: *Gamma Titanium Aluminides,* eds. Y.-W. Kim, R. Wagner, M. Yamaguchi (TMS, Warrendale, PA, 1995), p. 509.

182 R. Imayev, G. Salishchev, V. Imayev, M. Shagiev, V. Kuznetsov, in: *Gamma Titanium Aluminides,* eds. Y.-W. Kim, R. Wagner, M. Yamaguchi (TMS, Warrendale, PA, 1995), p. 665.

183 S. L. Semiatin, V. Seetharaman, I. Weiss, Mater. Sci. Eng. A243, 1 (1998).

184 M. Nobuki, K. Hashimoto, J. Takahashi, T. Tsujimoto, Mater. Trans. Japan Inst. Met. 31, 814 (1990).

185 R. Srinivasan, J. P. Singh, E. Tuval, I. Weiss, Scripta Mater. 34, 1295 (1996).

186 V. Seetharaman, S. L. Semiatin, Metall. Mater. Trans. 27A, 1987 (1996).

187 R. W. Cahn, M. Takeyama, J. A. Horton, C. T. Liu, J. Mater. Res. 6, 57 (1991).

188 R. M. Imayev, G. A. Salishchev, V. M. Imayev, M. R. Shagiev, M. R. Kuznetsov, F. Appel, M. Oehring, O. N. Senkov, F. H. Froes, in: *Gamma Titanium Aluminides 1999,* eds. Y.-W. Kim, D. M. Dimiduk, M. H. Loretto (TMS, Warrendale, PA, 1999), p. 565.

189 W.-J. Zhang, U. Lorenz, F. Appel, Acta Mater. 48, 2803 (2000).

190 S. Davey, M. H. Loretto, R. W. Evans, T. A. Dean, Z. W. Huang. P. Blekinsop, A. Jones, in: *Gamma Titanium Aluminides,* eds. Y.-W. Kim, R. Wagner, M. Yamaguchi (TMS, Warrendale, PA, 1995), p. 539.

191 R. M. Imayev, V. M. Imayev, G. A. Salishchev, J. Mater. Sci. 27, 4465 (1992).

192 F. Appel, H. Clemens, H. Kestler, in: *Intermetallic Compounds, Vol. 3, Principles and Practice,* eds. J. H. Westbrook, R. L. Fleischer, Chapter 29 (John Wiley, 2002) pp. 617–642.

193 S. L. Semiatin, V. Seetharaman, V. K. Jain, Metall. Mater. Trans. 25A, 2753 (1994).

194 J. Wesemann, G. Frommeyer, J. Kruse, Intermetallics 9, 73 (2001).

195 H. Clemens, H. Kestler, Adv. Eng. Mater. 2, 551 (2000).

196 F. Appel, U. Lorenz, M. Oehring, R. Wagner, German Patent DE 197 47 257 C2, 1997.

197 H. Mecking, C. Hartig, U. F. Kocks, Acta Mater. 44, 1309 (1996).

198 A. Bartels, C. Hartig, S. Willems, H. Uhlenhut, Mater. Sci. Eng. A239–240, 14 (1997).

199 H.-G. Brokmeier, M. Oehring, U. Lorenz, H. Clemens, F. Appel, Metall. Mat. Trans. A, in press.

5

Fatigue of Titanium Alloys

L. Wagner, *TU Clausthal, Institut für Werkstoffkunde und Werkstofftechnik, Clausthal-Zellerfeld, Germany*
J. K. Bigoney, *Springfield Metallurgical Services, Inc., Springfield, VT, USA*

5.1
Introduction

There are three main reasons to use titanium as a structural material: excellent resistance to chloride-containing fluids, high specific strength, and exceptional biocompatibility. Therefore, titanium and its alloys have primarily found application in the chemical and aerospace industry, as well as in biomedicine. During these applications titanium structures are often exposed to fatigue loading. The lifetime of such a cyclically loaded, initially defect-free component can be separated into a portion describing crack initiation (N_I) and a portion describing crack propagation (N_F).

Investigations of fatigue on titanium alloys have shown that for high stress or strain amplitudes, the crack initiation life can be very small compared to the overall fatigue life, i.e. $N_I/N_F=0.01$ [1, 2]. Therefore, under low-cycle fatigue (LCF) conditions the component lifetime is dominated by resistance to fatigue crack propagation. With decreasing load amplitudes, the portion attributable to crack initiation life continuously increases. Therefore, for titanium alloys, which are typically defect-free, the high-cycle fatigue (HCF) strength (the highest fatigue load amplitude a component endures without fracture after a large number of cycles, e.g. 10^7) can be considered a good measure of resistance to fatigue crack initiation.

It is useful to subdivide the fatigue crack propagation phase into components described by an initial stage of small surface crack or microcrack growth and a subsequent stage of macrocrack growth. Microstructural parameters such as grain size or phase dimensions can have contradictory influences on microcrack and macrocrack propagation [3, 4]. As a rule of thumb, the lifetime of small, highly stressed components (small critical crack length) is primarily controlled by the resistance to microcrack propagation whereas for large, low-stressed components (large critical crack length) component life is determined by the propagation of macrocracks.

The following chapter will highlight the most important metallurgical parameters which influence fatigue strength and fatigue crack propagation.

5.2
Influence of Microstructure

Depending on the alloy class, the parameters possibly having an influence on the fatigue life of titanium alloys include grain size (or phase dimension and morphology), age hardening condition, degree of work hardening, elastic constants, and crystallographic texture.

5.2.1
Commercially Pure Titanium, α Alloys

Usually the microstructure of α alloys consists exclusively of α grains. Consequently, grain size, interstitial oxygen content, and degree of work hardening can be varied. The influence of these parameters on the fatigue strength of commercially pure titanium is shown in Fig. 5.1 [5].

A reduction of grain size from 110 to 6 μm increases the fatigue strength of commercially pure titanium from 160 to 210 MPa (Fig. 5.1a). Increasing the oxygen content increases strength and thus improves fatigue strength (Fig. 5.1b). Likewise the fatigue strength increases after increasing strength via work hardening (Fig. 5.1c).

The da/dN-ΔK plots of Fig. 5.2 show the influence of two different grain sizes and oxygen contents on the propagation of long fatigue cracks for unalloyed titanium. Large grains reduce crack propagation rates, and increased oxygen content also has a beneficial influence on da/dN-ΔK behavior. These relationships of grain size and oxygen content on da/dN observed for long cracks are not necessarily the same for short surface cracks. Also, interaction effects can play a role. High oxygen content generally increases the influence of grain size on da/dN-ΔK behavior.

In addition to grain size and oxygen content, the fatigue behavior of α alloys is furthermore controlled by the degree of age hardening [6]. As an example, Fig. 5.3 shows the influence of fine coherent Ti_3Al particles on the high cycle fatigue strength of the experimental α alloy Ti-8.6Al. Tensile properties are listed in Tab. 5.1. Due to the tendency of Ti-8.6Al to planar slip, the increase in yield stress due to age hardening goes along with a strong reduction in ductility [8].

The effect of age hardening on fatigue strength is explained in a similar way to the way grain size and oxygen content control fatigue strength, namely, through their influence on yield stress.

In Ti-8.6Al fatigue cracks nucleate along planar slip bands within α grains (Fig. 5.4). At a given value of ΔK, microcracks propagate faster in coarse-grain structures than in fine-grained material (Fig. 5.5). This is a consequence of the higher grain boundary density [3], since grain boundaries are known to effectively hinder microcrack growth. The superior behavior of fine-grained material concerning microcrack growth is different from the behavior of macrocracks (Fig. 5.5) [9]. For comparable ΔK-values, macrocracks propagate much more slowly in coarse-grained structures than in fine-grained material. This difference is primarily due to the fact that for macrocracks additional crack retardation factors are effective,
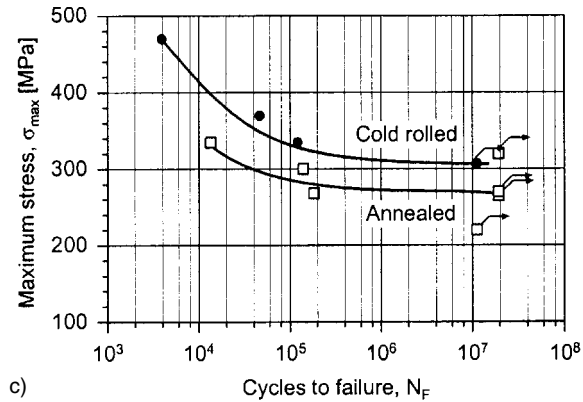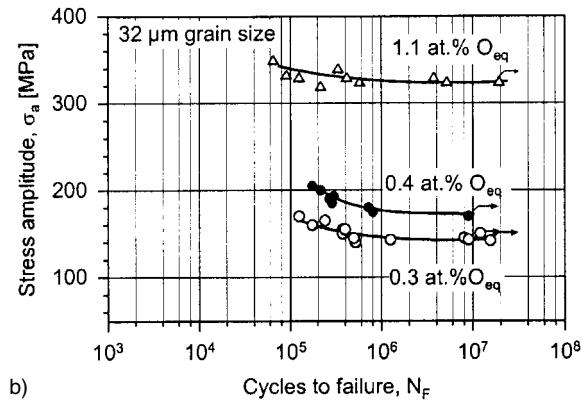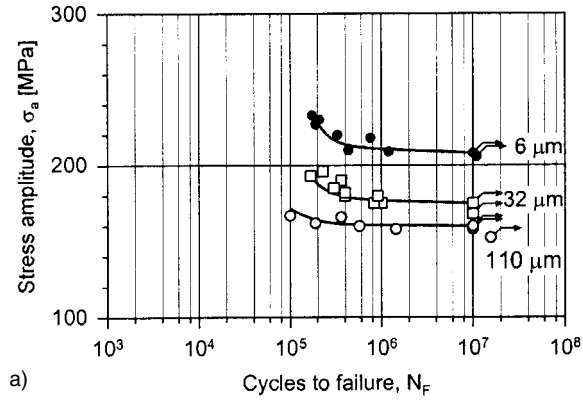
Fig. 5.1 High cycle fatigue behavior of commercially pure titanium: a) influence of grain size (R=−1); b) influence of oxygen content (R=−1); c) influence of cold work (R=0.1).
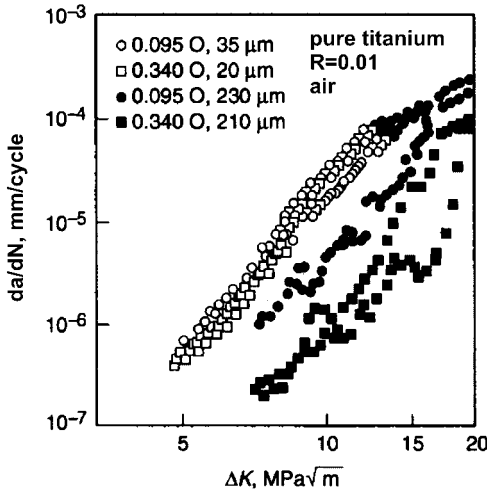
Fig. 5.2 Fatigue crack propagation in commercially pure titanium for two different grain sizes and two different oxygen contents at R=0.01 [6].
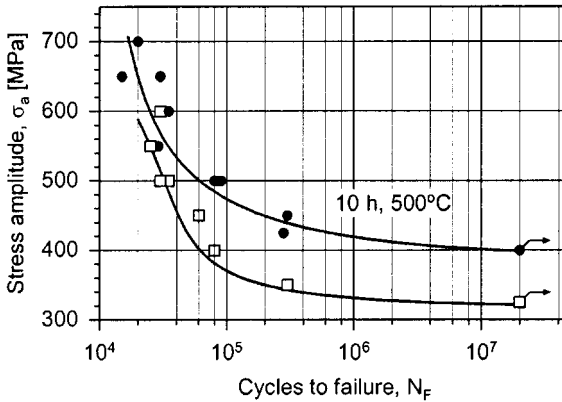
Fig. 5.3 Influence of age hardening on the high cycle fatigue behavior (R=−1) of Ti-8.6Al.

Tab. 5.1 Tensile properties of Ti-8.6Al (100 μm grain size).

Age hardening	$\sigma_{0.2}$/MPa	ε_F
–	775	0.38
10 h 500 °C	880	0.08

such as crack front geometry (i.e. all deviations from an ideal crack front) and so-called crack closure, which is particularly important at low R values [9–11]. Furthermore, increasing oxygen content or age hardening often intensifies the influence of grain size on macrocrack propagation through the influence on crack closure.
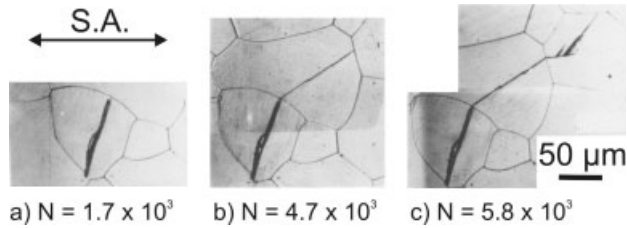
Fig. 5.4 Microcrack propagation in Ti-8.6Al (10 h/500 °C), $\sigma_a = 650$ MPa (R = −1).
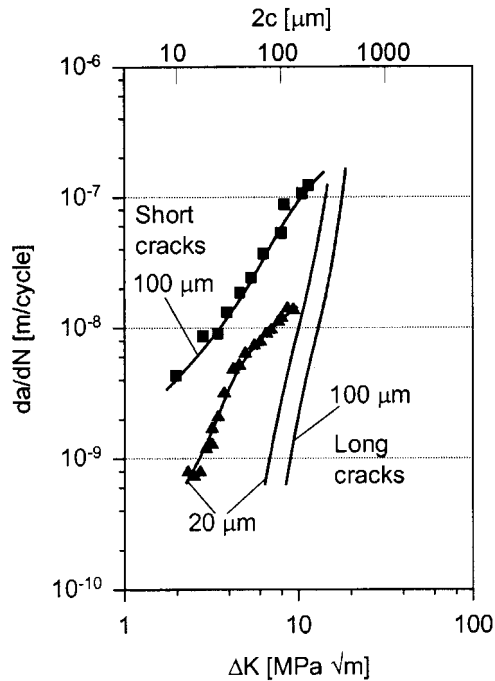
Fig. 5.5 Comparison of microcrack and macrocrack propagation in Ti-8.6Al (10 h/500 °C).

5.2.2
Near-α and α + β Alloys

In addition to α grain size, degree of age hardening, and oxygen content, the fatigue properties of two-phase near-α and α + β alloys are strongly influenced by the morphology and arrangements of the two phases α and β. Lamellar, equiaxed, and bimodal microstructures (primary α in a lamellar matrix) can be generated. Bimodal microstructures are also referred to as duplex structures. Important micro-

structural parameters include prior β grain size, colony size of α and β lamellae, and the width of α lamellae in lamellar microstructures. Additional parameters for duplex structures are grain size and volume fraction of the primary α phase.

Tab. 5.2 lists typical tensile properties for the alloy Ti-6Al-4V where the microstructural parameters α lamella width and α grain size are varied.

The high cycle fatigue behavior of these microstructures is shown in Fig. 5.6. Reducing the α lamellae width from 10 to 0.5 μm in lamellar microstructures raises the fatigue strength from 480 to 675 MPa (Fig. 5.6a) [12]. Similarly, reducing the grain size from 12 to 2 μm in equiaxed microstructures increases fatigue strength from 560 to 720 MPa (Fig. 5.6b) [12, 13]. For duplex structures, reducing the α lamellae width in a lamellar matrix from 1 to 0.5 μm leads to an increase in fatigue strength from 480 to 575 MPa (Fig. 5.6c) [14].

Fig. 5.7 shows typical crack initiation sites for these microstructures [15]. In lamellar microstructures (Fig. 5.7a), fatigue cracks initiate at slip bands within the α lamellae or at α along prior β grain boundaries [15]. Since the resistance to dislocation motion as well as fatigue crack initiation depends on the α lamellae width, there is a direct correlation between fatigue strength and yield stress. For equiaxed structures, fatigue cracks nucleate along slip bands within α grains (Fig. 5.7b). Thus, fatigue strength correlates directly with the grain size dependent yield stress (Tab. 5.2). In duplex structures, fatigue cracks can either initiate in the lamellar matrix, at the interface between the lamellar matrix and the primary α phase, or within the primary α phase. The precise crack initiation site depends on the cooling rate [16], and the volume fraction and size of the primary α phase [17, 18]. An example of crack initiation within the lamellar part of a duplex structure is shown in Fig. 5.7c.

Fig. 5.8 shows typical crack propagation behavior for microcracks in two extreme microstructures of Ti-6Al-4V, a coarse lamellar (Fig. 5.8a) and an equiaxed structure (Fig. 5.8b) [10].

The da/dN-ΔK plot (Fig. 5.9) clearly shows the inferior microcrack propagation behavior of the coarse lamellar structure compared to the equiaxed structure. However, the ranking of both microstructures changes for macrocrack propaga-

Tab. 5.2 Tensile properties of typical microstructures in Ti-6Al-4V (24 h/500 °C).

Microstructure	$\sigma_{0.2}$/MPa	ε_F
fine lamellar, 0.5 μm*	1040	0.20
lamellar, 1 μm*	980	0.25
coarse lamellar, 10 μm*	935	0.15
fine equiaxed, 2 μm**	1170	0.55
equiaxed, 6 μm**	1120	0.49
coarse equiaxed, 12 μm**	1075	0.38
duplex, 6 μm***, 40% α_p	1110	0.55
duplex, 25 μm***, 40% α_p	1075	0.45

* α lamella width, ** α grain size, *** α_p grain size
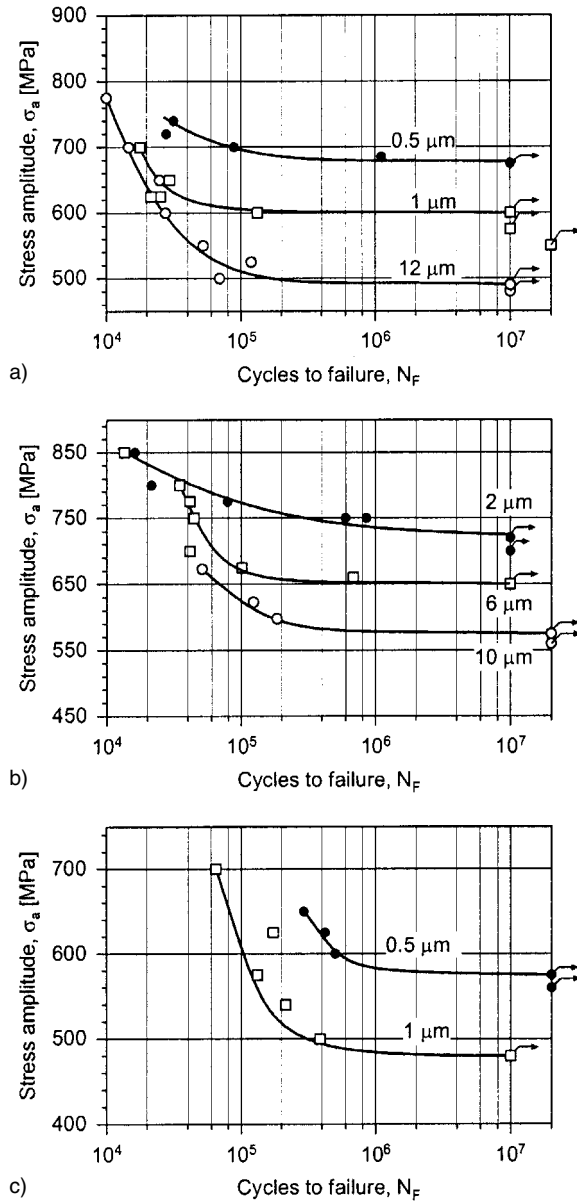
Fig. 5.6 High cycle fatigue behavior (R=−1) of Ti-6Al-4V: a) influence of lamella width (lamellar microstructure); b) influence of α grain size (equiaxed microstructure); c) influence of lamella width (duplex microstructure).
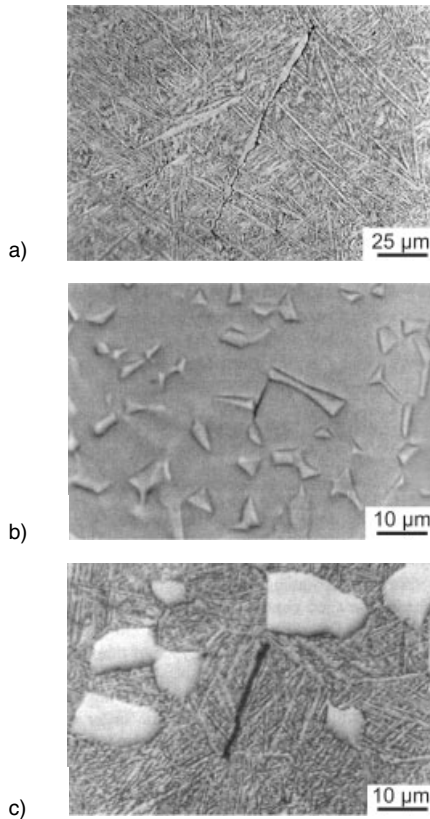
Fig. 5.7 Fatigue crack initiation in Ti-6Al-4V, σ_a=775 MPa (R=−1). a) Lamellar microstructure; b) equiaxed microstructure; c) duplex microstructure.

tion (Fig. 5.9). As already outlined in section 5.2.1, this is due to additional crack propagation resistance caused by crack front geometry and crack closure effects, which retard crack propagation compared to microcracks [15]. Similar results are reported for the α alloy Ti-2.5Cu [19]. The inferior microcrack propagation behavior of coarse structures correlates with the low density of phase boundaries in the coarse lamellar microstructures, which also leads to low ductility. Crack propagation tests on fine lamellar microstructures and duplex structures in Ti-6Al-4V have shown that these da/dN-ΔK curves fall in between those determined for coarse lamellar and equiaxed structures [10].

The microstructural morphology (lamellar, equiaxed, or a mixture of both (duplex)) has a substantial influence on fatigue crack propagation behavior, as will be demonstrated for the alloy Ti-6Al-4V (Fig. 5.10). The da/dN-ΔK curves reveal contradictory influences of microstructure for long cracks (Fig. 5.10a) and small surface cracks (Fig. 5.10b). For long cracks, fatigue crack growth behavior is superior for coarse lamellar structures compared to a fine equiaxed structure; the behavior is reversed for small cracks.
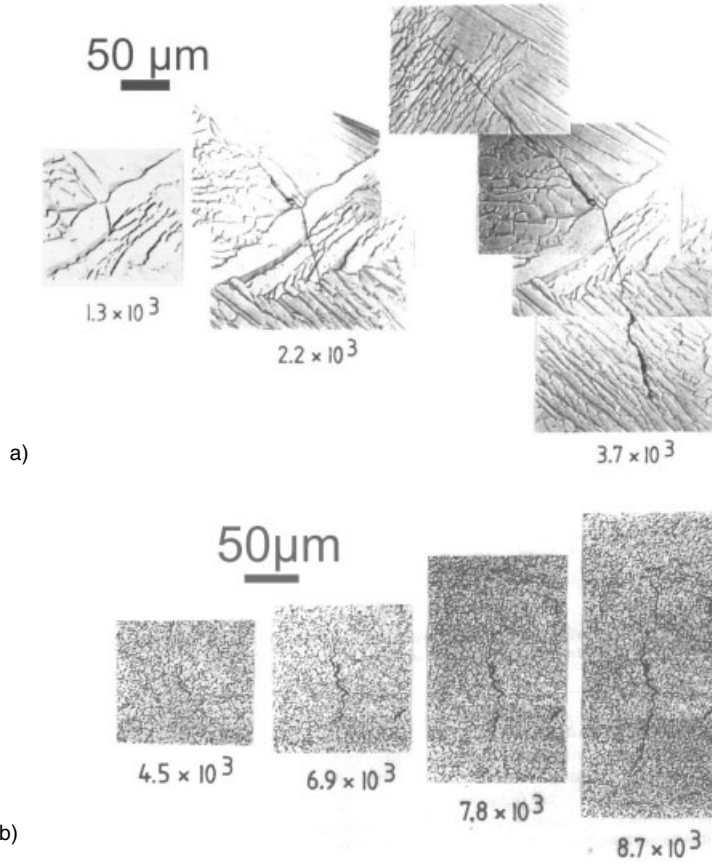
Fig. 5.8 Microcrack propagation in Ti-6Al-4V, σ_a=775 MPa (R=−1).
a) Coarse lamellar; b) equiaxed.

For a given microstructural type in near-α and α+β alloys, the influences of α grain size and oxygen content on fatigue crack growth are similar to those observed for α alloys. For a lamellar microstructure, lamellar width should be considered instead of grain size. Fig. 5.11a shows that for two-phase alloys, the reduction of crack growth rates by grain coarsening is quite measurable. However, due to the relatively small variations in absolute values, in this case from 2 μm to 12 μm, differences are not as pronounced as for α alloys, where grain variations from 20 μm to 200 μm are possible. For the same structural morphology and α grain size, the crack growth rate is slightly lower when the oxygen content is reduced (Fig. 5.11b). Often, however, an unambiguous determination of the influence of oxygen is difficult, due to its indirect effects on other microstructural parameters such as lamellae packet size [24, 25].

Because of the high silicon content (0.45 wt.%) in the near-α alloy TIMETAL 1100 and the resulting high silicide solvus temperature (T_{SS}), fine prior β grain

2c [μm]
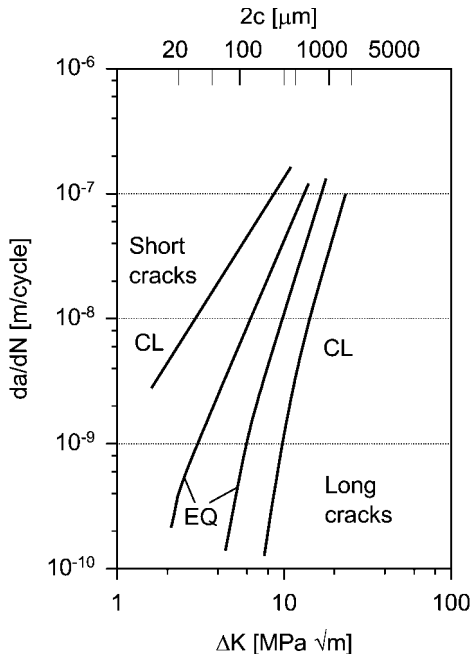
Fig. 5.9 Comparison of microcrack and macrocrack propagation in Ti-6Al-4V (CL: coarse lamellar, EQ: equiaxed).

a)

b)
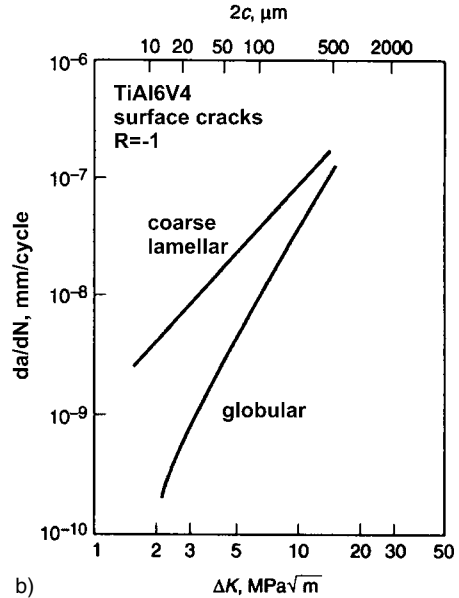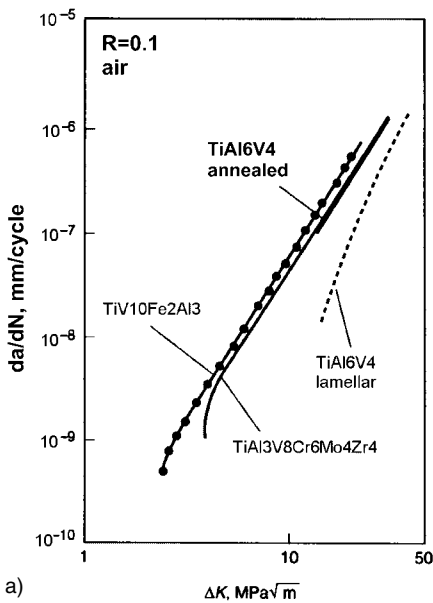
Fig. 5.10 a) Fatigue crack propagation in Ti-6Al-4V for two different microstructural morphologies [20] as well as in Ti-10V-2Fe-3Al [21] and Ti-13A-8V-6Cr-4Mo-4Zr [22]. b) Fatigue crack propagation of small surface cracks in Ti-6Al-4V with two different microstructural morphologies [23].
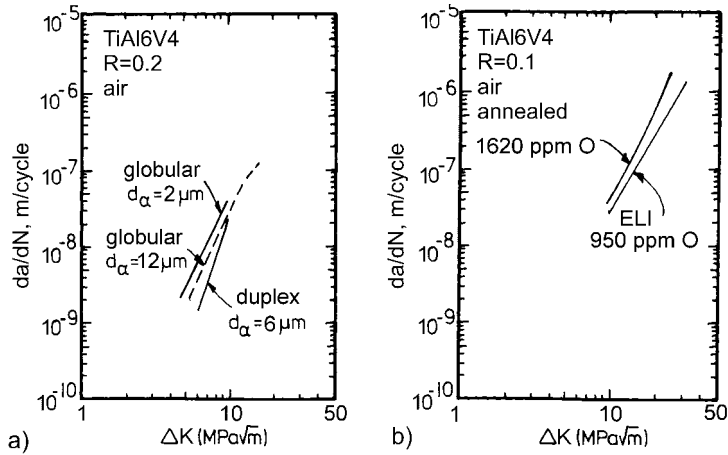
Fig. 5.11 a) Influence of grain size on fatigue crack propagation [26] in equiaxed microstructures and in duplex microstructure of an $\alpha + \beta$ alloy. b) Influence of oxygen contents on fatigue crack propagation in Ti-6Al-4V in the annealed condition [27].

sizes and correspondingly fine colony sizes can be generated after β-annealing below T_{SS} [28–30]. Tab. 5.3 compares tensile properties of fine and coarse grained lamellar microstructures with two duplex structures that only differ in primary α volume fraction.

A reduction of prior β grain size in lamellar structures significantly increases ductility (Tab. 5.3). There are, however, no significant differences in ductility noted for duplex structures when their primary α volume fraction is varied between 20 and 60%. Because of similar cooling conditions from the solution heat treatment temperature, lamellar and duplex structures show similar yield stress values. The fatigue strength behavior of TIMETAL 1100 is shown in Fig. 5.12.

A reduction of prior β grain size in lamellar microstructures (Fig. 5.12a) and a reduction of the primary α volume fraction in duplex structures (Fig. 5.12b) increases both LCF life as well as fatigue strength [31, 32]. Simultaneously, this structural modification increases the resistance to crack growth (Fig. 5.13). Therefore, the fine grained lamellar microstructure shows superior crack growth behavior over the coarse grained lamellar structure (Fig. 5.13a), while for duplex structures the lower primary α volume fraction is superior to the higher one

Tab. 5.3 Tensile properties of typical microstructures in TIMETAL 1100 (8 h/650 °C).

Microstructure	$\sigma_{0.2}$/MPa	ε_F
coarse grained lamellar, LC	955	0.10
fine grained lamellar, LF	935	0.22
duplex (60% α_P), D60	955	0.36
duplex (20% α_P), D20	965	0.32
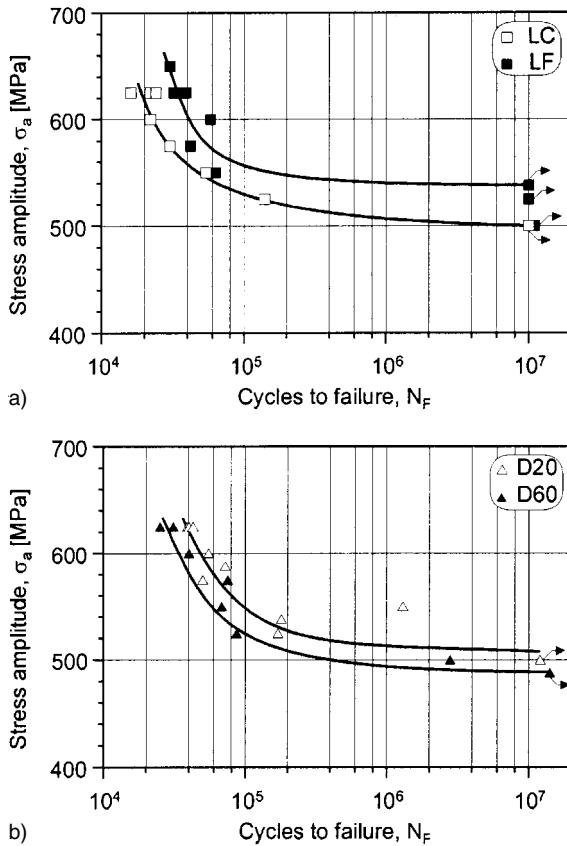
Fig. 5.12 High cycle fatigue behavior (R=−1) of TIMETAL 1100.
a) Lamellar microstructure (LC: coarse grained lamellar, LF: fine
grained lamellar); b) duplex microstructure (D20: 20% α_p con-
tent, D60: 60% α_p content).

(Fig. 5.13 b). The latter can probably be explained by the (near) absence or lower
presence of agglomerates of primary α grains and simultaneously reduced pri-
mary α volume fractions. These primary α clusters can act as large single grains,
which are easy for microcracks to propagate through [31, 32].

5.2.3
β Alloys

Depending on the alloy class (solute-rich or solute-lean β alloys), the following mi-
crostructural parameters are important for the control of the fatigue strength of β
alloys: β grain size, degree of age hardening, and precipitate-free zones in solute-
rich alloys such as Beta C. In addition, for solute-lean alloys such as Ti-10V-2Fe-
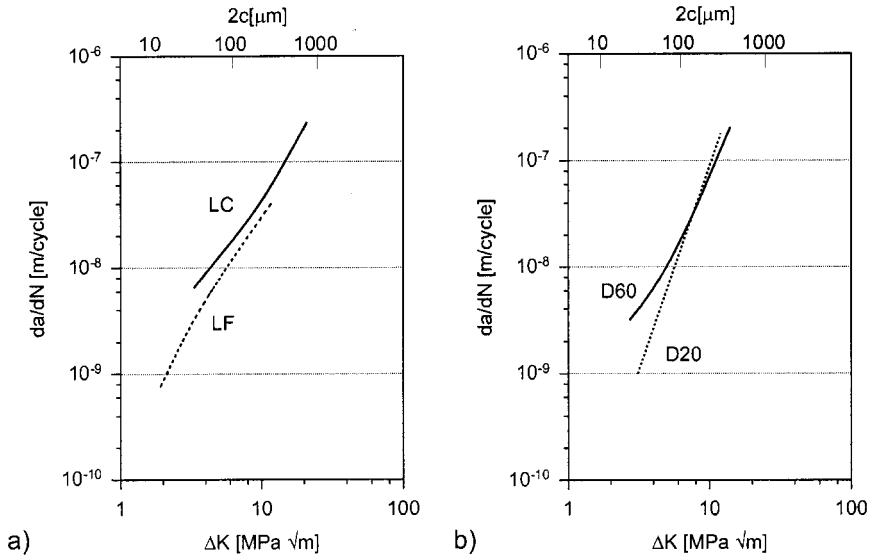
Fig. 5.13 Microcrack propagation in TIMETAL 1100, σ_a=625 MPa (R=−1). a) Lamellar microstructure (LC: coarse grained lamellar, LF: fine grained lamellar); b) duplex microstructure (D20: 20% α_p content, D60: 60% α_p content).

3Al, grain boundary α, primary α grain size and primary α volume fraction have to be considered [33].

Fig. 5.14 shows typical microstructures of Beta C: a conventional aging treatment (Fig. 5.14 a) is compared to two-step aging (Fig. 5.14 b) [34]. As opposed to conventional aging, two-step aging results in a homogeneous precipitation of α_s particles within the β grains. The tensile properties of these microstructures are listed in Tab. 5.4. The two-step aging treatment 4 h/440 °C + 16 h/560 °C was chosen to compare the fatigue behavior with conventional aging (16 h/540 °C) on the basis of identical yield stress.

The S-N curves for the different conditions of Beta C are compared in Fig. 5.15. While aging significantly increases fatigue strength as a result of increased yield stress, two-step aging is superior by about 50 MPa when compared to conventional
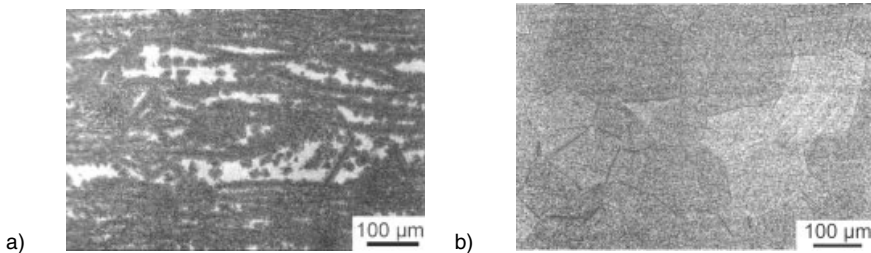
Fig. 5.14 Microstructures in Ti-3Al-8V-6Cr-4Mo-4Zr. a) Conventional aging; b) two-step aging.

Tab. 5.4 Tensile properties of Beta C.

Aging condition	$\sigma_{0.2}$/MPa	ε_F
–	850	0.97
16 h/540 °C	1085	0.26
4 h/440 °C + 16 h/560 °C	1085	0.27
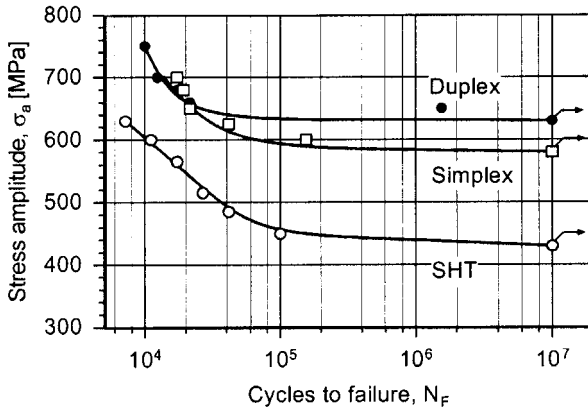
Fig. 5.15 High cycle fatigue behavior (R=–1) of Ti-3Al-8V-6Cr-4Mo-4Zr.

aging. The inferior behavior after conventional aging (Fig. 5.14 a) is caused by the presence of precipitate-free zones within the β grains [35, 36], which were identified as crack nucleation sites (Fig. 5.16). Microhardness measurements have revealed that these zones have a lower local yield stress than the solution treated condition [34].

Fig. 5.17 shows the microcrack growth behavior for different conditions of Beta C [34, 35]. No significant variations were observed between the different conditions. This result is consistent with tests on macrocracks performed on C(T) speci-
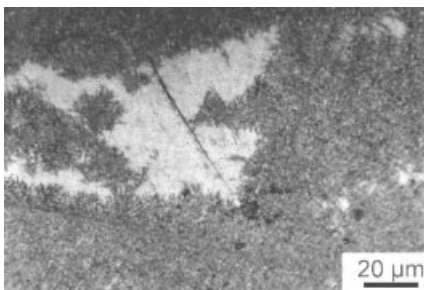
Fig. 5.16 Fatigue crack initiation in Ti-3Al-8V-6Cr-4Mo-4Zr, σ_a=675 MPa (R=–1).

Fig. 5.17 Microcrack propagation in Ti-3Al-8V-6Cr-4Mo-4Zr, σ_a=675 MPa (R=−1).
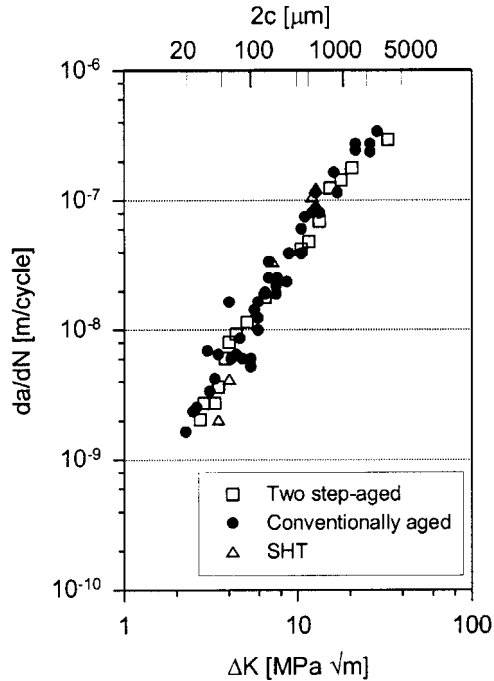
mens [37]. Obviously, the variation in fatigue crack growth resistance is much smaller for solute-rich β alloys than for α+β alloys.

The alloy Ti-10V-2Fe-3Al represents the class of solute-lean β alloys. Here microstructures can be more drastically varied due to the fact that primary α volume fractions can be generated in a manner similar to those of α+β alloys [38–41]. Typical microstructures for Ti-10V-2Fe-3Al with 15 and 30% primary α are shown in Fig. 5.18 [42, 43].

In Tab. 5.5 the tensile properties of these microstructures are compared with a β-annealed (without primary α) microstructure as well as a microstructure with 5% primary α.

Fig. 5.19 shows the S-N curves of the various microstructures. For these different conditions (Fig. 5.20), fatigue cracks nucleate at β grain boundaries in β-annealed structures (Fig. 5.20a), within β grains (Fig. 5.20b) and at thick α along β grain boundaries (Fig. 5.20c).

The superior behavior of the microstructures with low primary α volume fractions of 5 and 15% is probably due to the absence of a continuous grain boundary α film as well as to their relatively high strength values (Tab. 5.5). This is also documented in high $\sigma_a(10^7)/\sigma_{0.2}$ ratios of 0.58 and 0.55 for primary α volume fractions of 15 and 5%, respectively. For the β-annealed microstructure this ratio is only 0.45. This indicates that the presence of a soft grain boundary α film not only dramatically influences ductility (Tab. 5.5) but also reduces the resistance to fatigue crack initiation, without influencing the macroscopic yield stress. Increas-
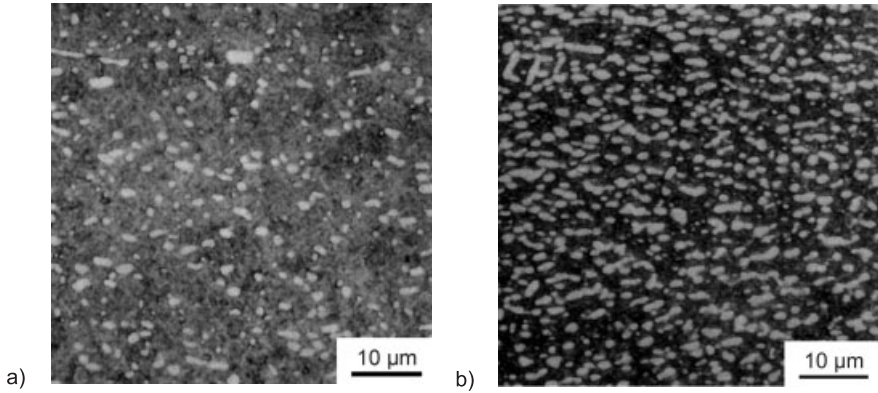
Fig. 5.18 Microstructures in Ti-10V-2Fe-3Al. a) 5% α_p content; b) 15% α_p content.

Tab. 5.5 Tensile properties of typical microstructures in Ti-10V-2Fe-3Al (8 h/480 °C).

Primary α content %	$\sigma_{0.2}$/MPa	ε_F
0	1555	0.02
5	1370	0.09
15	1330	0.11
30	1195	0.25
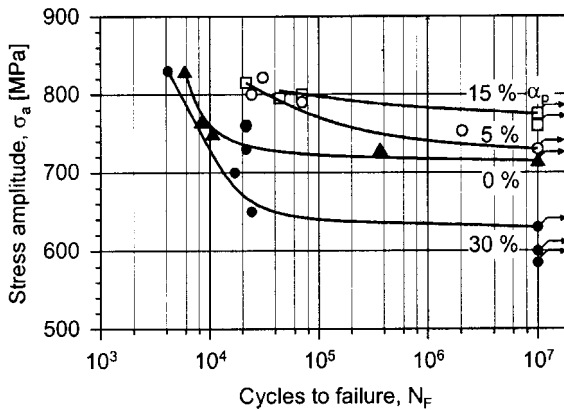
Fig. 5.19 High cycle fatigue behavior (R=−1) of Ti-10V-2Fe-3Al.

ing the primary α content to 30% raises the $\sigma_a(10^7)/\sigma_{0.2}$ ratio to 0.52. This corresponds to a decrease in strength difference between grain boundary α and the interior of the grain. In this case, the reduced macroscopic yield stress is caused by the contribution of the high volume fraction of primary α in the β matrix and consequently the reduced age hardening response from secondary α [42–44].
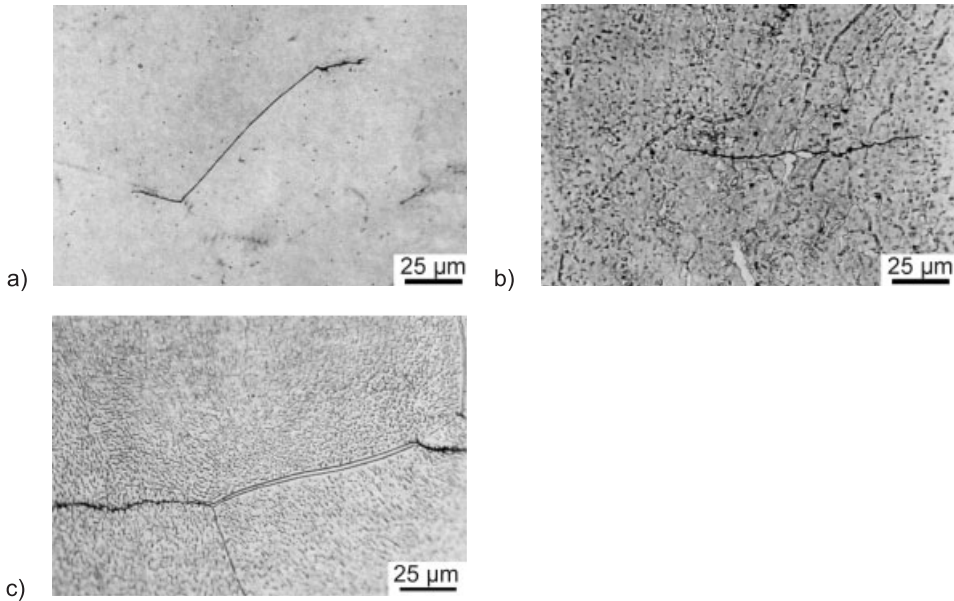
Fig. 5.20 Fatigue crack initiation in Ti-10V-2Fe-3Al, σ_a=825 MPa (R=−1). a) 0% α_p content; b) 5% α_p content; c) 30% α_p content.

5.3
Influence of Crystallographic Texture on Fatigue Life

Due to their body centered cubic crystal structure, β alloys are generally isotropic. The mechanical properties of α and α+β alloys can, however, be quite anisotropic due to the anisotropy of the hexagonal crystal structure. Not only single crystals possess strongly orientation-dependent properties, but textured polycrystalline materials with high volume fractions of α phase can also reveal quite anisotropic fatigue behavior. Since crystallographic textures can be more strongly varied in α+β alloys than in α and β alloys, the influence of texture on the fatigue behavior was primarily investigated on the alloy Ti-6Al-4V [45–50]. Various textures of the α phase are found in equiaxed microstructures [12].

The four basic types of textures are the basal texture (B), transversal texture (T), mixed texture (B/T), and a weak texture (W). These textures are generated by appropriate thermomechanical treatments [12].

Fig. 5.21 a and b show S-N curves for an equiaxed microstructure of the alloy Ti-6Al-4V with different types of sharp textures [12]. A B/T texture loaded parallel to the rolling direction (RD) showed the highest fatigue strength (725 MPa), while the lowest values (580 MPa) were found for a T texture loaded perpendicular to RD in the rolling plane (TD). When these results, which were generated in air (Fig. 5.21 a), are compared to tests performed in vacuum (Fig. 5.21 b), it is obvious that laboratory air has to be considered a corrosive environment for Ti-6Al-4V.
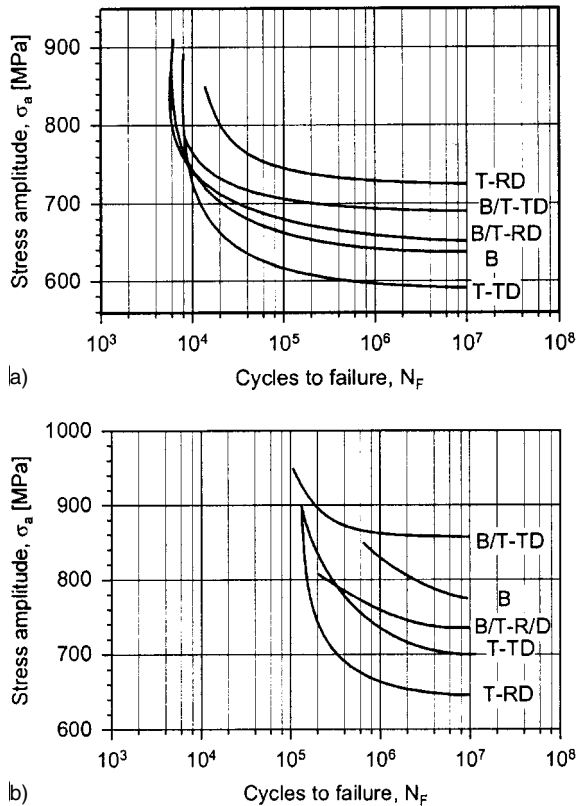
Fig. 5.21 High cycle fatigue behavior (R=−1) of Ti-6Al-4V (equiaxed microstructure). a) Laboratory air; b) vacuum.

Furthermore, the reduced fatigue strength caused by the environment strongly depends on the crystallographic texture and the loading direction [12]. For example, the reduction of fatigue strength is most pronounced for B/T and T textures loaded in directions with a high yield stress, owing to the fact that the stressed axis is perpendicular to basal planes (B/T-TD, T-TD). This behavior can probably be related to stress corrosion cracking of $\alpha+\beta$ titanium alloys, which is pronounced when the tensile axis is perpendicular to basal planes [12]. Compared to equiaxed and lamellar microstructures, the fatigue strength of duplex structures is less strongly influenced by the environment. Obviously, this behavior is due to the absence of α/α phase boundaries, i.e. isolated primary grains [12].

The influence of the degree of texture on fatigue strength of equiaxed microstructures is shown in Fig. 5.22. A reduction of the deformation from 75 to 60% for uniaxial rolling at 800 °C also results in a slight reduction of fatigue strength from 650 to 580 MPa [13].
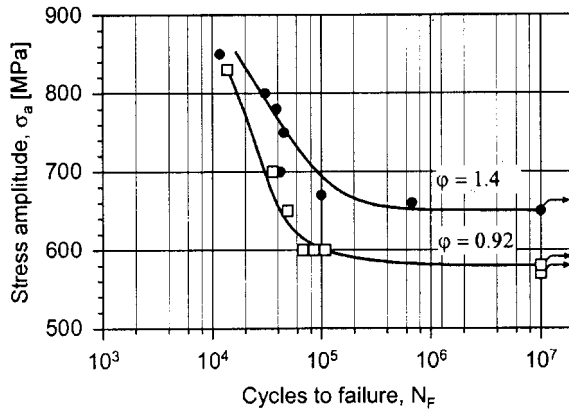
Fig. 5.22 High cycle fatigue behavior (R=−1) of Ti-6Al-4V (equiaxed microstructure).

5.4
Influence of Mean Stress on Fatigue Life

It has been known for quite some time that near-α and α+β alloys react quite sensitively to variations in mean stress during high cycle fatigue testing. This so-called anomalous mean stress effect is shown in the Smith diagram in Fig. 5.23, where the maximum stress for 10^7 cycles is plotted versus mean stress [51, 52].

For the alloy TIMETAL 1100 at low mean tensile stresses, the fatigue behavior at room temperature (Fig. 5.23a) of duplex structures is significantly inferior to lamellar structures [53]. These results confirm earlier work on the alloy Ti-6Al-4V [54]. Although the exact mechanism of the anomalous sensitivity on mean stress is not yet fully understood, the following statements can be made [55, 56]: The anomalous sensitivity on mean stress is controlled by crack initiation and is also present in an inert environment. Usually, β-annealed (lamellar) microstructures do not show this effect. For α+β-annealed microstructures (equiaxed or duplex structures) the degree of the anomalous sensitivity on mean stress depends on the crystallographic texture and on loading direction. Recent results on TIMETAL 1100 [56] point out the anomaly disappears at higher temperatures (Fig. 5.23b).

5.5
Influence of Mechanical Surface Treatments

Mechanical surface treatments such as shot peening, mechanical polishing, or deep rolling can be utilized to improve the fatigue life of titanium alloys [57, 58]. In most cases the following three surface properties are modified:

- surface roughness
- degree of cold work or dislocation density
- residual stresses.
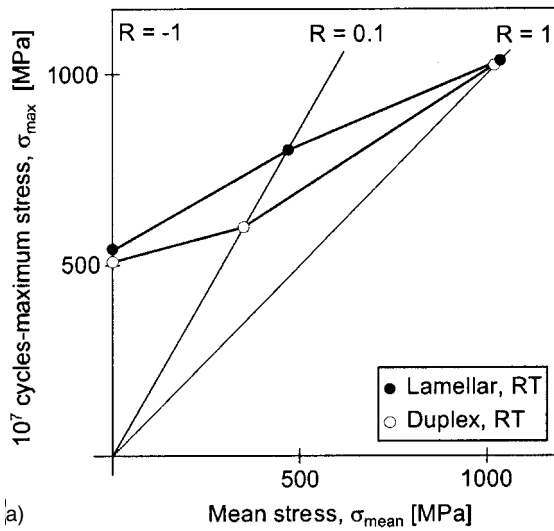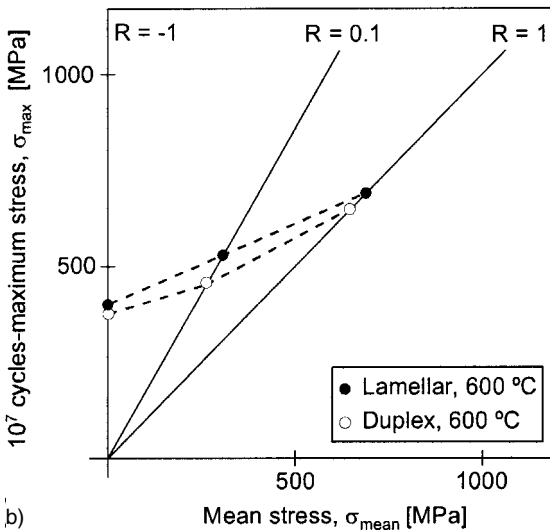
Fig. 5.23 Influence of mean stress on the high cycle fatigue behavior of TIMETAL 1100. a) Room temperature; b) 600 °C.

Since the fatigue life is simply the sum of the numbers of cycles to crack initiation and those of crack propagation, modifying surface properties using these treatments may well have contradictory effects on fatigue life. The surface roughness determines whether fatigue strength is primarily crack initiation (smooth surface) or crack propagation controlled (rough surface) [59]. For smooth surfaces, a hardened surface layer leads to a retardation of crack initiation owing to the increase in strength. For rough surfaces, there may even be no crack initiation

phase at all and the hardened surface layer is a disadvantage for crack propagation owing to the low residual ductility [60]. Compressive residual stresses in the surface layer are very favorable since they strongly retard microcrack propagation if cracks are present (Tab. 5.6) [61, 62].

However, one has to keep in mind that changes induced by mechanical surface treatments are not necessarily stable:

- Thermal or mechanical stress relief can eliminate or reduce residual stresses.
- Recovery and recrystallization can eliminate or reduce the amount of cold work (dislocation density).
- Further mechanical surface treatments, such as polishing, can reduce surface roughness.

Moreover, the favorable residual compressive stresses can also be reduced by fatigue (i.e. by the loads imposed on components in service). However, appropriate surface treatments can be tailored in the design phase according to the intended application of the titanium component.

Fig. 5.24, for example, shows a set of S-N curves for Ti-6Al-4V at ambient (Fig. 5.24a) and elevated temperature (Fig. 5.24b) [59, 60]. The electrolytically polished condition (EP) serves as a reference, since it is free of residual stresses, has a low dislocation density in the near-surface area, and has a very smooth surface. Compared to EP, shot peening (SP) significantly improves fatigue strength at room temperature (Fig. 5.24a). On the other hand, at elevated temperature, SP reduces fatigue strength when compared to the reference condition (Fig. 5.24b). To explain this behavior, the individual contributions of surface properties to fatigue life have to be considered. For example, stress relieving (SR) for one hour at $600\,^{\circ}$C after SP (SP+SR) leads to a decrease in fatigue strength at room temperature compared to SP. It does not, however, change the fatigue strength at $500\,^{\circ}$C. Indeed, SR has no influence at cyclic loading at elevated temperature. If residual compressive stresses were the only operating mechanism, one could argue that SP cannot improve fatigue behavior at elevated temperatures. On the other hand, an extra surface treatment which reduces surface roughness, in the present investigation electrolytic polishing (SP+EP), shows that work-hardening of near-surface layers can be utilized to improve fatigue strength, irrespective of stress relieving (SP+SR +EP). The amount of near-surface cold work (dislocation density) is only slightly changed by SR and therefore improves fatigue strength.

Tab. 5.6 Influence of surface properties on the fatigue behavior.

Surface Property	Crack Initiation	Microcrack Propagation
roughness	accelerated	–
cold work	retarded	accelerated
residual stresses	small influence	retarded
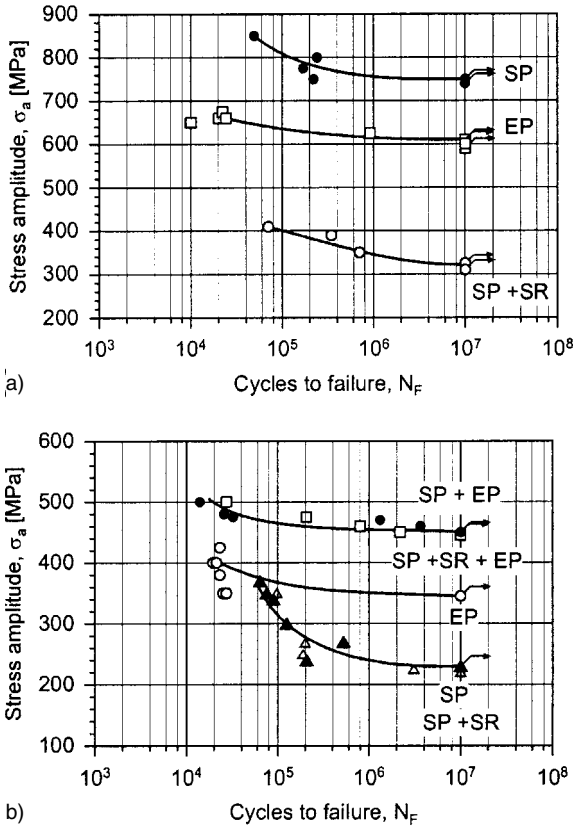
Fig. 5.24 High cycle fatigue behavior (R=−1) of Ti-6Al-4V. a) Room temperature; b) 500 °C.

Fig. 5.25 compares crack propagation rates of microcracks of conditions SP and SP + SR with the reference condition EP. At room temperature (Fig. 5.25 a), crack propagation is drastically retarded for SP, but accelerated by SP + SR when compared to EP. The difference in crack propagation rates between curves SP and SP + SR is caused by residual compressive stresses in SP, whereas the difference between curves SP + SR and EP is due to the high dislocation density in SP + SR. At higher temperature (Fig. 5.25 b), there is no difference in microcrack propagation rates between curves SP and SP + SR, since at these temperatures residual stresses are absent. The inferior behavior of SP and SP + SR compared to reference EP is caused by the negative influence a high dislocation density, and hence low residual ductility, has on crack propagation resistance [61–63].
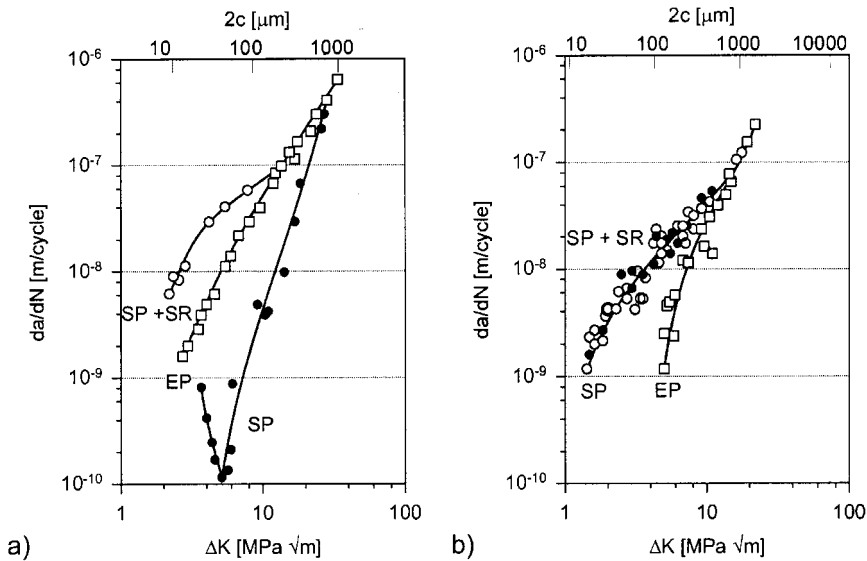
Fig. 5.25 Microcrack propagation in Ti-6Al-4V (R=−1). a) Room temperature (σ_a=775 MPa); b) 500 °C (σ_a=400 MPa).

5.6
Influence of Thermomechanical Surface Treatments

The near-surface microstructure of titanium alloys can be specifically modified to increase the resistance to crack initiation in the surface, leaving the initial microstructure unchanged in order to better fulfil the various requirements the material has to resist (similar to carburizing steel). As will be outlined in the following examples, cold work induced by mechanical surface treatments can be used to generate a near-surface microstructure different to the bulk material [64–66]. This allows the optimum properties of both structures to be combined. This is particularly important in cases where conventional thermomechanical treatments cannot be carried out, as in a thick section of large components. An explicit advantage of the modified near-surface microstructure is that these modifications are more stable than those induced by mechanical surface treatments alone.

5.6.1
α Alloys

A mechanical surface treatment combined with a subsequent recrystallization anneal offers the possibility to combine the high quasi-static strength and fatigue strength properties of fine grained structures with the superior macrocrack fatigue propagation resistance and the excellent fracture toughness of coarse grained structures. To optimize fatigue life in thick section components, fine grains are required
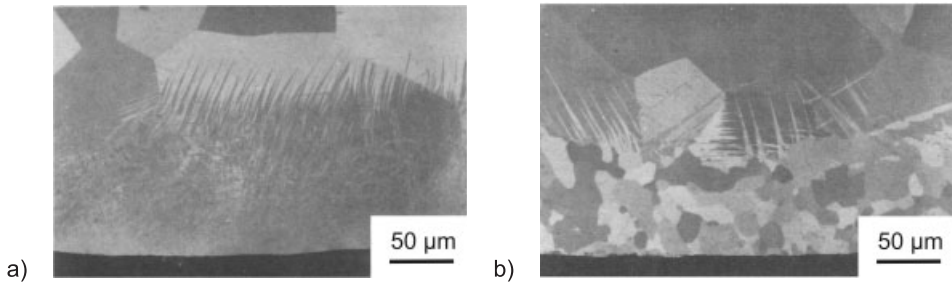
Fig. 5.26 Near-surface microstructure (cross section) of Ti-8.6Al. a) Shot peened; b) shot peened and recrystallized.
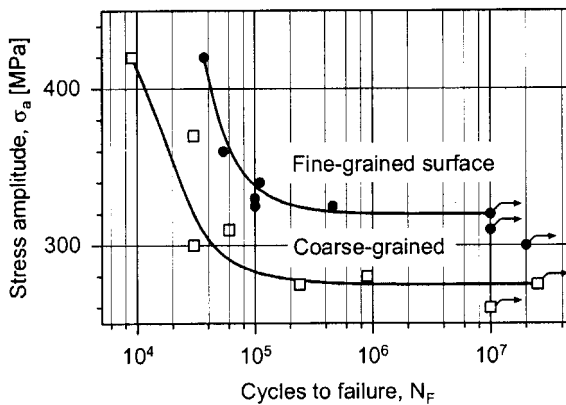
Fig. 5.27 High cycle fatigue behavior (R=−1) of Ti-8.6Al (T=350 °C).

at the surface where high resistance to crack initiation and microcrack propagation are essential. However, for the bulk of the component, coarse grains are required to reduce the driving force for propagation of long cracks. For the coarse-grained Ti-8.6Al model alloy, it was demonstrated that shot peening with subsequent heat treatment for 1 h at 820 °C led to localized cold work and recrystallization in the near-surface area (Fig. 5.26). The improvement of fatigue strength due to the fine-grained (20 μm) surface compared to the coarse-grained (100 μm) structure of the bulk material was significant: about 50 MPa at 350 °C (Fig. 5.27) [60].

5.6.2
Near-α and α+β Alloys

These two alloy classes, particularly near-α alloys, are usually considered for applications at elevated temperatures (e.g. in gas turbines), so that good creep behavior is important. Therefore, lamellar microstructures should be preferred. However,

Fig. 5.28 Near-surface microstructure (cross section) of Ti-6Al-2Sn-4Zr-2Mo, shot peened and recrystallized.
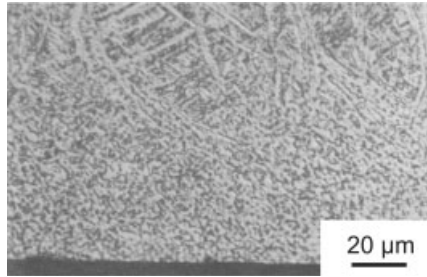
Fig. 5.29 High cycle fatigue behavior (R=−1) of Ti-6Al-2Sn-4Zr-2Mo (T=550°C).
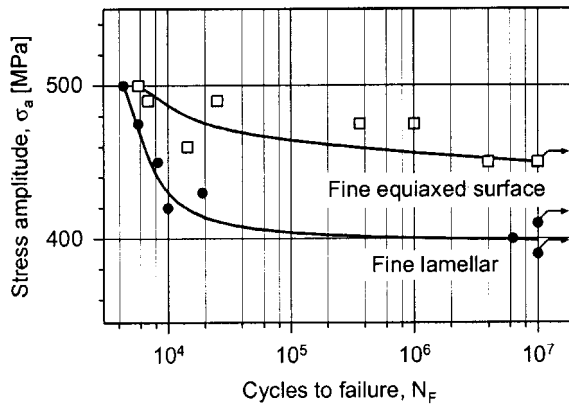
these structures show poor fatigue behavior, particularly under LCF conditions, where microcrack propagation determines lifetime. In these cases a change of phase morphology between the surface and the bulk of a component by means of shot peening and subsequent heat treatment can be advantageous (Fig. 5.28).

The improvement of the high cycle fatigue behavior at elevated temperature after such a thermomechanical treatment is shown in Fig. 5.29 for the alloy Ti-6242. Here the creep resistant lamellar bulk material was combined with a fine equiaxed surface layer to generate superior fatigue behavior [60].

5.6.3
β Alloys

Both shot peening and deep rolling, in combination with specially developed age-hardening treatments, were performed on Ti-3Al-8V-6Cr-4Mo-4Zr [66, 67] to exclusively harden the surface. These new thermomechanical surface treatments demonstrated a high potential for application in a high-strength spring or fastener alloy.

Fig. 5.30 shows the near-surface region of shot peened material after selective surface aging (SSA). The high strength in the surface layer is aimed at increasing the fatigue strength beyond the values of conventional age hardening, while the
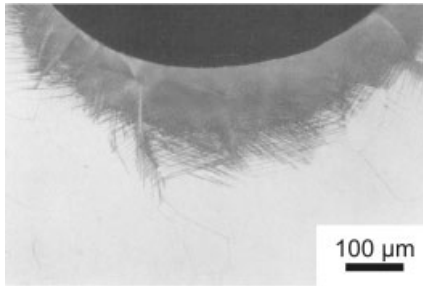
Fig. 5.30 Near-surface microstructure of Ti-3Al-6Cr-4Mo-4Zr, shot peened and aged.
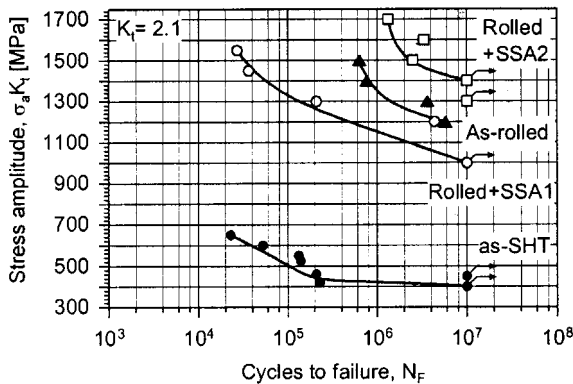
Fig. 5.31 High cycle fatigue behavior (R=–1) notched conditions (k_t=2.1) in Ti-3Al-6Cr-4Mo-4Zr.

high ductility of the solution heat treated condition (SHT) in the bulk of the material results in high notch ductility and fracture toughness [67].

Fig. 5.31 shows the changes to the high cycle fatigue behavior after deep rolling or deep rolling followed by selective surface aging. Deep rolling alone improves notch fatigue strength ($\sigma_a \cdot k_t$) of the SHT structure from the low value of 400 MPa to 1100 MPa. Depending on the subsequent aging treatment, the HCF behavior can slightly deteriorate (SSA 1) or be substantially improved (SSA 2) (Fig. 5.31). These results indicate that residual compressive stresses can be substantially reduced after deep rolling in condition SSA 1, however not for condition SSA 2 [67].

5.7
Titanium Aluminides

For titanium aluminides based on the α_2 phase (Ti$_3$Al), da/dN-ΔK curves of macrocracks show slightly higher threshold values and crack propagation rates than near-α and $\alpha+\beta$ titanium alloys. Fig. 5.32 shows fatigue crack propagation curves for alloys Ti-24Al-11Nb and Super Alpha 2. Both alloys exhibit equiaxed α_2 grains with the β phase at grain boundaries. The α_2 volume fraction is 74% for

Fig. 5.32 Fatigue crack propagation curves for the titanium aluminides Ti-24Al-11Nb and Super Alpha 2 [68] compared with Ti-6Al-4V [69] and CORONA-5.
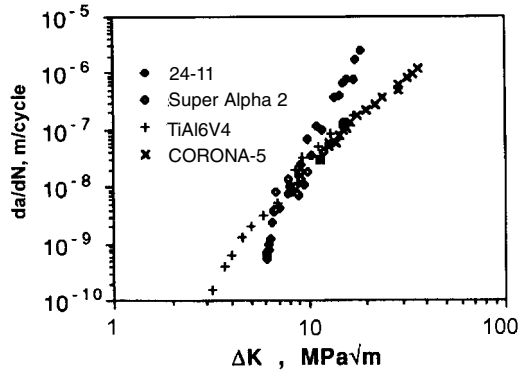
Ti-24Al-11Nb and 50% for Super Alpha 2. However, these differences are not important for fatigue crack propagation.

Detailed investigations of the influence of microstructure on fatigue crack propagation of macrocracks in γ titanium aluminides based on TiAl demonstrate that the behavior is similar to that observed for $\alpha+\beta$ alloys. The da/dN crack growth rates decrease in the order near-gamma (equiaxed), duplex, and lamellar (Fig. 5.33). Similar to $\alpha+\beta$ alloys, chemical composition is of less importance. In Fig. 5.34, three γ TiAl alloys having a lamellar microstructure are compared. The material containing boron additions has a lamellae packet size of 150 μm, the two other alloys have substantially larger lamellae packet sizes (500–1000 μm for Ti-48Al-2Nb-2Cr and 1200–1400 μm for Ti-47Al-2.6Nb-2(Cr+V)). The finer microstructure exhibits slightly higher crack propagation rates than the coarse structure.
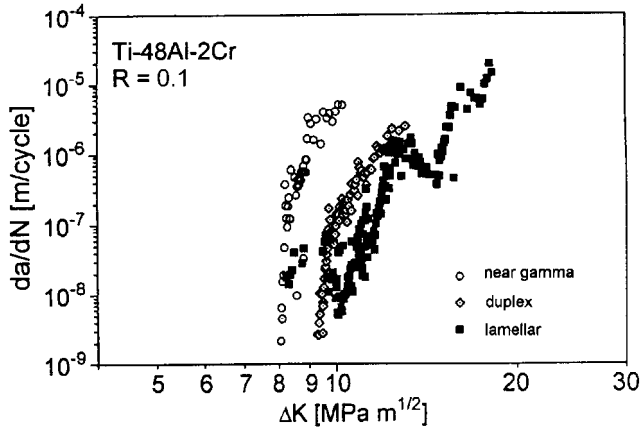
Fig. 5.33 Fatigue crack propagation curves for the γ TiAl alloy Ti-48Al-2Cr [70].
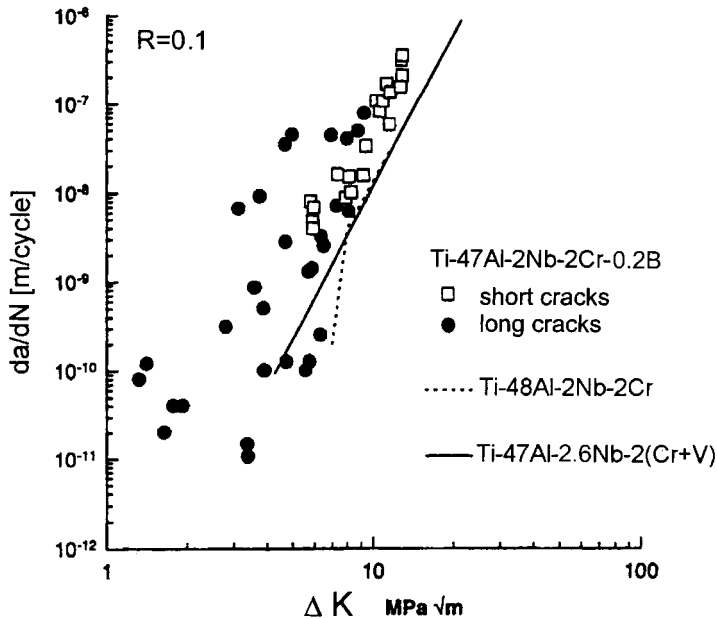
Fig. 5.34 Fatigue crack propagation curves for three different γ TiAl alloys with lamellar microstructure: Ti-47Al-2Nb-2Cr-0.2Nb with fine lamella packet size [71] Ti-48Al-2Nb-2Cr [72] and Ti-47Al-2Nb-2(Cr+V) with coarse lamella packet size [73].

5.8
Composite Materials

Metal-matrix composites based on titanium alloys provide an alternative to fiber-reinforced polymers since they can also be used at elevated temperatures. Generally, the properties of composites are largely controlled by the interface between fiber and matrix. A strong bonding between fiber and matrix is beneficial for the strength perpendicular to the fiber direction. However, for fatigue crack propagation perpendicular to the fibers, weak bonding is preferred since cracks then propagate parallel to the loading direction, dissipating energy in the delamination process at the interfaces. The influence of the interface on crack propagation in a composite material is shown in Fig. 5.35. If no delamination occurs, the crack path is perpendicular to the fiber direction and da/dN-ΔK curve (a) is measured. However, if specimens show pronounced delamination, crack propagation and crack branching occur along fiber/matrix interfaces (curve (b)).

Since titanium-based metal matrix composites are considered for high temperature use, the stability of the adhesion between fiber and matrix at high temperatures plays a dominant role for long-term applications. For this reason, the influence of annealing on fatigue crack propagation was investigated for various types of fibers [74–76]. In most cases, annealing led to a reduction of da/dN [75, 76]. An example
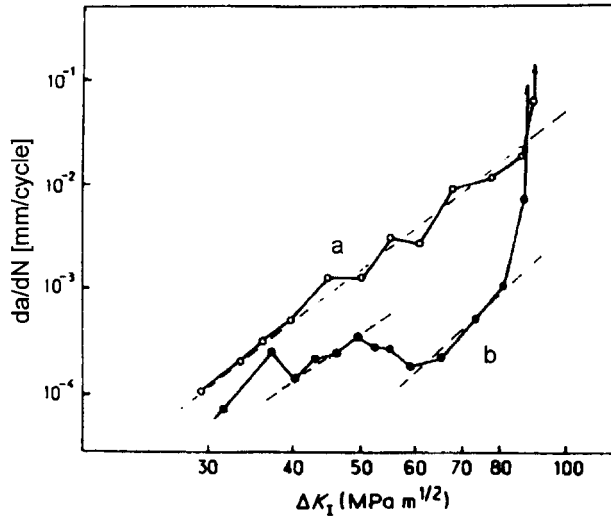
Fig. 5.35 Influence of bonding between fiber and matrix on da/dN-ΔK: curve (a): strong bonding, crack propagation perpendicular to fibers; curve (b): weak bonding, crack propagation and crack deflection parallel to fibers [74].

is shown in Fig. 5.36 for the alloy Ti-6Al-4V reinforced with B fibers, which had been coated with boron carbide. Annealing for 4.5 h at 900 °C and for 7 days at 500 °C shifts the da/dN-ΔK curves to lower crack propagation rates. It was also reported that annealing for 9 h at 850 °C could lead to higher da/dN rates in Ti-6Al-4V reinforced with uncoated boron fibers [75]. Only longer annealing times cause a reduction of the crack propagation rate due to delamination mechanisms. If the boron fibers are coated with B_4C, this effect occurs after 30 hours; for Ti-6Al-4V reinforced with SiC fibers delamination is observed only after 60 hours [74].

5.9
Summary

The most important microstructural parameters controlling fatigue crack initiation and propagation behavior of conventional titanium alloys were presented using typical examples for the respective α, α+β, and β alloy classes. In addition, crack propagation results on titanium aluminides and titanium matrix composite materials were highlighted.

Mechanical surface treatments such as shot peening and/or deep rolling, either alone or in combination with thermal treatments, can guarantee optimum fatigue properties in mechanically stressed components. The specific treatments should be tailored to the needs of the various alloy types (α, α+β, or β), to provide optimum properties through heat treatment and/or thermomechanical treatment.
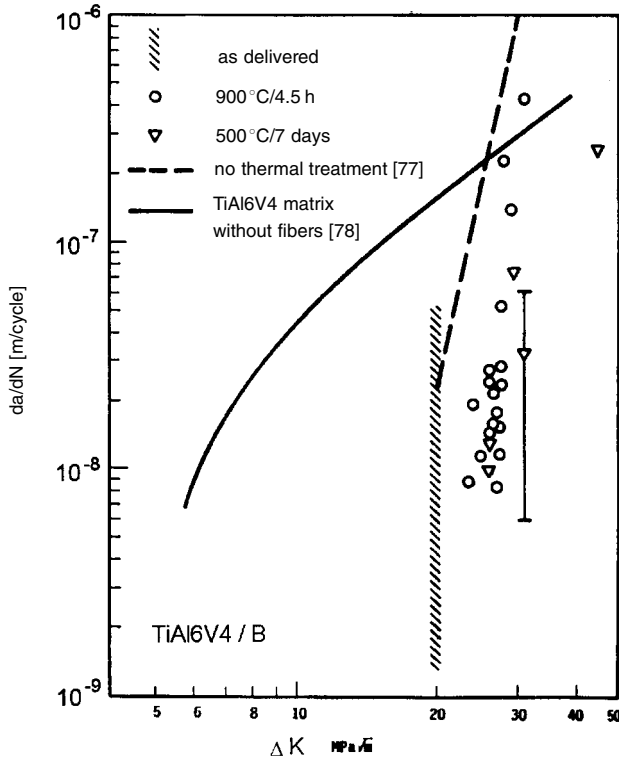
Fig. 5.36 Influence of annealing on fatigue crack propagation (macrocracks) in Ti-6Al-4V with B$_4$C coated B-fibers. Monolithic Ti-6Al-4V data is plotted as reference [78, 79].

5.10
Referenced Literature and Further Reading

1 C. H. WELLS and C. P. SULLIVAN: Trans. ASM, Vol. 62 (1969) 263

2 D. K. BENSON, J. C. GROSSKREUTZ and G. G. SHAW: Met. Trans., Vol. 3A (1972) 1239

3 L. WAGNER, J. K. GREGORY, A. GYSLER and G. LÜTJERING: in Small Fatigue Cracks, R. O. RITCHIE and J. LANKFORD (eds.), TMS (1986) 117

4 J. K. GREGORY: in Handbook of Fatigue Crack Propagation in Metallic Structures, A. CARPINTERI (ed.), Elsevier Science B. V. (1994) 281

5 N. G. TURNER and W. T. ROBERTS: Trans. TMS-AIME, Vol. 242 (1968) 1223

6 J. L. ROBINSON and C. J. BEEVERS: The Effects of Load Ratio, Interstitial Content and Grain Size on Low-Stress Fatigue Crack Propagation in α-Titanium, Met. Sci. J., 7 (1973) 153–159

7 H. CONRAD et al.: Critical Review: Deformation and Fracture, Titanium Science and Technology, Plenum Press (1973) 996

8 A. GYSLER, J. LINDIGKEIT and G. LÜTJERING: in Strength of Metals and Alloys, P. HAASEN, V. GEROLD and G. KOSTORZ (eds.), Pergamon Press (1979) 1113

9 G. T. GRAY and G. LÜTJERING: in Fatigue '84, C. J. BEEVERS (ed.), EMAS (1984) 707

10 L. WAGNER and G. LÜTJERING, in Titanium '88: Science and Technology, Les Editions de Physique (1988) 345

11 J.M. LARSEN, T. NICHOLAS, A.W. THOMPSON and J.C. WILLIAMS: in Small Fatigue Cracks, R.O. RITCHIE and J. LANKFORD (eds.), TMS (1986) 499

12 M. PETERS and G. LÜTJERING: Report CS-2933, Electric Power Research Institute (1983)

13 W. TROJAHN: diploma thesis, Ruhr University Bochum (1980)

14 L. WAGNER, G. LÜTJERING and R.I. JAFFEE: in Microstructure/Property Relationships in Titanium Aluminides and Alloys, TMS-AIME (1991) 521

15 L. WAGNER and G. LÜTJERING: Z. Metallkde, Vol. 87 (1987) 369

16 G.W. KUHLMAN: in Microstructure/Property Relationships in Titanium Aluminides and Alloys, TMS-AIME (1991) 465

17 R.R. BOYER and J.A. HALL: in Titanium '92: Science and Technology, F.H. FROES and I. CAPLAN (eds.), TMS (1993) 77

18 H. PUSCHNIK, J. FLADISCHER, G. LÜTJERING and R.I. JAFFEE: in Titanium '92: Science and Technology, F.H. FROES and I. CAPLAN (eds.), TMS (1993) 131

19 J.K. GREGORY and L. WAGNER: in Fatigue '90, H. KITAGAWA and T. TANAKA (eds.), MCEP (1990) 191

20 G.R. YODER, L.A. COOLEY, T.W. CROOKER: Observations on Microstructurally Sensitive Fatigue Crack Growth in a Widmanstätten Ti-6Al-4V Alloy, Metall. Trans., 8A (1977) 1737–1743

21 T.W. DUERIG, J.E. ALLISON and J.C. WILLIAMS: Microstructural Influences on Fatigue Crack Propagation in Ti-10V-2Fe-3Al, Metall. Trans. A, 16A (1985) 739–751

22 C.G. RHODES and N.E. PATON: The Influence of Microstructure on Mechanical Properties in Ti-3Al-6Cr-4Mo-4Zr (Beta-C), Metall. Trans. A, 8A (1977) 1749–1761

23 L. WAGNER, G. LÜTJERING, Propagation of Small Fatigue Cracks in Ti Alloys: in Titanium '88 Science and Technology, Vol. I, P. LACOMBE, R. TRICOT, G. BÉRANGER, (eds.), les éditions de physique, Les Ulis Cedex (1988) 345–350

24 G.R. YODER, L.A. COOLEY T.W. CROOKER: Fatigue Crack Propagation Resistance of Beta-Annealed Ti-6Al-4V Alloys of Differing Interstitial Contents, Metall. Trans. A, 9A (1978) 1413–1420

25 G.R. YODER, F.H. FROES, D. EYLON: Effect of Microstructure, Strength, and Oxygen Content on Fatigue Crack Growth Rate of Ti-4.5Al-5.0Mo-1.5Cr (CORONA 5), Metall. Trans. A, 15A (1984) 183–197

26 M. PETERS, A. GYSLER and G. LÜTJERING: Influence of Microstructure on the Fatigue Behavior of Ti-6Al-4V, in Titanium '80 Science and Technology, H. KIMURA, O. IZUMI, (eds.), TMS-AIME, (1980) 1777–1786

27 P. BANIA and D. EYLON: Fatigue Crack Propagation of Titanium Alloys under Dwell-Time Conditions, Metall. Trans. A, 9A (1978) 847–855

28 M. PETERS, Y.T. LEE, K.J. GRUNDHOFF, H. SCHURMANN and G. WELSCH: in Microstructure/Property Relationships in Titanium Aluminides and Alloys, TMS-AIME (1991) 533

29 M. PETERS, V. BACHMANN, K.H. TRAUTMANN, H. SCHURMANN, Y.T. LEE and C.H. WARD: in Titanium '92: Science and Technology, F.H. FROES and I. CAPLAN (eds.), TMS (1993) 303

30 A. STYCZYNSKI, L. WAGNER, C. MÜLLER and H.E. EXNER: in Microstructure/Property Relationships of Titanium Alloys, p. 83 ANKEM and J.A. HALL (eds.), TMS-AIME (1994)

31 A. BERG, J. KIESE and L. WAGNER: in Light-Weight Alloys for Aerospace Applications III, E.W. LEE, K.V. JATA, N.J. KIM and W.E. FRAZIER (eds.), TMS (1995) 407

32 J. LINDEMANN, A. STYCZYNSKI and L. WAGNER: in Light-Weight Alloys for Aerospace Applications III, E.W. LEE, K.V. JATA, N.J. KIM and W.E. FRAZIER (eds.), TMS (1995) 391

33 G. TERLINDE and G. FISCHER: in Titanium '95, Science and Technology, P.A. BLENKINSOP, W.J. EVANS and H.M. FLOWER (eds.) (1995) 2177

34 J.K. GREGORY and L. WAGNER: GKSS-Report 92/E/7 (1992)

35 J.K. GREGORY, L. WAGNER and C. MÜLLER: in Beta Titanium Alloys, A. VASSEL,

D. Eylon and Y. Combres (eds.), Editions de la Revue de Métallurgie (1994) 229

36 A. Styczynski, J. Kiese and L. Wagner: in Fatigue '96, G. Lütjering and H. Nowack (eds.), Pergamon Press (1996) 911

37 H.-E. Krugmann and J. K. Gregory: in Microstructure/Property Relationships in Titanium Aluminides and Alloys, TMS-AIME (1991) 549

38 T. W. Duerig, G. Terlinde and J. C. Williams: Met. Trans., Vol. 11A (1980) 1987

39 T. W. Duerig, J. E. Allison and J. C. Williams: Met. Trans., Vol. 16A (1985) 739

40 R. R. Boyer: J. Metals (1980) 61

41 C. C. Chen, J. A. Hall and R. R. Boyer: in Titanium '80: Science and Technology, H. Kimura and O. Izumi (eds.) (1980) 457

42 J. Kiese and L. Wagner: in Fatigue '96, G. Lütjering and H. Nowack (eds.), Pergamon Press (1996) 959

43 A. Drechsler, T. Dörr, J. Kiese and L. Wagner: Light-Weight Alloys for Aerospace Applications IV, E. W. Lee, W. E. Frazier, K. Jata and N. J. Kim (eds.), TMS (1997) 151

44 A. Drechsler: Ph.-D. thesis, BTU Cottbus (2001)

45 F. Larson and A. Zarkades: MCIC Report 74-20, Battelle Columbus Labs (1974)

46 F. Larson, A. Zarkades and D. H. Avery: Titanium Sci. Technol., Vol. 2 (1973) 1169

47 A. W. Sommer and M. Creager: Report TR-76-222, AFML (1977)

48 M. J. Blackburn, J. A. Feeney and T. R. Beck: Adv. Corros. Sci. Technol., Vol. 3, 1973, p. 67

49 D. A. Meyer and G. Sandoz: Trans. AIME, Vol. 245 (1969) 1253

50 G. Lütjering and L. Wagner: in Directional Properties of Materials, H. J. Bunge (eds.), DGM (1988) 177

51 R. K. Steele and A. J. McEvily: Eng. Fract. Mech., Vol. 8 (1976) 31

52 R. K. Steele and A. J. McEvily: in Fracture Mechanics and Technology, G. C. Sih and C. L. Chow (eds.), Sijthoff and Nordhoff, The Netherlands (1977) 33

53 J. Lindemann and L. Wagner: Mat. Sci. Eng. A (1997) 1118

54 S. Adachi, L. Wagner and G. Lütjering: in Fatigue Eng. Mat. Struct., ImechE, (1986) 67

55 J. Lindemann and L. Wagner: Mat. Sci. Eng. A (1997) 1118

56 J. Lindemann: Ph.-D. thesis, BTU Cottbus (1999)

57 M. Bauccio: Technical Note 9: Descaling and Special Surface Treatments, Materials Properties Handbook: Titanium Alloys, ASM International (1994) 1145

58 L. Wagner and G. Lütjering: in Shot Peening, Niku Lari (ed.), Pergamon Press, (1982) 453

59 L. Wagner and G. Lütjering: in Fatigue '90, H. Kitagawa and T. Tanaka (eds.), MCEP (1990) 323

60 H. Gray, L. Wagner and G. Lütjering: in Shot Peening, H. Wohlfahrt, R. Kopp and O. Vöhringer (eds.), DGM (1987) 467

61 T. Dörr and L. Wagner: Surface Performance of Titanium Alloys, J. K. Gregory, H. J. Rack and D. Eylon (eds.), TMS-AIME (1996) 231

62 T. Dörr and L. Wagner: Surface Treatment IV, C. A. Brebbia and J. M. Kenny (Eds.), WIT-Press (1999) 281

63 T. Dörr: Ph.-D. thesis, BTU Cottbus (2000)

64 J. K. Gregory, L. Wagner and C. Müller: in Surface Engineering, P. Mayr (eds.), DGM (1993) 435

65 J. K. Gregory and L. Wagner: in Fatigue '93, J.-P. Bailon and J. I. Dickson (eds.), EMAS (1993) 177

66 A. Berg, J. Kiese and L. Wagner: Mat. Sci. Eng. A (1998) 146

67 A. Berg: Ph.-D. thesis, BTU Cottbus (2000)

68 D. L. Davidson: Titanium Alloys: Fatigue Crack Growth Mechanisms and Crack Tip Micromechanics, Microstructure/Property Relationships in Titanium Alloys and Aluminides, Y.-W. Kim and R. R. Boyer (eds.), TMS-AIME (1991) 447–461

69 P. E. Irving, C. J. Beevers: The Effect of Air and Vacuum Environments on Fatigue Crack Growth Rates in Ti-6Al-4V, Metall. Trans. A, 5A (1974) 391–398.

70 H. Clemens, W. Glatz, P. Schretter, C. Koeppe, A. Bartels, R. Behr, A. Wanner: Processing and mechanical properties of gamma-TiAl based alloy sheet material, in Gamma Titanium Aluminides, Y.-W. Kim, R. Wagner, M. Yamaguchi, (Eds.), The Minerals, Metals and Materials Society, Warrendale, PA, (1995) 717–726

71 K. S. Chan, D. S. Shih: Fatigue and Fracture Behavior of a Fine-Grained Lamellar TiAl Alloy, Metall. Trans. A, 28A (1997) 79–90

72 J. M. Larsen, B. D. Worth, S. J. Balsone, J. W. Jones: An Overview of the Structural Capability of Available Gamma Titanium Aluminide Alloys, in Gamma Titanium Aluminides, Y.-W. Kim, R. Wagner, M. Yamaguchi (eds.), The Minerals, Metals and Materials Society, Warrendale, PA, (1995) 821–834

73 D. L. Davidson, J. B. Campbell: Fatigue Crack Growth Through the Lamellar Microstructure of an Alloy Based on TiAl at 25 and 800 °C, Metall. Trans. A, 24A (1993) 1555–1574

74 P. Soumelidis, J. M. Quenisset, R. Nalsain, N. S. Stoloff: Effect of the Filament Nature on Fatigue Crack Growth in Titanium Based Composites Reinforced by Boron, B(B$_4$C) and SiC Filaments. J. Mater. Sci. 21 (1986) 895–903

75 J. M. Quenisset, P. Soumelidis, R. Pailler, R. Nalsain, N. S. Stoloff: Effect of Isothermal Exposure on Fatigue Crack Growth in Boron-Titanium Composites. J. Mater. Sci. 20 (1985) 4532–4552

76 K. S. Chan, D. L. Davidson: Effects of Interfacial Strength on Fatigue Crack Growth in a Fiber-Reinforced Ti-Alloy Composite, Metall. Trans. A, 21A (1990) 1603–1612

77 D. S. Mahulikar, Y. H. Park, H. L. Marcus: ASTM STP 791, ASTM, Philadelphia, PA (1981) 101–113

78 D. L. Davidson, J. Lankford: Metall. Trans. A, 15A (1984) 1931–40

6

Oxidation and Protection of Titanium Alloys and Titanium Aluminides

C. Leyens, *DLR – German Aerospace Center, Cologne, Germany*

6.1
Introduction

Excellent mechanical properties combined with a low density make titanium alloys and titanium aluminides attractive structural materials for aerospace applications with maximum service temperatures in the range of to 540 and 800 °C, respectively. The use of these materials, e.g. in the compressor section of a gas turbine engine, is mainly determined by their mechanical properties. However, the high temperature capability of these alloys is often limited by relatively poor resistance against hot gas.

The formation of corrosion reaction products (mainly oxides) results in a loss of the load-bearing cross section and may eventually limit the time at temperature to maintain integrity of the component. Further, oxygen and nitrogen ingress into the subsurface zone of a component directly affect mechanical properties by embrittlement. Both modes of degradation, reaction product formation and embrittlement, require specific attention for component design and usage. Hot corrosion attack during high temperature exposure can limit the lifetime of a component and, like mechanical properties, must be considered carefully.

In the following the oxidation behavior of titanium alloys and titanium aluminides will be described in a general way. For in-depth information the reader is referred to the literature where appropriate. The phenomena described in this chapter apply to both monolithic and long-fiber reinforced titanium-based materials (see Chapter 12); however, only monolithic materials will be considered to simplify the discussion.

Despite the fact that titanium alloys used in industrial environments may be exposed to molten salt deposits, and titanium aluminides may be in contact with hot combustion gases, the majority of work has so far been focussed on the effect of oxygen and nitrogen on the environmental resistance of these materials. As a major constituent of the surrounding air, nitrogen has drawn much attention with regard to its effect on oxidation of γ TiAl-based alloys.

Following a general overview of the basics of high temperature oxidation of metallic materials, the oxidation behavior of titanium alloys and titanium aluminides will be addressed, including the effect of oxidation phenomena on mechanical

properties. Furthermore, measures to improve environmental resistance through alloying, pre-oxidation, and coatings will be described. By far not complete, this chapter aims at making the reader acquainted to the wide field of high temperature corrosion of titanium-based alloys.

6.2
Fundamentals of Oxidation of Metals

The following description of the fundamentals of oxidation of metals aims at providing general information to the reader and tries to give an overview of the major aspects of materials behavior at moderately elevated or high temperatures. The general topic is addressed in much more detail in monographs and publications by O. Kubaschewski and B. E. Hopkins [1], P. Kofstad [2–5] as well as A. Rahmel [6]. The first part of this chapter is mainly based on these references. In this context, the outstanding work of Carl Wagner must be highlighted, who paved the way to modern oxidation and hot corrosion science in the 1950s [7, 8].

In a simple chemical reaction, oxidation of a metal M in pure oxygen O_2 forming an oxide M_xO_y as a reaction product can be described by the following equation:

$$x \cdot M + \frac{y}{2} O_2 \Leftrightarrow M_xO_y \tag{eqn. 6.1}$$

In the real world, the oxidation behavior of materials can usually not be described by this simple equation. A number of parameters and, depending on the materials and the environment, their sometimes completely different effect on materials behavior, make oxidation and hot corrosion highly complex processes — particularly for industrially relevant material systems in service environments. Due to metal consumption during oxide scale formation an oxidation reaction is usually not desired. However, knowledge of the relevant degradation mechanisms and adequate measures of protection enables the use of these materials under harsh industrial conditions.

Notably, use of metallic materials at high temperatures for long service times (e.g. 1000 °C for >20 000 hours in stationary gas turbines for power generation) would be impossible without the oxidation reaction mechanism described in eqn. 6.1. The formation of an oxide scale separates the metal surface from the environment, thus providing a barrier layer that slows down further oxidation reaction and reduces metal consumption. Therefore, the key issue for all metallic high temperature materials in terms of their resistance to hot gas is the ability to form protective oxides scales that provide long-term protection under the particular service conditions a component is expected to operate.

Since oxidation and hot corrosion reactions predominantly occur at the material's surface, studies can be limited to areas close to the component surface; the interface between the metal and the oxide as well as between the oxide scales them-

selves, the latter of which are usually of major interest. Depending on the operating conditions, the oxide scales must fulfill some or all of the following requirements:

- high thermodynamic stability in the respective operating environment
- low interdiffusion of the oxide scale-forming elements (low oxide scale growth rate)
- low vapor pressure of the oxide
- crack healing ability
- good adhesion with the metal
- thermomechanical compatibility with the metal.

Technically, Cr_2O_3, SiO_2 and Al_2O_3 are the oxides that meet the requirements best. However, Cr_2O_3-forming materials are limited to service temperatures below 1000 °C due to the formation of volatile CrO_3; and at low O_2 partial pressures, SiO_2 dissociates to volatile SiO.

Since Cr-containing steels are widely used in industrial applications, Cr_2O_3-formers cover a large portion of metals used at high temperatures. For the highest temperature applications only nickel- or cobalt-based superalloys can be used. These are usually Al_2O_3-formers similar to metallic coatings of MCrAlY type (M = Ni, Co, Ni+Co), which are widely used to further improve hot corrosion and oxidation resistance of superalloys.

As common for all chemical reactions, oxidation reactions depend on thermodynamic and kinetic aspects. While the equilibrium of a reaction and the stability of the reaction products can be described by thermodynamics, the time dependence of the reaction is a matter of kinetics.

6.2.1
Thermodynamics of Oxidation

Thermodynamically, the oxidation reaction in eqn. 6.1 can be described by the change of the free enthalpy ΔG, e.g. by the difference between the free enthalpy of the reaction product M_xO_y and the reactants M und O_2. For $\Delta G < 0$ the reaction proceeds in the direction considered (from metal to oxide), while for $\Delta G > 0$ there is the tendency for reaction in the opposite direction (reduction from oxide to metal in this case). For $\Delta G = 0$ equilibrium conditions have been established, so both reaction products and reactants are present. Since G depends on the concentration of the reactants and the products, it is usually replaced by the standard enthalpy of formation, $\Delta G°$, where the normal state of the reaction is defined when the activities of the reacting metal M and the metal oxide M_xO_y are set to one. For almost all metals relevant to industrial applications, the standard enthalpy of formation is negative, so the oxides are usually stable in oxygen-containing environments while the respective metals are unstable. The enthalpy of formation is correlated to the standard enthalpy of reaction, $\Delta H°$, the entropy of formation, $\Delta S°$, and the reaction temperature, T:

$$\Delta G^\circ = \Delta H^\circ - T \cdot \Delta S^\circ \qquad \text{(eqn. 6.2)}$$

Since formation of an oxide reduces the entropy of the system, ΔG° increases at the same time, resulting in a decrease in oxide stability with increasing temperatures. The standard enthalpy of formation is temperature dependent and correlated to the oxygen partial pressure, p_{O_2}, of the oxide according to

$$\Delta G^\circ = RT \ln p_{O_2} \qquad \text{(eqn. 6.3)}$$

where R describes the general gas constant and T the absolute temperature.

The dissociation pressure describes the O_2 partial pressure at which, for a given temperature, the oxide is still stable. Below this pressure, the oxide decomposes into metal and oxygen. Fig. 6.1 shows the dissociation pressures as a function of temperature for several oxides, according to eqn. 6.3. With the exception of some noble metals, the oxygen partial pressures necessary for dissociation are very low or the temperatures where dissociation occurs are above the boiling temperatures of the metals or alloys, so that for major industrial applications at high temperatures oxidation occurs. In addition to the stability of the oxide of a particular metal, Fig. 6.1 allows comparison of relative stabilities for different oxides. For alloys, the oxide with the lowest dissociation pressure at a given temperature is thermodynamically the most stable one. For example, for Fe-Cr alloys Cr_2O_3 is more stable than FeO.

Thermodynamic data such as standard enthalpy of formation and dissociation pressure allow predictions to be made about the oxidation products formed; they
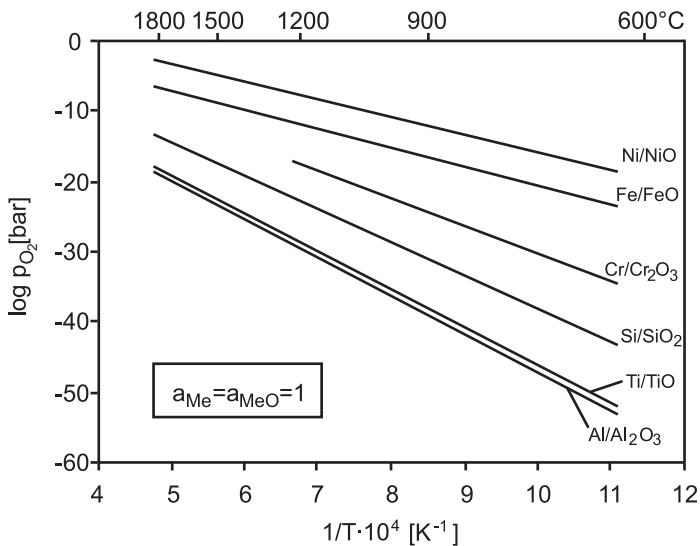
Fig. 6.1 Dissociation pressures of selected oxides vs. temperature. Curves for TiO and Al_2O_3 are close together.

do not, however, provide any information about the reaction rates. In industrially relevant systems, the formation of thermodynamically favorable oxide phases can be sufficiently slow such that less stable oxides form first. Furthermore, it should be mentioned that the activity of a single element in an alloy is lower than unity, compounds could be formed or there might be complete or limited miscibility in the solid state. Hence, in many cases the findings for binary alloys cannot be translated to more complex alloy chemistries. In this context ternary or multi-component phase diagrams are needed, in particular for different gas mixtures; however, their availability is so far very limited.

6.2.2
Oxidation Kinetics

Considering a pure metal surface, formation of an oxide scale can be divided into four steps (Fig. 6.2):

a)   oxygen adsorption at the surface
b)   oxide nucleation
c)   lateral growth of the nuclei
d)   formation of a compact oxide scale.

When lateral growth of the nuclei is concluded, the metal surface is completely covered with a thin oxide film and thus separated from the gaseous environment. At elevated temperatures and sufficiently high oxygen partial pressures, steps (a–c) occur very rapidly, hence having only a minor effect on the oxidation kinetics. However, the initial phase of oxidation can substantially influence the formation of the oxide scale, as will be shown later.

Once a thin, compact film has been formed on the metal surface, further growth of the oxide scale is controlled by mass transport through the oxide scale.
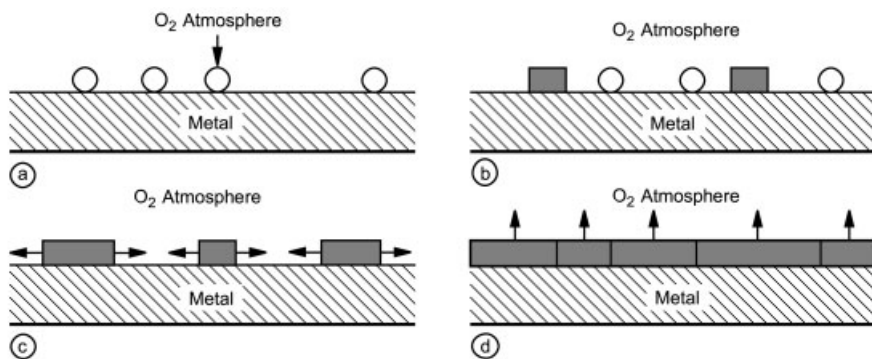
Fig. 6.2   Model of oxide scale formation on a metallic surface. (a) Oxygen adsorption at the surface, (b) formation of nuclei, (c) lateral growth of nuclei, and (d) growth of the compact oxide scale.

Depending on the type and morphology of the oxide scale, the following mechanisms can contribute to mass transport to varying extents:

- gas transport through micro/macro cracks and voids
- grain boundary diffusion
- volume diffusion.

The single transport mechanisms can effect the growth rate of the oxide scale. At low temperatures, mass transport is predominantly influenced by grain boundary diffusion due to its lower activation energy, and by cracks and voids that may provide direct access of oxygen to the metal surface. At elevated temperatures, mass transport can be dominated by volume diffusion. Along with temperature, the oxygen partial pressure, oxidation time, surface condition, and pretreatment of the metal may substantially affect oxidation kinetics.

6.2.2.1 Disorder Features in Oxides

Oxides are compounds characterized by a high portion of ionic bonding. Metal ions and oxygen ions form cation and anion partial lattices, which, as a whole, form an electrically neutral lattice. Continuing oxide scale growth is only possible if diffusion processes through the oxide scale provide mass transport (Fig. 6.3).

Determination of the oxide scale growth, the diffusion rate of the reactants, and the migration mechanisms is closely linked to the disorder of the reaction product. Particularly at elevated temperatures, any solid matter deviates from the ideal crystallographic lattice configuration. Point defects such as vacant lattice sites (vacancies), or interstitial lattice sites are important for mass transport. During oxidation the following reaction products can be formed:

- compounds with stoichiometric composition
- compounds with non-stoichiometric composition.

For stoichiometric compounds, four borderline cases can be distinguished that each describes anion or cation mobility or diffusion of both species (Frenkel and Schottky disorder). For oxides that deviate from stoichiometric composition, maintaining electroneutrality dictates electron disorder in addition to ion disorder. Since electron mobility is several orders of magnitude higher than ion mobility,
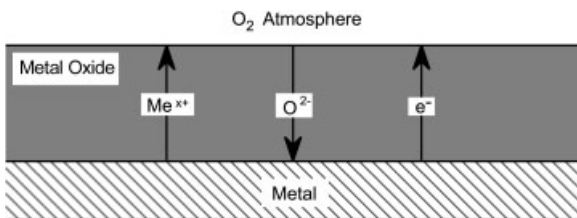
Fig. 6.3 Schematic representation of mass transport (anions, cations and electrons) through oxide scales.

these compounds are practically pure electron conductors (semiconductors). Semiconductors are divided into the following groups relevant to describe oxidation processes:

- electron excess conductors (n-conductors) with
  – metal excess (metal ions located at interstitials)
  – non-metal deficit (non-metal ion vacancies)
- electron defect conductors (p-conductors) with
  – metal deficit (metal ion vacancies)
  – non-metal excess (non-metal ions located at interstitials).

NiO is an example of an electron defect conductor with metal deficit; the oxide has a NaCl structure (Fig. 6.4). Due to the electroneutrality condition, the nickel vacancies must be compensated by a corresponding number of positive charges. In a simplistic description this can be achieved by Ni^{3+} ions that are incorporated into the Ni^{2+} lattice resulting in electroneutrality of the complete crystal.

For both electron excess and electron defect conductors, the dependency of the vacancy concentration on the oxygen partial pressure can be calculated by:

$$\text{n-conductor: } [\text{vacancies}] \approx p_{O_2}^{\frac{-1}{v}} \qquad \text{(eqn. 6.4)}$$

$$\text{p-conductor: } [\text{vacancies}] \approx p_{O_2}^{\frac{1}{v}} . \qquad \text{(eqn. 6.5)}$$

The value of v depends on the composition of the oxide formed and is typically between 2 and 8. Therefore, the disorder of the oxide determines which species are mobile in the course of oxidation. The driving force for diffusion is the concentration gradient of the vacancies in the oxide such that, e.g. in NiO, nickel
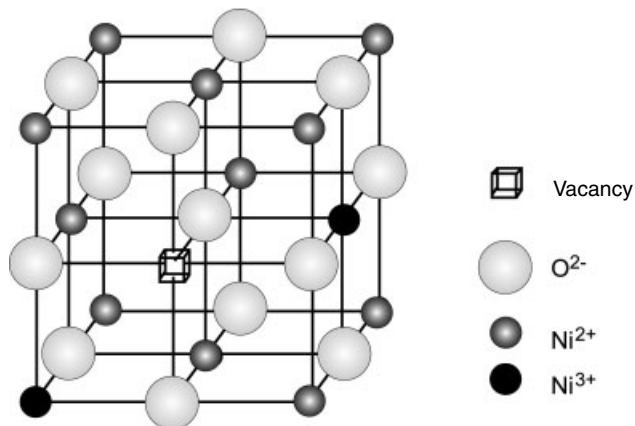
Fig. 6.4 Model of disorder in NiO. Since NiO is an electron defect conductor, diffusion is via nickel ion vacancies. For electroneutrality bivalent nickel ions are replaced by trivalent nickel ions.
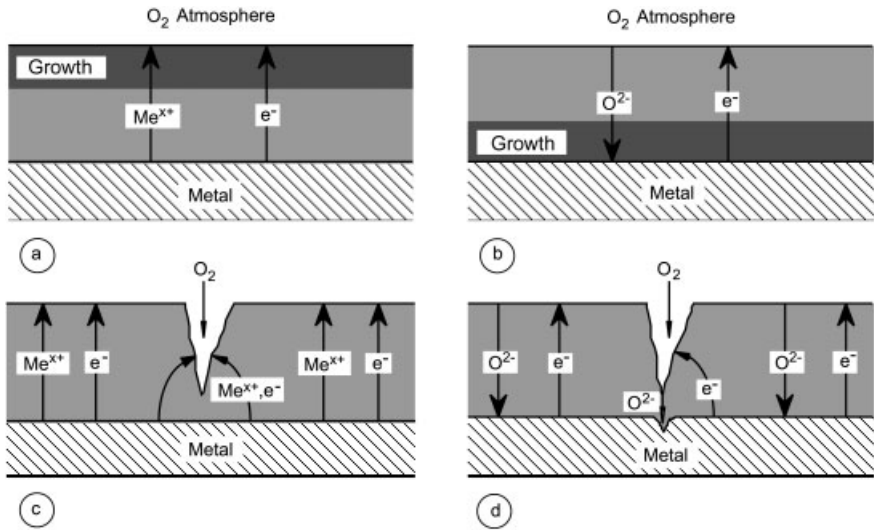
Fig. 6.5 Transport mechanisms through oxide scales without (a, b) and with (c, d) crack formation. Oxide scales with cation conductivity grow at the metal-oxide interface and can heal cracks by oxide formation (a and c).

ions diffuse outward since, according to eqn. 6.5, the nickel vacancy concentration is highest at the oxide/oxygen interface.

Therefore, disorder in oxides does not only determine the location for scale growth, but also influences the crack healing capability of the oxide scale, i.e. the ability of the oxide scale to close cracks by oxide re-growth during high temperature exposure (Fig. 6.5).

Oxide layers with predominantly cation conductivity grow at the oxide-gas interface (Fig. 6.5 a), while predominantly anion conductivity leads to scale growth at the metal-oxide interface (Fig. 6.5 b). Obviously only oxide scales with cation conductivity can close cracks (Fig. 6.5 c). Crack formation in oxide scales with anion conductivity results in enhanced local attack of the base material (Fig. 6.5 d) since these cracks can not heal and oxygen is continuously supplied to the crack tip.

6.2.2.2 Kinetics

Growth of the oxide scales as a function of time can be described by growth laws. For diffusion-controlled scale growth a parabolic dependency is found:

$$\frac{dx}{dt} = \frac{k'_p}{x} \qquad \text{(eqn. 6.6)}$$

or

$$x^2 = k_p \cdot t + C \qquad \text{(eqn. 6.7)}$$
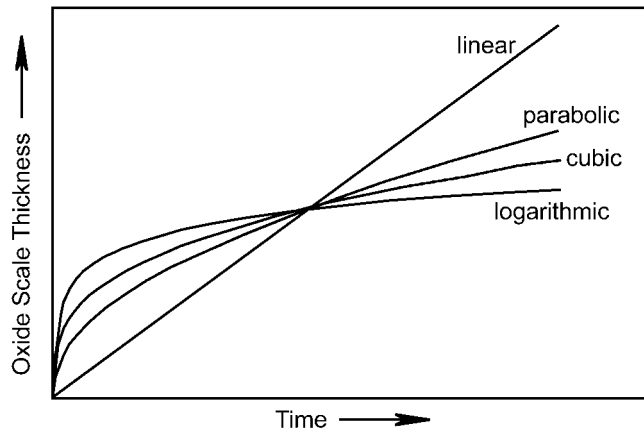
Fig. 6.6 Schematic representation of rate laws for oxide scale formation. In practice, often more complex and combined rate laws are observed.

where x is the thickness of the oxide scale, k_p is the parabolic rate constant, and C is an integration constant. In practical applications a number of different growth laws are reported, some of the borderline cases are displayed in Fig. 6.6.

However, even more complex or combined growth laws can be observed, for example, if the oxide scale grows linearly after initial parabolic oxidation, or if linear kinetics are followed by the formation of a protective oxide layer leading to parabolic, cubic, or logarithmic growth. However, often the parabolic rate constant, k_p, is used as a measure to characterize and compare the oxidation resistance of different materials.

The temperature dependency of the rate constant, k, of the reaction can be described with an Arrhenius law:

$$k = k_0 \cdot e^{-\left(\frac{Q}{RT}\right)}$$
(eqn. 6.8)

where k_0 is a temperature-independent pre-factor, Q is the activation energy, R is the general gas constant, and T the absolute temperature. Arrhenius diagrams, where the parabolic rate constant k_p, or log k_p, are displayed vs. 1/T, enable comparison of the oxidation resistance of different materials over a wide temperature range, and allow calculation of the activation energy, Q, of the oxidation reaction.

6.2.3
Oxidation of Alloys

In principle, the oxidation of multi-component alloys does not differ from that of pure metals. Depending on the type, quantity, and number of alloying elements, the oxidation behavior of an alloy can be substantially different compared to pure metals. The following factors must be considered:

- influence of the base metal
- alloy composition
- enthalpy of formation of the relevant oxides
- effect of dissolved oxides of the alloying elements on the disorder of the protective oxide scale
- formation of mixed oxides
- formation of ternary oxides (e.g. spinels)
- diffusion within the alloy
- solubility and diffusion of oxygen in the metal phase (internal oxidation)
- ratio of the rate of formation of different oxides.

In the following, two phenomena will be briefly described which are typically observed during oxidation of alloys: selective oxidation (usually desired) and internal oxidation (usually not desired). Both types can be influenced by some of the parameters listed above.

6.2.3.1 **Selective Oxidation**

Selective oxidation is often observed in alloys with widely differing stabilities of the alloying elements. The less noble element forms a continuous oxide layer, which, under ideal conditions, remains stable for long service times and effectively reduces the corrosion rate of the material. As already mentioned, the selective oxidation of alloying elements forming continuous SiO_2, Al_2O_3, and Cr_2O_3 scales is key for the good oxidation resistance of high temperature materials. For example, nickel-based superalloys rely on the selective oxidation of aluminum (5–8 wt.%), which forms continuous alumina scales.

Selective oxidation is not only influenced by the type of alloying addition, but also depends on temperature and oxygen partial pressure. As already discussed in section 6.2.1, the latter parameters decide whether or not the respective oxide scales can be formed from a thermodynamic standpoint (Fig. 6.1). For example, in Al-containing superalloys the dissociation pressure of alumina is much lower than that of nickel oxide thus making alumina the thermodynamically stable oxide.

Moreover, for a particular alloy system, and given oxidation conditions, a critical content of the active constituent is required to bring about selective oxidation. Considering an A-B alloy that does not form mixed oxides or spinels, and where B is the less noble element, three borderline cases can be distinguished (Fig. 6.7):

a) For low B concentrations, only A forms an oxide (Fig. 6.7a). B is enriched at the alloy/A oxide interface until the critical concentration to form B oxide is reached.
b) If the concentration of B is sufficiently high, only B oxide is formed and A diffuses into the alloy (Fig. 6.7b). Once the B content falls below a critical value, e.g. due to A enrichment in the diffusion zone, A oxide can be formed.
c) For intermediate concentrations of A and B, both A and B oxide form (Fig. 6.7c).
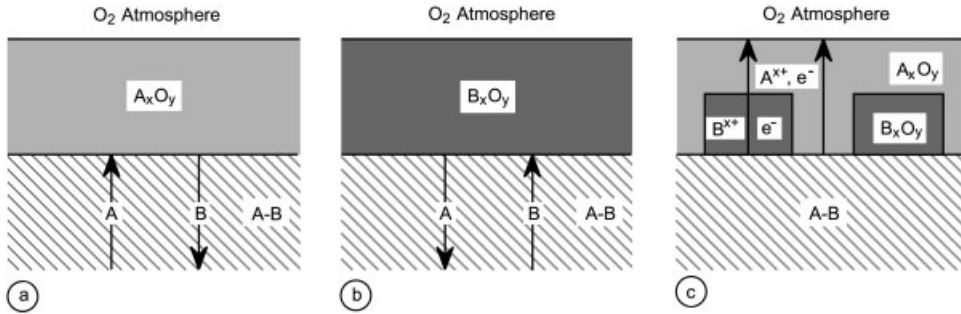
Fig. 6.7 Diffusion processes during oxidation of a binary A-B alloy. Selective oxidation to form a continuous protective layer is for case (b) only.

According to Wagner [7, 8], the critical concentration, N_{crit}^B, beyond which only B oxide is formed can be expressed for compact and void-free oxide scales by:

$$N_{crit.}^B = \frac{V}{z_B \cdot M_0} \left(\frac{\pi \cdot k_p}{D} \right)^{\frac{1}{2}} \qquad \text{(eqn. 6.9)}$$

where: V: molar volume of the alloy

z_B: valency of the B atoms

M_0:   atomic weight of oxygen

D: self-diffusion coefficient of B in the alloy

k_p: parabolic rate constant for exclusive formation of B oxide.

For many materials used in industrial applications the critical content can be calculated with reasonable accuracy. However, there are exceptions where the calculations are not in agreement with the experimental data. A detailed description can be found in [7, 8].

6.2.3.2 Internal Oxidation

If oxygen can be dissolved in an A-B alloy during oxidation, oxide formation of the less noble constituent, i.e. B, can occur within the alloy. The following prerequisites for this to happen must be fulfilled:

- Oxygen solubility in metal A and alloy A-B
- B has a greater oxygen affinity than A
- oxygen must have a higher diffusion rate into the alloy than B diffuses to the surface
- B must not exceed a maximum concentration leading to external oxide scale formation.

A transition from internal to external (selective) oxidation is observed if a critical concentration is reached by enrichment of the less noble B constituent, which re-

sults in formation of an external B oxide layer. According to Wagner [7, 8], the critical concentration for the transition from internal oxidation to external scale formation can be expressed by the following relationship:

$$N_B^* = \left(\frac{\pi g^* N_O D_O V_M}{2 D_B V_{Ox}}\right)^{\frac{1}{2}}$$ (eqn. 6.10)

where $N_O D_O$ is the oxygen permeability in A, D_B the diffusivity of B, g^* a factor (typically ~ 0.3) and V_M and V_{Ox} are the molar volumes of the alloy and the oxide, respectively.

Wagner's theory for internal oxidation is based on a number of idealizations, which often are not fulfilled in a real system; so, in practical applications, many examples seem to contradict his theory. A critical review of this topic has been published by Douglass [9], who focused particularly on the following issues: (a) effect of alloy element concentration and the effect on the reaction kinetics, (b) morphology of precipitates, (c) internal oxide bands, (d) intergranular internal oxidation, (e) non-stoichiometric precipitates, (f) precipitates with a high solubility product, and (g) absence of further oxidants. Douglass concludes from his work that indeed there are many examples for which Wagner's theory does not apply; however, it is undoubtedly the basis for a better understanding of oxidation phenomena [9].

6.3
Oxidation Behavior of Titanium Alloys and Titanium Aluminides

As already discussed in detail in Chapter 1, the classic high temperature titanium alloys are from the classes of $\alpha + \beta$ or near-α alloys, which provide the best combination of mechanical properties and oxidation resistance. For higher application temperatures, these conventional alloys are supplemented by titanium aluminides. In both classes of alloys, aluminum is the most important alloying element. Modern conventional high temperature titanium alloys contain up to 6 wt.% aluminum, while the aluminum content of titanium aluminides is typically between 25 and 50 at.%.

There are two principal effects relevant to the oxidation of titanium alloys and titanium aluminides:

- formation of an oxide scale
- dissolution of non-metals in the subsurface zone of the alloys.

Depending on the alloys, both phenomena can have different effects on the oxidation behavior and the mechanical properties of the entire system. Since many of the aspects discussed in the following are common for titanium alloys and titanium aluminides, there will be no explicit distinction between the alloy classes unless stated otherwise.

6.3.1
Oxide Scale Formation

6.3.1.1 Ti-Al-O Phase Diagram

Unlike high temperature materials based on Fe, Ni, or Co, where excellent oxidation resistance relies on the formation of thermodynamically stable Cr_2O_3, Al_2O_3, or SiO_2 scales, the stability of Al_2O_3 and TiO are very similar (Fig. 6.1). This fact hinders the selective oxidation of Al to form Al_2O_3, so the titanium base metal is oxidized as well. Due to the strong disorder in their lattice structure, TiO and other titanium oxides are fast growing and do not form protective oxide scales; therefore, sufficient oxidation resistance can only be achieved by the formation of an Al_2O_3 layer. Note, in the following discussion Al_2O_3 (or alumina) will always refer to the α-Al_2O_3 phase since for titanium-based alloys the corundum phase is almost always found at relatively low oxidation temperatures. Moreover, in practice TiO_2 is usually found rather than TiO since the monoxide is rapidly oxidized to the dioxide. However, for thermodynamic consideration, TiO is typically used in the literature.

A prediction of the stability of TiO or Al_2O_3 in equilibrium with one or more metal phases of an alloy is only possible if the activities of Ti and Al in the respective phases are known. For the Ti-Al system the activities of the constituents Ti and Al deviate from ideal Raoult behavior, which predicts a linear relationship of the activities and the chemistry. This deviation is mainly caused by the formation of intermetallic phases. Therefore, the stability of TiO and Al_2O_3 depend on the composition of the respective metallic phases. Initial thermodynamic calculation by Rahmel and Spencer [10] as well as by Luthra [11] have indicated that alumina is more stable than titania if the aluminum content is in excess of 50–55 at.%. The resulting ternary Ti-Al-O phase diagram is shown in Fig. 6.8a. More recent calculations based on the measurement of the Al and Ti activities in the Ti-Al system provide evidence that TiO is more stable than Al_2O_3 [12, 13]. However, exactly the opposite effect was found by experimental investigation of the phase equilibria in the Ti-Al-O system, namely Al_2O_3 being more stable than TiO. Surprisingly, this is not only true for the γ and $\gamma + \alpha_2$ regions relevant to titanium aluminides, but also for aluminum contents between 1 and 25 at.% [14–16]; the resulting ternary phase diagram is shown in Fig. 6.8b [17]. This result is particularly surprising since there obviously does not exist a thermodynamic barrier for the formation of Al_2O_3 layers over the entire region of industrially relevant compositions of the Ti-Al system. However, in practice, protective alumina scales are rarely found, particularly for low Al contents as present in conventional titanium alloys, α_2 titanium aluminides, and orthorhombic Ti_2AlNb-based titanium aluminides (see Chapter 3).

Among the potential reasons for the differences in the thermodynamic calculations and the experimentally determined Ti-Al-O phase diagram, differing oxygen solubilities in the various Ti-Al phases are believed to play a key role. These were neglected in the early thermodynamic calculations and might be important for the formation of the relevant oxide phases [15, 18]. Thermodynamic modeling has re-
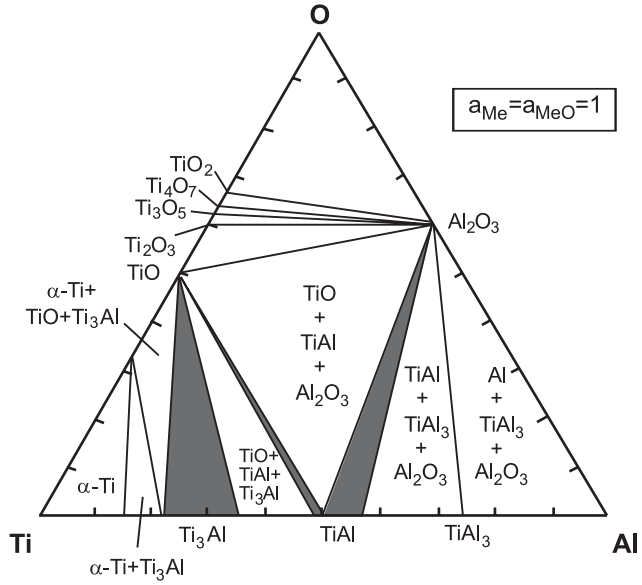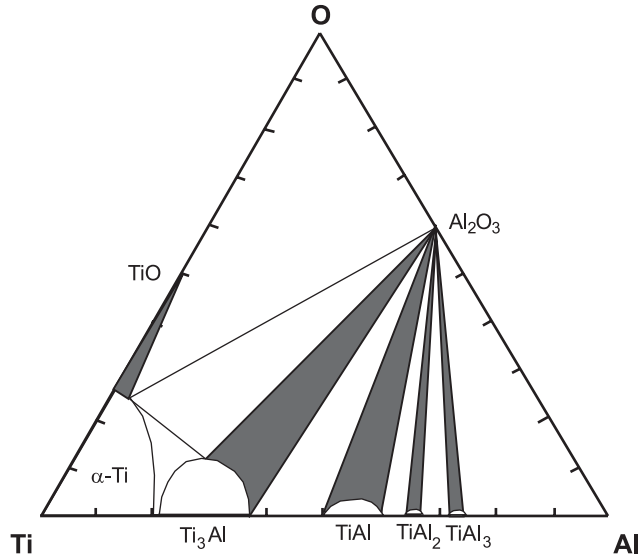
Fig. 6.8 Isothermal section of the Ti-Al-O phase diagram: (a) calculated at 800 °C after Luthra [11], (b) after experimental data [17].

vealed that calculations of the Ti-Al-O phase diagram can be adjusted more precisely to experimental findings when oxygen solubilities are considered [15, 19].

Moreover, formation of a new ternary $Ti_xAl_yO_z$ phase is discussed, designated as "Z"or "X" phase. This phase (or phases), which has a composition range of Ti-(25–35)Al-(15–20)O (at.%), is particularly found in the Al-depleted, oxygen-rich zone beneath the oxide scale on γ titanium aluminides. The existence of this Ti-Al-O phase, whose thermodynamic properties are largely unknown and whose stability [20] or metastability [21] is not clear yet, might also contribute to the discrepancy between calculated and experimentally verified phase equilibria in the Ti-Al-O system reported above [22]. Obviously, intensive research efforts are necessary to clarify the phase equilibria in the Ti-Al-O system. However, it should be mentioned again that contrary to common sense, alumina is the thermodynamically stable oxide phase for γ and $\gamma + \alpha_2$ alloys, so there is no thermodynamic barrier for the formation of alumina layers on these alloys. Kinetic effects that hinder the formation of protective alumina layers on industrial alloys have not yet been identified [17].

Even if the discussion of the Ti-Al-O phase diagram has not been concluded yet, it clearly indicates the issues of protective alumina scale formation particularly for low Al-containing titanium alloys. Therefore, phenomenological aspects of titanium alloy and titanium aluminide oxidation will be discussed to help general understanding of material behavior under oxidizing conditions, rather than provide detailed knowledge for specific alloys. The oxidation behavior of orthorhombic titanium aluminides is described in more detail in Chapter 3.

6.3.1.2 Oxide Scale Growth

The formation of an oxide scale during thermal exposure of titanium alloys is directly influenced by thermodynamics, such as the similar stabilities of TiO and Al_2O_3, and kinetic aspects, such as the high growth rate of TiO_2 relative to Al_2O_3. Fig. 6.9 shows a sketch of the oxide scale and oxygen interdiffusion zone of titanium-based alloys with different aluminum contents exposed to identical thermal conditions. For pure titanium, more than 50% of the oxygen is incorporated into the metal forming an oxygen diffusion zone, while a minor amount contributes to formation of an external TiO_2 layer. The reasons for, and the impact of, the high oxygen solubility in titanium will be addressed in more detail in section 6.3.2. Addition of aluminum decreases the width of the oxygen-affected zone while, on a relative basis, the portion of the external oxide scale increases. The oxide scale typically now has a multilayer microstructure consisting of a heterogeneous mixture of TiO_2 and Al_2O_3 in varying proportions and of a TiO_2 top layer [23–27]. Addition of more aluminum leads to a reduction in oxide scale thickness, e.g. the oxidation resistance of the oxide scale is generally improved. However, formation of alumina scale alone is observed for $TiAl_3$, which also yields a very thin oxygen-affected subsurface zone.

Beneath the oxide scale within the oxygen-enriched zone, an aluminum-depleted zone can form as a result of scale-forming aluminum depletion, which in turn has a direct effect on the stability of the types of oxides formed (see also sec-
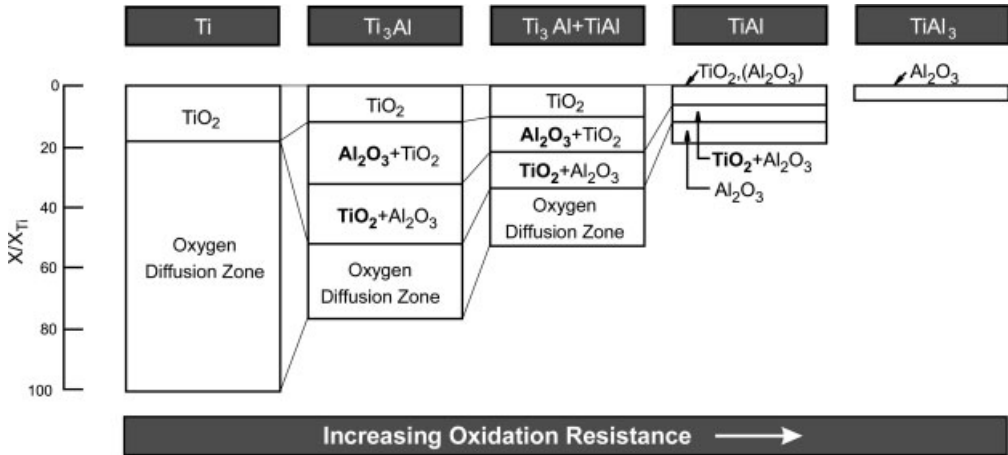
Fig. 6.9 Schematic representation of oxide scales and oxygen diffusion zones of titanium-base alloys (after Smialek et al. [149]).

tion 6.3.1.1). According to eqn. 6.9, defining the critical aluminum content that must not fall below a certain level in order to form alumina, the rate at which the critical level is reached strongly depends on the oxidation kinetics and the diffusivity of aluminum. It is therefore possible that after initial formation of a protective alumina scale a heterogeneous mixture of TiO_2 and Al_2O_3 can be formed during extended exposure. This is particularly relevant in the case of phase transformations (e.g. $TiAl \rightarrow Ti_3Al$). In this context it must be noted that most titanium alloys have multiphase microstructures, so the alloy microstructure can also influence the formation of the oxide scale. For example, a coarse cast microstructure of a ($Ti_3Al+TiAl$) alloy promotes formation of a heterogeneous TiO_2-Al_2O_3 scale while for a fine lamellar arrangement of Ti_3Al exclusive formation of Al_2O_3 was observed, resulting in low oxidation rates [28]. A similar effect was found for conventional titanium alloys. Near-α alloy TIMETAL 1100 with a lamellar microstructure has a greater oxidation resistance than with a bimodal microstructure [29].

The schematic presentation in Fig. 6.9 does not describe the arrangement of oxide scales of particular alloys in a universally valid way; however, it provides a clue about principal differences. Oxide scale formation in isolated cases depends on a number of parameters such as alloy chemistry, exposure temperature and time, as well as oxidizing atmosphere. The structure of oxide scales on multi-component alloy systems can be far more complex than that shown in Fig. 6.9. In Fig. 6.10 a cross section through the oxide scale of γ TiAl alloy Ti-45Al-8Nb is shown after 200 h oxidation in air at 1000 °C. The multilayer oxide scale consists of an outer alumina scale that is locally interrupted by TiO_2. Underneath this layer a two-phase zone is formed with TiO_2 being the predominant oxide phase present. Almost mid-way, a zone consisting of a mixture of NbO_x and Al_2O_3 is observed, again followed by a mixture of TiO_2 and Al_2O_3. In the oxide-metal transition zone

a Nb-rich layer is evident. Locally enhanced oxidation occurs for this alloy (after 200 h at 900 °C in this case) accompanied by internal oxidation (Fig. 6.10 b). The area of internal oxidation is characterized by the formation of needle-like oxides, mainly Al_2O_3, TiO_2, and Nb_2O_5.

Fig. 6.11 gives an impression of the surface topology of near-α alloy TIMETAL 834 oxidized at 750 °C for 100 h. While major parts of the surface are covered with characteristic rutile (TiO_2) crystals (Fig. 6.11 a), locally cube-like oxides are formed (Fig. 6.11 b) indicative of Al_2O_3. The behavior of the oxide scale under thermal cyclic conditions strongly depends on the alloy composition, which determines type and extent of the oxide scales formed. Fig. 6.12 shows the macroscopic appearance of the surfaces of near-α alloy TIMETAL 834 (a), orthorhombic tita-

a)

b)
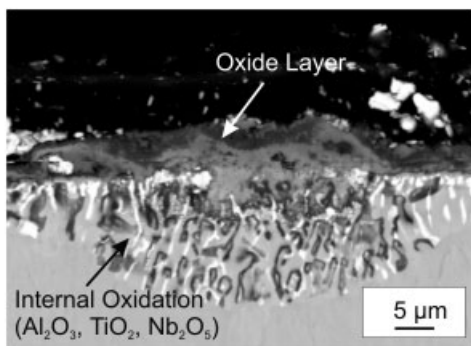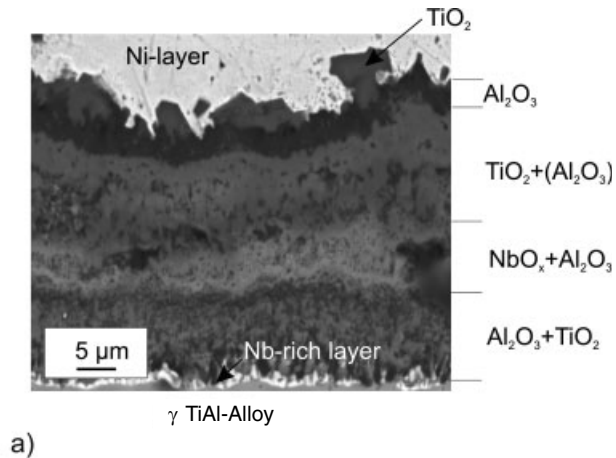
Fig. 6.10 Metallographic cross-section through the oxide scale of Ti-45Al-8Nb after air exposure: (a) 200 h/1000 °C, (b) 200 h/900 °C.
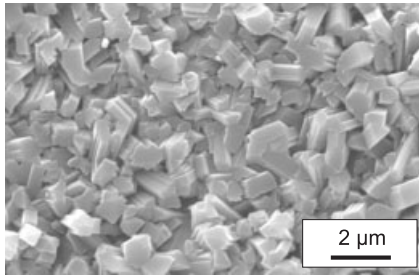
a)
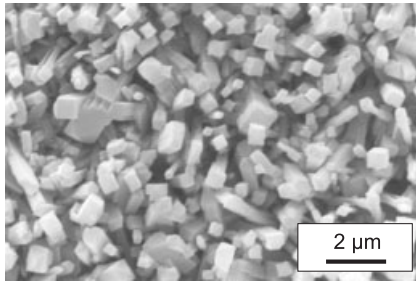
b)

Fig. 6.11 Different oxide morphologies on TIMETAL 1100 after 100 h air exposure at 750 °C (top view).

nium aluminide alloy Ti-22Al-25Nb (b) and γ TiAl alloy Ti-45Al-8Nb (c) after 1000 h oxidation in air at 750 °C. For the near-α alloy, rapidly growing oxide scales tend to spall during cooling after a critical thickness has been reached and, subsequently, new oxide forms (dark areas on the surface, Fig. 6.12 a). However, the oxide scales formed on the orthorhombic alloy demonstrate reasonable adhesion except at the edges, where these scales tend to spall as well but do not typically expose the metal surface (Fig. 6.12 b). There is no sign of oxide scale spallation for the γ TiAl alloy (Fig. 6.12 c); the thin gray alumina scale is still intact after 1000 h oxidation.

a)   b)   c)

5 mm
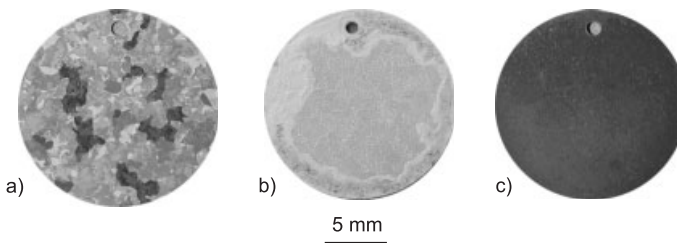
Fig. 6.12 Macrographs of three titanium alloys after 1000 h cyclic oxidation at 750 °C, (a) near-α alloy TIMETAL 834, (b) orthorhombic titanium aluminide Ti-22Al-25Nb, (c) γ TiAl alloy Ti-45Al-8Nb.

Different kinetics of oxide scale growth of titanium alloys and titanium alumi-
nides are shown in Fig. 6.13. While the two γ alloys Ti-48Al-2Cr-2Nb and Ti-45Al-
8Nb show moderate oxide scale growth under isothermal (a) and cyclic (b) condi-
tions, significant mass changes due to rapid oxide scale growth and subsequent
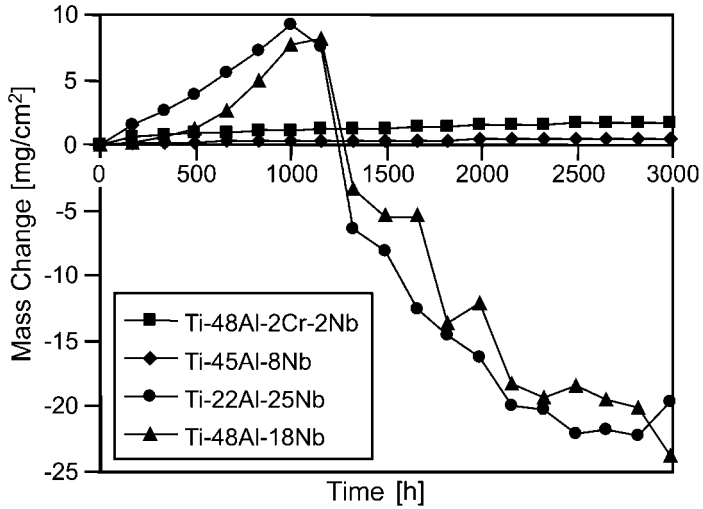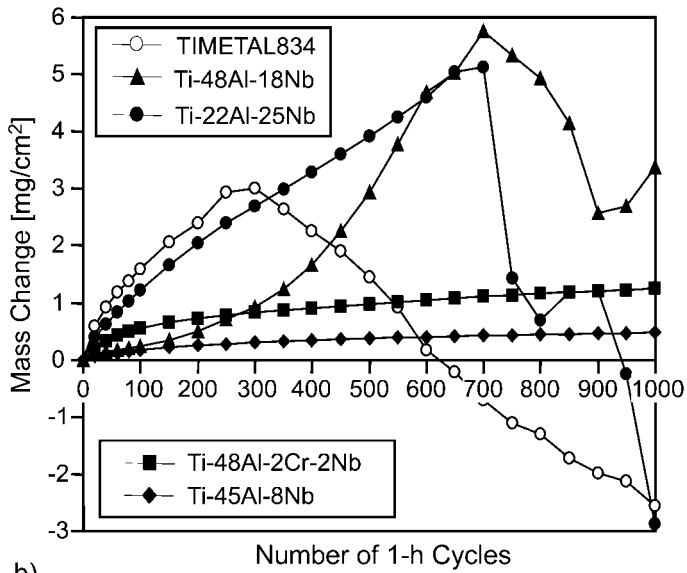
Fig. 6.13 (a) Quasi-isothermal and (b) cyclic oxidation behavior of different
titanium-based alloys in air at 750 °C.

scale spallation are obvious for near-α alloy TIMETAL 834, orthorhombic Ti-22Al-25Nb and high Nb-containing Ti-48Al-18Nb. Notably, failure of the oxide scales can generally not be attributed to a certain (critical) oxide scale thickness, but depends on various factors such as the type of oxide scale and the alloy itself. This is particularly evident by comparing the cyclic oxidation behavior of TIMETAL 834 to Ti-22Al-25Nb and Ti-48Al-18Nb. As can be concluded qualitatively by the greater mass increase experienced by Ti-22Al-25Nb and Ti-48Al-18Nb, the oxide scale thickness attained before scale spallation occurs can be much greater than for TIMETAL 834. For Ti-22Al-25Nb it is expected that the reasonable adhesion of the oxide scale is particularly related to the equiaxed morphology of the oxide phases formed, which obviously provides some damage tolerance [30].

The effect of temperature and alloy chemistry can be concluded from the Arrhenius plot (according to Eqn. 6.8) shown in Fig. 6.14. The rate constant increases with temperature, i.e. according to Eqn. 6.7, so the oxide scales formed during identical oxidation times are thicker. With increasing Al content, oxidation kinetics approach that of heterogeneous oxide scale formation and Al_2O_3 formation, respectively, so the protection provided by the oxide scales is increased. Additional alloying elements can significantly change oxidation resistance of titanium alloys (see also section 6.3.1.3); e.g. Nb can improve oxidation of Ti_3Al-based alloys significantly. As an alloy from the class of near-α alloys, TIMETAL 1100 follows TiO_2 kinetics, since the aluminum content of about 6 wt.% is too low, so the oxide scales grow rapidly and lack of protection.
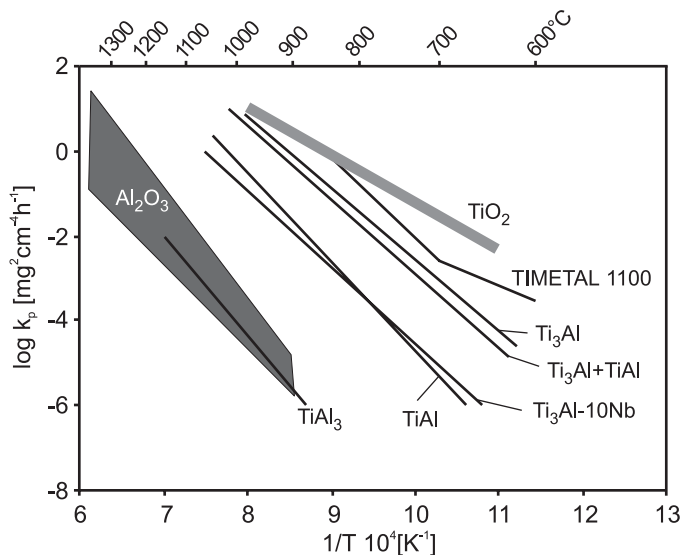
Fig. 6.14 Arrhenius plot of the parabolic rate law for Ti-Al alloys (after [76]). The borderline curves for TiO_2- and Al_2O_3-formers are included.

Relative to TiO_2, alumina has limited disorder, therefore mass transport is mainly within the titanium dioxide or along phase boundaries in the case of heterogeneous $Al_2O_3+TiO_2$ formation. Disorder of TiO_2 is strongly dependent on the environmental conditions. At low pressures and high temperatures, interstitial titanium ions are the major defects; while at high oxygen pressures and low temperatures, disorder is dominated by oxygen anion vacancies – therefore the composition of titanium oxide can be described more generally as $Ti_{1+x}O_{2-y}$ [3]. Transport processes in the oxide scale and its growth direction can be influenced by alloying elements. For example, the number of oxygen anion vacancies can be reduced by interstitial dissolution of Al in TiO_2 [31] (see also section 6.3.1.3). Therefore, outward growth of the oxide scale by cation transport is 10% for pure titanium, while for TiAl 30% of the oxide scale grows outwardly [32].

The crack healing capability of oxide scales is an important feature for application of high temperature materials since the protective nature of the oxide scale for long-term applications, and potentially under mechanical loading, can only be maintained if cracks can be closed by oxide formation during exposure. Crack healing can only be achieved by the outwardly growing part of the oxide scale [33]. Furthermore, crack healing requires a strain rate low enough to close the crack by oxide formation; the rate of which depends on the rate of formation of the oxide scale [32]. For binary TiAl, the critical strain rate for crack healing is on the order of 10^{-5} s^{-1}. The addition of 2% Nb can increase the strain rate by one order of magnitude [34]. No systematic studies on the crack healing behavior of conventional titanium alloys have been reported yet.

6.3.1.3 Effect of Alloying Elements

The effect of alloying additions, other than aluminum, in titanium alloys is limited to selective formation and stabilization of the alumina scale or reduction of the growth rate of the $Al_2O_3+TiO_2$ mixed oxide scale, since there is no oxide that forms slow-growing scales with a higher thermodynamic stability than TiO_2 or Al_2O_3 [32].

In addition to the thermodynamic requirements for alumina formation, protection can only be achieved if the conditions for continuous alumina scale formation are fulfilled, as described by eqn. 6.10. Although in most real systems formation of transient oxides of the base metal, for example, require the portion of scale-forming elements to be higher than calculated, eqn. 6.10 shows a qualitative way to improve oxidation of titanium-based alloys by alloying additions. The critical aluminum content, N_{Al}^*, can be reduced by such alloying additions, which decrease the oxygen solubility and diffusivity (N_O, D_O) and/or increase the aluminum diffusivity (D_{Al}) [35, 36]. The β-stabilizing elements show a major effect that is limited, however, to temperatures above 1200 °C, and thus far beyond the application temperatures even for titanium aluminides. Furthermore, formation of Al_2O_3 can be promoted by higher aluminum activities, and the mass transport in TiO_2 can be altered by doping. However, there is no information available about elements that substantially increase the aluminum activity.

Doping TiO_2 can influence its disorder when Ti^{4+} ions are replaced by ions with higher valencies, such as Nb^{5+}. Thus, the oxygen vacancy concentration $V_O^{\bullet\bullet}$ according to eqn. 6.11 is reduced [37]:

$$Nb_2O_5 + V_O^{\bullet\bullet} \xrightarrow{\text{Rutil}} 2Nb_{Ti}^{\bullet} + 2TiO_2 \qquad \text{(eqn. 6.11)}$$
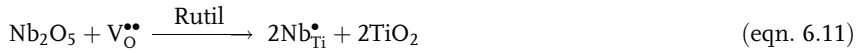
On the other hand, elements with a lower valency increase the vacancy concentration in rutile, given that they occupy the titanium sites in the oxide lattice. However, it appears fairly unlikely that doping can reduce the growth rate of the rutile to that of alumina [32]. Elements with lower valency increase the number of vacancies, i.e. low amounts of aluminum accelerate the oxide scale growth rate by the formation of Al^{3+} unless the content is high enough to form discrete Al_2O_3 scales.

Niobium is known to particularly improve the oxidation resistance of γ TiAl and α_2 Ti_3Al titanium aluminides. Fig. 6.15 [38] summarizes literature data of alloys in the composition range Ti-(22–25)Al-(0–27)Nb (at.%). Depending on the exposure temperature, between 10–15 at.% Nb is most effective; the parabolic rate constants are lowest, indicating the best oxidation resistance. For γ TiAl alloys the beneficial effect of Nb has been well known for quite some time (see e.g. Fig. 6.13); quite obviously, an optimum concentration must be found. While 8–10 at.% Nb typically improves oxidation resistance, 18 at.% leads to formation of less protective oxides scales. Similar to the findings for alloys in the Ti-(22–25)Al-(22–27)Nb (at.%) range, Nb-containing oxide scales absent a continuous alumina scale form if the Nb content is too high (see also Chapter 3).

The mechanistic reasons for the Nb effect have been discussed in the literature for a while. The following mechanisms have been proposed (after [39]):
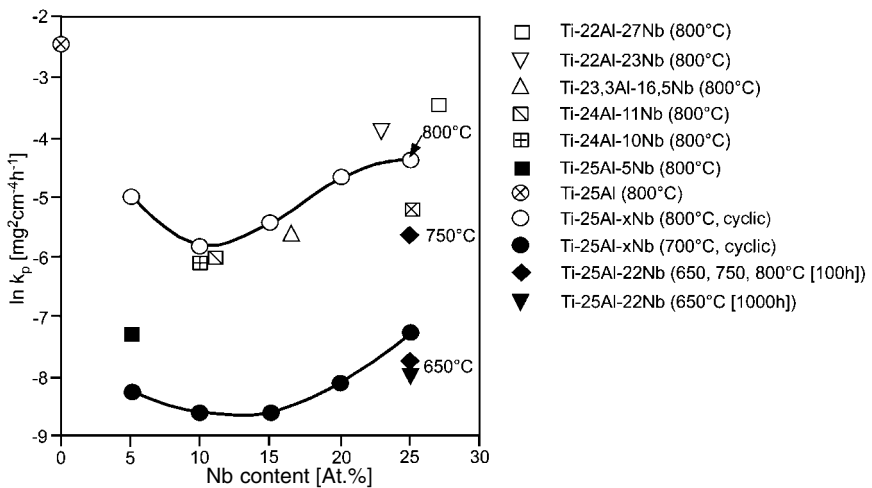
Fig. 6.15 Influence of the Nb content of Ti-(22–25)Al-xNb alloys on the parabolic rate constant of oxidation.

- Formation of a stable Ti-rich nitride layer at the metal-oxide interface that acts as a diffusion barrier against anion and/or cation mass transport.
- Increase of the aluminum activity relative to titanium, thus promoting formation of an alumina scale.
- Enrichment of Nb just below the oxide scale that alters diffusion processes such that the transport of metal ions and/or oxygen ions is reduced.
- Doping of the TiO_2 lattice by Nb^{5+} ions (see above).
- Formation of Nb_2O_5 that forms mixed oxides with TiO_2 and Al_2O_3, thus improving adhesion of the oxide scale and blocking diffusion paths.
- Reduction of oxygen solubility in the alloy.

At this point the only mechanism that can be ruled out is that Nb is assumed to increase the Al activity relative to titanium. Measurements of the activities in the Ti-Al-Nb system have shown that the addition of Nb to γ TiAl alloys reduced the Al activity, which should promote formation of TiO_2 rather than alumina [40]. All other mechanisms appear to be realistic so far, and it is very likely that more than one mechanism plays a key role in the improvement of oxidation resistance.

Examples of the effects of further alloying elements on the oxidation resistance of titanium alloys will be discussed in section 6.4.1.

6.3.1.4 **Effect of Atmosphere**

Comparative studies on the oxidation behavior of conventional titanium alloys and Ti_3Al-based alloys in air and in pure oxygen have typically shown a better oxidation resistance in air. On the contrary, for γ TiAl-base alloys, higher and lower oxidation rates have been reported in air or pure oxygen depending on alloy composition and oxidation time; this behavior is designated the "nitrogen effect". Although a number of mechanistic studies have been performed on the nitrogen effect (e.g. [18, 41–44]) universally valid statements are difficult to make and in most cases the mechanisms are not yet fully understood. It has been often reported that oxygen appears to promote the formation of Al_2O_3, while nitrogen hinders the formation of a protective alumina scale. This is particularly seen in the initial stages of oxidation due to formation of a TiN layer, which facilitates formation of heterogeneous TiO_2-Al_2O_3 oxide scales. As a consequence the oxidation rate in air is higher than in pure oxygen, where alumina scale can form undisturbed. Although the nitride layer is often dissolved after extended exposure, a continuous alumina scale can no longer be formed. On the other hand, the nitride layer can act as a diffusion barrier, thus reducing the aluminum depletion underneath the oxide scale, which in turn promotes formation of Al_2O_3 leading to improved oxidation resistance.

As shown in Fig. 6.16 for γ TiAl alloy Ti-45Al-8Nb, temperature has a significant effect on oxidation kinetics. While at 900 °C the oxidation reaction is slower in oxygen than in air, breakaway oxidation occurs in oxygen at 1000 °C after initial low mass gain, which finally leads to more rapid oxide scale growth compared to air. Breakaway oxidation in air is retarded at extended exposure times.
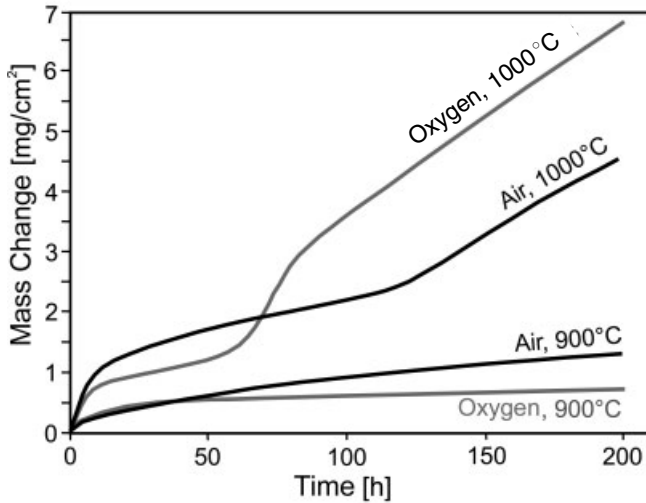
Fig. 6.16 Oxidation behavior of Ti-45Al-8Nb depending on atmosphere and temperature.

The effect of other media on the corrosion resistance of titanium alloys and titanium aluminides has been far less extensively studied than oxygen and air, where exposure to air is certainly the most relevant in view of industrial applications. However, it has been known that titanium-based alloys are prone to hot corrosion attack. In the temperature range between 650 and 750 °C, the envisaged temperature range for the use of γ TiAl alloys, the rate of metal consumption by hot corrosion attack is on the order of 20 times higher than that caused by oxidation attack alone [45].

6.3.2
Dissolution of Non-metals in the Subsurface Zone of Alloys

According to the Ti-O phase diagram, α Ti can dissolve up to 33 at.% oxygen (Fig. 6.17), which is interstitially incorporated into the lattice, either randomly or ordered at alternating (0002) planes of the hexagonal titanium lattice [37, 46]. Due to oxygen incorporation, the titanium ions are shifted towards the c-axis [46]. Up to 22 at.% nitrogen can be dissolved in Ti and also changes the lattice parameter [47]. Incorporation of oxygen and/or nitrogen leads to anisotropic lattice distortion, thus hindering dislocation mobility and alters the sliding behavior. Similar to α Ti, the intermetallic phases α_2 Ti$_3$Al and γ TiAl can dissolve oxygen and nitrogen; however, to a more limited extent. The oxygen solubility of Ti$_3$Al is reported to be between 10–20 at.% [14, 18, 48], while γ TiAl can only dissolve 1–2 at. % [14].

Since the oxygen/nitrogen diffusion zone is the major contributor to the environmentally affected cross section for titanium alloys (see Fig. 6.9), it is quite obvious that embrittlement caused by the dissolved oxygen and nitrogen is a critical issue in terms of mechanical properties of the materials.
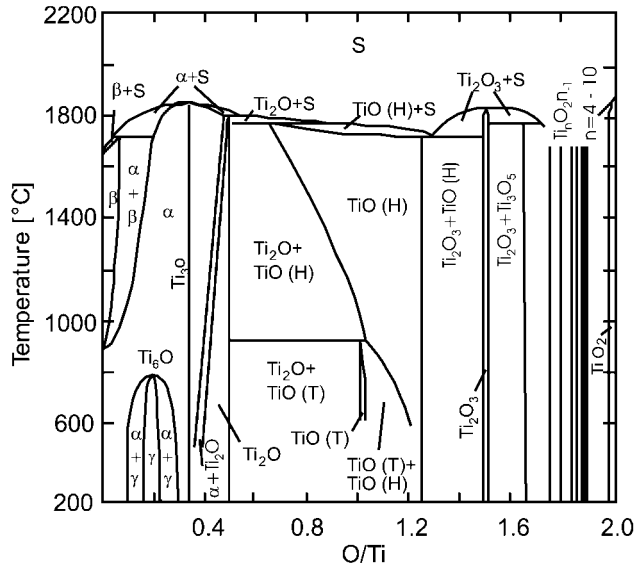
Fig. 6.17 Ti-O phase diagram (after [37]).

6.3.2.1 **Effect of Non-metal Dissolution on the Mechanical Properties**

Lattice distortion and preferred phase formation caused by oxygen dissolution result in hardening (embrittlement) of the affected subsurface zone of the alloy. Fig. 6.18 shows the microhardness profile of near-α titanium alloy TIMETAL 1100 after 500 h oxidation in air at 600 and 700 °C. The bright zone in the metallographic cross-section represents the α case, the oxygen diffusion zone. For conventional titanium alloys, hardness can be described by a square root function:

$$H = H_0 + b[O]^{\frac{1}{2}} \qquad\qquad (\text{eqn. } 6.12)$$

where H_0 represents the hardness of the unaffected base material, b is a constant and [O] is the oxygen concentration in the metal.

Increasing oxygen content leads to an increase in metal hardness. The penetration depth x can be described by a simple diffusion law, such as

$$x = \sqrt{Dt} \qquad\qquad (\text{eqn. } 6.13)$$

where t is exposure time and D represents the temperature-dependent diffusion constant. According to an Arrhenius relationship, D increases exponentially with temperature, resulting in a greater oxygen penetration depth for a given exposure time, as shown in Fig. 6.18. The maximum hardness depends on the oxygen content and, since the maximum solubility was reached, is identical at both temperatures.

Thin-walled components can be rapidly degraded across the entire cross-section, particularly along grain boundaries where diffusion is accelerated relative to the
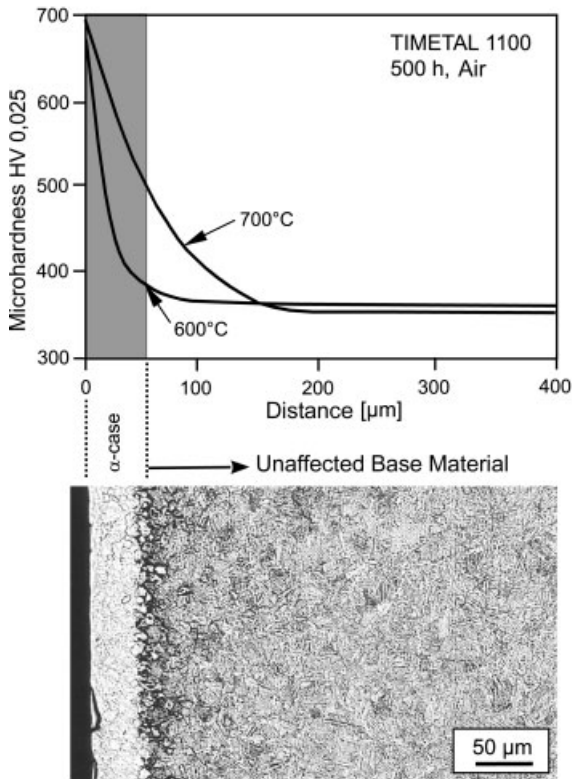
volume. However, ductility of the material is already degraded by the presence of thin embrittled surface layers (Fig. 6.19). For example, after short-term exposure at 600 °C ductility of TIMETAL 1100 is significantly reduced and the fracture strain after 100 h is only 50% of the initial strain value (Fig. 6.19 a). As can be concluded from Fig. 6.18, the embrittled zone after 100 h exposure at 600 °C is much thinner than 50 µm, nevertheless causing a drastic macroscopic embrittlement of the entire cross-section of the material.

This loss in ductility is clearly caused by crack formation within the embrittled zone, which leads to rapid crack propagation into the unaffected cross-section. While the center of the cylindrical sample indicated ductile fracture, the outer part of the cross-section fails by brittle fracture. Similar effects are known for Ti_3Al alloys. According to Fig. 6.9 the embrittlement effect of γ TiAl is less pronounced, due to lower oxygen solubility in the γ phase. Furthermore, these alloys are inherently much less ductile than conventional alloys, making the embrittlement effect more difficult to detect. However, embrittlement of titanium aluminides must be taken seriously, particularly for Ti_3Al- and orthorhombic Ti_2AlNb-based alloys [17, 38].
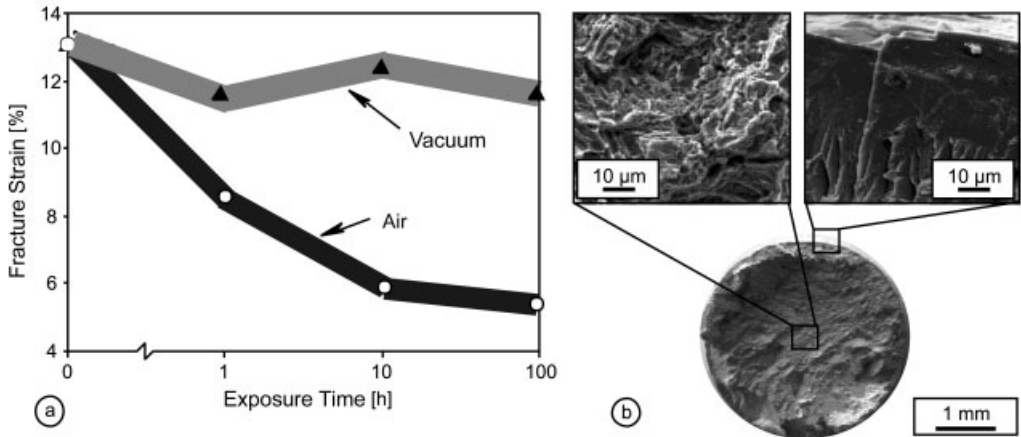
Fig. 6.19 (a) Fracture strain of TIMETAL 1100 vs. exposure time at 600 °C and (b) corresponding fractograph [38].

6.4
Measures to Improve Oxidation Resistance

Measures to improve resistance of a material to a particular environment must be taken by materials modifications since the service conditions (temperature, atmosphere, loading and life time) usually can not be changed. In general, there are three different ways to improve the oxidation resistance of titanium-based alloys: 1) addition of alloying elements, 2) pre-oxidation and 3) coatings.

6.4.1
Alloying Elements

As already mentioned in section 6.3.1.3, the oxidation resistance of titanium alloys can be influenced by the addition of alloying elements. Aluminum is undoubtedly the most effective alloying addition for titanium alloys (see Fig. 6.9). However, quite large amounts must be added, which substantially changes the mechanical properties of the material. This is certainly a general issue for many other alloying elements, which always requires an optimization process of oxidation resistance and mechanical properties.

For conventional titanium alloys, there is a lack of extensive systematic studies on the effects of alloying elements in the open literature. Si, Nb, W, and in certain cases also Cr, can reduce mass increase by oxide scale formation on these alloys; occasionally, adherence of the oxide layer can be improved (Tab. 6.1). V is known to reduce the oxidation resistance of conventional titanium alloys.

The effect of alloying additions has been studied in more detail for titanium aluminides based on the intermetallic phases α_2 Ti$_3$Al and γ TiAl. Tab. 6.1 displays the oxidation resistance (the key parameter), adherence of the oxide scale,

Tab. 6.1 Effect of alloying elements on the oxidation behavior of titanium alloys and titanium aluminides.

Alloy		Si	Ti	V	Cr	Mn	Y	Nb	Mo	Ta	W	Re
Ti Alloy	a	↑		↓	↑,↓			↑			↑	
	b	↑,↓			↑,↓							
	c											
	d	+		?	+			?				
Ti₃Al	a			↑,↓	↑			↑	↑,↓			↑
	b											
	c			↑,↓	↑			↑	↑		↑	
	d			+	+			+	+			
TiAl	a	↑	↑,↓	↑,↓	↑	↓	↑	↑,↓	↑,↓	↑	↑	↑
	b											
	c	↑	↑,↓	↑	↑			↑,↓	↑	↑		
	d	+	+	+	+	+	+	+	+	+	+	
TiAl₃	a	↑		↓	↑	↓	↑	↑				
	b	↑					↑					
	c			↓	↑	↓		↑				
	d			+		+						

↑ improvement; ↓ deterioration; + influence on oxidation mechanism; a: oxidation resistance; b: oxide scale adherence; c: Al_2O_3 protective layer formation; d: effect on oxidation mechanism. Sources: Ti₃Al, TiAl und TiAl₃ after [76]; Ti alloys: Si: [77–80], Cr: [77, 81], Nb: [79, 82], W: [82], V: [79]

formation of alumina, and the effect on oxidation mechanisms for various elements. Note, no distinction between different test temperatures and atmospheres is made, but a general tendency is given on the basis of a variety of literature data. Furthermore, this qualitative collection does not provide hard numbers for the concentration of the alloying additions. As experience shows, these can vary from 0.1 to a few 10%, depending on the alloying element. The important effect of Nb on the oxidation behavior of titanium aluminides was already addressed in more detail in section 6.3.1.3.

Recently, a detailed study on the effect of alloying elements on the oxidation behavior of γ TiAl was published [49, 50]. In a screening test, different elements were added to binary alloy Ti-48.6Al (at.%), ranging from maximum 6 wt.% for metals and 1 wt.% for non-metals. For the test temperature of 900 °C, the elements were classified into

a) detrimental (V, Cr, Mn, Pd, Pt, Cu)
b) neutral (Y, Zr, Hf, Ta, Fe, Co, Ni, Ag, Au, Sn, O)
c) beneficial (Nb, Mo, W, Si, Al, C, B).

The classification was based on the mass gain after 100 h isothermal oxidation in air. For Cr, Mn, Mo, and W the same classification was found at 800 and 1000 °C. Based on their experiments, the authors divided the oxide scales formed on the different alloys into five types [49], which mainly differed in the arrangement of the single phases in the oxide scale and in the formation of a continuous alumina scale.

Assessment of single alloying elements requires consideration of their total amount in the alloy. For example, while up to 6 wt.% Cr in γ TiAl demonstrates a detrimental effect on oxidation resistance [49], 12% Cr substantially improves oxidation behavior. [51]. TiAl$_3$ alloys containing 8 at.% Cr exhibit excellent oxidation resistance compared to binary TiAl$_3$, particularly under thermal cyclic conditions [52, 53].

Despite numerous and partly extensive studies on the effect of alloying elements on the oxidation resistance of titanium-based alloys, general recommendations for the use of specific additions are difficult to give. Moreover, alloys typically require a number of alloying elements to adjust the mechanical properties, whose interaction is usually unpredictable or even fairly unknown. Therefore, extensive empirical studies are necessary to select an appropriate alloy for specific applications [54].

Recently, the microalloying effect of Cl, P, I, B, C, and Br has been discussed for titanium aluminides. Particularly, Cl and Br demonstrated significant improvement in the oxidation resistance of γ TiAl alloys [55–59]. Added in small amounts, microalloying elements promote selective Al oxidation to form alumina and thereby change growth kinetics from TiO$_2$/Al$_2$O$_3$ kinetics to pure Al$_2$O$_3$ kinetics [59]. To take full advantage of the microalloying effect, a tight control of the amount of additions is necessary. The technical potential of this method to improve the oxidation resistance of γ TiAl alloys has not yet been fully explored. The low amount of additions is expected to have a certain advantage over classical alloying additions, since minor or negligible effects of microalloying elements on the mechanical properties of the intermetallic alloys are expected.

6.4.2
Pre-oxidation

The basic idea behind improving the oxidation resistance of titanium-based alloys through pre-oxidation is to initially form a protective Al$_2$O$_3$ scale before the component is exposed to service conditions. According to thermodynamic equilibrium conditions, depending on the temperature, selective Al oxidation in TiAl alloys requires an oxygen partial pressure lower than 10^{-20} Pa (see Fig. 6.1). However, oxidation studies on γ TiAl at 1000 °C indicated exclusive alumina formation at oxygen partial pressures of $6.7 \cdot 10^{-3}$ Pa. As a consequence of these findings, a number of different powder mixtures such as Cr$_2$O$_3$ [60], Cr/Cr$_2$O$_3$ [61], TiO$_2$ [62], and SiO$_2$ [63] were used to achieve well-defined oxygen partial pressures, thereby selectively oxidizing Al to form Al$_2$O$_3$. After pre-oxidation, oxidation resistance under atmospheric pressure was substantially better than for the untreated reference materials. However, long-term effectiveness of the pre-oxidation procedure has not yet been demonstrated. After extended exposure times (>20 h), breakaway oxidation was found for the pre-oxidized alloys, and it shifted towards longer times

with increasing Al content of the alloy [64]. Obviously, the Al reservoir available at the metal-oxide interface plays a major role.

6.4.3
Coatings

As addressed in the previous sections, the dilemma of titanium alloys and titanium aluminides used at elevated temperatures is characterized by the necessity for improved oxidation resistance and the requirements for mechanical properties. Measures to improve one property often lead to degradation of the other. Since oxidation attack is mainly limited to the outer region of a component, and mechanical properties are determined by the entire cross-section, a promising approach to optimize both mechanical properties and oxidation resistance is the use of surface modification technologies, particularly coating techniques.

A large variety of different coating systems have been applied to titanium alloys and titanium aluminides for more than 30 years now. Tab. 6.2 summarizes the major coating systems and fabrication techniques published in the open literature. Although ion plating is not a coating technique in the sense of forming an overlay coating, since this technique modifies the surface-near area only, it has been included into this overview.

The variety of the deposition techniques used, and the fact that several different material classes have been studied, suggest that even contemporary research and development has not yet brought an optimum solution to oxidation protection of titanium alloys and titanium aluminides. To date, no coating system has proven usable in service. As will be addressed in the following, coating systems have been recently developed that are believed to have a realistic chance for practical application in the near future.

With regard to practical application, the following key issues for the oxidation protection of titanium alloys and titanium aluminides have been identified:

1) adhesion of the coatings
2) long-term stability of the coating
3) degradation of the mechanical properties of the substrate.

Adhesion of the coating is a prerequisite for its effectiveness. The deposition process itself largely determines the adhesion of the coatings in the initial stages. While "hot" processes such as CVD, plasma spraying, or EB-PVD promote diffusion during coating fabrication and thus provide coatings with typically good adherence, coatings produced by "cold" processes such as sputtering or arc PVD often require bond layers or post-deposition heat treatment to provide adequate adhesion. Moreover, residual stresses as a consequence of the deposition process influence adhesion of the coatings. During exposure at elevated temperatures, different coefficients of thermal expansion between substrate and coating, non-relaxed residual stresses in the coating, formation of brittle intermetallic phases at the substrate-coating interface [65], and also potentially superimposed mechanical loads may play a key role.

Table 6.2 Overview of several coating systems and fabrication processes for titanium alloys and titanium aluminides.

Coating	Substrate	Deposition process	Source, Year
Ni, NiTi	Ti-6-4, Ti-6-2-4-2	electroplating	[65], 1973
Pt, Pt/C, Au, Ni/Au	Ti-11, Ti-6-2-4-2	ion plating	[83], 1977
Pt	Ti-6-2-4-2	ion plating	[67], 1978
Pt	cp-Ti, Ti-5Al-2.5Sn	ion plating	[84], 1979
Pt	Ti-6-2-4-2	ion plating	[85], 1979
Pt, Pt/Rh, Au	Ti-6-2-4-6	ion plating	[68], 1979
Pt	Ti-6-2-4-2-S	ion plating	[66], 1980
Pt	Ti-6-2-4-2	ion plating	[69], 1980
Ti-Si	cp-Ti	CVD	[86], 1982
Si	cp-Ti	ion plating	[87], 1985
Al	Cp-Ti, Ti-6-2-4-2	EB-PVD	[88], 1985
Pt	Ti-6-2-4-2	ion plating	[89], 1985
TiAl, $TiAl_3$	Cp-Ti	CVD	[90], 1986
Al, Silicates, Al-Silicates, SiO_2, Al-SiO_2	Ti-6-2-4-2	EB-PVD, CVD, sputtering	[91], 1987
Al_2O_3, Al_2O_3/Ni, Al_2O_3/Ni-Cr, Al_2O_3/TiO_2	KS 50	plasma spraying	[92], 1988
$TiAl_3$	Ti-14Al-24Nb	CVD	[93], 1988
Ti-Si	Ti	CVD	[94], 1988
Cr, Pt, TiAl, Ni, Ti_3Al+Nb, NiCr, FeCrAlY	IMI 829	sputtering	[95], 1988
Ti-Si	IMI 829	sputtering	[96], 1989
Ni-Cr	Cp-Ti, Ti-6-4	electroplating, sputtering	[97], 1989
Ni-Cr, SiC, Si_3N_4, Al	Cp-Ti	sputtering	[98], 1989
MgO, Y_2O_3, ZrO_2, HfO_2, SiO_2, B_2O_3, Al_2O_3, Na_2O, CaO, CaF_2, YF_3	Ti-14Al-21Nb	sputtering, sol-gel	[99], 1989
$TiAl_3$	TiAl	CVD	[100], 1989
Cr_2O_3	Ti 685	EB-ion implantation	[101], 1989
$TiAl_3$	Ti-14Al-21Nb	CVD	[102], 1990
$TiAl_3$	Ti-25Al-10Nb-3V-1Mo	CVD	[103], 1990
SiO_2/Al, Ni-Al, NiCoCrAlY	Ti-6-2-4-2	plasma spraying, EB-PVD	[104], 1990
Al, Al-O	Ti-6-4, Ti-14Al-21Nb, TiAl	sputtering	[105], 1991
SiO_2, B_2O_3, P_2O_5, MgO, Al_2O_3, ZrO_2, duplex- and tri-plex systems	Cp-Ti, Ti-14Al-21Nb	sol-gel	[99], 1991
Si_3N_4/Cr	IMI 829	IBAD	[106], 1991
Al, Al-Si	Ti-15-3-3-3, Ti-21Al-14Nb-3V-Mo	slurry technique	[107, 108], 1991
Al_2O_3, Al-Si-O	TiAl, Ti_3Al	sol-gel	[109], 1991
Al_2O_3	TiAl	CVD	[110], 1991
CrN, Cr	Ti-6-4	sputtering	[111], 1991

Table 6.2 (cont.)

Coating	Substrate	Deposition process	Source, Year
$BaTiO_3$, $SrTiO_3$, $CaTiO_3$	TiAl	hydrothermal treatment	[112], 1993
FeCrAlY, NiCrAlY, NiCr, CoCrWFeNi	Ti-6-4, Ti-6-2-4-2	arc-PVD	[113], 1993
Al, Ni, Ni-Cr, Cr, Cr_2N	cp-Ti, Ti-6-4	sputtering	[114], 1993
Ti-44Al-28Cr	Ti-47Al-2Cr-4Ta	sputtering, LPPS, HVOF, slurry technique	[115], 1993
$TiAl_3$, Al+glass	Beta-21S	EB-PVD, sol-gel	[116], 1993
CoCrAl	TiAl	sputtering	[117], 1993
CoCrAl, CoCrAlY	TiAl	sputtering	[118], 1993
$TiAl_3$	Ti_3Al	CVD	[119], 1993
MCrAlY, MCr/W	Ti-24Al-12.5Nb-1.5Mo, Ti-24Al-8Nb-2Mo-2Ta	plasma spraying	[120], 1993
SiC	TiAl	CVD, sputtering	[121], 1993
Si_3N_4	TiAl	IBED	[122], 1993
Ti-25Al-10Nb	IMI 829	sputtering	[48], 1994
Si, Pt, Al-Ti, NiCoCrAlY, NiCrAlTiSi	TIMETAL 1100	sputtering	[123], 1994
Nb	cp-Ti, Ti-6-4	arc-PVD	[124], 1995
Al	cp-Ti	laser alloying	[125], 1995
Cr, Y	TiAl	ion implantation	[126], 1995
Al-Y	TiAl	CVD	[127], 1995
HfN	cp-Ti, Ti-6-4	arc-PVD	[128], 1996
Ti-Si+B, Ge	cp-Ti, Ti-24-Al-11Nb, Ti-22Al-27Nb, Ti-20Al-22Nb	CVD	[71], 1996
Al, Si	TiAl	pack cementation	[129], 1996
Nb	TiAl	ion implantation	[39], 1996
TiAl, graded, multilayer	TIMETAL 1100	magnetron sputtering	[130], 1997
CoCrAlY, NiCoCrAlY, TiAlCr	TiAl	sputtering	[131], 1997
FeCrAlY	TiAl	sputter ion plating	[132], 1997
Al_2O_3, Y_2O_3-ZrO_2, $TiAl_3$	Ti-48Al-2Cr-2Nb	sol-gel, pack cementation	[133], 1997
TiAlCr	TIMETAL 834, Ti-48Al-2Cr-22Nb	magnetron sputtering	[134], 1998
SiAlN	TiAl	sputtering	[135], 1998
TiAl, TiAlCr	TiAl	plasma spraying	[136], 1998
Ti-47Al-2Cr-2Nb, Ti-6242S	$(Al, Cr)_3Ti$	plasma spraying	[137], 1998
Al, CoCrAlY, TiAlCr, Al_2O_3	TiAl	sputtering, pack cementation	[138], 1998
$(Al,Cr)_3Ti$	TiAl	pack cementation	[139], 1999
Ti-61Al-14Cr	Ti-43Al-5Cr	pack cementation	[140], 1999
$(Al,Cr)_3Ti$	TiAl	pack cementation	[141], 1999
Al_2O_3, enamel	TiAl	sputtering, enamel	[142], 2000
Cl	TiAl	ion implantation	[143], 2000
TiAl/TiAl-SiC	TiAl	EB-PVD	[144], 2000
Al-Cr	TiAl	pack cementation	[145], 2000

Table 6.2 (cont.)

Coating	Substrate	Deposition process	Source, Year
Si, Mo	TiAl	ion implantation	[146], 2000
Ti-48Al-2Ag	TiAl	sputtering	[72], 2001
Si, Nb	TiAl	ion implantation	[147], 2001
P	TiAl	etching	[148], 2002
TiAlCrYN	TIMETAL 834, TiAl	sputtering	[73], 2002

Long-term stability is among the most important properties of the coatings. Even though many of the coating systems studied so far have demonstrated improved oxidation resistance visible by reduced mass gain and/or reduced dissolution of interstitials, exposure times were usually in the range between 10–100 h only. These short-term experiments allow a ranking of different coating systems, but cannot provide information about the long-term properties after hundreds or thousands of hours exposure at elevated temperatures as required for many applications. It is well known from studies on bulk material and coatings that breakaway oxidation can occur after extended exposure, which is not captured by short-term experiments. Rapid oxidation can be caused by several phenomena. For example, interdiffusion between the substrate and the coating can lead to depletion of scale-forming elements in the coating, which then promotes formation of fast-growing TiO_2. Extensive interdiffusion can also result in the formation of Kirkendall pores, which reduce the adhesion of the coating on the scale [65]. Crack formation within the coating can also lead to TiO_2 formation within the crack, which might subsequently cover large parts of the component surface. This effect is particularly detrimental for coatings that can not heal cracks since, once formed, cracks are closed by substrate oxidation. Ceramic coatings and coating systems with a great difference between the coefficients of thermal expansion of coating and substrate are particularly prone to crack formation under thermal cyclic conditions.

The effect of coatings on the mechanical properties of the base titanium alloy or titanium aluminide is a key aspect for practical application of coatings, which has often been neglected in the literature. Detailed mechanical tests were performed for Pt ion implanted titanium alloys. Thin coatings (ca. 1 μm) improved the creep behavior [66] and the fatigue resistance of conventional titanium alloys [67–69]. However, overlay coatings were often shown to degrade the mechanical properties, particularly the fatigue behavior of the substrate material [39, 70, 71]. This fact is considered to be a major hurdle for oxidation resistant coating to make their way into service on titanium-based alloys.

Novel coating concepts are based on metallic overlay coatings from the Ti-Al-Ag system [72] or on nitride coatings [73]. In addition to good oxidation resistance, nitride coatings offer the advantage of wear resistance at high temperatures, an important property for applications in the compressor of gas turbine engines. Fig. 6.20 gives an overview of some of today's most advanced coating systems for conven-

tional titanium alloys and titanium aluminides. At 750 °C in air, TiAlCrYN coatings improve the oxidation resistance of already reasonably oxidation resistant γ TiAl alloy Ti-45Al-8Nb by one order of magnitude (Fig. 6.20). After 3000 h exposure, the coatings were fully intact and lacking any sign of degradation. Ti-Al-Ag coatings tested at 800 °C also demonstrated excellent oxidation resistance. Under cyclic ther-

a)

b)
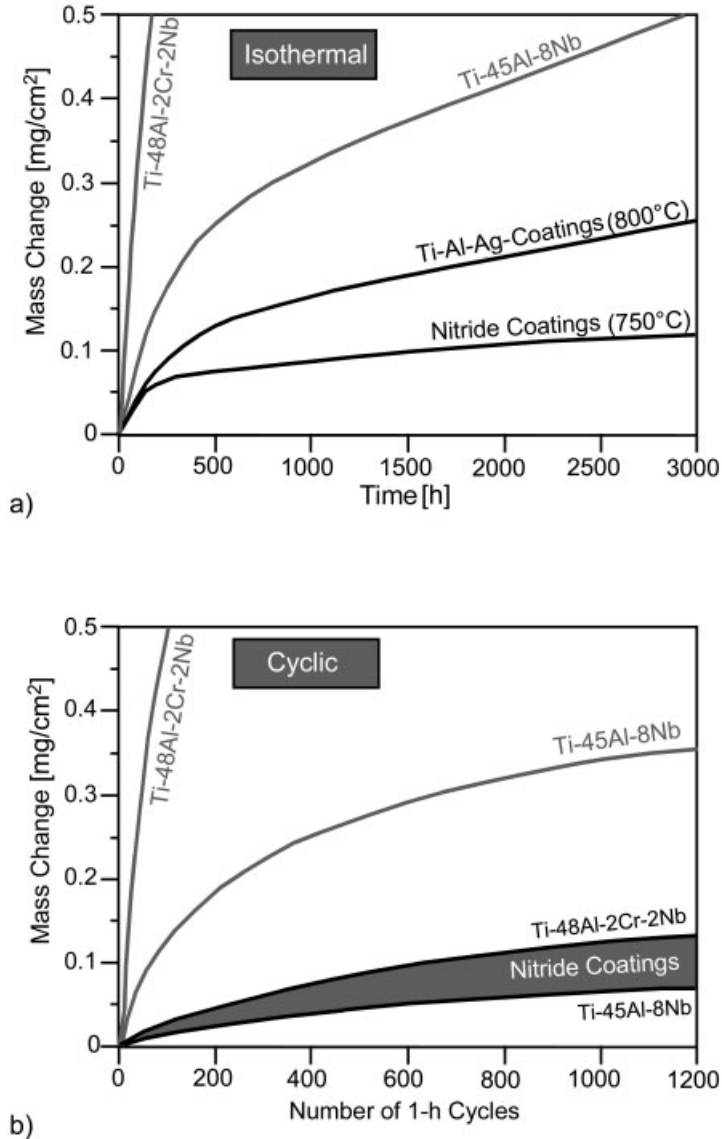
Fig. 6.20 (a) Quasi-isothermal and (b) cyclic oxidation behavior of coated and uncoated γ TiAl alloys at 750 °C.

mal conditions, TiAlCrYN coatings provide excellent protection for more than 1000 h of exposure. Even at temperatures up to 900 °C the coating systems appear to provide reasonable protection. However, mechanical tests yet have to prove the potential of these coatings for use at high temperatures in demanding applications.

In earlier studies performed on model coating systems from the binary Ti-Al system it was demonstrated that protection of the surface against oxygen/nitrogen penetration directly influences the mechanical properties of the base material. Fig. 6.21 shows significant differences of the surfaces of creep samples after testing at 600 °C in air at 250 MPa. While the bare sample is damaged by extensive
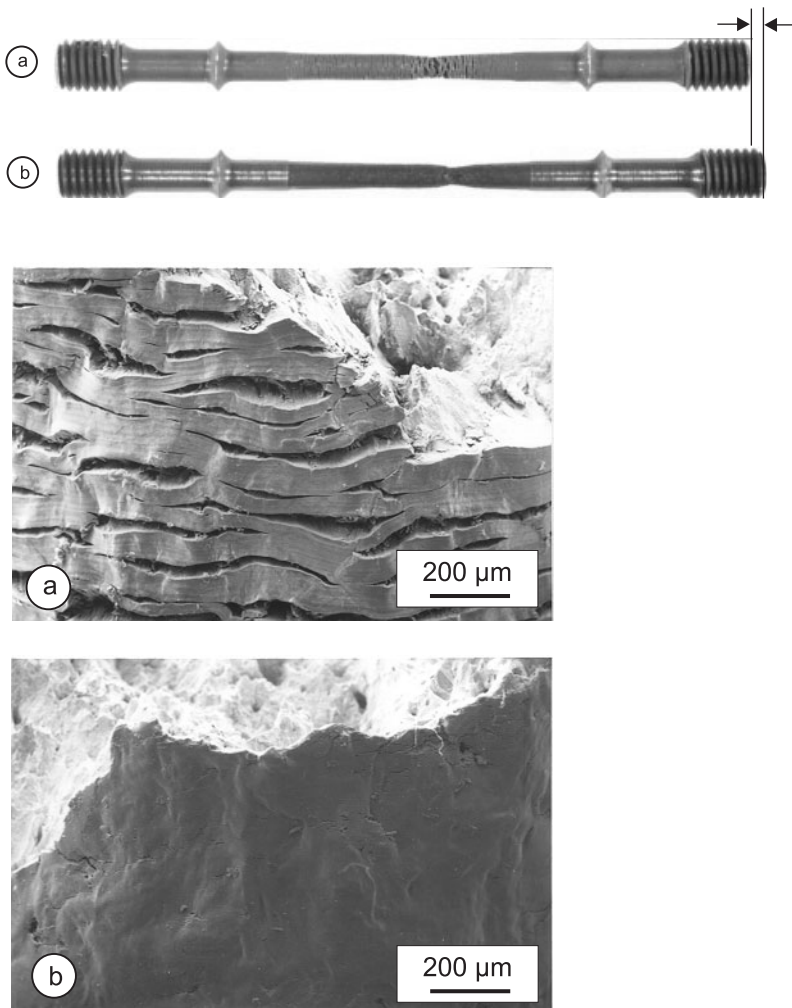
Fig. 6.21 Macrograph of TIMETAL 1100 after creep testing at 600 °C, (a) uncoated, (b) TiAl-coated.

crack formation at the embrittled surface (a) embrittlement can be avoided by the coating, which leads to a nearly crack-free surface even after extreme plastic deformation (b).

The beneficial effect of the protected surface on the mechanical properties can be directly concluded from the creep curves (Fig. 6.22 a). Unlike the uncoated reference material, the coated counterparts endured higher fracture strains and dem-
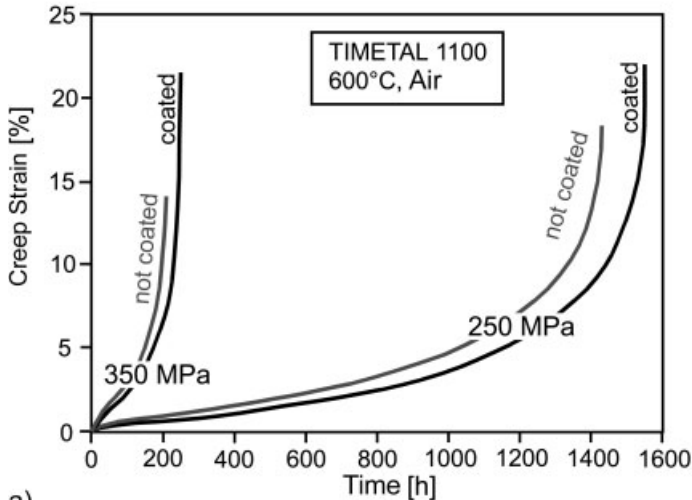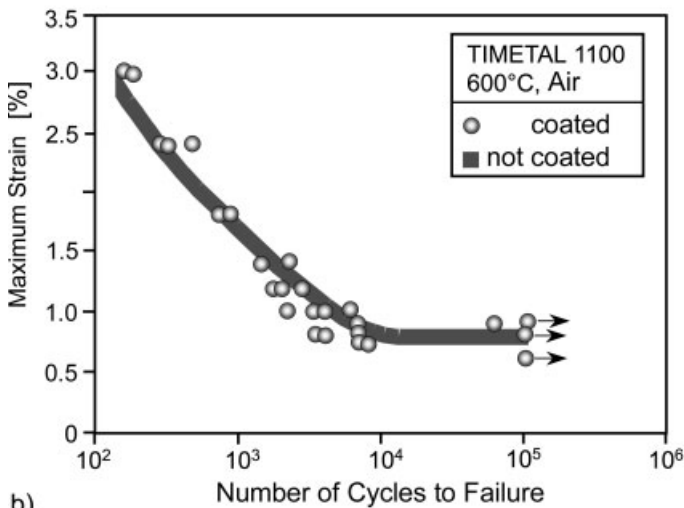
Fig. 6.22 Results of (a) creep tests at 600 °C and constant loads of 250 and 350 MPa, (b) fatigue tests at 600 °C and constant strain for uncoated and TiAl-coated TIMETAL 1100.

onstrated impressive protection under plastic deformation [74]. Moreover, protection of the surface leads to an increase in life time in the creep test by up to 20%.

Importantly, TiAl coatings were shown to have no detrimental effect on the fatigue resistance of the base metal (Fig. 6.22 b), a fact that has not yet been appreciated in earlier research and development work [75]. All newly developed coating systems must finally be tested with regard to their effect on the fatigue resistance of the base metal before they will be considered for practical use.

As a final remark, today's status of research and development in the field of protective coatings for titanium-based alloys indicates that some of these coating systems will be mature for use in modern high temperature titanium alloys and/ or titanium aluminides in the near future.

6.4
Summary and Outlook

Use of titanium alloys and titanium aluminides is limited, among other factors, by their poor environmental resistance in oxidizing atmospheres. Detailed knowledge of the oxidation and corrosion processes is required to ensure safe, long-term operation of components under various environmental conditions. Formation and growth of the oxide scales and their long-term stability, as well as embrittlement by dissolution of interstitials in the outer surface of a component are key issues to be understood. However, in order to fully use the high temperature potential of both titanium alloys and titanium aluminides, protective coatings are required. Due to the complexity of the environmental impact, current and future materials development must adopt a systems approach to optimize the properties of a material system consisting of a base material optimized for structural applications and a surface modified and optimized for environmental protection.

6.5
Referenced Literature and Further Reading

1 O. Kubaschewski and B. E. Hopkins, *Oxidation of Metals and Alloys.* 1962, London: Butterworths.

2 P. Kofstad, *Nonstoichiometry, diffusion and electric conductivity in binary metal oxides.* 1983, Malaba, Florida: R. E. Krieger Publishing Company.

3 P. Kofstad, *High Temperature Corrosion.* 1988, London, New York: Elsevier Applied Science. 558.

4 P. Kofstad, *Fundamental aspects of corrosion by hot gases.* Materials Science and Engineering, 1989. **A120**: p. 25–29.

5 P. Kofstad, *Defects and Transport Properties of Metal Oxides.* Oxidation of Metals, 1995. **44**(1/2): p. 3–27.

6 A. Rahmel, ed. *Aufbau von Oxidschichten auf Hochtemperaturwerkstoffen und ihre technische Bedeutung,* 1983, Deutsche Gesellschaft für Materialskunde e. V.: Oberursel.

7 C. Wagner, *Formation of composite scales consisting of oxides of different metals.* Journal of the Electrochemical Society, 1956. **103**(11): p. 627–633.

8 C. Wagner, *Reaktionstypen bei der Oxydation von Legierungen.* Elektrochemie, 1959. **63**: p. 772–782.

9 D. L. Douglass, *A critique of internal oxidation in alloys during the Post-Wagner era.* Oxidation of Metals, 1995. **44**(1/2): p. 81–111.

10 A. Rahmel and P. J. Spencer, *Thermodynamic Aspects of TiAl and TiSi$_2$ oxidation: The Al-Ti-O and Si-Ti-O phase diagrams.* Oxidation of Metals, 1990. **35**(1/2): p. 53–68.

11 K. L. Luthra, *Stability of Protective Oxide Films on Ti-Base Alloys.* Oxidation of Metals, 1991. **36**: p. 274–290.

12 M. Eckert, L. Bencze, D. Kath, H. Nickel and K. Hilpert, *Thermodynamic Activities in the Alloys of the Ti-Al System.* Ber. Bunsenges. Phys. Chem., 1996. **100**(4): p. 418–424.

13 N. S. Jacobson, M. P. Brady and G. M. Mehrotra, *Thermodynamics of selected Ti-Al and Ti-Al-Cr alloys.* Oxidation of Metals, 1999. **52**(5/6): p. 537–556.

14 M. Zhang, K. Hsieh, J. deKock and Y. A. Chang, *Phase diagram of Ti-Al-O at 1100°C.* Scripta Metallurgica et Materialia, 1992. **27**: p. 1361–1366.

15 X. L. Li, R. Hillel, F. Teyssandier and S. J. Chou, *Reactions and phase relations in the Ti-Al-O system.* Acta metall. mater., 1992. **40**(11): p. 3149–3157.

16 G. P. Kelkar and A. H. Carim, Journal of the American Ceramic Society, 1995. **78**(3): p. 572–576.

17 M. P. Brady, B. A. Pint, P. F. Tortorelli, I. G. Wright and R. J. Hanrahan, *High-temperature oxidation and corrosion of intermetallics,* in *Corrosion and Environmental Degradation of Materials,* M. Schütze, Editor. 2000, Wiley-VCH: Weinheim, Germany.

18 S. Becker, A. Rahmel, M. Schorr and M. Schütze, *Mechanism of isothermal oxidation of the intermetallic TiAl and of TiAl alloys.* Oxidation of Metals, 1992. **38**(5/6): p. 425–464.

19 B.-J. Lee and N. Saunders, *Thermodynamic evaluation of the Ti-Al-O ternary system.* Zeitschrift für Metallkunde, 1997. **88**: p. 152–161.

20 V. Shemet, P. Karduck, H. Hoven, B. Grushko, W. Fischer and W. J. Quadakkers, *Synthesis of the cubic Z-Phase in the Ti-Al-O system by a powder metallurgical method.* Intermetallics, 1997. **5**: p. 271–280.

21 E. H. Copland, B. Gleeson and D. J. Young, *Formation of Z-Ti$_{50}$Al$_{30}$O$_{20}$ in the sub-oxide zones of γ-TiAl-based alloys during oxidation at 1000°C.* Acta Materialia, 1999. **47**(10): p. 2937–2949.

22 N. Zheng, W. Fischer, H. Grübmeier, V. Shemet and W. J. Quadakkers, *The significance of subsurface depletion layer composition for the oxidation behavior of gamma-titanium aluminides.* Scripta Metallurgica et Materialia, 1995. **33**(1): p. 47–53.

23 S. Taniguchi, T. Shibata and S. Itoh, *Oxidation behavior of TiAl at high temperatures in purified oxygen.* Materials Transactions, 1991. **32**(2): p. 151–156.

24 T. A. Wallace, R. K. Clark, K. E. Wiedemann and S. N. Sankaran, *Oxidation characteristics of Ti-25Al-10Nb-3V-1Mo.* Oxidation of Metals, 1992. **37**: p. 111–124.

25 T. Shimizu, T. Ikubo and S. Isobe, *Cyclic Oxidation Resistance of an intermetallic compound TiAl.* Materials Science and Engineering, 1992. **A153**: p. 602–607.

26 J. S. Fish and D. J. Duquette, *Isothermal and cyclic oxidation of TiAl compounds.* in *Proc. 3rd Int. Conf. on High Temperature Corrosion and Protection of Materials.* 1993: Journal de Physique IV, Les Editions de Physique, Les Ulix Cedex, France.

27 J. Rakowski, D. Monceau, F. S. Pettit, G. H. Meier and R. A. Perkins. *The Oxidation and embrittlement of α$_2$ (Ti$_3$Al) titanium aluminides.* in *Proc. of the 2nd Int. Conf. on the Microscopy of Oxydation.* 1993: The Institute of Materials, London.

28 A. Gil, H. Hoven, E. Wallura and W. Quadakkers, *The effect of microstructure on the oxidation behavior of TiAl-based intermetallics.* Corrosion Science, 1993. **34**(4): p. 615–630.

29 C. Leyens, M. Peters and W. A. Kaysser, *Influence of Microstructure on Oxidation Behaviour of Near-Alpha Titanium Alloys.* Materials Science and Technology, 1996. **A12**: p. 213–218.

30 C. Leyens, *Environmental effects on orthorhombic alloy Ti-22Al-25Nb in air between*

*650 and 1000°C. Oxidation of Metals, 2000. **52**(5/6): p. 474–503.*

31 S. Becker, *Mechanismus der isothermen Oxidation der intermetallischen Phase TiAl und von TiAl mit Zusätzen von C, V und Nb*, 1993, RWTH Aachen: Aachen.

32 A. Rahmel, W.J. Quadakkers and M. Schütze, *Fundamentals of TiAl oxidation – a critical review*. Materials and corrosion, 1995. **46**: p. 271–285.

33 M. Schmitz-Niederau and M. Schütze, *Cracking and healing of oxide scales on Ti-Al alloys at 900°C*. Oxidation of Metals, 1999. **52**(3/4): p. 241–276.

34 M. Schütze and M. Schmitz-Niederau, *Interaction of mechanical loading and oxidation at 900°C for TiAl*. Gamma Titanium Aluminides, 1995: p. 83–92.

35 R.A. Perkins, K.T. Chiang, G.H. Meier and R. Miller, *Formation of alumina on niobium and titanium alloys*, in *Oxidation of High-Temperature Intermetallics*, T. Grobstein and J. Doychak, Editors. 1989.

36 R.A. Perkins and K.T. Chiang, *Formation of alumina of TiAl alloys*. Scripta Metallurgica, 1987. **21**: p. 1505–1510.

37 G. Welsch and A.I. Kahveci, *Oxidation behavior of titanium aluminide alloys*, in *Oxidation of High Temperature Intermetallics*, T. Gobstein and J. Doychak, Editors. 1989, The Minerals, Metals and Materials Society: Warrendale, PA. p. 207–218.

38 C. Leyens and H. Gedanitz, *Long-term oxidation of orthorhombic Alloy Ti–22Al–25Nb in Air Between 650 and 800°C*. Scripta Materialia, 1999. **41**(8): p. 901–906.

39 M.F. Stroosnijder, N. Zheng, W.J. Quadakkers, R. Hofman, A. Gil and F. Lanza, *The Effect of Niobium Ion Implantation on the Oxidation Behavior of a γ-TiAl-Based Intermetallic*. Oxidation of Metals, 1996. **46**(1/2): p. 19–35.

40 K. Hilpert, M. Albers, M. Eckert and D. Kath, *Vaporization Studies of Nickel and Titanium Aluminides*, in *Structural Intermetallics 1997*, M.V. Nathal et al., Editors. 1997, TMS: Warrendale, PA. p. 63–71.

41 G.H. Meier, D. Appalonia, R.A. Perkins and K.T. Chiang, *Oxidation of Ti-base alloys*, in *Oxidation of High-Temperature Intermetallics*. 1989. p. 185–193.

42 J.M. Rakowski, F.S. Pettit, G.H. Meier, F. Dettenwanger, E. Schumann and M. Rühle, *The Effect of Nitrogen on the Oxidation of γ-TiAl*. Scripta Materialia, 1996. **33**(6): p. 997–1003.

43 N. Zheng, W.J. Quadakkers, A. Gil and H. Nickel, *Studies Concerning the Effect of Nitrogen on the Oxidation Behavior of Ti-Al Based Intermetallics at 900°C*. Oxidation of Metals, 1995. **44**: p. 477–499.

44 W.J. Quadakkers, P. Schaaf and N. Zheng, *Beneficial and Detrimental Effects of Nitrogen on the Oxidation Behaviour of TiAl-based Intermetallics*. Materials and Corrosion, 1997. **48**: p. 28–34.

45 J.R. Nicholls, J. Leggett and P. Andrews, *Hot salt corrosion of titanium aluminides*. Materials and Corrosion, 1997. **48**: p. 56–64.

46 S. Yamaguchi, *Interstitial order-disorder transformation in the Ti-O solid solution. I. ordered arrangements of oxygen*. Journal Physical Soc. Japan, 1969: p. 155–163.

47 J.-P. Bars, D. David, E. Etchessahar and J. Debuigne, *Titanium alpha-Nitrogen solid solution formed by high temperature nitriding: diffusion of Nitrogen, hardness and crystallographic parameters*. Metallurgical Transactions A, 1983. **14A**: p. 1537–1543.

48 L. Gauer, S. Alperine, P. Steinmetz and A. Vassel, *Influence of Niobium Additions on High-Temperature Oxidation Behavior of Ti₃Al Alloys and Coatings*. Oxidation of Metals, 1994. **42**(1/2): p. 49–74.

49 Y. Shida and H. Anada, *The effect of various ternary additives on the oxidation behavior of TiAl in high temperature air*. Oxidation of Metals, 1996. **45**(1/2): p. 197–218.

50 Y. Shida and H. Anada, *Role of W, Mo, Nb, and Si on oxidation of TiAl on air at high temperatures*. Materials Transactions, 1994. **35**(9): p. 623–631.

51 D.A. Berztiss, *Oxidation of intermetallics: molybdenum disilicide, titanium aluminum chromium alloys and nickel aluminide*, 1996, University of Pittsburgh: Pittsburgh.

52 L.J. Parfitt, J.L. Smialek, J.P. Nic and D.E. Mikkola, *Oxidation behavior of cu-*

bic phases formed by Al₃Ti with Cr and Mn. Scripta Metallurgica et Materialia, 1991. **25**: p. 727–731.

53 M. P. Brady and J. L. Smialek, *Modification of microstructure for improved oxidation resistance in g-based Ti-Al-X alloys*. Materials and Manufacturing Processes, 1996. **11**(4): p. 635–653.

54 J. C. Schaeffer, C. M. Austin and F. Kaempf, *Effect of alloying on the environmental resistance of cast gamma alloys*. Gamma Titanium Aluminides, 1995: p. 71–82.

55 G. Schumacher, C. Lang, M. Schütze, U. Hornauer, E. Richter, E. Wieser and W. Möller, *Improvement of the oxidation resistance of gamma titanium aluminides by microalloying with chorine using ion implantation*. Materials and Corrosion, 1999. **50**: p. 162–165.

56 G. Schumacher, F. Dettenwanger, M. Schütze, U. Hornauer, E. Richter, E. Wieser and W. Möller, *Microalloying Effects in the Oxidation of TiAl Alloys*. Intermetallics, 1999. **7**: p. 1113–1120.

57 G. Schumacher, F. Dettenwanger, M. Schütze, A. Iberl and D. Reil, *XRD investigations of the phosphorous effect on the oxidation of TiAl alloys by high-resolution methods*. Oxidation of Metals, 2000. **54**(3/4): p. 317–337.

58 M. Schütze and M. Hald, *Improvement of the Oxidation Resistance of TiAl Alloys by Using the Chlorine Effect*. Materials Science and Engineering, 1997. **A240**: p. 847–858.

59 M. Schütze, G. Schumacher, F. Dettenwanger, U. Hornauer, E. Richter, E. Wieser and W. Möller, *The halogen effect in the oxidation of intermetallic titanium aluminides*. Corrosion Science, 2002. **44**(2): p. 303–318.

60 S. Taniguchi, T. Shibata, A. Murakami and K. Chiahra, *Improvement in the oxidation resistance of TiAl by preoxidation in a Cr₂O₃ powder pack*. Materials Transactions, 1994. **35**(9): p. 616–622.

61 S. Taniguchi, T. Shibata and S. Sakon, *Improvement in oxidation of TiAl by preoxidation at 1200 K in a pack mixture of Cr₂O₃ and Cr powders*. Zairyo-to-Kankyo, 1992. **41**: p. 453–460.

62 S. Taniguchi, T. Shibata, A. Murakami and K. Chihara, *Improvement in the oxidation resistance of TiAl by preoxidation in a TiO₂-powder pack*. Oxidation of Metals, 1994. **42**(1/2): p. 17–29.

63 S. Taniguchi and T. Shibata, *Improvement in the oxidation resistance of TiAl by preoxidation in a TiO₂-powder pack*. Oxidation of Metals, 1994. **41**: p. 103–113.

64 T. Suzuki, M. Goto, M. Yoshihara and R. Tanaka, *Improvement in oxidation resistance of the Ti-31 ∼39 mass% Al alloys by heat treatment under a low partial pressure oxygen atmosphere*. Materials Transactions, 1991. **32**(11): p. 1017–1023.

65 J. K. Tien, J. C. Chesnutt, D. H. Boone and C. W. Goward, *Metallurgy of Nickel-base coatings on Titanium alloys*, in *Titanium Science and Technology*, R. I. Jaffee and H. M. Burte, Editors. 1973, Plenum Press: New York. p. 2517–2525.

66 S. Fujishiro and D. Eylon. *Improved mechanical properties of α+β Ti alloys by Pt ion plating*. in *Titanium*. 1980.

67 S. Fujishiro and D. Eylon, *Improved high temperature mechanical properties of titanium alloys by platinum ion plating*. Thin Solid Films, 1978. **54**: p. 309–315.

68 T. Eckler, B. Manty and S. Fujishiro. *Evaluation of ion-plated coatings on titanium alloys*. in *IPAT '70*. 1979. London.

69 S. Fujishiro and D. Eylon, *Improvement of Ti alloy fatigue properties by Pt ion plating*. Metallurgical Transactions A, 1980. **11A**(8): p. 1259–1263.

70 M. A. Daeubler and D. Helm. *Surfaces and Elevated Temperature Effects*. in *Titanium '92, Science and Technology*. 1992: The Minerals, Metals and Materials Society, Warrendale, PA, USA.

71 B. Cockeram and R. A. Rapp, *Isothermal and cyclic oxidation resistance of boron-modified and germanium-doped silicide coatings for titanium alloys*. Oxidation of Metals, 1996. **45**(5/6): p. 427–467.

72 L. Niewolak, V. Shemet, A. Gil, L. Singheiser and W. J. Quadakkers, *Alumina-forming coatings for titanium and titanium aluminides*. Advanced Engineering Materials, 2001. **3**(7): p. 496–500.

73 C. Leyens, M. Peters, P. E. Hovsepian, D. B. Lewis, Q. Luo and W.-D. Münz. *Advanced nitride coatings for oxidation pro-*

tection of titanium alloys. in *Materials for Advanced Power Engineering*. 2002

74 C. Leyens, M. Peters and W. A. Kaysser, *Influence of Intermetallic Ti-Al Coatings on the Creep Properties of TIMETAL 1100*. Scripta Materialia, 1996. **35**(12): p. 1423–1428.

75 C. Leyens, K.-H. Trautmann, M. Peters and W. A. Kaysser, *Influence of Intermetallic Ti-Al Coatings on the Fatigue Properties of TIMETAL 1100*. Scripta Materialia, 1997. **36**(11): p. 1309–1314.

76 J. Doychak, *Oxidation Behavior of High-Temperature Intermetallics*, in *Intermetallic Compounds*, J. H. Westbrook and R. L. Fleischer, Editors. 1994, John Wiley & Sons: New York. p. 977–1016.

77 A. M. Chaze, G. Béranger and C. Coddet, *A comparison of the influence of Si, Al and Cr additions on the high temperature oxidation behaviour of Titanium*, in *Titanium-Science and Technology*, G. Lütjering, U. Zwicker, and W. Bunk, Editors. 1985, DGM: Oberursel. p. 2665–2672.

78 A. M. Chaze and C. Coddet, *Influence of the nature of alloying elements on the adherence of Oxide films formed on Titanium alloys*. Oxidation of Metals, 1987. **28**(1/2): p. 61–71.

79 T. J. Johnson, M. H. Loretto and M. W. Kearns. *Oxidation of high temperature Titanium alloys*. in *Titanium '92, Science and Technology*. 1993: TMS, Warrendale, PA.

80 T. J. Johnson, M. H. Loretto, C. M. Younes and M. W. Kearns. *A study of the role of alloying additions during the high temperature oxidation of IMI 834*. in *Second International Conference on the Microscopy of Oxidation*. 1993.

81 A. M. Chaze, C. Coddet and G. Beranger. *Dissolution of Oxygen in the metallic phase during high temperature oxidation of Titanium and some alloys*. in *Sixth World Conference on Titanium*. 1988. France.

82 H. Chuanxi and L. Bingnan. *Effect of Nb and W on mechanical properties and oxidation resistance of high temperature Titanium alloys*. in *Titanium*. 1992.

83 S. Fujishiro and D. Eylon, *Effect of Environment and Coating on the Creep Behavior of Commercial Ti Alloys*. Scripta Met., 1977. **11**: p. 1011–1016.

84 S. Fujishiro and D. Eylon, *Effect of Pt ion plating on the creep behavior of alpha-Ti*. Scripta Metallurgica, 1979. **13**: p. 201–203.

85 S. Fujishiro, D. Eylon and R. W. Gehring, *Creep Property improvement of $\alpha + \beta$ Titanium Alloys by Platinum Ion Plating*. Thin Solid Films, 1979. **63**: p. 55–60.

86 A. Abba, A. Galerie and M. Caillet, *High temperature oxidation of titanium silicide coatings on titanium*. Oxidation of Metals, 1981. **17**(1): p. 43–54.

87 A. Galerie and G. Dearnaley, *Production of Ti-Si Surface Alloys on Titanium by Ion Beam Mixing, and their Oxidation Behaviour*. Materials Science and Engineering, 1985. **69**: p. 381–390.

88 J. Unnam, R. N. Shenoy, K. E. Wiedemann and R. K. Clark. *Use of aluminum as an oxidation barrier for titanium*. in *30th. Nat. SAMPE Symposium and Exhibition*. 1985. Anaheim.

89 D. Eylon, S. Fujishiro and R. W. Gehring. *Improved creep resistance of titanium alloy tubular sections by platinum ion plating*. in *Fifth International Conference on Titanium*. 1984. Munich.

90 J. Subrahmanyam and J. Annapurna, *High temperature cyclic oxidation of Aluminide layers on Titanium*. Oxidation of Metals, 1986. **26**(3/4): p. 275–285.

91 R. K. Clark, J. Unnam and K. E. Wiedemann, *Effect of coatings on oxidation of Ti-6Al-2Sn-4Zr-2-Mo foil*. Oxidation of Metals, 1987. **28**(5/6): p. 391–405.

92 H. Matsumoto, N. Kamio and T. Sugimoto. *Alumina coating on titanium by plasma spraying*. in *6th World Conference on Titanium*. 1988. France.

93 J. Subrahmanyam, *Cyclic oxidation of aluminized Ti-14Al-24Nb alloy*. Journal of Materials Science, 1988. **23**: p. 1906–1910.

94 J. Guille, L. Matini and A. Clauss. *Obtaining silicide coatings on titanium by pack-cementation*. in *Fifth International Conference on Titanium*. 1984. Munich.

95 N. W. Kearns and J. E. Restall. *Oxidation Resistant Coatings for Titanium Alloys*. in *Sixth World Conference on Titanium*. 1988: Les Editions de Physique, Les Ulis Cedex, France.

96 C. Indrigo, S. Naka and R. Mévrel. *High temperature oxidation resistance of sputter-deposited Ti-Si coatings.* in *IPAT 89 – Ion and Plasma Assisted Techniques.* 1989.

97 R. Suchentrunk, M. Meyer and H. Schweinberger. *Beschichtung von Titanwekstoffen durch kombinierte Oberflächentechniken.* in *Surtec '98.* 1989. Berlin.

98 M. Meyer and R. Suchentrunck. *High temperature oxidation barriers on Titanium- the oxidation behavior of thin sputtered NiCr-, SiC-, Si$_3$N$_4$ and Al-layers.* in *IPAT '89, 7th International Conference.* 1989.

99 K. E. Wiedemann, P. J. Taylor, R. K. Clark and T. A. Wallace, *Thin coatings for protecting titanium aluminides in high temperature oxidizing environments.* Environmental Effects on Advanced Materials, 1991: p. 108–121.

100 H. Mabuchi, T. Asai and Y. Nakayama, *Aluminide Coatings on TiAl Compound.* Scripta Metallurgica, 1989. **23**: p. 685–689.

101 A. Galerie. *Ion Beam Assisted Deposition of Chromium Oxide Coatings on Ti–685 Alloy and their Oxidation Behaviour.* in *IPAT 98 – Ion and Plasma Assisted Techniques.* 1989. Gent.

102 J. L. Smialek, M. A. Gedwill and P. K. Brindley, *Cyclic Oxidation of Aluminide Coatings on Ti$_3$Al + Nb.* Scripta Metallurgica et Materialia, 1990. **24**: p. 1291–1296.

103 S. Kung, *High temperature coating for titanium aluminides using the pack-cementation technique.* Oxidation of Metals, 1990. **34**(3/4): p. 217–228.

104 R. C. McCune and S. W. Choi. *A comparison of several surface treatments for minimizing oxygen diffusion in b-processed titanium–6242 at 800 °C.* in *17th International Conference and 8th International Conference on thin films.* 1990. San Diego, CA.

105 P. Grahle, B. Heine and E. Fromm, *Schutzschichten für Ti$_3$Al gegen Hochtemperaturoxidation.* Werkstoffe und Korrosion, 1991. **42**: p. 12–18.

106 C. J. Bedell, H. E. Bishop, G. Dearnaly, J. W. Desport, H. Romary and J.-M. Romary, *Oxidation-resistant coatings on titanium alloys by ion beam assisted deposi-*

tion. Nuclear Instruments and Methods in Physics Research, Section B, 1991. **59–60**(1): p. 245–248.

107 B. G. McMordie and A. K. Isaacs. *Slurry aluminide coating processes for gas turbine components at overhaul.* in *The Annual Gas Turbine Conference and Exhibition.* 1991. Harrogate, UK.

108 B. G. McMordie, *Oxidation resistance of slurry aluminides on high temperature titanium alloys.* Surface and Coatings Technology, 1991. **49**: p. 18–23.

109 J. Covino and K. Klemm, *Coatings for hypersonic applications.* Materials Performance, 1991. **30**(5): p. 75–79.

110 S. Taniguchi, T. Shibata and K. Takeuchi, *Protectiveness of a CVD-Al$_2$O$_3$ Film on TiAl Intermetallic Compound against High-Temperature Oxidation.* Materials Transactions, 1991. **32**: p. 299–301.

111 H. Benien, M. Meyer and R. Suchentrunk, *D. C. magnetron sputtering of oxidation-resistant chromium and ArN films monitored by optical emission spectrometry.* Materials Science and Engineering, 1991. **A139**: p. 126–131.

112 M. Yoshimura, W. Urushihara, M. Yashima and M. Kakihana. *Titanate film coating on TiAl by solvothermal processing.* in *3rd Japan International SAMPE Symposium.* 1993.

113 D. W. McKee and K. L. Luthera, *Plasma-sprayed coatings for titanium alloy oxidation protection.* Surface and Coatings Technology, 1993. **56**(2): p. 109–117.

114 M. Meyer, R. Suchentrunk and H. Franz. *Sputter ion plating on Ti6Al4V and Ti (cp) – preparation and properties of oxidation and wear resistant coatings.* in *Titanium.* 1992.

115 R. L. McCarron, J. C. Schaeffer, G. H. Meier, D. Berztiss, R. A. Perkins and J. Cullinan, *Protective Coatings for Titanium Aluminide Intermetallics,* in *Titanium '92 – Science and Technology,* F. H. Froes and I. Caplan, Editors. 1992, TMS: Warrendale, PA. p. 1971–1978.

116 K. E. Wiedemann, R. K. Bird, T. A. Wallace and R. K. Clark. *Mechanical properties of coated titanium beta–21S after exposures to air at 700 and 800°C.* in *Titanium.* 1992.

117 S. Taniguchi, T. Shibata, N. Asanuma and H. Luo, *Oxidation resistance of TiAl improved by a CoCrAl coating.* Journal de Physique IV, 1993. **3**(12): p. 403–410.

118 S. Taniguchi, A. N, T. Shibata, F. Wang, H. Lou and W. Wu, *Oxidation resistance of TiAl improved by CoCrAl and CoCrAlY coating.* Japan Institute of Materials, 1993. **57**(7): p. 781–789.

119 J. L. Smialek, *Oxidation behavior of TiAl₃ coating and alloys.* Corrosion Science, 1993 (5–8): p. 1199–1209.

120 D. W. McKee. *Oxidation and protection of Ti₃Al based intermetallic alloys.* in *Mat. Res. Soc. Symp.* 1993.

121 S.-K. Wu and R. Y. Lin. *Coating of SiC on titanium aluminide.* in *Mat. Res. Soc. Symp.* 1993.

122 S. Taniguchi, T. Shibata, T. Yamada, X. Liu and S. Zou, *High temperature oxidation resistance of TiAl improved by IBED Si₃N₄ coating.* ISIJ International, 1993. **33**(8): p. 869–876.

123 C. Leyens, M. Peters and W. A. Kaysser. *Oxidationsverhalten von IMI 834 und TIMETAL 1100 und deren Schutz durch Coatings.* in *DLR-Werkstoff-Kolloquium '94.* 1994. Köln: DLR, Institut für Werkstoff-Forschung.

124 H. L. Du, P. K. Datta and J. S. Burnell-Gray, *Effect of Nb coating on the sulphidation/oxidation behavior of Ti and Ti–6Al–4V alloy.* Journal of Materials Science, 1995. **30**: p. 2640–2647.

125 M. Li, A. Kar, V. Desai and A. Khanna, *High temperature oxidation of titanium using laser surface alloying.* Journal of Materials Science, 1995. **30**: p. 5093–5098.

126 A. Gil, B. Rajchel and N. Zheng, *The influence of implanted chromium and yttrium on the oxidation behavior of TiAl-based intermetallics.* 1995.

127 H. Inoue, N. Sasaki and Y. Omori. *Oxidation behavior of the aluminum-yttrium coating layer on a titanium-aluminum alloy at elevated temperatures.* in *Advanced Materials '93.* 1993.

128 H. L. Du, P. K. Datta, D. B. Lewis and J. S. Burnell-Gray, *Enhancement of oxidation/sulphidation resistance of Ti and Ti–6Al–4V alloy by HfN coating.* Materials Science and Engineering A, 1996. **A205**: p. 199–208.

129 T. C. Munro and G. B., *The Deposition of Aluminide and Silicide Coatings on γ-TiAl Using the Halide-Activated Pack Cementation Method.* Metallurgical and Materials Transactions, 1996. **27A**: p. 3761–3772.

130 C. Leyens, *Oxidationsverhalten und Oxidationsschutz von Titanlegierungen für den Hochtemperatureinsatz in Flugtriebwerken.* Dissertation RWTH Aachen. 1997, Aachen: Verlag Shaker, p.113.

131 Z. Tang, F. Wang and W. Wu, *Improvement of Oxidation Resistance of Titanium Aluminide Intermetallics by Coatings,* in *Structural Intermetallics 1997,* M. V. Nathal, et al., Editors. 1997, TMS: Warrendale, PA. p. 341–346.

132 M. J. Bennett and S. J. Bull, *Coatings of Titanium Aluminides by FeCrAlY Coatings.* Materials and Corrosion, 1997. **48**: p. 48–55.

133 B. D. Prasad, S. N. Sankaran, K. E. Wiedemann and D. E. Glass, *Multilayer coating for protection of titanium aluminides from oxidation and hydrogen embrittlement,* in *Structural Intermetallics 1997,* M. V. Nathal, et al., Editors. 1997, TMS: Warrendale. p. 295–303.

134 C. Leyens, J.-W. van Liere, M. Peters and W. A. Kaysser, *Magnetron-Sputtered Ti-Cr-Al Coatings for Oxidation Protection of Titanium Alloys.* Surface and Coatings Technology, 1998. **108–109**: p. 30-35.

135 E. Lugscheider, C. Siry and S. R. J. Suanders, *The Behaviour of PVD SiAlN-Type Coatings Deposited on γ-TiAl,* in *Advanced Materials for Power Engineering,* J. Lecomte-Beckers, F. Schubert, and P. J. Ennis, Editors. 1998, Forschungszentrum Jülich. p. 1319–1327.

136 M. P. Brady, J. L. Smialek and W. J. Brindley, *Two-Phase (TiAl + TiAlCr) Coating Alloys for Titanium Aluminides,* 1998: USA.

137 T. D. Wood, D. K. Dewald and D. E. Mikkola. *High Cycle Fatigue Behavior of Ti-47Al-2Cr-2Nb and Ti-6242S with (Al,Cr)₃Ti Plasma Spray Protective Coatings.* in *Surface Modification Technologies 12.* 1998. Rosemont, IL: ASM International.

138 Z. Tang, F. Wang and W. Gao, *The effects of several coatings on cyclic oxidation resistance of TiAl intermetallics.* Surface

and Coatings Technology, 1998. **108–109**: p. 57–61.

139 T. Kawakami, H. Mabuchi, H. Tsuda, T. Matsui and K. Morii, *Oxidation Resistant Coating of L1₂-(Al, Cr)₃Ti on TiAl Alloys by Pack Cementation.* Materials Transactions, JIM, 1999. **40**(5): p. 381–384.

140 H. Mabuchi, H. Tsuda, T. Kawakami, S. Nakamatsu, T. Matsui and K. Morii, *Oxidation-resistant coating for gamma titanium aluminides by pack cementation.* Scripta Materialia, 1999. **41**(5): p. 511–516.

141 H. N. Lee, Z. M. Park, M. H. Oh, K. Y. Kim and D. M. Wee, *Oxidation behavior and mechanical properties of yttrium-doped L12 (Al,Cr)₃Ti coating on TiAl alloys.* Scripta Materialia, 1999. **41**(10): p. 1073–1078.

142 Z. Tang, F. Wang and W. Wu, *Effect of Al₂O₃ and enamel coatings on 900°C oxidation and hot corrosion behaviors of gamma-TiAl.* Materials Science and Engineering, 2000. **A276**: p. 70–75.

143 U. Hornauer, R. Günzel, H. Reuther, E. Richter, E. Wieser, W. Möller, G. Schumacher, F. Dettenwanger and M. Schütze, *Protection of γ-based TiAl against high temperature oxidation using ion implantation of chlorine.* Surface and coatings technology, 2000. **125**: p. 89–93.

144 S. Gong, H. Xu, Q. Yu and C. Zhou, *Oxidation behaviour of TiAl/TiAl-SiC gra-dient coatings on gamma titanium aluminides.* Surface and Coatings Technology, 2000. **130**: p. 128–132.

145 C. Zhou, H. Xu, S. Gong, Y. Yang and K. Y. Kim, *A study on aluminide and Cr-modified aluminide coatings on TiAl alloys by pack cementation method.* Surface and Coatings Technology, 2000. **132**: p. 117–123.

146 U. Hornauer, E. Richter, W. Matz, H. Reuther, A. Mücklich, E. Wieser, W. Möller, G. Schumacher and M. Schütze, *Microstructure and Oxidation Kinetics of Intermetallic TiAl after Si- and Mo-Ion Implantation.* Surface and Coatings Technology, 2000: p. 418–422.

147 X. Y. Li, S. Taniguchi, Y.-C. Zhu, K. Fujita, N. Iwamoto, Y. Matsunaga and K. Nakagawa, *Oxidation behavior of TiAl protected by Si+Nb combined ion implantation.* Intermetallics, 2001. **9**(5): p. 443–449.

148 M.-R. Yang and S. K. Wu, *The improvement of high-temperature oxidation of Ti-50Al by anodic coating in the phosphoric acid.* Acta Materialia, 2002. **50**(4): p. 691–701.

149 J. L. Smialek, J. A. Nesbitt, W. J. Brindley, M. P. Brady and J. Doychak. *Service Limitations for Oxidation Resistant Intermetallic Compounds.* in *Mat. Res. Soc. Symp. Proc.* 1995: Materials Research Society.

7
Titanium and Titanium Alloys –
From Raw Material to Semi-finished Products

H. Sibum, *Deutsche Titan GmbH, Essen, Germany*

7.1
Introduction

With a total of 0.6%, titanium ranks fourth among metals, behind iron, aluminum, and magnesium, and ninth among all elements in the Earth's crust. However, even today it has not yet lost the air of an exotic and expensive material.

The majority of titanium is used as oxide (about 95%) in the paint industry as whitener or filler material. Not many people are aware of the fact that titanium as oxide is part of everyday life, e.g. in toothpaste, white paint, sun blockers, etc.

The main reason behind the late use of titanium as a metal is the difficult and costly reduction of oxide to metal.

7.2
Titanium Sponge

As already mentioned, titanium deposits are enormous; today's estimates assume a worldwide reserve of 650 billion metric tons of titanium oxide. Fig. 7.1 shows an overview of the global distribution of the deposits. Titanium oxide is part of almost all minerals, sands, and rock. However, mainly rutile (TiO_2) and ilmenite ($FeTiO_3$) are considered for use. Deposits suitable for mining can be found in Australia, South Africa, Canada, Norway, and Ukraine. Recently, new deposits have been developed in northeast Russia and Kazakhstan.

After pre-cleaning and initial enrichment at the deposits, particularly inexpensive ilmenite is separated from iron using a metallurgical process, enriching the slag to the point where a concentration comparable to rutile can be achieved. Tab. 7.1 compares the composition of rutile and titanium slag from different sources. Both ilmenite and rutile are reduced to metallic titanium using the extended "Kroll process" (Fig. 7.2).

Introduced at the end of the 1940s, this reduction process is the only one that has survived for economic reasons. Of particular importance is the intermediate step where titanium oxide is transformed into titanium tetrachloride. Magnesium is used for final reduction. The magnesium chloride formed by this reaction is
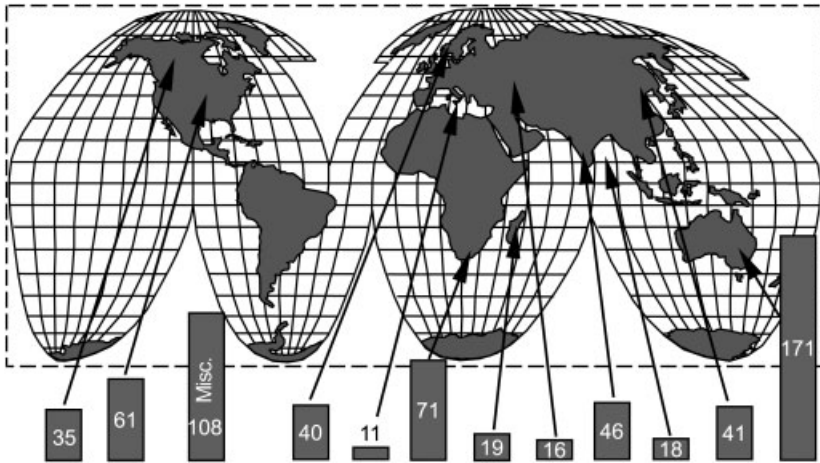
Fig. 7.1 Distribution of global titanium oxide deposits (in billions of metric tons, 1999).

Tab. 7.1a Composition of several titanium slags.

		TiO_2	FeO	SiO_2	Al_2O_3	MnO	MgO	CaO
Canada	Sorel slag	80	9	2.4	2.9	0.25	5	0.6
South Africa	UGS	95	1.2	2	0.6	0.05	0.6	0.14
Norway	Namakwa	86	10	1.8	1.4	1.7	0.7	0.16
	Richards Bay	85	11	2.1	1.3	1.7	1.1	0.17
	Sulfate	75	7.6	5.3	1.2		7.9	
	Chloride	85	10	1.8	1.2		0.7	

Tab. 7.1b Examples of rutile compositions.

		TiO_2	Fe_2O_3	SiO_2	MnO	MgO	CaO
Australia	BHP	96.0–96.5	0.50–0.80	0.60–0.90		0.08–0.14	0.01–0.06
South Africa	Cable Sands	95.5	0.8	0.60	0.03	0.03	0.04
USA	Namakwa	94.5		2.0	<0.01	0.05	0.12
	Richards Bay	95.0		1.4	0.50	0.05	0.05
	RGC Min. Sands	94.2		0.4			

Source: TZMI Mineral Sands Annual Review 1998

subsequently electrolytically reduced to magnesium and chlorine, which are re-cycled back into the process (Fig. 7.2).

High purity titanium tetrachloride is obtained by multiple condensation and fractionating steps. Final purity of the sponge is determined by the contamination
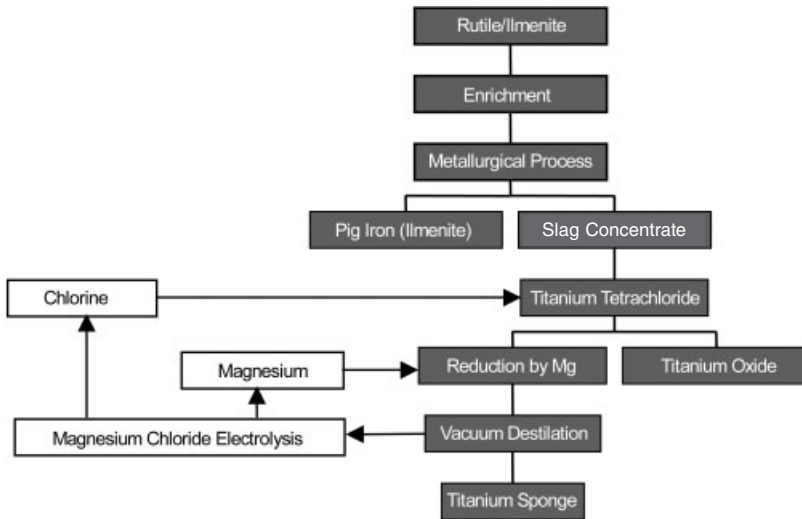
Fig. 7.2 Extended Kroll process for titanium sponge production.
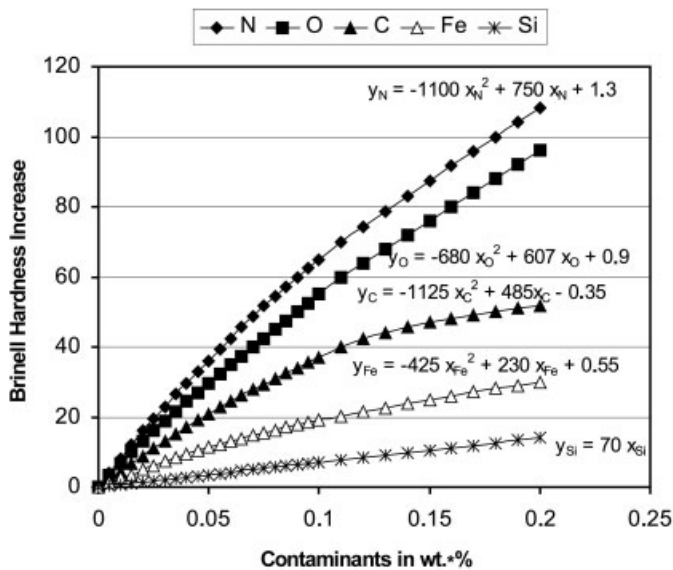
Fig. 7.3 Effect of residual contaminants on the Brinell hardness of titanium.

level of the magnesium (mainly oxygen) and by reaction with the reactor walls (mainly iron). The effect of different contaminant levels on the Brinell hardness is shown in Fig. 7.3. The final product of the reduction process is titanium sponge (Fig. 7.4).

Fig. 7.4 Titanium sponge as a raw material for titanium and titanium alloy production as well as an alloying addition for steel.

Major producers of titanium sponge can be found in the countries of the former Soviet Union, Japan and the USA, and cover the current worldwide titanium sponge requirement.

According to thermodynamic calculations, alternative processes for direct reduction of titanium oxide to metal (e.g. by electrolytic processes) are believed to be less expensive than the Kroll process. However, the feasibility of alternative processing routes has only been demonstrated on a laboratory scale and not yet in large-scale production.

7.3
From Sponge to Ingot

Along with a certain portion of secondary raw materials, titanium sponge is the base material for production of all titanium-based semi-finished products as well as for alloying additions to titanium-stabilized special steels.

Multiple re-melting is necessary due to the remaining contaminants from the magnesium reduction process, the morphology of the sponge, and adjustment of the final alloy composition. Volatile contaminants (e.g. chlorides) can be removed by the repeated melting process. Depending on the specific melting process, castings, ingots and slabs can be produced with a homogeneity required for further processing.

In a first step, the titanium sponge (density 1.2–3 g cm^{-3}) is pre-densified in a hydraulic press. These compacts are then assembled to an electrode for the melting process. In order to obtain specific alloy compositions, the compacts are adequately alloyed with pre-alloys or elements. Furthermore, small-piece scrap metal can be added to the compacts.

Due to the high oxygen affinity of titanium, the compacts must be welded in a plasma-welding chamber at low-pressure argon to an electrode. Electrodes of 13 tons maximum can be welded.
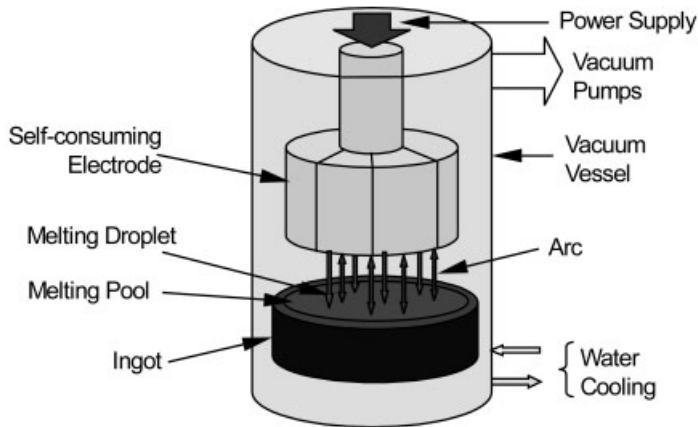
Fig. 7.5 Sketch of a vacuum arc melter.

In the classic case, the electrodes are then at least double re-melted in a vacuum arc furnace. Fig. 7.5 shows a sketch of such a furnace. Between the electrode and some swarf placed on the water-cooled bottom of the crucible, an arc is ignited. Due to the high energy of the arc, the self-consuming electrode is melted and forms an ingot in the crucible. The complete process is run in vacuum. The melting temperature is computer-controlled and, as usual for materials for critical applications, process parameters are stored for decades. Fig. 7.6 shows a vacuum arc furnace (VAR) in service.

Figures 7.7 and 7.8 show sketches of further developments in melting technologies. These processes are mainly used for melting scrap material (up to 100%).

Fig. 7.6 Vacuum arc melter in service.
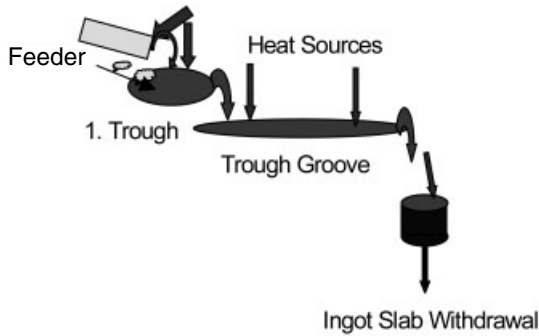
Fig. 7.7 Sketch of a cold hearth melter. Electron beam
guns or plasma sources are used as heat sources.
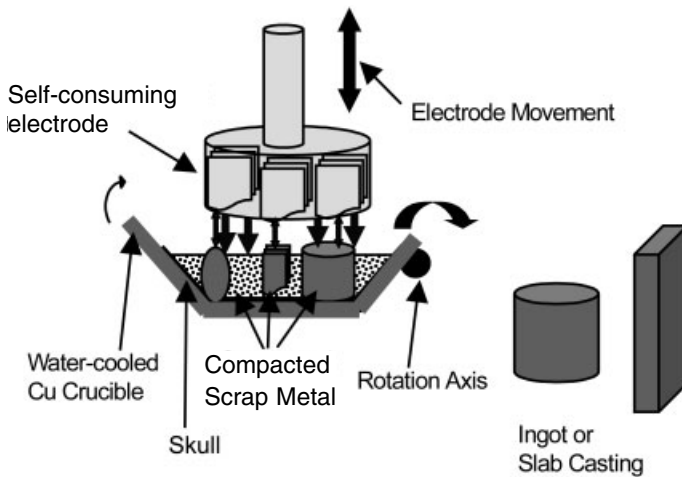
Fig. 7.8 Sketch of a skull melter.

Furthermore, slab-shape formats can be easily produced by these methods. Typical heat sources are electron and plasma guns (EB-CHM = *e*lectron *b*eam-*c*old *h*earth *m*elting or Plasma-CHM = plasma-*c*old *h*earth *m*elting) or, as used for skull melters, classic arc technology. For critical applications (e.g. premium quality or disk quality in aerospace), final re-melting must be performed in a vacuum arc furnace.

7.4
Titanium, Titanium Alloys and Special Alloys

Since high purity titanium has poor strength and is hence not used for industrial applications, the alloy composition desired is set during manufacture of the electrodes. Pure titanium is alloyed by small and well-defined amounts of oxygen (in-

terstitial element), while titanium alloys rely on the addition of substitutional elements such as aluminum, vanadium, zinc, molybdenum, zirconium, etc. Depending on the objectives, these elements stabilize the different titanium phases. Aluminum is the most important alloying element, stabilizing titanium's α phase. The α-stabilizers and their relative ability to stabilize the α phase, expressed as an aluminum equivalence, are summarized in Fig. 7.9. Molybdenum has analogous significance for the β phase. Since this topic has already been discussed in more detail in Chapter 1, only a few properties of pure titanium and some titanium alloys are summarized here (Tab. 7.2 and Tab. 7.3).

In the following, some of the advantages of titanium alloys and their applications will be discussed. Fig. 7.10 displays the range of applications and the relevant alloying elements for mechanical and physical properties.

In summary, the major advantages of titanium and its alloys are:

- high/highest corrosion resistance
- good oxidation resistance at T < 600 °C
- low density

Tab. 7.2 Effect of chemical composition on the mechanical properties of titanium alloys.

DTG-brand TIKRUTAN®	Fe_{max} [wt.%]	O_{max} [wt.%]	YS [MPa]	UTS [MPa]	%El	%RA
RT 12 (Pd)	0.20	0.10	180	290–410	30	35
RT 15 (Pd)	0.25	0.20	250	390–540	22	30
RT 18 (Pd)	0.30	0.25	320	460–590	18	30
RT 20	0.35	0.30	390	540–740	16	25
LT 27 (Ti-0.8Ni-0.3Mo)	0.25	0.25	345	480	18	25

Tab. 7.3 Titanium alloys (examples).

Modification	Alloy example	YS [MPa]	UTS [MPa]	%El	Remark
α	Ti-5Al-2.5Sn	830	860	15	
near α	Ti-6Al-2Sn-4Zr-2Mo	820	890	8	high strength at elevated temperatures
α/β	Ti-6Al-4V	1030	1100	8	universal
near β	Ti-10V-2Fe-3Al	1000	1100	6	cold workable
β	Ti-15V-3Cr-3Al-3Sn	965	1000	7	cold workable
γ	Ti-34Al-1Cr-1Nb-0.2Si	450	520	1	high strength at high temperatures, low RT ductility

Fig. 7.9 α and β-stabilizing elements for titanium.
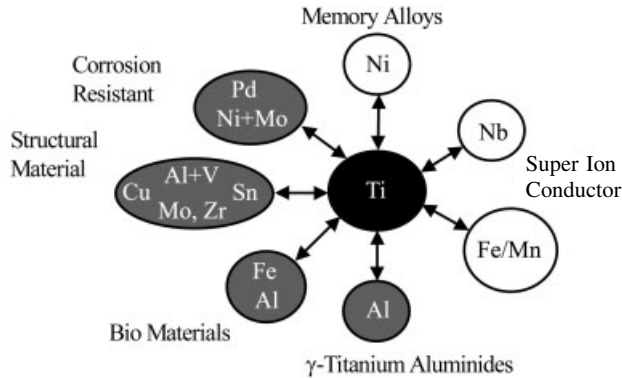
Fig. 7.10 Areas of application for titanium.

- high specific strength
- outstanding yield strength/ultimate tensile strength ratio
- excellent bio-compatibility
- decorative appearance.

7.5
Processing to Semi-finished Products

The production of semi-finished titanium products is usually similar to that of specialty steels. Typical forming processes such as forging, extrusion, rolling, pulling as well as precision and compact casting of titanium have been adopted from steel production by adjusting appropriate parameters for titanium. Using hardware from the steel industry contributes to cost-effective, large-scale production of titanium.

In the following, some examples of the broad production and application range of titanium alloys will be demonstrated.

Forging is the first forming process in the manufacture of slabs, bars, flat rolled material as well as open die forged parts such as rings, shafts, disks etc. Fig. 7.11 shows some forged titanium parts fabricated by swaging or open die forging.

Slabs and plates are the base products for the fabrication of coils, single rolled sheets, and plates in conventional rolling facilities (Fig. 7.12).

Bars are often cut into disks and die-forged to near-net-shape parts, thin bars are rolled to wire and finally to thin filaments, and raw billets can be extruded to complex shapes. Tubes can be fabricated by crossrolling or pilgering using punched blanks.

Fig. 7.13 gives an (incomplete) overview of several manufacturing processes. Particularly the titanium-specific processes should be noted. For example, complex structures can be fabricated by superplastic forming (SPF), possibly combined with diffusion bonding (DB).
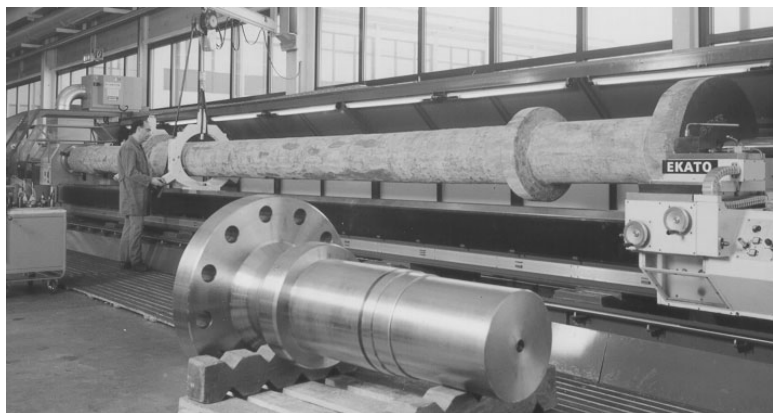
Fig. 7.11 Examples of forged titanium parts: a) open die forged part, b) swaged part.

Fig. 7.12 Hot wide strip mill for sheet production.
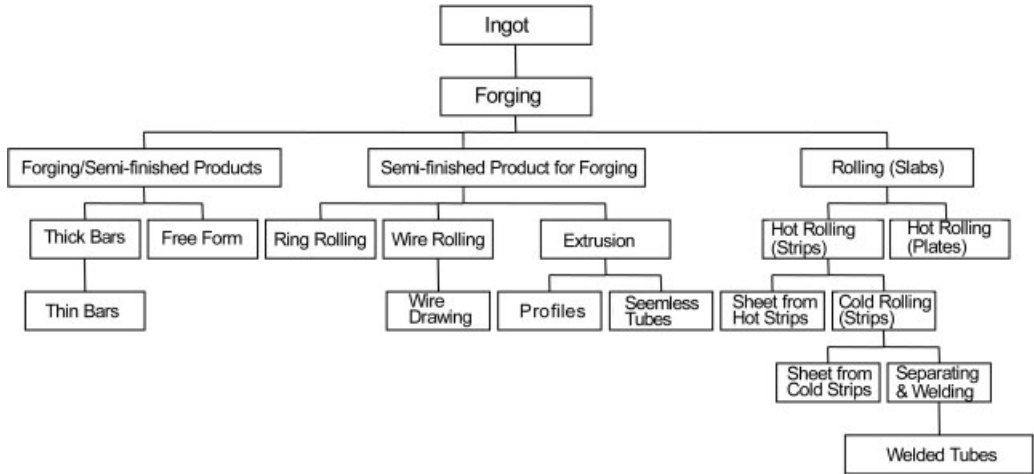
Fig. 7.13 Flow chart for semi-finished product manufacture. Not mentioned are intermediate and final annealing, pickling, grinding, machining and adjusting.

Furthermore, surface modification processes should be mentioned. Anodic oxidation of titanium surfaces offers endless possibilities for the fantasies of architects and designers. In addition to its spectacular appearance, techniques are available to produce resilient, weather resistant surfaces that guarantee excellent visual effects for many years.

Tribological properties of titanium alloys can be significantly improved, e.g. by laser gas alloying. With the help of a laser beam, the component surface can be reactively melted in specific atmospheres (nitrogen, methane) or a surface layer (boron, carbon) can be melted, thus locally hardening the surface.

Detonation cladding of titanium on steel or roller plating on aluminum allows the production of composites with tailored, optimized materials properties.

7.6
Applications

Aerospace applications, where the specific strengths at low and elevated temperatures are prime considerations, are described in more detail in Chapter 13. The perspectives for the use of titanium in automotive applications are presented in Chapter 18.

The good corrosion resistance of titanium alloys has already been mentioned. In addition to some examples summarized in Tab. 7.4, it is essential that the integrity of the titanium oxide scale present on the surface of titanium must not be damaged to guarantee good corrosion resistance, or there must at least be the chance that once damaged the oxide scale can be reformed in the particular environment. Therefore,

Tab. 7.4 Corrosion behavior of titanium.

Resistant	Limited resistance	Not resistant
nitric acid	sulfuric acid	fluorine
chromium acid	hydrochloric acid	dry chlorine gas
sulfurous acid	phosphoric acid	red smoking nitric acid
alkaline solutions	oxalic acid	
ammonia	formic acid	
aqueous chlorides		
brine		
seawater		
wet chlorine gas		
acetic acid		
maleic acid		
ethanol		
carbamate		
dimethylhydrazine		
liquid hydrogen		
Increasing	*← Resistance →*	*Decreasing*
oxidizing conditions, Fe^{3+}, Cu^{2+}, Ti^{4+}, Cr, Si, Mn, Pd in titanium		reducing conditions, increasing concentrations, higher temperatures, fluorine, fluorine compounds

in oxidizing atmospheres, titanium alloys have long-term corrosion resistance; traces of oxygen and water are sufficient to form protective oxide scales.

The corrosion resistance of titanium can be improved by the addition of noble metals (often palladium and ruthenium), nickel and molybdenum, or by the use of inhibitors in the machine. Extensive corrosion data banks provide information about specific alloys in different media.

Examples of some applications where corrosion resistance plays a major role, plate and tube heat exchangers for the chemical, power generation, or food industries, are shown in Fig. 7.14.

Excellent corrosion resistance is needed in onshore/offshore applications. For mechanical, technological and corrosion reasons, new generation floating platforms have many kilometers of conveyor and supply pipelines.

Furthermore, medical applications rely on the biocompatibility of titanium alloys. Hip and knee-joint prostheses and other permanent implants (casing for cardiac pacemakers, bond fixtures, orthodontic and dental implants) are made of titanium today.

However, there is no other area with a higher rate of increasing production than the sporting goods industry. Professionals and amateurs alike desire not only bicycle frames, but also titanium golf clubs. For a time, the demand for titanium in golf equipment was on the order of 5000 t/a and represented about 10% of the worldwide consumption of titanium.
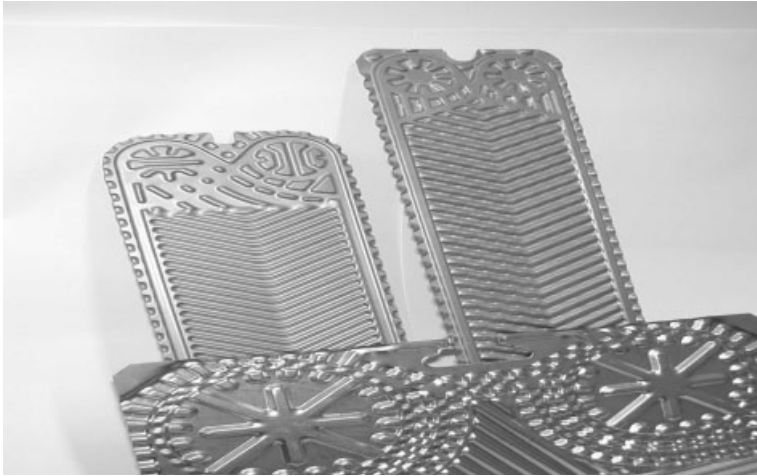
Fig. 7.14   Titanium heat exchanger plates.

7.7
Recycling

Today, no material can succeed if not environmentally friendly and recyclable. After adequate cleaning and refining procedures, high-quality titanium scrap can be used to make ingots and slabs and can thus be put back into circulation again. Melting processes such as cold hearth melting with electron beam or plasma heating can guarantee titanium qualities for high demands if the final re-melting step is done by vacuum arc re-melting.

If the scrap material cannot be used for high-quality titanium ingot, it can still be used as an alloying addition to titanium-stabilized specialty steels, either directly or as ferro-titanium.

The need for titanium recycling is directly evident by looking at the materials cycle. On average, only 0.4 kg of each 1.3 kg titanium sponge used ends up in the finished product (Fig. 7.15). In some cases, the portion machined away of a component can be above 90% of the input material.
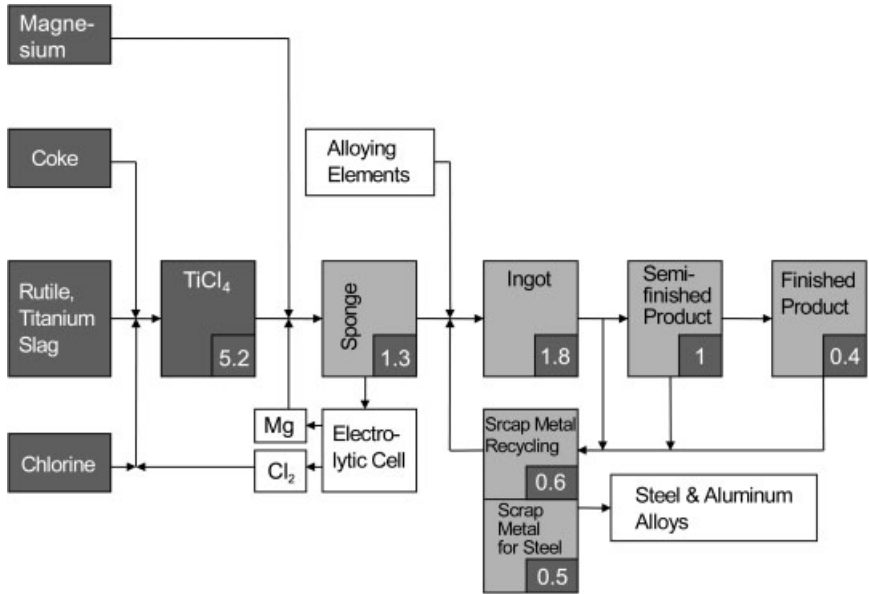
Fig. 7.15 Flow chart and mass balance sheet for titanium product fabrication from ore.

7.8
Summary and Outlook

This chapter has described the production processes from sponge to semi-finished products. Many of them are identical to that of large-scale production in the steel industry. Examples of major applications demonstrate the advantages typical for titanium.

To achieve wider use of titanium, which is certainly justified in terms of its properties, production costs must be drastically reduced.

8

Fabrication of Titanium Alloys

M. Peters and C. Leyens, *DLR – German Aerospace Center, Cologne, Germany*

8.1
Introduction

To build a usable component from titanium or titanium alloys with the required properties, the semi-finished products have to be put into a final shape. This requires similar forming methods to those used for metals in general. Since the starting titanium products are already relatively expensive, attempts are made to minimize the machining costs for final component design. Therefore, cost-optimized titanium parts are almost always a result of a carefully selected processing route. In particular, "near-net-shape" processing has the potential to substantially reduce the manufacturing costs and simultaneously increase the material output factor, which is called the "fly-to-buy-ratio" in the aerospace sector. In the following, first machining procedures for titanium alloys will be described. Then, manufacturing methods with a high net-shape potential like casting, welding, superplastic forming in combination with diffusion bonding, as well as powder metallurgy will be highlighted.

8.2
Machining of Titanium Alloys

To a large extent, machining of titanium and titanium alloys follows criteria that are also applied to common metallic materials. Compared to high strength steels, however, some restrictions have to be recognized, which are due to the unique physical and chemical properties of titanium:

- The lower thermal conductivity of titanium hinders quick dissipation of the heat caused by machining. This leads to increased wear of the cutting tools.
- The lower modulus of elasticity of titanium leads to significant spring back after deformation under load. This causes titanium parts to move away from the cutting tool during machining.
- The lower hardness of titanium and its higher chemical reactivity leads to a tendency for galling of titanium with the cutting tool.

Therefore, some general guidelines should be adhered to for successful machining of titanium parts:

- The workpiece should be as short as possible and mounted to be vibration-free into the grips of the working machine.
- Sharp cutting tools should be used and replaced at the first sign of wear. Tool failure occurs quickly after a small initial amount of wear.
- A stiff working machine and stiff grips are required.
- The titanium parts have to be effectively cooled by use of copious amounts of cutting fluid. This allows the heat to dissipate quickly, but also fire can be prevented, since titanium fines, turnings, or chips can cause a fire hazard. Water-based soluble oils can be used, as well as solutions of vapor-phase rust inhibitors of the nitrite amine type.
- Low cutting speeds should be used while feed rates should be high. Never stop feeding while the cutting tool and work piece are in moving contact, since this could promote smearing or galling, and rapid tool destruction.
- Hard surface scales should be removed before machining, either by grit blasting or pickling in a solution of 2% hydrofluoric acid and 20% nitric acid.

High-speed cobalt-based steel tools are mostly used for machining titanium because of their flexibility and low cost. High feed rates and speeds or rough surfaces may, however, require special qualities found in cemented carbides or stellites.

Because of titanium's tendency to smear and gall with the tooling, milling turns out to be more difficult than turning. Generally, cut-down milling is preferred to conventional milling since damage to the milling cutter from built-up edges and chip welding to the cutting edge are minimized. Clearance angles for face milling cutters should be greater than those used for steel. Use of sharp tools is a must. End milling of titanium is best performed by using short length cutters, which should have sufficient flute space to prevent chip clogging.

For drilling, the workpiece should be clamped as rigidly as possible. This usually prohibits manual drilling. The drill, preferably high-speed cobalt-containing steel with short cutting length, should be sharpened and cleaned. The feed rate can be high, the cutting speed, however, must be low. To avoid excessive friction, cooling with chlorinated cutting oil is required. The drill should be put on strongly, and drilling chips should be removed by raising the drill frequently. To allow a free flow of chips, the rake angle of the drill must be sufficiently large to avoid welding between the drill and the workpiece.

The tendency of titanium for fretting and galling is a particular concern during thread cutting. For this reason, the use of chemically active lubricants is recommend, e.g. sulfurous cutting oils or mixtures including carbon tetrachloride, molybdenum sulfide or graphite. Straight, clean holes must be drilled to ensure good tapping results. To avoid unnecessarily shortening tool life, threads shouldn't be cut manually where possible. Male threads have to be cut on a lathe since cutting dies can fret, thus preventing sound threads. The thread depth should be increased gradually. For cutting female threads a drill with a strong core and a short

cutting edge should be used. The tap drill should be extra tapered and flank relieved.

Titanium can be sawn using conventional band sawing or power hacksawing. Because of titanium's poor heat dissipation, the saw speed should be reduced by about one quarter compared to steel. Appropriate cooling also has to be provided here, preferably on the basis of sulfurous or chlorinated oils. The contact pressure of the saw blade should be high. Carbide-tipped tooling increases sawing speed. Since hard oxide surface scales increase tool wear, they should be removed before sawing by grit blasting, grinding or chemical agents.

The low thermal conductivity of titanium is most noticeable during surface grinding operations. Here it can even come to chemical reactions between the grinding media and the titanium surface, leading to smearing or even to intense sparking, which can cause a fire hazard. Therefore, the use of reduced wheel speeds – half to one third of conventional operating speeds – and ample coolant is therefore essential to get the best results with titanium. As abrasive grinding media, aluminum oxide and silicon carbide wheels as well as resin-bonded diamond wheels have proved to be successful. For smooth surfaces with minimum roughness, oil emulsions including nitrite-amine-based fluids should be used.

8.3
Casting

Casting can be considered to be the classic (near-)net-shape process. Due to often very extensive metal removal by machining from the ingot to the final component, and the relative expense of titanium material, casting offers a high cost saving potential. Furthermore, casting enables to do without extensive post-processing of cast components. Often complex components can be produced for which conventional production methods would be too complex or expensive. Compared to forged parts, however, strength and ductility penalties have to be accepted. These can at least be partly compensated for by intelligent casting-specific component design. The two casting methods used are rammed graphite mold casting and investment casting.

Rammed graphite mold casting is similar to sand casting. It is considered an inexpensive process and particularly suitable for large castings. Wooden, plastic epoxy, or metal patterns are used to shape the molds. Coring offers the possibility to produce hollow castings. The mold for the external shape is made in two halves, and the separately made core is then located by core prints between them. The location of the gates and risers have to suit each casting design. The completed molds are then embedded on a casting table for centrifugal casting. Cast components of up to 2750 kg have already been successfully produced (see also Chapter 19). Even larger structures are likely, but can also be manufactured by welding together two or more individual castings. Also, permanent molds of machined graphite blocks may be used. Here sprays have to be used to prevent metal-mold reaction during pouring and to keep the solidified part from sticking

to the mold. Permanent molds are preferably used for simple, symmetrical thin section shapes with large flat areas, e.g. plates or missile wings.

Investment casting is used in preference to graphite mold casting when close tolerances, thinner sections, smaller draft angles, and better surface finishes are required. Due to the high reactivity of the liquid titanium, casting must be carried out in vacuum and water-cooled crucibles have to be used. The lost-wax process is preferred since it yields high surface quality and precise dimensional components. Often theses parts require no extra post-processing and are ready to install. First, a wax model is manufactured from a dimensionally stable metal form, e.g. of aluminum. This form takes into account that the wax model must be bigger than the final titanium cast part due to shrinkage of both the wax and the titanium alloy. The wax models are then assembled in a cluster, coated with ceramic slurry, and dried. In the next production step, the ceramic green bodies are de-waxed in an autoclave. Burning provides the required stability to the ceramic form for the actual casting process and, simultaneously, removes left wax residues.

Casting then is carried out in a vacuum arc furnace with a self-consuming electrode (Fig. 8.1). The titanium alloy melt drips into a water-cooled copper crucible, forms a thin titanium scull, which then acts as the crucible. Centrifugal casting is used to fill the final mold. After cooling, the casting is removed from the mold by breaking off the ceramic mold (lost wax). After removing stays, risers, and channels the final cast piece is ready. Due to the reaction of the titanium with the ceramic mold, a thin reaction zone is formed during casting, which has an adverse effect on the mechanical properties and must therefore be removed by pickling. To eliminate inevitable porosity, it is a common practice for cast aerospace parts to be hot isostatically pressed (HIP) just below the beta transus temperature at pressures of around 100 MPa.
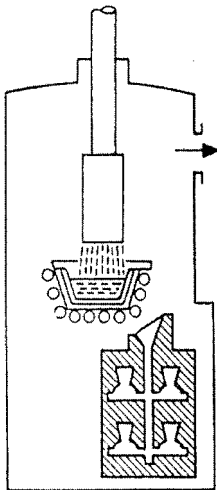
Fig. 8.1 Principle of titanium investment casting (courtesy: Tital, Bestwig).

Fig. 8.2 Cast Ti-6Al-4V jet engine fan frames of 130 and 150 cm diameter for GE engines CF6-80C and GE 90 respectively (Precision Castparts Corporation).
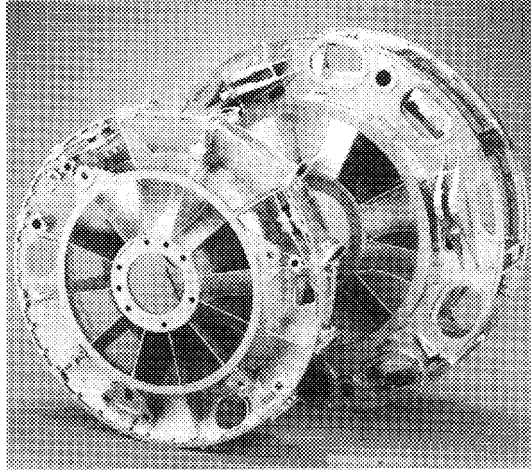
The main fields of application for investment castings are high performance parts for the aerospace and non-aerospace industry. Titanium cast parts are used as static components in jet engines, e.g. as casings (Fig. 8.2), compressor casings or as exhaust gas pipes of auxiliary gas turbines (Fig. 8.3). The casings shown in Fig. 8.2 not only have to carry the fan case, but also have to transfer a large portion of the engine's thrust. The mid-frame casting of the GE 90 is among the larg-
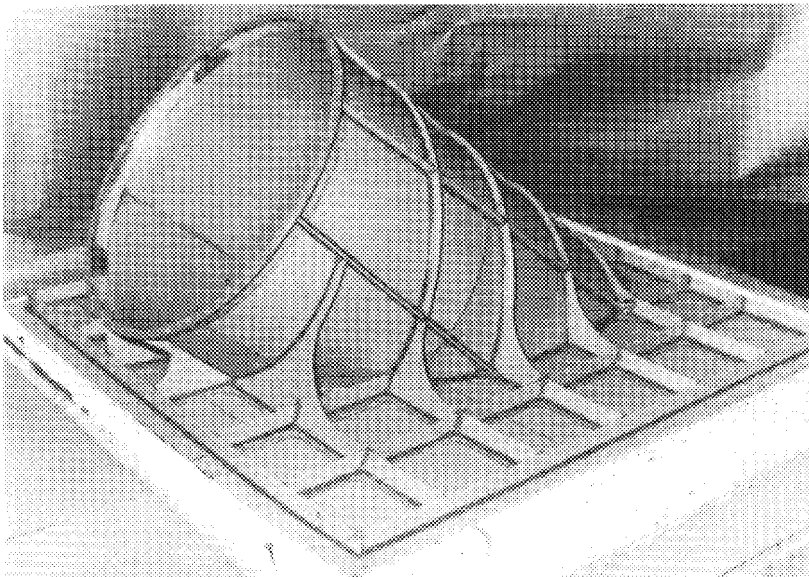
Fig. 8.3 Gas duct of the auxiliary turbine for the Boeing 777: Ti-6Al-4V cast part (Boeing; Howmet).

Fig. 8.4 Cast Ti-6Al-4V hip implant (R&D development project) (Tital, Bestwig).

est titanium aerospace cast parts worldwide. Furthermore, cast parts from titanium are used in the automotive industry (valves, turbocharger rotors), medical engineering (implants, Fig. 8.4), dental technology as well as the electronics industry. The 1990s experienced a boom in the manufacture of investment-cast titanium golf club heads. In the future, the development of special titanium alloys for casting is likely, as already successfully practiced for decades for Ni-based superalloys. Chapter 9 deals with titanium investment casting in more detail.

8.4
Welding

Titanium and most industrial titanium alloys are readily weldable. Fusion, resistance, flash butt, electron beam, diffusion bonding, and pressure welding techniques are available and are widely practiced to produce joints in titanium and titanium alloys. Techniques are also available to weld titanium under a wide range of conditions in the open fabrication shop, in a weld chamber, or in the field. Since during welding the metal locally melts, measures have to be taken to avoid that titanium molten metal comes into contact with reactive gases, including oxygen and nitrogen from the air. Generally, a clean environment has to be provided to avoid an embrittlement of the workpiece. Two principle approaches are followed. In one, all metal parts exposed to temperatures greater than 250–400 °C

are protected by an inert gas shield. In the other, the whole component is placed in a vacuum chamber, which is flushed with an inert gas. Gas tungsten-arc welding (GTA), also called tungsten electrode inert gas welding (TIG), and gas metal-arc welding (GMA), also called metal inert gas welding (MIG), work according to the first principle; while electron beam welding (EB) is a classic representative of the second principle. GTA/TIG welding is most commonly used for titanium alloys, while plasma, laser, resistance, electron beam, and friction welding are applied for specific applications.

8.4.1
Fusion Welding

GTA/TIG and GMA/MIG welding are primarily applied in pressure vessels and in process equipment construction, while the aerospace sector requires high-quality electron beam welding. Heavier sections generally require the use of filler metal and grooved joints. Either GTA/TIG or GMA/MIG welding can be used, although the economy of GMA/MIG welding increases with plate thickness. If the GTA/TIG process is used, care has to be taken to avoid contact of the tungsten electrode with the molten puddle to prevent tungsten pickup. Small diameter thoriated tungsten electrodes should be used for titanium alloys. For GMA/MIG welding the weld speeds are fast and the weld puddle is relatively large and agitated, so optimum gas shielding is required. Conventional power supplies are used for both GTA/TIG and GMA/MIG welding. For the former, DC straight polarity is used, while the latter uses reverse polarity.

Usually, filler wire matching the properties and composition of the titanium base metal is used. However, for c.p. titanium a weld wire one strength level below the base metal may be selected to compensate for the nearly unavoidable slight hardening of the weld due to atmospheric gas pick-up.

Shielding is of central importance for the quality of the weld. Because titanium reacts with the atmosphere, all parts at temperature above 300 °C must be provided with a protective gas shield. Therefore, during GTA and GMA welding, argon or helium shielding gases of welding grade (99.99% purity) with dewpoint of −45 °C or lower are used to provide the necessary protection. Three separate gas supplies are needed for primary shielding of the molten weld puddle, secondary, or "trailing", shielding of cooling weld deposit and associated heat affected zone, and backup shielding of the backside of the weld. The argon used must be of the highest purity available. To avoid weld defects, the weld area should be cleaned of surface contaminants directly before welding using sanding, brushing, or degreasing and pickling in aqueous acid solutions. After the cleaning procedure, the parts to be welded and the filler material should be handled with lint-free gloves and cloth. Bare hands should never be used to handle cleaned titanium since even hand sweat can be harmful.

For welding small parts, a purge chamber is a way to surround the titanium parts with argon to ensure contamination-free welds. Purge chambers are usually large domed-shaped plastic bubbles with access ports for the torch and the

welder's hands. Because the argon is heavier than the surrounding atmosphere, it falls to the bottom of the chamber and forces the atmosphere up and out through a valve at the top of the chamber.

Titanium alloys can be welded up to 20 mm thick. For sheets more than 2 mm thick, usually two or more welding passes are necessary. Once welded, visual inspection of the weld can indicate if contaminants are present. A bright silver weld indicates absence of contaminants. A golden or straw-like color indicates that some embrittlement is present. Hardness testing gives the safest measurement of the weld condition. A good weld should only reveal a slight increase in hardness compared to the base metal. Usually, stress relief annealing is not required and is only recommended for thick, complex components where multiple welding passes were applied.

8.4.2
Friction Welding

In principle, friction welding is a press welding method. Intensive friction leads to local heating between two components so that the parts finally weld together without reaching the liquid phase. Therefore, friction welding can be done in air. By intensive rubbing and additional pressure, the surfaces are heated up to temperatures where usually hot forming takes place, i.e. kinetic energy is converted into heat to bring about controlled degrees of fusion. Although cylindrical workpieces like shafts or flanges are particularly suitable for this method, friction welding has recently attained a special attention for the production of "blisks" (bladed disks) in jet engine compressors (see Chapters 12 and 13). Here the individual blades are attached by linear friction welding to the compressor disk. Friction welding offers cost advantages, particularly for larger blisk sizes.

8.4.3
Electron Beam Welding

Electron beam welding (EB) leads to very high integrity welds (Fig. 8.5) and is frequently used where highest weld quality is desired, particularly in the aerospace industry. Therefore, it is superior to GTA and GMA welding, but is also more expensive since all welding is done in a high-vacuum chamber by mechanized equipment. This also restricts the size of the components to be welded as well as the freedom of movement in the weld chamber. Due to the high power density of the electron beam, the heat penetration depth is low. The resultant fusion and heat-affected zones yield a high depth-to-width ratio, which results in low distortion EB weld structures. Weld speeds are very high, and excellent reproducibility of the welds can be guaranteed. Even thick plates up to 100 mm can be welded without filler metals. If filler metal is required, the same alloy is used.
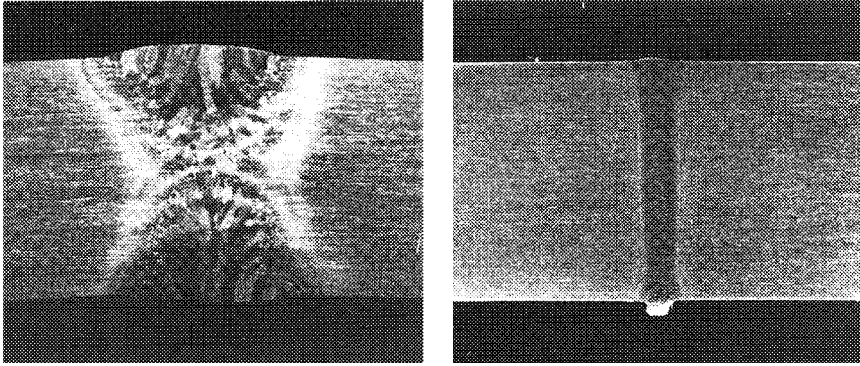
Fig. 8.5 Comparison of Ti-6Al-4V TIG and EB welds.

8.4.4
Laser Beam Welding

Similar to EB welding, laser beam welding also offers advantages of high speed, good automated manufacturing, and highly reproducible, narrow welds with low risk of distortion. Furthermore, laser beam welding can be performed at ambient atmosphere so that large and complex formed structures can be easily welded. However, like for fusion welding, the welds have to be protected by gas shielding due to the reactivity of titanium with atmosphere. Furthermore, hard to access areas can be laser beam welded since the laser beam can be easily deflected by lenses and mirrors, or optical fibers. Both CO_2 lasers and Nd:YAG lasers are used.

8.4.5
Spot Welding

Resistance spot welding is performed on titanium in much the same way as for other metals. In fact, the lower electrical and thermal conductivity of titanium makes it more readily weldable than aluminum and many of the carbon and low alloy steels. As known from arc welding, the surfaces have to be clean, free of scale, oxide, dirt, paint, grease or oil. The close proximity of mating surfaces in combination with the very short duration of the resistance weld cycle and squeeze pressure exclude air from the weld zone. Therefore, inert gas shielding is not required. Equipment and parameters for resistance spot welding titanium are about the same as required for austenitic stainless steel.

8.4.6
Properties of Welded Structures

During a weld path the titanium alloy locally melts, leaving behind two well-defined areas, the fusion zone (FZ) and the heat-affected zone (HAZ). In the FZ,

the melting temperature of the titanium alloy is exceeded, and upon cooling a very coarse-grained cast microstructure develops. The HAZ limits are given by the melting temperature at the upper end, and by the β transus temperature at the lower end. Due to the temperature gradient in this zone a graded, lamellar structure develops during cooling (Fig. 8.6).
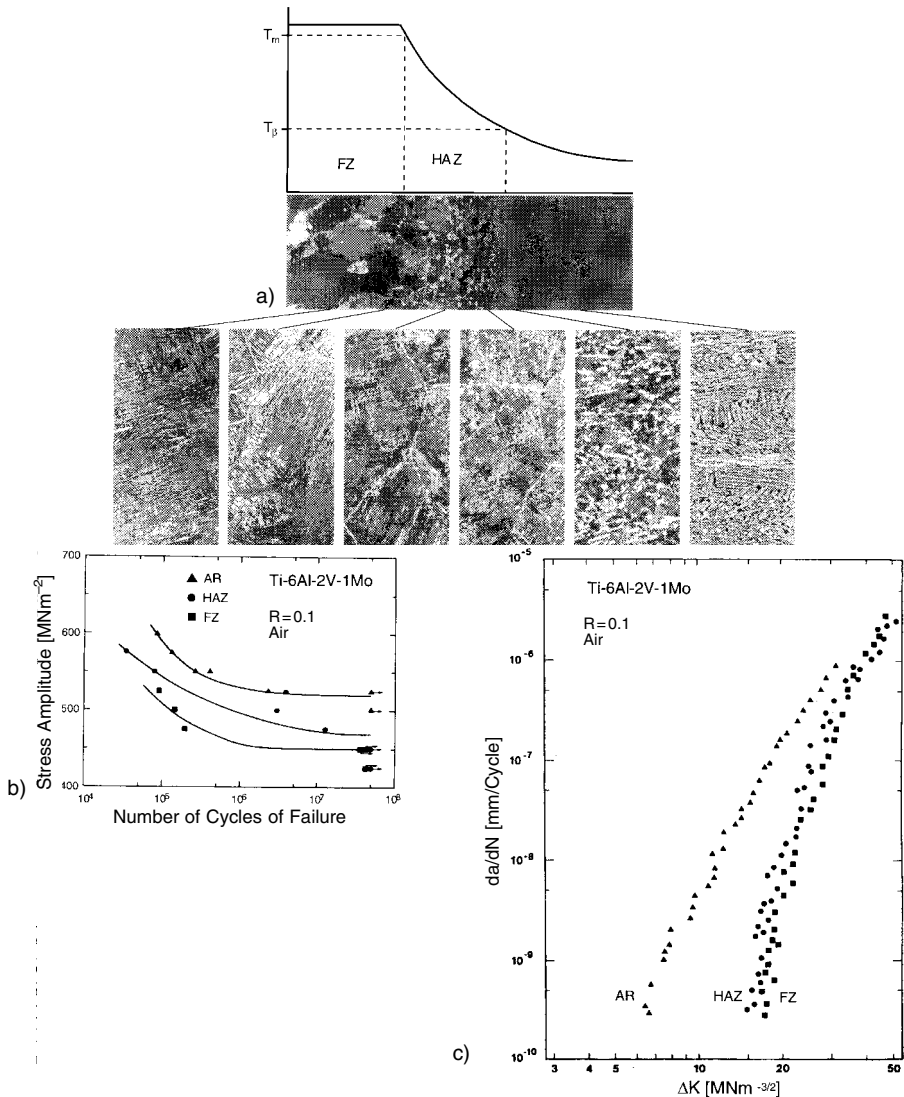
Fig. 8.6 a) Formation of fusion zone (FZ) and heat affected zone (HAZ) after TIG welding of an α + β titanium alloy. b) Microstructure of FZ, HAZ and base material. c) High-cycle fatigue and fatigue crack growth behavior of FZ, HAZ and base material.

Both alloy composition and microstructure determine the weldability of titanium alloys. Unalloyed titanium and α alloys are easy weldable. Generally, conventional titanium alloys become easier to weld with increasing volume fraction of the α phase. Usually, α+β alloys like Ti-6Al-4V are weldable in the annealed condition. Metastable β alloys have only limited weldability since their FZ and HAZ can embrittle due to phase transformations occurring during welding or upon post-weld heat treatments. Welding titanium with other metals generally presents great difficulties due to embrittlement caused by the formation of intermetallic phases.

The mechanical properties of welded structures seldom reach the values of the base material, and usually correspond to those known for lamellar cast structures. Typically yield and tensile strength, ductility, and fatigue strength are reduced (Fig. 8.6). However, those properties that are known to be superior with lamellar microstructures also reveal improved weld properties. This applies, for example, to the fatigue crack growth behavior (Fig. 8.6), the creep properties, and the fracture toughness. Prerequisite are, however, high-quality welds. Defects like pores as a result of a careless surface cleaning before welding or segregations should be avoided. For large, complex shaped parts stress-relief annealing may be necessary to remove residual stresses.

8.5
Superplastic Forming/Diffusion Bonding

Superplastic forming (SPF) in combination with diffusion bonding (DB) is probably the most spectacular near-net shape process. Superplasticity describes the ability of a metallic material to deform to very high plastic strains without macroscopic necking, assuming the appropriate (high) forming temperatures and (slow) strain rates are provided. Analogous to blow forming in plastics, complex thin walled titanium components can be manufactured in a single step. Often diffusion bonding is incorporated in the hot metal forming process to create hollow or honeycomb structures.

The phenomenon of "superplasticity" has been known for a long time. In 1934 SnBi-alloys were deformed more than 2000%. For a long time this material property was considered as exotic. However, its potential as an economic manufacturing tool for complex formed titanium sheet components was discovered in the 1970s and 1980s. Today SPF is mainly applied for aircraft parts like ducting, aircraft wing access panels, nozzles, and engine casings and blades, but also for non-aerospace products like high-pressure oil field sample bottles.

There are several requirements for superplasticity. The deformation temperature should be about half that of the melting temperature; for titanium alloys this is about 90% of the β-transus temperature. The deformation rate has to be low. Since plastic deformation at these high temperatures is primarily due to creep, there are two metallurgical requirements that favor creep deformation: extremely fine microstructures, since creep is primarily controlled by grain boundary gliding, and stability of the fine structures at the high deformation temperatures.

Usually, fine-grained equiaxed or bi-modal structures of $\alpha + \beta$ alloys fulfill these requirements. The typical grain sizes of 5 to 15 µm of these alloys reveal sufficiently high grain boundary density. Furthermore, the two-phase structures effectively hinder grain growth during SPF.

At high temperatures, the strain rate sensitivity, m, only depends on strain rate, $\dot{\varepsilon}$, and flow stress, σ:

$$m = d \ln \sigma / d \ln \dot{\varepsilon} \qquad \text{(eqn. 8.1)}$$

The highest superplastic deformation degrees are achieved for maximum m values, as shown for Ti-6Al-4V in Fig. 8.7. Values for m should exceed 0.3 to generate sufficient superplastic performance.

The SPF process involves placing titanium sheet between the two halves of a die and heating to the deformation temperature of about 925 °C for Ti-6Al-4V. Then, hot argon gas is pumped into the die and the appropriate pressure forces the sheet to deform superplastically into the final shape of the lower die. Typical strain rates range from 10^{-1} to 10^{-4} s^{-1}, and plastic deformation degrees of more than 1000% are achieved for Ti-6Al-4V. Furthermore, local bonding via diffusion processes enables formation of complex three-dimensional sheet structures. SPF/DB as a single manufacturing operation is shown in Figures 8.8 and 8.9. The bond produced is of high integrity, thus making specific areas of separate sheets metallurgically a single sheet. Due to the high affinity of titanium to oxygen, processing has to be performed either in vacuum or in protective gas atmosphere.

Superplastic forming is firmly established, particularly in the aerospace industry, and allows the economic production of thin-walled sheet components. Fig. 8.10 shows a service panel for the Airbus A300/310 superplastically manufactured from Ti-6Al-4V sheet. Even for complex formed components, only little post-processing is required.
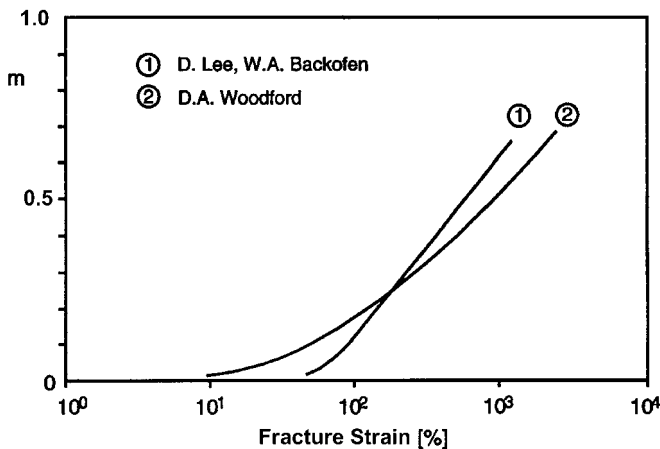
Fig. 8.7 Effect of m value on SPF deformation degree (Ti-6Al-4V).

Fig. 8.8 Principle of SPF/DB processing of a sandwich structure.
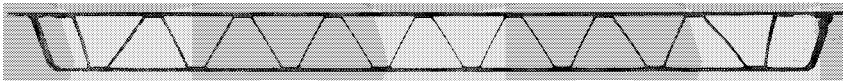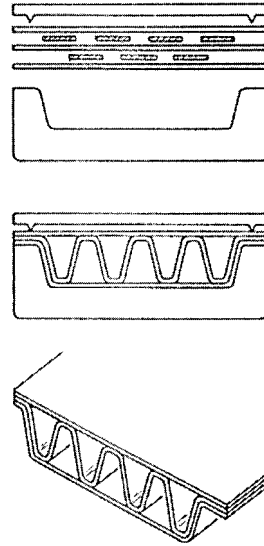
Fig. 8.9 Cross section of a SPF/DB sandwich structure (Ti-6Al-4V).
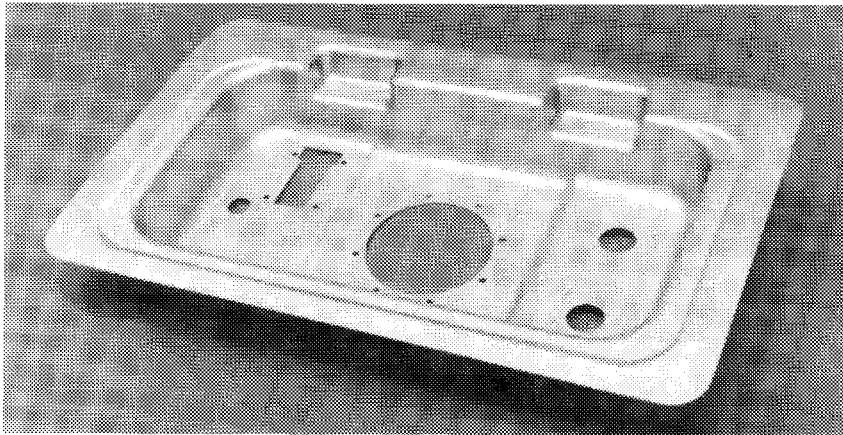
Fig. 8.10 Service panel for the Airbus A300/310 (SPF Ti-6Al-4V).

To even further improve the economy of the SPF process, efforts have been undertaken to increase strain rates and/or reduce deformation temperature. Thus, the throughput and the tool life can be increased, while energy costs go down. Here the Japanese β-titanium alloy SP-700 (Ti-4.5Al-3V-2Mo-2Fe) is of interest.

Owing to its extremely fine microstructure and low β-transus temperature, SP-700 is superplastically formable at temperatures below 800 °C without significant increase in flow stress. More advantageously, diffusion bonding is also accomplished around this temperature. The low temperature SPF-DB process not only saves die material life and process costs, but also reduces alloy degradation from exposure at elevated temperatures, e.g. grain growth and oxidation. SPF-DB is reviewed in more detail in Chapter 10.

8.6
Powder Metallurgy

Powder metallurgy (PM) offers a viable tool to produce complex components with little machining, thus keeping production costs down. This applies particularly to relatively expensive materials like titanium alloys, where often up to 95% of the metal has to be removed depending on the complexity of the component.

The powder-metallurgical production of titanium parts covers both the powder production with the help of rapid solidification methods and the compaction of these powders to the final component by hot isostatic pressing (HIP).

The powder manufacturing methods are subdivided into arc and electron-beam melting methods. Arc melting is carried out under protective gas atmosphere. Pulverization is provided by centrifugal forces either with the rotation of a self-consuming titanium electrode (REP- Rotating Electrode Process) or by a rotating crucible or plate on which the melted titanium drops. During rapid cooling by the protective gas, the liquid droplets solidify and retain their spherical shape. The resultant martensitic structure is shown in Fig. 8.11. Unfortunately, the economic REP process leads to unwanted tungsten impurities from the tungsten cathode. Therefore, this method is no longer applied today. Contamination can be avoided with the PREP method (Powder Rotating Electrode Process), where a plasma is used instead of an arc to melt the rotating titanium electrode. Since the electron
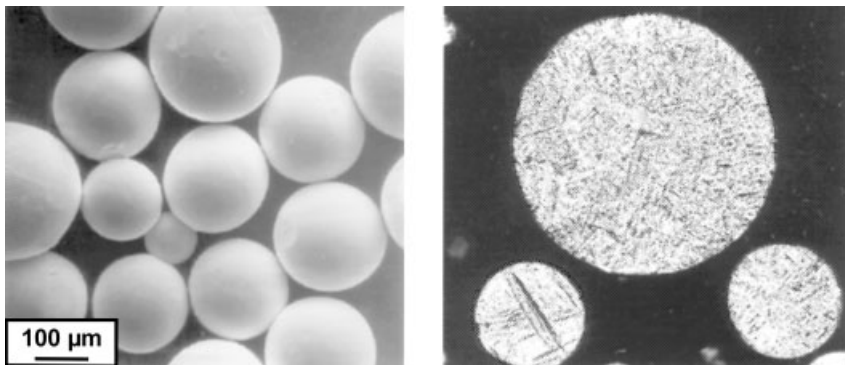
Fig. 8.11 Ti-6Al-4V PREP powder (SEM and OM).

beam process is under vacuum, inherently lower impurity levels of the powders are guaranteed. The method itself is, however, more expensive due to the more complex rapid solidification technology.

Before the resulting powders are consolidated in the hot press they have to be encapsulated, degassed, and evacuated. This ensures that no adsorbed gases remain on the particle surfaces as they can prevent complete consolidation by pore formation during HIP, or impair the sintering behavior by formation of oxide skins. If the capsule already compensates for shrinkage in the final component shape, then hot isostatic pressing can come close to the final component shape. A typical HIP process for Ti-6Al-4V powder is carried out for 1–3 hours at about 920–970 °C and a pressure of about 2000 bar.

Normally, the mechanical properties of PM titanium alloys are superior to cast alloys and partly correspond to those of forged alloys.

Initially, the powder-metallurgical route was primarily considered to be a method for economic production of near-net shape components. Titanium alloys, however, could not live up to this expectation, since they are neither cheap nor was the degree of material usage high. Currently, the high process cost of rapid solidification and subsequent compaction can be justified only in cases in which new titanium alloys are not producible by ingot metallurgy or where powder metallurgy is used as a vehicle for the production of titanium matrix composites.

Indeed, titanium powder metallurgy has experienced a certain renaissance due to the possibility of producing particle reinforced titanium alloys. For the production of stiff, wear resistant components, particle reinforced Ti-PM alloys could be an economic alternative as demonstrated by the series of commercial CermeTi alloys. These consist of elemental powder mixtures with up to 20% TiC particles. Such alloys are, for instance, used for aerospace components due to their high stiffness, but are also applied in the sport and leisure industry (Fig. 8.12).

The high expectations of the PM process to develop advanced, dispersion strengthened, high-temperature alloys have not been not fulfilled. The activities are however concentrated on titanium aluminides, since a large increase in the use temperature can be expected. Here the powder route can be helpful for the production of semi-finished products from titanium and aluminum elemental
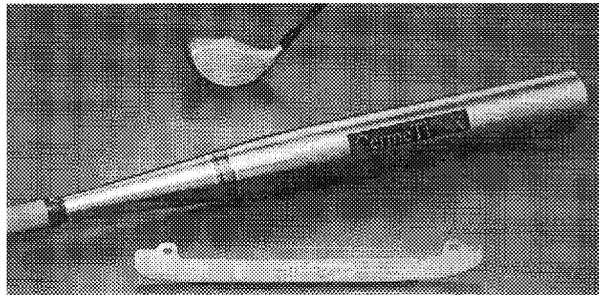
Fig. 8.12 CermeTi leisure components (Dynamet Technology, Inc. Burlington, MA, USA).
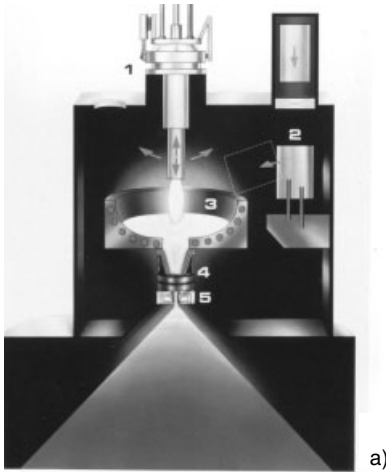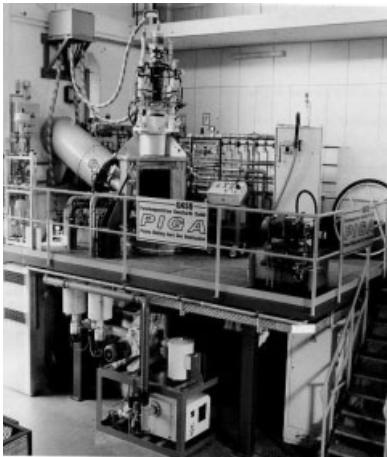
Fig. 8.13 Plasma melting induction guiding gas atomizer PIGA at GKSS-Forschungszentrum Geesthacht; a) schematic, b) process equipment.

a)

b)

powders, or, generally, for the production of complex intermetallic titanium-based alloys. GKSS operates the PIGA (Plasma melting Induction Guiding Gas Atomization) unit, which was developed especially for the production of intermetallic titanium-based alloys powders (Fig. 8.13). With the help of a plasma burner, the alloy is melted in a water-cooled copper crucible and then poured into the chamber and simultaneously atomized by inert gas (Fig. 8.13 a).

8.7
Referenced Literature and Further Reading

1 R. R. BOYER: Titanium for Aerospace: Rationale and Applications, Advanced Performance Materials **2** (1995) 349–368

2 K. FOLKERS: Die Technologie des Titan-Feingießens, METALL **47** (1993) 538–540

3 F. H. FROES: Developments in Titanium Applications, Light Metal Age (Oct. 1995) 6–8

4 F. H. FROES, D. EYLON: Titanium Net Shape Technologies, TMS, Warrendale, PA (1984)

5 R. GERLING, H. CLEMENS, F. P. SCHIMANSKY, G. WEGMANN: PM-Processing of an Advanced γ-TiAl Alloy: Technologies, Microstructures and Mechanical Properties, in Structural Intermetallics 2001, H. CLEMENS ET AL. (eds.), TMS, Warrendale, PA, USA (2001) 139–148

6 A. K. GHOSH, T. R. BIELER, (eds.): Superplasticity and Superplastic Forming, TMS, Warrendale, PA, USA (1998)

7 W. A. KAYSSER, M. PETERS: Pulvermetallurgische Werkstofflösungen am Beispiel der Luftfahrt, in: Innovative und wirtschaftliche Bauteile durch Pulvermetallurgie, VDI-Verlag, Düsseldorf (1993) 100–128

8 V. S. MOXSON, O. N. SENKOV, F. H. FROES: Innovations in Titanium Powder Processing, JOM, 52 (May 2000) 24–26

9 T. G. NIEH, L. M. HSIUNG, J. WADSWORTH: Superplastic behavior of a powder metallurgy TiAl alloy with a metastable microstructure, Intermetallics 7 (1999) 163–170

10 N. E. PATON, C. H. HAMILTON: Superplastic Forming of Structural Alloys, TMS, Warrendale, PA (1982)

11 M. PETERS, J. C. WILLIAMS: Microstructure and Mechanical Properties of a Welded α + β Ti Alloy, Metallurgical Transactions A **15** (1984) 1589–1596

12 M. PETERS, W. A. KAYSSER: Das Potential metallischer Leichtbauwerkstoffe in der Luft- und Raumfahrt, VDI-Bericht 1080, VDI, Düsseldorf (1994) 483–490

13 A. V. SERGUEEVA, V. V. STOLYAROV, R. Z. VALIEV, A. K. MUKHERJEE: Superplastic behavior of ultrafine-grained Ti-6Al-4V alloys, Materials Science and Engineering **323A** (2002) 318–325

14 G. WEGMANN, R. GERLING, F.-P. SCHIMANSKY, H. CLEMENS, A. BARTELS: High-temperature mechanical properties of hot isostatically pressed and forged gamma titanium aluminide alloy powder, Intermetallics **10** (2002) 511–517

15 P.-J. WINKLER, M. A. DÄUBLER, M. PETERS: Applications of Titanium Alloys in the European Aerospace Industry, in: Titanium '92: Science and Technology, TMS, Warrendale, PA, USA (1993) 2877–2890

16 P.-J. WINKLER, M. PETERS: Leichtmetalle in der Luft- und Raumfahrt: II. Stand und Perspektiven neuer Fertigungsverfahren, METALL **47** (1993) 531–538

17 Merkblatt DVS 2713 "Schweißen von Titanwerkstoffen", Deutscher Verlag für Schweißtechnik (DVS), Düsseldorf

18 B817-98 Standard Specification for Powder Metallurgy (P/M) Titanium Alloy Structural Components, ASTM International, West Conshohocken, PA, USA (2002)

9
Investment Casting of Titanium

H.-P. Nicolai and Chr. Liesner, *Titan-Aluminium-Feinguss GmbH, Bestwig, Germany*

9.1
Titanium

This chapter provides an introduction to the manufacturing of cast parts made of titanium alloys. It is a comprehensive description of the process, rather than an explanation of its basic principles. The previous chapters of this book dealt with reports about ore deposits and the extraction of such, as well as about the production of the metal itself. These pages will deal with the primary molding in liquid phase. It is now clear that titanium has a privileged rank among conventional metals: its melting point is elevated and its affinity to the oxygen and nitrogen of the ambient air is extremely strong. On the other hand, properties of titanium such as specific weight, strength, and corrosion resistance are encouraging. In spite of challenges, mentioned later, in the field of handling liquid titanium, processes such as melting, pouring, and making of cast parts are all proven technologies. Certain procedures and knowledge of the handling of liquid titanium are needed, but there are a sufficient number of titanium foundries around the world that can meet these requirements. Titanium castings are successfully being implemented as cost-effective alternatives to forged and wrought products for high performance and increasingly cost-sensitive applications such as military and commercial aircraft airframe structures. In some instances, these castings have been produced for half the cost of comparable forged and machined parts. For most of the last two decades, investment casting has been the preferred processing route for sophisticated titanium castings.

9.2
Cast Alloys

Breaking from conventional custom, titanium alloys have not been developed to accommodate the processing routes, as had been done for iron, bronze and aluminum; rather, titanium alloys have been developed basically to fit their application. So foundrymen have learned how to deal with alloys that are, actually, wrought alloys. Consequently, titanium alloys' negatives with respect to castability and feed-

ing have been countered by adapting the casting process. We can therefore safely state that all commercial titanium alloys can be used for making cast parts.

A favorable casting route can be suggested leading to the appropriate properties required by the customer. When the entire package of static and dynamic properties, chemical resistance, weight and specific requests with regard to shape complexity is taken in due consideration, the casting of titanium alloys ends up being profitable.

Even if one takes into account the reactivity of molten titanium on mold architecture and composition as well as its repercussion on the price of the molds, savings that are brought about by castings easily offset such cost differentials. The limiting factor so far has been the number of customers. These customers are definitely not eager to explore the total number of choices in the alloy chemistries available that could suit their requirements and needs. They will not select the "best new" alloy, but rather the "best known" alloy only, relying on proven compositions to design future parts. Tab. 9.1 shows the alloys that are used for casting. This list is not exhaustive; it should rather be used as a general guide. As mentioned previously, all titanium alloys are castable.

Tab. 9.2 shows typical static mechanical strength data for investment cast titanium alloys.

Tab. 9.1 Examples of cast titanium alloys.

Alloy Designation	Preferred Property	Application
cp-Ti (Pd, DIN 17 865)	corrosion resistance	chemical industry
Ti-64 (EN 3352)	strength, weight	universal application
Ti-6242 (WL 3.7141)	temperature capability, creep	moderately elevated temperatures
TIMETAL 834	temperature capability, creep	high temperatures
γ TiAl	weight, temperature capability	very high temperatures (under development)

Tab. 9.2 Typical mechanical properties of cast titanium alloys.

Alloy Designation	UTS [MPa]	YS [MPa]	%El	max. T [°C]
cp-Ti (DIN 17 865)	350	280	15	350
Ti-64 (EN 3352)	880	815	5	350
Ti-6242 (WL 3.7141)	860	760	6	450
TIMETAL 834	1020	900	4	600
γ TiAl	500–600	400–500	1–2	800

9.3
Melting Units

Different types of furnaces are available for melting and pouring. All titanium and titanium alloy melting furnaces have in common vacuum or inert atmosphere melting (typically argon). Some of these units are more of historical interest or are sometimes used for niche applications, while the others are still the "workhorses" with the largest share of casting production (Tab. 9.3).

9.4
Molding Materials

The making of castings is a result of filling molten metals into a hollow mold with the interior shape of the future cast part. So the molten metal comes in close contact with the molding material and might, in the worst-case scenario, cause a metal-mold-reaction with detrimental effects. Therefore, the molding materials should be non-reactive (which is nearly impossible, according to thermodynamic laws) or should at least react in a delayed way and then minimally with the molten titanium. The objective of minimizing the metal-mold reaction in an efficient manner can be reached through the selection of molding materials as well as the control of molding parameters. Conventional molding materials commonly used in non-titanium casting applications having a typical composition of Al_2O_3-SiO_2 are not suitable for titanium (investment) casting. The molten titanium will react with both oxides and dissolve the elements Al and Si as well as the oxygen. Thus, the titanium consumes the mold and, at the extreme, there is a real risk of titanium spilling into the furnace. Any chance of getting a suitable casting from this is nil.

In order to counter this reactive tendency, there are measures and methods to make molds for titanium casting where a bit more design effort is needed than with conventional molding. Typically, there are three alternatives (Tab. 9.4).

Tab. 9.3 Melting and casting processes for titanium.

Type of Furnace	*Special Features*	*Overheating*	*Use*
Electron beam furnace (high vacuum)	re-chargeable, alloy modifications possible	yes	rare (evaporation of alloying elements)
DESU (pressure or vacuum)	recycling of scrap titanium possible	n.a.	rare
VAR (self-consuming electrode=ingot)	Ingot on demand	no	typical melting equipment, "workhorse"
KIC (cold wall induction crucible)	re-chargeable, alloy modifications possible	principally yes	introduction phase, small mass product parts
Plasma (gas filled furnace)	re-chargeable, alloy modifications possible	yes	re-melting/refining

Tab. 9.4 Mold variants for cast titanium.

Mold Material	Special Features	Application
refractory metals	melting point of the mold material is higher than that of liquid titanium, low solubility of the mold material	investment casting, chill casting
chill material	formation of a solid titanium skin (solid-solid reaction between titanium and mold only)	chill casting, pressure die casting, crucible material
ceramics	melting point of the mold material is higher than that of liquid titanium, enthalpy of formation of the oxide is greater than that of Ti_xO_y	investment casting, compact casting

9.5
Casting Design

The basic philosophy for designing cast parts can be spelled out as: the more complex the shapes are, the more economically advantageous they are designed as cast parts. If there is any doubt about whether the design is economically complex or not, a dialogue should be undertaken in earnest with "the local titanium foundry" right away. Simple designs using conventional titanium-based alloys are better off as a forging, while for the γ titanium alloys with a narrow forging window, the boundary for choosing casting over forging is shifted towards the more simple design. Complex shapes generally mean: 3D design from the beginning, load path optimized design, and integration of several assemblies into one cast structure. Known and proven valuations of castings show a cost benefit of about 50% in comparison to the assembled version they are meant to replace. As titanium alloys are not genuinely castable alloys, there are some limits with regard to complexity and wall thickness when compared to aluminum investment cast parts, for instance. Nevertheless, one should not hesitate to dare get out of the envelope and to think complex.

9.6
Finishing

Process procedures for the finishing of titanium (investment) cast parts are mainly determined by the properties of the molten titanium, especially the reactivity and the feeding properties during mold filling.

9.6.1
Pickling (Chemical Milling)

As a rule, titanium picks up some constituents from the molding material or from the residual gases in the furnace's atmosphere during the manufacturing process. These constituents diffuse into the surface and form the "α-case", with a thickness of a few tenths of a millimeter. This *a*-case is later removed by pickling (chemical milling). This method is used very effectively on the surface of three-dimensional cast parts.

9.6.2
Hot Isostatic Pressing (HIP)

We have previously mentioned the formation of defects with respect to castability and feeding. During solidification, poor feeding causes residual shrinkage cavities in the core areas (e.g. in the center line/center plane, nodal points, and heavy sections). Contrary to other cast metals, these cavities cannot be economically prevented by improved gating. Instead, the HIP process (Hot Isostatic Pressing) is used. The HIP procedure typically uses 1000 bar pressure of an inert atmosphere at about 900 °C (e.g. for Ti-6-4). At these temperatures and pressures the material can creep without adversely affecting macroscopic dimensional stability. In the final phase of the process, the walls of the former cavity join and completely diffusion weld together. A tensile test bar across this area shows no indications of what has happened; and the mechanical strength shows no difference compared to other areas. With the HIP procedure, titanium investment castings will reach strength levels that may be compared to those of wrought parts.

9.6.3
Welding

Welding can be classified in two separate categories: structural welding, and cosmetic (surface) welding. Structural welding is either used to assemble two castings (two sections of the part) or to fit a casting to other structural elements, thus forming a bigger unit. The techniques that are preferably used for this purpose are either EB (electron beam) welding or laser welding. As it is known that TIG welding in a glove box under inert (argon) atmosphere has no detrimental effect on the properties of castings, TIG welding can also be used to fill out small surface flaws.

9.7
Examples of Cast Parts

Fig. 9.1 to 9.8 are illustrations of typical success stories for titanium investment castings. They show the broad spectrum of what is possible today: from small to
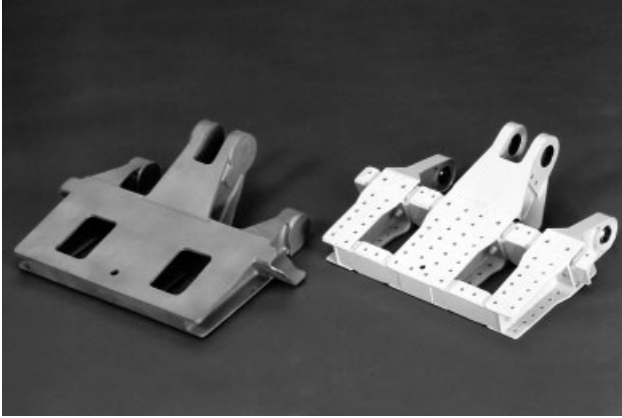
Fig. 9.1 Cast (left) and assembled (right) variant of a spoiler fitting.
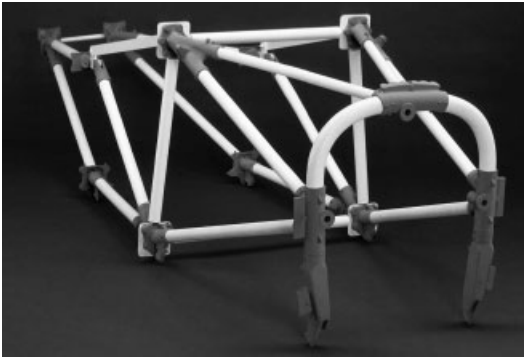
Fig. 9.2 Full-scale model of an engine mount for the Dornier DO 328.

Fig. 9.3 Different knot elements.

Fig. 9.4   Various investment cast parts for applications in the low temperature section of a gas turbine engine.

Fig. 9.5   Air inlet suspension for the Eurofighter aircraft.
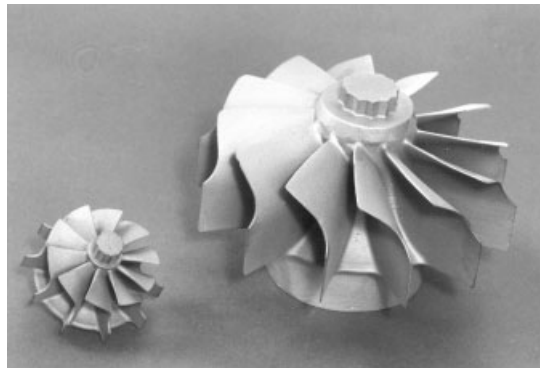
Fig. 9.6   Exhaust gas turbocharger rotors made from TiAl.

Fig. 9.7 γ-TiAl turbine blades.

a)

b)
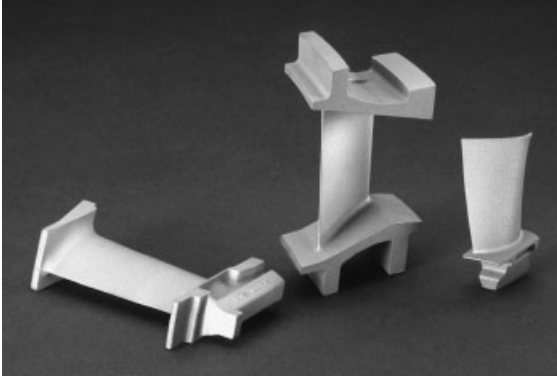
Fig. 9.8 Intermediate casing for large jet engines. (a) Diameter 152 cm, weight 173 kg; (b) diameter 150 cm, weight 240 kg. (Courtesy of PCC-Wyman Gordon)

large sizes, and from simple designs to complex shapes, from parts for aerospace applications to parts used in medicine and surgical applications.

Fig. 9.1 shows a cast (left) and an assembled (right) variant of a spoiler fitting, which is the joint that actuates the air deflectors on the upper side of an aircraft wing. Fabrication costs of the cast variant are only 50% of that of the assembled variant. A full-scale model of the engine mount for the Dornier DO328 is shown in Fig. 9.2. Titanium tubes are used for the straight parts, while investment castings are used for the knot elements. Fig. 9.3 shows examples of these knot elements. A few examples of parts used in the cold section of a gas turbine engine are shown in Fig. 9.4. Fig. 9.5 shows the air inlet suspension for the Eurofighter

military aircraft. For symmetry reasons, "left" and "right" variants are available. Different sized γ TiAl turbocharger rotors are displayed in Fig. 9.6, while γ TiAl turbine blades are shown in Fig. 9.7. The latter two applications are in the transition phase between laboratory and industrial application. Fig. 9.8, courtesy of PCC-Wyman Gordon, shows large intermediate casings for jet engines. The casings are located where the incoming air is ducted either into the engine by-pass or the core engine. Their primary function is to bear the rotating parts as well as to suspend the entire engine.

10

Superplastic Forming and Diffusion Bonding of Titanium and Titanium Alloys

W. Beck, *FormTech GmbH, Weyhe, Germany*

10.1
Introduction

Due to their unique property profile, titanium materials are considered for a wide range of industrial applications. Primarily their high specific strength and excellent corrosion behavior were deciding factors for use particularly in the aerospace industry, but also in other applications like offshore and medicine. Despite significantly higher prices and more complex processing compared to steel, it is often worthwhile and economical to use titanium. Concerning specific processing requirements, especially for sheet components manufactured via conventional cold forming techniques, some difficulties have to be overcome.

The high strength, anisotropic sheet properties, tendency to fret when in contact with steel tooling, and strong springback make the cold forming process technically difficult and cost intensive. Commercially pure titanium is relatively easy to handle and comparable to stainless steel with respect to attainable levels of deformation, provided the titanium-specific process conditions are mastered. So, in a swift test deep-drawing grades of $\beta > 2.3$ are realistic. Also springback, notorious for all titanium materials, can be as high as 20 degrees. Sometimes it may even develop after long storage times, but it can, however, be completely avoided by a subsequent hot calibration, as will be outlined later.

For titanium alloys, forming problems are formidable. The maximum strain is low; the forming forces, and thus tooling loads, are high due to high flow stresses (e.g. for Ti-6Al-4V, the yield stress is 870 MPa). Therefore, deep drawing and stretch forming cannot be applied. Only parts with simple bends are commonly made from titanium alloys. Therefore, sheet constructions made from titanium alloys are rarely found.

Titanium's plasticity increases, however, with increasing temperature. This is utilized for sheet forming, similar as in solid forming operations. Creep forming, or warm calibration, is primarily used for conventional sheet forming of commercially pure titanium. At temperatures of about 480 to 650 °C the low flow stresses and increased plasticity are utilized during hot working. Cold pre-deformed blanks, which are strained a few percent and then stress relieved after each deformation cycle, are hot calibrated in a two-piece device in this temperature range

for a defined time. The components, which usually show only a few percent of deformation, are afterwards stress relieved. In welded constructions, single parts are mostly employed; and commercially pure titanium Grades 1 to 4 are primarily used. Due to its favorable property spectrum of high strength and ductility, and excellent corrosion resistance, Grade 2 is explicitly preferred.

Hot working of titanium alloys is performed at temperatures up to 850 °C. Mostly a combination of hot calibration and deep drawing or stretch forming at low strains is applied. This requires high strength, thermally stable, two-piece tools. After hot working, the components have to be pickled to completely remove the oxide layers formed on the surface of titanium at temperatures above about 550 °C. When in service, an insufficiently removed oxide layer (α-case) embrittles the surface and leads to a strong reduction in fatigue strength.

Expensive processing initially led to a quite limited use for sheet structures made of titanium. However, increasing performance requirements in military and civil aerospace projects raised titanium use in the 1960s, as high strength aluminum alloys could no longer meet the higher stress and temperature needs. This situation stimulated the development of new, economic titanium sheet processing methods.

Since the 1920s it has been known that some materials can endure enormous tensile strains without necking (Table 10.1) [1]. Since then, the underlying material phenomenon, called "superplasticity" (much higher plasticity than usually observed), has been scientifically investigated. In the beginning, activities primarily concentrated in research laboratories in England and the former Soviet Union, were entirely directed towards the exploration of basic material science. The materials investigated appeared not to be sufficiently attractive for real products.

However, this changed with the development of the supersonic Concorde aircraft, with high requirements for power density and skin temperature. Meanwhile, substantial knowledge on superplastic materials, including the α+β titanium alloy Ti-6Al-4V, was established, primarily by the English scientist Roger

Tab. 10.1 Historic milestones of research on the phenomenon of superplasticity and SPF materials [1].

Authors	Alloys	Year
Bengough	α+β brass	1912
Rosenhain et al.	Zn-Al-Cu	1920
Hargreaves and Hills	Pb-Sn	1928
Jenkins	Cd-Sn, Pb-Sn	1928
Pearson	Pb-Sn, Bi-Sn	1934
Chaston	Pb	1935
Bochvar and Sviderskaja	Zn-Al	1945
Presniakov and Chervjakova	Al-Cu	1958
Underwood	overview on Soviet Union data	1962
Backofen et al.	Zn-22Al	1964

Pearce. So it was just a matter of time before the phenomenon was transformed into an industrial sheet forming process called "superplastic forming" (SPF).

At that time, sandwich structures were considered and obviously inspired investigations on titanium in bonding and welding techniques and also, later on, "diffusion bonding" (DB). The first structures were relatively thick-walled, integrally stiffened DB plates and SPF/DB sandwich structures, which were first commercialized in both the Concorde and the US B-1 project.

Interestingly, the scientists in the former Soviet Union concentrated their activities on hot bulk deformation in a superplastic state for gas turbine engine applications, a process today called "isothermal forging".

10.2
Superplasticity

During the 4th International World Conference on Superplasticity of Advanced Materials (ICSAM), held in Osaka in 1991, a general definition of the term superplasticity was formulated for the first time [2]:

Superplasticity is the ability of a polycrystalline material to exhibit, in a generally isotropic manner, very high tensile elongations prior to failure.

SPF materials were generally described as:

Metallic, ceramic, composite, or intermetallic multiphase materials with uniform or non-uniform relatively coarse (20 μm) to ultrafine (30 nm) grain size that has isotropic or anisotropic grain (phase) shape, size, or orientation.

Conventional $\alpha + \beta$ titanium materials fulfill both these definitions (Table 10.2). This is particularly true for the most widely used alloy, Ti-6Al-4V. In isothermal tensile tests at about 50% of the melting temperature (0.5 T_M), this alloy in its conventionally specified two-phase structure easily exceeds tensile elongations of

Tab. 10.2 Titanium alloys with SPF behavior [3].

Alloy	Test temperature [°C]	Strain rate [s⁻¹]	m Value
Ti-6Al-4V	840–870	1.3×10^{-4} to 10^{-3}	0.75
Ti-6Al-5V	850	8×10^{-4}	0.5
Ti-6Al-2Sn-4Zr-2Mo	900	2×10^{-4}	0.67
Ti-4.5Al-5M0-1.5Cr	870	2×10^{-4}	0.63–0.81
Ti-6Al-4V-2Ni	815	2×10^{-4}	0.85
Ti-6Al-4V-2Co	815	2×10^{-4}	0.53
Ti-6Al-4V-2Fe	815	2×10^{-4}	0.54
Ti-5Al-2.5Sn	1000	2×10^{-4}	0.49
Ti-15V-3Cr-3Sn-3Al	815	2×10^{-4}	0.5
SP700*	775	1.3×10^{-5} to 1.3×10^{-3}	0.59–0.38

* RMI data

1000% without necking. Furthermore, at about 900 °C and slow SPF deformation rates, the as-received fine-grained material shows only limited grain growth. Typically, SPF titanium alloys possess a grain size of less than 10 µm, an equiaxed grain shape, and a relatively homogeneous microstructure.

The theoretical approach to explaining the macrostructural processes leading to such large strains is based on three simultaneously acting mechanisms:

- grain boundary sliding
- grain rotation
- grain boundary diffusion.

Still today, however, a consistent model that completely formulates and proves the superplastic behavior is missing.

Tensile test have shown that the common relationship for hot deformation of metallic materials is also true for SPF materials:

$$k_f = A \times \varphi^n \times \dot{\varphi}^m \qquad \text{(eqn. 10.1)}$$

corresponds to USA/UK:

$$\sigma = A \times \varepsilon^n \times \dot{\varepsilon}^m \qquad \text{(eqn. 10.2)}$$

Assuming that during hot forming the term ε^n tends to 1 and correspondingly the strain hardening exponent n to 0, the flow stress only depends on the strain rate considering a constant factor A. Thus, the exponent m characterizes the intensity of flow stress dependence on flow rate. If arbitrary necking occurs at an incidental position, the local strain rate increases since displacement per time unit imposed by the tensile test machine is concentrated on this neck. The "dynamic strain hardening", characterized by the exponent "m", then causes an increase in flow stress and thus stabilizes the potential necking area. Local necking is suppressed, and the specimen is homogeneously strained further along its entire gauge length. This process is repeated multiple times until after several hundred percent straining a weak point finally leads to local necking and fracture of the specimen.

In contrast to other hot formed materials, SPF alloys usually have an m-value of m > 0.5. To determine the m-value, a stepped strain test is chosen. During the test the strain rate is step-wise increased, always after a short period of constant strain rate (Fig. 10.1).

A plot of the individual flow stresses σ versus the corresponding strain rates $\dot{\varepsilon}$ leads to a typical s-shaped curve. The strain-rate sensitivity is discussed in terms of three regions, as shown in Fig. 10.2. In region 1 slow strain rates dominate, and grain coarsening during long-term high temperature exposure is hindered. The typical SPF behavior is found in transition region 2. At the high strain rates in region 3, a similar behavior is observed as in forgings. Here strain hardening due to increased dislocation density leads to premature necking once the strain limit is exceeded. The m-values calculated from the slopes of the curves in Fig. 10.2 and plotted versus flow rates, result in a bell-shaped curve, as shown in Fig. 10.3.
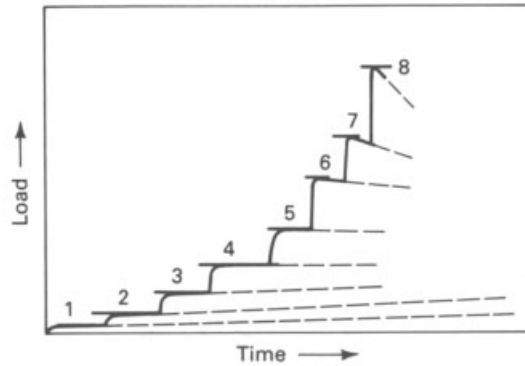
Fig. 10.1 Stepped strain test [4].
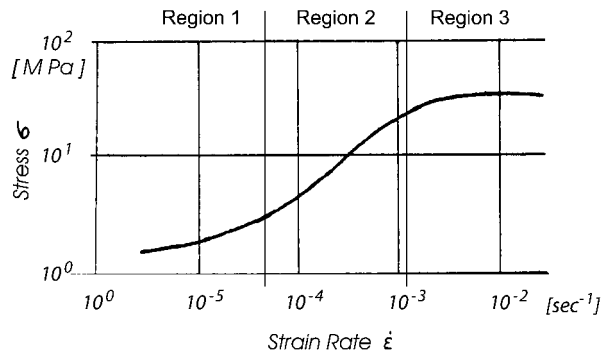
Fig. 10.2 Flow stress versus flow rate.
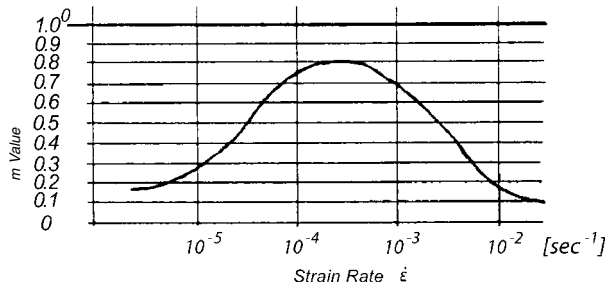
Fig. 10.3 m-Value versus flow rate.

The curves' maxima show the highest m-values and the corresponding flow rates. Thus, the optimum deformation rate for high elongation without necking is found for materials and test temperatures investigated for uniaxial loading. For standard SPF titanium alloys, typical parameters for a potential SPF processing window are as follows:

Fig. 10.4   Ti-6Al-4V tensile specimen deformed 830%.

- T_{SPF}: $\sim$ 700 to 1000 °C
- $\dot{\varepsilon}$: $\sim$ 1.3$\times$10^{-4} to 10^{-3} s^{-1}
- σ: $\sim$ 2 to 20 MPa.

Fig. 10.4 shows a Ti-6Al-4V specimen after tensile deformation of about 830% without necking.

Today it is assumed that nearly all polycrystalline materials can exhibit high tensile strains at the appropriate temperatures and strain rates, provided they can be processed in a sufficiently fine-grained structure and thus exhibit an adequate high resistance to grain growth during the SPF hot forming procedure. For polycrystalline materials, there are essentially two TMT (thermo-mechanical treatment) processes known to produce a fine-grained microstructure with grains of "sub-micrometer" to $\sim$ 20 nanometer size.

During the hot torsion process and the ECAE (equal channel angular extrusion) process additional slip planes are activated, which favor grain refinement. Neither process is yet commercialized. Titanium alloys treated by these measures, demonstrate the following SPF property improvements:

- reduction of deformation temperature by about 150 to 200 °C
- significant increase of deformation rate and overall strains.

10.3
Diffusion Bonding

Titanium materials are primarily corrosion resistant since they are able to form a dense oxide layer after a short period of time in air. This protective layer has the tendency to diffuse into the material at high temperatures. This "self-cleaning" characteristic of titanium, together with the good solid-state diffusion, is used for planar bonding of titanium sheet. The resultant bonding strength reaches the level of the base materials.

If bare titanium surfaces are pressed against each other at a temperature of about 0.5 T_M, diffusion takes place and both surfaces combine. A continuous microstructure is observed and prior interfaces can no longer be distinguished, as schematically outlined in Fig. 10.5.

Since joining occurs by avoiding the liquid phase state, no needle-like, strength-reducing weld-type structure is observed. Consequently, the process is therefore referred to as "diffusion bonding" (DB). DB temperatures are similar to SPF temperatures. Other important process parameters for diffusion bonding are time and pressure. As an example, the following parameters are common knowledge for Ti-6Al-4V:

Physical Processes

$$dm = -D \frac{c}{x} \Big/ A \, dt$$

dm =   Mass transported across the diffusion plane

D =   Diffusion coefficient

C/x = Concentration gradient across the diffusion plane

A =   Surface

dt =   Unit of time

Diffusion Bonding Mechanisms

First contact of a few roughness peaks

Deformation of roughness peaks

Grain boundary diffusion and grain boundary motion

Volume diffusion of atoms with vacancies

Fig. 10.5 Solid-state diffusion and mechanisms of diffusion bonding [5].

- T_{DB} : ~920 to 950 °C
- t_{DB}: ~2 to 3 h
- p_{DB} : ~20 to 60 bar = 2 to 6 MPa

10.4
The SPF Process

Today superplastic forming of Ti alloys is a standard industrial practice accepted worldwide. Due to the high temperatures and simultaneously relatively low flow stresses, deformation by means of gas pressure has found wide spread application. Because of titanium's high affinity to oxygen and hydrogen, inert gases are exclusively used as the pressure medium. Depending on component quality requirements, different purity grades of argon, for example, are used. The SPF process is schematically shown in Fig. 10.6.

First, the sheet exhibiting appropriate superplastic behavior is placed into the hot forming device. Today's applications cover sheet thicknesses ranging from 0.1 to more than 20 mm. The device is then placed into a special SPF hot press and pre-heated to the forming temperature. During SPF forming the projected temperature, e.g. 900 °C, has to be reached and kept at this value within small tolerances, mostly +/– 1 to 2% of the reference value.

After a short soaking time of the sheet, and after gas-tight closure of the apparatus with support of the press, the pressure for the forming process is increased. The component requires adaptive pressure control, which just depends on the ge-
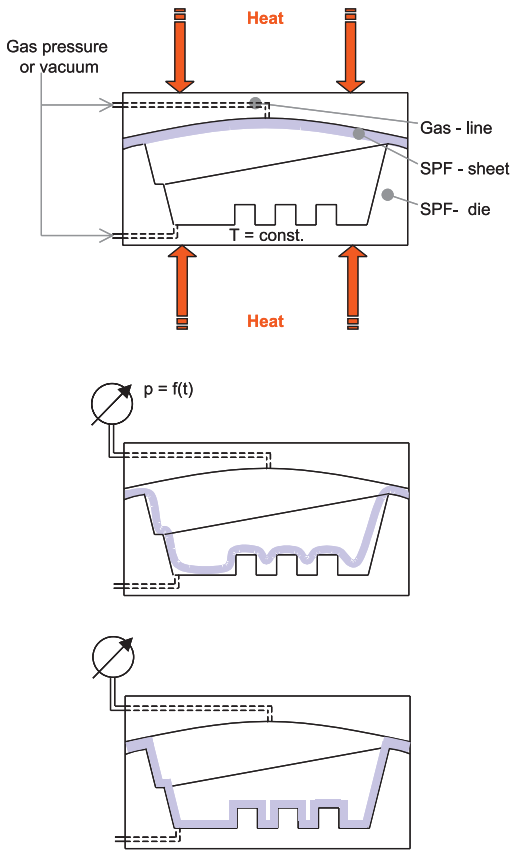
Fig. 10.6 SPF process scheme [7].

ometry. The cycle time is primarily dependent on the geometry of the component. For example, a deep, V-shaped structure has a higher final deformation degree in the bottom section than a flat, dish-shaped structure. For a first approximation, the deformation time for a known or estimated deformation level at the critical location, and the material-inherent, optimum deformation rate can be calculated. As a rule of thumb, the following equation can be used:

$$d\dot{\varepsilon} = d\varepsilon/dt \qquad\qquad (eqn.\ 10.3)$$

Components typically reveal deformation degrees of $\varepsilon < 300\%$. For a flow rate of $\dot{\varepsilon} = 3 \times 10^{-3}\ s^{-1}$, the deformation time, t_{SPF}, amounts to about 5.5 minutes.

The pressure curve and other process parameters, like the resulting wall thickness distribution of the final component, can be calculated by means of finite element (FE) simulation (Fig. 10.7).

The titanium sheet is tightly fixed between the cover and the forming device so that there is no after flow from the flange. An ironing of the material takes place.
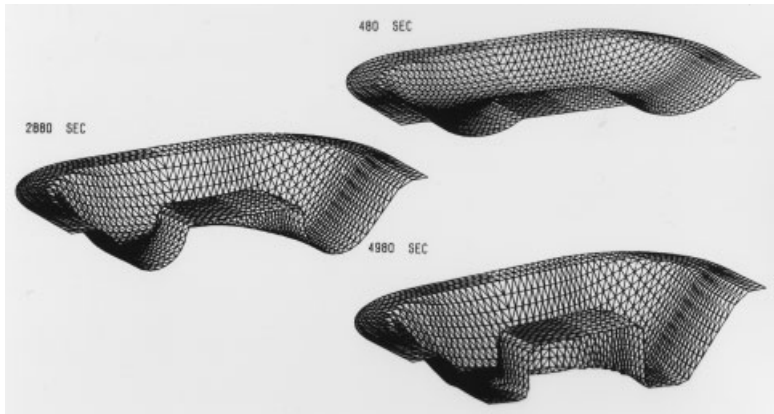
Fig. 10.7   FE simulation of SPF.

Therefore, the SPF process can also be considered to be a variant of stretch forming. The entire increase in area to form the final component geometry results from the unfixed area of the sheet membrane. The highest deformation degrees, and thus the thinnest wall thicknesses, are attained for that part of the sheet that finally touches the form. To properly control the required minimum wall thickness, extra measures are helpful like, for example, tailored blanks, pre-bulging or (however, with minor influence) various lubricants and variable pressure control.

10.5
SPF-Material Investigations for Parameter Definition

The above investigations on tensile behavior allow to make material and sheet thickness related forecasts for required temperatures, strain rates and expected deformation degrees. However, there are often discrepancies when the data are transferred to real component manufacturing. Most likely the reason is the different deformation mode: uniaxial tensile test versus biaxial SPF processing. Therefore, the "cone-test" has been developed as a process-relevant test (Fig. 10.8).

To establish the processing parameters for new SPF materials, or to screen the SPF behavior of batches of semi-fabricated products, the cone-test represents a practical and cost-effective test procedure, which can also be carried out in a commercial SPF press. The special advantage of this test is the very simple control of a constant flow stress. To adjust the flow stress and the accompanying constant flow rate, only a fixed deformation pressure is required. An example of such a set-up is shown in Fig. 10.8. The dome height and the minimum wall thickness achieved are directly readable from the test cones, which are deformed until fracture. Wall thickness reduction across the cone wall, a characteristic of the material used and process parameters applied, give further indications of the deformation degrees usable in practice. Due to its simplicity and lower cost, the cone test is

Fig. 10.8 Principle of cone-test [8].

also employed for performance tests and to analyze the validity of finite element programs.

A special feature of the test is the online recording of the deformation degrees actually reached during the forming operation, as shown in Fig. 10.8. Possible variations of flow stress, e.g. through grain growth, are thus detectable.

For novel sheet metals, a matrix of temperature and flow stress values is prepared based just on tensile test results. Data analyses provide the optimum parameters for temperature and strain rate of the specific materials. For incoming material, data of batches can be compared to known values. SPF formability can thus be simply verified (Fig. 10.9).
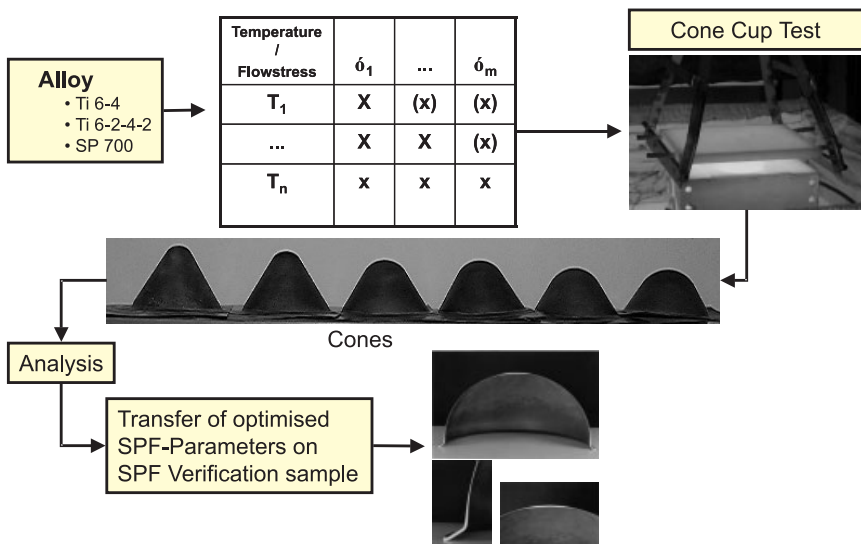
Fig. 10.9 Investigation of material on SPF-behavior with the help of the cone-test (FormTech GmbH, Germany).

10.6
SPF Tooling

Due to the high process temperatures, molding dies for mass production have to be made from scale-free and heat-resistant steels. For alloy selection, the sensitivity of titanium to nickel as an alloying element has to be considered. When properly designed, steel tooling has a long lifetime. It is possible to manufacture several thousand components in a single device without subsequent finishing work. For feasibility studies and small lots, ceramic dies may be used (Fig. 10.10). Lead times and material cost can be significantly reduced. However, even today the limited lifetime and the sensitivity to tensile stresses are major drawbacks for widespread application.

10.7
Examples of SPF Components

Due to high material and processing costs, the use of titanium is primarily concentrated in areas where one can take full advantage of the material's properties. In aerospace, these are primarily components that require increased temperature capability, high loads, and superior corrosion resistance.

Fig. 10.11 shows three SPF-manufactured components. The tank half shell (Fig. 10.11 a) is made from Ti-6Al-4V, since the tanks have to withstand high internal pressure and are exposed to aggressive corrosive media. In contrast to the competing forging process, it was possible to avoid machining for contouring the final half shells, thus gaining substantial savings in manufacturing time and costs. The close tolerance in the final wall thickness of the half shell is achieved by pre-machining the blanks before SPF as well as by wall thickness modulation during SPF. After the SPF cycle only the weld areas are machined to size and the surface is pickled. The α-stabilized zone formed during contact with the atmosphere while feeding and withdrawing parts has to be completely removed.

Fig. 10.10 SPF ceramic mold form.

a)
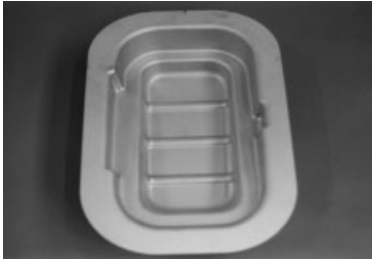
b)
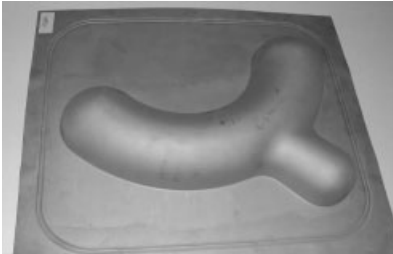
c)

Fig. 10.11 Examples of SPF components: half shells and casings [8] (ASTRIUM, AIR-BUS and PFW).

The half shell of a Y-duct shown in Fig. 10.11 c is manufactured from alloy SP700. This alloy can be superplastically deformed at temperatures as low as about 700 °C. Compared to conventional titanium alloys, this is a low SPF temperature. Also, since no oxide film forms, no pickling is required. Titanium was chosen for the Y-duct since hot gases are passed through the tubing system. Contrary to conventional structures from pure titanium, SPF is more cost effective since individual parts can be integrated into the final component. This reduces manufacturing and joining expenditures.

The component shown in Fig. 10.11 c replaces a hardware assembly consisting of many individual parts. The integral construction leads to substantial cost advantages and clearly demonstrates the potential of SPF technology. The complex geometry with a convex flange area, an inclined spacer flange, and multiple shapes is formed in a single SPF cycle.

10.8
SPF Forming Presses

Due to the complexity of the SPF process (see also Fig. 10.6) and the applied pressures and temperatures, it is common to use special hot presses. State-of-the-art SPF presses feature an integrated heater, as well as control systems to monitor the pressure of the forming medium and appropriate counteracting hydraulic locking systems to insulate tooling. To easily feed and unload large, thin-walled SPF components, the lower platen can often be driven out and thus features a "shuttle" design. Fig. 10.12 shows such a press. Presses are offered for platen dimensions ranging from about 0.5 m×0.5 m to 4.5 m×2.0 m, and press forces from about 10 MN to 250 MN.

10.9
SPF/DB Processing

SPF and DB processing can be combined into one press cycle. Since diffusion bonding also allows thin flat sheet to be bonded along a plane, complex sandwich structures can be realized. The process follows the steps outlined in Fig. 10.13:

- To separate sheet surfaces, a special parting agent is applied.
- For subsequent diffusion bonding, these areas remain untouched.
- Stacking of single sheets.
- Diffusion bonding in the press.
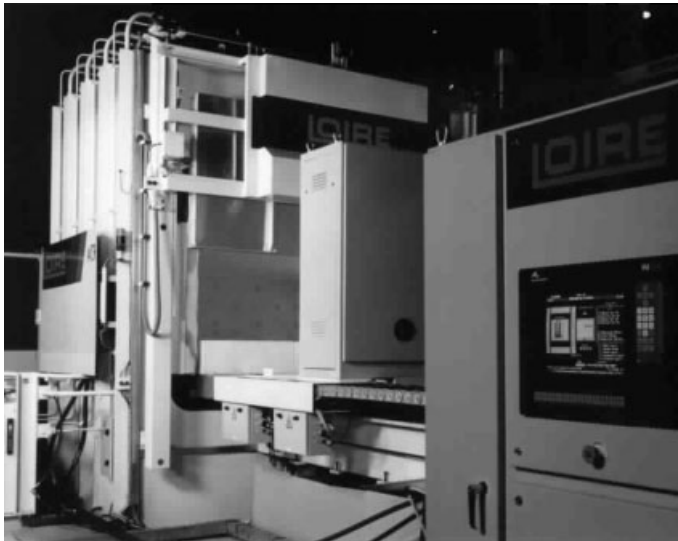
Fig. 10.12   SPF press (courtesy: ACB Pressure Systems) [9].

3 sheets   **4 sheets**

stop-off   stop-off

bonding of 1& 3 on 2	forming of 1 & 4 - bonding of 2 on 3.
forming	forming of 2 & 3.
calibration	bonding of 2 on1 & 2. bonding of 3 on 3 & 4.
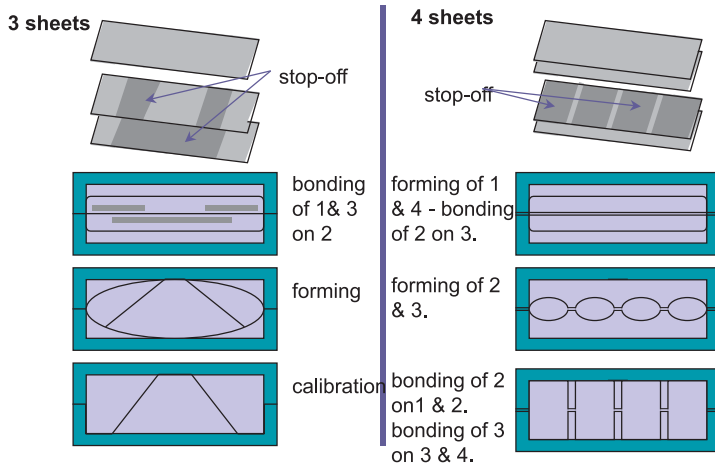
Fig. 10.13 SPF/DB process (schematically) [10].

- SPF to form the molded article. In this process the cell walls of the sandwich structure align with the intended design.

10.10
SPF/DB Structures and Components

Fig. 10.14 shows three different structures and the corresponding model components. The upper, "three-sheet structure" is particularly suitable for thin sandwich components. The outer skin sheets are thicker than the web sheets. This bridge girder design translates into exceptional stiffness in the web direction. Applications include highly loaded and fire-resistant gas turbine engine firewalls, integrally stiffened exhaust gas ducts, and gas turbine engine fan blades.

The integrally stiffened component consists of four individual pieces and can be manufactured from very thin sheet. The ribs can be designed as uniaxial or, for example, honeycomb structure. The stiffness can be varied to a large extent. Adequate cell size provided, the surface sheets are nearly continuously supported. Furthermore, the outer skins can be manufactured from sheets of high-temperature titanium alloys, which do not require a particularly high deformation potential since the deformation degree of the skin sheets is low. Such constructions are applied, for example, in temperature-stressed wings or fuselage panels for hypersonic missiles.

The final design has multiple uses. It is possible to achieve a quasi-continuous outer sheet support or to realize very large sandwich cross sections. An integrally stiffened hot air supply pipe with a large component height is shown. The channel replaces a multitude of individually manufactured sheet components that were welded together afterwards. The sandwich plate with a small rib distance
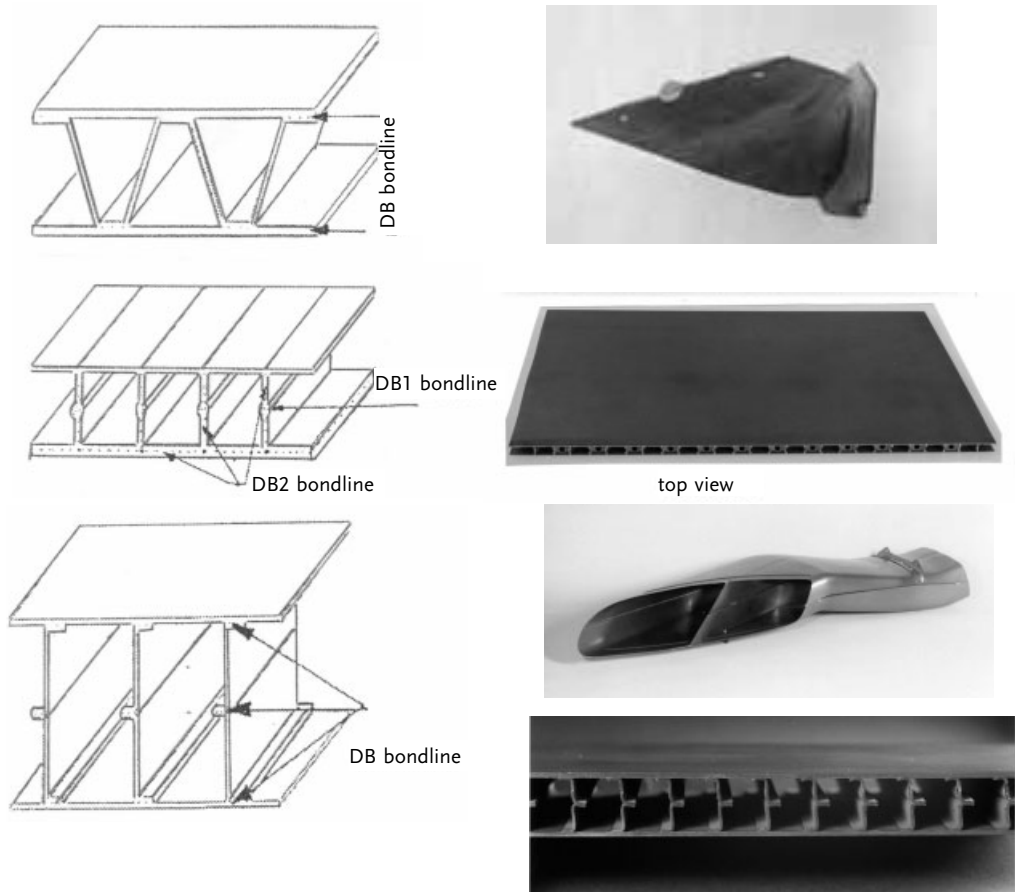
Fig. 10.14 Example of SPF/DB components [11].

serves as a demonstrator design that effectively improves laminar flow over aerodynamic surfaces.

10.11
Summary

Today the phenomenon of superplasticity offers the designer substantially increased design variability. For titanium and titanium alloys, SPF and SPF/DB have been industrially implemented to manufacture a multitude of thin-walled structural components. Forming of otherwise hard-to-process high strength titanium alloys and improvement of the functionality of SPF and SPF/DB processes are of prime importance. Compared with conventional forming and shaping methods, significant cost and weight savings have been reported. Cost reductions result

from material savings, reduced tooling costs, and reduced efforts due to single component manufacturing. Weight savings are almost always achieved by replacement with alternative materials, e.g. replacement of pure titanium or stainless steel. If titanium alloys replace pure titanium, significant wall thickness reductions of about 40% are possible due to the strength advantage of the alloys. Compared to stainless steel, the reduced specific weight of about 50% is another striking argument.

Sheet material of $\alpha+\beta$ titanium alloys is particularly suitable for SPF/DB since it already exhibits a sufficiently fine-grained structure in the as-received condition, and does not tend to excessive grain growth. The efficiency of the SPF process can be further increased for titanium, allowing lower deformation temperatures and higher flow rates. The development of alloy SP 700 points to this direction. To evaluate SPF materials' properties, the cone-test and special tensile tests are available.

In summary, SPF and SPF/DB have today matured to an economic manufacturing technique for complex titanium sheet structures.

10.12
Referenced Literature and Further Reading

1 O.A. KAIBYSHEV: Superplasticity of Alloys, Intermetallics and Ceramics, Springer-Verlag (1992)

2 S. HORI, M. TOKIZANE, N. FURUSHIRO (eds.): Superplasticity in Advanced Materials – Summery of conference, ICSAM-91 (1991)

3 ASM Handbook: Materials Properties Handbook: Titanium Alloys, ASM International (1994)

4 ASM Handbook: Forming and Forging, Volume 14, ASM International (1988)

5 W. BECK, P. Knepper: Superplastic forming and diffusion bonding of a cell component of Ti6Al4V, DVS-Berichte (1985) (in German)

6 P.-J. WINKLER: Diffusion Bonding and Super Plastic Forming, Two Complementary Manufacturing Techniques, Mitteilungen aus dem Zentrallabor **17** (1989)

7 W. BECK, O. KRAATZ: Actual SPF and SPF/DB Applications, DGM, Materialsweek 2001, Munich, Germany

8 W. BECK: SPF and SPF/DB, Material and Process Development Projects, EuroSPF-1, 2001, Villard de Lans, in print

9 N.N., Forming Presses for the Aerospace Industry, ACB Pressure Systems, Nantes, France

10 A. PETIOT, B. PELLETIER: SPF and SPF/DB from the Viewpoint of a Press Manufacturer, DGM, Materialsweek 2001, Munich, Germany.

11 W. BECK, P.-J. WINKLER: Superplastic Forming and Diffusion Bonding of Sheet Metal Sandwich Structure Components, International Symposium on Superplasticity, ASM, Materials Solutions, Indianapolis, 2001

11
Forging of Titanium

G. Terlinde, T. Witulski and G. Fischer, *OTTO FUCHS Metallwerke, Meinerzhagen, Germany*

11.1
Introduction

Since they were first developed in the 1940s, titanium and titanium alloys have become an important alternative to existing materials like steel, aluminum, and nickel-base superalloys. Their attractiveness is primarily based on an excellent combination of specific strength and corrosion resistance. With a density of about 4.5 g cm^{-3}, titanium is just in between aluminum (2.7 g cm^{-3}) and steel (7.8 g cm^{-3}). The yield strength range of technical interest at room temperature varies from 800 to 1300 MPa.

Titanium products are manufactured by forging, casting, as well as powder metallurgy. Forging is by far the most applied processing route. It offers the ability to precisely tailor microstructures and properties through deformation and heat treatment. Compared to casting, forging enables production of larger cross sections. By appropriate processing and strict process control, highly reproducible properties are possible.

The following will present some general properties and applications of titanium alloys. The potential of thermomechanical treatment and forging process design will be addressed next. Finally, an example for the thermomechanical optimization of a gas turbine engine alloy will be presented as well as some typical forged components.

11.2
General Properties and Applications

Depending on their chemical composition, titanium alloys are classified as α, $\alpha + \beta$ or β alloys [1]. The various alloys, consisting of the hexagonal α phase, the body-centered cubic β phase, or of both phases, show quite specific properties (Fig. 11.1).

For example, α or near-α alloys are preferentially used for gas turbine engine applications due to their good creep behavior and weldability, while β alloys have a high strength potential that comes at the expense of weldability and elevated temperature capability.
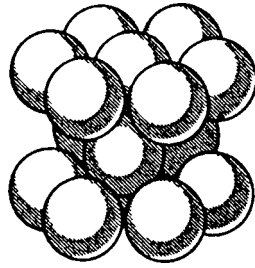
(α) hexagonal
close packed [hcp]
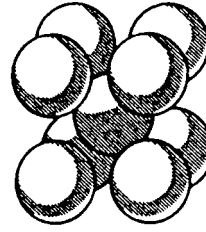
(β) body centered
cubic [bcc]

Alpha-stabilizing
elements

For example:
aluminum
oxygen
nitrogen

Beta-stabilizing
elements

For example:
molybdenum
iron
vanadium
chromium
manganese

Increasing quantities of alpha stabilizers promote alpha phase.

Increasing quantities of beta stabilizers promote beta phase.
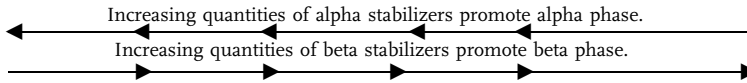
Alpha structure	Near-alpha (some beta)		Mixed alpha-beta structure		Near-beta (some alpha)		Beta structure	
Unalloyed Ti	Ti-5Al-6Sn-2Zr-1Mo-0.2Si	Ti-6Al-2Sn-4Zr-2Mo	Ti-6Al-4V	Ti-6Al-6V-2Sn	Ti-6Al-2Sn-4Zr-6Mo-	Ti-8Mn	Ti-8Mo-8V-2Fe-3Al	Ti-11.5Mo-6Zr-4.5Sn
Ti-5Al-2.5Sn		Ti-8Al-1Mo-1V						Ti-13V-11Cr-3Al

Higher density

Increasing heat-treatment response

Higher short-time strength

Higher creep strength

Increasing strain rate sensitivity

Improved weldability

Improved fabricability
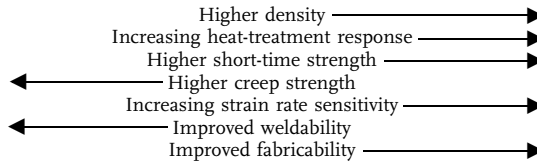
Fig. 11.1 Classification of titanium alloys based on their crystal lattice structure [1].

Besides chemical composition, the microstructure has a dominating influence on properties. In Fig. 11.2, typical microstructures of an $\alpha+\beta$ alloy are shown with respect to a schematic phase diagram. In both figures on the left lamellar microstructures are compared, which are produced by β annealing and β forging, respectively. It is obvious that deformation avoids the pronounced and harmful
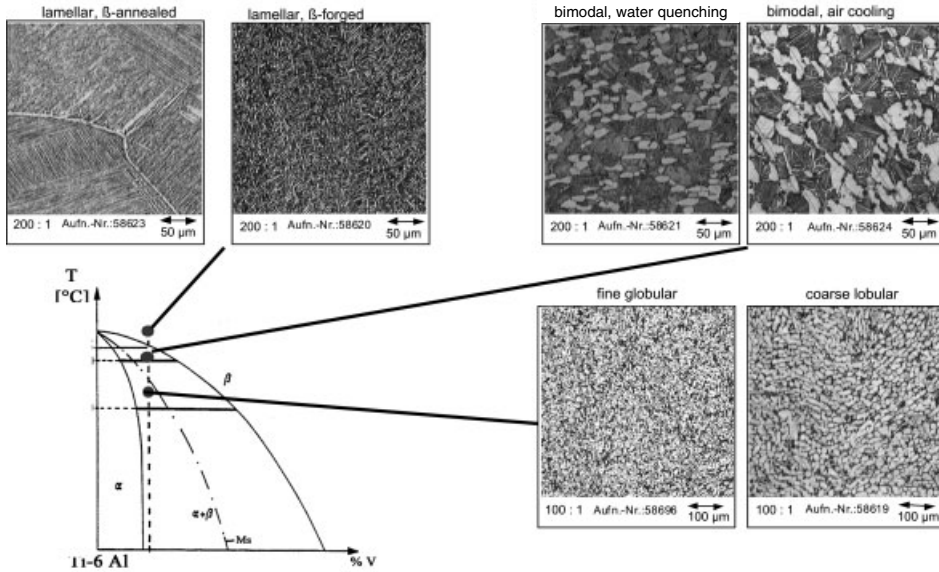
Fig. 11.2 Microstructures of the alloy Ti-6Al-4V.

Fig. 11.3 Applications of titanium alloys.

decoration of grain boundaries with α phase. The two upper right figures show bi-modal microstructures, i.e. equiaxed α in a transformed β structure. The solution heat treatment temperature and the cooling rate can modify the α volume fraction and the fineness of the transformed structure after solution heat treatment. Deformation at relatively low temperatures or slow cooling rates after deformation result in equiaxed microstructures with high α volume fraction. Depending on their processing history, the structures differ in fineness.
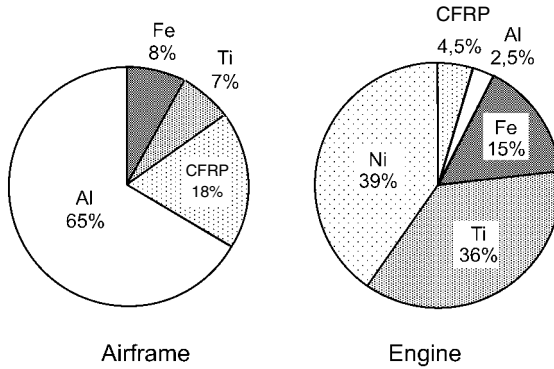
Fig. 11.4 Share of titanium alloys in aerospace compared to other materials [2].

There is a large spectrum for the application of titanium alloys. Although aerospace still dominates, other market sectors are broadening titanium's application such as in medical devices, construction engineering, and automotive components (Fig. 11.3). Fig. 11.4 shows the portion of titanium alloys used in the aviation industry subdivided into airframe and engine materials. In tables 11.1 and 11.2 the most common titanium forging alloys are listed. The tables describe strength, toughness, maximum thickness for heat treatment, and show typical properties and fields of application of the alloys. Ti-6Al-4V is the by far the most often used titanium alloy since it offers the best property balance.

11.3
Thermomechanical Treatment of Titanium Alloys

11.3.1
Processing of Forging Stock

High quality forged titanium products can only be achieved if the material is given a thermomechanical treatment tailored to its requirements for application. For the production of forging stock, titanium sponge and master alloys are mixed, then pressed to briquettes, welded to electrodes, and then double or triple vacuum arc re-melted (Fig. 11.5). The resulting cylindrical cast ingots are then processed to billets or bars by hand forging and/or radial forging. Alternate forging above and below the β transus temperature is performed to break up the cast structure and to produce a fine-grained equiaxed α/β microstructure. In a final α/β deformation step, the required diameter for the subsequent hand or die forging is achieved. Since the thermomechanical treatment of the starting material considerably influences the later properties, these processes are often coordinated at an early stage between material supplier, forger, and customer.

Tab. 11.1 Titanium alloys and their applications.

Alloy	Alloy Type	Properties and Applications
Ti 99.5	α	High corrosion resistance, good weldability, highly formable
Ti 99.4	α	Like Ti 99.5, higher strength
Ti 99.2	α	Highest strength of unalloyed titanium, weldable, otherwise comparable to Ti 99.5 and Ti 99.4
Ti-2Cu	α	Alloy with moderate strength, good elevated temperature strength and creep strength at 200–500 °C, relatively difficult to deform, weldable
Ti-5Al-2.5Sn	α	Weldable alloy of moderate strength, heat-treatable, good forgeability
Ti-6Al-2Sn-4Zr-2Mo-0.1Si	α + β	High temperature alloy, primarily used in gas turbine engines up to about 520 °C, weldable
Ti-5.8Al-4Sn-3.5Zr-0.7Nb-0.5Mo-0.35Si	α + β	High temperature alloy, primarily used in gas turbine engines up to about 600 °C, weldable
Ti-5Al-2.5Fe	α + β	Implant alloy, corrosion resistant, biocompatible
Ti-6Al-4V	α + β	Most widely used, high strength, heat-treatable titanium alloy, multiple applications, weldable, good forgeability, good toughness
Ti-6Al-4V ELI	α + β	Like Ti-6-4, but increased toughness
Ti-4Al-4Mo-2Sn	α + β	High strength, good heat-treatability, high toughness α + β alloy, used in aerospace for structure and engine
Ti-6Al-6V-2Sn	α + β	Highest strength α + β alloy, good forgeability, used in aerospace structures
Ti-6Al-2Sn-4Zr-6Mo	α + β	High strength, good heat-treatability, alloy with moderate high temperature strength; used for gas turbine engine components
Ti-10V-2Fe-3Al	Meta-stable β	Good heat-treatability, metastable β alloy, medium to very high strength (900–1400 MPa), excellent fatigue behavior, excellent combination of yield strength and toughness at high strength levels, good forgeability, used in aero structures, landing gear, helicopter rotor head

11.3.2
Forgings

Further processing of the forging stock in the forge can be principally divided into α/β forging and β forging (Fig. 11.6). During α/β forging the material is heated to a temperature 30 °C to 100 °C below the β transus ($T_β$). The temperature is chosen sufficiently high that crack-free forging is possible at high degrees of deformation. Additionally, heating of the workpiece during deformation has to be consid-

Tab. 11.2 Properties of titanium alloys.

Alloy	Density [g cm⁻³]	Heat Treatment	Heat Treatment Thickness d [mm]	YS [MPa]	UTS [MPa]	%El	%RA	K_{Ic} [MPa $\sqrt{m}$]	
								min	typical
Ti 99.5	4.5	annealed	≤80	200	290–420	24	–	–	–
Ti 99.4	4.5	annealed	≤80	290	390–540	20	30	–	–
Ti 99.2	4.5	annealed	≤80	490	540–740	15	25	–	–
Ti-2Cu	4.56	annealed	≤80	400	540	16	35	–	–
		aged	≤80	540	650	10	30	–	–
Ti-5Al-2.5Sn	4.46	annealed	≤100	760	790	10	25	–	70
Ti-6Al-2Sn-4Zr-2Mo-0.1Si	4.55	aged	≤80	830	900	8	20	50	60
Ti-5.8Al-4Sn-3.5Zr-0.7Nb-0.5Mo-0.35Si	4.55	aged	≤75	880	1000	6	15	–	45
Ti-5Al-2.5Fe	4.45	annealed	≤50	780	860	8	25	–	–
		annealed	50<d≤160	780	860	8	20	–	–
Ti-6Al-4V	4.43	annealed	≤80	830	900	10	25	50	70
		annealed	80<d≤150	830	900	8	20	–	70
		aged	≤13	1030	1100	8	15	–	45
		aged	13<d≤25	1000	1070	8	15	–	–
Ti-6Al-4V ELI	4.43	annealed	≤75	795	860	10	25	–	95
		annealed	75<d≤100	760	830	10	20	–	95
Ti-4Al-4Mo-2Sn	4.60	aged	≤100	920	1050	9	20	–	60
		aged	100<d≤150	870	1000	9	20	–	60
Ti-6Al-6V-2Sn	4.54	annealed	≤80	930	1000	8	20	–	45
		aged	≤25	1100	1200	6	15	–	35
Ti-6Al-2Sn-4Zr-6Mo	4.65	aged	≤150	940	1080	4	–	55 (β)	75(β)
Ti-10V-2Fe-3Al	4.65	aged highest strength	≤75	1105	1195	4	–	44	55
		aged high strength	≤100	1035	1100	6	–	60	75
		aged medium strength	≤100	895	965	8	20	88	100

ered in order to avoid overheating of the microstructure by going above the β transus temperature. Deformation degree and deformation rate have to be carefully selected so that desired microstructural developments, e.g. recrystallization, lead to an equiaxed shape of the α phase. Usually cooling after α/β forging is done in air.

β forged titanium alloys are much more sensitive to deformation conditions. The material is first heated above the β transus temperature, and the forging pro-
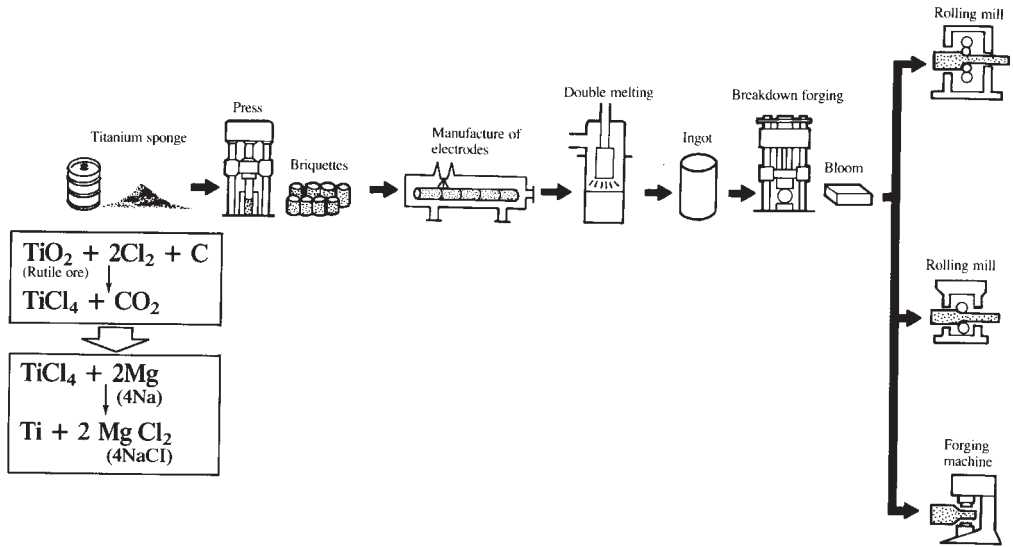
Fig. 11.5 Production of forging stock [1].

cess has to be finished before the β to α transformation starts. Here the hold time at deformation temperature before forging is of prime concern since at these higher temperatures grain coarsening and detrimental hydrogen pickup can occur. To avoid detrimental microstructures, e.g. decoration of grain boundaries with

Parameters	Effects (Examples)
– Temperature:	Workability, Microstructure (α/β or β) Grain Coarsening (T>T_β), H_2
– Dwell Time:	Hydrogen Absorption, Microstructure Coarsening, esp. for T>T_β
– Deformation Degree:	Workability, Microstructure (e.g. Recrystallization, Grain Structure, Formation of α Phase)
– Deformation Rate:	Workability, Kinetic Heating during Deformation, Recrystallization
– Cooling Rate after Forging:	Transformation and Precipitation Behavior

Fig. 11.6 Parameters influencing forging of titanium alloys.

α, a sufficient β deformation and a controlled cooling after β forging have to be chosen. Here the cooling rate has to be adapted to the transformation characteristics of the alloy. So cooling of near-α alloys, for example, has to be done in water, while for more slowly transforming β alloys air cooling may be sufficient.

11.3.3
Heat Treatment

Similar to forging, heat treatment is also distinguished between a β solution heat treatment and an α/β solution heat treatment (Fig. 11.7). Annealing above the β-transus leads to a lamellar or Widmanstätten microstructure (Fig. 11.2). This microstructure is characterized by high fracture toughness and reduced ductility. Annealing below the β transus leads to a bimodal microstructure. This structure is composed of an equiaxed α phase, with a volume fraction determined by the temperature, and a transformation structure that is controlled by the cooling rate from the solution heat treatment temperature. After solution heat treatment, a stress relief annealing is usually performed, or an aging treatment to increase the alloy's strength.

11.4
Process Design

11.4.1
Geometric Requirements

Considering the variety of applications for titanium forgings, process design is necessarily adjusted to the particular part. The majority of forged aerospace parts will be
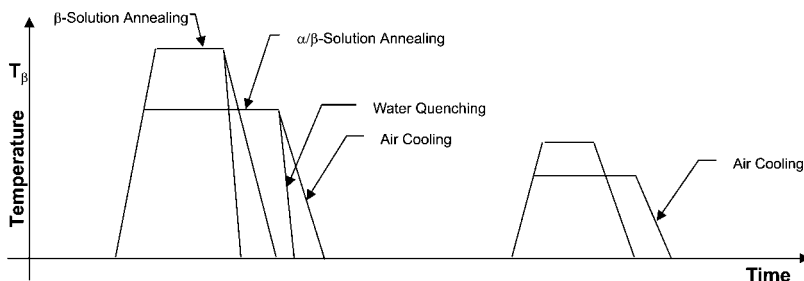
Solution Annealing	
– Temperature:	**Lamellar/Bimodal Microstructures** $(T > T_\beta / T < T_\beta)$ **Various Bimodal Microstructures (α_p)**
– Time:	**Grain Coarsening ($T > T_\beta$) Hydrogen Absorption**
– Cooling Rate:	**Transformation Behavior**

Ageing	
– Temperature:	**Precipitation, Stress Relief Annealing**
– Time:	**Precipitation, Stress Relief Annealing**

Fig. 11.7   Heat treatment of titanium alloys.

1. Machining Tolerance
2. Die Tolerance
3. Straightness
4. Die Closure Tolerance
5. Mismatch
6. Thermal Expansion
7. Draft Angle
8. Flash
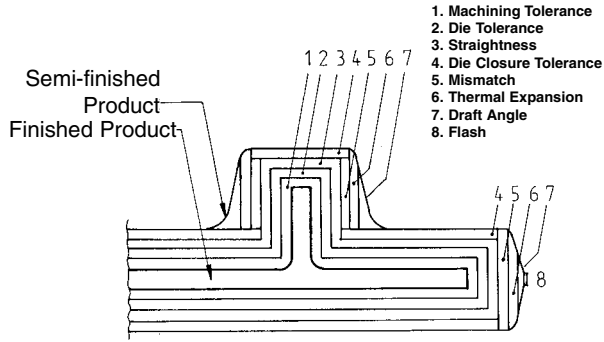
Fig. 11.8 Tolerances for forged components.
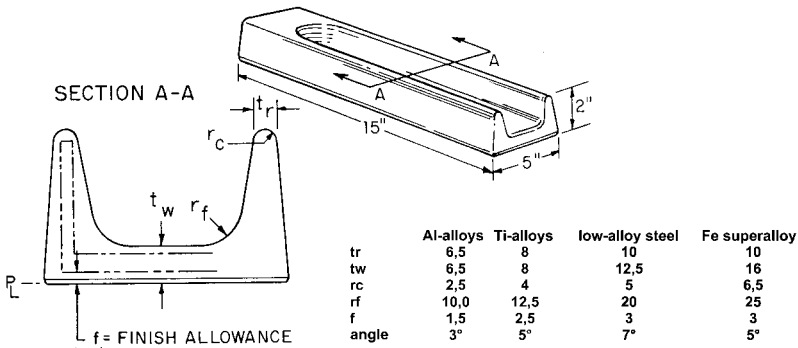
Fig. 11.9 Design of forged components [3].

	Al-alloys	Ti-alloys	low-alloy steel	Fe superalloy
tr	6,5	8	10	10
tw	6,5	8	12,5	16
rc	2,5	4	5	6,5
rf	10,0	12,5	20	25
f	1,5	2,5	3	3
angle	3°	5°	7°	5°

machined in their entirety. Apart from considering the standard tolerances (Fig. 11.8) for titanium alloys, the α-case layer, which evolves during manufacturing, also has to be taken into account. Oxygen diffusion into the material leads to a highly enriched zone of α resulting in a hard and brittle surface layer about 0.2 mm thick. Before further machining, the layer has to be removed by shot peening and pickling.

The actual forging part geometry is developed based on these tolerances. In Fig. 11.9 typical draft angles, radii, and web and rib thicknesses are compared to other materials.

11.4.2
Forged Components and Forging Equipment

Besides typical hand-forged parts, die-forged parts are primarily manufactured. Die forging is also economic for small batches due to the high material costs. Often so called "blocker type" die-forged parts are manufactured. These parts are frequently simple and thick-walled, and tooling costs are lower than for conventional tools.
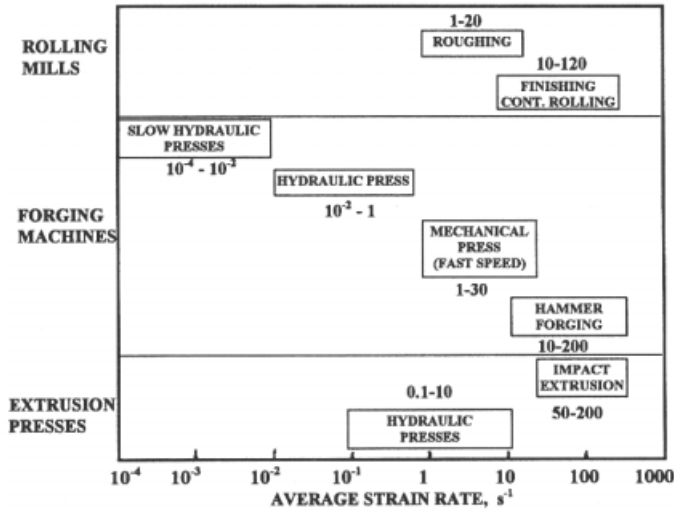
Fig. 11.10 Forging equipment and their strain rates [4].

In special cases, precision-forged parts are also manufactured, which are at, or close to the net shape. Substantially tighter tolerances can often only be achieved by isothermal forging, which substantially increases production costs.

In principle, all kinds of forging presses can be used for die forging (Fig. 11.10). However, fast mechanical presses and hammers are less appropriate due to the high deformation rates and thus the risk of cracking and overheating from the deformation energy introduced. Therefore, hydraulic presses are often used for difficult to deform materials or complex geometries, allowing a better control of the deformation rate (Fig. 11.11).

11.4.3
Processing Window for Forgings

For a deformation process the important design parameters are temperature, degree, and rate of deformation. In addition, friction conditions, tooling temperature, transfer times between furnace/press and press/cooling, microstructure, and deformation history of the starting material have to be considered.

Plotting flow curves allows to estimate the deformation resistance and therefore the required loads. In Fig. 11.12, the flow stresses for some titanium alloys are shown in relation to their β transformation temperatures. For all alloys listed the flow stress strongly drops until the β transus temperature is reached. Above the β transus the temperature dependence on flow stress is less pronounced.

For many materials the flow stress alone is not sufficient to design the processing route since it provides no information on deformation capability and microstructural development. In [4] a procedure is described which enables one to develop so called "processing maps" by analyzing the flow curve in combination

Fig. 11.11   30 000 t hydraulic press.
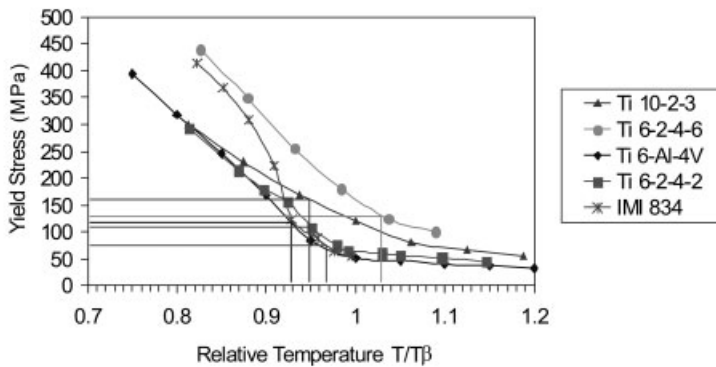
Fig. 11.12   Flow curves of titanium alloys.

with investigations on the microstructure of compression specimens. Such a dia-
gram is shown in Fig. 11.13 for the alloy Ti-6-2-4-2. The contour lines specify the
efficiency of energy introduction into the material, which indirectly gives informa-
tion about the tendency of the material to recrystallize or to form shear bands. In
Ti-6-2-4-2, for instance, dynamic recrystallization of α is observed at temperatures
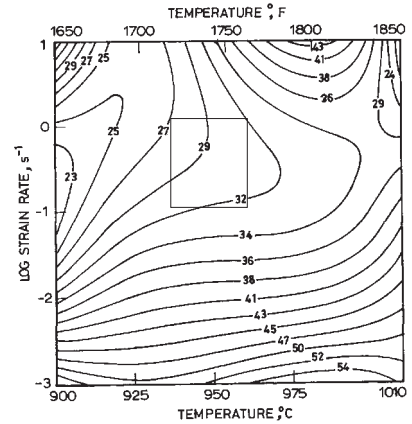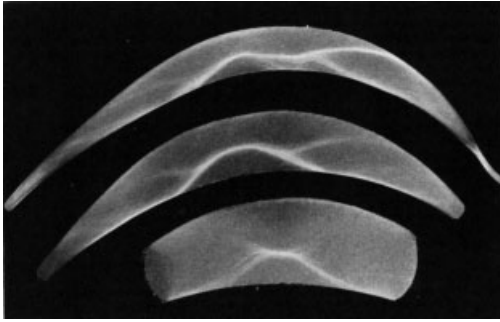
Fig. 11.13 Shear bands in forged blades of Ti 6-2-6-2 S [5] and processing map of alloy Ti-6-2-4-2 S [4].

between 950 °C and 990 °C and deformation rates between 1 and 10 s^{-1}. At lower temperatures (900–925 °C) and high deformation rates (1–10 s^{-1}) shear bands form in areas with high deformation, which can lead to material separation (Fig. 11.13). Therefore, forging parameters can be chosen which avoid undesired reactions.

Apart from these entirely isothermal observations, workpiece heating during deformation as well as cooling of the component surfaces by the substantially cooler dies (the "die chill zone") during deformation also have to be considered. In the next paragraph, the potential of finite element (FE) simulation as a tool for modeling complex forging processes will be presented.

11.4.4
Finite Element Simulation

FE programs to simulate deformation have been used for quite some time. Increased computer capacity and improved simulation programs now allow 3D component calculations. Apart from mere calculation and optimization of loads, material flow and tooling loads, there is the chance to calculate the microstructural development and so indirectly the component properties [6]. Currently, predictions of microstructures for titanium alloys are not yet possible due to the lack of metallurgical models. Nevertheless, FE simulations can be used to design and optimize processes with respect to modeling of component properties.

This is shown in Fig. 11.14 for a β-forged gas turbine engine compressor disk made of Ti-6-2-4-2. To avoid a continuous precipitation of the α phase at grain boundaries during processing, rapid cooling of the forged component after die forging is essential. As the temperature distribution in the left figure shows, immediately after deformation large portions of the parts are still above the β-transus
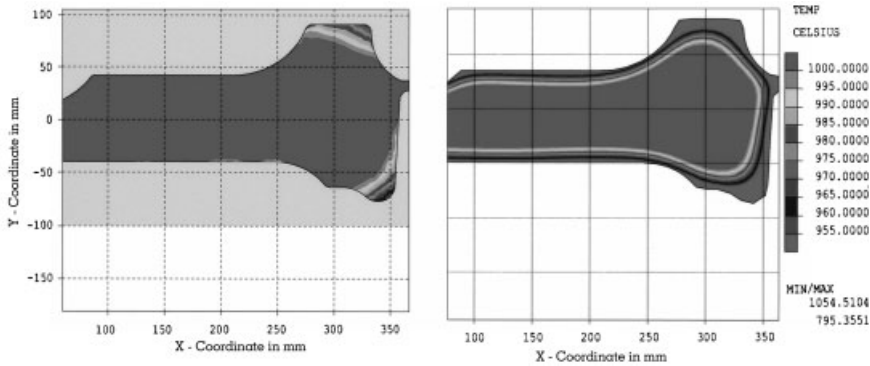
Fig. 11.14 Use of FEM to calculate the "die chill zone" (Ti-6-2-4-2 engine disk).

temperature (1000 °C). 30 s after deformation the temperature near the surface has already dropped 50 °C below the β-transus. Knowing the time-dependent α/β transformation behavior (e.g. from TTT diagrams) the thickness of the "die chill zone", which shows an undesirable microstructure, can be estimated. If included in the forging allowance, this zone can be removed during subsequent machining without leaving a negative influence on the final component.

An important future task will be the development of metallurgical models, which also include pre- and post-forging process steps (billet heating, cooling after forging, thermal treatment) and further optimization of properties at simultaneously reduced material input and production costs.

11.5
Examples for Process Optimization and Applications

The possibilities of process optimization are subsequently shown for two typical titanium forged parts, a gas turbine engine disk made from TIMETAL 834 and a structural Ti-6Al-4V component.

TIMETAL 834 is the most advanced conventional elevated temperature titanium alloy available today for gas turbine engine applications. Fig. 11.15 summarizes how properties can be tailored by using various forging routes. As an example, two alternative α/β-processing routes result in different α/β microstructures and consequently lead to an improved LCF lifetime for the finer microstructure. Forging in the β phase field leads to a lamellar microstructure and thus an improvement of creep strength and fracture toughness, at the expense of ductility, however. Depending on requirements, heat treatment, i.e. variation of solution heat-treatment temperature, quenching, and aging conditions, also allows a wide variation of properties. Fig. 11.16 shows a pre-machined compressor disc made from TIMETAL 834.

Apart from metallurgical requirements, the Ti-6Al-4V component in Fig. 11.17 represents a particular challenge for forging technology. Prior to die forging a complex

	α/β Route 1	α/β Route 2	β-Route
Tensile Test 600°C			
YS (MPa)	536	551	542
TS (MPa)	673	679	683
% El	14.7	13.3	8.5
% RA	45	42	26
K_{Ic} **(MPa√m)** RT	43.4	42.7	58.3
Creep Test			
Creep Strain A_p (%) 600°C, 100 h, 175 MPa	0.13	0.17	0.07
LCF Test			
R_{max} = 900 MPa R = 0.05, 0.3 Hz, RT Life Time (cycles)	6451	11606	5764
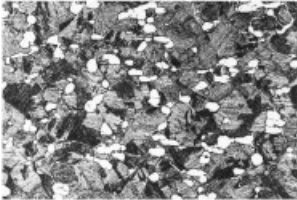
α/β-Route 1   0,2 mm
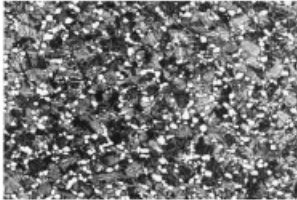
α/β-Route 2   0,2 mm
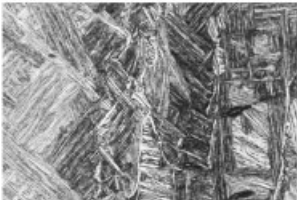
β-Route   0,2 mm

Fig. 11.15 Hot-die forged compressor disk of TIMETAL 834; mechanical properties for different process routes (average values) and corresponding microstructures.

Fig. 11.16 Machined compressor disc "Stage 3 blisk" made from TIMETAL 834; about 40 kg; $\varnothing$ = 500 mm.
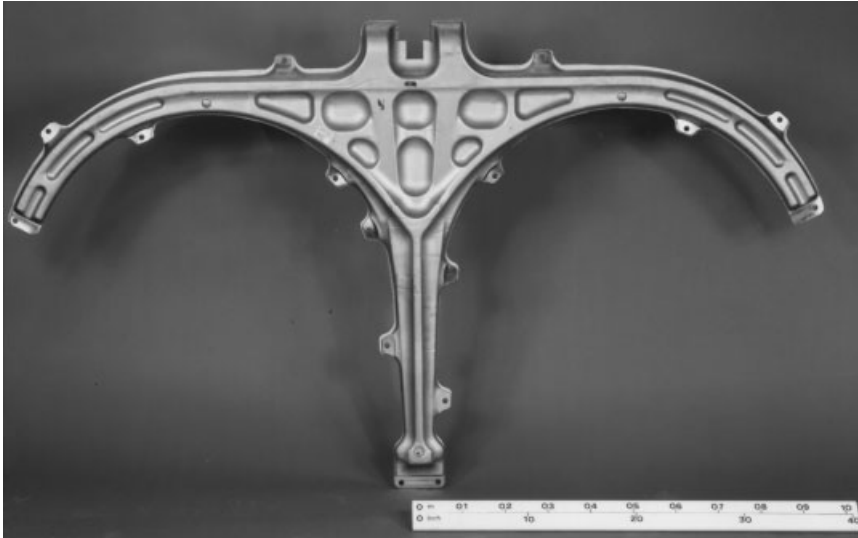
Fig. 11.17 Die-forged component "frame" made of Ti-6Al-4V.

pre-form has to be manufactured from cylindrical forging stock. This is done by multiple die forging in a block die combined with a hand forging step and a bending operation. Only by such a route can a minimization of the metal input, and thus economical processing, be possible. After flash removal and stress relief annealing, tensile data are generated for each part on a specimen taken from the forging.

Compared to forging parts for the automotive industry, forged components for aerospace applications are produced in much smaller quantities of about 100–5000 parts per year. Nevertheless, particularly highly stressed components, e.g. gas turbine engine compressor disks, are also subjected to a statistical control. The aim is to monitor processing variations, but also – in cases with stable production – to minimize cost intensive tests. Tab. 11.3 shows the statistical evaluation of mechanical tests for a compressor disk. The results of the control ring, taken from each part after heat treatment, were analyzed. After having proven a reproducible production (Cpk > 1) the amount of testing was reduced from 100% initially to 10%.

Minimization of scatter during processing and, at the same time, reduction of costs for production and testing are the central future needs. This necessitates that the entire process chain, starting from production of forging stock and ending with machining of forged components, is continuously monitored and optimized. Advanced tools like forging and microstructural simulation can significantly contribute to a successful future development of forging technology.

11.6
Referenced Literature and Further Reading

1 M. J. Donachie: Titanium A Technical Guide, ASM (1988)

2 M. Peters, J. Kumpfert, C. H. Ward, C. Leyens: this reference, Chapter 13

3 A. M. Sabroff, F. W. Boulger, H. J. Henning: Forging Materials and Practices (1968)

4 Y. V. R. K. Prasad, S. Sasidhara: Hot Working Guide, ASM (1997)

5 T. G. Byrer, S. L. Semiatin, D. C. Vollmer: Forging Handbook, ASM (1985)

6 K. F. Karhausen: Integrierte Prozess- und Gefügesimulation bei der Warmumformung, Umformtechnische Schriften, Band 52

12

Continuous Fiber Reinforced Titanium Matrix Composites: Fabrication, Properties and Applications

C. Leyens, J. Hausmann and J. Kumpfert*, *DLR-German Aerospace Center, Cologne, Germany, * Airbus Industrie, Blagnac, France*

12.1
Introduction

Titanium alloys and titanium aluminides exhibit excellent mechanical properties, distinguishing themselves as lightweight materials for applications where high specific strength, high ductility and toughness, good corrosion resistance as well as high creep and fatigue resistance are required. The service temperatures range from room temperature and below, to 750 °C and potentially higher for the titanium aluminides. Today, the useful service temperature of titanium alloys is limited to about 550 °C where near-α titanium alloys are used. However, a general trend clearly emerges toward higher temperature requirements that is driven by the aerospace industry. Here, new design concepts for compressors and turbines in gas turbine engines will result in higher mechanical and thermal loading of the components, increasing the overall performance of the engines. Since lightweight structures are always a major requirement for gas turbine engines, new materials concepts must be developed beyond the classical monolithic titanium alloys. While titanium aluminides, particularly gamma titanium aluminides (see Chapters 4 and 14), may broaden the spectrum to higher temperatures, the use of titanium-based composites in highly loaded components would prove to be a quantum leap for materials design, hence opening unknown possibilities to engine designers.

Such titanium matrix composites (TMCs) are obviously an innovative materials concept that combines the high strength, stiffness, and creep resistance of silicon carbide (SiC) monofilaments with the damage tolerance of titanium alloys and titanium aluminides. Moreover, introducing SiC fibers into a titanium matrix further reduces the density of the material. Provided there is complete implementation of composite technology in the future, the availability of these lightweight materials capable of extreme mechanical loading at elevated temperatures would certainly revolutionize engine design and other high performance areas of mechanical engineering. TMCs have already demonstrated the enormous potential of this class of material in niche applications, but to make the vision become reality in the near future, several materials issues must be addressed. It is believed that the successful use of TMCs in these niche applications will eventually pave the

way for wider use. Obviously, the success of TMCs will not depend on materials properties alone, but will ultimately be controlled by the life-cycle costs of a particular component. Economic considerations will finally decide whether TMCs can make the step from an exotic and expensive special material, to a lightweight material with a broader range of applications within the medium- or long-term.

12.2
Fabrication Processes

Due to the high reactivity of titanium alloys with the SiC monofilaments, fabrication processes that place the least possible thermal load on the composite during manufacturing are given preference. Neither melt infiltration nor powder metallurgy routes have yet been established for TMC fabrication. The favored routes for TMCs today are the foil-fiber-foil technique (Fig. 12.1 a), the mono tape technique (Fig. 12.1 b) and the matrix-coated fiber technique (Fig. 12 c).

For the foil-fiber-foil (FFF) technique, fibers are placed between foils, stacked to a multilayer arrangement, and then consolidated at high temperatures. In spite of its simplicity, some major technical disadvantages are related to this fabrication method. First, the process is limited to titanium matrices that can be fabricated as thin foils and, second, it is fairly difficult to obtain a homogeneous fiber distribution. Due to the long flow distances that must be overcome by the matrix during the consolidation process, fibers can easily become shifted, resulting in processing-related fiber rupture and fiber-fiber contact, which lead to premature failure of the composite (see also section 12.3.5.1). Methods to keep the SiC fibers in place, e.g. by interweaving the fibers with tungsten or polymer fibers, have been developed. However, the auxiliary fiber leaves a certain degree of contamination in the composite.

The mono tape technique (MT) relies on the production of fiber reinforced tapes as starting material that can be fabricated, for example, by coating flat fiber bundles using plasma spraying. The tapes can be stacked or bundled and subsequently consolidated to form the component. Similar to the FFF technique, the homogeneous fiber distribution in the final composite is a major technical challenge.

Composites with optimum fiber distribution can be fabricated using the matrix-coated fiber (MCF) technique. By far the most costly method, the starting product
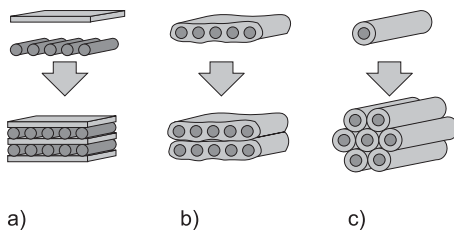
Fig. 12.1 Fabrication methods for titanium matrix composites:
a) foil-fiber-foil (FFF) technique
b) mono tape technique (MT) and
c) matrix-coated fiber technique (MCF).

is a homogeneously matrix coated fiber (monofilament) that allows fabrication of composites with excellent fiber arrangement, as will be shown in the following. In the past, three different processes for matrix coating deposition have been explored: melt levitation process, electron beam physical vapor deposition, and magnetron sputtering; the latter two processes are the more mature methods. Currently, a low-cost coating process via matrix powder polymer dispersion is under development; however, it is also expected to introduce contaminants into the composite, which must be carefully removed [1]. While the coating is fabricated from the melt for the melt levitation process, coatings produced by EB-PVD and magnetron sputtering are deposited from the vapor phase. Despite the higher deposition rate of the EB-PVD technique, magnetron sputtering also allows to fabricate considerable amounts of coated fibers, if appropriate equipment is available. Today's daily productivity of pilot coaters is on the order of 2–5 km of matrix coated fibers; however, this does not represent materials fabrication on an industrial scale, which can be achieved on demand.

Unlike the EB-PVD technique, where the processing and hardware expenses increase with increasing chemical complexity of the matrix alloy, magnetron sputtering is a very versatile process to produce coatings of almost any chemistry [2]. While for EB-PVD different vapor pressures of the component in the melting pool might hinder a reproducible and robust deposition process, the physical vaporization of the target material in the magnetron sputtering process allows easy fabrication of multi-component systems with tightly controlled chemistries.

Magnetron sputtering was explored in the early 1980's as a deposition process for titanium matrices on monofilaments [3–6]. Matrix deposition onto the fibers is the first step of a multiple step processing chain, shown in Fig. 12.2. To start, fibers are coated with the titanium matrix, where the residual gas atmosphere as well as the deposition parameters such as sputtering rate and bias voltage have a crucial effect on the quality and the properties of the different matrix materials. The fiber volume content of the composite can be easily adjusted by the matrix coating thickness. In addition to batch processes, where an ultimate length of fiber can be coated and which are appropriate for laboratory use, the development of so-called inline systems will enable a continuous deposition process leading to fibers of "infinite" length [7]. Furthermore, a significant reduction of TMC fabrication costs can be expected, which, currently, is considered to be two-thirds dominated by the deposition process.

In the second step, the matrix-coated fibers are bundled or arranged using, for example, winding techniques to achieve the desired component geometry, encapsulated, and subsequently hot-isostatically pressed at temperatures around 950 °C and pressures of about 2000 bar. Careful processing results in a SiC/Ti composite with regular fiber distribution and excellent mechanical properties. The high quality TMCs available by the matrix-coated fiber technique are a direct consequence of an optimized fabrication procedure.

In the final step, the component is machined. It is important that machining must not damage the fiber-reinforced section of the component, neither mechanically nor chemically, such that only the unreinforced areas can be machined. Ob-
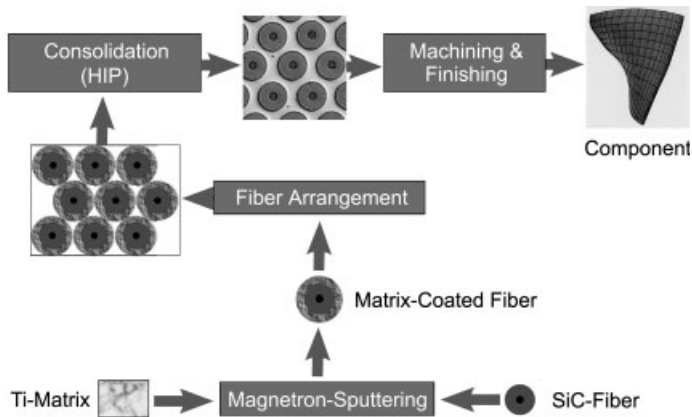
Fig. 12.2 Flow chart of the complete processing chain for fabrication of TMC-reinforced components.

viously, fabrication of components requires a detailed knowledge of deformation and shrinkage of the specific part.

On the one hand, the large number of processing steps requires precise information about the influencing parameters of each single step on the properties of the material or the component, as well as complete process control in order to obtain reproducible high quality products. On the other hand, it opens the possibility to specifically modify the properties of the composite at different stages of its fabrication. In Fig. 12.3 the coating process, consolidation, and post-consolidation heat treatment are shown. The parameters of each step determine the microstructure of the matrix alloy and the formation of the fiber-matrix interface, which is important in determining mechanical properties.

With regard to composite properties, the consolidation process by hot isostatic pressing is a crucial step. Relatively high temperatures are needed to obtain a fully compacted composite; however, after cooling down from fabrication temperatures, residual stresses are generated caused by the differences in the coefficients of thermal expansion between the fiber and the matrix. Furthermore, exposure at high temperatures leads to reaction between the matrix and the carbon protective layer on the fiber. The carbon layer is applied to the SiC fiber by the fiber producer to protect the fiber against the reactive titanium matrix. In general, reaction between the matrix and the carbon layer can not be excluded completely; therefore, the consolidation process must be conducted carefully to minimize the carbon-titanium reaction while still fully consolidating the composite. Obviously, acceptable consolidation parameters strongly depend on the matrix alloy chemistry and microstructure, which influence formability and reactivity.

In Fig. 12.4, different material qualities from the early days of TMC development and today are compared. Note, it is expected that the ideal fiber distribution shown in Fig. 12.4b is unlikely to be feasible in real components. However, comparison of irregularities in the fiber distribution can be made by the introduction
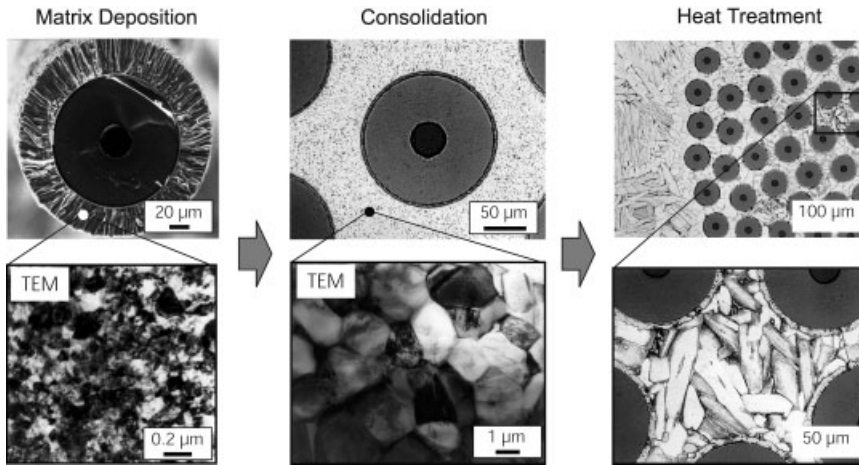
Fig. 12.3 The microstructure of titanium matrix composites can be tailored by the deposition parameters during coating fabrication (a), during the consolidation process (b) and by post-consolidation heat treatment procedures (c).

(a)

(b)
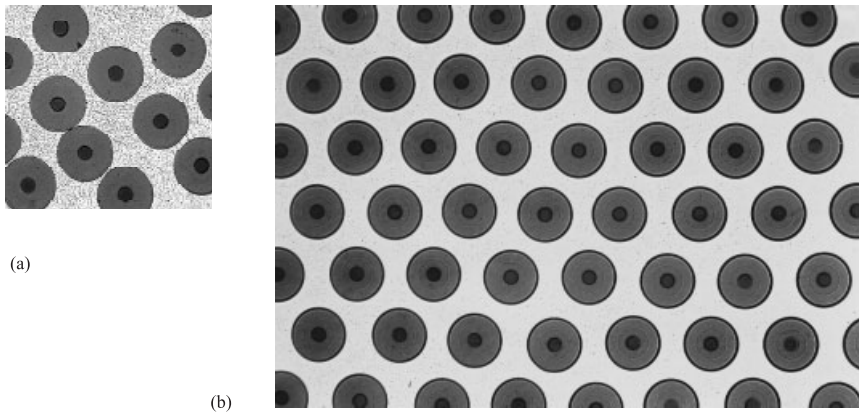
Fig. 12.4 Differences in TMC quality using the matrix-coated fiber technique. While early material exhibited a irregular fiber distribution (a), today's TMCs stand out for minor deviation from the ideal fiber distribution (b).

of a quality parameter, Q [8], that describes the average deviation of the fiber distance from the average fiber distance. While Q = 1.0 represents an ideal fiber distribution, Q = 1.65 denotes fiber-fiber contacts. Fig. 12.5 shows some examples of quality parameters of TMCs fabricated by different processing routes. This comparison impressively underlines the high quality level obtained by the matrix-coated fiber technique.
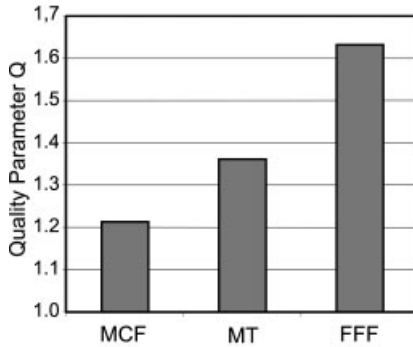
Fig. 12.5 Quality parameter Q for assessment of fiber distribution of matrix coated fiber (MCF), mono tape (MT) and foil-fiber-foil (FFF) techniques. Q=1.0 represents an ideal fiber distribution while Q=1.65 indicates presence of fiber-fiber contacts. Only the MCF technique seems to deliver optimum materials quality.

12.3
Properties

In general, composite properties strongly depend on the properties of the single constituents. Knowledge of the interaction between the constituents is always the basis for successful materials system development; optimization of the composite properties almost always relies on the optimization of these interactions. These general remarks are equally valid for SiC/Ti composites.

If the properties of the fibers and the matrix are known, strength and stiffness of TMCs in the longitudinal direction can be determined with sufficient accuracy by the rule of mixtures. Other properties follow a more complex relationship, which have to be determined experimentally or by simulation. Important properties of the SiC fiber and a typical titanium matrix are summarized in Tab. 12.1. These data are also used for modeling (see section 12.5) of the material and analytical calculations.

Tab. 12.1 Examples of fiber and matrix properties; these are also used in analytical calculations [29].

Property	Unit	Matrix		Fiber	
		20 °C	300 °C	20 °C	300 °C
Young's modulus	GPa	110	96	400	394
Poisson's ratio	1	0.3	0.3	0.25	0.25
Yield strength	MPa	770	560	–	–
Rupture stress	MPa	1050	780	4000	3980
Density	g cm^{-3}	4.55		3.0	
Coefficient of thermal expansion	ppm K^{-1}	10.36	10.70	1.61	3.90
Thermal conductivity	W (mK)$^{-1}$	10		25	
Specific heat capacity	J (kgK)$^{-1}$	550		670	

12.3.1
Strength and Stiffness

High strength and stiffness in the longitudinal direction up to elevated service temperatures are certainly the most outstanding properties of unidirectionally (unidirectional = all fibers are oriented in one direction) reinforced TMCs. For many applications where the use of TMCs is reasonable or essential, these two mechanical properties are the key driving forces for development. Strength, or more precisely specific strength, i.e. strength related to density, is a key parameter for lightweight structures and is an important property of major interest to the designer.

The specific strength data of typical aerospace materials and TMCs are displayed in Fig. 12.6a for maximum service temperatures up to 800 °C. While the specific strength (or the rupture length) of classical near-α titanium alloys, α_2-Ti$_3$Al or orthorhombic (Ti$_2$AlNb) titanium aluminides, γ-TiAl alloys as well as nickel-based superalloys (here IN 718) range from 10 to 30 km at room temperature and from 10 to 15 km at 800 °C, the maximum specific strength of TMCs is between 40 and 55 km at room temperature and still as high as 50 km at 700 °C. The maximum strength strongly depends on the fiber volume fraction; maximum values were obtained from 40% fiber volume fraction. For SiC/TIMETAL 834, a room temperature tensile strength of 2400 MPa can be reproducibly obtained, which is in good agreement with the calculations according to the rule of mixtures. Note, for good results the rule of mixtures requires a minimum of 3% matrix ductility.

Strength of TMCs at high temperatures is not limited by insufficient strength of the fiber – the fiber is stable far beyond 800 °C – but by the high temperature capability of the matrix material. The service temperature limitations of the matrix are caused by the loss of strength and, much more importantly, by environmental degradation of the matrix material. Therefore, the choice of matrix material determines the service temperature limit of the composite. Similar to the environmental protection required by monolithic titanium alloys at elevated temperatures, the full potential of TMCs at high temperatures can only be used if sufficient environmental resistance of the matrix, e.g. by the use of protective coatings (see Chapter 6), is provided.

Moreover, interaction between the fiber and the matrix might become an issue at elevated service temperatures. While at low service temperatures reaction between the matrix and the fiber's carbon layer is limited to the consolidation process, this reaction can proceed at higher temperatures, leading to continued consumption of the protective carbon layer. This may finally result in attack of the fiber; and gradual damage of the fibers leads to degradation of the mechanical properties of the composite. For elevated service temperatures, orthorhombic titanium aluminides (see Chapter 3) have been considered as matrices that might expand the service spectrum of TMCs to 700 °C. Along with the required minimum room temperature ductility and a relatively low coefficient of thermal expansion with better match to the SiC fiber, this class of alloys has good chemical compatibility with the SiC fiber at elevated temperatures.
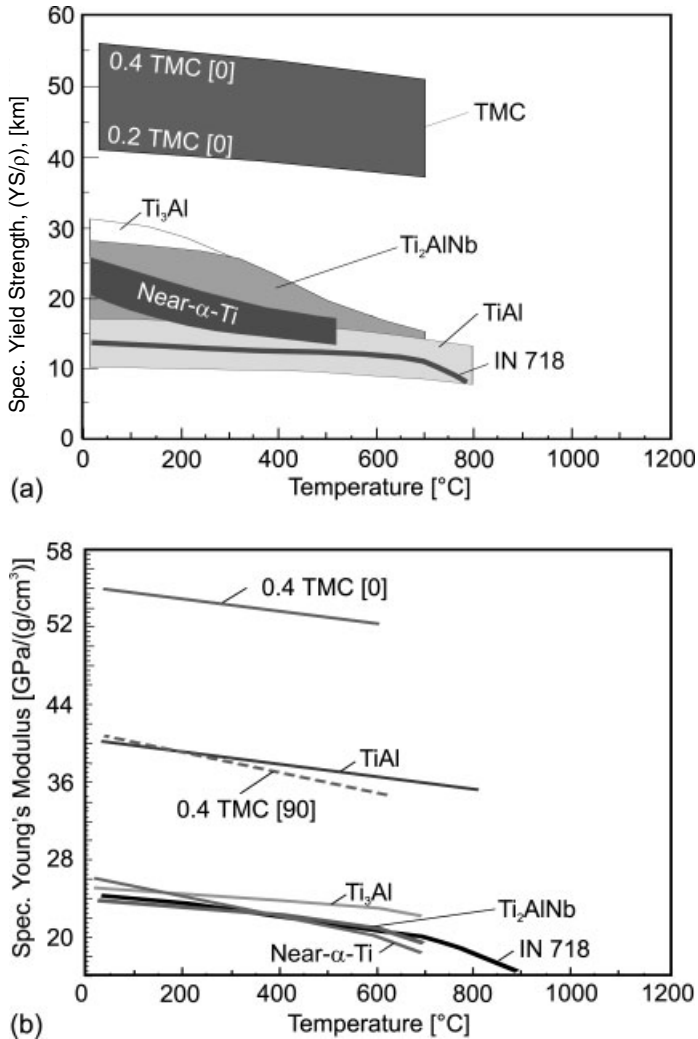
Fig. 12.6 The specific yield strength of TMCs goes far beyond that of advanced aerospace materials. The strength level depends on the fiber volume content (a). The specific Young's modulus of TMCs significantly exceeds that of monolithic titanium alloys. Even for transverse loading, stiffness of the TMCs is similar to what is found for γ TiAl (b).

The specific Young's modulus as a measure of stiffness is plotted vs. temperature in Fig. 12.6 b. Note, the data for near-α titanium alloys, Ti_3Al-based and orthorhombic titanium aluminides is similar to that of nickel-based superalloy IN 718. Titanium aluminides based on γ TiAl exhibit much higher specific Young's moduli, which are greatly surpassed by TMCs tested in the longitudinal direction. In spite of the anisotropy of the properties caused by unidirectional reinforcement, the transverse (i.e. perpendicular to the fiber elongation) stiffness of TMCs is still in the same

range of γ TiAl. A more detailed description of the special features of TMCs related to the anisotropy of their properties is given in section 12.3.4.

12.3.2
Creep Properties

Creep resistance of TMCs is of particular interest for aerospace applications at elevated temperatures. Since stiffness, strength and creep resistance of the SiC fiber are significantly greater than that of the matrix, it is obvious that during creep exposure the load placed on the composite is mainly endured by the fibers. Thus, the creep resistance of the composite is substantially improved relative to the matrix where the fiber reinforcement hinders matrix creep. Obviously, the relevant creep deformation mechanisms in TMCs are greatly different from that known for monolithic titanium alloys.

It is well known today that a number of factors impair the creep resistance of TMCs. Among others, fiber strength and distribution, chemical composition and creep behavior of the matrix, type and properties of the fiber-matrix interface, fiber orientation, residual stresses, applied stresses as well as environmental conditions all play a certain role. A detailed discussion on the creep behavior of TMCs is given in [9]. In the following, the creep behavior of TMCs under longitudinal loading is only addressed. The special features of creep behavior under transverse loading are given in section 12.3.4.

Fig. 12.7 shows typical creep curves for SiC-reinforced Ti-6Al-4V [9]. The SiC fiber used is SCS-6, developed by Specialty Materials, Inc. (formerly Textron). At 538 °C, loads as high as 1000 MPa can be applied without failure of the material (Fig. 12.7 a). Increasing the load leads to failure of the TMCs; the secondary creep regime is shortened with increasing load. Notably, the strain at rupture is lower than 1% in all cases. Fig. 12.7 b shows the effect of temperature on the creep behavior of TMCs at constant load; increasing temperatures have the same effect as increasing loads. At 427 °C the SiC/Ti shows asymptotic behavior, while at 538 °C marked secondary creep is observed. Above 538 °C creep rate and time of rupture strongly depend on temperature. Moreover, the transition creep behavior is temperature-dependent.

As can be concluded from the Larson-Miller plot in Fig. 12.8, TMCs exhibit significantly better creep resistance than monolithic titanium alloys. However, creep properties are clearly highly anisotropic, as demonstrated for a SiC/Ti-24Al-11Nb composite. The minimum creep rates for longitudinal loading of TMCs containing different matrix alloys are given in Fig. 12.9 [9]. Remarkably, the stress exponents of all composites are fairly similar, indicating that the predominant creep mechanisms are equally similar. Moreover, the stress exponents of the TMCs are greater than that of the monolithic matrix alloys. Based on microstructure observations, which would exceed the purpose of this chapter, the following conclusions can be drawn.

During the loading phase of the test, load is gradually transferred from the matrix to the fibers. As a consequence of load sharing by the fibers, stress relaxation
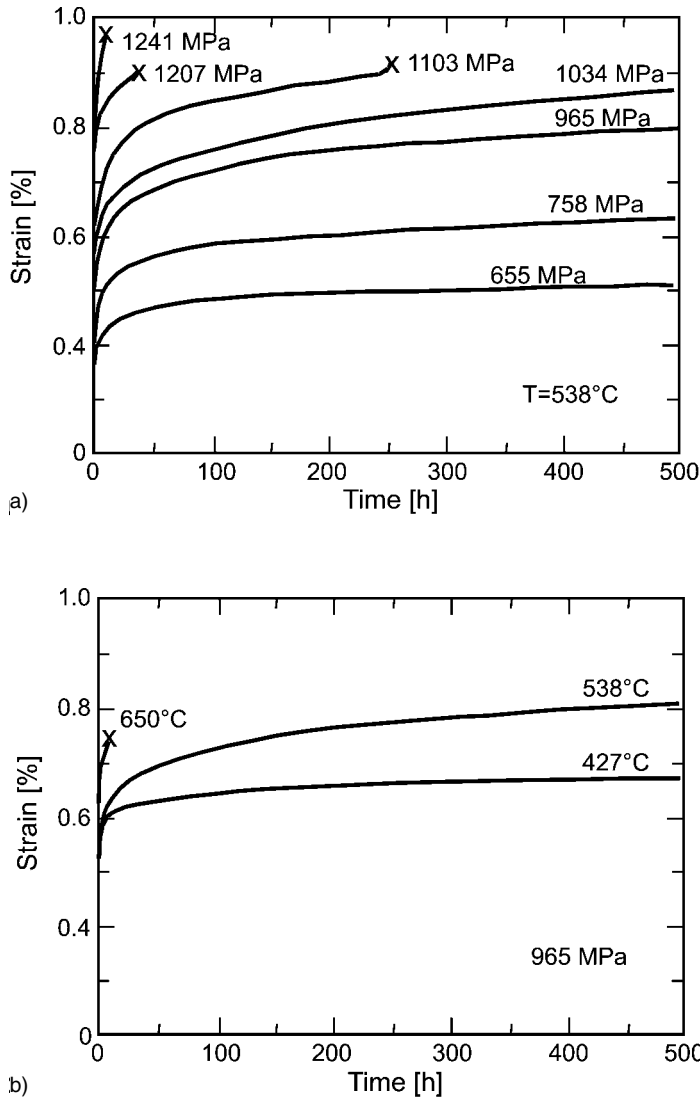
Fig. 12.7 Creep behavior of SCS-6/Ti-6Al-4V [9]. At 538 °C good creep resistance is maintained up to 1034 MPa (a). For a constant load of 965 MPa creep behavior at 427 °C shows an asymptotic, at 538 °C a continuous slowly increasing course, while at 650 °C rapid failure occurs (b).

in the matrix occurs. The highly loaded fibers break at locations where stresses are maximum, and where flaws are accumulated. At these locations, load is transferred from the fiber to the matrix; as a consequence, further creep deformation is maintained. Plastic deformation of the matrix results in local stress re-distribution until intact fiber segments near the location where fiber rupture occurred can
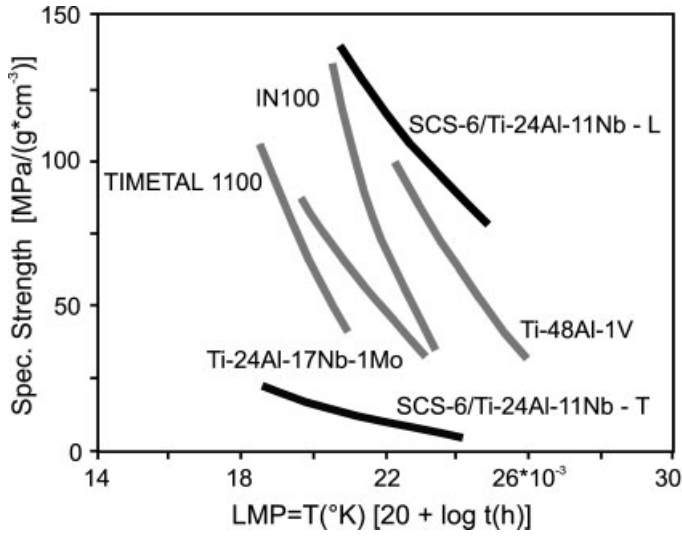
Fig. 12.8 Larson-Miller plot of the creep behavior of a monolithic titanium alloy, titanium aluminides, and nickel-base alloy IN 100. Fiber-reinforced Ti-24Al-11Nb exhibits outstanding creep resistance in longitudinal direction while transverse creep properties are inferior to the monolithic titanium alloy.
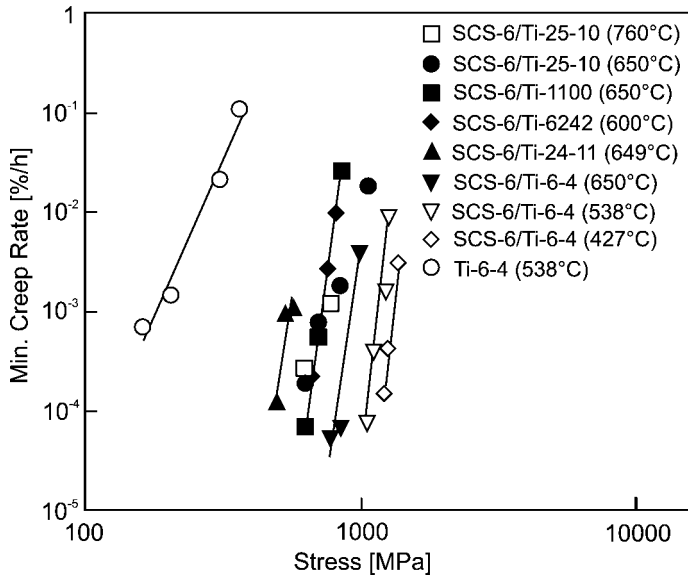
Fig. 12.9 Minimum creep rate vs. strength for different reinforced and monolithic titanium alloys [9]. Note, the stress exponents of the various materials are fairly similar.

take up stresses, thus relieving the matrix. A constant creep rate is reached if the rate of load transfer from the matrix to the fibers and subsequent fiber rupture is in equilibrium with load re-distribution to the fibers. For continuing creep loads, this process occurs throughout the entire composite length, which leads to multiple fiber rupture. Failure of the composite is a consequence of accumulated micro-damage, where fiber rupture, environmentally induced matrix damage, reduction of fiber strength, and interface degradation play important roles [9].

12.3.3
Fatigue Properties

The use of TMCs in rotating components of future jet engine compressors requires fatigue resistance; where fatigue behavior under high stress loading is one of the most important design criteria. Fig. 12.10 shows the cyclic strength of unreinforced and SiC-fiber reinforced TIMETAL 834 under tension-tension loading at room temperature and 600 °C, respectively [10]. The application of TMCs has a positive effect, particularly at 600 °C. The maximum cyclic stress for TMCs in the LCF (**l**ow **c**ycle **f**atigue) regime as well as in the HCF (**h**igh **c**ycle **f**atigue) regime is at least 100% higher than that of the unreinforced material. While the endurance limit of the unreinforced alloy is about 400 MPa, SiC/Ti reaches an endurance limit of more than 1000 MPa at 600 °C.

At room temperature, the maximum stress for the unreinforced matrix is superior compared to 600 °C, although the difference is higher in the LCF-regime than in the HCF-regime. Thus, the endurance limit at both temperatures is comparable.
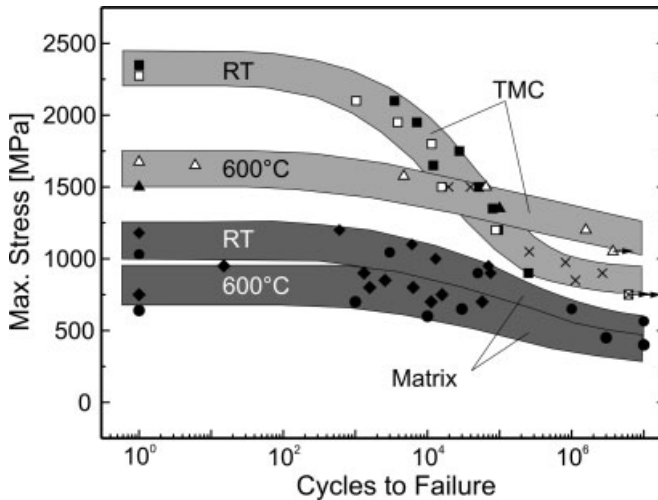
Fig. 12.10 Fatigue behavior of SCS-6/TIMETAL 834 at room temperature and 600 °C compared with the monolithic titanium alloy [30].

High levels of static strength caused by the fiber reinforcement induces the highest maximum stresses in the LCF-regime. In contrast to the unreinforced material and to the SiC/Ti composite at elevated temperatures, there is a distinct transition zone between 10^2 and 10^4 cycles corresponding to a significant drop of strength at room temperature. The endurance limit at room temperature is lower than at 600 °C; however, it is above that of the unreinforced matrix material.

The significant drop in the endurance limit at room temperature is caused by premature emergence of matrix cracks, which quickly grow during fatigue loading due to the reduced ductility of the matrix compared to 600 °C. Although such matrix cracks are bridged by intact fibers, they may reach a length critical for failure. The bridging mechanism is controlled by the fiber-matrix interface. Strong fiber-matrix bonding reduces the stress intensity factor at the crack tip, but, on the other hand, the load is transferred to the intact fibers, which may fail due to overloading. In contrast, a moderate strength of the fiber-matrix interface is favorable for the fatigue behavior of TMCs. For predictions of the crack growth rate, the strength as well as friction of the fiber-matrix interface must be considered [10, 11].

Thermal residual stresses induced during processing of TMCs may reduce the fatigue loading capabilities of the composite, especially at room temperature, since they are tensile in the matrix. The origin of residual stresses and their influence on the fatigue behavior will be discussed in section 12.3.5 in detail. At elevated temperatures (e.g. 600 °C), residual stresses due to processing are reduced by about 80% compared to room temperature; thus, their influence on the fatigue behavior at elevated temperatures is negligible. Furthermore, considering the lower susceptibility against cracking of the matrix, the endurance limit of the composite is higher at 600 °C than at room temperature.

Fatigue properties of TMCs show a strong dependence on the processing technique used. Excellent fatigue properties can only be reached by TMCs produced by the matrix coated fiber (MCF) route. Due to the minor homogeneity in the fiber distribution (Fig. 12.5) of composites produced by the foil-fiber-foil (FFF) technique, the endurance of the TMC is at the same level as that of the unreinforced matrix material (Fig. 12.11) [12].

12.3.4
Anisotropy of TMCs

Due to their specific morphology, continuous fiber reinforced materials show inferior properties under loading out of the fiber axis (Fig. 12.12a). This impacts the tensile and compressive strengths, as well as the stiffness. However, this effect is somewhat less pronounced for TMCs compared to fiber-reinforced plastics or ceramics due to the high-strength titanium matrix (Fig. 12.12b). In general, independent of the reinforcement material, polymer-matrix composites show very low strengths normal to the fiber direction. Therefore, multidirectional alignment of the fibers is usually necessary, which reduces the maximum strength of the composite in the principal direction. However, TMCs show superior strength in the transverse direction. Thus, in spite of the existing anisotropy, a unidirectional re-
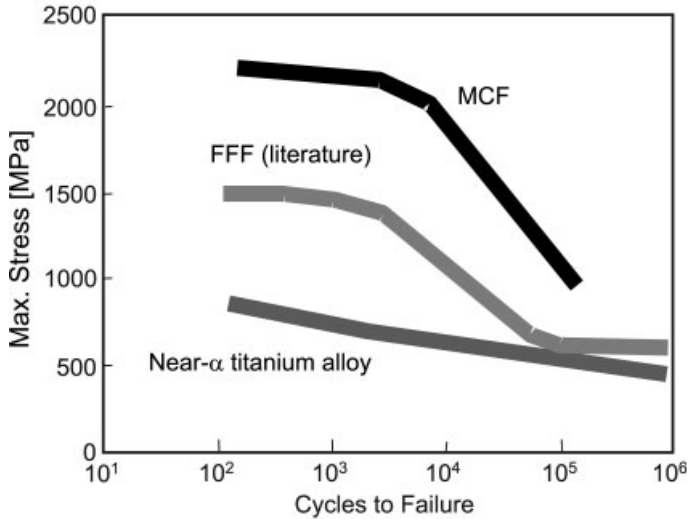
Fig. 12.11 Effect of processing technology on the fatigue properties of TMCs. The matrix coated fiber (MCF) technique reveals TMCs with optimum fatigue behavior while the fatigue limit of materials produced by the foil-fiber-foil (FFF) technique is similar to that of the monolithic matrix material.

inforcement can be applied and the capabilities in the fiber direction can be completely obtained. Tab. 12.2 shows the anisotropy ratio of TMCs in comparison with some other materials. It can be seen that the anisotropy of the Young's modulus is lower than that of the tensile strength.

The properties in the transverse direction (normal to the fibers) are dominated by the properties of matrix and interface. Fig. 12.13 schematically shows the stress-strain response under transverse tension loading at room temperature [13]. In region I the composite is fully elastic and the stiffness is increased by the fibers. Shear stresses induced by the stress gradient exceed the shear strength of the interface in region II, which causes mode II failure of the interface. However, the crack surface is kept closed due to thermal residual stresses and thus the stiffness is unchanged in region II [14]. Under static loading this interface shear crack is irrelevant, while it may be the threshold for fracture under long-term cyclic loading. If the applied stress exceeds the sum of the thermal residual stress and the interface tensile strength, fiber and matrix separate (region III, Mode I-failure). This is marked by a sudden drop in stiffness [15, 16]. With further loading, the fibers bear no stress and the composite stiffness is lower than that of the unreinforced matrix material. Subsequently, the matrix deforms plastically, leading to a further decrease of the Young's modulus in region IV. Finally, the composite fails completely.

Similar damage mechanisms occur under creep and fatigue loading. However, they may occur at lower stresses. Fig. 12.14 shows the transverse creep behavior
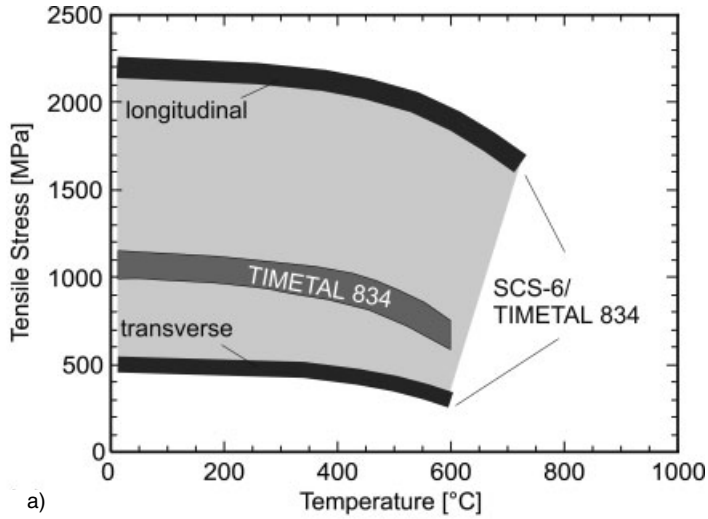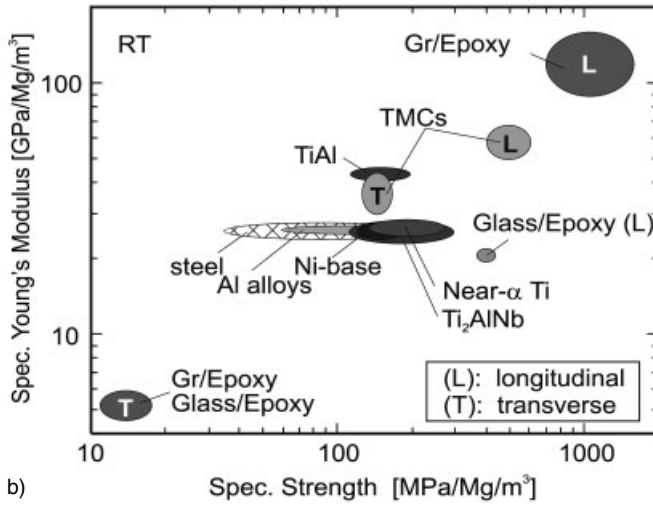
Fig. 12.12 Anisotropy of the mechanical properties of TMCs. The strength in fiber direction (longitudinal) is extremely high due to the fiber reinforcement, while the strength in transverse direction (normal to the fibers) is below that of the unreinforced matrix (a). In comparison to fiber reinforced plastics, the anisotropy of TMCs is moderate resulting in a transverse stiffness of TMCs that is superior to the unreinforced material.

of TMCs. Below a threshold, the creep resistance is higher than that of the unreinforced matrix material. Above this threshold, the matrix separates from the fibers, designated as *debonding* in region III under static loading in Fig. 12.13. The region of the time-dependent debonding marks a stress transfer due to creep,

Tab. 12.2 Anisotropy ratio of different materials.

Material	$E_\perp/E_\parallel$	$\sigma_\perp/\sigma_\parallel$
Isotropic materials	1.0	1.0
Metals, rolled	~ 1.0	$0.9 \sim 1.1$
Glass fiber reinforced polymer (GFRP-UD)	$0.1 \sim 0.15$	$0.05 \sim 0.1$
Carbon fiber reinforced polymer (CFRP-UD)	$0.02 \sim 0.1$	$0.02 \sim 0.1$
TMC (UD)	$0.7 \sim 0.8$	$0.15 \sim 0.2$
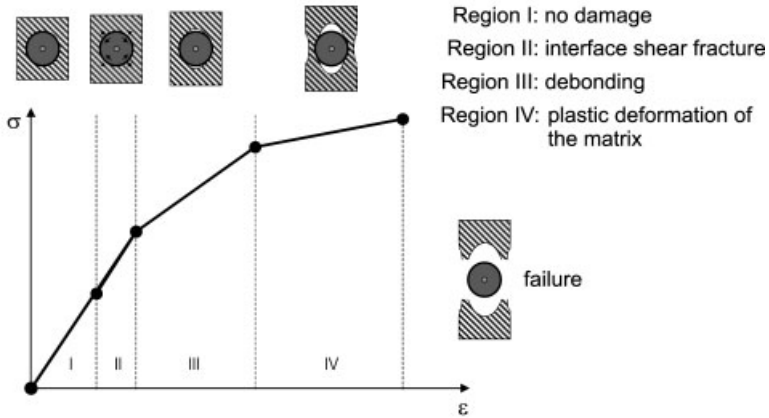
Fig. 12.13 Stress-strain response and damage events under transverse tension (schematic).

leading to a time-dependent failure of the interface [17]. Analogous to the expositions in section 12.3.2, the matrix stresses are reduced due to creep. The stress is transferred from the matrix to the neighboring fibers, and especially the weak fiber matrix interface. The interface stress increases, inducing the effect of time-dependent debonding shown in Fig. 12.14 b. Once the interface has been separated, the creep rate increases suddenly, since the fibers bear no load. The fibers produce a similar effect to voids, resulting in a higher creep rate compared to the unreinforced matrix material.

12.3.5
Thermal Residual Stresses

As previously mentioned, TMCs are consolidated at a temperature in the range of 920 °C to 980 °C, depending on the matrix alloy used [4]. Thermal residual stresses are induced due to the mismatch of the coefficients of thermal expansion, which is relatively low for fibers compared to matrix. Basically, the fibers are under compression while the matrix is in tension. Only in the direction normal to the fiber/matrix interface is the matrix in compression [18]. Depending on the
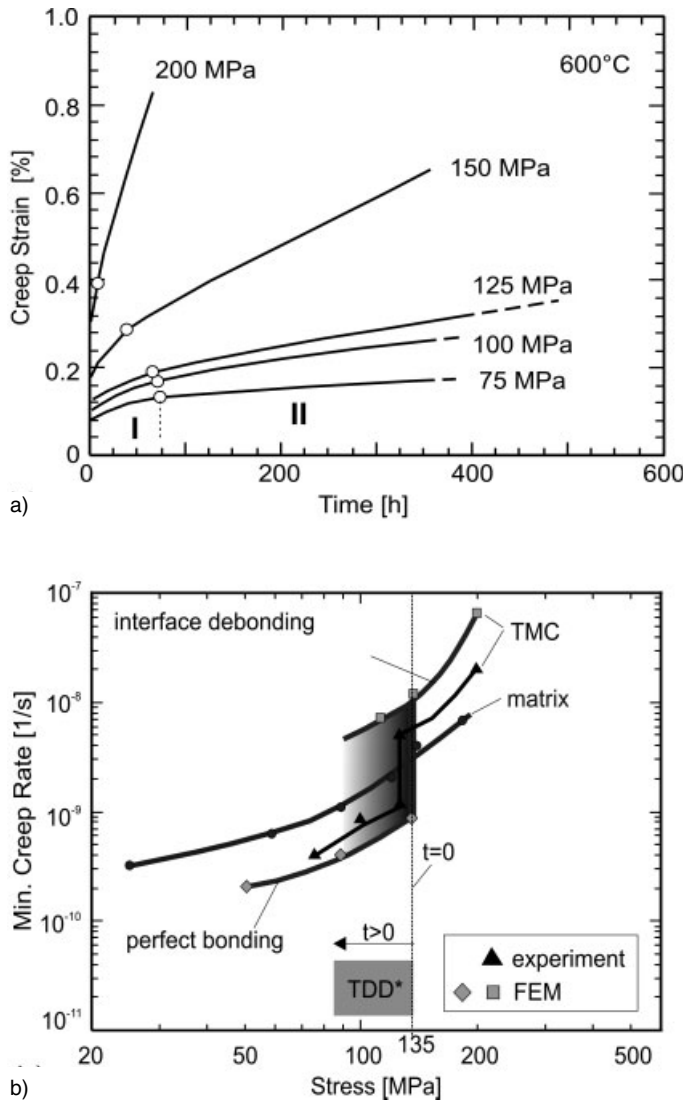
Fig. 12.14 Transverse creep behavior of TMCs. The maximum loads at 600 °C are low (a). The strength of the fiber matrix interface is the major factor. Exceeding a threshold induces debonding and thus a sudden increase of the minimum creep rate (b). TDD = time dependent debonding.

matrix alloy, the fiber volume content and the processing route, thermal residual stresses reach up to 30–80% of the tensile strength of the matrix material. This illustrates the great influence of residual stresses on the mechanical properties of TMCs [19]. Since residual stresses are directly dependent on the temperature, different damage mechanisms prevail with changing temperature.

12.3.5.1 **Influence of the Fiber Distribution on Residual Stresses**

Not only the materials, but also the type and regularity of fiber distribution influence thermal residual stresses. A square fiber arrangement results in a smaller fiber distance compared to a hexagonal arrangement (Fig. 12.15), based on a constant fiber volume content [20]. Since fiber distance influences the interface normal stress, its maximum is higher when fibers are arranged in a square. This causes higher transverse strengths under loading parallel to a line of lowest fiber distances [21, 22]. Otherwise, the capabilities in the diagonal direction are lower. In contrast, in a hexagonal fiber arrangement there are lower maximum and higher minimum values of residual stresses resulting in a more homogeneous stress and, thus, property distribution. It exhibits a more tolerant behavior with respect to the loading direction. Furthermore, processing aspects prefer the hexagonal fiber arrangement due to the preferred packing density. Manufacturing a defined rectangular or square arrangement requires costly measures, which are difficult to realize. Therefore, the square fiber arrangement is relevant in special circumstances only and in the following, a hexagonal arrangement is assumed.

The processing route used influences the homogeneity of the fiber distribution. Irregularities induce stress peaks, which may reduce the allowable composite stresses [18, 23]. Fig. 12.16 shows the simulated result of a finite element analyses

hexagonal and square fiber arrangement

fiber distance $l_q = 0{,}73\ l_h$
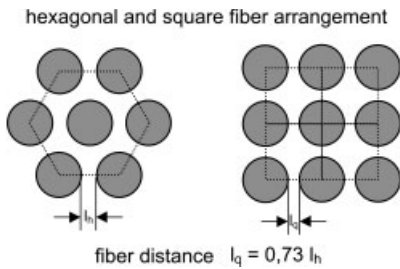
Fig. 12.15 Comparison of hexagonal and square fiber arrangement at constant fiber volume content of 50%.
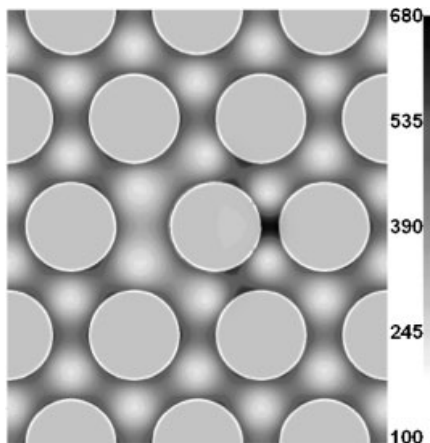
Fig. 12.16 Stress distribution in an irregular hexagonal unit cell (von Mises equivalent stress [MPa]).
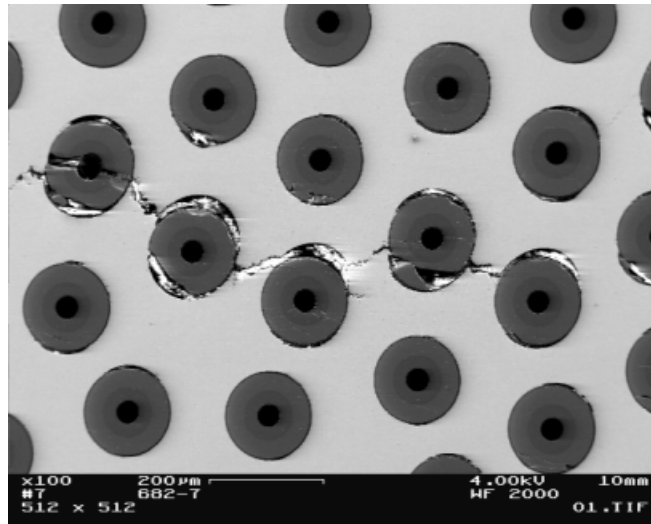
Fig. 12.17 Crack path in a transverse creep specimen.
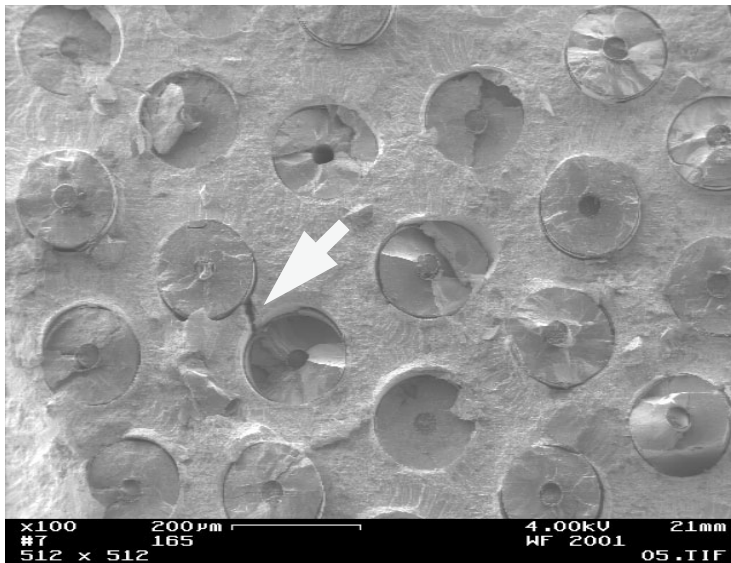
Fig. 12.18 Fracture surface of a fatigue specimen.

(FEA) of an irregular hexagonal cell. The stress peak in the region where the fibers are closest is obvious. This relatively low irregularity leads to a maximum stress that is about 50% above the average value. On the other hand, stress minima can be distinguished. Depending on the load case, both may reduce the allowable composite stress. Fig. 12.17 shows the crack path in a transverse creep speci-

men. It is obvious that the crack follows a line where the fibers are closest. Fig. 12.18 shows the fracture surface of a fatigue specimen. In the region of irregularities, cracks are detected that are even normal to the fracture surface. Both examples confirm the FEA prediction of stress peaks in the presence of inhomogeneities. Thus, the quality of fiber distribution has a strong impact on the load carrying capability of the composite. To obtain the full performance of TMCs, optimum processing routes have to be chosen. The MCF route offers the greatest safety to avoid matrix defects.

12.3.5.2 Residual Stresses and Fatigue

Due to a reduction in thermal residual stresses at elevated temperatures (~ 400–$600\,°C$), they are of minor relevance for high temperature applications. Furthermore, matrix stresses tend to zero by the reduced creep resistance [24]. Thus, long-term loading (static or cyclic) leads to the load being mainly carried by the fibers [25]. This implies that the reinforcing effect of the fibers is highest at elevated temperatures, of which the mechanical properties are only slightly temperature dependent.

Generally, high tensile loading at room temperature conditions induces plastic deformation of the ductile titanium matrix. The remaining deformation reduces residual stresses after unloading. As a result, residual stresses are of minor relevance at low cycle fatigue (LCF) conditions with high stress levels. On the other hand, high cycle fatigue (HCF) loading with low stress levels induces no plastic deformation. The thermal residual stresses add to the applied stress, leading to overloading of the matrix and, thus, become the dominating factor. The beneficial effect of reinforcement by the fibers is reduced drastically.

This effect can be eliminated by a well defined modification of residual stresses [23]. Fig. 12.19 shows the results of fatigue testing specimens in an as-processed condition and with modified residual stresses. A significant improvement of the HCF-strength is obvious. The modification has been carried out by a single tension loading up to a value below the rupture strain of the fibers. This reduces residual stresses by about 37%. It reduces the matrix stresses in the loaded composite in general, and reduces stress peaks in the presence of irregularities. Furthermore, the matrix is hardened by the *Bauschinger* effect [26]. Optimized procedures can lead to a further reduction of residual stresses and an even greater improvement in HCF strength. Limits for any mechanical or thermal treatment are fiber breakage or nucleation of oxidation reactions.

12.4
Dimensioning and Design with TMCs

Local reinforcement of components using TMCs promises the best cost-benefit ratio. By selective interception of stress peaks with a local reinforcement, a well-defined stress state can be obtained and allowing the use of elements with unidirec-
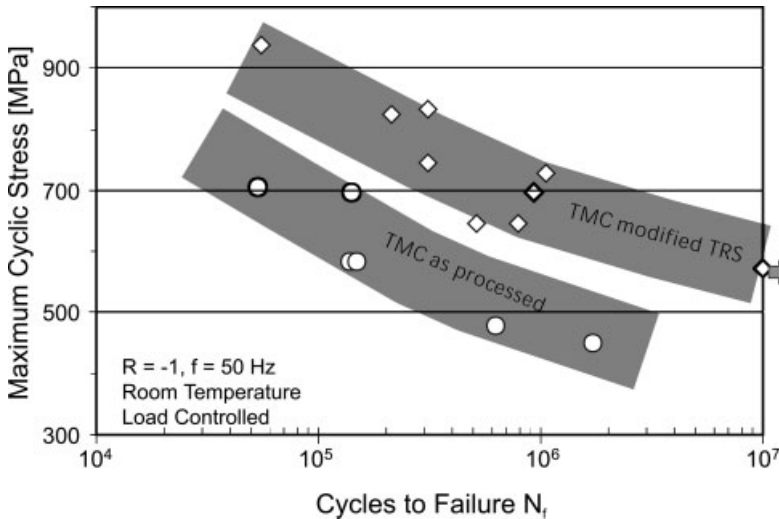
Fig. 12.19 Improvement of fatigue strength due to residual stress modification.

tional reinforcement. With this, the designer gains freedom to design highly loaded components with new concepts. The state of thermal residual stresses depend on the processing temperature and the way of component fabrication. For computation, the reinforcement is depicted by the orthotropic properties of the composite.

The lay-up of multidirectional laminates may be necessary in special cases only. Due to the difference in the rupture strains in the longitudinal and transverse directions, in general, the material capabilities are used less efficiently. Furthermore, thermal stresses due to the interaction of the layers reduce the strength of off-axis loaded layers. Thus, a design concept should be applied at which either a unidirectional reinforcement is sufficient, or an interaction of the layers is avoided.

12.5
Material Modeling

To determine elastic and physical properties of TMCs, classic rules known for polymer matrix composites are sufficiently exact. Also, strengths can be roughly estimated by these rules. Usually, the calculated values mark a theoretical upper limit. Values that can be reached in practice depend on the processing route and the quality of the materials used.

To obtain insight into internal damage mechanisms of the composite, numerical methods are useful. The finite element analysis (FEA) enables two- and three-dimensional modeling of the composite. Depending on the required results, a non-linear computation with temperature-dependent material properties is recom-

fiber coating   **fibers**   **matrix**
1899 elements   1477 elements   2087 elements
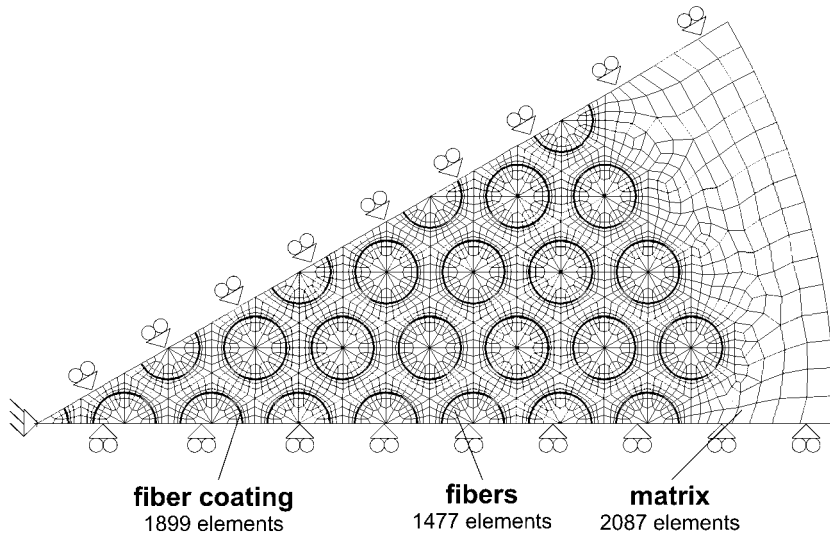
Fig. 12.20 FE-Model of a circular TMC-specimen (30°-segment).

mended. The model should consider the single fibers and the carbon protective layer. Fig. 12.20 shows a model of a circular specimen. It is a 30°-segment with a thickness of one element to carry out three-dimensional computations. First, the state of thermal residual stresses has to be determined. This can be done by a simulation of cooling from processing to ambient temperature. To avoid the simulation of any creep behavior in the upper temperature region, it has been proven successful to use an upper reference temperature that is about 20–30% below the real consolidation temperature and to use this as starting point for a time-independent computation [16]. The result is the state of thermal residual stresses, which can be examined for locations where stress limits are exceeded. Now, mechanical loads can be applied in the model. A useful scaling of the load steps enables the determination of the failure of the different constituents. Of course, this requires a knowledge of the maximum stresses for the fiber, carbon layer, and matrix constituents divided into tensile, compressive, and shear failure, as well as either a static or cyclic loading condition. Furthermore, yield and creep behavior of the matrix may be considered in the simulation.

12.6
Applications

The development of TMCs has been decisively spurred by the requirements of the gas turbine engine industry. With increasing demands placed on lightweight properties in engine design, development of materials operating at elevated temperatures for long times, providing damage tolerance and extreme mechanical proper-

ties has become necessary. In the USA, the IHPTET program (**I**ntegrated **H**igh **P**erformance **T**urbine **E**ngine **T**echnology) was among the most powerful programs for the development and introduction of TMCs into aerospace applications [26]. To date, a number of different components have been developed with TMCs, such as hollow airfoils, compressor rotors, casing structures, connecting elements, and actuators. With the introduction of the F-22 for the U.S. Air Force, TMCs have arrived in the operational world. Pratt & Whitney's F119 engine that powers the F-22 has TMC actuators used for nozzle control.

The potential areas for TMC application in aerospace can be ranked with regard to the benefits and to the risks taken with the component at failure [27]. Static structural components, such as fan casings, whose primary role is just to maintain component shape or to provide a well defined tip clearance, typically rely on the stiffness of TMCs and are thus considered low-risk components. For large civil aircraft engines, such as the GE 90, weight savings of the order of 10–15% have been projected for the fan casing [27]. TMC ducts offer 40% greater stiffness and 25% weight savings relative to monolithic titanium alloys [26]. Similarly, TMCs used in connecting elements or actuators are capable of 40% savings in structural weight compared with nickel-based alloys or steels [28].

Rotating components used at ambient temperature are considered moderate- or high-risk components. Recently, fan airfoil design concepts have been developed based on a locally TMC-reinforced airfoil (Fig. 12.21). Due to the high stiffness of the airfoils, innovative aerodynamic designs can be approached that reveal significantly improved efficiency and higher specific performance than achievable with monolithic titanium alloys today. Safety requirements, particularly with regard to foreign object damage (e.g. bird strike) are contemporary issues that need to be adequately addressed before TMC technology can be introduced into large-scale fan airfoils. Obviously, for low service temperatures, TMCs are not only in competition with monolithic metallic materials, but also fiber reinforced polymers.
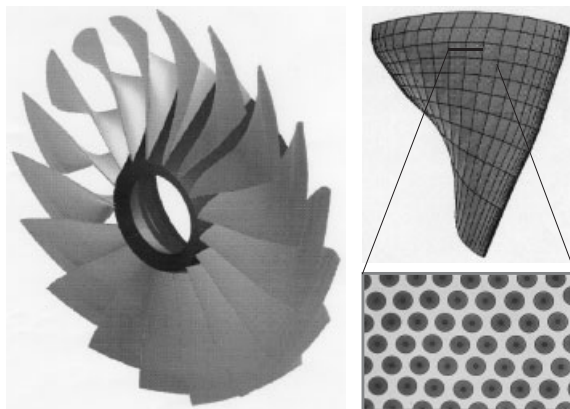
Fig. 12.21 Fiber reinforced fan blades enable innovative compressor concepts with improved power density.

Another design where TMCs play a major role is in the bling (bladed ring) concept (Fig. 12.22) that aims to revolutionize current compressor design. Along with extended design limits in the compressor (Fig. 12.22 a), substantial weight savings are feasible by replacing the heavy compressor disks by bladed rings (Fig. 12.22 b). In these components, the benefits of TMCs can be used in an ideal way since loading is strongly unidirectional. It is expected that weight savings in the order of 50% relative to conventional compressor design can be realized. Moreover, realization of the bling concept would make better use of the elevated temperature potential of TMCs than in fan applications, since materials temperatures in the high pressure compressor can exceed 600 °C. The consequent application of the bling concept would therefore allow an all titanium compressor design. However, these
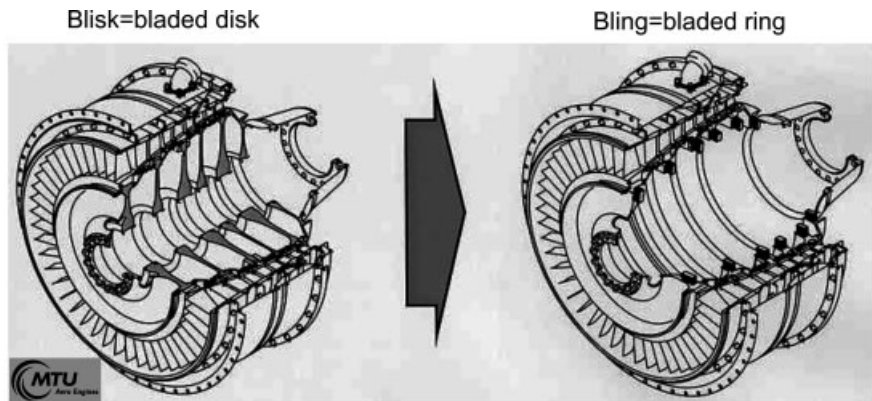
a)
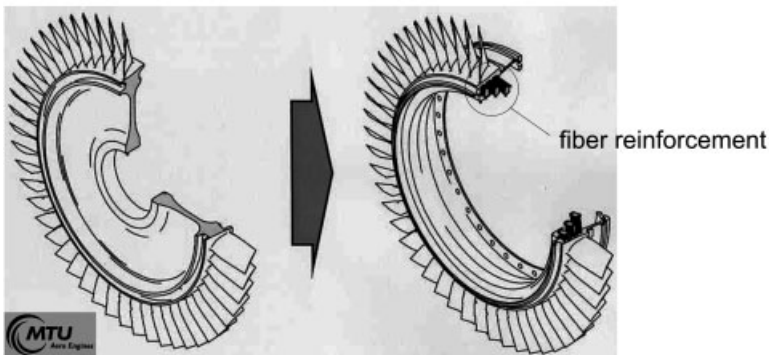
b)

Fig. 12.22 The transfer of the blisk (bladed disk) design to the bling (bladed ring) enables dramatic weight savings in connection with extended design limits (a). Due to extreme mechanical loading, the replacement of disks by rings can only be realized by fiber reinforced titanium alloys (b). (Courtesy: MTU Aero Engines)

Fig. 12.23 Slug of a shaft before consolidation. Fiber reinforced shafts or hollow bodies are distinctly stiffer than unreinforced components.

rotating components would be high-risk applications, since in the case of failure the entire engine might be damaged. Reliability of the materials and the components are therefore of uppermost importance. Moreover, a reasonable balance between the expenditures necessary to produce high-quality TMCs and the final component costs must be found.

Shafts are a further example of safety-relevant components in gas turbine engines. Again, fiber reinforcement would result in a significant increase in component stiffness. Fig. 12.23 shows a semi-finished model shaft before the consolidation process. Particularly for large-scale components, marked technical hurdles must be taken before high quality shafts can be manufactured that meet all the materials and design requirements.

12.7
Summary and Outlook

Outstanding mechanical properties including high strength, stiffness, creep and fatigue resistance make long-fiber reinforced titanium matrix composites (TMCs) ideal materials for demanding high technology applications, e.g. in gas turbine engines. Due to extremely high materials costs and lack of knowledge on materials properties, their use has so far been limited to niche applications. Even here, TMCs compete against alternative materials and must prove their advantages, particularly to justify the high materials costs. While today most TMC applications are focused on low or moderately elevated temperatures, high temperature applications are likely the future of TMCs. Here, TMCs are in direct competition with nickel-based alloys and steels, where they are expected to expand the application spectrum of titanium alloys and titanium aluminides to higher mechanical loads and temperatures.

12.8
Referenced Literature and Further Reading

1 Z. X. Guo, N. R. F. Beeley: *A Novel Powder Coated Fibre Pre-processing Route to Metal Matrix Composites,* Advanced Engineering Materials **3**(4) (2001) 223–226

2 C. Leyens: *Wechselwirkung zwischen Herstellungsparametern und Schichteigenschaften ausgewählter metallischer und keramischer Systeme bei der Magnetron-Kathodenzerstäubung,* Fortschritt-Berichte VDI, Reihe 5, Nr. 534, Düsseldorf: VDI-Verlag (1998)

3 H. J. Dudek, R. Leucht and G. Ziegler: *Auger Electron Spectroscopy of the Interface of SiC Fiber Reinforced Titanium Alloys.* in *Titanium – Science and Technology,* DGM, Frankfurt (1984)

4 H. J. Dudek, R. Leucht and W. A. Kaysser: *Development of Metal Matrix Composites by Fiber Coating and HIPing,* in *ICCM-10,* Woodhead Publ. Ltd., Canada (1995)

5 R. Leucht and H. J. Dudek: *Properties of SiC-fibre reinforced titanium alloys processed by fibre coating and hot isostatic pressing,* Materials Science & Engineering A **188** (1994) 201–210

6 R. Leucht, H. J. Dudek, K. Weber and A. Werner: *Magnetron Sputtering for Metal Matrix Composite Processing,* Z. Metallkd. **87** (1996) 424–427

7 *Wirtschaftliche Faserbeschichtung,* in *CemeCon Facts: Components,* Aachen, Germany (2001) 8–9

8 J. Hausmann, J. Hemptenmacher and J. Kumpfert: *Modelling of the influence of fibre distribution on residual stresses and strength of titanium matrix composites.* in *ICCM 13,* Beijing, China (2001)

9 J.-M. Yang: *Creep Behavior,* in *Titanium Matrix Composites: Mechanical Behavior,* S. Mall and T. Nicholas, eds., Technomic Publishing Co, Inc.: Lacaster, Basel (1998) 273–312

10 P. W. M. Peters, Z. Xia, J. Hemptenmacher and H. Assler: *Influence of interfacial stress transfer on fatigue crack growth in SiC-fibre reinforced titanium alloys,* Composites A**32** (2001) 561–567

11 T. P. Gabb, J. Gayda, B. A. Lerch and G. R. Halford: *The Effect of Matrix Mechanical Properties on $[0]_8$ Unidirectional SIC/Ti Composite Fatigue Resistance,* Scripta Metallurgica et Materialia, **25** (1991) 2879–2884

12 J. Hausmann, H. Assler, J. Kumpfert: *Modellierung der transversalen Eigenschaften von Titanmatrix-Verbundwerkstoffen (TMCs),* in *Werkstoff-Kolloquium,* Cologne: DLR, Institut für Werkstoff-Forschung (2000)

13 S. G. Warrier, B. S. Majumdar, D. B. Gundel and D. B. Miracle: *Implications of Tangential Shear Stress Induced Failure During Transverse Loading of Sic/Ti-6Al-4V Composites.* Acta Materialia **45**(8) (1997) 3469–3480

14 S. R. Gunawardena, S. Jansson, F. A. Leckie, *Modelling of anisotropic Behavior of weakly bonded Fiber reinforced MMC's.* Acta metall. mater. **41**(11) (1993) 3147–3156

15 D. B. Gundel, S. G. Warrier and D. B. Miracle: *The transverse tensile behavior of SiC-fiber/Ti-6Al-4V composites 2. Stress distribution and interface failure.* Composites Science & Technology **59**(7) (1999) 1087–1096

16 J. Kumpfert, H. Assler, D. B. Miracle, J. E. Spowart: *Transverse Properties of Titanium Matrix Composites,* in *Materials Week 2000* Munich (2000)

17 J. L. Bobet, C. Masuda and Y. Kagawa: *Estimation of residual stresses in SiC/Ti-15-3 composites and their relaxation during a fatigue test,* Journal of Materials Science **32**(23) (1997) 6357–6369

18 N. Chandra, C. R. Ananth, H. Garmestani: *Micromechanical Modeling of Process-Induced Residual Stresses in Ti-24Al-11Nb/SCS-6 Composites,* Journal of Composites Technology and Research **16**(1) (1994) 37–46

19 J. F. Durodola, B. Derby: *An Analysis of Thermal Residual Stresses in SiC and Al_2O_3-Fibres,* Acta Metall. Mater. **42**(5) (1994) 1525–1534

20 W. Ding, J. Liu and P. Bowen: *Effects of fiber inter-ply distance on the transverse tensile behavior of titanium matrix composites,* Scripta Materialia **44**(3) (2001) 443–448

21 H. E. DEVE: *Effect of fiber spatial arrangement on the transverse strength of titanium matrix composites,* Metallurgical & Materials Transactions A **30**(9) (1999) 2513–2522

22 J. HAUSMANN, C. LEYENS, J. HEMPTENMACHER and W. A. KAYSSER: *Optimization of the Fatigue Resistance of Titanium Matrix Composites,* Advanced Engineering Materials **4**(7) (2002) 497–500

23 M. P. THOMAS, G. HOWARD, R. PATHER, M. R. BROWN and P. H. TRANTER: *Comparison of low cycle fatigue performance of several [0] Sigma fibre reinforced titanium matrix composites,* International Journal of Fatigue **23**(10) (2001) 851–856

24 T. NICHOLAS, M. G. CASTELLI, M. L. GAMBONE: *Fiber Breakage in Metal Matrix Composites – Reality or Artifact?,* Scripta Materialia **36**(5) (1997) 585–592

25 S. TIMOSHENKO: *Strength of Materials – Part II Advanced Theory and Problems,* 3 ed. Vol. 2., New York: Van Nostrand Reinhold Ltd. (1958)

26 S. MALL, T. FECKE and M. A. FORINGER: *in Titanium Matrix Composites: Mechanical Behavior,* S. MALL and T. NICHOLAS, eds., Technomic Publishing Co, Inc.: Lancaster, Basel (1998) 1–22

27 S. A. SINGERMAN and J. J. JACKSON: *Titanium Metal Matrix Composites for Aerospace Applications,* in *Superalloys 1996,* TMS, Warrendale, PA (1996)

28 M. LAVITT: *First TMC Aircraft Part to Help Power F-22,* in *Aviation Week & Space Technology* (1997) 74–75

29 H. ASSLER: *Charakterisierung und Modellierung der mechanischen Eigenschaften von SiC-faserverstärkten Titanmatrix-Verbundwerkstoffen,* Ph. D. thesis RWTH Aachen, Germany (1999)

30 J. HEMPTENMACHER, P. PETERS, H. ASSLER and Z. XIA: *Fatigue of a SiC-Fibre Reinforced Titanium Matrix Composite: Experimental Results and Modelling.* in *EUROMAT 99* (1999)

13

Titanium Alloys for Aerospace Applications

M. Peters*, J. Kumpfert**, C. H. Ward*** and C. Leyens*,
*DLR – German Aerospace Center, Cologne, Germany, **Airbus Industrie, Blagnac, France,
***US Air Force Research Laboratory, EOARD, London, UK

13.1
Introduction

An increasing scarcity of resources and their growing expense demands a reduction in energy consumption for passenger and goods transportation. Here the aerospace sector plays a special role with respect to the application of new materials. Compared to land-based transportation systems, the much lower system quantities and much higher specific energy consumption allow designers to tolerate orders of magnitude higher cost for weight savings. For example, while one kilogram of weight saved in the automotive industry can not cost more than about € 10, the aerospace industry is willing to pay up to about € 1000. For space applications, more than € 10 000 may oftentimes still be economically attractive. This comparison is even more dramatic if weight savings are compared on a percentage basis. Due to a much higher payoff over a system's life cycle, the tolerable material prices in the aerospace sector are about three to five orders of magnitude higher than those in the automotive industry (Tab. 13.1).

The much higher payoff for weight reduction in aircraft, and especially spacecraft, is rationalized by the much lower payload capacity compared to land-based vehicles. As an example, a Boeing 747 carries about 100 tons of fuel, which is approximately one third the take-off weight of the jumbo jet. This would correspond to a tank volume of about 500 liters for a mid-sized passenger car. Accordingly, the remaining payload is quite limited. If fuel consumption is lowered by only 10%, a simple estimate shows one could increase the payload of the Boeing 747 by 10 tons.

Tab. 13.1 Tolerable extra costs for weight reductions of 1 kg or 1% of the structural weight.

	T€/kg	T€/wt.%
Automobile	0.01	0.1
Regional aircraft	0.5	100
Large Aircraft	1	1 000
Space	10	10 000

Alternatively, as less fuel means less weight, the use of smaller, lighter engines would be possible. Landing gears, wings, support structure, etc., could similarly be downsized as well. This "snowball effect" leads to secondary weight savings, which are almost as high as that due to the installation of the lighter component itself.

What possibilities do materials offer for weight savings in the aerospace arena? A Lockheed study provides some insight to this question. Although based on military aircraft, it still delivers good, general guidelines. The study reasons that if metal density is reduced by 10%, the weight of the component is also reduced by 10%. The same component weight reduction can also be achieved by increasing the strength, but by 35%. Likewise, the stiffness would have to be increased by 50%, and the damage tolerance by 100% to achieve the same 10% weight savings. This underlines the sustained importance of light metals as materials of choice in the aerospace sector.

13.2
Titanium Alloys in Aircraft

Compared to steels or aluminum alloys, titanium alloys must be considered a much younger structural material. The first alloys were developed at the end of the 1940s in the USA. Among these was the classic titanium alloy, Ti-6Al-4V, which still captures a large portion of aerospace applications today.

The outstanding properties of titanium alloys include high specific strength and excellent corrosion resistance. Therefore, titanium alloys are found in aerospace applications where the combination of weight, strength, corrosion resistance, and/ or high temperature stability of aluminum alloys, high strength steels, or nickel-based superalloys are insufficient. The main drivers for titanium's use in aerospace applications are:

- weight reduction (substitute for steels and Ni-based superalloys)
- application temperature (substitute for Al alloys, Ni-based superalloys, and steels)
- corrosion resistance (substitute for Al alloys and low-alloyed steels)
- galvanic compatibility with polymer matrix composites (substitute for Al alloys)
- space limitation (substitute for Al alloys and steels).

Fig. 13.1 shows the percentage of structural weight for various material classes in modern large commercial aircraft, distinguished between airframe and engine materials. The fuselage of the Airbus A330/340, for example, is manufactured of nearly two thirds aluminum. At about 7%, titanium alloys have a similar share of the structural weight as steels. However, at over a third the structural weight, titanium is the second most common material in the jet engine following Ni-based superalloys; and by volume, titanium alloys are the most abundant material in the engine.

In addition to material properties, cost is a determining factor in the selection of materials for design. This extends beyond raw material costs to the production
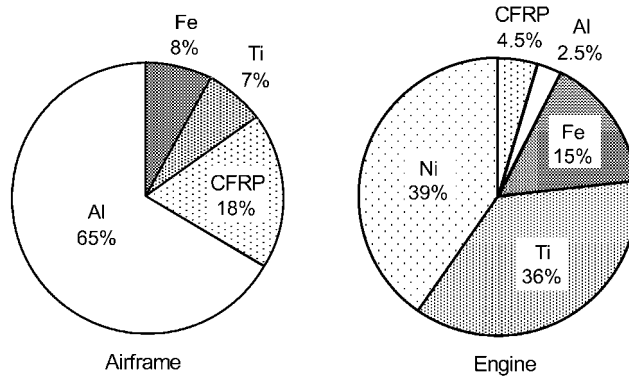
Fig. 13.1 Percentage of aluminum, titanium, and steel alloys and FRP of the structural weight of modern large commercial aircraft and gas turbine engines.

costs for the finished component. Therefore, besides the mechanical properties required for component integrity, a material's producibility measured by its castability, machinability, (plastic) formability, and weldability represents an important factor impacting cost. Particularly imperative in the aerospace industry is to adopt a life cycle approach to material selection by considering the cost implications of maintenance and repair over the expected lifetime of a component. The aircraft manufacturers, as well as producers and manufacturers of titanium alloys, are subject to the airlines' demands to maximize component performance while simultaneously reducing overall costs.

Applications of titanium alloys in the aerospace sector will be highlighted in the following sections. First, fixed-wing aircraft will be addressed, then the use of titanium in jet engines will be highlighted, and finally examples for helicopter and space applications will be given.

13.2.1
Airframe

Oftentimes, saving weight is the major reason for choosing titanium alloys in fuselage applications, thus making use of the high specific strength of the metal. Frequently, the substitution for high-strength steels is worthwhile even if steel's strength is higher, or for aluminum-based alloys even if aluminum's density is lower. This has led to increased use of titanium alloys in fuselages over the past four decades. Fig. 13.2 charts the steady growth of titanium use in Boeing commercial aircraft since titanium's introduction to fuselages in the 1950s. Today, it accounts for approximately 9% of the structural weight of the Boeing 777. Similar numbers are found for Airbus aircraft. In the following, typical fuselage applications for titanium alloys are highlighted.

Titanium alloys are used to stop fatigue crack growth in aircraft fuselages. They are applied as thin, narrow rings placed around the aluminum aircraft fuselage
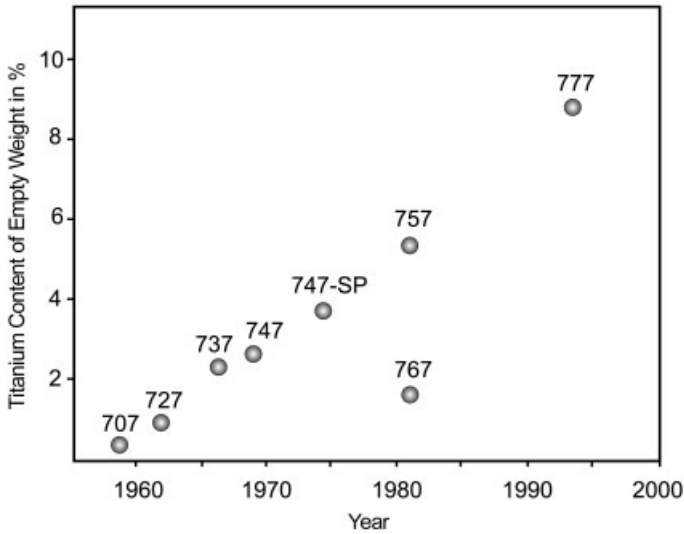
Fig. 13.2 Increase in application of titanium alloys in commercial Boeing aircraft.

like a "belly band", preventing potential fatigue cracks from propagating catastrophically in the outer skin.

Nowadays, titanium alloys are also used for hydraulic tubing of modern aircraft. Compared to steel tubes, weight savings of up to 40% are possible. The $\alpha + \beta$ alloy Ti-3Al-2.5V is primarily used for this application as it is easily deformed and demonstrates sufficient strength.

Where high corrosion resistance is required at moderate strengths, commercially pure titanium is used. Aircraft floors surrounding on-board kitchens and toilets are an example where the corrosive environment dictates titanium's use.

The piping system for de-icing equipment is manufactured from unalloyed titanium. Here strength is less important than thermal stability. Since temperatures can well exceed 200 °C, aluminum alloys may no longer be used. Furthermore, excellent corrosion resistance is required since warm aggressive media have to be transported.

Despite higher initial cost, primary components of aircraft landing gear are increasingly manufactured from forged titanium alloys. The higher up front cost pays off over the long term as high-strength steels typically need to be replaced at least once in an aircraft's lifetime due to their susceptibility to stress corrosion. Landing gear component replacement is avoided if made from titanium alloys; and the Boeing 777 (Figs. 13.3 and 13.4) has set the trend for their use. Here the main landing gear is almost completely manufactured from forged components of TIMETAL 10-2-3, which nearly doubled the amount of titanium used on the 777. The weight savings amounted to approximately 270 kg per aircraft.
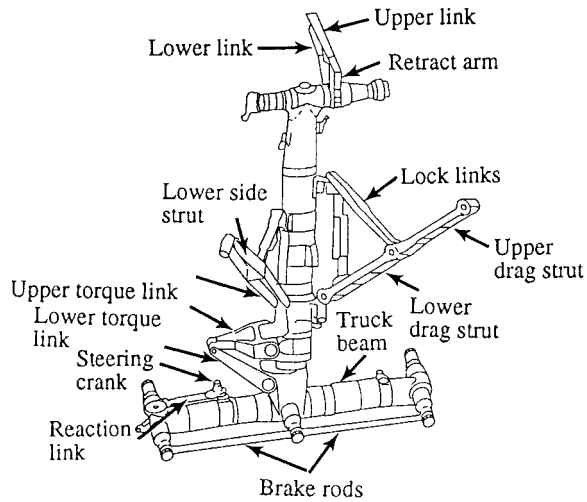
Fig. 13.3 Main landing gear of the Boeing 777 of forged TIME-TAL 10-2-3 parts (Boeing Commercial Aircraft, Seattle, WA, USA).

Fig. 13.4 The main landing gear of the Boeing 777 primarily uses forged parts of Ti-10V-2Fe-3Al, among others the truck beam "Bogie Beam" (Shultz Steel, South Gate, CA, USA).

Due to potentially high loads, e.g. from bird strikes, the frames of cockpit windows are manufactured from forged titanium alloys (Fig. 13.5), while aluminum-based alloys provide sufficient strength for other window frames. Titanium alloys are preferred to support the vertical and horizontal stabilizer structure in a carbon fiber reinforced polymer (CFRP) tail assembly. This use is primarily dictated by

Fig. 13.5 Window frames of Ti-6Al-4V for the cockpit of a commercial aircraft (Shultz Steel, South Gate, CA, USA).

the close match between titanium's coefficient of thermal expansion, compared to aluminum's, and that of polymer matrix composites. Additionally, titanium alloys are chemically more compatible with carbon fibers than aluminum and are used to avoid galvanic corrosion problems.

Compared with the commercial aircraft market, the use of titanium alloys is considerably higher in military fighter aircraft. The greater use is driven by design in response to the larger thermal and mechanical loads associated with greater maneuverability and supersonic cruise speed. The proportion of titanium alloys in military aircraft fuselages can exceed 50%; for the SR-71 "Blackbird" it was 95%. Due to the aero kinetic heating of the surface skin, titanium alloys were used since the temperature capability of the most advanced elevated temperature aluminum alloys was insufficient. Today, titanium accounts for about 35 to 50% of the weight of a modern fighter aircraft. The most common area to find titanium is in the engine bay of fighter aircraft, where temperatures can quickly exceed aluminum's capability. For example, conventional titanium sheet and rivet construction was used extensively in the aft end of the US F-15 aircraft. However, with the redesign to the F-15E model, advanced techniques using superplastic forming and diffusion bonding (SPF-DB) were extensively employed for the same structure. This change in manufacturing technique eliminated 726 part details and 10 000 fasteners, enhancing the maintainability of the aircraft.

Newer alloys such as Ti-6Al-2Zr-2Sn-2Mo-2Cr-0.25Si are used in the airframes of the US F-22 and Joint Strike Fighter projects. This alloy has moderate temperature capability and is used primarily in engine bay bulkheads of these aircraft where fuselage temperatures are highest. Generally speaking, meeting the high performance requirements of military aircraft is of greater importance compared to commercial aircraft, where overall cost effectiveness is the primary driver. The biggest, and probably also most spectacular, titanium structure in military aircraft is the wing box, which carries the load from the wings and can sometimes incorporate a swing-wing design. Fig. 13.6 shows an example of a mid-fuselage bulkhead for the US F-22, which makes up part of the wing box. With a width of 4.90 m, a depth of 1.80 m, and a height of 0.2 m, it is one of the largest titanium
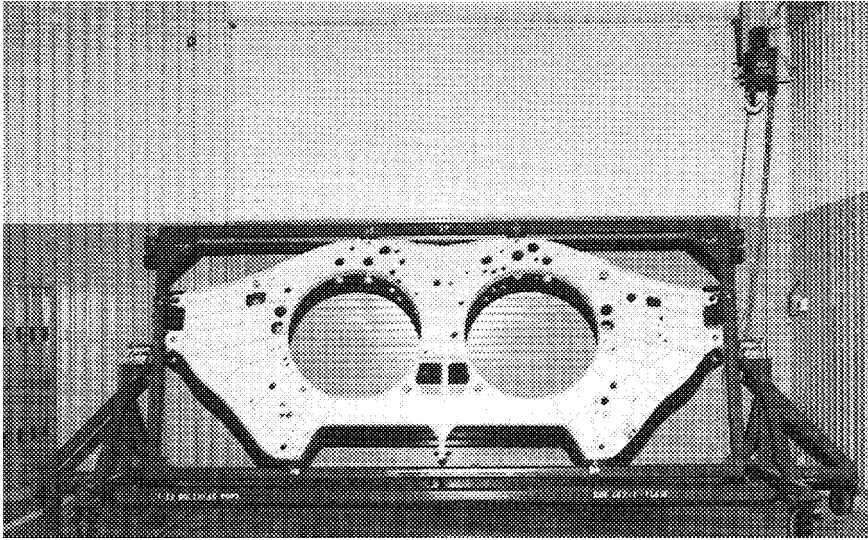
Fig. 13.6 Center bulkhead of the F-22 (Lockheed-Martin Aeronautics, Fort Worth, TX, USA).

forgings ever produced. Although the final component only weighs about 150 kg, it was initially forged from a single cast ingot of almost 3000 kg. This example clearly exhibits the extremely high machining losses, 95%, which can be found in Ti forgings, and demonstrates the opportunity for optimization of the forging process in the future.

Titanium alloys are exceptionally well suited as a spring material. Here, in comparison with high strength steels, the density-corrected modulus of elasticity can lead to weight savings of up to 70%, a simultaneous volume savings of up to 50%, and improved corrosion resistance. Due to their higher strengths, β alloys such as Beta C or Ti-15V-3Cr-3Sn-3Al are preferred alloy candidates.

13.2.2
Gas Turbine Engines

The main area of application for aerospace titanium alloys is in the gas turbine engine. Approximately one third the structural weight of modern turbine engines is made up of titanium. Besides nickel-based superalloys, titanium alloys are the standard engine material. Indeed, the first jet engines introduced at the beginning of the 1950s by Pratt & Whitney in the USA and Rolls-Royce in England contained titanium alloys. Since then the titanium content has steadily increased, as illustrated for Rolls-Royce engines in Fig. 13.7. Furthermore, over the years an evolutionary trend in alloy design is observed from the α + β alloys to the elevated temperature near-α alloys.

Compressor blades were the first engine components to be made from titanium, titanium compressor disks being introduced next. The large front fan
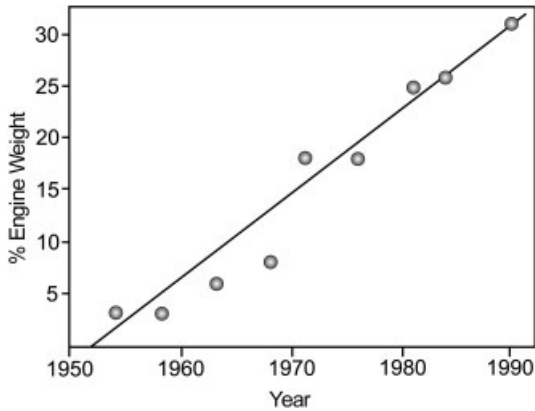
blades of modern jet engines are now often made from titanium alloys too. Fig. 13.8 shows the scale of such components represented by the Rolls-Royce Trent jet engine series. Due to steadily increasing engine by-pass ratios, the newest blade designs exceed lengths of one meter. At these dimensions, fan blade flutter can become a serious problem since the blade tips may reach the velocity of sound and cause mixed supersonic/subsonic flow fields and generate associated shock waves. To increase their stiffness, *shrouds*, or *snubbers*, were added to the middle of the blades. Although these mid-span shrouds were able to control vibration, they adversely affected the aerodynamic efficiency of the fan and lowered fuel efficiency. Advanced fan designs have eliminated shrouds by improving blade stiffness through an increase in chord width and have led to a reduction in the number of blades by about one third. Today, these *wide chord fan blades* are employed in the latest generation jet engines. However, the large mass of these blades dictates designs other than the previously used solid titanium alloy forgings.

Fig. 13.8 Front fans of commercial Rolls-Royce Trent engines made of Ti-6Al-4V (Rolls Royce plc., Derby, UK).

The major engine manufacturers have pursued different concepts for the production of lightweight wide chord fan blades for their latest large jet engines. General Electric was the first to use fiber reinforced polymer composites in the fan blades of their GE90. However, to meet erosion resistance requirements, the blades are designed with leading edges made from titanium. Rolls-Royce and Pratt & Whitney have continued to use designs based on titanium. To reduce the weight of their engines both have moved to hollow titanium fan blade technology. Early hollow fan blade designs were comprised of machined titanium face sheets that were liquid-phase diffusion bonded to a titanium honeycomb core. Advances in manufacturing techniques now allow the blades to be produced from Ti sheet via superplastic forming and solid-state diffusion bonding (SPF-DB). The drawing in Fig. 13.9 shows that the external skins of the bonded construction are expanded at elevated temperatures by pressurized inert gas to the aerodynamically contoured metal dies. For details on SPF-DB see Chapters 8 and 10. The new engines for the Airbus A380 from both Rolls-Royce (Trent 900) and the GE/Pratt & Whitney Engine Alliance (GP7200) will have fan diameters of approximately three meters and will incorporate hollow titanium fan blades.

Evolutionary engine design stresses the need to further decrease the weight of the compressor blades and disks, while extending component life or inspection intervals. This can be achieved using an integrally bladed disk, or "blisk", design. The finished blisk is a single assembly where disk and blades are metallurgically bonded together. For small blade heights up to about 60 to 80 mm, it is more cost effective to machine a blisk from an oversized forged disk. Larger blades are generally attached to the disk by linear friction welding.
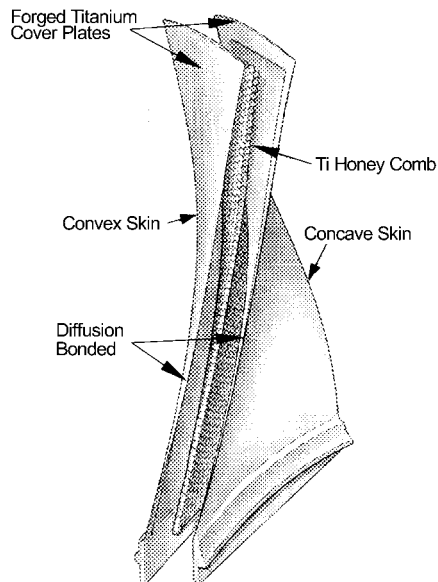
Fig. 13.9 Hollow fan construction for the first generation of 'wide chord fan blades' (Rolls-Royce plc., Derby, UK).

In addition to the weight reduction from a blisk design, the lack of a mechanical interface between the blades and the disks eliminates a common site for fatigue crack initiation. This can result in extended inspection intervals. An example of a blisk compressor stage manufactured by MTU Aero Engines is shown in Fig. 13.10. Blisk technology is now standard technology in small and medium size category compressors of commercial and military engines. In the Eurofighter's EJ200 engine, for example, all three stages of the fan section are a blisk design; the first two being manufactured using linear friction welding, the third by electrochemical machining (ECM).

Since fan blades and disks are used at low temperatures, they are normally manufactured from Ti-6Al-4V. The maximum temperature limit for this alloy is about 315 °C. Therefore, the disks and blades of the first 4 to 5 stages of the compressor (low-pressure compressor) can also be made from Ti-6Al-4V. However, elevated temperature near-α alloys are used in the high-pressure compressor. Today, the maximum temperature limit for these alloys is about 540 °C. This upper bound is not limited by the elevated temperature strength or creep resistance of the near-α alloys, but by their moderate oxidation resistance (see Chapter 6), especially in comparison to nickel-based superalloys. In long-term elevated temperature applications titanium alloys form an "α-case" at the surface, i.e. a zone with a brittle α phase caused by oxygen enrichment, which leads to a drastic reduction in ductility and fatigue strength.

For rotating components, titanium's temperature limit can be even lower due to its propensity to burn. This condition is created when a rotating blade rubs on the inside wall of the engine casing causing localized heating at the blade tip. At elevated temperatures and in a high-pressure air environment, this can lead to very rapid oxidation of the titanium. These conditions are encountered in the high-pressure compressor of the engine. The oxidation process, which is exothermic, can become self-propagating and cause a titanium fire. To mitigate this problem, Pratt & Whitney developed a highly stabilized β-alloy called Alloy C (Ti-35V-15Cr)
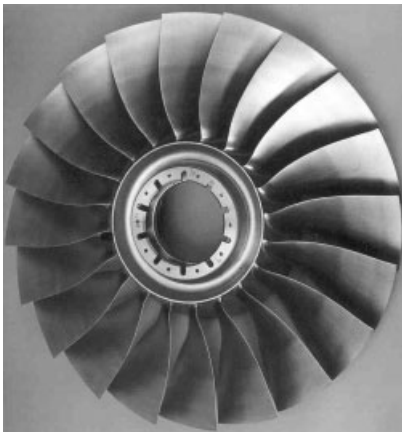
Fig. 13.10 Titanium blisks for compressor applications (MTU Aero Engines, Munich, Germany).

that is resistant to burning. This alloy is finding application in the F-22's F119 engine in compressor stators as well as augmentor and nozzle components.

These temperature limitations for titanium alloys mean the hottest parts in the compressor, i.e. the disks and blades of the last compressor stages, have to be manufactured from Ni-based superalloys at nearly twice the weight. Additionally, problems arise associated with the different thermal expansion behavior and the bonding techniques of the two alloy systems. Therefore, enormous efforts are underway to develop a compressor made completely of titanium. Titanium alloys are required that can be used at temperatures of 600 °C or higher. This has been the impetus for extensive research and development work in the area of elevated temperature titanium alloys. As shown in Fig. 13.11, the maximum application temperature of titanium alloys has been raised from about 300 °C to nearly 600 °C over the last 40 years.

Within the last few years, the near-α class of elevated temperature titanium alloys has been the subject of particular development interest. An example of the state-of-the-art of this development is IMI 834 (Ti-5.8Al-4Sn-3.5Zr-0.7Nb-0.5Mo-0.35Si), developed jointly in the United Kingdom by IMI Titanium Ltd. and Rolls-Royce in the 1980s. With a potential use temperature of almost 600 °C, the alloy was aimed at replacing the IMI 685 and IMI 829 alloys preferred in European jet engines. After IMI was acquired by Titanium Metals Corporation (TIMET), this alloy was given the trade name TIMETAL 834 and has since found its way into European military jet engines. Presently it is also used as a compressor disk material in the last two stages of the medium-pressure compressor, and the first four stages of the high-pressure compressor in variants of the Rolls-Royce Trent series commercial jet engine. A bimodal microstructure with a primary α volume fraction of 15% has proven to be an optimum microstructure for this particular appli-
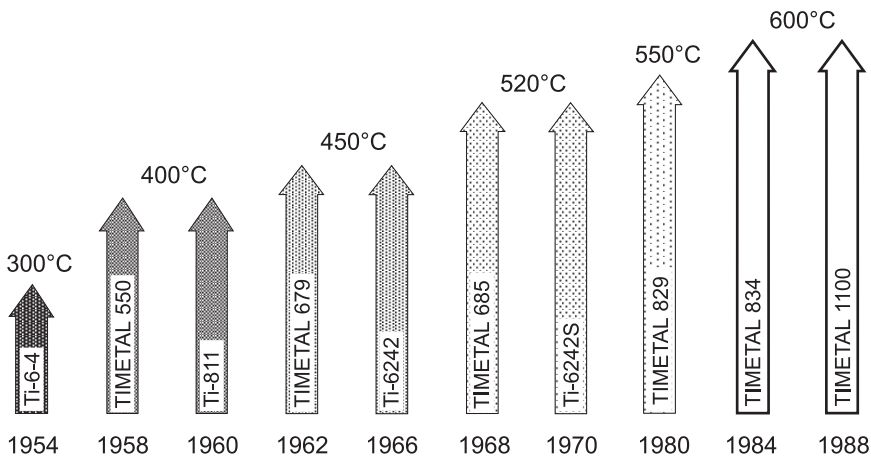
Fig. 13.11 Increase of maximum application temperatures of titanium alloys.

cation. In the United States, the mature Ti-6-2-4-2S is still the preferred high temperature alloy for jet engine applications.

Despite the discussion of near-α titanium alloys, the objective to further increase high temperature strength is addressed with the development of titanium aluminides. These materials, based on the intermetallic compounds $\alpha_2(Ti_3Al)$ and $\gamma(TiAl)$, have been studied for their potential to raise the application temperatures of titanium alloys to 650 °C and 800 °C, respectively (see Chapters 4 and 14). Their excellent creep resistance is due to the ordered nature of the crystal structure. However, this structure also makes the intermetallics relatively brittle and correspondingly hard to deform. Alloying with Nb, Cr, V, Mn or Mo and microstructural optimization are two approaches to gain increased ductility.

Another important aspect for the use of titanium aluminides in turbine engines is the resistance of these materials to initiating a titanium fire, as shown in Fig. 13.12. TiAl-based alloys in particular minimize the risk of titanium fire. Compressor blades of future high-pressure compressors are therefore a potential application of TiAl alloys. Sufficient damage tolerance, a satisfactory oxidation behavior, and producibility (cost) are critical parameters that will ultimately determine the use of titanium aluminides in aerospace. The prospect for potential application of TiAl-based alloys is much higher for jet engine components with less stringent damage tolerance requirements.

Fig. 13.13 shows the fifth stage of the low-pressure turbine in the GE CF6-80C2 jet engine with turbine blades manufactured from a cast Ti-47Al-2Cr-2Nb alloy. Each of the 98 blades has a length of 50 cm, and, at 217 g, the blades are only about 55% the weight of a conventional nickel-based superalloy blade. The reduced weight of the titanium aluminide blades would further enable an even lighter weight design of the entire turbine due to the lower centrifugal forces imposed on the disk. Use of these alloys in a large jet engine like the GE90 could
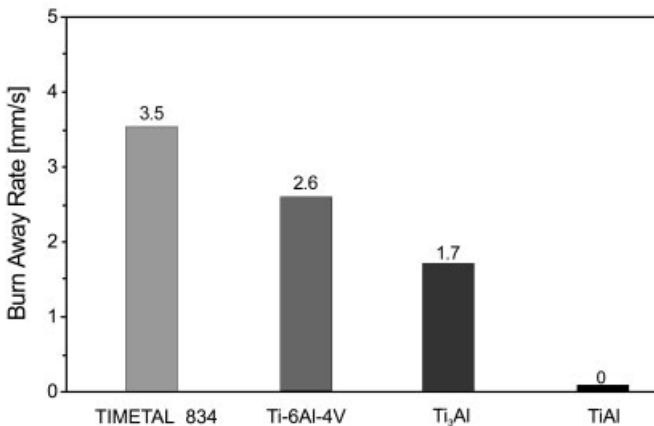
Fig. 13.12 Burn resistance of titanium aluminides compared to conventional titanium alloys (W. Smarsly, MTU Aero Engines, Munich, Germany).
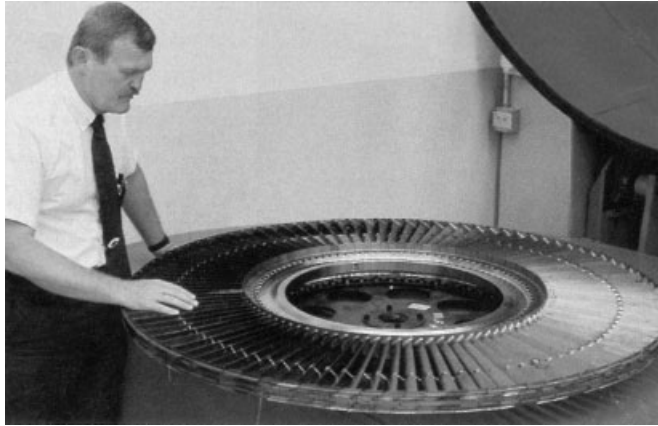
Fig. 13.13 TiAl low-pressure turbine blades for the CF6-80C2 (GE Aircraft Engines, Evandale, OH, USA).

save more than 150 kg. Due to cost, the casting route is favored for the production of TiAl low-pressure turbine blades. At present, the production of TiAl blades is delayed primarily due to cost considerations.

Increased stiffness and elevated temperature strength are the primary goals for the development of long fiber reinforced titanium matrix composites (TMCs). Potential areas for application in jet engines are high-stiffness, high-strength fan blades, and thermally stable cylindrical components in the high-pressure compressor. Most investigations have been carried out on SiC long fiber reinforced Ti-6Al-4V. Matrices of near-α alloys and titanium aluminides, stable at higher temperatures, are also of interest. The availability of TMCs enables previously untenable design approaches, such as the integrally bladed compressor ring, or *bling*. The bling design eliminates the hub of the disk, significantly reducing the component weight by up to 70%. However, in order to accomplish this, the strength of the material at the base of the blades must be much higher to support the centrifugal loads and calls for use of metal matrix composite reinforcement. As with blisks, the number of parts is drastically reduced, substantially reducing maintenance costs compared to conventionally bladed rotors. Such improvements are likely to justify the high manufacturing costs, and will allow compressors and jet engines themselves to be built considerably more compact (see Chapter 12). Continued research and development, particularly in processing and component life management techniques, still have to be completed before these composite materials are put into rotating components. The first aerospace use of continuously reinforced titanium composite material is a low risk application as an actuator piston on the F-22's F119 engine.

Aerospace hydraulic fluid is one of the few corrosive media to otherwise usually corrosion-resistant titanium alloys. Above 130 °C hydraulic fluid forms an acid that etches the titanium and leads to hydrogen embrittlement of the component.
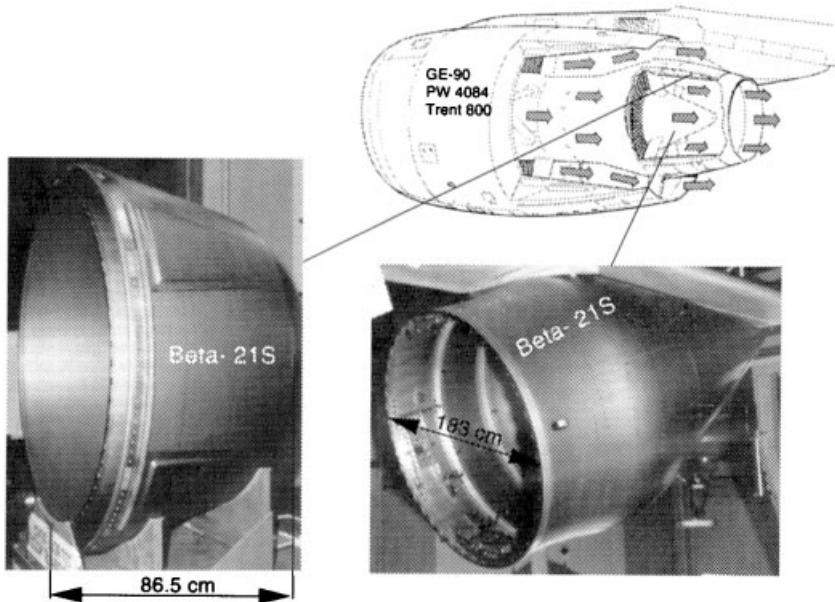
Fig. 13.14 Applications of TIMETAL 21S in the nozzle area of the Boeing 777.

One of the few alloys that appears to be immune to this attack is the β alloy TIMETAL 21S. For this reason, the Boeing Company uses TIMETAL 21S for the plug and other parts of the nozzle assembly on its 777 aircraft (Fig. 13.14). The 777 uses the largest jet engines GE90, PW4084 and Trent 875. Pratt & Whitney also plans to use similar components manufactured from TIMETAL 21S for its PW4168 engine that flies on the Airbus A330.

13.2.3
Helicopters

For helicopters, titanium alloys are used in the most highly stressed component: the rotor head. Fig. 13.15 shows examples of forged Ti-6Al-4V rotor heads for the Eurocopter BO 105 and BK 117 helicopters. However, intensive studies are on-going for the high-strength β alloy replacements (see Chapter 2). For example, the β alloy TIMETAL 10-2-3 has replaced Ti-6Al-4V for the main rotor head of the Westland Super Lynx helicopter. Today β alloys are also established in other helicopter programs. TIMETAL 10-2-3 is used for the rotor mast and rotor head for the US RAH-66 Comanche helicopter. The same alloy is also being applied in the yoke assembly of the tiltrotor V-22 Osprey.
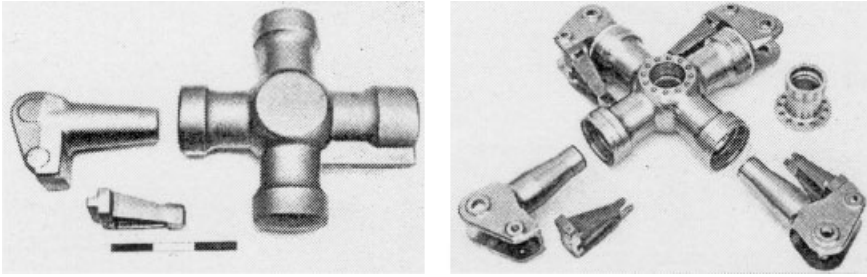
Fig. 13.15 Forged rotor head of the BO 105 and BK 117 helicopters.

13.3
Space Applications

Due to the comparatively small payload of space vehicles, saving weight in these structures is even more important than in aircraft (see Tab. 13.1). For this reason, titanium alloys were used extensively in the first Apollo and Mercury programs. Fuel and satellite tanks are regarded as a standard application for titanium alloys. Titanium's low weight, high strength, and long term chemical compatibility with fuel give titanium alloys an advantage over high-strength steels. Furthermore, the integrity of the tanks must be reliably nondestructively tested before being sent into orbit, which is most consistently done for metallic tanks. Non-metallic components require additional efforts to ensure their integrity. Fig. 13.16 shows pressure vessels made from titanium alloys for the US Space Shuttle program.

Fig. 13.16 Pressure tanks manufactured from titanium for space transportation systems (TIMET, Henderson, NV, USA).

The requirement for extremely lightweight satellite component construction dictates very intensive, weight-optimizing manufacturing techniques. Under favorable conditions, the final fuel tank wall thickness in commonly used satellite propulsion systems is machined from 25 mm thick forged half-shells to less than 1 mm. This exceptionally high degree of machining can be drastically reduced by superplastic forming (see Chapters 8 and 10). Titanium sheet, 6 to 10 mm thick, can be superplastically formed to hemispheres and either simultaneously diffusion bonded or later conventionally welded to form a tank. Compared to conventional production by forging and machining, clear cost savings are obtained. Fig. 13.17 shows a tank used for the Attitude Control System (SCA) on the Ariane 5. It was produced from two SPF half-shells that were TIG welded together.

In addition to superplastic forming, cold-formable β alloys provide another cost effective route. MAN Technologie AG uses such an approach to produce the fuel tanks for the ESA on the Automated Transfer Vehicle (ATV) for the International Space Station (ISS). The Ti-15-3 tank half-shells are formed by a special, patented cold rolling process called *counter-role spin forming*.

The sequence in Fig. 13.18 demonstrates how half-shells for satellite tanks can also be manufactured by simple spin forming of the alloy Ti-15-3. Compared to SPF processing, the required infrastructure and tooling are substantially cheaper. Furthermore, the β alloy shows very good mechanical properties. Among others, spin forming is used for the production of the half-shells of the Storable Propellant Stage (EPS) tanks for the upper stage of the Ariane 5.

Ti-3Al-2.5V was developed, among others, for low temperature applications and shows good toughness and ductility down to cryogenic temperatures. Therefore, it is used for high-pressure piping in the hydrogen pumping systems of the US Space Shuttle.

Fig. 13.17 Attitude Control System (SCA) tank of welded Ti-6Al-4V SPF half shells (Astrium GmbH, Bremen, Germany)

Fig. 13.18 Sequences during spin forming of Ti-15-3 half shells (Astrium GmbH, Bremen, Germany)

a)

b)

c)
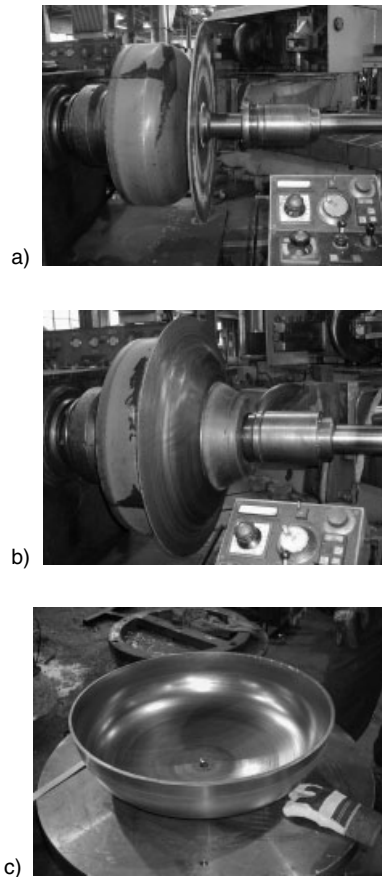
13.4
Referenced Literature and Further Reading

1 F. Appel, U. Brossmann, U. Christoph, S. Eggert, P. Janschek, U. Lorenz, J. Müllauer, M. Oehring, J.D.H. Paul: Recent Progress in the Development of Gamma Titanium Aluminide Alloys, *Advanced Engineering Materials* **2** (2000) 699–720

2 R.R. Boyer: An Overview on the Use of Titanium in Aerospace Industry, *Materials Science & Engineering* **A213** (1996) 103–114

3 R.R. Boyer, J.C. Williams, N.E. Paton: Evolving Aerospace Applications for Ti Alloys, in *Titanium '99: Science and Technology*, CRISM "Prometey", St. Petersburg, Russia (2000) 1007–1016

4 H. Clemens, H. Kestler: Processing and Applications of Intermetallic γ-TiAl-Based Alloys, *Advanced Engineering Materials* **2** (2000) 551–570

5 S. Djanarthany, J.-C. Viala, J. Bouix: An Overview of Monolithic Titanium Aluminides Based on Ti_3Al and TiAl, *Materials Chemistry and Physics* **72** (2001) 301–319

6 J.M. Donachie: *Titanium, A Technical Guide*, ASM International, Metals Park, OH (1988)

7 D. Eylon, S. R. Seagle: State of Titanium in the USA – the First 50 Years, in *Titanium '99: Science and Technology*, CRISM "Prometey", St. Petersburg (2000) 37–41

8 F. H. Froes: Developments in Titanium Applications, *Light Metal Age*, **Oct.** (1995) 6–8

9 A. Gilchrist, T. M. Pollock: Cast Gamma Titanium Aluminides for low-pressure Turbine Blades, in *Structural Intermetallics*, eds. K. J. Hemker and D. M. Dimiduk, TMS, Warrendale, PA (2001) 3–12

10 K. J. Hemker, D. M. Dimiduk, H. Clemens, R. Darolia, H. Inui, J. M. Larsen, V. K. Sikka, M. Thomas, J. D. Whittenberger, eds.: Structural Intermetallics 2001, TMS, Warrendale, 2001

11 Y.-W. Kim, H. Clemens, A. H. Rosenberger, eds.: Gamma Titanium Aluminides 2003, TMS, Warrendale, PA (2003)

12 H. A. Lipsitt: Titanium Aluminides – An Overview, in High-Temperature Ordered Intermetallic Alloys, MRS, Pittsburgh, PA (1985) 351–364

13 E. A. Loria: Gamma Titanium Aluminides as Prospective Structural Materials, *Intermetallics* **8** (2000) 1339–1345

14 G. Lütjering: Potential von Titanlegierungen, *BDLI-Werkstofftag '91*, BDLI, Bonn (1992) 139–148

15 R. Martin, D. Evans: Reducing Cost in Aircraft, *Journal of Metals* **52** (2000) 24–29

16 M. Peters: Titanium Alloys for Aerospace Applications, *Titanium World* **2** (1995) 15–17

17 M. Peters, R. Braun: Light Alloys for Aerospace Applications, in *4th European Conference on Advanced Materials and Processes – EUROMAT 95*, Associazione Italiana di Metallurgia, Milano (1995) 55–64

18 M. Peters, C. Leyens, W. A. Kaysser (eds.): *IMI 834 and TIMETAL 1100*, DLR, Cologne (1994) 1–76

19 U. Rieck: Near Net Shape Forming Technology for Propellant Tanks, in *Advanced Aerospace Materials*, eds. M. Peters and W. A. Kaysser, DGLR, Bad Godesberg (2001) 213–219

20 A. Vassel, J. Y. Guedou: Aero-Engine Applications: Present and Future, in *Titanium '99: Science and Technology*, CRISM "Prometey", St. Petersburg (2000) 1017–1026

21 C. H. Ward: Microstructure Evolution and its Effect on the Fracture Behavior of Ti_3Al Intermetallics, *International Materials Reviews* **38** (1993) 79–101

22 J. C. Williams: Alternative Materials Choices – Some Challenges to the Increased Use of Ti Alloys, *Materials Science and Engineering* **A263** (1999) 107–111

23 P.-J. Winkler, M. A. Däubler, M. Peters: Applications of Titanium Alloys in the European Aerospace Industry, in *Titanium '92: Science and Technology*, TMS, Warrendale, PA (1993) 2877–2890

14

Production, Processing and Application of γ(TiAl)-Based Alloys

H. Kestler and H. Clemens*, PLANSEE AG, Technology Center, Reutte, Austria
*GKSS Research Center, Institute for Materials Research, Geesthacht, Germany, now with
Department of Physical Metallurgy and Materials Testing, University of Leoben, Austria

14.1
Introduction

Because of their attractive properties, γ(TiAl)-based alloys are considered for high-temperature applications in aerospace and automotive industries [1–10]. These properties include low density (~ 3.9–4.1 g cm^{-3}), high specific yield strength (yield strength/density), high specific stiffness (modulus of elasticity/density), good oxidation resistance, resistance against "titanium fire", and good creep properties at high temperatures. The variation of the specific yield strength and the specific stiffness with temperature of typical γ(TiAl) based alloys in comparison with commercial Ni-based superalloys and Ti-alloys is shown in Fig. 14.1.

Particularly at temperatures between 600 °C and 800 °C γ(TiAl)-based alloys are superior to Ti-alloys in terms of their specific strength. Compared to the heavier Ni-based alloys, their specific strength is at least similar if not higher. In the last
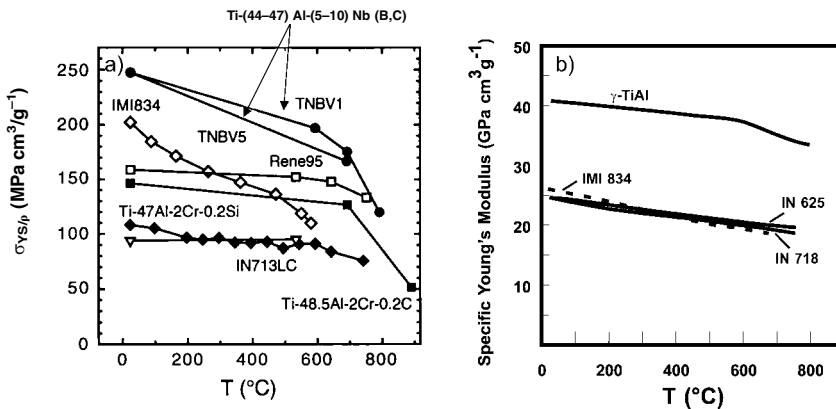
Fig. 14.1 (a) Variation of the specific yield strength [11], and (b) the specific Young's modulus with temperature for conventional engineering γ(TiAl)-based alloys and high-strength TNB alloys in comparison with some Ti-based alloys and superalloys used in aerospace applications.

years a promising family of high-strength γ(TiAl)-based alloys have been developed (Fig. 14.1a). These so-called TNB-alloys are characterized by a Nb-content ranging between 5–10 atomic percent. At room temperature yield strength levels >1000 MPa can be achieved after proper thermomechanical processing. It is important to note that the high temperature properties, such as creep resistance, are also remarkably increased, thus extending the application range of γ(TiAl)-based alloys to higher temperatures. For further detailed information the reader is referred to Chapter 4. Additionally, the high specific stiffness that is retained at elevated temperatures is most advantageous for the design of lightweight structural parts in aerospace and automotive applications.

In order to make use of these advantages, it is necessary to provide suitable alloy compositions as well as industrial manufacturing and processing technologies that are appropriately adapted to this material class. Therefore, the emphasis of this chapter is centered mainly on thermomechanical processing of γ(TiAl)-based alloys because it provides the control of microstructure and hence of the resulting mechanical properties necessary to exploit the potential of this new class of high-temperature structural materials.

14.2
Constitution of γ(TiAl)-Based Alloys

Single-phase γ(TiAl), even with low interstitial impurity levels (<1000 wt. ppm), tends to fracture at room temperature before reaching 0.5–1% plastic strain in tension [12–15]. This brittle behavior was improved by alloying modifications; however, no practical breakthrough was made. Furthermore, single-phase γ(TiAl) alloys are sensitive to unacceptable grain growth during hot-working and subsequent heat treatments. Consequently, extensive research and development activities have led to the introduction of *two-phase* γ(TiAl)-based alloys with appropriate combinations of alloying elements to overcome the above mentioned deficiencies of single-phase TiAl alloys [1, 2, 12]. Two-phase γ(TiAl)-based alloys of engineering interest consist of γ(TiAl) (ordered face-centered tetragonal $L1_0$ structure) and α_2-Ti_3Al (ordered hexagonal DO_{19} structure). The crystal structures of the two phases are shown in Fig. 14.2.

The unit cell of the γ(TiAl) phase is only slightly distorted (c/a ≈ 1.02) and consists of alternating planes of Ti and Al atoms in the [001] direction. In thermodynamic equilibrium, the α_2/γ volume fraction is controlled by the Al-content, and additional alloying elements, and typically is in the range of 0.05 to 0.2 [1, 2]. However, thermomechanical processing and heat treatments have a strong influence on the actual γ/α_2 volume fraction in γ(TiAl)-based alloys (see sections 14.3 and 14.4.3). Although the α_2-Ti_3Al phase is more brittle than the γ(TiAl) phase, it has a significant effect on the mechanical properties and deformation behavior of γ(TiAl)-based alloys. Because of the higher solubility of interstitial impurities in the α_2-Ti_3Al phase (especially oxygen), the γ(TiAl) phase is essentially "gettered", and thus its ability to deform plastically even at low temperatures is increased. The-
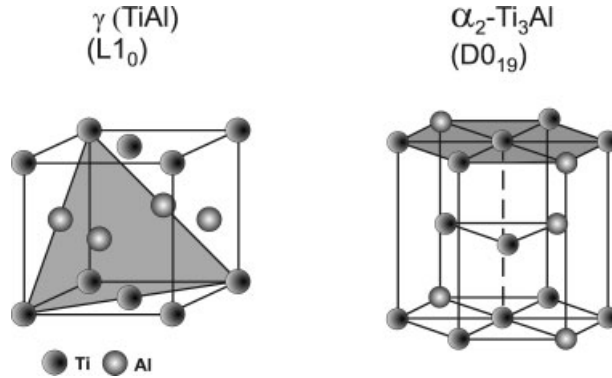
Fig. 14.2 Crystal structure of γ(TiAl) (left) and α_2-Ti$_3$Al (right). The close-packed planes $(111)_\gamma$ and $(0001)_{\alpha_2}$ are shaded.

oretical calculations have shown that the "Peierls force" acting on dislocations is reduced by minimizing the interstitial impurities in the γ(TiAl) phase. As a consequence, the mobility of dislocations is increased and, in contrast to single phase γ(TiAl), mechanical twinning is activated as an additional deformation mechanism [1, 16]. Additionally, the tetragonality of the γ(TiAl) phase decreases with decreasing Al-content, which also has a positive effect on dislocation mobility and therefore on low temperature ductility. Besides γ(TiAl) and α_2-Ti$_3$Al, some alloys additionally show the presence of β/B2 (disordered bcc structure/ordered CsCl structure) phase in particle form, whose formation is favored by additions of Cr, Mo, and W [2, 12, 17, 18]. Borides and/or silicides are present if the amount of B and/or Si exceeds a certain alloying concentration [2, 12, 19, 20]. For some alloys, the existence of Laves phase (C14 and C15 structure) has been reported [21–24].

The ductility and strength of γ(TiAl) alloys are controlled by chemistry and microstructure. For fine-grained binary alloys, the room temperature elongation to fracture varies with Al-content, exhibiting a maximum centered around the two-phase composition Ti-48at%Al [1, 12]. Since low temperature ductility is a major concern for structural application, γ(TiAl) alloys of engineering importance are based on Ti-(45–48)at%Al [1, 2, 12]. However, it has been shown that binary two-phase alloys generally cannot be used due to their inability to meet specific requirements such as creep strength and resistance to oxidation. As a consequence, the effect of alloying elements on the mechanical properties of two-phase γ(TiAl)-based alloys with specific types of microstructure has been investigated within the framework of extensive development programs [1–3, 12, 19, 25–28]. The composition of conventional engineering γ(TiAl)-based alloys, or "2nd generation" alloys, can be summarized as follows:

Ti-Al$(45 - 48)$at%-X$(1 - 3)$ at%-Y$(2 - 5)$at%-Z(< 1) at%

where, X = Cr, Mn, V; Y = Nb, Ta, W, Mo; Z = Si, B, C

Fig. 14.3 shows a section of the binary Ti-Al phase diagram in which the range of existence of the two-phase γ(TiAl)-based alloys is indicated.

It should be noted that all alloying elements marked with X, Y, and Z affect the position of the phase boundaries to a greater or lesser extent [1, 3, 12, 29]. While Cr, Mn and V lower the stacking fault energy and thus increase the ductility of the alloys at room temperature by increasing the propensity for mechanical twinning, the other alloying elements improve their high temperature properties (resistance to oxidation, creep strength, etc.). Boron is typically used as a grain-refining agent. Engineering γ(TiAl)-based alloys on the 2nd generation contain at least one ductilizing element and one refractory element, which improve oxidation and creep resistance. However, like in the case of currently used superalloys, γ(TiAl) alloys can contain up to 5 to 8 different alloying elements. Depending on alloy chemistry and microstructure, these alloys exhibit good workability, good tensile properties (Fig. 14.1), tensile fracture strains in the range of 1% to 3% at room temperature, and fracture toughness in the range of 10 to 35 MPa m$^{0.5}$ [30]. However, the creep resistance of these alloys seems to limit the maximum application temperature to 700 °C, especially if long-term service is considered. This is probably a direct consequence of thermally activated dislocation processes that make the mechanical behavior of γ(TiAl) alloys strongly rate-dependent. Thus, the strength degrades at low strain rates, which normally occur under creep conditions [16]. Additional limitations might arise from microstructural instabilities (see section 14.3), which are also expected to degrade the creep properties.

In order to increase the high-temperature capabilities of γ(TiAl)-based alloys, current alloy development programs are focused on high Nb-containing alloys as well as C-containing alloys (see Chapter 4). γ(TiAl) alloys with Nb contents in the range of 5 to 10 at% are 3rd generation alloys or referred to as GKSS TNB alloys. This class of alloys exhibits improved strength properties and oxidation resistance when compared with conventional γ(TiAl)-based alloys [31, 32]. For example, a room temperature tensile strength of more than 1100 MPa was reported for a hot-extruded Ti-45at%Al-(5–10)at%Nb alloy. Remarkably, a plastic fracture strain of > 2% was obtained. The relatively high fracture strain has been attributed to the high Nb content, which decreases the stacking fault energy in γ(TiAl) and thus facilitates mechanical twinning. Large Nb additions also reduce the diffusion rates in γ(TiAl) [33], which is beneficial for creep resistance. Improvements in creep strength of conventional γ(TiAl)-based alloys have also been achieved by carbon additions in the range of 0.2–0.4 at% [2, 34]. Annealing and quenching result in a carbon solid solution, whereas Ti_3AlC perovskite-type precipitates are formed by subsequent ageing. Implementation of precipitation hardening often tends to embrittle the material, which is of particular concern in the case of less ductile alloys like γ(TiAl)-based intermetallics. However, it was demonstrated that adequate processing could lead to a homogeneous and relatively fine microstructure. For example, hot extrusion resulted in well-balanced mechanical properties, which are characterized by a good creep resistance and an appreciable room temperature ductility of 2.5% [34]. Thus, precipitation-hardened γ(TiAl)-based alloys appear to be promising for high-temperature service. However, the thermal stability of the Ti_3AlC
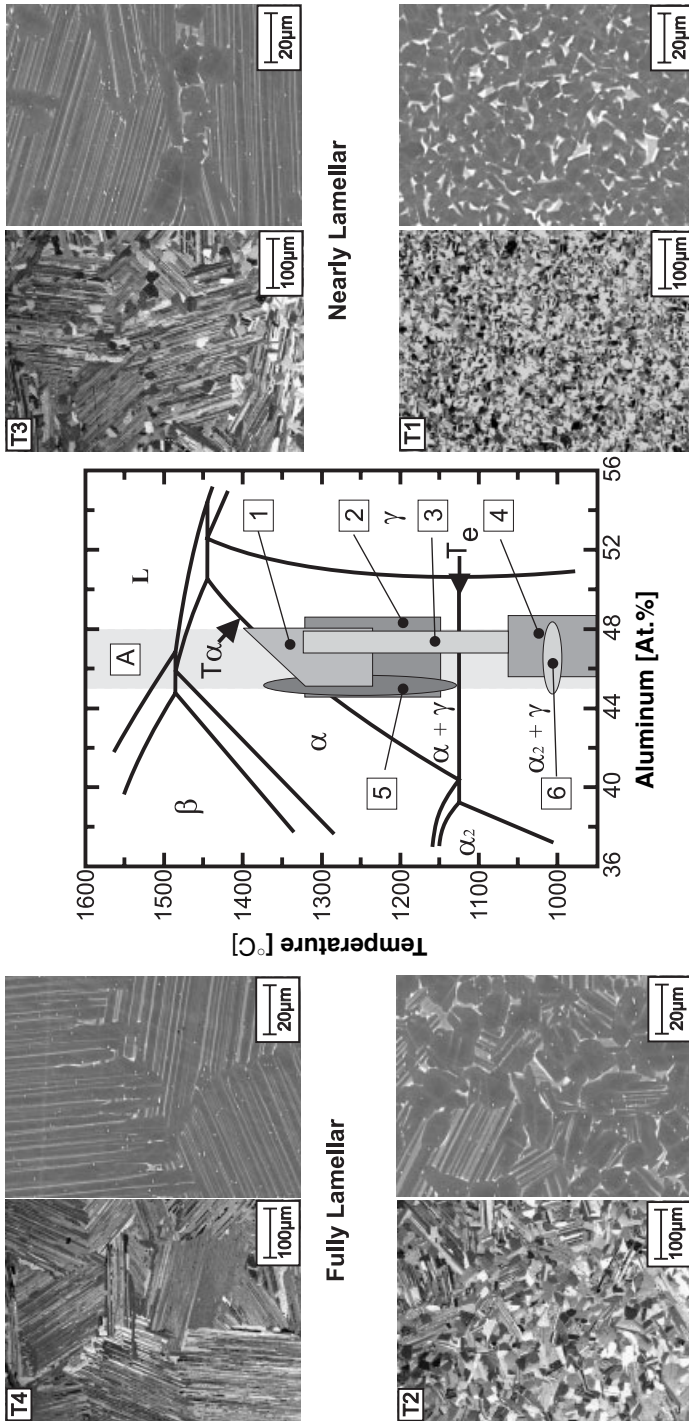
Fig. 14.3 Mid-section of the binary Ti-Al phase diagram and corresponding microstructures (left hand side micrographs: light microscopy (polarized light) and, right, scanning electron micrographs (back-scattered electron contrast)). The shaded areas indicate the base for engineering γ(TiAl)-based alloys (A) and the temperature regions for thermomechanical processing and subsequent heat-treatments: (1) extrusion; (2) rolling; (3) forging; (4) superplastic and conventional hot-forming of sheet material; (5) heat-treatments: (i) annealing above T_α and subsequent cooling at moderate rates → fully lamellar microstructures are formed (T4); (ii) slightly below T_α → nearly lamellar microstructures (T3); (iii) between T_e and T_α → duplex microstructures with varying volume fraction of lamellar grains (T2); (iii) close to T_e → near gamma microstructures; (6) flattening and residual stress reducing heat-treatment for γ(TiAl) sheets after rolling (primary annealing). T_α: α-transus temperature; T_e: eutectoid temperature.

precipitates against coarsening, for example under long-term creep conditions, has to be proven. Besides perovskite phases, silicide or Laves phases may be attractive for increasing the creep strength of γ(TiAl) alloys [2, 12, 16]. In order to compete with superalloys within a wider temperatures range, future γ(TiAl)-based alloys must exhibit increased high temperature capabilities (creep, oxidation) with appreciable room temperature ductility and fracture toughness. Based on the current status of research, it is believed that high Nb-containing γ(TiAl) alloys with precipitation hardening are the most promising candidates to fulfill these demands (see Chapter 4) [26].

14.3
Controlled Microstructures by Heat-Treatments

Generally, the influence of microstructure on mechanical properties of γ(TiAl)-based alloys can be summarized as follows: coarse-grained, fully lamellar microstructures exhibit relatively good fracture toughness and excellent creep resistance, but poor tensile ductility and strength, especially at room temperature. The high Nb-containing alloys exhibiting a fully lamellar microstructure show improved stress levels; however, they are more susceptible to embrittlement. Relatively fine-grained, equiaxed primary annealed, near-gamma, duplex microstructures with only small amounts of lamellar colonies show low fracture toughness and creep resistance but moderate tensile ductility and strength at room and elevated temperatures. This inverse correlation between tensile properties and resistance to fracture (fracture toughness) calls for a carefully selected microstructure for service while at the same time making microstructural optimization for achieving balanced engineering properties difficult.

Normally, wrought γ(TiAl)-based alloys exhibit a fine-grained microstructure that can be altered over a wide range by heat-treatments, see Fig. 14.3. Annealing above the eutectoid temperature and subsequent slow cooling to room temperature leads to the formation of a near-gamma microstructure. This microstructure consists of equiaxed γ grains and, in accordance with the lever rule, a small amount of $α_2$ situated at triple points and grain boundaries of γ grains. Heat-treatments in the middle of the $α + γ$ region followed by cooling to room temperature result in the evolution of a duplex microstructure composed of γ grains and $γ/α_2$ colonies, and a small volume fraction of $α_2$ precipitates in the γ grains. The volume fraction of the lamellar colonies and the average lamellae spacing depends on the applied cooling rate. The γ and $α_2$ lamellae within the colonies possess the following crystallographic relationship: $(111)_γ//(0001)_{α_2}$ and $[110]_γ//[11\overline{2}0]_{α_2}$ [35]. This relationship becomes quite clear if the atomic matching of the $(111)_γ$ plane and the $(0001)_{α_2}$ basal plane is taken into account (Fig. 14.2).

With increasing annealing temperature in the $α + γ$ phase region (or with increasing annealing time at a fixed temperature), the proportion of lamellar colonies increases. The lamellar spacing in the colonies strongly depends on the applied cooling rate. Nearly lamellar or fully lamellar microstructures are generated

upon cooling when wrought γ(TiAl)-based alloys are heat-treated about 10 °C below or 10 °C to 20 °C above the α-transus temperature, respectively. Here it should be noted that heat-treating in the single α-phase field bears the risk of uncontrolled grain growth due to the absence of a second phase. Especially for basic γ(TiAl)-based alloys, colony sizes in the range of 100 μm to 500 μm are readily obtained after annealing above the α-transus temperature for only a few minutes. However, such coarse-grained fully lamellar microstructures cannot be used because of their inherently low tensile ductility at room temperature. In this context, boron proved to be very beneficial for obviating uncontrolled growth of α grains when cast as well as wrought γ(TiAl) alloys are heat-treated above the α-transus temperature [2, 19, 36].

The transformation of the high-temperature phase to lamellar α + γ phases upon cooling is well known. The reaction occurs in the α + γ phase field by introduction of stacking faults in the hexagonal α-phase (spreading of Shockley partial dislocations on the basal planes), which produce the correct stacking sequence for the $L1_0$ structure, followed by diffusional growth and chemical equilibration of the γ-phase [35, 37]. It was shown that lamellar formation occurs rapidly below the α-transus temperature; however, the degree of undercooling required for nucleation of the reaction is strongly dependent upon cooling rate, alloy composition and α-grain size [18]. From such studies, continuous cooling transformation (CCT) diagrams have been established for several γ(TiAl)-based alloys as reported in Refs. [18, 38].

For engineering γ(TiAl)-based alloys with compositions similar to Ti-46.5at% Al-4at% (Cr,Nb,Ta,B), the optimum balance between fracture toughness and creep resistance on one side, and room temperature tensile ductility and strength on the other side, is expected for fully lamellar microstructures with small colony sizes (50 to 400 μm) exhibiting narrow lamellar spacing [2, 39]. In order to realize these "designed" fully lamellar microstructures by using industrial annealing furnaces, the transformation behavior of the γ(TiAl) alloys must be exactly known, e.g. variation of the α-transus temperature within the limits of the specified composition range.

Problems that arise when heat treatments are transferred from small laboratory furnaces to large industrial furnaces include temperature overshoot that leads to undesired grain growth; non-uniform temperature distribution, which is of particular concern in case of large sheets; and, limited cooling rates that do not allow fine lamellar spacing adjustment. In the case of sheet material, additional requirements must be fulfilled, i.e. a minimum number of lamellar colonies having a maximum variation with respect to the lamellae habit planes of such colonies within the sheet thickness [9, 36]. Otherwise, a local anisotropic material behavior might be expected.

The beneficial effect of boron is exemplified in Fig. 14.4a, where the dependence of the colony size on holding time at 1350 °C is shown for two hot-rolled γ(TiAl) alloys with the following compositions and corresponding α-transus temperatures: Ti-46at%Al-4at%(Cr, Nb, Ta, B) with $T_\alpha = 1325$ °C, and Ti-46.7at%Al-3.7at%(Cr, Nb, Ta) with $T_\alpha = 1345$ °C. The main difference between these two al-

loys is that the alloy with the lower α-transus temperature contains boron, which reacts to form (Ti, Ta)-borides. From Fig. 14.4 a it is evident that the growth of the α grains is impeded by the presence of the borides, and therefore a controlled adjustment of a fully lamellar microstructure is achieved more easily than in the case of the boron-free alloy. Furthermore, the colony size obtained is in a range that fulfils the requirements for sheet material mentioned above. From TEM investigations it might be speculated that the boride particles act by a "Zener-drag effect" that effectively restricts the size of the α grains during annealing in the α-phase field [41]. The size of the α grains, which corresponds to the lamellar colo-
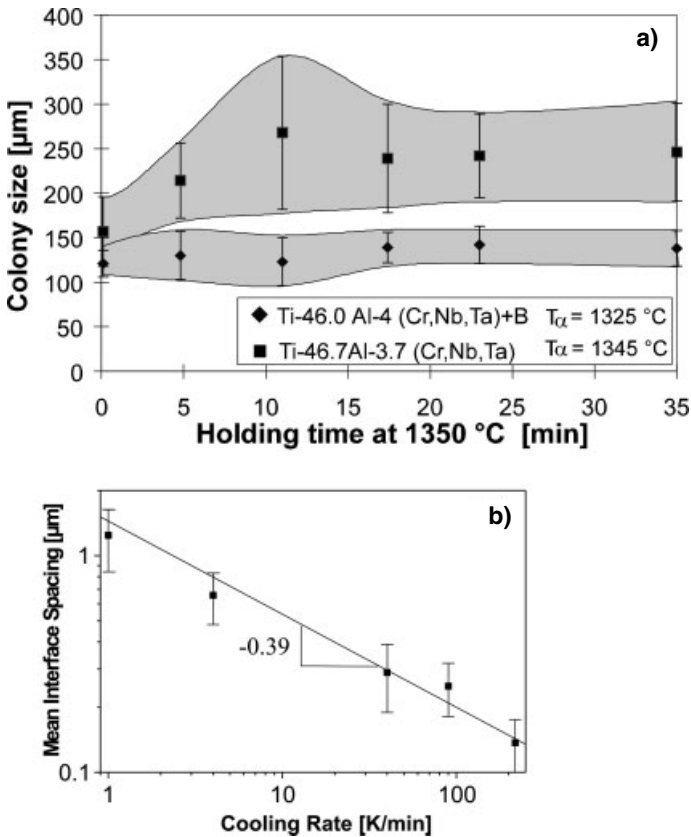
Fig. 14.4 (a) Variation of colony size with holding time at 1350 °C for γ(TiAl) sheet material with and without boron additions. Heating and cooling conditions were identical for both alloys. Alloy compositions and corresponding α-transus temperatures are given in the inset. (b) Dependence of the mean interface spacing on cooling rate obtained for Ti-46.5at%Al-4at%(Cr, Nb, Ta, B) sheet material. Prior to cooling the specimens were annealed for 6 min at 1350 °C, which corresponds to a temperature 5 °C above the α-transus temperature [40]. The slope of ≈ 0.5 indicates that the formation of the lamellar structure is a diffusion controlled process.

ny size upon cooling, depends mainly on particle size and volume fraction of the borides [41, 42]. Heat treatments in the α phase field destroy the "modified cube" texture present in as-rolled sheet material (section 14.6). After transformation to a fully lamellar microstructure the appearance of a random cube texture or a weak [110] fiber texture has been observed, which is reflected in almost isotropic mechanical properties [43–45].

The dependence of the average interface spacing on cooling rate as obtained for fully lamellar Ti-46at%Al-4at%(Cr, Nb, Ta, B) sheet is shown in Fig. 14.4b. With increasing cooling rate, the kinetics of the $\alpha \to \gamma$ transformation is slowed down. Hence, the α_2 volume fraction increases to values that are significantly higher than those predicted for thermodynamic equilibrium [31, 40, 46, 47]. However, in order to obtain a fully lamellar microstructure without any formation of primary grains along lamellar colony boundaries, a certain cooling rate has to be exceeded, which in turn leads to α_2 volume fractions far from thermodynamic equilibrium [41]. For example, in the case of the Ti-46at%Al-4at%(Cr, Nb, Ta, B) alloy, a cooling rate of 40 K min^{-1} leads to an α_2 volume fraction of about 30%, which is higher by a factor three than that expected for equilibrium condition [41]. Such non-equilibrium conditions, however, provide one of the driving forces responsible for structural changes in lamellar microstructures on exposure at temperatures in the range of 700 °C to 800 °C [18, 31, 41, 46]. An additional driving force arises from interfacial energy. This contribution increases with decreasing lamellar spacing. In a recent study it was shown that the ''chemical'' driving force arising from non-equilibrium conditions plays the major role, whereas the contribution from interfacial energy is of secondary importance [48].

Fig. 14.5a shows a SEM image of a fully lamellar microstructure in a Ti-46at%Al-4at%(Cr, Nb, Ta, B) alloy after exposure to 800 °C for 3500 h. The bright particles at colony boundaries and within the colonies represent a Cr-rich B2 phase, which has been formed during the dissolution process of the original α_2-lamellae [40, 49]. The elongated particles are (Ti, Ta)-borides, which have aligned themselves in the rolling direction during deformation [49]. The bright-field TEM image shown in Fig. 14.5b reveals that thinning and dissolution of the α_2-lamellae took place during long-term exposure. In addition, in high-resolution TEM investigations, the formation of C14-type Laves phase particles at lamellar interfaces was observed. Again, the formation of these particles is connected with the dissolution process of the α_2-lamellae, which requires a redistribution of the alloying elements [23].

More detailed information concerning microstructural changes in lamellar microstructures, as well as a description of the underlying mechanisms, can be found in Refs. [23, 31, 26, 47, 49]. However, from the observations reported here, it is evident that there is an upper temperature limit for the use of lamellar microstructures since these structural changes are accompanied by significant changes in mechanical properties [34, 46, 47]. In addition, it is assumed that these microstructural changes will be accelerated under creep conditions. Therefore, future research efforts must be aimed at the development of γ(TiAl)-based alloys that allow the adjustment of microstructures exhibiting a higher thermodynamic stability.
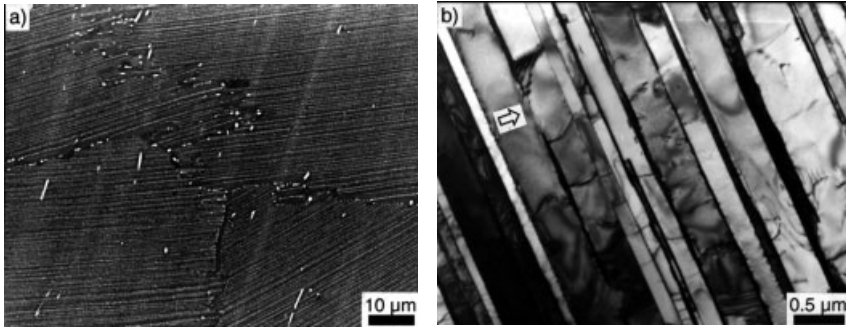
Fig. 14.5 Microstructural changes in a fully lamellar Ti-46.5at%Al-4at%(Cr, Nb, Ta, B) alloy during long-term exposure at 800 °C for 3500 hours: (a) SEM micrograph showing B2 particles (bright contrast) at colony boundaries and within α_2(Ti$_3$Al) lamellae; (b) bright-field TEM image obtained from a lamellar colony. Arrow: partly dissolved α_2 lamellae.

However, it is uncertain if this target can be achieved with conventional γ(TiAl) alloys, as described in section 14.2. Presently, heat treatments in the range of 800 °C to 900 °C are employed in order to stabilize fully lamellar microstructures [2, 16, 31]. The intention of such heat treatments is to produce microstructures that are closer to thermodynamic equilibrium. However, further studies must prove whether these stabilized microstructures can guarantee the required long-term stability. Another way to overcome these problems is to develop γ(TiAl) alloys with high-temperature properties that do not rely on lamellar microstructures. In this context, high Nb-containing and/or precipitation-strengthened γ(TiAl) alloys are of particular interest.

14.4
Processing of γ(TiAl)-Based Alloys

In many aspects the industrial-scale processing routes established for γ(TiAl)-based alloys are similar to those employed for Ni-based and conventional Ti alloys. The processing routes used today are summarized in Fig. 14.6. In the following sections, ingot and powder processing, forging of large ingots, single-step and multi-step extrusion as well as processing of sheets by hot rolling are described.

14.4.1
Ingot Production

As a consequence of the progress in processing γ(TiAl)-based alloys to semi-finished products, the availability of industrial-scale ingots with a defined homogeneous element distribution is required. In the following, the processing of large ingots by means of Vacuum Arc Remelting (VAR), as employed by GfE – Metalle und Materialien GmbH (Germany), is described [50]. In general, the processing
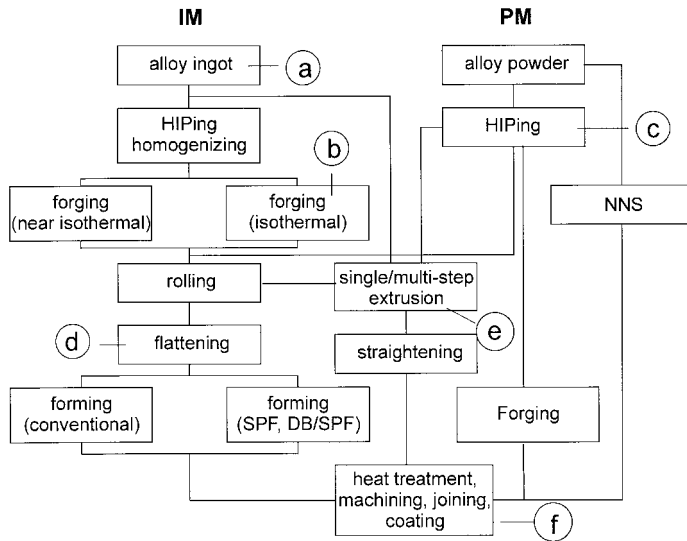
Fig. 14.6 Manufacturing and processing routes for γ(TiAl)-based alloys used at PLANSEE AG [36]. The circles contain the lettering of the corresponding microstructure shown in Fig. 14.11. IM: ingot metallurgy; PM: powder metallurgy; HIP: hot-isostatic pressing; DB: diffusion bonding; SPF: superplastic forming; NNS: near-net shape.

route for γ(TiAl) ingots shown in Fig. 14.7 is equivalent to the processing of Ti alloys, which is used for the production of rotating parts in the aerospace industry.

First, small electrodes are pressed from a mixture of alloy components. The composition of the electrodes is chosen to compensate for the known evaporation loss of Al and specific alloying elements during the VAR process. A final electrode is assembled by welding the single pressed electrodes. In the first VAR-step, the electrode is melted in a water-cooled crucible to a primary ingot. In the second VAR-step, the primary ingot is remelted in order to improve the chemical homogeneity of the entire ingot. Fig. 14.11a shows a representative microstructure of a Ti-47at%Al-4at%(Cr, Nb, Mo, B) ingot. The cast microstructure consists of colonies comprised of γ and α_2 lamellae. Due to the large differences in melting points and densities of the constituting elements and the occurring peritectic solidification reactions (see Fig. 14.3), segregation effects resulting in, for example, macroscopic fluctuations of the Al content by more than ± 2 atomic percent are often obtained. Additionally, the lamellar microstructure obtained from the casting process shows chemical inhomogeneities even on a microscopic scale from one lamellae to the next within a single lamellar grain [51]. However, such deviations make subsequent thermomechanical processing steps, e.g. forging and extrusion, difficult to control and lead to semi-finished products showing an inhomogeneous microstructure, which is reflected in a strong variation of the mechanical properties.
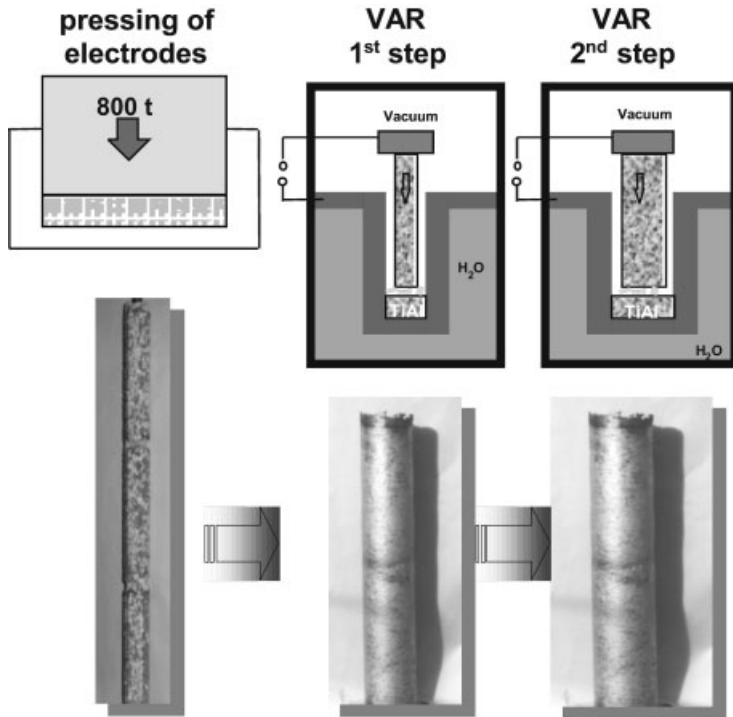
Fig. 14.7 Processing of γ(TiAl) ingots on an industrial scale by means of vacuum arc remelting by GfE – Metalle und Materialien GmbH (Germany) [50]. A representative microstructure of a double vacuum arc melted ingot is shown in Fig. 14.11 a.

Chemical inhomogeneities on microscopic scale can be improved through heat treatments in the α phase field [2, 4, 52]. A promising way to improve the macroscopic element distribution within the γ(TiAl) ingot is to add the alloying elements via masteralloys, a procedure well known in the Ti industry. In this context, GfE has developed particular masteralloys suitable for the processing of γ(TiAl)-based alloys. These multi-component masteralloys, e.g. CrBAl, CrAlSi and NbAlTiC, are produced by an aluminothermic reaction and exhibit good homogeneity and low impurity levels of undesired interstitial elements, such as oxygen and nitrogen. Industrial-scale TiAl ingots (diameter 300 mm, length 1500 mm) of various compositions have been manufactured by using optimized masteralloys. The ingots exhibit satisfactory microstructural homogeneity and alloying element distribution as well as impurity concentrations well below 700 wt. ppm. For a Ti-46.5at%Al-4at%(Cr, Nb, Ta, B) ingot, which was analyzed for Al distribution, it was demonstrated that the Al deviation is about ±0.7 atomic percent [50]. Fig. 14.8 shows the variation of the Al content along the middle axis of an 800 mm long, double-melted TiAl ingot with a nominal Al composition of 46.5 at%.

Fig. 14.8 Aluminum concentration along the middle axis of an 800 mm long TiAl ingot (double VAR remelted; nominal Al content: 46.5 at%).
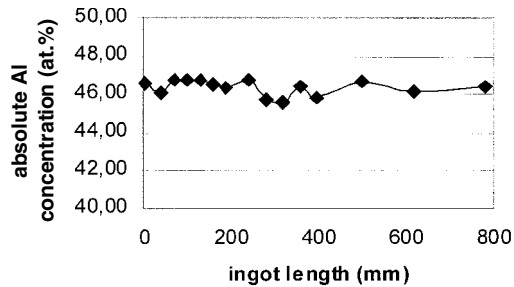
Nevertheless, in the case of Ti-46.5at%Al-4at%(Cr, Nb, Ta, B) ingots, it was occasionally found that refractory alloying elements (e.g. Ta) are not fully dissolved in the matrix during the VAR process, thus leading to unwanted high-melting inclusions. Although significant world-wide progress in γ(TiAl) ingot processing on an industrial-scale has been achieved over the last few years, additional research and development activities are required in order to ensure ingot processing and quality control are on a level already established for commercial aerospace materials. With respect to cost, the processing of γ(TiAl) ingots must be optimized in order to prevent cost-intensive HIPing and/or homogenization heat treatments, which have been frequently applied in the evaluation phase to ensure a defined ingot quality on the macroscopic and microscopic scale. A particular challenge will be large-scale production of the promising "next-generation" γ(TiAl)-based alloys, which have a high Nb content, high carbon levels, or a combination of both (see also: Chapter 4).

14.4.2
Powder Processing and Compaction

Recent developments in clean powder production methods [53, 54] and improved consolidation techniques have increased the interest in powder metallurgical (PM) materials. In this context, the PM route offers an attractive alternative for the production of feedstock for sheet rolling because γ(TiAl)-based alloy powder can be hot isostatically pressed (HIP) to a billet that can be rolled to sheet without prior homogenizing heat treatments and forging [4, 5, 36, 54]. Due to near-net shape HIPing, the yield from the PM route is much higher than from ingot metallurgy (IM), where a significant part of the forged ingot cannot be processed. Furthermore, the PM route enables production of large γ(TiAl)-based alloy sheets because HIPing of material is possible in almost any dimension. However, it was shown recently that through the use of extruded feedstock, the yield of the IM is significantly increased.

Prealloyed γ(TiAl) powders can be produced in large quantities by means of high-pressure Ar gas atomization, which yields fine, almost segregation-free powders [53, 54]. For example, Fig. 14.9 shows the basic set-up of the Plasma Melting Inert Gas Atomization (PIGA) facility, as employed at the GKSS Research Center (Germany) [53].
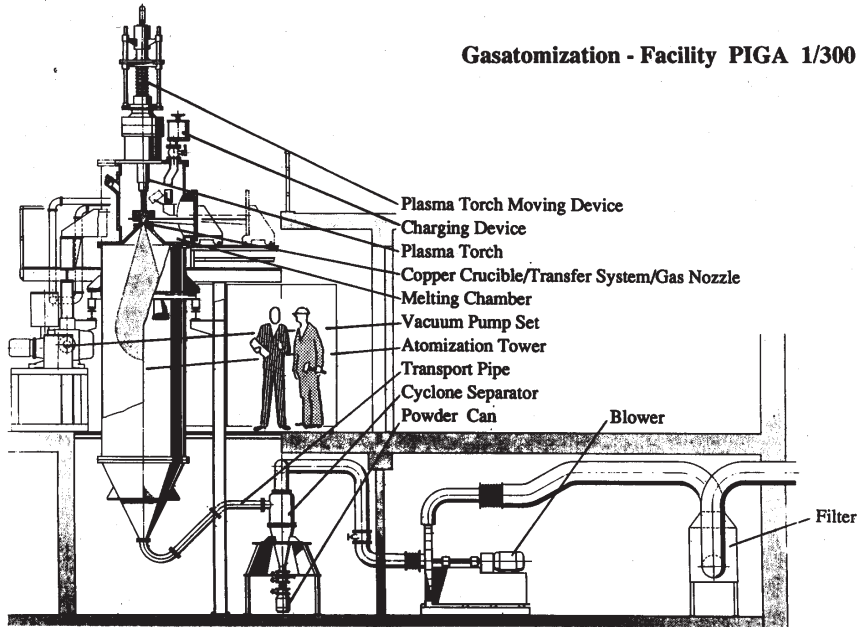
Fig. 14.9 Schematic drawing of the PIGA facility used at GKSS Research Center.

By means of a plasma torch, the elemental constituents are melted in a water-cooled copper crucible using skull melting. At the bottom of the crucible, a novel transfer system consisting of an induction-heated, water-cooled copper funnel forms a melt stream and guides it into the gas nozzle, which can be operated either with helium or argon. The complete facility consists of a melting chamber, an atomization tower, the transport pipe, a cyclone separator, the powder can, the blower, and an exhaust pipe. A detailed technical description of the PIGA concept as well as processing parameters, cooling rates, and results of powder analyses are given in Ref [53]. The powders are generally spherical with few satellites, as shown in Fig. 14.10 a.

Spherical powders with no or few satellites are desirable because they show the best flow behavior and highest packing densities. The powders exhibit a cellular microstructure with cell sizes of few micrometers (Fig. 14.10 b). This solidification structure indicates a high degree of undercooling [54]. Detailed information on the distribution of the constituting elements in gas-atomized γ(TiAl) powders can be found in Refs. [54, 55]. After atomization the powders are subsequently sieved in order to obtain a desired particle size distribution. As a result of their spherical shape, smooth surface and high hardness, γ(TiAl) powders cannot be compacted by cold pressing. Normally, the powders are filled in a Ti can, evacuated at elevated temperature, sealed and then HIPed under proper conditions in order to obtain complete densification [36, 54]. Fig. 14.11 c shows a typical microstructure of PM Ti-46.5at%Al-4at%(Cr, Nb, Ta, B) after HIPing in the $\alpha + \gamma$ phase field. The
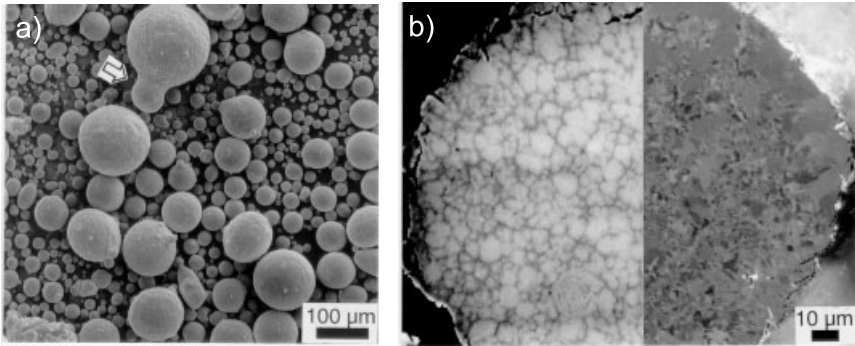
Fig. 14.10 (a) Ti-46.5at%Al-4at%(Cr,Nb,Ta,B) powder produced by inert gas atomization on an industrial scale [54]. Occasionally satellites appear (arrow); (b) section through a powder particle (light micrograph/SEM image taken in back-scattered electron mode).

microstructure is fine-grained and shows an improved homogeneity in terms of grain size, phase distribution and distribution of alloying elements when compared to that of a forged ingot (Fig. 14.11 b).

Nevertheless, microstructural defects sometimes still exist. These defects, e.g. coarse lamellar particles with a diameter up to 150 μm, originate from local chemical fluctuations in the melt [55]. In addition, the appearance of ceramic inclusions has been reported [56]. The negative impact of such microstructural irregularities and inclusions on mechanical properties of γ(TiAl) material in as-HIPed condition is treated in Refs. [36, 56]. During thermomechanical processing, e.g. hot-rolling, these microstructural defects can be eliminated and no degrading effect on the mechanical properties (e.g. tensile ductility at room temperature) has been found [36]. Another effect directly related to the atomization process is the appearance of microporosity [4, 5, 36]. Metallographic examinations conducted on γ(TiAl) powders, heat-treated and HIPed materials as well as hot-rolled sheets have revealed that the mechanism by which these micropores are formed is related to thermally induced porosity due to gaseous argon, which is entrapped in powder particles. These hollow, argon-filled powder particles are formed during the atomization process ("umbrella" effect). In contrast to argon that is adsorbed on the powder surface, the entrapped argon cannot be removed by the degassing process mentioned above prior to HIPing [57]. Recently, a quantitative investigation on the argon content in gas-atomized powders was reported in [57]. Although the fraction of hollow particles in the atomized powders is rather low, their presence is reflected in a finite Thermally Induced Porosity (TIP). For sheet material it has been shown that these micropores are too small to have an influence on short-term tensile properties [36, 43]. Recently, room temperature high-cycle fatigue tests at low and high frequencies have been conducted on PM γ(TiAl) sheets. As in the case of static tensile tests, no influence of the micropores on fatigue properties was found [43]. The negative impact of these micropores on tensile elongation at elevated temperatures and superplastic properties will be discussed in a following section.
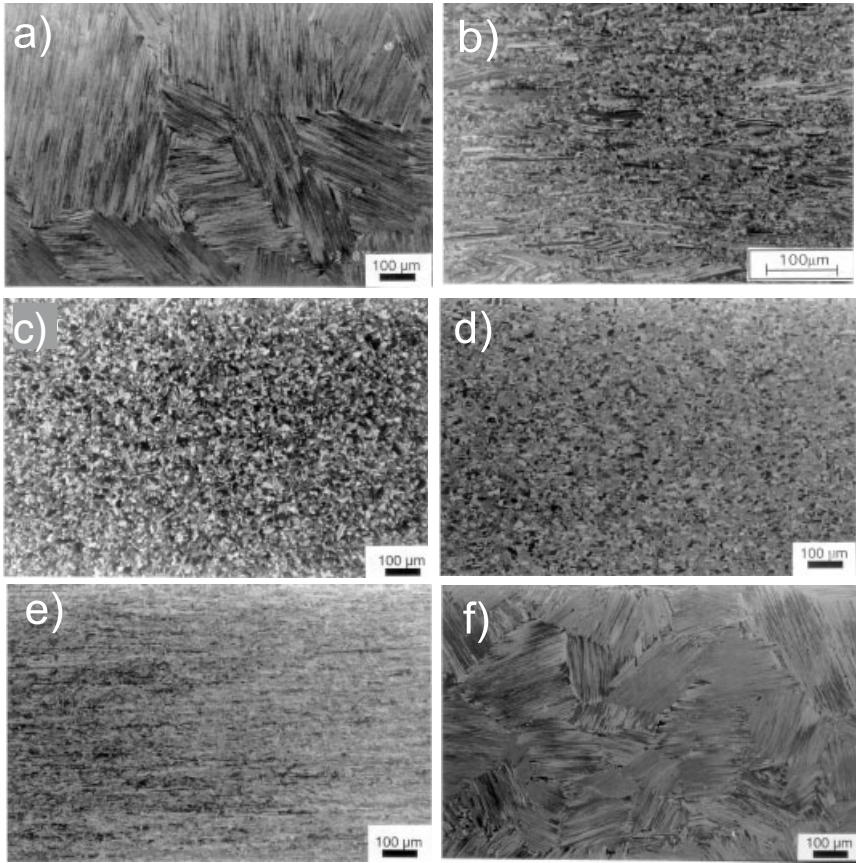
Fig. 14.11 Microstructure of engineering γ(TiAl)-based alloys (light micrographs): (a) Ti-47at%Al-4at%(Cr, Nb, Mo, B) ingot produced by vacuum arc remelting; (b) isothermally forged Ti-47at%Al-3.5at% (Cr, Mn, Nb, Si, B) ingot. Forging was conducted within the α₂+γ phase field (forging direction is vertical); (c) HIPed Ti-46.5at%Al-4at%(Cr, Nb, Ta, B) prealloyed powder; (d) Ti-46.5at%Al-4at%(Cr, Nb, Ta, B) sheet rolled in the α+γ phase field and subsequently flattened by annealing at 1000 °C for 2 hours under load. The microstructure obtained is referred to as primary annealed (rolling direction is horizontal); (e) hot-extruded Ti-46.5at%Al-4at%(Cr, Nb, Ta, B) ingot. The extrusion process was conducted in the middle of the α+γ phase field (extrusion ratio: approximately 14:1); (f) designed fully lamellar microstructure in Ti-46.5at%Al-4at%(Cr, Nb, Ta, B) sheet material. The designed fully lamellar microstructure was adjusted by short-term annealing in the α-phase field followed by controlled cooling through the α+γ phase field.

14.4.3
Thermomechanical Processing

Hot-working of γ(TiAl) alloys is conducted exclusively above their brittle-to-ductile transition temperature (BDTT), i.e. at temperatures $\gg 700\,°C$, and might be distinguished in primary and secondary hot-working steps. The aim of the primary hot-working step of cast ingots is to convert (or break down) the coarse-grained microstructure into a fine-grained and uniform microstructure suitable for subsequent wrought-processing or heat-treatments [11]. This is usually accomplished employing hot-working parameters at which dynamic recrystallization is prevalent, and macroscopic as well as microstructural damage is negligible, i.e. at temperatures between T_e and T_α (see Fig. 14.3) and relatively low deformation rates ($< 1\ s^{-1}$). A fine-grained, homogeneous microstructure is probably the most important precondition for successful secondary hot-working steps because it provides improved workability due to reduced flow stresses and increased fracture resistance [17].

Because hot-working temperatures are usually selected with reference to a specific phase transformation, e.g. $\alpha + \gamma \rightarrow \alpha$ for γ(TiAl)-based alloys, the area for engineering γ(TiAl)-based alloys as well as the temperature regions for thermomechanical processing and subsequent heat-treatments are indicated in Fig. 14.3 within the $\alpha + \gamma$ phase field, e.g. hot-rolling. Whereas, annealing in the α phase field is used to produce Designed Fully Lamellar (DFL) microstructures that show balanced mechanical properties. Therefore, the α-transus temperature (T_α), which strongly depends on the alloy composition, is of particular importance in order to define processing temperatures. The phase diagram shown in Fig. 14.3 gives only an estimate of the α-transus temperature of two-phase γ(TiAl) alloys because almost every alloying element tends to alter the shape of the phase fields and consequently the α-transus temperature. It is therefore a requirement that the α-transus temperature of the specific γ(TiAl) alloy under consideration must be determined before proper processing can be conducted.

In the past few years a considerable variety of different conventional engineering γ(TiAl) alloys, including the promising high Nb-containing TNB alloys, have been successfully processed according to the routes shown in Fig. 14.6.

For the practical application of hot-working of γ(TiAl) based alloys, e.g. extrusion or forging of small to medium sized parts, it is necessary to meet a relatively narrow processing window in terms of strain-rate, strain and temperature. Especially when hot-working small parts, the requirements in temperature and strain-rate control are more demanding when compared to large-scale wrought processing. These demands predominantly arise because γ(TiAl) alloys in general exhibit a strong dependence of flow stress on strain-rate and temperature. This is particularly important for components with thin sections, such as turbine blades, where heat loss due to radiation during transfer operations, and chilling from heat conduction into the tools during non-isothermal or near-isothermal forming operations is unavoidable and, thus, can lead to unstable flow behavior and damage.

14.4.4
Forging

Little is found in the open literature concerning practical forging of γ(TiAl)-based alloys. Most of the published work was carried out on ingot breakdown routes and the kinetics associated with microstructural refinement and chemical homogenization of the cast microstructure. However, activity in practical hot-forging of γ(TiAl) increased substantially during the nineties and concentrated on components for gas turbine engines [10, 58–60] and high-performance automotive valves [30, 61]. As is clear from the last chapter, conventional forging is not appropriate for γ(TiAl)-based alloys due to rather cold tools and high strain rates; therefore, most of the components have been forged isothermally.

14.4.4.1 **Forging of Large Ingots**

In the early nineties, forging of γ(TiAl) ingots under non-isothermal conditions was developed within the framework of a German Materials Research (Matfo) project. The target was to provide feedstock for sheet rolling, which was developed simultaneously [4, 62]. Ingots with diameters of 190 mm and weights up to 150 kg have been produced by Rotating Electrode (Rotel) vacuum melting and skull casting. Prior to forging, the ingots were hot isostatically pressed to close casting porosity and then homogenized in the α phase region to minimize microsegregation, which appears as a consequence of the peritectic solidification reactions. Ingots of about 500 mm length were appropriately canned in order to avoid excessive heat loss during deformation on a hydraulic press. Single-step forging was conducted in the $\alpha + \gamma$ temperature range at the slowest strain rate that could be achieved ($\approx$ approximately $1\,s^{-1}$). Pancakes with final diameters up to 570 mm have been forged. The microstructure obtained by non-isothermal forging is fine-grained. However, striped zones of coarse γ(TiAl) grains and isolated lamellar areas have been detected [4, 62]. It has been shown that distinct microstructural inhomogeneities (e.g. striped zones of coarse γ(TiAl) grains) cannot be completely eliminated by the subsequent rolling process [62, 63]. The homogeneity of the sheet microstructure, however, is extremely important with respect to the mechanical properties; in particular to the ductility below the brittle-to-ductile transition temperature [64].

The microstructural quality can be improved significantly by forging under isothermal conditions at low strain rates. Especially in the USA, many development programs have been aimed at producing high-quality pancakes utilizing isothermal forging techniques [65]. In Germany, researchers of the GKSS have established isothermal forging of large ingots on an industrial scale. For example, γ(TiAl) ingots with dimensions of 270 mm diameter and 250 mm length have been single-step forged in the $\alpha_2 + \gamma$ phase field to pancakes with diameters up to 600 mm [11]. A typical microstructure of an isothermally forged Ti-47at%Al-3.5at%(Cr, Mn, Nb, Si, B) ingot is shown in Fig. 14.11 b. The material shows a recrystallized, fine-grained microstructure with a small amount of remaining lamel-

lar grains. Because of its superior quality, at present only isothermally forged γ(TiAl) ingots are used as feedstock for sheet rolling.

14.4.4.2 Forging of Components

An example of the successful combination of different secondary hot-forming processes is the work of [61], where non-isothermal multi-step extrusion, hot bulging, and isothermal near-net-shape forging were employed to manufacture γ(TiAl) valves. The individual processing steps are depicted schematically in Fig. 14.12. These valves were produced entirely using industrial production equipment. The valves had homogeneous, fine-grained microstructures and have been successfully tested in engines. However, as in primary wrought processing, microstructural refinement during secondary hot-working operations is one of the key concepts to improving processing reliability and optimizing mechanical properties.

Isothermal closed-die forging of high-pressure compressor blades was reported by Appel and co-workers [60]. The use of extruded γ(TiAl) bar with a refined microstructure as starting material reduced the susceptibility to cracking during hot-working. More than 200 blades were forged in this study using the optimum processing parameters obtained from laboratory compression tests.

Closed impression die forging of γ(TiAl)-based alloys has been evaluated for the manufacture of complex shaped demonstration components, including subscale disks and turbine blades [66]. A refined, uniform billet material for the component forging operation was obtained through ingot conversion by isothermal forging. From this billet with a near-gamma microstructure, preforms with two different starting geometries were produced by machining for subsequent blade forging. The closed die forging operation was accomplished in a single step with isothermal forging temperatures between 1165 °C and 1205 °C. The results of the forging trails were prototype blade components with excellent die impression fill. The forging flash was removed by means of abrasive cutting. The forged blade had a very good surface finish and good dimensional control. The typical airfoil leading/trailing edge was ≈ 1.6 mm, whereas the root sections had a thickness of ≈ 11 mm. The length of the airfoil was ≈ 70 mm. The flash that developed around the closed die component was typically 0.8 mm thick. For further process details, alloy, microstructure of the forged part as well as additional post-forging heat-treatments the reader is referred to [66].

Tetsui *et al.* have also reported the manufacture of a TiAl blade [67]. Here, a Ti-42at%Al-5at%Mn alloy was heated to the vicinity of 1300 °C in the $\beta+\alpha$ region and then forged during cooling in a conventional facility. Then the blade (Fig. 14.13) was machined from the forged square using conventional milling and a chip-free technique.

Insight into the microstructural processes and the corresponding flow behavior during forging of γ(TiAl)-based alloys has been reported by Millet et al. [59] and Brooks et al. [58], who studied isothermal forging of gas turbine engine airfoils. In this work, a flow stress model was incorporated into a finite element code, allowing specification of the forging process itself, the microstructural evolution, and the flow-softening behavior of γ(TiAl) during hot working.

1 Ingot Metallurgy
Argon Arc Melting Technique

2 Hot extrusion

3 Hot Bulging

4 Quasi-isothermal Die Forging
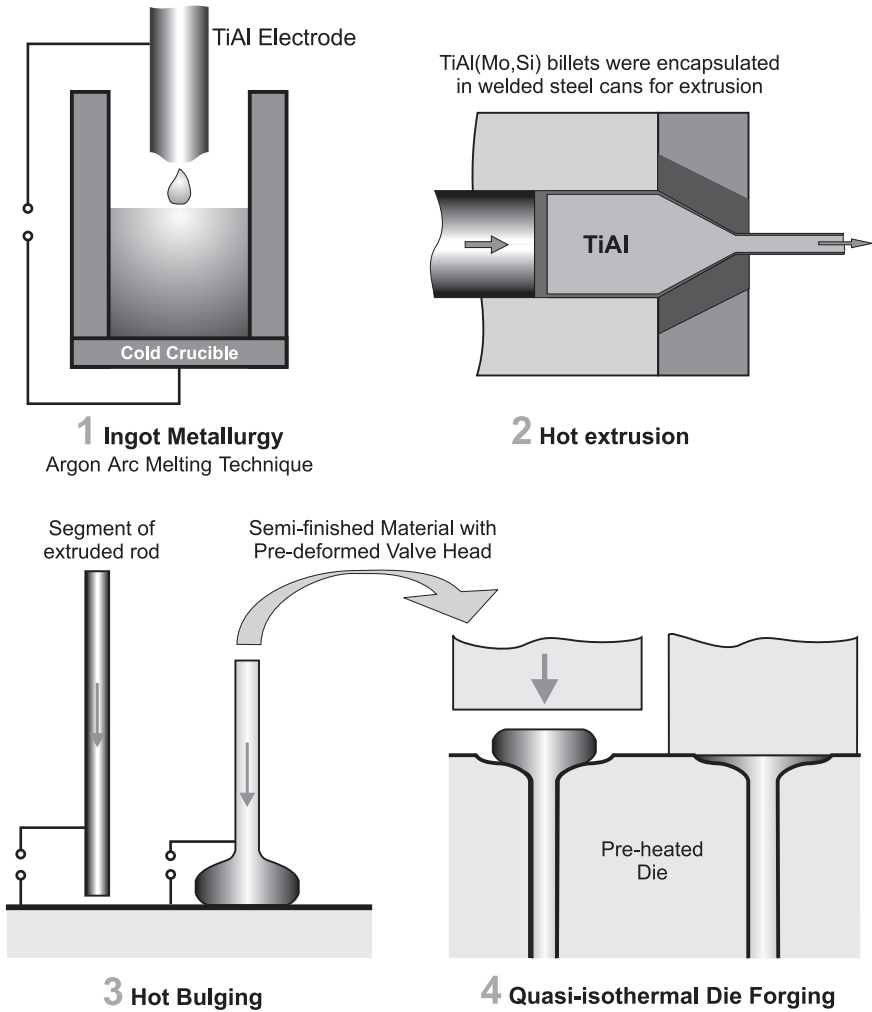
Fig. 14.12 Basic steps of the fabrication process for TiAl(Mo,Si) automotive valves based on ingot metallurgy and thermomechanical processing-hot extrusion, hot bulging and quasi-isothermal die forging [61].

14.4.5
Single and Multi-Step Extrusion

Extruded γ(TiAl)-based alloys have a high potential to be used for the production of various automotive parts (e.g. exhaust valves, connecting rods, piston pins etc.) and blades for gas turbine engines. For example, it has been demonstrated that near-net shape valve blanks can be produced by hot bulging extruded rod segments followed by subsequent quasi-isothermal die-forging of the valve head (see
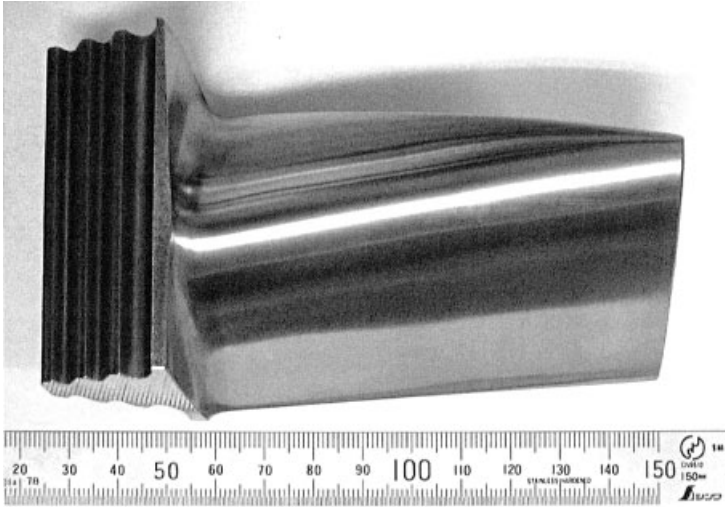
Fig. 14.13 TiAl blade machined from forged square bar [67]. Reproduced by permission of Elsevier Science Ltd.

section 14.4.4.2). The first successful processing of large γ(TiAl) alloy ingots on an industrial hot-extrusion press was reported by US researchers [68]. In Austria and Germany, hot-extrusion of γ(TiAl)-based alloys on laboratory as well as industrial scale has been established within the framework of several research programs that were initiated after industry had identified their need of rod material for the production of components as stated above.

Fig. 14.14 schematically summarizes the sequence for a double-step extrusion process as used at PLANSEE AG [36]. Usually mild steel is used as canning material. A diffusion barrier between can and ingot prevents the formation of low melting phases. A typical dimension of the extrusion billet is 250 mm (diameter) × 500 mm (length). In the first step, the canned material is extruded to an outer diameter of about 60 mm (length: ≈ 5 m). In order to obtain fine-grained material, extrusion is conducted in the center of the α + γ phase field. Fig. 14.11 e shows the microstructure of a Ti-46.5at%Al-4at%(Cr, Nb, Ta, B) ingot after the first extrusion step. The microstructure of the cast starting material consisted predominantly of lamellar colonies with a size of several hundred micrometers. After extrusion, an equiaxed and obviously fully recrystallized microstructure is obtained, which, however, shows banded regions of small and coarser γ(TiAl) grains. Such banded microstructures are frequently observed after hot-working of γ(TiAl) ingots, and their origin is attributed to the segregation of Al during peritectic solidification [64, 69, 70].

After the first extrusion step, the material is treated as shown in Fig. 14.14. The billet is extruded at the same temperature to a diameter in the range of 15–20 mm, which corresponds to a total extrusion ratio in the range of approximately 100–250. During the second extrusion step, a further refinement of grain size takes
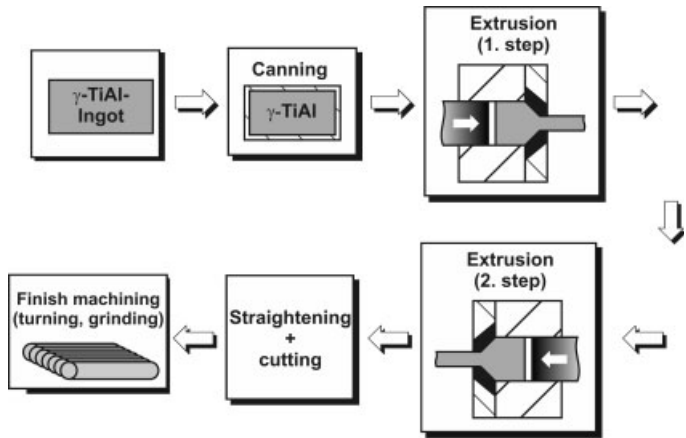
Fig. 14.14 Two-step extrusion of γ(TiAl)-based alloys. A representative microstructure of a Ti-46.5at%Al-4at% (Cr,Nb,Ta,B) alloy after the first extrusion step is shown in Fig. 14.11 e.

place along with an increase in microstructural homogeneity. Banded regions, however, are still present but their volume fraction decreases significantly with increasing extrusion ratio [36, 62, 71]. After a hot-straightening operation, the rods are cut to length and the can material is removed by turning. Further processing of the rods to valves includes upsetting of the valve heads (see Fig. 14.12). For this process, rod material with high straightness is required. The straightening process developed for γ(TiAl) provides rod material with lengths in the range of 200–500 mm and exhibiting a straightness comparable to that specified for valve-steel rods. Extrusion above the α-transus temperature offers the possibility of adjusting fine-grained, fully lamellar microstructures. These microstructures show a fine lamellar spacing, which leads to enhanced creep strength [72, 73]. Several γ(TiAl) alloys were successfully single-step extruded within the α-phase field using an industrial extrusion press. Mechanical properties of γ(TiAl) rod material extruded below and above the α-transus temperature are summarized in the following references: [2, 5, 36, 61, 72–75]. PLANSEE AG and GKSS have both developed the extrusion of rectangular shapes. Typical dimensions are 120×30×4000 mm. This product form is then used as starting material for further processing of components.

14.4.6
Rolling of Sheet and Foil

Especially in Japan and the USA, several R&D programs were initiated in the late eighties focusing on rolling techniques, such as isothermal rolling in the former [76, 77], and conventional hot-pack rolling in the latter [17, 78]. The fundamental research carried out by Semiatin and co-workers [17, 78–81] established a sound understanding of the interaction of process variables and the evolution of micro-

structures as well as an insight into failure mechanisms during hot-pack rolling. In Europe, driven by the Hermes and Sänger programs, γ(TiAl) sheet rolling activities were intensified in the early nineties with the aim of establishing a process feasible for industrial equipment and capable of providing scale-up potential. In the course of these activities, Clemens and co-workers developed the "Advanced Sheet Rolling Process" (ASRP), which allows processing of large γ(TiAl) sheets on a conventional hot-rolling mill [82, 83].

In general, the requirements for rolling γ(TiAl)-based alloys are mainly linked to an accurate choice of the processing variables, which have to be adapted to the specific properties of the rolling stock (the alloy and its thermomechanical history), as well as to the rolling equipment used. In the layout of rolling schedules, besides control of strain rates and strain per rolling pass, the main issue was shown to be temperature control [17, 80, 83].

Precise temperature control within an extremely narrow window is, firstly, important to optimize flow characteristics of the γ(TiAl) alloy and to avoid microstructural damage such as wedge cracks and cavitation, but, secondly, is important in achieving optimum microstructural uniformity. Temperature control is needed not only for the rolling temperature itself but also for preheat temperatures [17]. Temperature transients during rolling arise from workpiece chilling due to contact of workpiece and rollers during transfer operations [80]; and pronounced temperature gradients along the rolling direction of the workpiece evolve due to finite processing times (low rolling speed) [80, 82]. Considering this, isothermal rolling of γ(TiAl) sheet [76, 77] seems to be the process of choice. However, scale-up considerations, cost issues, and a lack of available large, industrial-scale isothermal rolling equipment are making conventional hot pack-rolling techniques, as developed in Europe and the USA, more attractive. Again, the most challenging task with hot pack-rolling is temperature control. Therefore, techniques have been successfully developed to provide accurate heat control throughout the rolling process by canning the workpiece [80, 82].

In order to ensure the homogeneity and quality of the sheets, it is important that the as-rolled γ/α_2 phase distribution, which very sensitively depends on the rolling temperature, should be uniform over the whole sheet area. Fig. 14.15 shows the γ/α_2 phase distribution at different positions of a 1 m long Ti-48Al-2Cr sheet rolled at a temperature in the middle of the $\alpha+\gamma$ phase field [84]. Note that there is no significant change in phase distribution between the ends.

From this finding it is evident that even when employing conventional rolling equipment, it is feasible to minimize temperature gradients and, therefore, to provide quasi-isothermal rolling conditions. This is further confirmed by the absence of any edge cracks over the entire sheet length. In addition, Fig. 14.15 shows the γ/α_2 phase distribution of a 700 mm long Ti-48Al-2Cr sheet that was rolled under non-optimized rolling conditions. It is obvious that during rolling under non-isothermal conditions substantial heat loss takes place, which in turn limits the maximum sheet length.

Employing the ASRP process, successful scale up of sheet dimensions as well as excellent microstructural homogeneity and mechanical properties were
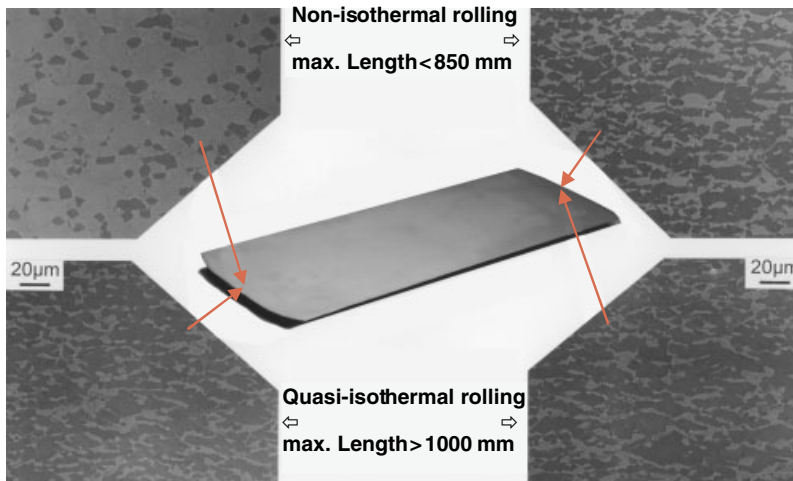
Fig. 14.15 γ/α_2 phase distribution within Ti-48Al-2Cr sheet after processing under quasi-isothermal rolling conditions (lower half) and non-isothermal rolling conditions (upper half). Note: the α_2 appears brighter than the γ(TiAl) phase. (SEM micrographs taken in back-scattered electron mode)

achieved [36]. Currently, γ(TiAl) alloy sheets in dimensions of about $800 \times 400 \times 1.0$ mm can be routinely produced. The dimensions of the largest γ(TiAl) sheets that have been rolled so far are approximately $2000 \times 500 \times 1.0$ mm. Further scale up of sheet dimensions seems to be feasible as far as the rolling process is concerned. However, factors that limit both sheet dimensions and microstructural homogeneity may depend on the particular feedstock used, as is generally true for other forming processes. The availability of rolling feedstock in adequate dimensions and also homogeneous in chemical composition is mandatory for the scale up of sheet dimensions. Although wrought-processed γ(TiAl) feedstock is available in the form of forged pancakes or extruded bar material (see sect. 14.4.5) the use of these materials is considered to be relatively costly because of the expense of ingot breakdown and the low yield, especially when rectangular rolling slabs are prepared from circular forged pancakes.

An important factor limiting sheet quality is improper, or at least not homogeneous, starting microstructure. The importance of close control of the Al content must not be underestimated, and can easily be figured out when the rolling temperature relative to the α-transus temperature (and thus the width of a potential processing window) of a specific γ(TiAl) alloy is considered. As stated above, the processing temperature relative to T_α and its interaction with other process variables govern the formability and the resulting microstructure of rolled γ(TiAl) sheet. Translating the Al content variation into a relative temperature shift, fluctuations of 1 at% in Al content would lead to an uncertainty in T_α of about 25 °C (as can be estimated from the binary Ti-Al phase diagram, Fig. 14.3) and therefore cannot be tolerated. Even these small Al fluctuations (which normally occur in

larger ingots) would lead to a scatter in the mechanical properties from sheet to sheet and also to varying, and thus unpredictable, sheet forming behavior. In this context, there is a certain advantage of the powder-metallurgy (PM) route over the ingot metallurgy route (IM). However, recent achievements in ingot production have shown that a close control of the Al content and other alloying elements is both possible and reproducible [36].

The texture of γ(TiAl) sheets in the as-rolled condition and after subsequent heat-treatment has been investigated thoroughly [45, 71, 85]. For example, sheet material rolled at a temperature within the $\alpha + \gamma$ phase field and subsequently annealed at 1000 °C for 2 hours shows the following texture components: $\{110\}\langle 21\bar{1}\rangle$ brass, $\{112\}\langle 11\bar{1}\rangle$ copper $\{123\}\langle 63\bar{4}\rangle$-S and $\{010\}\langle 100\rangle$-cube. A special feature of the cube component is that the c-axis of the γ(TiAl) lattice is aligned in the sheet plane perpendicular to the rolling direction. The influence of texture on tensile and creep properties in rolling and transverse direction are reported in references [45, 86, 87].

For advanced thermal protection systems and honeycomb structures, thin sheets and foils with a thickness of ~50 µm are required [9]. Currently, thin foils with a thickness down to 150 µm have been rolled [88]. For processing of γ(TiAl)-based alloy foils to industrially relevant dimensions, however, the requirements for rolling are more challenging than for sheet processing. A critical point is the surface quality that is developed during the rolling process. In the case of foil processing, surface quality must be good enough that any final treatments become unnecessary. However, before industrial production of γ(TiAl)-based alloy foils can be considered, additional research and development is required. All processing parameters must be defined and accompanying quality-control regulations established with well-defined test standards for foils. Because of the problem in achieving fully lamellar microstructures with colony sizes well below 50 µm, it is anticipated that thin sheets and foils will have to be used in the fine-grained condition. Thus, the choice of a suitable alloy is a prerequisite in order to achieve sufficient mechanical properties, e.g. creep strength.

14.4.7
Superplastic Forming

Superplastic forming (SPF) can be used for the manufacture of complex shaped parts. Especially in aerospace industry, SPF is widely used for processing Ti-based alloys. The superplastic behavior of sheet material processed via the ingot (IM) and powder (PM) metallurgy routes (Fig. 14.6) was investigated intensively over the last several years [36, 43, 63, 71, 88–90]. Microstructural investigations of specimens that have been tested under different conditions have revealed that conventional γ(TiAl)-based alloys do not obey the classic theory of superplasticity [71]. Grain boundary sliding accommodated by diffusion controlled dislocation motion is the essential deformation mode, but the grain size dependence of superplastic properties holds only for the beginning of deformation. After an incubation strain, a steady-state grain size is produced that is related to the deformation conditions. It has been shown that for SPF the steady-state grain size can be related to the

deformation strain rate and the temperature through the Zener-Hollomon parameter [63, 71, 89]. Thus, if the initial grain size is smaller than at steady-state, dynamic coarsening is observed, whereas grain refinement due to dynamic recrystallization takes place if the initial grain size is larger than at steady-state. For example, Fig. 14.16 shows the peak flow stress and the strain rate sensitivity exponent (m)

a)

b)
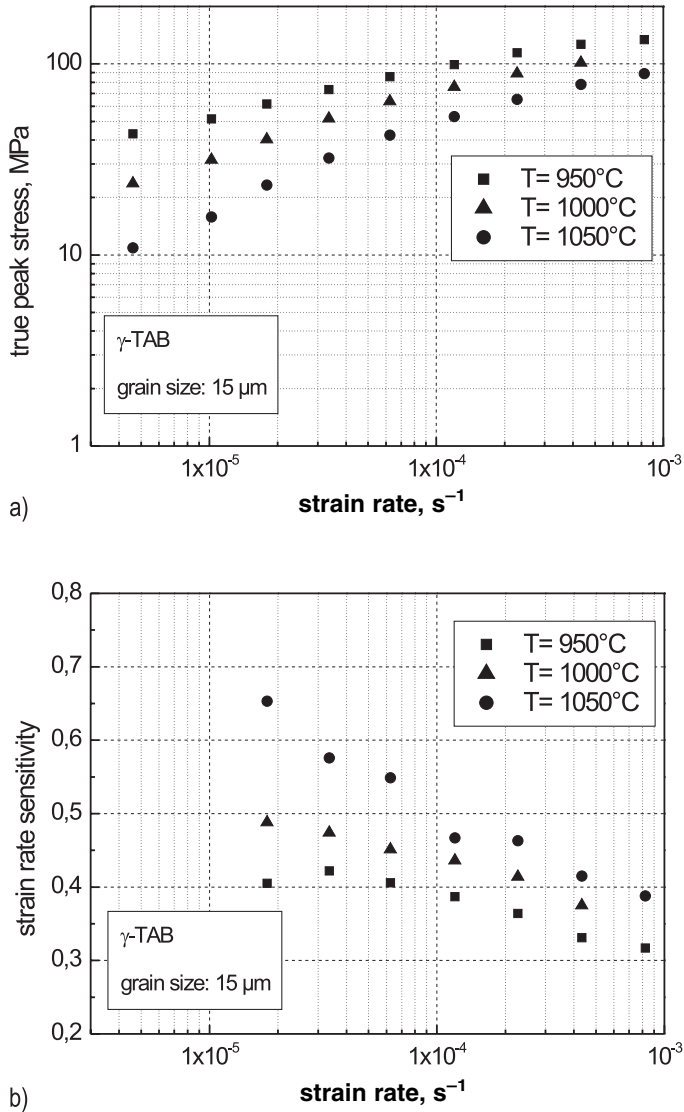
Fig. 14.16 (a) Variation of peak-stress and (b) strain-rate sensitivity exponent m with strain rate and temperature for a γ(TiAl) sheet material with a fine-grained, equiaxed microstructure.

as a function of strain rate and temperature for a primary annealed IM γ(TiAl) sheet, as determined from strain rate step tests under tensile conditions.

It should be noted that a similar behavior was found for PM sheet material [36]. From Fig. 14.16 it is evident that the sheet material exhibits a good potential for SPF even at temperatures below 1100 °C. This is important because SPF facilities that are in use for Ti alloys can also be used for SPF of γ(TiAl)-based alloys. From the Woodford correlation between m and tensile ductility, ductility values considerably higher than 200% might be expected for γ(TiAl) alloys that show m-values between 0.4–0.7 [91]. However, at 1000 °C maximum elongations only up to 180% have been measured in the case of IM Ti-47Al-2Cr-0.2Si sheet material, whereas in the case of PM sheets, elongations less than 100% were observed [36]. This difference in fracture elongation between PM and IM sheets was also found in high-temperature tensile tests. The reason for the low ductility lies in the development of moderate-to-extensive cavitation, and thus fracture-controlled failure takes place [36, 92]. Metallographic studies have revealed that grain boundary separation takes place in the early stages of deformation, which leads to the formation of massive isolated cavities during further deformation. In the case of PM sheet material, cavitation starts at relatively low strains [36]. Failure is then caused by subsequent growth of these cavities. At present, no complete explanation for the degraded SPF behavior of PM sheet material can be given. However, it can be assumed that also in case of superplastic deformation the presence of thermally induced microporosity (see section 14.4.2) eases grain boundary separation and consequently enhances the nucleation rate for microvoids.

It should be noted that a distinct superplastic behavior has been reported for hot-isostatically pressed and forged γ(TiAl) alloy powder [93]. Due to isothermal forging at a relatively low temperature of 850 °C, the resulting near-gamma microstructure is extremely fine with an average grain size of 0.9 μm. The forged material exhibits excellent superplastic properties at temperatures as low as 900 °C to 1100 °C, and quite high deformation rates in the range of 10^{-4} s^{-1} to 10^{-3} s^{-1}. At 1000 °C with a nominal strain-rate of 1.5×10^{-3} s^{-1}, a tensile elongation of 920% was achieved with a low level of cavitation, which might be attributed to improved accommodation processes due to the very fine grain size.

SPF experiments on a laboratory scale have been performed to show the formability of γ(TiAl)-based alloy sheet materials. For example, biaxial gas-forming tests have been conducted on IM sheet material and a maximum true strain of 600% was realized [63]. In addition, tests on industrial SPF facilities have demonstrated that shaping of complex geometries is feasible, as illustrated in Fig. 14.17 [4, 9].

Generally, the best results are obtained for γ(TiAl) alloys when SPF techniques used for other superplastic materials showing deformation enhanced cavitation are applied. For example, in utilizing driver sheet techniques or by applying a "back-pressure" during SPF, the onset of cavitation is shifted to higher elongations, a fact that is highly beneficial in the case of PM sheets. At present, the main challenge is to establish a large-scale production of optimized γ(TiAl) powders that exhibit an insignificant content of entrapped atomization gas and an non-critical content of non-metallic inclusions.
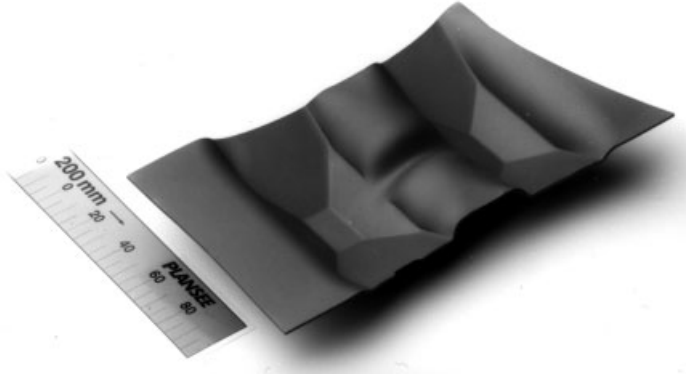
Fig. 14.17 Ti-47Al-2Cr-0.2Si part formed on an industrial SPF facility at 1000 °C.

14.5
Further Processing

For the future application of γ(TiAl)-based alloys, appropriate joining and machining methods must be made available. Despite increasing interest in the use of γ(TiAl) in aerospace and automotive industries, and the significant progress in alloy design, forming, casting, joining and machining issues have been investigated to a lesser extent. The following paragraphs aim to summarize the relevant features regarding joining and machining of γ(TiAl)-based alloys, and to give an outlook on the feasibility of industrialization of these techniques.

14.5.1
Joining

In the last few years, several studies have been performed to investigate the weldability of γ(TiAl) alloys with the aim of establishing reliable joining techniques. Generally, it is concluded that this material class exhibits limited weldability and precautions have to be taken to achieve sound joints.

Studies on fusion welding have focused on tungsten inert gas (TIG) welding [94–98], electron beam (EB) welding [8, 94, 99–102], and laser beam welding [103, 104]. The consistent result was that γ(TiAl) has a tendency to cold cracking. Due to the low ductility below the BDTT, the material may not be able to withstand the high thermal residual stresses arising from the welding operation. Moreover, fusion welding significantly changes the optimized microstructure of the base material in the region of weld and heat affected zone, resulting in a decrease of mechanical properties in the joints. However, sound joints can be demonstrated by a careful selection of the process parameters and a suitable post weld heat treatment. The optimized welding strategy includes preheating above the BDTT, and control of the cooling rate and temperature gradient. The thermal residual stresses can be minimized as they are accommodated in the higher temperature regime by plastic deformation.

Solid-state processes like friction welding and diffusion bonding have been proved to be successful in several applications [105–107], although there may be limitations regarding geometry of the components. Sound joints by application of friction welding have been achieved for components symmetric in rotation. Attention, however, has to be paid to the low ductility of γ(TiAl) at ambient temperatures by applying only a relatively low pressure force during the friction phase. Due to the high plastic deformation and temperature, microstructural changes within joints, e.g. change of the grain size, are often observed. A post weld heat treatment may be required to obtain the desired microstructure and joint properties.

Furthermore, friction welding is well suited to join dissimilar materials. In the case of γ(TiAl), joining with steels [108, 109], titanium alloys [105], and Ni-based [108] alloys has been investigated with relevance to applications in the automotive industry, as pointed out by a number of patents. Diffusion bonding experiments have shown that excellent joints with mechanical properties comparable to the base material can be realized. Typical process parameters, depending on the alloy composition and microstructure, are temperatures in the regime of 1000–1200 °C, bonding times of several hours and pressure values of 10 MPa–40 MPa [110–112]. If the degree of plastic deformation at the joining interface is sufficient, recrystallization can be initiated and grain growth across the joint line may occur. Despite high equipment costs and long processing times, this process is especially interesting in combination with superplastic forming techniques for the production of γ(TiAl) sheet-based lightweight structures. The feasibility of such a concept to produce a hollow jet engine turbine blade was investigated within a MATECH research project [43].

Brazing techniques have the advantage that the component is exposed to low thermal and mechanical stresses, while complex geometries and different materials can be joined. However, in the case of γ(TiAl), with its highly optimized alloy composition, the selection of a braze material is difficult to fulfill all the requirements regarding brazing temperature, wetting behavior, chemical, and mechanical properties of the joint. The use of high temperature braze alloys to join γ(TiAl) and heterogeneous material combinations was investigated and reviewed in [108]. Ni and Co-based braze alloys contain additions of B, C and Si as melt temperature depressants, which lead to the formation of undesired brittle precipitates in the joints. Precious braze alloys exhibit pore formation due to bad wetting behavior and strong erosion of the base material. Good results regarding mechanical properties and quality of the joint were obtained by using Ti-based braze foils [6, 74, 90, 108]. In the development of honeycomb structures for aerospace applications, an important issue beside mechanical properties is the oxidation resistance of the joints. For this purpose, innovative brazing techniques like transient liquid phase bonding are under evaluation [7].

14.5.2
Machining

γ(TiAl)-based alloys can be conventionally machined in as-cast as well as in the wrought condition as far as its limited ductility is considered. Machining of γ(TiAl) sheets and rods of different compositions and microstructures has been investigated thoroughly. All important machining methods were tested without major problems. A comprehensive compilation of conditions and systematic parameter evaluations for successful machining via turning, milling, grinding, electro-discharge machining (EDM), electrochemical milling (ECM) and water-jet machining is given in Refs. [113, 114]. For example, Fig. 14.18 shows a complex γ(TiAl) part that was machined at PLANSEE AG.

14.6
Requirements, Components, Tests and Applications

14.6.1
Gas Turbine Engines

It has been forecasted that for every 15 years of traffic growth, a doubling of transport capacity will be needed. This prediction underlines the importance of improving the environmental compatibility, economic performance, and the safety of transport systems. Advanced engine concepts that incorporate new lightweight materials show potential for improvement in these fields. Compared to metallic materials used in automotive and gas turbine industries today, titanium aluminides based on γ(TiAl) alloys have a lower density and a higher modulus of elasti-
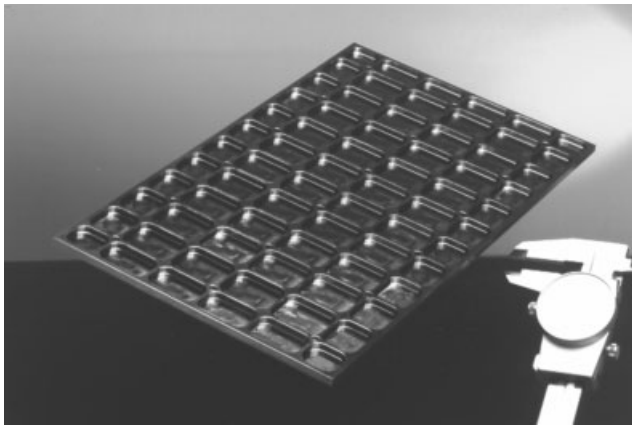
Fig. 14.18 Complex γ(TiAl) part machined at PLANSEE AG (dimensions: 270 mm×145 mm×4 mm) employing EDM, grinding and milling.

city. Additionally, γ(TiAl)-based alloys have a high specific strength and creep resistance. The maximum temperature for long-term operation without oxidation protection is as high as 750 °C and, therefore, titanium aluminides are able to close the gap between high-temperature titanium alloys and nickel-based superalloys [115].

Until the year 2010, the German Engine 3E (Environment, Efficiency, Economy) and the European Commission "Target Research Action on Efficient and Environmentally Friendly Aeroengines (EEAF)" aerospace research programs, are funding research on the development of high bypass geared turbo-fan engines, with a bypass ratio >10 that are equipped with a low emission combustion chamber. Significant potential for reducing specific fuel consumption is offered by turbines designed for energy recovery [115].

In this design, a heat exchanger cools the turbine gas and heats the air entering the combustion chamber from the compressor stages. In the medium term, high-bypass turbines with gearing between the fan and low-pressure turbine are being developed for the Airbus A320 family and the Boeing 737. This requires low-pressure turbines (LPTs) having increased revolutions, higher flow Mach numbers and increased entry temperature that are capable of operating at higher efficiency compared with conventional LPTs. As the potential for weight reduction is highest in the low-pressure turbine, γ(TiAl) will be introduced in the near future for the turbine's rear rotor blades. Analysis has shown that the future engine market requires up to one million γ(TiAl) low-pressure turbine blades per annum, replacing the state-of-the-art, heavy IN713 nickel alloy blades in the last stage of present and advanced turbines. For engine compressors, potential applications are the rotor blades as well as vanes in the high-pressure module in order to increase the overall thrust-to-weight ratio of the engine [115].

There are at least three major payoff areas for γ(TiAl)-based alloys in advanced jet engines [2, 8, 19, 116]: (a) γ(TiAl) has a specific stiffness 50% greater than structural materials commonly used in aircraft engines. Generally, stiffness is valuable wherever clearances are concerned, such as frames, seal supports, cases, and linings (e.g. consisting of honeycomb structures). The higher specific stiffness (E/ρ) also shifts acoustically excited vibrations towards higher frequencies, which is usually beneficial for structural components, e.g. turbine blades, disks, and parts within the exhaust nozzle area. (b) The good creep resistance of advanced γ(TiAl)-based alloys in the temperature regime of 600 °C to 700 °C, enables the substitution for Ni-based alloys (twice the density as γ(TiAl) alloys) in certain applications. (c) The high burn resistance of γ(TiAl)-based alloys (nearly as resistant as Ni-based alloys) can enable the substitution for heavy and expensive Ti-based alloy components designed to be fire-resistant. Design considerations and requirements on ductility for aircraft engines have been discussed in Refs. [8, 117–120]. An analysis for a component with complex geometry has suggested that ductility requirements are generally small [119], but more detailed analyses combined with component tests are required. The greatest issue in design of γ(TiAl)-based alloy components is damage tolerance. Low ductility and low fracture toughness along with high crack growth rates will increase the possibility of damage.

Therefore, extensive work is still needed to characterize and catalogue the likely range of damage and the resulting effects on life. For example, the suitability of γ(TiAl)-based alloys for blade application in the low-pressure turbine section is determined by the following requirements [117]:

- High cycle fatigue strength (10^7 cycles): ≥350 MPa at RT and 700 °C,
- Low cycle fatigue strength (10^4 cycles): ≥350 MPa at 700 °C,
- Time to 1% creep ≥1000 h at 150 MPa and 700 °C,
- Room temperature ductility: ≥1%,
- Sufficient oxidation and corrosion resistance at 700 °C,
- Domestic object damage (DOD) tolerance.

In 1992, MTU Aero Engines GmbH (Germany) successfully performed the first spin test of investment-cast γ(TiAl) blades in a rotor of a low-pressure turbine at 700 °C and 16 000 rpm [116]. In 1993, General Electric (USA) conducted their first engine test [8]. A full set of 98 low-pressure turbine blades were installed in a CF6-80C2, an engine used in large commercial transports. The engine test included over 1000 simulated flight cycles as part of a normal endurance test.

In advanced gas turbine engine concepts, rod and sheet materials are under consideration for fabrication of rotating and stationary compressor components, such as high-pressure compressor blades, nozzle components, such as flaps, nacelle structures, acoustic honeycombs, as well as substructures [2, 8, 9, 12, 115, 116, 121]. For example, γ(TiAl) sheet material to be used in the exhaust nozzle area must withstand hundreds of hours between 600 °C and 900 °C in a jet engine exhaust gas environment.

In the second half of the nineties, a German materials technology program (MaTech) was completed, the goal of which was to demonstrate the feasibility of hollow low-pressure turbine blades out of γ(TiAl) sheet material by using SPF and diffusion bonding technologies [43]. The selected γ(TiAl)-based alloy was developed by GKSS within the framework of a preceding German Matfo project [19].

Within the framework of another German materials research program, GKSS, Thyssen Umformtechnik and Rolls-Royce Deutschland developed the complete processing technology for the production of a high-pressure gas turbine engine compressor blade [60]. The processing route included hot-extrusion, closed-die forging and electro-chemical milling for final shaping. The alloy used in this study had the composition of Ti-47Al-3.7(Nb, Cr, Mn, Si)-0.5B at%. Compression-test flow curves of the extruded starting material were used to determine a suitable processing window for secondary hot-working, and to model the isothermal closed-die forging behavior. Using optimal forging conditions, more than 200 blades were successfully produced.

14.6.2
Aerospace

The requirements for high-temperature aerospace components are demanding. Several metallic alloy families are candidates for these components, but each family has its own temperature niche. These niches can be roughly defined as follows: 300 °C to 600 °C for titanium alloys; 500 °C to 1000 °C for superalloys and metal matrix composites; 900 °C to 1200 °C for oxide dispersion strengthened superalloys; and 1100 °C to 1600 °C for carbon/carbon and ceramic matrix composites [9]. γ(TiAl)-based alloys are targeted for the 600 °C to 900 °C range, as a material substitute for superalloys, and must survive hundreds of hours in this temperature range in space entry/re-entry environments. In addition, there are specific tensile, fatigue and creep requirements that have to be met. Furthermore, any material candidate must eventually be able to be economically manufactured into reliable high temperature components. γ(TiAl)-based alloys are of special interest as structural materials for advanced propulsion systems, hot structures, thermal protection systems (TPS), and, in the long-term, as matrix materials of intermetallic matrix composites. γ(TiAl) sheet is being considered as a material candidate in current major American aerospace programs which include: 1) the Reusable Launch Vehicle, representing a Single Stage-to-Orbit vehicle, which is planned to replace the Space Shuttle; 2) the NASA Future X Plane; 3) the Joint Strike Fighter; 4) the X-38 Crew Rescue Vehicle; 5) the Military Space Plane (a reusable launch vehicle type spacecraft); 6) the Space Maneuverable Vehicle; and 7) supersonic transport aircraft [9].

For example, in supersonic civil transport aircraft, advanced technologies are required to reduce exhaust and noise pollution in order to meet the stringent environmental goals established by different nations. A part of the strategy for noise attenuation is the use of an extremely large exhaust nozzle [6]. In the nozzle, several critical components are planned to be fabricated from γ(TiAl)-based alloys. The divergent flap, situated in the exhaust nozzle, uses wrought γ(TiAl), whereas the nozzle sidewall is a hybrid fabrication of both wrought γ(TiAl) face sheet and a cast γ(TiAl) substructure. Within the framework of the High Speed Civil Transport (HSCT) program, γ(TiAl) sheet material was down-selected over cast γ(TiAl) as the prime divergent flap material [6]. The divergent flap is a relatively large component (3.0×1.8 m) designed for small deflections. It is comprised of two superalloy box beams supporting a series of sub-elements made of γ(TiAl) sheet, as shown in Fig. 14.19.

The sub-elements were manufactured by BF Goodrich Aerostructures Group (USA) using Ti-46.5at%Al-4at%(Cr, Nb, Ta, B) sheets with a thickness of 0.635 mm. The structures shown in Fig. 14.19 were fabricated using production equipment at production fabrication rates [6, 90]. The forming and joining processes were developed at NASA Glenn Research Center and Pratt & Whitney. The corrugations were hot-formed at relatively low temperatures in an argon environment using standard tooling. The parts were assembled by brazing in vacuum employing a TiCuNi filler alloy [6, 90]. The overall dimensions of the part are approximately 65 mm (height)×145 mm (width)×610 mm (length). It is a trusscore type of geometry, typical for static structures in both propulsion and airframe components.
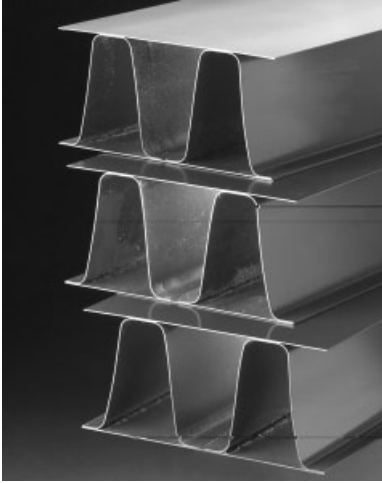
Fig. 14.19 Sheet TiAl sub-elements of the divergent flap concept for the HSCT with salient features of the full-scale flap [6, 122]. The parts are made from Ti-46.5at%Al-4at%(Cr, Nb, Ta, B) sheet and the overall dimensions are approximately 66 mm (height)×146 mm (width) ×610 mm (length). Sheet thickness: 0.025″ (0.635 mm). Courtesy of NASA Glenn Research Center.

The mechanical properties of the sub-element were characterized at room temperature in a three-point bend test using a uniform pressure instead of a point load. Detailed information concerning experimental set-up, test procedure as well as achieved test results are reported in Ref. [6]. However, this test revealed that γ(TiAl) sheet has a tremendous potential for future supersonic propulsion systems.

In the mid-nineties, within the framework of a German Hypersonic Technology Program, the feasibility of hot-structure γ(TiAl) components was investigated. At the end of 1995, a panel structure (Fig. 14.20) was fabricated from wrought
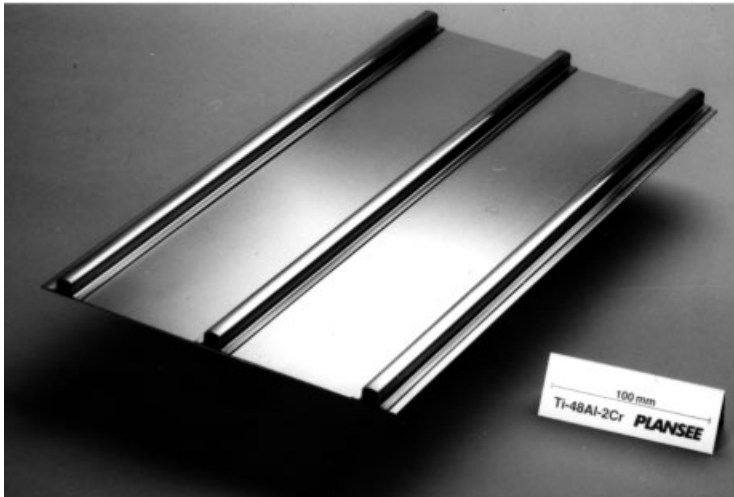
Fig. 14.20 Stiffened, lightweight γ(TiAl) sheet-based panel. Sheet and stringers were joined employing CO_2-laser welding [123].

γ(TiAl) sheet. The results of a structural stability test conducted on the γ(TiAl) panel shown are summarized in [123].

In the European Community, the development of γ(TiAl)-based alloy sheets for applications in hot-structure and TPS has been included in the framework of the Future European Space Transport Investigations Program (FESTIP) [124] and current follow-up programs.

14.6.3
Automotive Engines

The demand for reduced fuel consumption, emissions, and noise in cars and trucks is continuing to increase. New legislation concerning emissions from mid- to large-size Diesel engines will soon be enforced in the USA and Europe. On the basis of the upcoming 2005 EURO-IV emissions rules, automotive manufacturers are facing increasing requirements for:

- weight reduction,
- reduced noise and pollution,
- decreased fuel consumption,
- reduced production and maintenance costs,
- enhanced lifetime and reliability.

The European automotive industry is meeting this challenge by, for example, further downsizing of their conventional combustion engines. In addition, engine performance and efficiency will be enhanced by increasing combustion gas temperatures up to 1050 °C (gasoline) and 850 °C (Diesel), while gas pressures and engine rpm are rising. Consequently, the requirements for oscillating and rotating components operating at high temperatures are steadily increasing. Thus new lightweight, high-temperature materials and cost-effective production techniques must be developed and applied. The properties of TiAl exhibit a promising combination of low density and high temperature strength [125].

In 1999, the first commercial application of γ(TiAl)-based alloys was announced with their use for turbochargers in a Mitsubishi sports car (Lancer 6) [126]. The turbine wheels were produced by means of the LEVICAST process [127], a variation of the lost wax precision casting method.

Exhaust engine valves appear to be another ideal application for γ(TiAl)-based alloys. Generally, there are three major benefits that could be exploited by the use of lightweight engine valves: (a) higher fuel economy, (b) better performance and (c) reduced noise and vibration. For exhaust valve application in automotive engines, the requirements are as follows [117]:

- High cycle fatigue strength (10^7 cycles) of $\geq$250 MPa at 800 °C,
- thermo-shock resistance,
- oxidation resistance,
- wear resistance.

So far, casting and reactive sintering are the two mostly investigated processing methods [2, 127–129]. In Germany, a new manufacturing process based on cold induction melting and permanent mold centrifugal casting has been developed [61, 123, 130].

Recently, the start of a pilot plant was announced. The prototype furnace enables the production of 50 valves per melt and the production relevant cycle time of approximately 30 minutes. Assuming a three-shift operation, the productivity of the plant is approximately 600 000 valves per year. Based on experience with the production route of conventional valves (bimetal design), new machining parameters have been developed for the TiAl near-net shape blanks. Depending on the design of the TiAl valves, it is possible to save about ten machining steps in comparison to the bimetal valves [131].

However, wrought processing of γ(TiAl) valves from extruded rod material [61, 117, 132] might be a potential alternative. The first short-term engine tests conducted on γ(TiAl) valves have shown that protection against wear, especially at the top of the valve stem, is required. In this context, suitable coatings and coating techniques for wear protection have been developed and tested [117]. Good results have been obtained using brazes and hard surface layers produced by micro plasma welding.

Exhaust valves manufactured by near-net shape technology based on PM (see section 14.4.2) as well as by thermomechanical processing of extruded ingots (see section 14.4.4.2) were long-term engine tested in passenger cars powered by diesel (2200 cm^3) and Otto type engines (2300 cm^3) [117]. The geometry of the γ(TiAl) valves was identical to those of conventional steel valves. The valves endured more than 100 000 km without any failure. In order to study the effect of wear, the valves were inspected at certain intervals. After 140 000 km, an indication of slight material loss due to wear was found at the coated end of the stem. However, the observed wear is expected to be non-critical. The valve seat shows minor damage caused by indentation of hard carbon particles, however, no cracks were detected. The engine tests demonstrated the applicability of γ(TiAl) valves as well as the chosen wear protection layers.

In early 2002 PLANSEE AG started the commercial production of wrought processed high-performance γ(TiAl) valves. The processing route is a variant of the multi-step extrusion process described in section 14.4.5. Further processing steps include high-precision machining and coating (see Fig. 14.21).

14.7
Concluding Remarks

Intermetallic γ(TiAl)-based alloys are considered to be very important candidate materials for advanced applications in aerospace, automotive and related industries. Research and development on γ(TiAl) alloys have progressed significantly over the last 10 years. This research has led to a better understanding of the fundamental influence of alloy composition and microstructure on mechanical properties and processing behavior.

Fig. 14.21 γ(TiAl) high-performance car valves (PLANSEE AG).

Industry appears to be on the threshold of significant use of this new class of material. In particular, all major aircraft and automotive engine manufacturers are advancing the qualification and introduction of γ(TiAl) components. γ(TiAl)-based alloys can be processed using conventional metallurgical methods; a factor that is necessary for these materials to be economically competitive with other state-of-the-art materials. The processing of γ(TiAl) alloys via ingot and powder metallurgy routes on an industrial scale has been successfully demonstrated. Also, the feasibility of sheet forming by means of superplastic forming and other forming techniques has been successfully transferred from laboratory to industrial facilities.

However, for the widespread application of γ(TiAl) alloys it must be shown that semi-finished products and components with specified mechanical properties can be manufactured in large quantities at reasonable cost. From today's point of view, it is expected that cost issues will be minimized as soon as γ(TiAl)-based alloys are produced in industrially relevant quantities.

Further, for structural applications, appropriate joining and repairing methods must be available that guarantee processing of reliable joints exhibiting good mechanical properties, especially at temperatures below the brittle-to-ductile transition temperature. Engineering γ(TiAl)-based alloys should exhibit a more improved balance between room temperature ductility, fracture toughness, high-temperature strength, creep and oxidation resistance. Presently, the next-generation, high Nb-containing γ(TiAl)-based alloys are under development, aiming to provide these improved properties.

14.8

Referenced Literature and Further Reading

1 Y.-W. Kim, *JOM* **1989**, *41*, 24.

2 Y.-W. Kim, *JOM* **1994**, *46*, 30.

3 Y.-W. Kim, D. M. Dimiduk, *JOM* **1991**, *43*, 40.

4 H. Clemens, *Z. Metallkd.* **1995**, *86(12)*, 814.

5 H. Clemens, A. Lorich, N. Eberhardt, W. Glatz, W. Knabl, and H. Kestler, *Z. Metallkd.* **1999**, *90(8)*, 569.

6 P. A. Bartolotta, D. L. Krause, in *Gamma Titanium Aluminides* (eds. Y.-W. Kim, D. M. Dimiduk, and M. H. Loretto), TMS, Warrendale, PA, **1999**, p. 3.

7 R. Leholm and M. Martinez, in *Titanium 95 – Science and Technology* (eds. P. A. Blenkinsop, W. J. Evans, and H. M. Flower), The Institute of Metals, London, **1996**, p. 1617.

8 C. M. Austin, T. J. Kelly, K. G. McAllister, and J. C. Chesnutt, in *Structural Intermetallics* (eds. M. V. Nathal, R. Darolia, C. T. Liu, P. L. Martin, D. B. Miracle, R. Wagner, and M. Yamaguchi), TMS, Warrendale, PA, **1997**, p. 413.

9 R. Leholm, H. Clemens, and H. Kestler, in *Gamma Titanium Aluminides 1999* (eds. Y.-W. Kim, D. M. Dimiduk, and M. H. Loretto), TMS, Warrendale, PA, **1999**, p. 25.

10 T. Tetsui, H. Higuchi, and K. Takita, *Mitsubishi Heavy Industries, Ltd. Technical Review* **1997**, *34(1)*, 35.

11 F. Appel, H. Kestler, and H. Clemens, *Intermetallic Compounds: Principles and Practice – Progress*, Vol. 3, Chap. 29, Wiley VCH, **2002**, p. 617.

12 S. C. Huang and J. C. Chesnutt, in *Intermetallic Compounds – Principles and Practice* Vol. 2, Chap. 4 (eds. J. W. Westbrook and R. L. Fleischer), John Wiley and Sons Ltd., **1994**, p. 73.

13 S. C. Huang, in *Structural Intermetallics* (eds. R. Dariola, J. J. Lewandowsky, C. T. Liu, P. L. Martin, D. B. Miracle, and M. V. Nathal), TMS, Warrendale, PA, **1993**, p. 299.

14 S. C. Huang and D. S. Shih, in *Microstructure Property Relationships in Titanium Aluminides and Alloys* (eds. Y.-W. Kim and R. R. Boyer), TMS, Warrendale, PA, **1991**, p. 105.

15 D. Shechtman, M. J. Blackburn, and H. A. Lipsitt, *Metall. Trans.* **1974**, *5*, 1373.

16 F. Appel and R. Wagner, *Mater. Sci. Eng.* **1998**, *R22*, 187.

17 S. L. Semiatin and V. Seetharaman, *Metall. Trans.* **1995**, *26A*, 371.

18 D. M. Dimiduk and V. K. Vasudevan, in *Gamma Titanium Aluminides 1999* (eds. Y.-W. Kim, D. M. Dimiduk, and M. H. Loretto), TMS, Warrendale, PA, **1999**, p. 239.

19 R. Wagner, F. Appel, D. Dogan, P. J. Ennis, U. Lorenz, J. Müllauer, H. P. Nicolai, W. Quadakkers, L. Singheiser, W. Smarsly, W. Vaida, and K. Wurzwallner, in *Gamma Titanium Aluminides* (eds. Y.-W. Kim, R. Wagner, and M. Yamaguchi), TMS, Warrendale, PA, **1995**, p. 387.

20 S. C. Huang, in *Structural Intermetallics* (eds. R. Dariola, J. J. Lewandowski, C. T. Liu, P. L. Martin, D. B. Miracle, and M. V. Nathal), TMS, Warrendale, PA, **1993**, p. 299.

21 Z. Guo and W. Sha, *Intermetallics* **2002**, *10*, 945.

22 M. Beschliesser, H. Clemens, H. Kestler, and F. Jeglitsch, *to be published in Scripta Mat.* **2003**.

23 A. Chatterjee, G. Dehm, C. Scheu, and H. Clemens, *Z. Metallkd.* **2000**, *91(9)*, 755.

24 D. Hu, A. B. Godfrey, and M. H. Loretto, in *Gamma Titanium Aluminides 1999* (eds. Y.-W. Kim, D. M. Dimiduk, and M. H. Loretto), TMS, Warrendale, PA, **1999**, p. 409.

25 Y.-W. Kim, D. M. Dimiduk, and M. H. Loretto eds., *Gamma Titanium Aluminides 1999*, TMS, Warrendale, PA, **1999**.

26 Y.-W. Kim, H. Clemens, and A. Rosenberger eds., *Gamma Titanium Aluminides 2003*, TMS, Warrendale, PA, **2003**.

27 M. V. Nathal, R. Dariola, C. T. Liu, P. L. Martin, D. B. Miracle, R. Wagner, and M. Yamaguchi eds., *Structural Intermetallics 1997*, TMS, Warrendale, PA, **1997**.

28 K. J. Hemker, D. M. Dimiduk, H. Clemens, R. Dariola, H. Inui, J. M. Larsen, V. K. Sikka, M. Thomas, and J. D.

WHITTENBERGER eds., *Structural Interme-tallics 2001*, TMS, Warrendale, PA, **2002**.

29 E.L. HALL and S.C. HUANG, in *Micro-structure/Property Relationships in Tita-nium Aluminides and Alloys* (eds. Y.-W. KIM and R.R. BOYER), TMS, Warrendale, PA, **1991**, p. 47.

30 Y.-W. KIM, *JOM* **1994**, *7*, 30.

31 F. APPEL, U. LORENZ, J.D.H. PAUL, and M. OEHRING, in *Gamma Titanium Alu-minides* (eds. Y.-W. KIM, D.M. DIMIDUK, and M.H. LORETTO), TMS, Warrendale, PA, **1999**, p. 381.

32 G.L. CHEN, W.J. ZHANG, Z.C. LIU, S.J. LI, and Y.-W. KIM, in *Gamma Titanium Aluminides 1999* (eds. Y.-W. KIM, D.M. DIMIDUK and M.H. LORETTO), TMS, Warrendale, PA, **1999**, p. 371.

33 Y. MISHIN and CHR. HERZIG, *Acta Mater.* **2000**, *48*, 589.

34 F. APPEL, M. OEHRING, and P.J. ENNIS, in *Gamma Titanium Aluminides* (eds. Y.-W. KIM, D.M. DIMIDUK, and M.H. LO-RETTO), TMS, Warrendale, PA, **1999**, p. 603.

35 M.J. BLACKBURN, in *The Science, Technol-ogy and Application of Titanium Alloys* (eds. R.I. JAFFEE and N.E. PROMISEL), Plenum Press, New York, **1970**, p. 633.

36 H. CLEMENS, H. KESTLER, N. EBERHARDT, and W. KNABL, in *Gamma Titanium Alu-minides 1999* (eds. Y.-W. KIM, D.M. DIMI-DUK, and M.H. LORETTO), TMS, Warren-dale, PA, **1999**, p. 209.

37 S.A. JONES and M.J. KAUFMANN *Acta Mater.* **1993**, *41*, 387.

38 M. TAKEYAMA, T. KUMAGAI, M. NAKA-MURA and M. KIKUCHI, in *Structural In-termetallics* (eds. R. DARIOLA, J.J. LEWAN-DOWSKI, C.T. LIU, P.L. MARTIN, D.B. MIRACLE, and M.V. NATHAL), TMS, War-rendale, PA, **1993**, p. 167.

39 Y.-W. KIM, in *Gamma Titanium Alumi-nides* (eds. Y.-W. KIM, R. WAGNER, and M. YAMAGUCHI), TMS, Warrendale, PA, **1995**, p. 127.

40 A. CHATTERJEE, U. BOLAY, U. SATTLER, and H. CLEMENS, in *Intermetallics and Superalloys – EUROMAT 99*, Vol. 10 (eds. D.G. MORRIS, S. NAKA, and P. CARON), Wiley VCH, **2000**, p. 233.

41 U. BOLAY, *Master's thesis*, Universität Stuttgart, Germany, **1999**.

42 E. NES, N. RYUM, and O. HUNDERI, *Acta metall.* **1985**, *33*, 11.

43 H. KESTLER, H. CLEMENS, H. BAUR, R. JOOS, R. GERLING, G. CAM, A. BARTELS, C. SCHLEINZER, and W. SMARSLY, in *Gam-ma Titanium Aluminides 1999* (eds. Y.-W. KIM, D.M. DIMIDUK, and M.H. LORET-TO), TMS, Warrendale, PA, **1999**, p. 423.

44 A. CHATTERJEE, H. BAUR, F. APPEL, A. BARTELS, W. KNABL, H. KESTLER, and H. CLEMENS, in *Gamma Titanium Alumi-nides 1999* (eds. Y.-W. KIM, D.M. DIMI-DUK, and M.H. LORETTO), TMS, Warren-dale, PA, **1999**, p. 401.

45 A. BARTELS, H. KESTLER, and H. CLE-MENS, *Mater. Sci. Eng.* **2002**, *A329–331*, 153.

46 D. HU, A.B. GODFREY, and M.H. LORET-TO, *Intermetallics* **1998**, *6*, 414.

47 D. HU, A. GODFREY, P.A. BLENKINSOP, and M.H. LORETTO, *Metall. Trans.* **1998**, *29A*, 919.

48 M. BESCHLIESSER, *Thermische Stabilität and Mechanische Eigenschaften von Gamma-TiAl Basislegierungen*, PhD thesis, Monta-nuniversität Leoben, Austria, **2003**.

49 B.J. INKSON and H. CLEMENS, in *Mater. Res. Soc. Symp. Proc. Vol. 552* (eds. E.P. GEORGE, M.J. MILLS, and M. YAMAGU-CHI), MRS, Pittsburgh, PA, **1999**, KK3.12.1.

50 V. GÜTHER, A. OTTO, H. KESTLER, and H. CLEMENS, in *Gamma Titanium Alumi-nides 1999* (eds. Y.-W. KIM, D.M. DIMI-DUK, and M.H. LORETTO), TMS, Warren-dale, PA, **1999**, p. 225.

51 T. PFULLMANN and P.A. BEAVEN, *Scripta Metall.* **1993**, *28*, 275.

52 S.L. SEMIATIN, V. SEETHARAMAN, and I. WEISS, *Mater. Sci. Eng.* **1998**, *A243*, 1.

53 R. GERLING, F.P. SCHIMANSKY, and R. WAGNER, Institute for Materials Re-search, Geesthacht, **1992**, p. 215.

54 U. HABEL, C.F. YOLTON, and J.H. MOLL, in *Gamma Titanium Aluminides 1999* (eds. Y.-W. KIM, D.M. DIMIDUK, and M.H. LORETTO), TMS, Warrendale, PA, **1999**, p. 301.

55 P.I. GOUMA and M.H. LORETTO, in *Tita-nium '95 – Science and Technology* (eds. P.A. BLENKINSOP, W.J. EVANS, and H.M. FLOWER), The Institute of Metals, Lon-don, **1996**, p. 550.

56 N. Eberhardt, A. Lorich, R. Jörg, H. Kestler, W. Knabl, W. Köck, H. Baur, R. Joos, and H. Clemens, *Z. Metallkd.* **1998**, *89(11)*, 772.

57 G. Wegmann, R. Gerling, and F.-P. Schimansky, *to be published in Acta Mat.* **2003**.

58 J. W. Brooks, T. A. Dean, Z. M. Hu, and E. Wey, *Materials Processing Technology* **1998**, *80/81*, 149.

59 J. C. F. Millett, J. W. Brooks, and I. P. Jones, *Mater. Sci. Technology* **1999**, *15*, 697.

60 F. Appel, U. Brossman, and U. Christoph, *Adv. Eng. Mat.* **2000**, *2(11)*, 699.

61 S. Knippscheer and G. Frommeyer, *Adv. Eng. Mat.* **1999**, *1*, 187.

62 H. Clemens, P. Schretter, K. Wurzwallner, A. Bartels, and C. Koeppe, in *Structural Intermetallics* (eds. R. Dariola, J. J. Lewandowski, C. T. Liu, P. L. Martin, D. B. Miracle, and M. V. Nathal), TMS, Warrendale, PA, **1993**, p. 205.

63 H. Clemens, W. Glatz, N. Eberhardt, H.-P. Martinz, and W. Knabl, in *Mater. Res. Symp. Soc. Proc. Vol. 460* (eds. C. C. Koch, C. T. Liu, N. S. Stoloff, and A. Wanner), MRS, Pittsburgh, PA, **1997**, p. 29.

64 C. Koeppe, A. Bartels, J. Seeger, and H. Mecking, *Metall. Trans.* **1993**, *24A*, 1795.

65 S. L. Semiatin, in *Gamma Titanium Aluminides* (eds. Y.-W. Kim, R. Wagner, and M. Yamaguchi), TMS, Warrendale, PA, **1995**, p. 509.

66 D. U. Furrer, R. R. Hoffman, and Y.-W. Kim, in *Gamma Titanium Aluminides* (eds. Y.-W. Kim, R. Wagner, and M. Yamaguchi), TMS, Warrendale, PA, **1995**, p. 611.

67 T. Tetsui, K. Shindo, S. Kobayashi, and M. Takeyama, *Scripta Mat.* **2002**, *47*, 399.

68 P. L. Martin, D. A. Hardwick, D. R. Clemens, W. A. Konkel, and M. A. Stucke, in *Structural Intermetallics* (eds. M. V. Nathal, R. Dariola, C. T. Liu, P. L. Martin, D. B. Miracle, R. Wagner, and M. Yamaguchi), TMS, Warrendale, PA, **1997**, p. 387.

69 S. L. Semiatin, N. Frey, S. M. El-Soudani, and J. D. Bryant, *Metall. Trans.* **1992**, *23A*, 1719.

70 P. L. Martin, C. G. Rhodes, and P. A. McQuay, in *Structural Intermetallics* (eds. R. Dariola, J. J. Lewandowski, C. T. Liu,

P. L. Martin, D. B. Miracle, and M. V. Nathal), TMS, Warrendale, PA, **1993**, p. 177.

71 C. Koeppe, A. Bartels, H. Clemens, P. Schretter, and W. Glatz, *Mater. Sci. Eng.* **1995**, *A201/201*, 182.

72 C. T. Liu, P. J. Maziasz, D. R. Clemens, J. H. Schneibel, V. K. Sikka, T. G. Nieh, J. Wright, and L. R. Walker, in *Gamma Titanium Aluminides* (eds. Y.-W. Kim, R. Wagner, and M. Yamaguchi), TMS, Warrendale, PA, **1995**, p. 679.

73 P. J. Maziasz and C. T. Liu, *Metall. Trans.* **1998**, *29A*, 105.

74 H. Clemens, N. Eberhardt, W. Glatz, H.-P. Martinz, W. Knabl, and N. Reheis, in *Structural Intermetallics 1997* (eds. M. V. Nathal, R. Dariola, C. T. Liu, P. L. Martin, D. B. Miracle, R. Wagner, and M. Yamaguchi), TMS, Warrendale, PA, **1997**, p. 277.

75 M. Oehring, U. Lorenz, R. Niefanger, U. Christoph, F. Appel, R. Wagner, H. Clemens, and N. Eberhardt, in *Gamma Titanium Aluminides 1999* (eds. Y.-W. Kim, D. M. Dimiduk, and M. H. Loretto), TMS, Warrendale, PA, **1999**, p. 439.

76 N. Fujitsuna, Y. Miyamoto, and Y. Ashida, in *Structural Intermetallics* (eds. R. Dariola, J. J. Lewandowski, C. T. Liu, P. L. Martin, D. B. Miracle, and M. V. Nathal), TMS, Warrendale, PA, **1993**, p. 187.

77 A. Morita, N. Fujitsuna, and H. Shigeo, *Symp. Proc. Basic Technology for Future Industries High-performance* Materials for Severe Environment 4th meeting, **1993**, p. 215.

78 S. L. Semiatin and V. Seetharaman, *Metall. Trans.* **1994**, *25A*, 2539.

79 S. L. Semiatin, D. C. Vollmer, S. El-Soudani, and C. Su, *Scripta Metall. Mater.* **1990**, *24*, 1409.

80 S. L. Semiatin, M. Ohls, and W. R. Kerr, *Scripta Metall. Mater.* **1991**, *25*, 1851.

81 S. L. Semiatin, J. C. Soper, and R. Shivpuri, *Metall. Trans.* **1994**, *25A*, 1681.

82 H. Clemens, P. Schretter, W. Köck, and G. Kneringer, *Metall* **1993**, *46(6)*, 547.

83 H. Clemens, W. Glatz, P. Schretter, C. Koeppe, A. Bartels, R. Behr, and A. Wanner, in *Gamma Titanium Aluminides* (eds. Y.-W. Kim, R. Wagner, and M. Ya-

MAGUCHI), TMS, Warrendale, PA, **1995**, p. 717.

84 H. CLEMENS, W. GLATZ, N. EBERHARDT, H.-P. MARTINZ, and W. KNABL, in *Mat. Res. Soc. Symp. Proc. Vol. 460*, MRS, Pittsburgh, PA, **1997**, p. 29.

85 A. BARTELS, H. CLEMENS, H. HARTIG, and H. MECKING, in *Mater. Res. Soc. Symp. Prov. Vol. 460*, MRS, Pittsburgh, PA, **1997**, p. 141.

86 A. BARTELS, W. SCHILLINGER, A. CHATTERJEE, and H. CLEMENS, in *Mater. Res. Soc. Symp. Proc. Vol. 646*, MRS, Pittsburgh, PA, **2001**, N 1.5.1.

87 A. BARTELS, S. BYSTRZANOWSKY, R. GERLING, F.-P. SCHIMANSKY, H. KESTLER, M. WELLER, and H. CLEMENS, in *Mater. Res. Soc. Symp. Proc.*, MRS, Pittsburgh, PA, **2003**, B.B.3.3.1–B.B.3.3.6.

88 H. CLEMENS and H. KESTLER, *Adv. Eng. Mater.* **2000**, *2(9)*, 551.

89 H. CLEMENS, I. RUMBERG, P. SCHRETTER, and S. SCHWANTES, *Intermetallics* **1994**, *2*, 179.

90 G. DAS and H. CLEMENS, in *Gamma Titanium Aluminides 1999* (eds. Y.-W. KIM, D.M. DIMIDUK, and M.H. LORETTO), TMS, Warrendale, PA, **1999**, p. 281.

91 C.M. LOMBARD, A.K. GOSH, and S.L. SEMIATIN, in *Gamma Titanium Alloys* (eds. Y.-W. KIM, R. WAGNER, and M. YAMAGUCHI), TMS, Warrendale, PA, **1995**, p. 579.

92 H. CLEMENS, W. GLATZ, and P. SCHRETTER, *Prakt. Metallogr.* **1996**, *33*, 17.

93 G. WEGMANN, R. GERLING, F.-P. SCHIMANSKY, H. CLEMENS, and A. BARTELS, *Intermetallics* **2002**, *10*, 511.

94 P.L. THREADGILL and B.G. DANCE, *Technical Report 498*, The Welding Institute, London, **1994**.

95 V.L. ACOFF, A. PONNUSAMY, and D.J. BHARANI, in *Proc. 3rd Pacific Rim Int. Conf. Advanced Materials and Processings* (eds. M.A. IMAM, R. DENALE, S. HANADA, Z. ZHONG, and D.N. LEE), TMS, Warrendale, PA, **1998**, p. 2235.

96 D.J. BAHRANI and V.L. ACOFF, *Metall. Trans.* **1998**, *29A*, 927.

97 L.C. MALLORY, W.A. BAESLACK, and D. PHILLIPS, *Mater. Sci. Lett.* **1994**, *13*, 1061.

98 M. ARENAS and V.L. ACOFF, in *Proc. Mater. Sol. Conf. 99 on Joining of Advanced and Specialty Materials*, Cincinnatti, OH, **1999**, p. 184.

99 S.P. GODFREY, P.L. THREADGILL, and M. STRANGWOOD, in *Proc. of 4th European Conf. on Advanced Materials and Processing (EUROMAT 95)*, **1995**.

100 R.A. PATTERSON, P.L. MARTIN, B.K. DAMKROGER, and L. CHRISTODUOLOU, *Welding Research Supplement* **1990**, *1*, 39.

101 M.C. CHATURVEDI, N.L. RICHARDS, and Q. XU, *Mater. Sci. Eng.* **1997**, *A239/A240*, 605.

102 Q. XU, M.C. CHATURVEDI, and N.L. RICHARDS, *Metall. Trans.* **1999**, *30A*, 1717.

103 M. KLASSEN, E. SCHUBERT, and G. SEPOLD, in *Laser Treatment of Materials* (ed. F. DAUSINGER), Arbeitsgemeinschaft Wärmebehandlung und Werkstofftechnik, Stuttgart, Germany, **1996**, p. 193.

104 H. CRAMER, A. NENTWIG, and W. SMARSLY, *Schweissen und Schneiden* **1998**, *98*, 114.

105 W. SMARSLY, H. CRAMER, and A. NENTWIG, in *Werkstoffwoche 98* (ed. R. KOPP), Wiley VCH, **1998**, p. 295.

106 T. SHINODA, K. ITO, and C. HAYASHI, *Welding International* **1997**, *11(3)*, 200.

107 W.A. BAESLACK, T.F. BRODERICK, P.L. THREADGILL, and E.D. NICHOLAS, in *Titanium 95 – Science and Technology* (eds. P.A. BLENKINSOP, W.J. EVANS, and H.M. FLOWER), The Institute of Metals, London, **1995**, p. 424.

108 R. LISON, *Schweissen und Schneiden* **2000**, *52(2)*, 80.

109 H. HORN, in *Proc. of 13th Int. PLANSEE Seminar* (eds. H. BILDSTEIN and R. ECK), PLANSEE AG, Reutte, Austria, **1993**, p. 595.

110 Y. NAKAO, K. SHINOZAKI, and M. HAMADA, *ISIJ International* **1991**, *31*, 1260.

111 P. YAN and E.R. WALLACH, *Intermetallics* **1993**, *1*, 83.

112 S.P. GODFREY, P.L. THREADGILL, and M. STRANGWOOD, in *Mater. Res. Soc. Symp. Proc.*, Vol. 364 (eds. J.A. HORTON, I. BAKER, S. HANADA, R.D. NOEBE, and D.S. SCHWARTZ), MRS, Pittsburgh, PA, **1995**, p. 793.

113 E. AUST and H.R. NIEMANN, *Adv. Eng. Mat.* **1999**, *1(1)*, 53.

114 M. ECKSTEIN and W. SMARSLY, in *2nd Int. Conf. on Machining of Advanced Materials (MAM)*, VDI-Verlag, **1996**, p. 641.

115 W. Smarsly, H. Baur, G. Glitz, H. Clemens, T. Khan, and M. Thomas, in *Structural Intermetallics 2001* (eds. K. J. Hemker, D. M. Dimiduk, H. Clemens, R. Dariola, H. Inui, J. M. Larsen, V. K. Sikka, M. Thomas, and J. D. Whittenberger), TMS, Warrendale, PA, **2002**, p. 25.

116 W. Smarsly and L. Singheiser, in *Materials for Advanced Power Engineering, Part II* (eds. D. Coutsouradis, R. Wagner, and M. Yamaguchi), Kluwer Academic Publishers, Dordrecht, The Netherlands, **1994**, p. 1731.

117 H. Baur, R. Joos, W. Smarsly, and H. Clemens, in *Intermetallics and Superalloys EUROMAT 99*, Vol. 10 (eds. D. G. Morris, S. Naka, and P. Caron), Wiley VCH, Weinheim Germany, **2000**, p. 384.

118 J. C. Williams, in *Structural Intermetallics* (eds. R. Dariola, J. J. Lewandowski, C. T. Liu, P. L. Martin, D. B. Miracle, and M. V. Nathal), TMS, Warrendale, PA, **1993**, p. 839.

119 P. K. Wright, in *Structural Intermetallics* (eds. R. Dariola, J. J. Lewandowski, C. T. Liu, P. L. Martin, D. B. Miracle, and M. V. Nathal), TMS, Warrendale, PA, **1993**, p. 885.

120 D. Rugg, in *Gamma Titanium Aluminides 1999* (eds. Y.-W. Kim, D. M. Dimiduk, and M. H. Loretto), TMS, Warrendale, PA, **1999**, p. 11.

121 C. M. Austin and T. J. Kelly, in *Structural Intermetallics* (eds. R. Dariola, J. J. Lewandowski, C. T. Liu, P. L. Martin, D. B. Miracle, and M. V. Nathal), TMS, Warrendale, PA, **1993**, p. 143.

122 G. Das, P. A. Bartolotta, H. Kestler, and H. Clemens, in *Structural Intermetallics 2001* (eds. K. J. Hemker, D. M. Dimiduk, H. Clemens, R. Dariola, H. Inui, J. M. Larsen, V. K. Sikka, M. Thomas, and J. D. Whittenberger) TMS, Warrendale, PA, **2001**, p. 121.

123 H. Clemens, W. Glatz, P. Schretter, M. Klassen, E. Schubert, G. Sepold, T. Fleischer, H. W. Schrock, and R. Franke, in *Spacecraft Structures, Materials and Mechanical Testing*, European Space Agency, Noordwijk, The Netherlands, **1996**, p. 1297.

124 K. Krings, in *Spacecraft Structures, Materials and Mechanical Testing*, Vol. 3, SP-386, European Space Agency, Noordwijk, The Netherlands, **1996**, p. 1085.

125 H. Baur, D. B. Wortberg, and H. Clemens, in *to be publ. in Gamma Titanium Aluminides 2003*, TMS, Warrendale, PA, **2003**.

126 T. Tetsui, in *Gamma Titatnium Aluminides 1999* (eds. Y.-W. Kim, D. M. Dimiduk, and M. H. Loretto), TMS, Warrendale, PA, **1999**, p. 15.

127 T. Noda, *Intermetallics* **1998**, *6*, 709.

128 D. Eylon, M. M. Keller, and P. E. Jones, *Intermetallics* **1998**, *6*, 703.

129 M. Dahms and H. Clemens, in *Pulvermetallurgie in Wissenschaft und Praxis – Pulvertechnologische Wege in die Zukunft* (ed. H. Kolaska), DGM Informationsgesellschaft, Oberursel, Germany, **1995**, p. 113.

130 M. Blum, A. Choudhury, H. Scholz, G. Jarczyk, S. Pleier, P. Busse, G. Frommeyer, and S. Knippscher, in *Gamma Titanium Aluminides 1999* (eds. Y.-W. Kim, D. M. Dimiduk, and M. H. Loretto), TMS, Warrendale, PA, **1999**, p. 35.

131 M. Blum, in *Structural Intermetallics 2001*, TMS, Warrendale, PA, **2002**, p. 131.

132 S. Hurta, H. Clemens, G. Frommeyer, H.-P. Nicolai, and H. Sibum, in *Titanium 95 – Science and Technology* (eds. P. A. Blenkinsop, W. J. Evans, and H. M. Flower), The Institute of Metals, London, **1995**, p. 97.

15

Non-Aerospace Applications of Titanium and Titanium Alloys

M. Peters and C. Leyens, *DLR – German Aerospace Center, Cologne, Germany*

15.1
Introduction

Titanium and its alloys were specially developed for aerospace applications in the 1940s in the United States. Today the aerospace market accounts for about 50% of worldwide titanium consumption, and in the United States these figures have been as high as 70%. However the aerospace market, and in particular the military sector, is characterized by vigorous boom-to-bust demand and price cycles. Therefore, efforts have been made to substantially increase titanium consumption in less cyclic non-aerospace markets. Here the greatest obstacle has often proven to be the high cost of titanium components, which results from not only the price of the raw material, but also the higher secondary costs of semi-finished and final products.

Nowadays the exceptional properties, such as low weight at high strength and outstanding corrosion resistance, have paved the way for titanium and its alloys to enter applications in high-quality industrial and consumer products. Certainly, these are not yet mass-market products, but the trend to use titanium and its alloys outside the aerospace sector continues steadily. In particular, applications in the chemical industry, medical engineering, energy and transportation technology, as well as architecture, sports and leisure have played pioneering roles. In the following examples of such new applications outside aerospace will be given. For more detailed information the reader is referred to the subsequent special chapters in this book.

15.2
Chemical, Process and Power Generation Industries

Although titanium is a very reactive metal, it is extremely corrosion resistant. This is due to the high affinity of titanium to oxygen and moisture in the air. As a result, at room temperature a highly stable, tenacious and permanent thin oxide film (TiO_2) forms on the metal surface and immediately regenerates after being damaged. This property largely explains the popularity titanium has gained in the chemical, process and power generation industry where harsh environments are the order of the day. Usually titanium requires no corrosion allowance, so often

the higher up-front costs are compensated soon by less down time and reduced maintenance costs. In Japan, for example, about 30% of the titanium used is for chemical plants.

Titanium was first used in the chemical industry in the 1960s, initially and mainly for applications involving control of processes with oxidizing chloride environments. Today it is also used for other aggressive media including acetic and nitric acids, wet bromine, and acetone. Titanium is further very stable in formic, citric, tartaric, stearic, and tannic acids, and can be used for equipment to handle organic acids mixed with inorganic acids, organic solvents, and salts. Alkaline environments up to pH 12 and 75 °C usually offer no problem for titanium. However, in the presence of galvanic coupling to a more active material at temperatures above 75 °C and a pH of less than 3 or greater than 12, atomic hydrogen can be generated, and thus hydrogen embrittlement can be a problem. Furthermore, stress corrosion cracking can occur when titanium is exposed to methyl alcohol at water contents below 1.5%.

Usually, titanium is used in areas in which austenitic stainless steels no longer provide sufficient corrosion resistance. Therefore, titanium finds preferred application in equipment exposed to salt acidic solutions containing oxidants. In chemical process engineering, titanium is applied for containers, mixers, pumps, columns, heat exchangers, pipes, tanks, agitators, coolers, pressure reactors, etc.

Since particularly in chemical applications the main requirement is corrosion resistance, and to a lesser extent strength, unalloyed and low-alloy titanium grades are preferred. For increased corrosion resistance the Pd-containing Grade 7 or Ti-0.3Mo-0.8Ni (Grade 12) are recommended, particularly to avoid crevice corrosion. Alloys are mainly provided in the form of thin foils, sheet and plates (heat exchanger plates, linings, plating, etc.), as well as piping (heat exchangers, condensers, etc.).

15.2.1
Heat Exchangers and Condensers

The good thermal conductivity of titanium, which is roughly 50% higher than for stainless steel, makes it a preferred material in applications for heat exchangers in which the cooling medium is seawater, brackish water, and also polluted water. Here the commercially pure titanium grades have demonstrated their superior corrosion resistance for decades. Both tubular and more compact plate-type heat exchangers (Fig. 15.1) are routinely applied in land based oil refineries and on offshore oilrigs. Moreover, experience has shown that even water speeds of 10 m s^{-1} do not cause any erosion corrosion, cavitation, or impingement attack in the tubes. Therefore, particularly thin-walled condenser tubing can often be used with zero corrosion allowance. Worldwide millions of meters of welded and seamless titanium tubing in steam turbine power plants, refineries, chemical plants, air conditioning systems, multi-stage flash distillation, desalination and vapor compression plants, offshore platforms, surface ships and submarines, as well as for swimming pool heat pumps have documented titanium's life span and dependability compared

a)

b)
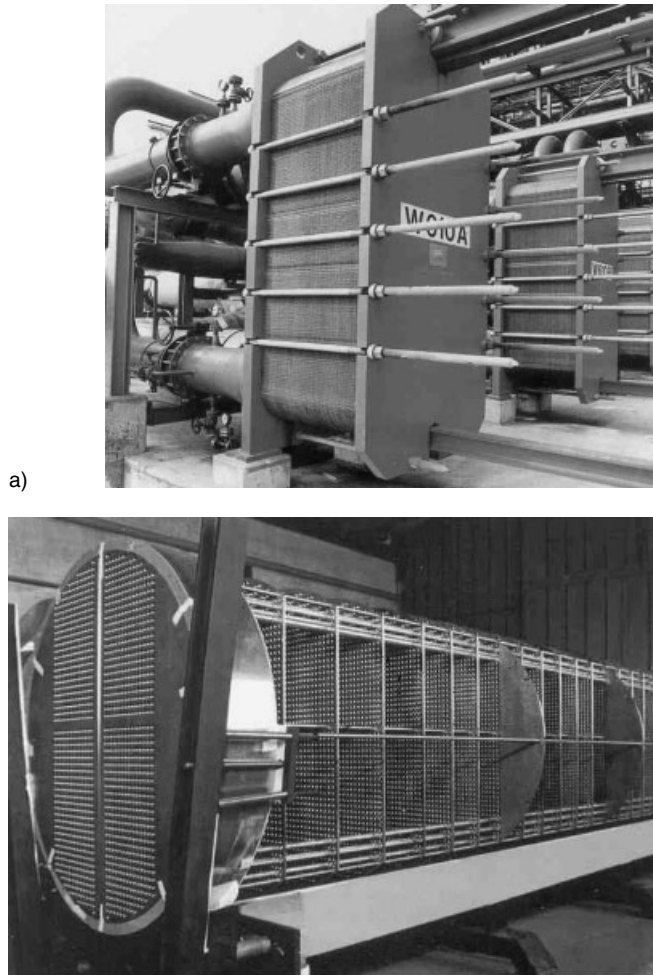
Fig. 15.1 a) Plate and b) tube heat exchangers manufactured from titanium (DTG, Essen, Germany).

to previously used copper-nickel alloys and stainless steel. In Japan, for example, condenser tubes consume about 20% of the domestic titanium use.

15.2.2
Containers and Apparatus Manufacturing

The high corrosion resistance, particularly in water, makes titanium an ideal material for the chemical, electrochemical, and petrochemical industries. Since titanium is mainly applied for containment and tank construction, commercially pure titanium is utilized with Grade 2.

For manufacturing of containers and apparatus from titanium, one distinguishes full wall structures, loose linings, and plated construction styles. Full wall structures are produced economically to wall thicknesses of about 15 mm. This is mainly due to the limited thermal stressing of the titanium. Above 250 °C, the strength strongly decreases and the material starts to creep. Therefore, for pressure vessels made from c.p. titanium, such operating temperatures can not be recommended for pressures of more than 20 bars. Moreover, with an increasing wall thickness, welding of titanium becomes problematic since stress corrosion cracking can occur in the welds.

Thin-walled linings of titanium are restricted to pressureless containers or internally pressurized components with inside heating or cooling. Titanium electroplated steel sheets can be used for both pressure and vacuum containers. Compared to loose linings, plating has the advantage of better heat conduction and protection against wrinkling from thermal changes or sudden exposure to vacuum. Also mounts, heating or cooling devices, stiffeners, etc., can be welded directly outside onto conventional steel containers. However, the high costs of plating and difficult technical processing represent major obstacles.

Titanium is also used in electroplating on, for example, a variety of current carrying attachment structures that are connected as anode to the parts to be refined. This way, removal of material can be almost completely eliminated so that the cross-section of the structures and the contacts remain unchanged. Titanium anode baskets are suitable for use in electrolytes like copper, zinc, tin, cadmium and other mainly sour baths. Also, for heating or cooling of the baths, systems of titanium are used such as titanium-jacketed immersion bath heaters, boiler tubes, heat exchangers, registers, and spiral tubes. Due to the excellent heat transfer properties of thin-walled titanium tubing, a spiral made from titanium often allows much reduced tube lengths. Because of the lower weight, less excessive mountings and anchorage can be used. In most cases the higher initial costs of a titanium construction pay off very fast.

15.2.3
Dimensionally Stable Anodes – Extractive Metallurgy

Use of titanium anodes for chlorine and sodium chlorate has been successful through the use of thin noble metal, platinum-type or ruthenium oxide surface coatings to maintain electrical contact with the electrolyte. Such anodes possess the low overvoltage characteristic of the platinum metal. This permits considerable reduction in power consumption in cells for the electrolytic production of chlorine compared to using conventional graphite anodes. Therefore, titanium-based anodes not only offer higher current efficiencies, they are also dimensionally stable and cause less contamination of both the cell electrolyte and the chlorine.

The use of titanium electrodes for electro-winning and electro-refining of metals like copper, gold, nickel, manganese, and manganese dioxide from sulfides dissolved in sulfuric acid solutions has been established as an environmentally

friendly alternative to smelting processes by avoiding roasting of the sulfide ores. The main reasons to use titanium in electrolytic extraction is titanium's excellent corrosion resistance and the fact that its oxide film serves as an excellent parting agent. Titanium electrodes are also used for electrophoresis and electro-osmosis – generally speaking, for applications where long-term electrode stability is required.

15.2.4
Petrochemical Refineries

Titanium has also gained central importance in the petrochemical industry. Due to its outstanding corrosion resistance, c.p. titanium grades and Ta or Pd containing alloys are applied in production facilities for acetaldehyde and acetone, acrylic fibers, and urea. Initial applications were focused on heat exchanger tubing for corrosive cooling media. More recently lower quality crude oil with increased hydrogen sulfide and carbon dioxide contents have forced refineries to improve their processing equipment by changing to titanium. The higher initial investment costs were soon recovered by longer equipment life, less downtime and maintenance, and the ability to use the lower cost crude oil. Titanium is used today in refinery heat exchangers, vessels, scrubbers, columns, piping systems, and other related equipment.

15.2.5
Flue Gas Desulphurization

It has been accepted worldwide that pollutants play a major role in the damage of lakes and forests by acid rain fallout from sulfur containing gases being emitted from fossil fuel burning power stations. The need to respect the environment has boosted worldwide installation of flue gas desulphurization plants, a current state-of-the-art technology to remove most of the sulfur from the flue gases. For major SO_2 emitters, the most widely used desulphurization technology is wet scrubbing. For more than 25 years, titanium has been used in major installations in the outlet ductwork and stacks of flue gas desulphurization plants and has proven its exceptional resistance to the highly aggressive conditions encountered. Here titanium has also demonstrated to be most effective on a life cycle cost basis so that primarily Grade 2 titanium sheet is now routinely applied in stacks and chimney linings.

15.2.6
Steam Turbine Blades

A considerable portion of the down time of power plants for energy generation can directly be related to failures of steam turbine components. Of these failures, the majority occurs in low-pressure steam turbines, primarily at the steam-moisture transition zone in the last two rows of blades (L-1 and L). High operating

a)   b)
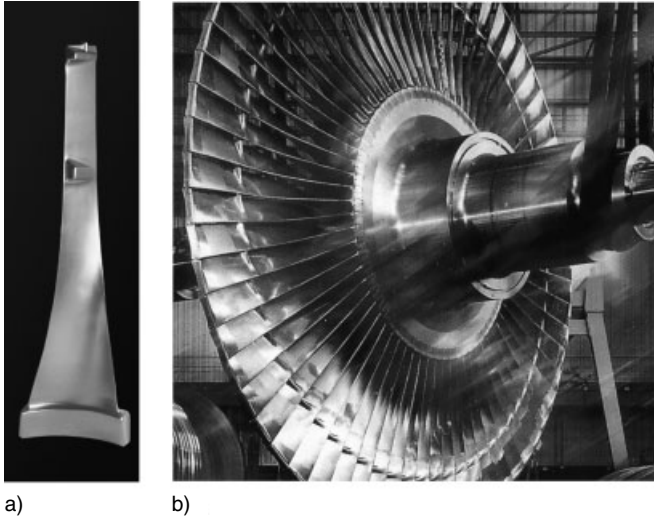
Fig. 15.2 Presently the largest forged titanium blade has a length of 1650 mm (a) and is used for L-0 rows of steam turbines (b); (courtesy: ThyssenKrupp Turbinenkomponenten, Remscheid, Germany).

stresses, poor corrosion-resistant materials, and hostile operating environments are identified as prime failure causes. In the 1980s, the first trials on US steam turbines of replacing the standard 12Cr steel with Ti-6Al-4V retrofit blades proved to be quite successful. Titanium test blades have performed in service for more than 20 years without failure. Therefore, titanium alloys are today increasingly used for advanced steam turbine blades. The primary reasons are weight reductions of close to 60% compared to steel blades and high resistance to oxygenated acid chlorides, corrosion fatigue, and stress corrosion cracking.

Compared with steel blades, the lighter titanium alloys also permit longer blades for the same root stress, thus increasing turbine efficiency. Presently ThyssenKrupp Turbinenkomponenten, Remscheid, Germany, the leading manufacturer of envelope and precision forged titanium low-pressure steam turbine airfoils, is manufacturing the largest forged steam turbine blade in the world, measuring 1650 mm in length (Fig. 15.2). For increased strength, new titanium alloys like Ti-6Al-6V-2Sn are proposed in Japan by Hitachi, as well as alloy SP-700. Although the cost of titanium blades are estimated to be twice that for steel blades, avoiding a single forced outage pays for more than the additional cost of a titanium blade row.

15.2.7
Other Applications

Titanium's excellent corrosion and erosion resistance has made it the prime material choice for use in critical segments of desalination plants. In particular, thin-walled tubing has shown to be superior in cost effectiveness and dependability over traditional copper-nickel alloys. In the food, brewing, winery, and pharmaceutical industry, titanium's excellent biocompatibility has been an additional argument to replace existing stainless steel equipment. Further advantages include ease of cleaning and disinfecting, low maintenance, and reduced life-cycle costs.

In the bleaching sections of textile or pulp and paper plants, titanium is frequently used for equipment that is subjected to aggressive bleaching agents, particularly chloride dioxide chemicals. Largely c.p. titanium grades are used for the bleaching process itself and also for recycling of waste fluids, e.g. for drum washers, filters, reaction vessels, mixers, valves pumps, and piping systems. The higher initial investment costs are soon compensated by increased reliability and extended lifetime of the titanium equipment.

Titanium's high strength-to-weight ratio and its excellent fatigue and corrosion resistance are the prime reasons for selecting it for high-speed centrifuges, among other applications in the medical field. Finally, titanium may be selected as a candidate material for the safe storage of nuclear waste in multi-wall disposal systems.

15.3
Marine and Offshore Applications

Exceptional corrosion resistance, both in seawater and in sour hydrocarbons, has made titanium and titanium alloys a preferred material for use in marine technology, particularly in petroleum and gas exploration in saline environments like the North Sea. Gas and oil raisers on drilling platforms are now manufactured from titanium alloys on a large scale (see also Chapter 19). In particular, very high requirements are met for taper stress-joints, which connect the drill head on the seabed with the actual riser piping system. This metallic tubular fitting has to be extremely flexible since it must compensate for the movements of the floating drilling platform caused by waves, wind, and the tides. The special requirements for these tube connections are in addition to corrosion resistance and high fatigue strength. Furthermore, the low elastic modulus compared to steel provides the titanium structure with higher flexibility. Using titanium alloys permits smaller tube diameters and reduces the allowable bend radii, which not only saves weight but also allows more economic use of space on the drilling platform. Such connections, as shown in Fig. 15.3, weigh approximately 4500 kg and have been extruded from a single Ti-6Al-4V ingot. Tube flanges were attached by electron beam welding. The largest titanium cast part ever produced is a globe valve body also used in offshore operations. The component, which is made from Grade 2

commercially pure titanium, weighs almost 3000 kg and was cast in Russia for the Norwegian company Alba (see also Chapter 19, Fig. 19.5).

Apart from corrosion resistance, the high strength and the low specific weight of titanium compared to high-strength steels are also deciding factors for the choice of titanium in offshore services. The development of cold bending of thin-wall titanium pipe has provided a breakthrough in the overall competitiveness of titanium systems. Currently cooling water, supply, and waste water piping, sea water lift pipes, anchor system piping, sprinkler and ballast water systems on drilling rigs, and also on supply ships, are manufactured from titanium.

Since new gas and oil wells are increasingly required at greater depths, minimizing weight becomes ever more important. Today, new sources have already been explored in water depths of more than 7 km, giving the idea of "offshore" quite a new meaning. Here, weight loading on vessels or semi-submersible platforms becomes even more critical. Particularly lightweight riser pipe materials can substantially reduce hang off weight, which causes a multiple weight reduction in the floating platform itself.

Also the outer skin of unmanned, deep-sea submersibles, which are used for inspection and light repairs in large depths of water, is manufactured from titanium. In fact, only the substitution of steel and aluminum parts by titanium allowed the increase in water depth from 1800 to 3600 m for the manned research diving boat "Alvin". For this boat and for the diving boats that followed it, the use of titanium alloys for the pressure hull was essential. Since the water pressure increases by approximately 10 kPa per meter of water depth, alloys like Ti-6Al-4V (ELI) or Ti-6Al-2Nb-1Ta-0.8Mo were chosen. Today's deep-sea, titanium-hulled submersibles can dive as deep as 6000 m.

In the 1970s and 1980s, the Russian navy operated submarines that were the first with a hull completely manufactured from titanium. The 80 m long nuclear powered Project 705 Alfa class submarines were the world's fastest and deepest
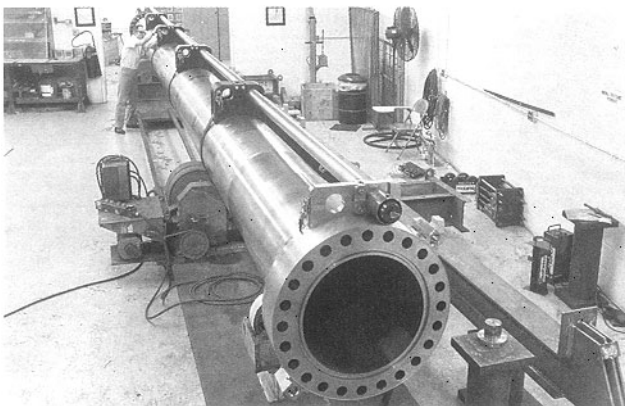
Fig. 15.3 A drilling riser of titanium for the offshore industry at RTI Energy Systems (RTI International Metals Inc., USA).

diving of their time. Using titanium allowed the thickness and weight of the hull to be reduced, producing a remarkably small and very fast submarine. The prototype, completed in 1972 at the Sudomekh shipyard in Leningrad, could accelerate to a speed of 45 knots. In the early 1990s, the last of the few prototypes built was decommissioned.

Excellent corrosion resistance to seawater was the prime reason for the launch of the first all-titanium fishing boat in Japan in the late 1990s. The Eto Shipbuilding Co. in Karatsu, Saga Prefecture, Kyushu Island, used about 3 metric tons of c.p. titanium to build the 12.5 m long and 2.8 m wide vessel that can travel at 30 knots with improved fuel efficiency. The hull thickness is only 2.5 mm, compared to 5 mm for an aluminum construction. As opposed to fiber-reinforced plastic or aluminum alloys, the titanium boat is virtually maintenance-free: she needs no painting, and biofouling can be easily removed from the titanium hull. Larger ships are planned, not only for fishing, but also as pleasure boats, yachts, or high-speed police boats. High-tech anchors are also offered from titanium. They are much lighter than steel, corrosion and maintenance free, and have a lifetime warranty. In marine applications, titanium is currently also being used for water jet propulsion systems, propeller shafts and propellers, shipboard cooling and piping systems, snap shackle and ring kits for sailboats, as well as fishing poles and kayak paddles.

15.4
Automotive Industry

In the mid-1950s, titanium was already first used in the automotive industry. The turbine-driven, experimental vehicle of General Motors, the Titanium Firebird II, had an outer skin manufactured completely from titanium (Fig. 15.4). The vehicle, which never went into production, also remained the only car with a titanium skin; except for ground-bound high speed racing cars developed later, which needed temperature protection from aero-kinetic heating.

Since then, however, it has been a constant objective of the titanium industry to penetrate the mass market of the automotive industry, even if it were only with niche products. Growing demand for fuel-efficient and environmentally friendly cars requires reduced weight at simultaneously improved performance. Titanium alloys, with their high specific strength and excellent corrosion resistance, were the materials of primary choice. The higher price of titanium has, however, proven to be a major stumbling block for wide spread automotive application, and use was initially limited to the racing and high performance sports car sector such as Formula 1 racing cars, competition motorcycles, and high-end automobiles, such as Ferrari.

In the late 1990s, Toyota succeeded in being the first mass production automobile manufacturer to introduce titanium engine valves into a series production vehicle in Japan. But the "Altezza" is a mid-size family car and not, as one might have expected from the higher costs of titanium, an automobile in the high price

Fig. 15.4 Titanium Firebird II of General Motors Corp., USA (Conklin Systems, USA).

market. A powder metallurgy route is used to manufacture the titanium valves. Ti-6Al-4V/TiB powders are used for the intake valves, while the high temperature outlet valves are manufactured from Ti-Al-Zr-Sn-Nb-Mo-Si/TiB powders. The Altezza's 2-l engine has 16 valves, which together weigh only about 400 g compared to almost 700 g for steel valves. The lower weight allowed valve springs to be re-dimensioned with corresponding additional weight savings. Other titanium applications in the power train connecting rods in the Acura NSX V-6 engine and engine valves in Nissan's Infiniti V-8 motor. Also, Yamaha uses titanium valves for one of its recent 250 cm^3 motocross engines.

Automotive coil springs are ideal components for which substitution of steel by titanium can be quite economic. In particular, the relatively low modulus of elasticity or, more exactly, the low shear modulus of titanium alloys, which is only about half that of steel, is of central importance. Compared to conventional automotive coil spring material, the lower modulus translates to increased coil deflection, resulting in fewer coil turns for a given spring application. Therefore, weight is not only reduced by the lower density of titanium, but also by the more compact height of the springs, thus allowing increased payload, and increasing engine or passenger compartment space. Theoretically, titanium springs would account for a "lightweight factor" of 3 to 4. However, due to the portion of inactive coil, weight savings in practical applications amount for little more than 50%. Finally, titanium springs need no corrosion allowance or coating due to their inherent corrosion resistance.

For quite some time, Formula 1 racing cars have made use of the advantages of titanium springs, which are also used in motorcycle racing. However, the Volkswagen group was the first in the world to introduce titanium springs into a series

Fig. 15.5 Worldwide first commercial series production of titanium springs for rear suspension of the Volkswagen Lupo FSI (Volkswagen AG, Germany).

production vehicle. Again, it wasn't an expensive model of the upper class, but the Lupo "FSI", a compact car that has been equipped with titanium rear suspension springs since the year 2000 (Fig. 15.5). TIMETAL LCB (Ti-6.8Mo-4.5Fe-1.5Al) was chosen instead of the traditional Ti-6Al-4V alloy. On the one hand, since it is a beta alloy, it has a particularly low shear modulus, which is even lower than that of standard $\alpha + \beta$ alloys and thus further increases the physical advantage. Additionally, the alloy is also cheaper than Ti-6Al-4V. Like the name LCB (low-cost beta) implies, expensive vanadium was replaced by iron, allowing less-expensive Fe-Mo master alloys to be used. To keep the production costs of the springs at acceptable levels, the spring manufacturer, Muhr and Bender in Attendorn, Germany, paid much attention to adapt existing processes utilized for steel to the production of the titanium coil springs.

The exhaust system is another attractive component in the automotive industry for using titanium. The Austrian sports motorcycle manufacturer KTM uses a rally exhaust system manufactured from titanium for its motocross engine "LC8". The wall thickness of the muffler is as thin as 0.3 mm for weight reduction. Remus, a world-wide leader in sport exhaust systems, offers sport exhausts for motorcycles with a titanium casing weighing as little as 2.5 kg (Fig. 15.6). Reduced weight and even more – a lifetime guarantee – were primarily decisive for the introduction of the first series production titanium exhaust system in the automotive industry. Since 2001, General Motors Corp.'s sports car Chevrolet Corvette Z06 has been equipped with exhaust system subassemblies completely manufactured from titanium Grade 2. Compared with 18.6 kg for the stainless steel alternative, the titanium muffler weighs only 11 kg (Fig. 15.7).

Although worldwide consumption of titanium for automotive applications exceeded 1000 tons in 2002, which is more than an order of magnitude higher than in 1995, the high cost of the raw material is still a central problem for widespread

Fig. 16.6 The titanium sport exhaust system weighs as little as 2.5 kg (courtesy: REMUS Innovation, Bärnbach, Austria).

Fig. 15.7 The dual exhaust system (here shown the right section) of the 2001 Corvette Z06 is completely manufactured from titanium Grade 2 (ArvinMeritor Inc., Troy, MI, USA).

application. For the near future it is not expected that titanium prices will lower drastically. Hopes are, however, that in a high-volume industrial market, prices could very well be reduced to half or one third those known for aerospace, which would in turn open new opportunities for titanium in the automotive industry.

Chapter 18 describes in more detail the advantages, and limits of titanium and titanium alloys for automotive applications.

15.5
Architecture

A more recent field of application for titanium is in architecture. It is not surprising that the pioneering work started in Japan, since this country with only a small aerospace industry has looked from an early stage to extend the use of titanium into non-aerospace fields. The first building with a titanium roof was installed in 1973. Since the 1980s, titanium has been increasingly used as exterior and interior cladding material for roofing, curtain walls, column covers, soffits, fascias, canopies, protective cladding for piers, artwork, sculptures, plaques, and monuments. The annual consumption in Japan increased by the mid-1990s to 350 tons. By the turn of the century, more than 2000 tons of titanium has been used in architectural applications worldwide, representing over one million square meters of roofing and cladding. In 1997, the Guggenheim Museum in Bilbao, Spain, opened – probably the most spectacular "titanium building" so far (Fig. 15.8). The curvilinear design of the American architect Frank O. Gehry features an exterior cladding consisting of 33 000 plates of Grade 1 titanium. Although only 0.35 mm thick, 60 tons were used for the building. In fact, the museum has attracted worldwide attention since then and sparked architectural interest in the use of titanium.

Titanium is mostly used for parts that are exposed to aggressive atmospheric conditions like urban pollution, marine environments, acid rain, volcanic ash residue, or industrial emissions. Here titanium can play its trump card, the superior

Fig. 15.8 The exterior cladding of the Guggenheim museum in Bilbao, Spain, is completely manufactured from commercially pure titanium.

immunity to atmospheric corrosion. It results from the stable adherent protective oxide film, which even restores itself instantaneously after the surface is scratched or otherwise damaged.

Since titanium is virtually immune to stress, pitting, and crevice corrosion, as well as other types of corrosion caused by acid rain, manufacturers can provide a 100-year performance warranty for facades and roofs. This in turn leads to reduced maintenance and repair costs, which can usually overcompensate the initial high material expenditure. The immunity to corrosion makes titanium also an environmentally friendly metal, since no corrosion or harmful run off to contaminate rainwater occurs. Since titanium does not degrade during service, it is 100% recyclable. Therefore, on a life-cycle basis, titanium is the most competitive of all architectural metals. Aesthetics aside, the high immunity to corrosion is the prime reason to select titanium for architectural applications. Commercially pure titanium – mostly Grade 1 – is used, allowing wall thicknesses typically ranging from as thin as 0.4 to only 1 mm.

Usually titanium claddings are used in their natural appearance, giving the structure a soft reflectivity and subtle silver-gray color. However, annealing and pickling can reveal a reflective metallic surface finish, while anodizing offers the opportunity for a wide range of surface textures and colors with a color spectrum from dark-bronze and light green to red-violet.

Another advantage of titanium is its low coefficient of thermal expansion, which is only half that of stainless steel and only one-third of aluminum. This favors titanium over other metals for structures with a lot of glass or concrete, which also have a low coefficient of thermal expansion. As a result, for large titanium structures like movable roofs, thermal stresses resulting from day and night temperature cycling are substantially reduced due to minimized expansion and contraction. Consequently, such huge titanium structures are preferably installed for roofs of arenas, theaters or temples, which can be opened or closed depending on weather conditions.

Most of these large mobile structures can only be realized because of the reduced weight of titanium. Low weight means that large areas of roofing can be supported by less massive structures, with corresponding cost savings. Furthermore, lightweight structures allow an increase in the floor space, giving the architects extra flexibility. Examples of impressive structures made of titanium include the roof of the Naya Temple in Fukui, the Fukuoka Dome, the Miyazaki Ocean Dome, the International Conference Building in Tokyo, the Shimane Prefecture Art Museum in Matsue, Japan, the futuristic curtain wall of the Showa-Kan building in Kudan, Tokyo, the Glasgow Museum of Science with its adjacent IMAX theatre, as well as the roof of the Titanium Dome, and the Chinese Grand National Theater planned on the Tiananmen Square in Beijing, designed by the French architect Paul Andreu. The controversial ellipsoid building will be made of two large titanium shells opening on both sides onto a wide glass wall.

The Abu Dhabi airport is the world's first structural application of titanium in the context of architecture. Due to their high specific strength, titanium beams can be significantly smaller than steel beams, which give architects extended freedom in design and realization of their aesthetic visions.

Apart from superior environmental resistance, the optical impression due to titanium's unique and subtle reflectivity also plays a role in choosing the light metal. But the status surrounding titanium with the mystique of a luxurious "aerospace" material can also be a decision-maker for a more prestigious material choice. Not surprisingly, among the buildings featuring titanium roofs and facades, a striking majority are museums or public buildings. Apart from the Guggenheim Museum in Bilbao, these include the MTRC Central Station in Hong Kong, the National Scottish Science Center in Glasgow, as well as the Van Gogh and the Scheepvaart Museum in Amsterdam. Opened in 2001, the new Cerritos Millennium Library in Cerritos, California, is the first titanium-clad building in the United States.

For a metal, titanium is an excellent insulator. Its thermal conductivity of $21.6 \, \mathrm{W \, m^{-1} K^{-1}}$ ($0–100\,°\mathrm{C}$) is only one tenth that of aluminum, increasing a building's energy efficiency. Particularly in cases where architects are restricted to metal structures, titanium proves to be a very energy-efficient material with a positive impact on the building's economy.

15.6
Sports and Leisure

Due to the extreme requirements of the aerospace sector, titanium alloys are considered high-performance materials. In looking for new fields of applications it is therefore obvious to consider areas that are also based on high-performance. This particularly applies to high-performance sports, but also includes the moderate versions of recreational activities and leisure sports.

15.6.1
Golf

In golf, the prime aim is to drive the golf ball as far as possible. Here the head of the golf club plays a central role. Originally, the club head was manufactured from high-strength persimmon wood, hence the name "wood". Nowadays, golf clubs usually have "metallic" woods, which were first manufactured from high-strength steel. In the mid-1990s, the first "metal woods" made from titanium alloys came on the market and have become quite popular since then (Fig. 15.9).

The advantage of using the light metal allows the club maker to manufacture bigger club heads that still have little weight. Advanced heads have a volume of up to $400 \, \mathrm{cm^3}$, thus considerably widening the sweet spot, i.e. the potential hit point of ball and head. Commonly, the hollow golf club heads are manufactured by investment casting using the lost wax process. Ti-6Al-4V is preferred, but also other $\alpha + \beta$ titanium alloys like Ti-3Al-2.5V are cast. In Japan, drivers with club heads made of SP-700 are available.

But it isn't the size of the club head alone that makes the difference. The club hitting face should be as thin as possible and show a spring effect. Like a trampo-

Fig. 15.9 Golf club heads of Ti-6Al-4V (BIAM, China) (a) and with forged club hitting face of the beta alloy Ti-15-3-3-3 (Tour Edge Golf Mfg., Inc., Saint Charles, IL, USA) (b).

line, the spring face softens the impact by storing and returning energy to the ball over a longer impact time, all of which guarantees the player longer distances without having to swing harder. Due to the lower Young's modulus of beta titanium alloys, this effect is particularly pronounced for these alloys. Furthermore, the high strength of forged beta alloys permits the use of forged club faces with wall thickness of less than 3 mm. Especially for application as thin structure, Kobe Steel has developed a new titanium $\alpha + \beta$ alloy, Ti-2Mo-1.6V-0.5Fe-4.5Al-0.3Si-0.03C, which can be produced as coil and thus is relatively cheap.

Not only the heads of golf clubs, but also shafts are manufactured from titanium. Due to the reduced weight, irons can be accelerated faster, which translates into a higher speed swing and therefore more distance. With a shaft length of 1.17 m, club head speeds can exceed 175 km h^{-1} and allow the golf ball to be driven as much as 280 m. Beside irons, putters made from titanium are also available.

Also, parts of golf balls are produced from titanium. Particularly golf balls that are used by children or teenagers should have a lower weight to protect kid's joints. Youth golf balls have about 15% less weight due to their special internal construction, and have a softer outer skin.

15.6.2
Tennis Racquets, Baseball Bats and Pool Cues

As in the case of golf, for any kind of sport where balls have to be hit fast and far, weight savings is of advantage. Therefore, it is not surprising that the frames of tennis racquets and baseball bats are also offered in titanium; not only to professionals, but also with increasing success to recreational players. Pool cue shafts, e.g. manufactured from Ti-3Al-2.5V, are also on the marketplace. Generally, Ti-3Al-2.5V has been a very popular tubing material used in sporting applications since the alloy combines a good strength-to-weight ratio and corrosion resistance, with a low modulus of elasticity that translates into favorable dampening characteristics.

15.6.3
Bicycles: Not only Frames

In high-speed cycling, weight savings of a couple of grams can mean the difference between winning and losing. High strength and high corrosion resistance with low density make titanium alloys an ideal material. So it is obvious to use lightweight titanium alloys as a substitute for high-strength steels in frames for racing, mountain, and triathlon bikes. Frames are mainly manufactured from Ti-6Al-4V, Ti-6Al-4V ELI, and Ti-3Al-2.5V tubes. The first racing bike with a titanium frame was ridden by Tour-de-France legend Eddie Merckx in 1972. Frames are hand-made and usually welded together from tubes (Fig. 15.10). Recently, the first custom titanium hand-cranked tricycle, with two front wheels, was offered for handicapped riders who are unable to use their legs. Particularly for this application, the low elastic stiffness

Fig. 15.10 The Ti-6Al-4V bicycle frame weighs only 1.45 kg (MORATI Titanium Bicycle Components, Mariánské Údolí, Czech Republic).

provides comfortable absorption and damping of shocks and vibrations. Also, titanium racing wheelchairs are offered to racing teams.

Unfortunately, titanium's ideal properties, like high fatigue strength at low weight and excellent corrosion resistance, often go along with high prices of the equipment – often four times or more above steel or aluminum – that has hindered their widespread use. It is not the expensive manufacturing process alone, but often much higher prices for semi-finished products than in the aerospace sector have to be paid due to the small batch quantities. On the other hand, high prices often add to the appeal of titanium goods among professionals. So, lately, titanium alloys have experienced competition from carbon fiber reinforced composites. Cyclists who favor a stiff frame and do not want the extra spring of a low modulus titanium frame prefer these materials. Consequently oval-shaped titanium tubes are offered to give back stiffness to the frame; however, they also increase weight.

Certainly the frame is the largest single titanium bicycle component. However, other parts are also manufactured from titanium alloys, primarily for weight savings. These include handlebars and handlebar stems, fasteners, seat posts, high-end saddles with titanium rails, forks, crank arms, bearings and bearing axis, spokes for ultra-light road and off-road bikes, chains and chain rings, and other accessories like racks, or casings for wrist microcomputers that monitor time, temperature, pulse, or bicycle computers that control speed, height, pedal frequency, or angle-of-sight level. Often titanium accessories can save as much as a kilogram off the weight of a bicycle.

15.6.4
Scuba Diving Equipment

The equipment of marine sport divers should be light, exhibit high strength, and be resistant to seawater. Where it comes in contact with the body, it also has to be gentle to the skin. Taking the sum of these requirements, titanium is superior to steel. Thus, a new field of application opens up for titanium alloys, the rapid spread of which is only prevented by the high price of the metal. Valves, gas cylinders, and air regulators made from titanium alloys are available, as are accessories needed by the sports diver such as knives, watches, and cases for underwater cameras. Even when exposed to saltwater, titanium equipment shows superior durability, is highly reliable, and almost maintenance-free.

15.6.5
Expedition and Trekking

For backpacking, hiking, rock climbing, camping, and expeditions, the desire to use equipment as light as possible is quite understandable. So, it is not surprising that the high-strength light metal can be found here, too. High strength climbing gear like snap shackles, hooks, rings and eyes, latches, locking carabineers, pins, clips, eye bolts, cliffhangers, and straps are usually manufactured from forged Ti-6Al-4V. Cookware like pots, pans, and drinking bottles, and eating utensils, like

spoons and forks, made from pure titanium not only substantially lower the weight to carry, they also do not ionize foods nor will they rust or leave an aftertaste. Stoves and propane gas canisters or fuel bottles made from titanium also contribute to reduce camping and expedition weight just as tent stakes do.

Also, in the snow and on glaciers, titanium equipment eases weight. This applies to snowboards and skis, for example. The advertising slogan "the Porsche among skis" indicates, however, that these items rather appeal to snobs. This is, however, different for titanium ice axes and ice screws, primarily engineered for high-altitude mountaineering. Apart from the axe, ice climbers also have to carry at least two ice screws, vital for their advancement in the ice rocks. Here the lower weight compared to steel equipment is certainly crucial for the choice of titanium. Also, titanium does not embrittle with decreasing temperature.

15.6.6
Knives

Due to its relatively poor hardness, titanium alloys weren't considered to be a material for cutting tools for a long time. However, the Heinr. Boeker Baumwerk company in Solingen, Germany, jointly with a Japanese company, managed to obtain outstanding cutting performance for titanium by introducing titanium carbide particles via powder-metallurgy processes. Not only was Boeker, a special manufacturer of high quality outdoor, sports and collector knives, the first to use titanium as a handle material, they also are the first to introduce titanium blades to the kitchen cutlery market. The sintered powder titanium blades hold an edge six times longer than conventional cutlery, do not rust, and weigh only half as much as stainless steel. Introduced in 1999, the titanium blades repulse germs in laboratory experiments, are antimagnetic and – unlike most current kitchen cutlery – discharge nearly zero metallic ions into the material being sliced, and eliminate unpleasant metallic taste in foods. Fig. 15.11 shows the unique styling of Boeker's "Titanum" knife designed

Fig. 15.11 Kitchen knife series "Titanum" (Heinr. Boeker Baumwerk GmbH, Solingen, Germany).

by the internationally recognized British designer Julien Brown, which was influenced by both esthetic and ergonomic aspects.

15.6.7
Winter Sport Equipment

Titanium's ability to conduct heat more slowly than steels has revealed applications of titanium alloys in high performance winter sports. So, for bobsled runners made from titanium, frictional warming will not be dissipated as fast as for steel. The resulting higher temperatures provide better gliding behavior, which can be decisive in high performance racing. In addition there is the weight advantage of titanium: Ti-6Al-4V runner have almost half the weight of comparable steel runners.

For similar reasons, ice skating blades are also made from titanium, just having only half the weight of steel blades. However, at a price of over € 1000, customers for the laser cut, hand-made blades are found among professional ice skaters. For figure skaters, the lower modulus of elasticity of titanium provides the blade much better spring for jumps than steel blades, and also a softer landing after high jumps.

If used in polar-regions as a material for runners of sleighs, one makes use of another quality of titanium: it will not rust.

15.6.8
Diverse Sports Applications

Certainly the advantage of using titanium equipment in highly competitive sports, and even more in popular sports, is not in all cases very obvious and one may suspect that there is also a certain portion of prestige and snobbery in the game. This may apply for horse sports, where horses carry a bridle made from titanium in their mouth. Titanium horseshoes are offered as well to provide horses an easy ride. For horse riders, high-end helmets with a titanium reinforcing stripe in the middle provides ultimate safety and comfort due to its light weight.

Weight is also decisive in the choice of titanium as a material for face protection on the helmet of American football players by using lightweight faceguards manufactured from titanium wire. And why shouldn't anglers use reels manufactured from titanium for their fishing rods? Sports marksmen can choose housings of pistols or guns made from titanium. Likewise, titanium weapon casings can also lighten the load for policemen or soldiers.

15.7
Medical Applications

Right at the beginning of the new millennium medicine history was written. But unlike the first successful heart transplantation on December 3rd, 1967, at the Groote-Schur hospital in Cape Town, South Africa, the implantation of the first ar-

tificial heart into the body of Robert Tools was almost unnoticeably carried out at the Jewish hospital in Louisville, Kentucky, USA, on July 2nd, 2001. The two surgeons from the University of Louisville, Laman Gray and Rob Dowling, will also probably never attain the fame and publicity of the South African surgeon Christian Barnard in the 1960s; however, the company ABIOMED from Danvers, Massachusetts, may possibly. They developed the first artificial implantable replacement heart AbioCor™ shown in Fig. 15.12. The fully implantable prosthetic system weighs nearly 1 kg, is about the size of a grapefruit, is entirely self-contained and estimated to cost about $ 70 000. Apart from many soft tissues and plastic tubing, the metallic parts of the artificial heart, like connectors, valves, etc., are manufactured from c.p. titanium.

This pioneering work underlines the important progress titanium and its alloys have made as surgical implant materials in medical engineering within the last 30 years. The excellent compatibility with the human body is regarded as a key property for the choice of titanium: Titanium is generally perceived as the biocompatible metallic material. Furthermore, titanium is extremely resistant to corrosion from body fluids, and is compatible with bone and living tissue, and is elastically deformable as thin foil material. Thus, pure titanium combines many of the attributes desirable for heart pacemaker cases and as the carrier structure for replacement heart valves.

If implants have to carry mechanical loads, titanium alloys are used. Their outstanding strength to weight ratio and excellent fatigue behavior are decisive for the choice of material for orthopedic devices. Favorable to other high-strength metallic materials, titanium has a relatively low modulus of elasticity, which reduces the differences in stiffness between the human bone and the implant. This is important, for example, to the traditional application of titanium alloys as hip implants (Fig. 15.13) and knee joints, but also to bone fracture plates and screws, and intramedullary nails or plates for cranial surgery. Titanium alloys are further

Fig. 15.12 The metallic parts of the first artificial heart are made of titanium (ABIOMED, Inc., Danvers, MA, USA).

Fig. 15.13 Components of a hip implant made from cast titanium (Tital, Bestwig, Germany).

used to substitute parts of the shoulder, the spine, the elbow, and the hand. External bone-fracture fixation provides another area for titanium applications. Since titanium withstands repeated sterilization, instruments for heart or eye surgery are made from titanium.

Initially, the standard titanium alloy Ti-6Al-4V was chosen for medical applications, since engineers could take advantage of an extensive database available from aerospace applications, particularly on fatigue behavior. However, in the course of the discussion around the toxicity of the element Vanadium, V-free alloys were specifically developed for medical applications. In alloys like Ti-5Al-2.5Fe, Ti-12Mo-6Zr-2Fe, Ti-15Mo-3Nb-3Al, Ti-6Al-7Nb, Ti-13Nb-13Zr, Ti-35Nb-7Zr-5Ta, and Ti-30Ta, Fe, Nb, Ta, or Mo replaces Vanadium. At the same time, orthopedic alloys gradually shifted from $\alpha + \beta$ alloys to metastable β alloys, since – compared to Ti-6Al-4V – they have a lower Young's modulus, which comes closer to that of the human bone (10–30 GPa) (see also Chapter 16.)

Titanium is non magnetic. This allows surgery in the magnetic field of a nuclear spin tomograph. Also, the risk of damage to small and sensitive implanted electronic devices is virtually eliminated.

In connection with medical applications, one class of titanium alloys is becoming integral to the design of a variety of new products. Actually, these are nickel-based titanium alloys and are better known as shape memory alloys: they remember their initial shape after being deformed. Moreover, they are able to undergo large elastic deformations and show high kink resistance and stability of shape. The super-elastic effect was discovered in the 1960s and has led to medical applications primarily for the Ni-Ti alloy Ti-56Ni. Like titanium alloys, they are also chemically and biologically compatible with the human body.

For shape memory alloys, generally one-way effects, two-way effects, and pseudo-elasticity, also described as super-elasticity, are distinguished.

Materials with a one-way effect remember their original shape after being deformed at lower temperatures. Once heated to a higher temperature, they spring

a)

b)
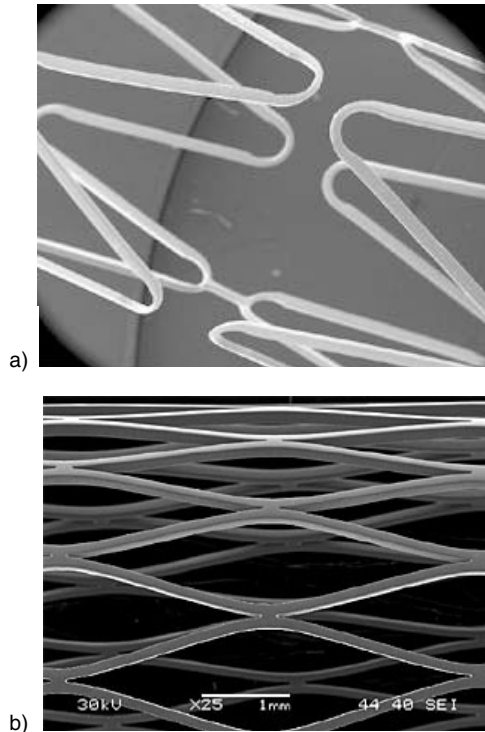
back to their original shape and keep it even when cooled down again. The metallurgical background of this phenomenon is that shape memory alloys undergo a phase transformation in their crystal structure when cooled from the stronger, high temperature austenite to the weaker, low temperature martensite. The potential transformation temperatures range from −20 °C to +80 °C and can be adjusted by slight changes in alloy composition and through heat treatment. Ni-Ti alloys, which can be deformed at room temperature and retransform at 50–70 °C, are used today in surgery as implants (osteosynthese) and for stiffening of weakened fabrics. Probably the most celebrated application is the self-expanding stent (Fig. 15.14) applied in the cardiovascular system. These permanent implants are deployed through a catheter and expand by simply returning to their equilibrium, non-deformed shape.

As the elasticity of Ni-Ti alloys can be more than 20 times greater than stainless steel, the shape memory effect is also employed for the occlusion of arterial defects thus avoiding open-heart surgery. A Ni-Ti wire mesh filled with polyester fabric is implanted through a catheter inserted in the patient's vein. Once the occlusion or hole in the arterial wall of the heart is reached, it springs open, expanding to its original shape and clamps the defect.

Applications outside medical engineering include pipe joints and body-bound rivets as well as plug-in connections of circuits.

For two-way effects, the shape memory process is reversible. Upon thermal cycling the material also deforms cyclically. This behavior is utilized for control of endoscopic instruments. Outside medical engineering, the two-way effect is used in electrical engineering and electronics for heat and electrical installations, as well as in the automotive industry as measuring and control elements, e.g. engine valves, manipulators, or small robots.

The third form is pseudo-elasticity, or super-elasticity. Here the reversible austenite-martensite-austenite transformation is forced by an external deformation. Such a pseudo-elastic material can bear very high deformations and is used as a material for braces, for example. In fact, orthodontic archwire was the first product to take advantage of this property. Ni-Ti wires are able to move with the teeth, applying a constant force over a very broad treatment time and tooth position. Another popular application outside medicine is as seals. Super-elastic eyeglass frames became the first successful Ni-Ti consumer product. Since Ni-Ti components show a ten-fold higher elastic straining than conventional spring materials, they are also suitable for applications where high damping is essential.

15.8
Dental Implants

Titanium alloys have also proven to be a mature material for dental implants. A major advantage of titanium in comparison with gold-based alloys is that titanium comes as a pure element, thus avoiding chemiophysical reactions in the mouth and excluding the danger of a metal allergy. Titanium is totally biocompatible. Fig. 15.15 shows a model casting from titanium. Grade 1 titanium can be combined with other dental materials like amalgam or gold, without the risk of electrochemical reactions from contact with these alloys in the mouth. Because of its high affinity for oxygen, titanium immediately forms an oxide film in the mouth, which creates this neutrality. Since the dielectric constant of titanium oxide is similar to that of water, titanium is also neutral in taste. Furthermore, its very low thermal conductivity, which is more than an order of magnitude below that of gold-based alloys, is of benefit to titanium: teeth that are equipped with titanium
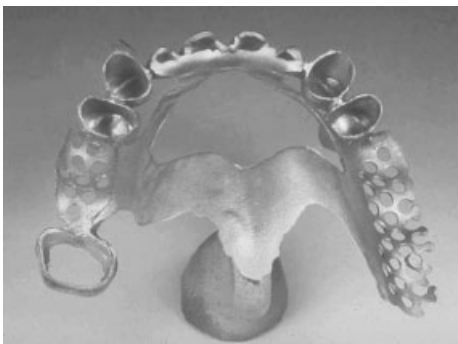
Fig. 15.15 Dental casting of c.p. titanium Grade 1 (Dentaurum J.P. Winkelstroeter KG, Germany).

react less sensitively to the fast temperature changes from hot or cold food and drinks. Titanium's lower density usually only plays a minor role in the material's choice. It is, however, of some advantage for large dental restorations like crowns, bridges, implant suprastructures, and removable partial dentures, where four-times heavier gold implants may occasionally feel like a foreign body.

Titanium implants have opened up new possibilities in restorative dental practice. The introduction of a titanium implant into the jawbone favors osseointegration before the superstructure is built onto the implant. Today, titanium is successfully used in prosthetic dentistry for implant screws, crowns, bridges, dental posts, inlays, and removable partial dentures. Since titanium is the only dental metal that can be easily X-rayed, a proper diagnosis of caries can be made without removing crowns or bridges. Detailed information about the use of titanium in dental technology is given in Chapter 17.

15.9
Jewelry and Fashion

Similar to its predecessors, gold, silver, and platinum, titanium has also made its appearance in the jewelry section. Certainly, the focus was primarily on its exclusiveness as a high quality "noble" metal, surrounded by the mystique and aura of its use in aerospace. There is, however, also the benefit of titanium's high biocompatibility, as known in medical engineering, which makes pure titanium superior to the classic jewelry alloys based on gold and silver.

At the beginning of the 1990s, the first watches with titanium casings were brought to market and were established in the upper price segment. However, since they were exclusively produced by relatively cheap investment casting, the high prices couldn't be maintained in the long run. Today titanium watchcases and bracelets differ only slightly in price from their competing noble metal counterparts.

Wedding and friendship rings are also offered in titanium, as well as rings and other pieces used as piercing jewelry. Almost exclusively, chemically pure titanium Grades 1 and 2 are used. Not being alloyed with elements like copper or nickel, which are found in karat gold, titanium is completely inert and does not irritate even sensitive skin. Particularly for piercing jewelry, the danger of allergic reactions is minimized and titanium does not affect the time required to heal wounds. The soft, unalloyed titanium also allows resizing of rings to a certain extent, and, in case of emergency, they can be easily removed from the finger. Also, wearing a titanium ring can provide a pleasant "lightweight" feeling on the finger.

Titanium is not only a popular choice for jewelry because of its hypoallergenic, lightweight, and corrosion resistant nature, designers also like the large range of surface finishes they can create by anodizing or heating the metal. Mechanically polished jewelry exhibits a beautiful, luster and natural color characteristic of titanium. Its attraction, however, is the ability to produce a large range of both bright and subtle colors by anodizing or heat tinting. The ultra-thin, permanent, and

Fig. 15.16 Examples for watch casings, jewelry and eyeglass frames made of titanium (Citizen Watch, Japan, Germany; Bluecat, Vienna, Austria; Eschenbach, Nürnberg, Germany).

transparent surface oxide film leads to exceptionally decorative coloration of the surface by absorbing and refracting the light. This effect can be further intensified by anodic oxidation using electrolytes on the basis of sulfur and phosphoric acid. The required layer thickness simply depends on the voltage and time used. Continuous variation in film thickness results in spectacular rainbow coloring. Thus a permanent and non-abrasive broad color spectrum can be achieved for titanium jewelry, ranging from silver to gold, red, violet and blue.

Further applications of titanium jewelry and fashion articles include cuff links, tiepins, brooches, pens, and spectacle frames. Particularly for the latter, light weight is of importance. Stylish ultra-light eyeglass frames are also made from Ni-Ti shape memory alloys, using fine wire or rolled products. The unique shape retention and extreme flexibility significantly enhance durability and usefulness of the eyeglasses, which enjoy widespread popularity. Fig. 15.16 shows examples of watches and bracelets, jewelry and stylish eyeglass frames all manufactured from titanium.

15.10
Musical Instruments

Titanium has also penetrated the musical instrument market. Here the elastic modulus, which is different from steel or wood, increases the acoustic response of the metal and creates a characteristically titanium sound spectrum. For example, concert or piccolo flutes are produced from titanium, since the metal is ideally suited to high audio frequencies. Usually only head joints are made from titanium, but US craftsman Jonathon Landell has also manufactured an entire titanium flute.

In the 1990s the first concert drums were manufactured from titanium, both in Japan and in the United States. Despite their lower weight, they produce a deep, rich, and dignified sound that wooden frames cannot create. Besides having
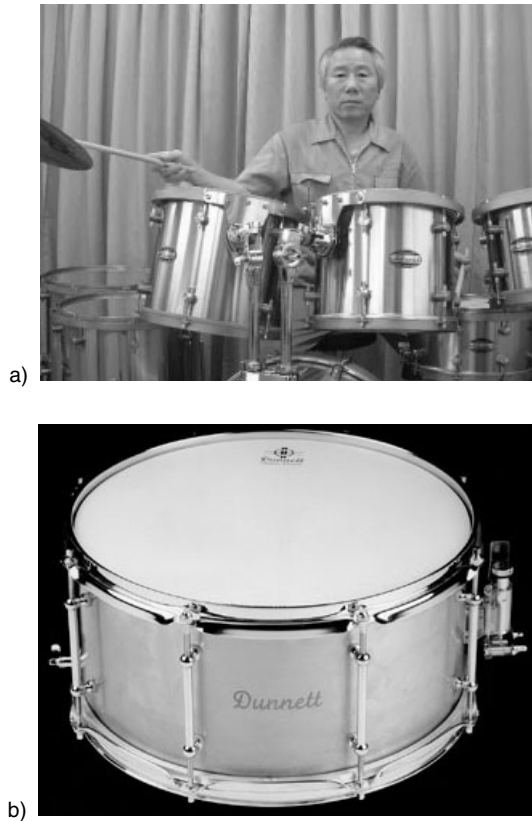
Fig. 15.17 Concert drums manufactured from titanium; (a) Kitana, Japan; (b) Dunnett Classic Drums, USA.

unique tonal qualities, they are also an optical attraction. But not only drums, also titanium beater shafts, hi-hat rods, and hoops, as well as titanium endpins, tailpieces and tail wire are hand-made to customer specifications (Fig. 15.17).

15.11
Optical Industry

In 1982, the single lens reflex camera Nikon FM2 was the first camera featuring a high-speed shutter with release times as fast as 1/4000 second. At that time, this was achieved with a lamellar-type shutter made from titanium, built into a production camera for the first time. Later, the titanium shutter was replaced by aluminum, which proved to be even faster with shutter speeds of up to 1/8000 s.

Also, camera casings or parts of the camera body were manufactured from c.p. titanium, particularly of expensive models such as the Nikon FM2/T. Since these

cameras were all placed in a high-price sector, their distribution was limited. The Nikon 5×15 T binoculars had an all-titanium body.

15.12
Information Technology

Titanium also penetrates into information technology. Right at the turn of the millennium, Apple Computer Inc. introduced the "Apple Titanium PowerBook G4", the first laptop with a casing made from Grade 1 titanium. The high specific strength of titanium was decisive for the material choice. To accomplish the very low height of only 25 mm and weight of only 2.4 kg, a thin titanium foil as the outer skin was wrapped around a very stiff carbon fiber lightweight support frame, providing the necessary structural rigidity. Thus, the Titanium Power Book G4 is one of the lightest and thinnest full-featured laptop computers worldwide.

Titanium is also considered a promising substrate candidate material for hard disk drives in the computer industry. The US company TitaniumX is presently evaluating titanium's potential for this application. Compared to aluminum, the material mainly used today, titanium offers significant advantages. Apart from higher strength, titanium's non-magnetic properties can prevent detrimental interference with the data storage process; its higher temperature stability permits higher temperatures during the coating process, thus improving disc production rates, and its purity permits closer read/write head tolerances that would increase disc storage capacity.

15.13
Safety and Security

Due to their high strength and light weight, titanium alloys can also be of substantial help to policemen, security personnel, fire brigades, and rescue crews. Here weight savings are obviously most helpful in reducing the workload on the user. Firefighters should be supplied with rescue tools as light as possible. This applies to the shovels, axes, crowbars, and pry bars firemen often have to use to force their way to the location of catastrophe. Since rescue tools must frequently be used overhead, weight is of particular concern. Manufactured from titanium alloys they usually weigh less than 40% of comparable steel products. Furthermore, titanium alloys are fire-resistant and do not corrode when used in saltwater, brine, polluted or any other waters and most chemicals. Since titanium is non-magnetic and non-sparking, titanium tools can also be used in areas where sensitive electronic equipment or inflammable fluids are present.

A new application for titanium in the security and protection field is safety vests for personal security (Fig. 15.18). Laser-cut 0.1 mm thin titanium foils are tailored into these vests and offer an efficient protection against firearms and stabbing. Furthermore, the titanium layers also offer protection against shrapnel, for

Fig. 15.18 Thin titanium foils tailored into safety vests provide ultimate protection (DTG, Deutsche Titan, Essen, Germany).

example after the explosion of a hand grenade. Titanium is particularly favored for this application due to the high specific strength, the thermal and mechanical loading, the compatibility with the human body and – most of all – the light weight, since first of all protective armor vests have to be comfortable and therefore as light as possible. Titanium-reinforced vests weigh only about 3 kg and are significantly lighter than conventional models with steel inlays. Worldwide there is large interest in this new product. Recently, Berlin policemen were the first to be supplied with the new lightweight body armor vests, the foils being supplied by Deutsche Titan GmbH, Essen, Germany.

High specific strength and superior ballistic properties make titanium also suitable for armor applications. Used as protective armor on personnel carriers and tanks, titanium offers considerable weight reduction over conventional steel and aluminum alloys and thus drastically affects transportability, portable-bridge-crossing capability, and maneuverability. As an example, the commander's hatch in the US M2 tank has been replaced by Ti-6Al-4V with a weight savings of about 35%. Further, a stretched version of the M113 armored personnel carrier also uses titanium appliqué armor. Marine forces try to employ titanium lightweight armor to reduce weight of their amphibious vehicles. Future artillery systems, like the Crusader howitzer, are likely to see titanium alloys used for carriage, trail, legs and forward outriggers as well as the recoil system, resulting in substantial weight savings. For their marine vessels the, US Navy plans to substitute steel and Cu-Ni seawater pipes in heat exchangers by titanium, thus reducing maintenance cost. After all, the higher price for titanium is still a major stumbling block for widespread application. Here lower-cost titanium alloys through the use of cold-hearth melting, as well as improved and less-costly fabrication processes, may be the solution.

15.14
Referenced Literature and Further Reading

D. M. Brunette, P. Tengvall, M. Textor, P. Thomson, eds.: Titanium in Medicine, Springer-Verlag, Berlin Heidelberg (2001) 1019

W. Diem: Titanium in the auto industry, Auto Technology **5** (2001) 36–37

T. W. Duerig, A. R. Pelton, D. Stöckel: Superelastic Nitinol for Medical Devices, Medical Plastics and Biomaterials, March 1997 (http://www.devicelink.com/mpb/archive/97/03/003.htm)

K. Faller, F. H. Froes: The Use of Titanium in Family Automobiles: Current Trends, JOM **53** (4) (2001) 27–28

F. H. Froes, P. G. Allen, M. Niinomi: Non-Aerospace Applications of Titanium, TMS, Warrendale, PA, USA (1998)

F. H. Froes: Developments in Titanium Applications, Light Metal Age (Oct. 1995) 6–8

F. H. Froes: Will the Titanium Golf Club be Tomorrow's Mashy Niblick?, Journal of Metals **51** (June 1999) 18–20

J. S. Grauman, B. Willey: Shedding New Light on Titanium in CPI Construction, Chemical Engineering, August 1998, 106–111

J. S. Montgomery, M. G. H. Wells: Titanium Armor Applications in Combat Vehicles, JOM, **53** (4) (2001) 29–32

M. Niinomi: Recent Titanium R&D for Biomedical Applications in Japan, JOM, **51** (5) (1999) 32–34

O. Schauerte, D. Metzner, R. Krafzig, K. Bennewitz, A. Kleemann: Fahrzeugfedern federleicht, ATZ Automobiltechnische Zeitschrift **103** (2001) 654–660

R. W. Schutz, C. F. Baxter, P. L. Boster: Applying Titanium Alloys in Drilling and Offshore Production Systems, JOM **53** (4) (2001) 33–35

M. Seiersten, L. Lunde: Titanium for Offshore and Marine Applications, Institute for Energy Technology, Kjeller, N (1999) 1–27

T. Tetsui: Application of TiAl in a Turbocharger for Passenger Vehicles, Advanced Engineering Materials **3** (2001) 307–310

Shaping the future with titanium, DTG – A company of ThyssenKrupp Steel (1998)

Architectural Titanium, Timet (http://www.timet.com/architecture/index.html)

RTI: a world of possibilities, Stainless Steel World, April 2001, 17–22

16

Titanium and its Alloys for Medical Applications

J. Breme, E. Eisenbarth and V. Biehl, *Universität des Saarlandes, Saarbrücken, Germany*

16.1
Introduction

Biomaterials must fulfill the following requirements:

a) corrosion resistance
b) biocompatibility
c) bioadhesion (osseointegration)
d) favorable mechanical properties, e.g. Young's Modulus, similar to that of the bone, fatigue strength according to the intended application
e) processability (casting, deformation, powder metallurgy, machinability, welding, brazing, etc.)
f) availability (low prices)

Because of these requirements the number of metallic materials that can be considered is limited. Until now the following groups of metallic materials have been used as biomaterials:

a) stainless steel, e.g. X2CrNiMo1812 (316L)
b) CoCr-based alloys (vitallium) in the as-cast condition, e.g. CoCr30Mo6, or in the as-wrought condition, e.g. CoNi35Cr20
c) cp-titanium and titanium alloys, e.g. Ti-6Al-4V
d) cp-niobium
e) cp-tantalum

In section 16.2 the various groups of biomaterials will be compared with respect to the above requirements, and the advantages of titanium and its alloys with their favorable properties will be elaborated. Since medical progress often makes special demands on the properties of the biomaterial, it has become necessary to develop tailor-made materials (metal-matrix composites based on titanium) according to the particular application. In section 16.3 examples of such tailor-made Ti-based materials are given.

16.2
Comparison of the Various Groups of Metallic Biomaterials

16.2.1
Corrosion Resistance

Under normal conditions in human body fluid, i.e. a solution of about 0.9% NaCl, the pH value amounts to about 7.4. Changes in the pH value can be caused by surgery, resulting in a rise to 7.8 and followed by a drop to 5.5. After a few days the normal value of 7.4 is re-established. In this medium the most corrosion resistant materials are titanium and its alloys, niobium, and tantalum, followed by wrought and cast vitallium, and by stainless steel [1]. Breakdown potential measurements of various implant materials in Hank's solution also showed a clear order of precedence. While cp-Ti and Ti-6Al-4V had high breakdown potentials of 2.4 and 2.0 V, respectively, the value for stainless steel and CoCr-alloys (cast and wrought) amounted to only 0.2 and 0.42 V, respectively (Tab. 16.1) [2]. As already described in a previous publication [3] Ti and its alloys, as well as Nb and Ta, belong to that group of metals which, in the body fluid, cannot undergo a breakdown of passivity. Nevertheless, in all materials the passive layer can be mechanically damaged, for example by fretting of metal against metal (plate/screw system) or by the instruments used during surgery. Therefore, the repassivation time of the passive oxide layer for these materials is very important. The repassivation behavior of the various materials in saline solution was measured by means of a method described in the literature [3]. The values for the repassivation time, t_e, and for the oxide growth, $t_{0.05}$, are given in Tab. 16.1. As compared to other mate-

Tab. 16.1 Breakdown potential of metallic biomaterials in Hank's solution and repassivation in 0.9% NaCl (pH = 7.4).

	Breakdown potential [2] (V)	**Repasssivation time [4] (msec)**			
		t_e		**$t_{0.05}$**	
		−0.5 V	**+0.5 V**	**−0.5 V**	**+0.5 V**
FeCrNiMo (316L)	0.2–0.3	>72 000	35	≫72 000	>6 000
CoCr (as cast)	+0.42	44.4	36	≫6 000	>6 000
CoNiCr (as wrought)	+0.42	35.5	41	>6 000	5300
Ti-6Al-4V	+2.0	37	41	43.4	45.8
cp-Ti	+2.4	43	44.4	47.4	49
cp-Ta	+2.25	41	40	43	45
cp-Nb	+2.5	47.6	43.1	47	85

rials the oxide growth on cp-Ti and its alloys $t_{0.05}$ is accelerated [4]. In order to avoid mechanical damage of the passive layer, a surface coating with hard layers, e.g. TiN, which also show a favorable fretting behavior, is recommended. Since the highest values of the acceleration tension are achieved by ion implantation, the best reaction and binding (compression residual stresses) can be expected with this procedure. By ion implantation of TiN on wrought vitallium, the corrosion resistance of the material in a 0.17 M saline solution was improved, in addition to the fretting behavior. The pitting potential for the surface treated material amounted to 1.16 V, while the material that had undergone no surface treatment had a potential of 0.83 V [5]. It is essential that these surface layers are dense. If there are any cracks or fissures in the layer, the corrosion rate will be accelerated due to the lower pH value in these crevices. A principle question that arises is the necessity for a surface treatment on materials other than Ti, since implants made of Ti and its alloys are available that can be more easily treated by nitrogen and that moreover, as shown, offer the best corrosion resistance. Experiments dealing with ion implantation of nitrogen in titanium surfaces gave good results with respect to the fretting behavior. Even the fatigue strength of the alloy surface treated by nitrogen ion implantation was reported to have increased because of the residual compression stresses generated by the high acceleration tension of the nitrogen ions [6]. Another possibility for hardening the surface of Ti and its alloys without diminishing the corrosion resistance and the fatigue properties is a pick-up of oxygen by an anodic or thermal oxidation, combined with an increase of the oxygen content in the surface region of the material [7].

16.2.2
Biocompatibility

In the implant/body system various interactions and reactions can lead to the following injuries:

a) By the corrosion process a flow of electrons in the implant metal and a flow of ions in the surrounding tissue is produced. This ion flow in the tissue may disturb the physiological ion movement of the nerve cells.

b) An inorganic reaction of the implant, or especially of primary corrosion products, with a large surface by solution of metal ions in the body fluid and transportation to various organs, where they become concentrated and can produce systemic or hypersensitive effects if the limit of toxicity for a certain metal is exceeded.

c) An organic, direct reaction of the implant or of the primary corrosion products with proteins of the tissue causing an allergy or inflammation.

d) Production of H_2O_2 by inflammatory cells and decomposition of H_2O_2 with the formation of a hydroxyl radical causing an injury of the biological system.

Whether any of these interactions occurs or not depends on the physical, chemical, and thermodynamic properties of the alloy in question. Ti, Ta, and Nb are reported to be biocompatible because they form protective surface layers of semi- or

nonconductive oxides. Because of their isolating effect, these oxides are able to prevent to a great extent a flow of ions. This isolating effect is demonstrated by the dielectric constants ε of the various metal oxides (Tab. 16.2). There are three groups of oxides. While TiO_2 (rutile), Fe_2O_3 and Nb_2O_5 have constants even higher than that of water, Al_2O_3, Cr_2O_3 and Ta_2O_5 have a lower isolating effect and therefore higher conductivity. For Ni- and V-oxides, dielectric constants are not available because of their high conductivity, so interactions with the surrounding tissue can be expected. Because of the isolating effect of an oxide layer with a dielectric constant similar to that of water, implants of Ti are not recognized by the bone or tissue as foreign bodies. Because of their large surface, the primary corrosion products are particularly responsible for inorganic and organic reactions. These corrosion products have a different thermodynamic stability. While the oxides and hydroxides of Al, Cr, Nb, Ta, Ti, and V are stable because of a greater negative heat of formation than that of water, the oxides and hydroxides of Co and Ni are less stable so that an interaction with body fluid may occur. Therefore, the thermodynamically stable corrosion products have a low solubility in body fluid. This is directly demonstrated by the p_K-values (negative logarithm) of the solution product of the primary corrosion products (Tab. 16.2). While Ti-, Ta-, Nb-, and Cr-oxides have p_K-values of >14, i.e. hydrolysis does not feature, Co-, Fe- and

Tab. 16.2 Physical and chemical properties of primary corrosion products of metallic biomaterials.

Primary Corrosion Product		ε	$-\Delta H^{\circ}_{298}$ *(kJ/mole)*	P_K
Al_2O_3		5–10	1675	+14.6
$Al(OH)_3$			916	
CoO			239	−12.6
Cr_2O_3		12	1141	+18.6
CrO_3			595	−1.8
$Cr(OH)_3$			988	
FeO			267	−13.3
Fe_2O_3		100	822	−14
$Fe(OH)_2$		30–38	568	+2.3
MoO_3			712	+3.7
NiO			240	−12.2
$Ni(OH)_2$			538	
NbO			486	
Nb_2O_5		280	1905	>20
Ta_2O_5		12	2090	>20
TiO			518	
TiO_2	anat.	48	935	
	brook.	78		
	rutile	110	943	+18
VO			410	
V_2O_5			1560	+10.3
H_2O		78	273	+14
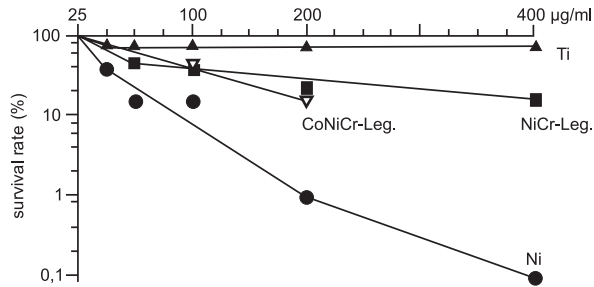
Fig. 16.1 Survival curves of L132 cells in the presence of different metal powder suspensions [9].

Ni-oxides possess negative p_K-values, which are the cause of considerable solubility. Thermodynamically stable, primary corrosion products with a low solubility in body fluid are in a stable equilibrium with only a low reactivity to the proteins of the surrounding tissue. These theoretical considerations have been confirmed by experimental results. In materials with inert or biocompatible behavior, the cells in the vicinity of the implant are still supplied with blood, while those cells in the neighborhood of implants of toxic elements (V, Cu etc.) showed an inflammatory reaction and died [8]. For the determination of the survival rate of L132 cells, different metal powder concentrations were added to the culture medium (Fig. 16.1). After a culture time of 78 hours, cp-Ti and Ti alloys showed a high survival rate of more than 80%, even in the highest powder concentration of 400 µg ml^{-1}. For cp-Ni, the lethal concentration, c_{50}-value (survival rate of cells=50%), amounts to only 20 µg ml^{-1}, for NiCr-alloys and CoNiNr-alloys to 50 and 75 µg ml^{-1}, respectively [9].

16.2.3
Bioadhesion (Osseointegration)

The integration of metallic implants by bone ingrowth was studied for a range of different materials and implant systems. The ingrowth behavior of miniplates made of cp-Ti, of Ti-5Al-2.5Fe, and of stainless steel (316L) was investigated by implantation of these plates to the legs of Hanford minipigs. The miniplates were fixed to the legs of these animals by screws. After removal following an exposure time of 8 weeks, a histological examination was performed by fluorescence microscopy. With all the animals where Ti-plates had been used, new bone formation in close contact with the surface of the screws and plates could be observed. In contrast to these results, new bone formation in the neighborhood of stainless steel plates was lower and, in addition, granulated tissue between the metallic surface and the surrounding bone was found [10]. This granulated tissue at the bone/implant interface has the disadvantage of not being supplied with blood. Therefore, the granulated connective tissue is not able to transfer or sustain high loads, so that a loosening of the implant will take place. This behavior was veri-

fied when the screws were removed. While the detaching moment for cp-titanium screws increased steadily with exposure time, the detaching moment was much lower for stainless steel screws and, furthermore, a maximum was observed after an exposure time of 6 weeks (Fig. 16.2).

Of all possible implant types, dental implants must fulfill the most critical requirements because they are in contact with three different types of tissue. In addition to an attachment to the alveolar bone (hard tissue) and to the periodontal ligament (connective tissue) for bone maintenance, an attachment to the gingiva (epithelium) for sealing purposes is the key problem. The sealing of that part of the implant that enters the oral cavity has to prevent inflammatory reactions caused by bacteria. Because of their good ingrowth behavior, Ti implants show no tendency of a downgrowth of the epithelium. Culturing cells with Ti powder particles showed adhesion of the gingiva to Ti. After just 24 hours, cells adhered to the powder and formed cytoplasmic bridges [11]. By contrast, when stainless steel was used as an implant material, the implant was separated from the tissue. A similar unfavorable behavior was observed after the implantation of CoCr implants in dogs. Histological findings showed that 28 days after implantation, newly formed bone fibrils were observed at the surface of the metal. However, because of a reduction of the newly formed bone caused by resorption, after 56 days the implant bed was enlarged, and after 112 days the CoCr-implant was lost. By
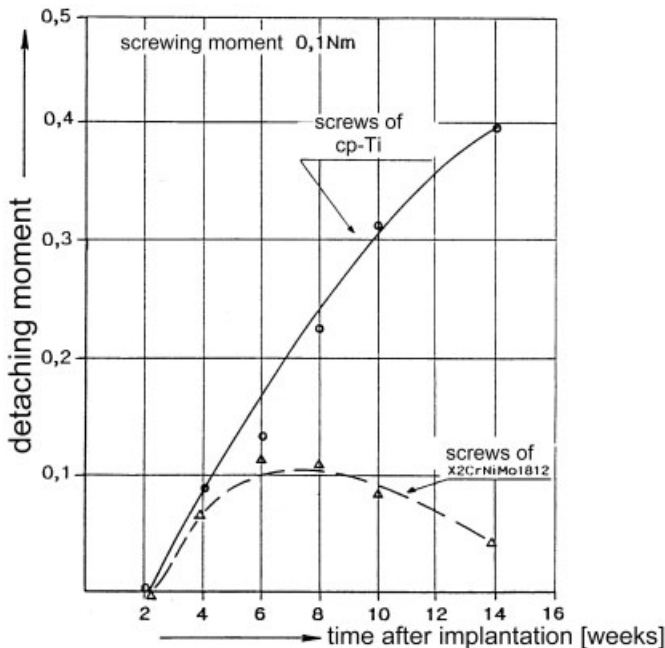
Fig. 16.2 Detaching moment of screws of X2CrNiMo1812 and of cp-Ti after different exposure times (time after implantation) with Hanford minipigs.

Fig. 16.3 Shear strength between plates of Ti with the bone [12].
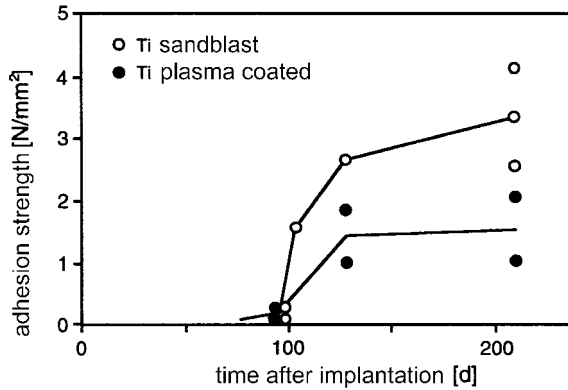
contrast, a vitallium implant, which had been plasma coated with Ti again, had close contact with the bone [12]. In order to guarantee perfect integration, the titanium implant must be unloaded for a period of about 3–4 weeks. An initial implant movement relative to the host bone can result in an attachment by a non-mineralized fibrous connective tissue layer with poor adhesion strength. Perfect osseointegration was observed when the movement of the implant relative to the bone did not exceed 28 μm [13]. After the ingrowth period, loading of the implant is desirable in order to transfer the stress, thus stimulating new bone formation. In vivo tests with Ti-implants to the ulna of monkeys showed that after just 100 days an adhesion strength was reached between Ti and the bone. In addition, an influence of the surface structure was observed (Fig. 16.3) [12]. Another study investigated the influence of the surface roughness of cylinders of Ti and Ti alloys, which had been implanted into the legs of rabbits. The results are shown in Fig. 16.4. A measurable adhesion could be observed only when a certain surface roughness (>22 μm) of the implant was present [14].

The adhesion strength is improved with increasing roughness, and exposure time after implantation also plays an important role. With Ti-6Al-4V implants, the tensile strength required for tearing the cylinders off the bone was more than doubled when the exposure time was increased from 84 to 168 days. After the short exposure time of 84 days, the Ti-5Al-2.5Fe implant already had an adhesion to the bone similar to an implant of bioglass. In contrast to the titanium alloys, the adhesion of the bioglass did not depend on the surface roughness [14]. These results show that growth with the formation of a strong bond of bone and tissue in close contact with Ti and its alloys must have, in addition to a biomechanical, a biochemical character. Furthermore, the enlargement of the implant surface by the surface roughness must be taken into account. Therefore, the tear-off force from the bone must be higher. It is known that in a pH region from 2.9–12.7 the titanium oxide is hydroxylated, i.e. at the surface OH^- groups exist which are able to react chemically with biomolecules [15]. Therefore in the oxide layer mineral ions from the biosystem, e.g. calcium and phosphorous, are incorporated [16, 17].
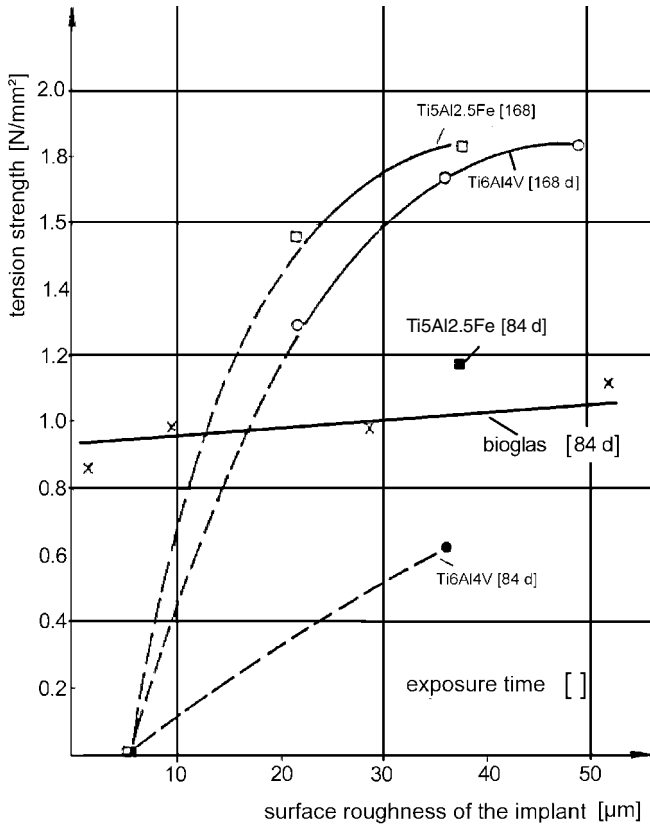
Fig. 16.4 Influence of the surface roughness and the exposure time of implants on the adhesion strength between the implant and the bone with rabbits (according to [14]).

These Ca- and P-deposits are able to bridge the gap between the collagen fibrils and the oxide surface layer with a maximum mechanical stability. Therefore, after tearing the implant off the bone, collagen fibrils were often observed on the surface of the implant [18].

16.2.4
Mechanical Properties, Processability, Availability

Tab. 16.3 shows typical values of the mechanical properties of metallic biomaterials. In addition to a Young's Modulus similar to that of the bone (10–30 GPa), adequate fatigue strength and elongation at fracture, %EL, are required. Ti, Ti-alloys, and niobium have an elastic modulus of about 100–120 GPa. This value is among all metallic biomaterials the closest to that of bone. In fatigue strength, titanium and its alloys are equal or even superior to other cp-materials and alloys. With regard to their bio-

Tab. 16.3 Characteristic mechanical properties of various metallic biomaterials.

	E (GPa)	YS (MPa)	σ_f (MPa)	%EL	$BF \cdot 10^{-3}$ [a]
FeCrNiMo (316L)	210	450	250	40	1.2
CoCr (as cast)	200	500	300	8	1.5
CoNiCr (as wrought)	220	850	500	20	2.3
TiAl6V4	105	900	550	13	5.2
TiAl5Fe2.5	105	900	550	15	5.2
cp-Ti	100	300	200	40	1.8
cp-Ta	200	300	200	40	1.3
cp-Nb	120	250	150	70	1.3

a) $BF = $ Biofunctionality $ = \sigma_f/E$

functionality value, which is given by the quotient of the fatigue strength and Young's Modulus, titanium and its alloys demonstrate their superiority to other biomaterials. In the calculation of the biofunctionality value, the great importance of Young's Modulus is taken into account. The lower Young's Modulus, the better the functional load on the implant can be transmitted whereby the formation of new bone is stimulated. A further decrease of Young's Modulus can be achieved by the use of porous implants or implants with a porous surface layer. Since titanium alloys are known to be notch sensitive, the fatigue strength of implants with porous surface layers will be diminished. From the different production procedures of these surface layers (plasma spraying, sintering and diffusion bonding) the best fatigue strength, which is about 10% lower than the fatigue strength of the bulk materials, was achieved by plasma spraying [20].

All current processing procedures are also possible for Ti and its alloys and are used for the fabrication of implants. While, for example, the shafts of hip prostheses are produced by forging or by CNC machining, the cups of the prostheses are often fabricated by precision casting via the lost-wax process.

Concerning the costs of semi-products, Ti and its alloys belong to the same group as stainless steel, while CoCr alloys, niobium, and, especially, tantalum are more expensive. A consideration of the premises of the foregoing sections 16.2.1–16.2.4 verifies that titanium and its alloys are the metallic biomaterials of choice because they possess the best corrosion resistance, biocompatibility, osseointegration, and biofunctionality. The processability of Ti and its alloys is unrestricted and, as for the economic aspects, the volume price (€ m^{-3}) is lower than that of CoCr-alloys, niobium, and tantalum.

16.3
Examples of Tailor-made Ti-based Composites

For special applications, biomaterials can be tailor-made in the form of composites wherever a single material is not able to fulfill the various requirements. In most cases, a functional surface layer with, for example, special mechanical, physical or biological properties can be used on a structural material – titanium and its alloys preferred. In order to produce such composite materials, various properties such as the difference in thermal expansion coefficients of the structural and functional materials must be considered. A change in the functional properties of the surface layers and/or a loss of the mechanical properties of the structural material should be avoided. In the following, four classes of composites based on titanium materials are described:

- Ti with a structured surface with special mechanical properties (isoelastic implants)
- Ti/ceramic composites with special biological properties (improved osseointegration)
- Ti/ceramic composites with special physical properties (heart pacemaker leads)
- Ti/ceramic composites with improved wear resistance

16.3.1
Structured Surfaces on Ti Materials with Special Mechanical Properties

Surface structuring is possible in the macroscopic, microscopic, and in the submicroscopic (nano) region. The surface structure of an implant has a significant influence on its anchorage and on the strength of adhesion to the tissue. Since strength is defined as the ratio of the loading force to the surface area on which the force is exerted, the load under service conditions can be higher the larger the surface is. From this simple consideration it is clear that a smooth implant surface will have a small area of contact to the tissue and, therefore, a lower adhesion strength as compared to a structured surface that may, in addition, provide mechanical anchoring of the implant by means of bone ingrowth. With increasing roughness the adhesion strength is enhanced [14]. From the point of view of applied mechanics, the ingrowth of the bone into the surface cavities has a favorable influence. The shear stress that is generated by the functional loads on the implant at the interface with the bone is decreased because, like the thread of a screw, the functional load causes, in addition to the normal stress perpendicular to the inclined area, only a low shear stress acting in the inclined area. Beside the favorable influence on anchorage, there is a further advantage of the surface structure. The ingrown bone, which under loading will be subjected to strain, produces calcium [21] and, in addition, the load stimulates new bone formation. This phenomenon will be improved by increasing load transfer, or by decreasing the stiffness of the implant. The stiffness, S, can be described by the product of the moment of inertia, I, and Young's modulus, E (Eqn. 16.1):

$$S = E \cdot I \qquad \text{(eqn. 16.1)}$$

Since an implant's moment of inertia is in most cases given by the geometry of the "landscape", in order to decrease the stiffness of the implant towards that of the bone (isoelastic behavior), the Young's modulus value for the implant material must be decreased. Because of the value of Young's modulus for Ti and its alloys, which amounts to only about 50% that of CoCr alloys and stainless steel, it is possible to produce the required stiffness in the porous surface layer at a lower porosity than in other materials. Fig. 16.5 shows Young's modulus of the porous material, E_p, as a function of the porosity, p, which is calculated by Eqn. 16.2 [22]:

$$E_p = E_o(1 - 1.21p^{2/3}) \qquad \text{(eqn. 16.2)}$$

where E_o is Young's modulus for the bulk material. While, with the near-β Ti alloy Ti-30Ta, a porosity of about 20% is sufficient to obtain the value of the cortical bone, alumina, the CoCr alloys and stainless steels, even with porosities of 50%, do not achieve an isoelastic behavior. The titanium alloy Ti-30Ta was originally developed for direct diffusion welding with alumina for the production of dental implants [23]. Due to a high portion of the β phase, this alloy has a decreased Young's modulus (E=80 GPa) as compared to cp-titanium. Similar behavior is observed with β Ti alloys that have been developed for use as biomaterials [24-26]. Tab. 16.5 gives a survey of the properties of different near-β and β alloys. With the alloy Ti-30Ta, a martensitic structure, which is produced by quenching from the β
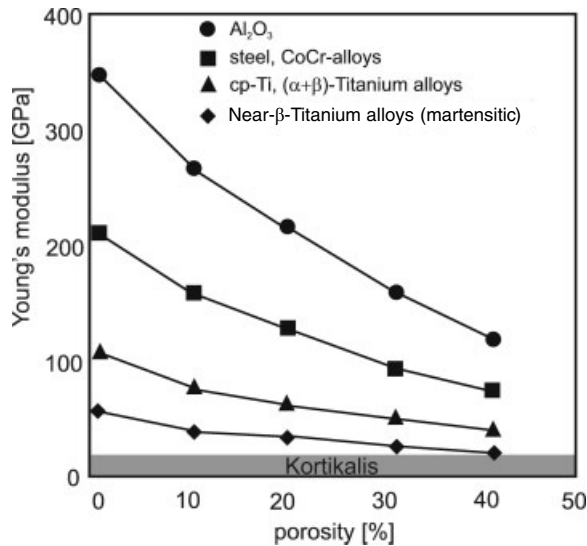
Fig. 16.5 Influence of the porosity on Young's Modulus of Al_2O_3, of steel and CoCr-alloys respectively, of cp-Ti and α+β Ti alloys respectively and of a near-β alloy Ti-30Ta (martensitic).

Tab. 16.4 Mechanical properties of Ti and Ti alloys.

Type	E (GPa)	YS (MPa)	UTS (MPa)	%EL	%RA
α cp-Ti (grade 2)	105–110	250	390–540	22	30
α + β Ti-6Al-4V	100–110	830–1070	920–1140	8	25
Ti-6Al-7Nb	110	810–1010	870–1016	7–16	24–55
Ti-5Al-2.5Fe	110–115	780	860	8	25
Ti-6Mn	110	1060	1095	11	26
β or Ti-12Mo-6Zr-2Fe	74–85	1000–1060	1060–1100	18–22	64–73
β-near Ti-13Nb-13Zr	64–83	435–905	705–1035	11–29	28–74
Ti-30Nb	63–80	500	700	20	60
Ti-30Ta	60–70	590	740	28	58

phase field, shows a further decrease in Young's modulus (60 GPa). Nevertheless, the reduction of the implant stiffness by means of a porous sintered surface layer results in a decrease in the mechanical properties, especially in fatigue strength because titanium materials are known for their notch sensitivity. Because of the poor fatigue properties of the transformed β microstructure, production of the porous surface layer by sintering in the β phase field should be avoided. During the production of surface layers of the alloy Ti-30Nb, (similar to Ti-30Ta) on the surface of bulk Ti-5Al-2.5Fe, an optimum fatigue strength can be obtained, resulting in a decrease of only 20% as compared to that of the bulk material. This is achieved by optimizing the sintering parameters, cold pressure, sintering temperature and time, grain size PGF, thickness of the surface layer and hydrogen content of the HDH powder C_H. Fig. 16.6 shows schematically the influence of the various parameters [27].
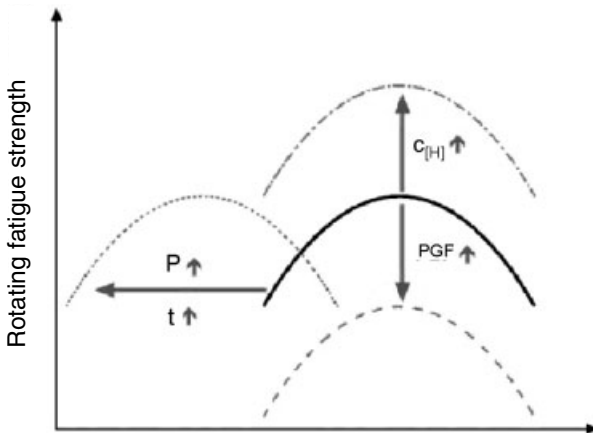
Fig. 16.6 Influence of the sintering temperature and time, of the hydrogen content and the powder grain size PGF on the fatigue strength of Ti materials with a porous surface layer (schematic).

On the other hand, since under service conditions dental implants are subjected to relatively low loads, the isoelastic concept is easily realized. In addition to the porosity itself, the pore size also plays an important role. It must be sufficiently large (approx. 50–100 µm) to allow the ingrowth of the bone [28]. Besides porous sintered implants, another type of implant with a special surface structure, which decreases the implant stiffness and imitates the natural anchorage of teeth, has been developed. A spiral of a cp-Ti wire was diffusion welded on a core made of Ti-30Ta. The ingrowth of the bone into the spiral's loops initiates the natural suspension by transmitting a damping capacity to the implant similar to the Sharpey fibers of the tooth. The functionality of both implant types (porous surface layer and loops) was determined in vitro as well as in vivo. For the in vitro experiments, an artificial jaw was constructed from a plastic material with the same elastic properties and geometry as a human jaw (inner part corresponding to the spongy bone, $E = 3$ GPa; outer part corresponding to the cortical bone, $E = 20$ GPa). The implants were inserted in the model and loaded in a testing machine. The strain and, therefore, the stresses were measured by means of strain gauges. In order to obtain a result concerning the influence of the implant stiffness, a systematic change in Young's modulus was studied by a comparison of implants consisting of various materials (Fig. 16.7 and 16.8). The Ti implants with the different surface structures showed an elasticity similar to that of the bone. For in vivo tests, both types of implants were inserted in the jaw of adult fox hounds. After a healing period of three months, the implants were provided with a dental prosthesis and functionally loaded for a period of six months. The ensuing histological investigation demonstrated a good interlocking of the bone and close bone contact to the implant surface [29].

As already mentioned, dental implants have to fulfill different requirements (close contact with the hard as well as to the soft tissue). Especially the soft tissue, the gingiva, must grow in close contact with the implant in order to avoid the mi-
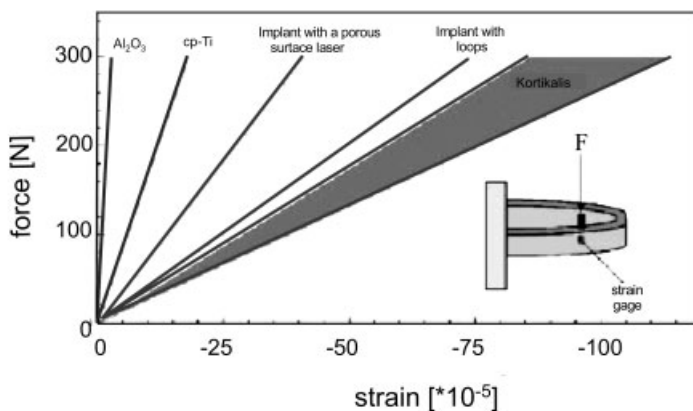
Fig. 16.7 Influence of the functional loading of implants of a differing elasticity on the strain in an artificial jaw.
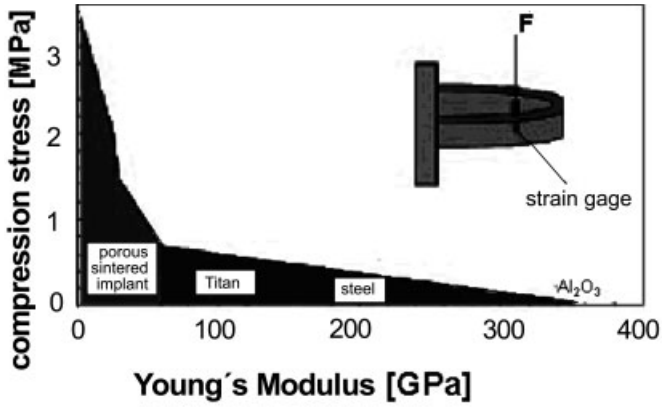
Fig. 16.8 Compression stresses in an artificial jaw under a functional load for various implants.
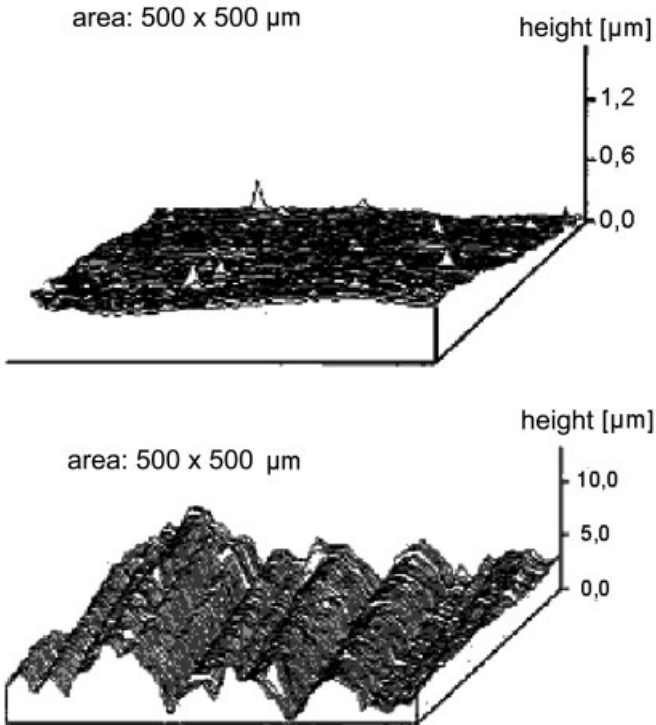
Fig. 16.9 Surface structure of polished (a) and roughened (b) samples of cp-Ti.
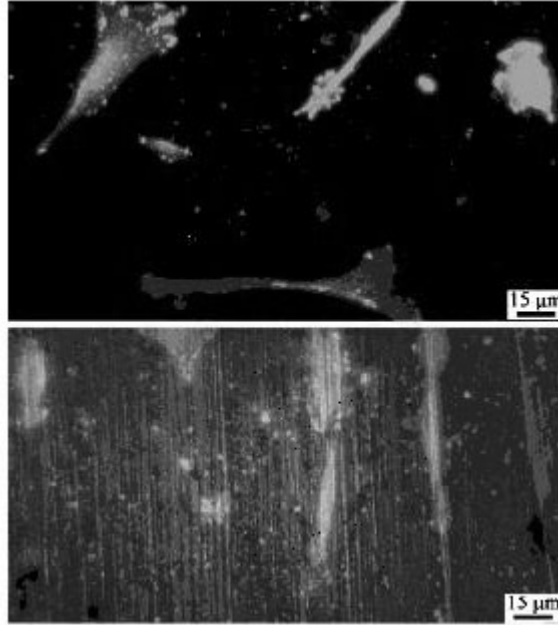
Fig. 16.10 Fibroblasts after cultivation on polished (a) and roughened (b) samples of cp-Ti.

gration of bacteria from the oral cavity to the implant bed. An optimization of the surface structure may help to solve this problem. In the microscopic region, the surface of cp-Ti has been structured by grinding with a different surface roughness (Fig. 16.9). Primary gingiva cells have been cultured on these surfaces. It was observed that the cells assumed an orientation corresponding to that of the surface structure. By contrast, on a polished surface the cells had a rounder shape and no significant orientation (Fig. 16.10). At the edges of the surface structure, the orientated cells formed more focal contacts with the substrate while increasing their adhesion strength. The orientation of the cells increased with increasing surface roughness (Fig. 16.11) [30].

16.3.2
Ti/Ceramic Composites with Special Biological Properties

Surface structured implants of titanium materials possess a strength of adhesion to the bone because the latter grows in close contact with implants and penetrates cavities and grooves on the implant surface. In order to provide a high shear strength between the bone and the implant during the healing period of about 100 days, perceptible relative implant/bone motion ($> 28 \, \mu m$) [13] must be avoided. Using hydroxyapatite (HA), with its osteoconductive properties, can decrease the healing period to about 20 days, and the bone is stimulated to bridge
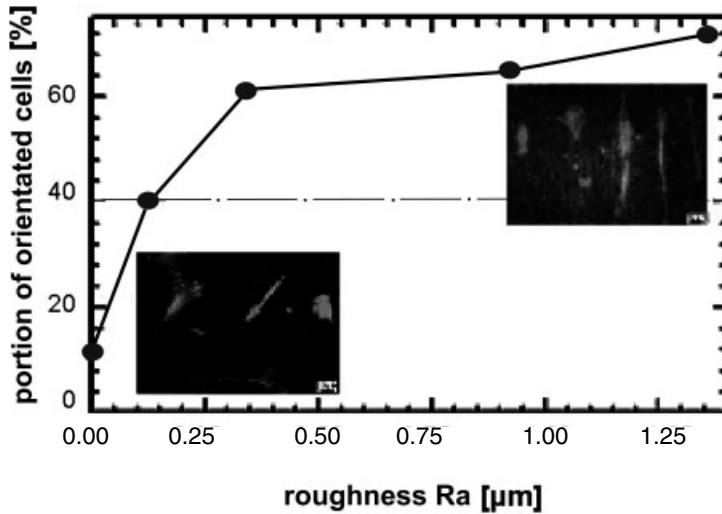
Fig. 16.11 Influence of the surface roughness on the orientation of fibroblasts.

the gap to the implant by the formation of a chemical bonding to the HA [31]. Since HA has inadequate mechanical properties under tensile stresses, it is of advantage only if it is used as a coating on a structural metallic material, i.e. a titanium alloy. Because of this fact, the problem of implant anchorage is shifted to the metal/ceramic interface. Nevertheless, a dense HA layer with a high strength of adhesion to the metallic substrate is required. This adhesion strength can be achieved only through chemical bonding by means of diffusion annealing. The difficulty of producing a dense HA layer on Ti arises from the mismatch of the thermal expansion coefficients, α, of both materials. Whereby, according to Eqn. 16.3, high residual stresses σ_{RS} are obtained, which produce pre-damage in the ceramic:

$$\sigma_{RS} = \overline{E}|(\alpha_M - \alpha_C)|\Delta T \qquad (\text{eqn. } 16.3)$$

$\overline{E}$ = Young's modulus of the interlayer metal/ceramic
$\alpha_{M,C}$ = thermal expansion coefficient of the metal and the ceramic respectively
ΔT = temperature difference annealing temperature/RT

Therefore, in order to overcome this problem, the aim was to develop a titanium alloy with a thermal expansion coefficient adapted to that of HA. Fig. 16.12 gives the results of the measurement of the thermal expansion coefficients of various Ti alloys compared with those of cp-Ti and HA. Alloys containing manganese (6–8 wt%; Mn is an important tracer element in the human body) as well as a Ti-30Nb alloy (the latter at T <700 °C) show a reduced misfit of the thermal expansion coefficients between the metallic and the ceramic material. Coating tests by means of sintering HA on cp-Ti and on the alloy Ti-6Mn, which was adapted in the thermal
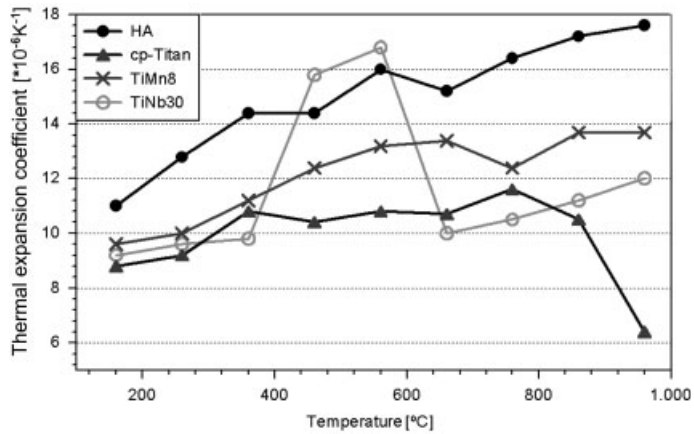
Fig. 16.12 Thermal expansion coefficients of Ti alloys as a function of temperature as compared with cp-Ti and HA.

expansion coefficient to HA, showed more than twice the shear strength of the composite Ti-6Mn/HA as compared to cp-Ti/HA because of the formation of cracks during cooling from the sintering temperature (Fig. 16.13) [32]. However, in accordance with theoretical considerations, the HA layer should be as thin as possible because, in the case of implants such as hip prostheses that are loaded by bending, the maximum bending strength occurs in the surface fiber that consists of HA. Because of this fact, especially thick HA layers risk being damaged. The sol-gel procedure was chosen as a coating method to provide the required thin layer. In accordance with theoretical considerations, it is clear that thin layers must have an advantage compared to thick layers due to better load bearing since during bending the maximum tensile stress appears in the surface fiber consisting of HA. The metallic samples were dip coated with a mixture of the starting materials CaO and triethylphosphate $(PO(OC_2H_5)_3)$. Dip coating followed by drying (1 h at 130 °C) produced a gel. Finally, the coating was developed by annealing at 600–800 °C (5–15 min). The HA produced
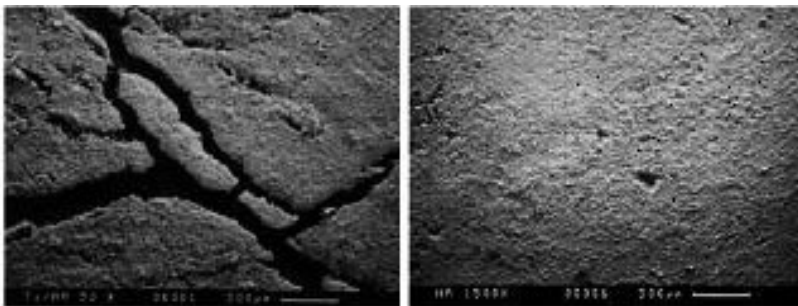
Fig. 16.13 HA coating produced by sintering on cp-Ti (a) and on Ti-6Mn (b).
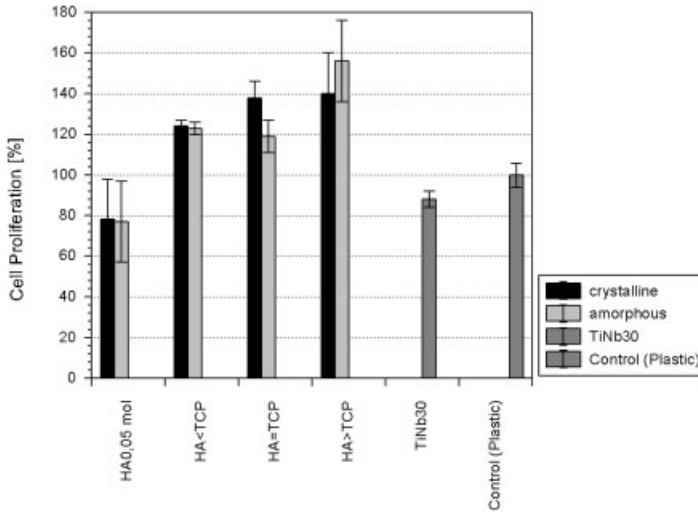
Fig. 16.14 Influence of the Ca:P ratio of HA on the cell proliferation.

at 600 °C was observed to be more amorphous than the coating produced at 800 °C. The adhesion strength of the HA layers was >70 MPa (value of the glue used for the bonding of the counterpart sample for the shear strength test) [32]. Due to the thin sol-gel HA layers, it is possible to maintain a surface structure of the metallic materials that is able to support the deposition of bone cells (cell guidance). Even the pores of the porous surface layers described above can be clad while maintaining the open porosity. A further advantage of the sol-gel process is the possibility to change the Ca:P ratio within close limits. The interaction of HA layers with differing Ca contents with cells (L132) was studied in proliferation tests and compared with a standard of plastic. The percentage of proliferation was calculated as the ratio to the number of initially cultured cells. Fig. 16.14 shows the results. There is no significant difference between the amorphous and the crystalline coatings. Nevertheless, a certain content of tricalciumphosphate seems to stimulate cell proliferation [33].

16.3.3
Ti/Ceramic Composites with Special Physical Properties

For artificial stimulation of the heart, an electric field is required that is determined by the electrical potential and the current of the pacing electrode. In the electrode itself, the current is carried by the electrons, whereas outside the ions are the main contributors to the current distribution. The coupling takes place at the electrode surface by the formation of an electrical double layer. The properties of the electrode/tissue interface are of major importance for the pacing leads because they must serve two important functions. They must

- conduct the electrical pulses from the pacemaker to the heart
- sense intracardiac signals and transmit them to the pulse generator.

Pacing and sensing performance may be improved by adjusting the electrochemical and physical parameters to the interface without disturbing the biological equilibrium. For long-term stability it is essential to avoid chemical reactions that irreversibly decrease the signal amplitude and increase the threshold. The behavior of the phase boundary can be explained by the structure of the double layer: a simplified equivalent circuit of the electrode/myocardium interface demonstrates that the potential distribution is determined by the Helmholtz capacity and the Faraday impedance. If the double layer capacity is large, the pacing losses will be low and the amplitudes of the depolarization signals will be high. This behavior explains in principal the advantage of porous electrodes as compared with smooth electrodes. The surface influence of the double layer capacity can be qualitatively described by Eqn. 16.4:

$$C = \varepsilon \cdot \varepsilon_0 \cdot \frac{A}{d} \qquad\qquad (eqn.\ 16.4)$$

where C=capacity, ε=dielectric constant of the electrolyte, ε_0=dielectric constant of the vacuum, A=surface area, and d=thickness of the layer. From this relation it is clear that an increase of the surface A produces the observed favorable behavior of the porous Ti electrodes. The various surface layers (e.g. TiN) produced by PVD are able to improve the electrical conductivity of the electrode surface (Tab. 16.5). TiN is also known to have a good biocompatibility, similar to that of TiO_2 [34, 35].

According to these considerations, porous sintered electrodes of titanium with conductive surface layers can have the following advantages:

- safe fixation to the myocardium due to ingrowth
- long-term stability of the electrode due to the corrosion resistance and biocompatibility of titanium materials
- relatively high electrical conductivity due to surface layers
- high capacity.

The physical properties, high electrical conductivity and high capacity, guarantee low losses and consequently a longer battery lifetime. For the sintering of the hemispherical shape of the electrode tip, HDH powder cp-Ti was used. Simultaneous with the sintering operation, a contact supplying tube of cp-Ti was diffusion bonded to the head of the electrode tip. After sintering at 950 °C, the average porosity of the electrode amounted to about 70%, the pore size to about 50 µm. An alternative as a conductive ceramic surface layer could be TiB_2 that, compared to TiN (Tab. 16.5), has an even lower specific electrical resistance. TiB_2 coatings on Ti electrodes can easily be realized by a solid-state reaction (electrodes embedded in oxygen-free boron powder). The results of the impedance measurements of TiB_2 coated porous Ti electrodes are given in Fig. 16.15. Compared to TiN coated samples, there is no significant difference in the results. Both layer

Tab. 16.5 Heat of formation, ΔH, and electrical resistance of various layers on heart pacemaker leads as compared to cp-Ti.

Material	Heat of Formation $-\Delta H$ (kJ mol^{-1})	Electric Resistance ρ ($\mu\Omega cm$)
Ti	–	41.8
TiO$_2$	890	10^{16}
TiN	309	25
TiB$_2$	320	14.4
Ir	–	5.3
IrO$_2$	189	49
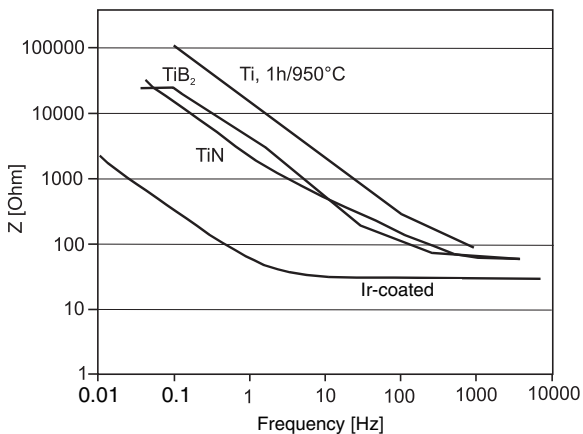
Fig. 16.15 Impedance of heart pacemaker leads of cp-Ti with different coatings: 1 – without coating, 2 – TiB$_2$ coating, 3 – TiN-coating, 4 – Ir-coating.

types (TiN and TiB$_2$) have the crucial disadvantage of a low thermodynamic stability as compared with TiO$_2$ (Tab. 16.5). Therefore, if anodic loading takes place, formation of the electroactive oxides, which have the disadvantage of a low electrical conductivity (Tab. 16.5), is inevitable. This problem can be overcome by the use of iridium coatings [36], which provide a metallic layer and an oxide layer (after anodic loading) with high electrical conductivity and high impedance (Fig. 16.15). The Ir layers can be produced by PVD and CVD. For the latter process, metal organic precursors such as (CH$_3$COCHCOCH$_3$) Ir can also be used, which decomposes at moderate temperatures under deposition of Ir [35, 36].

16.3.4

Ti/Ceramic Composite with Improved Wear Resistance

A disadvantage of Ti and its alloys is the poor wear resistance, which is observed with articulating devices such as knee joints or the heads of hip prostheses [37]. Some proposed solutions recommend hard layers consisting of Ti-nitrides, Ti-oxynitrides or Ti-oxides, or artificial diamond, which may be produced by CVD, PVD, or ion implantation [38–42]. A simple method has been reported for the surface hardening of heads of hip prostheses. This method is performed by induction heating in atmosphere whereby pick-up of oxygen in the surface layer takes place at, for example, 900 °C for 40 sec. After quenching in paraffin oil, the thickness of the oxide layer amounted to about 1–3 μm. After a measurement of the wear resistance in 0.9% NaCl at 37 °C, Ti-5Al-2.5Fe heads showed similar results compared to Al_2O_3 heads. Fig. 16.16 demonstrates the friction moments as a function of the applied force [38]. Nevertheless, these wear layers have some disadvantages, e.g. their low thickness (μm-range) combined with a relatively rapid abrasion, or the presence of residual tensile stresses in the layer/substrate region, that induces damage and a diminished adhesion strength, are induced [43]. On the other hand, because of poor adhesion strength, a break in the layer may occur ("egg-shell" effect). A further disadvantage of these layers is their relatively expensive production, so that optimization of wear resistant titanium materials has not yet been realized.

A possible solution to the problem could be the development of a Ti-based metal matrix composite reinforced with ceramic particles that, similar to carbides in cast CoCr alloys, improve the wear resistance. In most cases, these so-called cermets are produced by means of powder metallurgy. The powder metallurgical route includes blending of metal and inert ceramic powders, cold isostatic pressing (CIP), and vacuum sintering of the powder mixture or hot isostatic pressing (HIP) [44]. The processes have disadvantages that limit the function of the products. Thermodynamically stable ceramics of refractory metals such as oxides, borides, nitrides, and carbides do not show any chemical or metallurgical interaction with the metal matrix even at high temperatures. Thus, the particles are present in an incoherent manner with regard to the matrix. On the other hand, the thermal expansion coefficient of the reinforcements and the metal matrix often differ drastically. This is advantageous if the expansion coefficient of the metal matrix exceeds that of the ceramic, because this results in compression stresses on the brittle particles. An expansion coefficient of the ceramic higher than that of the matrix leads to undesirable tensile stresses at the interface. If these stresses are not reduced by plastic flow of the ductile matrix, they cause the formation and propagation of cracks originating from the interface. Binding problems between the matrix and the ceramic particles also often arise from a contamination of the particle surface from adsorbates. Thermodynamically stable ceramic particles that are precipitated in situ during the production process are thought to possess a better bonding to the matrix because their surfaces are free of contamination and the expansion coefficient of the matrix can be adapted to that of the reinforce-

ment. Titanium materials reinforced by ceramic particles have mainly been developed for improved high temperature properties, e.g. creep resistance. Many investigations deal with fiber or particle reinforcement with SiC [45]. Also, the use of TiB and TiB_2 as a ceramic in a Ti-matrix has been reported. By means of the powder metallurgical route, Ti-, TiB_2-, FeMo- and AlV-powders were mixed in order to produce an alloy, Ti-7Mo-7Fe-2.5Al-1.5V, with an increased creep resistance containing different fractions of TiB [46]. Also, the intermetallic compound Ti_3Al was improved with respect to its creep resistance by adding TiB. For the production of samples, powder mixtures of cp-Ti, NbAl and TiB_2 were prepared. After sintering, the alloy composition was Ti-14Al-11Nb with 10 wt.% TiB [47].

A prerequisite for an in situ reaction is a reactive metal with a high affinity to the elements forming the ceramic phase (boron, carbon, nitrogen, oxygen). The refractory metals Ti, Nb, Ta, and Zr are suitable for forming thermodynamically stable borides because of their high affinity to B. If they are combined with elemental B or a thermodynamically weaker B-containing compound, the refractory borides will be formed in situ. The standard enthalpy of formation, (293 K), of CoB, Cr_2B, FeB, and NiB compared with the standard enthalpy of the refractory metal borides (Tab. 16.6), suggests these borides are products. The value of the Gibbs free energy, ΔG, determines the exothermic or endothermic course of reaction. ΔG is defined as (Eqn. 16.5):

$$\Delta G = \Delta H - T\Delta S \qquad (eqn. 16.5)$$

A reaction can take place spontaneously only if ΔG is less than zero, while increasingly negative values of ΔG improve the possibility of a self-propagating reac-
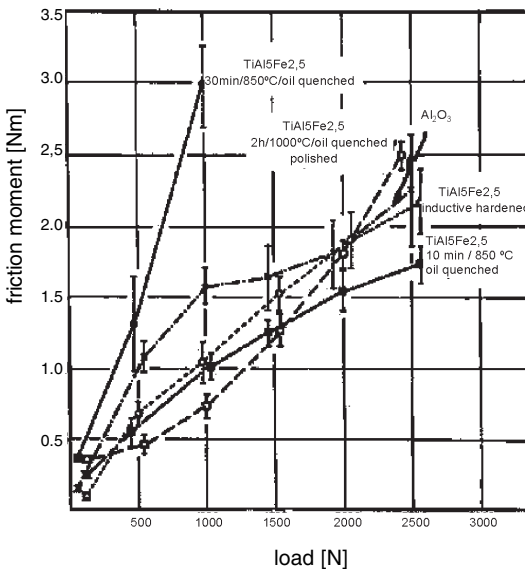
Fig. 16.16 Influence of the load on the friction moment of Ti-5Al-2.5Fe and of Al_2O_3 heads during wear tests to UHMW-polyethylene cups.

tion type. Under conditions of stoichiometric composition and complete transformation of the products, the reaction of Ti and FeB occurs as follows (Eqn. 16.6)

$$2Ti + FeB \rightarrow TiB + TiFe \qquad \text{(eqn. 16.6)}$$

The Gibbs free energy ΔG is related to the equilibrium constant K by Eqn. 16.7

$$\Delta G = -RT \ln K \qquad \text{(eqn. 16.7)}$$

The equilibrium constant K is defined by the law of mass action (Eqn. 16.8)

$$K = \frac{a_{TiB} \cdot a_{TiFe}}{a_{Ti}^2 \cdot a_{FeB}} \qquad \text{(eqn. 16.8)}$$

or

$$\ln K = \Sigma v_i \ln K_{f,i} \qquad \text{(eqn. 16.9)}$$

In the case of high titanium activity, Eqn. 16.8 yields a displacement of the equilibrium towards the products. The energies of the compounds as a function of temperature are shown in Fig. 16.17. The higher negative Gibbs free energy of TiB relative to FeB leads to the reduction of FeB followed by the formation of TiB. Free iron atoms react with titanium atoms to form the intermetallic compound TiFe.

Thermodynamic considerations do not provide information about the reaction velocity. In the case of a diffusion controlled reaction (for example the blended powder metallurgical route), the velocity depends strongly on the temperature and the grain size of the powder. In practical applications, the cermets should have an excess of the metal matrix to guarantee sufficient ductility. In this study the titanium content of all alloys examined exceeds 70 wt.%. The formation of TiB and TiFe takes place until FeB is completely consumed under equilibrium conditions.

Metal matrix composites were produced from grade 2 cp-titanium and Fe-B (18.6 wt.% B). Tab. 16.7 shows the chemical composition of the feedstock.

Tab. 16.6 Standard enthalpies of formation, ΔH_f^0 (293 K), of various metal borides.

	ΔH_f^0 (kJ mol^{-1})
CoB	–85.5
Cr$_2$B	–123.5
FeB	–64.5
NiB	–60
NbB$_2$	–228
TaB$_2$	–190
TiB	–150
TiB$_2$	–294.5
ZrB$_2$	–293
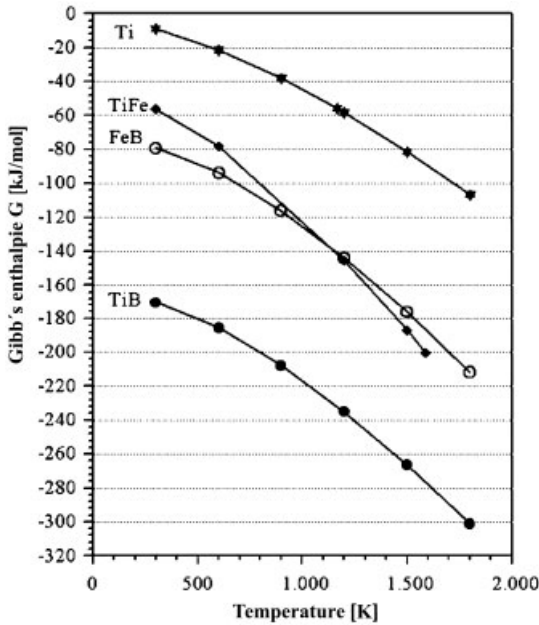
Tab. 16.7 Chemical composition of Ti grade 2 and FeB (wt.%).

Ti grade 2

Fe	O	N	C	H	Ti
0.15	0.11	0.04	0.05	0.007	Balance

Ferrobor

B	Al	C	Mn	Si	other	Fe
18.6	0.6	0.02	0.1	0.5	0.2	Balance

Tab. 16.8 summarizes the composition range of the Ti-Fe-B-alloys. The Ti-16.3Fe-3.7B alloy was chosen to examine the kinetics as a function of the production process. Samples were prepared by arc melting and powder metallurgical means. Arc melting was carried out in an electric arc furnace in combination with a water-cooled copper crucible ("skull melting"). The in-situ formation of TiB takes place during solidification from the melt (cooling rate $>600 \mathrm{~K~min}^{-1}$). One set of samples was annealed for 2 and 12 h at 550 °C in a vacuum of 10^{-4} Pa. In addition, samples were produced by centrifugal casting. After skull melting the melt was poured into a rotating copper mold. Both melting and casting were preformed in an argon atmosphere.

Powder metallurgical samples were prepared by mixing Ti and FeB powders ($<90 \mathrm{~\mu m}$) in a ball mill and by uniaxial pressing at 700 MPa. The samples were cylindrical in shape with a diameter of 10 mm and a length of 5 mm. The sinter-

Tab. 16.8 Chemical composition of alloys in the Ti-Fe-B system (wt.%).

	Ti	Fe	B
Ti + 5% FeB	95	4.1	0.9
Ti + 10% FeB	90	8.1	1.9
Ti + 15% FeB	85	12.2	2.8
Ti + 20% FeB	80	16.3	3.7
Ti + 25% FeB	75	20.4	4.6
Ti + 30% FeB	70	24.4	5.6

ing temperature varied from 850 to 1050 °C, with sintering times from 3 to 24 h. The sintering process was followed by furnace cooling (cooling rate 5 K min^{-1}). Additionally, some samples were hot isostatically pressed for 3 h at 950 °C and under 1000 bar.

The characterization of the phases present was performed by optical microscopy, scanning electron microscopy (SEM), and energy dispersive analysis (EDX). Transmission Mössbauer spectrometry was carried out at room temperature using a ^{57}Co/Rh-source. X-Ray diffraction (XRD) powder patterns (Cr K$_\alpha$) were used to identify all crystalline phases present in the samples. Pin-on-disc-tests were carried out at room temperature in air without a lubricant. The relative atmospheric humidity was 20–30%. For this experimental arrangement, the cermet was machined to a cylindrical disc with a polished surface. The wear couple was a 100Cr6 steel ball. A force of 2 N, a sliding distance of 1000 m, and a sliding speed of 0.1 m s^{-1} were selected for the rubbing condition. The wear rate is defined as the quotient of the wear volume, the force, and the sliding distance. The wear volume can be calculated from the cross section and the circumference of the wear track. The cross section was measured with a profilometer type machine.

Fig. 16.18 shows pieces that were produced by centrifugal casting of the alloy Ti-12.2Fe-2.8B. Fig. 16.19 demonstrates the microstructure of this alloy in the as-cast condition. The titanium borides, which are responsible for the wear resis-

Fig. 16.18 Examples for pieces of Ti-12.2Fe-2.8B produced by means of centrifugal casting.
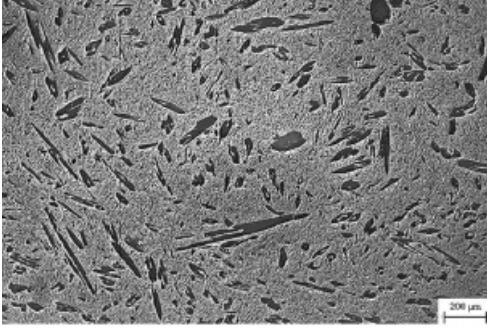
Fig. 16.19 Microstructure of centrifugally cast Ti-12.2Fe-2.8B.

tance, appear as plate-like precipitates or as round particles, if the plates are cut perpendicular to their longitudinal axes. Fig. 16.20 shows the results of the abrasion tests performed by the pin-on-disc test. The wear rate increases from the reference test sample of cp-Ti to samples with a content of 10% FeB. Samples containing 15 to 20% FeB in the as-hipped and as-cast condition, respectively, have a high wear resistance. Fig. 16.21 shows the microstructure of the various alloys after the abrasion test. The reference sample of cp-Ti suffered a high cold deformation whereby a relatively favorable abrasion behavior was achieved. With samples containing <10% FeB, this cold deformation could not be observed. TiB particles were ejected from the matrix, diminishing the wear resistance. In contrast, with a FeB content of >10% the alloys are extremely wear resistant because the shape and size of the borides provide an effective protection of the surface. Since an abrasive wear of the counterpart (100 Cr6) takes place, the metal matrix composite has total wear resistance.
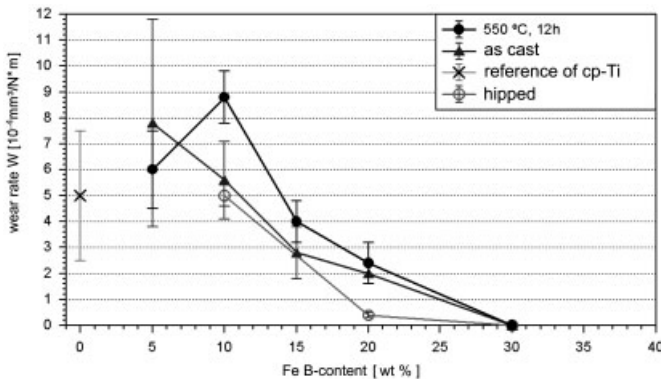
Fig. 16.20 Wear rates of pin-on-disc tests of Ti-Fe-B alloys as compared to cp-Ti.
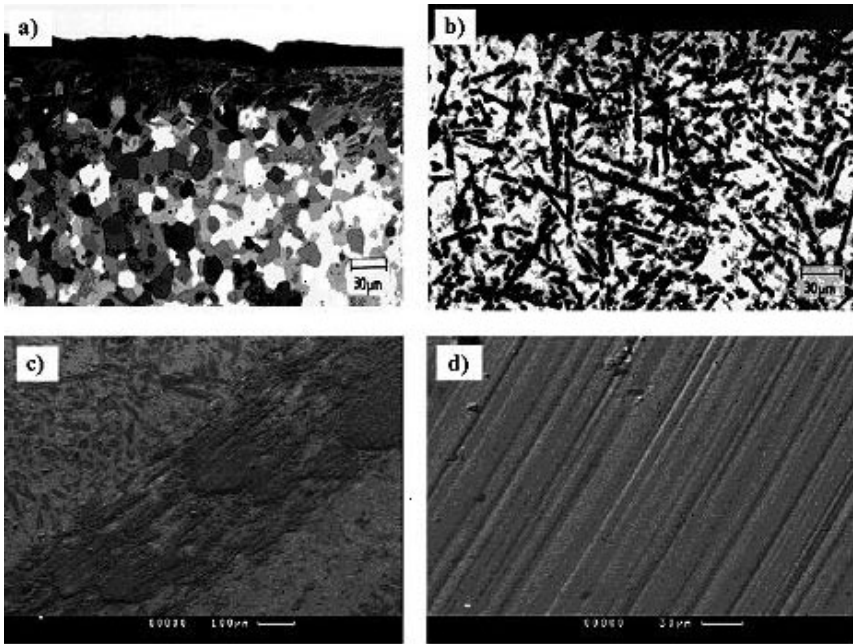
Fig. 16.21 Microstructure of the samples of the pin-on-disc test. a) Reference cp-Ti, b) FeB content <10 wt.%, c) FeB content >10 wt.%, counterpart 100Cr6.

16.4
Referenced Literature and Further Reading

1 ZITTER, H. PLENK JR.: The Electromechanical Behaviour of Metallic Implant Materials as an Indicator of their Biocompatibility, J. Biomed. Mater. Res. **21** (1987) 881

2 A.C. FRAKER, A.W. RUFF, P. SUNG, A.C. VAN ORDEN, K.M. SPECK: Surface Preparation and Corrosion Behaviour of Titanium Alloys for Surgical Implants. Ti '80 Science and Techn., Plenum Press (1980) 2447

3 H.J. RÄTZER-SCHEIBE, H. BUHL: Repassivation of Titanium and Titanium Alloys. Titanium Science and Technology AIME (1984) 2641

4 J. BREME, H.J. SCHMID: Implant System Based on Bioinert Metals, in G. HEIMKE: Oseo Integrated Implants. CRC Press, New York (1989) 31

5 P.A. HIGHAM: Ion Implantation as a Tool for Improving the Properties of Orthopedic Alloys. Proc. Conf. Biomed. Met., Boston, 1985 (1986) 253

6 J.M. WILLIAMS, R.A. CUBHANAN: Ion Implantation of Surgical TiAl6V4 Alloy. Mater. Sci. Eng. **69** (1985) 237

7 U. ZWICKER, J. BREME: Friction Behaviour of Oxidized Ti.5%Al-2.5%Fe Surface Layers on Implant Material. J. Less Common Met. **100** (1984) 371

8 S.G. STEINEMANN, S.M. PERREN: Titanium as Metallic Biomaterials. Ti '84 Science and Technology. Eds. G. Lütjering, U. Zwicker, W. Bunk (1984) 1327

9 K. ELAGLI, H.J. HILDEBRAND, J. BREME: Electrochemical and in vitro biological behaviour of Ti and its alloys. 20th Annual Meeting of the Society of Biomaterials, Boston (1994) 262

10 J. BREME, E. STEINHÄUSER, G. PAULUS: Plate/screw system according to Steinhäuser of cp-Ti for maxillofacial surgery, Biomaterials **9** (1988) 310

11 H. KAWAHARA: Cellular responses to implant materials: biological, physical and chemical factors, Int. Dent. J. **33** (1984) 350

12 A. KIRSCH: Titan-spritzbeschichtetes Zahnwurzelimplantat unter physiologischer Belastung beim Menschen, Dtsch. Zahnärztl. Z. **35** (1980) 112

13 R.W. PILLIAR, J.M. LEE, C. MAMATOPOULOS: Observations on the effect of movement on bone ingrowth into porous-surface implants, Clin. Ortho. Relat. Res. **208** (1986) 108

14 J. EULENBERGER, F. KELM, A. SCHROEDER, S.G. STEINEMANN: Haftung zwischen Knochen und Titan: 4. DVM-Vortragsreihe Implantate, Ed. DVM, (1983) 108

15 H.P. BOEHM: Disc. Faraday Soc. **32** (1971) 264

16 A. SCHRÖDER, O. POHLER, F. SUTTNER: Gewebereaktion auf ein Titan- Hohlzylinderimplantat mit Titan-Spritzschichtoberfläche, Schweiz. Montatsschr. Zahnheild. **86** (1976) 713

17 A.E. CLARK, L.L. HENCH, H.A. PASHALL: The influence of surface chemistry on implant interface histology: a theoretical basis for implant material selection, J. Biomed. Mater. Res. **10** (1976) 161

18 H. KRUPP: Particle adhesion-theory and experiments, Adv. Colloid Interface Sci. **1** (1967) 11

19 D.F. WILLIAMS: Implants in dental and maxillofacial surgery, Biomaterials **2** (1981) 133

20 W. PLITZ: Wie beeinträchtigen osteoinduktive Oberflächenstrukturen die Gestaltfestigkeit von Endoprothesen, 8, DVM-Vortragsreihe Implantate, Ed. DVM (1988) 25

21 D.B. JONES: in Metals as Biomaterials, J. HELSEN and J. BREME, eds., Wiley, Chichester (1998) 317

22 G. ONDRACEK: Proc. Colloqu, Interfaces in Materials, Brussels (1988) 113

23 J. BREME, V. WADEWITZ: Int. J. Oral Maxillofac. Impl. **4** (1989) 11

24 K. WANG, L. GUSTAVSON, J. DUMBLETON: in Ti'92 Science and Technology, F.H. Froes and I. Caplan, eds., TMS, Warrendale (1993) 2689

25 S.G. STEINEMANN, P.A. MÄNSLI, S. SZMUKLER-MONCLER, M. SEMLITSCH, P. PHOLER, H.E. HINTERMANN, S.M. PERREN: in Ti '92 Science and Technology, F.H. Froes and I. Caplan, eds., TMS, Warrendale (1993) 2689

26 S. OZAKI, S. RAO, Y. ITO, T. TATEISHI: Biomaterials **9** (1998) 1197

27 A. HOFFMANN: Dissertation, Saarbrücken (1999)

28 S.F. HULBERT, F.A. YOUNG, T.S. MATTHEWS, K. KLAWITTER, C.D. TALBOT, F.H. STELLING: Biomed. Mater. Res. **4** (1970) 433

29 B. D'HOEDT, W. SCHULTE, S. HANDTMANN, G. GOMEZ-RAMAN, M. MESCHENMOSER, K. DONATH, J. ORTLEPP, J. BREME, V. BIEHL, G. PETZOW, G. ELSSNER, D. KORN: in Proc. 43. Jahrestag der DGZPW (1994) 24

30 E. EISENBARTH, J. MEYLE, W. NACHTIGALL, J. BREME: Biomaterials **17** (1993) 1398

31 J.E. DALTON, S.D. COOK, K.A. THOMAS, J.F. KAY: J. Bone Joint Surg. **77A** (1995) 97

32 J. BREME, Y. ZHOU, L. GROH, BIOMATERIALS **16** (1995) 239

33 J. FLOQUET, A. RALISON, E. EISENBARTH, A. JOST, J. BREME, H.F. HILFEBRAND: Rév. Stomatol. Chir. Maxilofac. 98 (1997) 47

34 M. SCHALDACH, M. HUBMANN, M. HARDT, R. WEIKE, A. WEIKE: Biomed. Technol. **34** (1989) 185

35 M. SCHALDACH, A. BOLZ: Proc. Conf. Bioceram. Hum. Body, Faenza (1991) 82

36 J. RIEDMÜLLER, A. RZANY, R. FRÖHLICH, A. BOLZ, M SCHALDACH: Biomed. Technol. (1995) 37

37 J.A. DAVIDSON: Clin. Orthop. Relat. Res. **294** (1993) 361–366

38 U. ZWICKER, U. ETZOLD, T. MOSER: Titanium Science and Technology, G. Lütjering, U. Zwicker, and W. Bunk, eds.,

Deutsche Gesellschaft für Metallkunde, Oberursel (1985) 1343–1350

39 J. M. WILLIAMS, R. A. BUCHANAN: Mater. Sci. Eng. **69** (1985) 237–241

40 R. THULL, D. REPENING: Z. Biomed. Technik **25** (1990) 56–61

41 F. F. HENNIG, D. REPENING: Unfallchirurgie **98** (1995) 256–259

42 G. HEINRICH, S. ROSIWAL, R. F. SINGER: Werkstoffe für die Medizintecnik, H. Planck and H. Stallforth, eds. Wiley, VCH, Weinheim (1999) 11–16

43 H. MCKELLOP, T. V. RÖSTLUND: J. Biomed. Mat. Res. **24** (1980) 1413–1425

44 S. EMURA, M. HAGIWARA, Y. KAWABEL: Proc. of the 8th World Conf. on Ti, P.A. Blenkinsop ed., The Institute of Materials, London (1995) 2795–2802

45 N. AXÉN, S. JACOBSEN: Wear **174** (1994) 187–193

46 A. T. ALPES, J. ZANG: Metall. Mater. Trans A **25** (1994) 969–974

17

Titanium in Dentistry

J. Lindigkeit, *Dentaurum J. P. Winkelstroeter KG, Ispringen, Germany*

17.1
Introduction

Metals secured an important role long ago as dental materials with a wide range of applications for functional replacements. Metals have been used as filling materials in preservative dentistry, for fixed prostheses (inlays, onlays, crowns and bridges) as well as for complete and removable partial dentures and combined dentures with telescopic crowns or attachments in dental prosthetics, as materials for endosteal implants and implant-retained suprastructures in dental implantology, and for removable and fixed appliances (brackets, bands, wires, extension screws) in orthodontics. Although the oral cavity is comparatively small, a great variety of different metals and alloys can be found there. In the German dental market alone, more than 1000 dental alloys of different compositions are offered [1]. This spectrum includes alloys of noble gold-platinum, palladium-copper, silver-palladium, nickel-chromium, cobalt-chromium, stainless steel, titanium, and titanium alloys. Today one of the demands of dentistry is to use only materials with high corrosion resistance and a negligible release of ions from a toxicological point of view. Also, the number of different alloy systems in the mouth should be reduced wherever possible [2]. Therefore, due to its characteristics, the importance of titanium and titanium alloys in dentistry is continuously increasing.

17.2
Clinically Relevant Properties of Titanium and Titanium Alloys in Dentistry

The primary benefit of titanium and titanium alloys as materials for dentistry is due to their corrosion resistance and biocompatibility in the oral cavity compared to other metallic materials.

17.2.1
Corrosion Resistance

Today the so-called static immersion test, according to ISO 10271, is the standardized method for testing corrosion resistance of metallic dental materials [5]. Test specimens with a defined surface condition are immersed in a lactic acid/sodium chloride solution for 7 days. The loss of mass is measured after immersion, related to the specimen surface, and calculated as surface-related loss of mass, given in $\mu g\,cm^{-2}$. Results, compared to other dental alloys (Tab. 17.1 [6–10]), reveal that the corrosion reaction of pure titanium is the same order of magnitude as high gold alloys and the highly corrosion resistant CoCr and NiCr alloys with high Cr and Mo contents used in prosthetics.

Currently stainless steels are still the most commonly used material in orthodontic treatments for fixed and removable appliances [11]. Compared to titanium, these materials are less resistant to the conditions in the oral cavity, as seen by the relative loss of mass by corrosive attack shown in Fig. 17.1 [12].

Tab. 17.1 Loss of mass, dental metallic materials, test according to ISO 10271.

Material	Loss of mass ($\mu g\,cm^{-2}$)	Ref.
cp-Ti (Ti 99.5)	2	(6)
cp-Ti (Ti 99.5)	1.53	(7)
cp-Ti (Ti 99.5)	1–2	(8)
Co 61 Cr 25 Mo 7 W 5 Si Mn	0.65	(9)
Ni 61 Cr 26 Mo 11 Si 1,5	0.3	(10)
Ni 68 Cr 17.4 Mn 5.5 Mo 4.5 Si Cu Be 0.5	850	(10)
Au 68 Ag 12 Pd 6 Cu 6 Zn 3 Pt 1	1	(10)
Au 85.6 Pt 12.7 In Ga Zn	8.27	(7)
Cu 79.3 Al 7.8 Ni 4.3 Fe Zn	1528.32	(7)
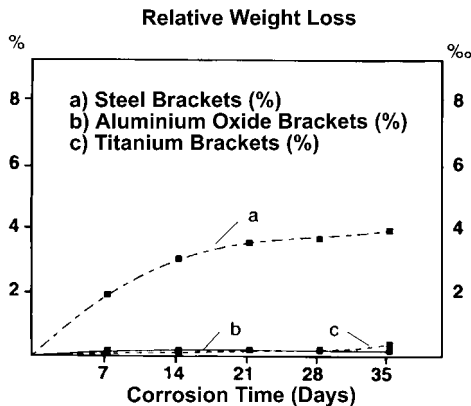
Fig. 17.1 Percentage loss of mass for fixed orthodontic appliances (brackets, upper jaw) [12].

17.2.1.1 Resistance Against Fluorine

It is well known that the resistance of titanium against attack of fluorine-containing agents may not be sufficient for technical applications under certain circumstances [13]. On the other hand, the inhibiting effect of fluoridating agents to caries in dentistry is unanimously recognized worldwide. In-vitro tests simulating the corrosive attack of titanium by fluoride-containing toothpastes and gels [14–16] reveal contradictory results with identical products. Therefore, it seems doubtful that those tests are suitable to clarify conditions and processes in the oral cavity. In addition, there are no clinical findings about corrosion due to fluorides in dentistry and it has been stated: "In practice, high affinity to fluorine is not a problem" [17]; and, "Up to now there does not exist any clinical investigation showing that this effect (release of titanium-ions due to fluoride) will induce any visible change of titanium in the oral cavity" [6]. However, regarding fluoridating treatments in combination with titanium restorations, a recommendation should be followed: "During local application of fluoride gels, liquids, and lacquers the dentist should protect titanium restorations from contact with fluoride ions. This may be done by limiting the application of the prophylactic agent only onto the areas of the natural teeth that have to be fluoridated, or by protecting the titanium surface by isolating with Vaseline or cocoa butter" [16].

17.2.2
Biocompatibility

Considering the total number of dental restorations, incompatibilities are comparatively rare in dentistry. Most of these cases are local inflammations induced by insufficient corrosion resistance, only very few are allergic reactions [18]. No allergies have been documented for pure titanium [19]. Biocompatibility has been proven experimentally [20] and confirmed clinically [21]. This is also valid for Ti-6Al-4V, which has been used as a material for endosteal implants in dental implantology. Special surface treatments by electrochemical and mechanical methods have been applied to increase the implant surface area in those implant areas with bone contact, promoting bone tissue growth on the titanium surface. This so called osseointegration is commonly accepted as a basis for clinical success of dental titanium implants [22]. The pronounced affinity of titanium to oxygen, even in aqueous solutions, may be considered the fundamental reason for titanium's biochemically inert behavior and biocompatibility [23].

The discussion about biocompatibility of dental materials, initiated in prosthetics, has also influenced orthodontics. Usually orthodontic treatments have been considered as being temporary. From this point of view, most investigations have accepted the corrosion resistance of stainless steels as being sufficient [24]. Since technical prerequisites for manufacturing brackets, buccal tubes, expansion screws, and wires from titanium are available today, the positive findings about titanium and titanium alloys are also considered in orthodontics [24] and the importance of biocompatibility is increasing [25].

17.2.3
Physical Properties

Beside corrosion resistance and biocompatibility, the physical properties of titanium and titanium alloys support their use in dentistry. For dental prosthetics, low thermal conductivity is important. From the view of dentistry, thermal conductivity should be as low as possible to reduce thermal irritation of the pulp of a crowned tooth. Compared to precious metal alloys, thermal conductivity is lower for Co- and Ni-based alloys. Titanium, however, exhibits the lowest thermal conductivity of all metallic materials in prosthetics (Tab. 17.2). Even in the case of large surface structures of cast partials, a reduction of hot and cold irritations is of immediate benefit to the patient.

Diagnostically, the X-ray transparency of titanium is of particular interest for dentistry. Attenuation of X-rays is proportional to the fourth power of the atomic number. Therefore, only titanium (atomic number 22) is X-ray transparent under realistic dental conditions with an X-ray tube voltage of 60–125 kV [26]. For exam-

Tab. 17.2 Thermal conductivity of metals used in dentistry; test according to ISO 10271.

Metal	Thermal Conductivity $(Wm^{-1}K^{-1})$
Gold	297
Nickel	92
Cobalt	71
Titanium	22
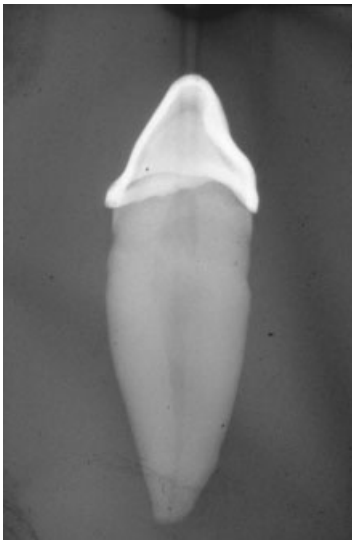
Fig. 17.2 Radiograph of a titanium crown in-situ.
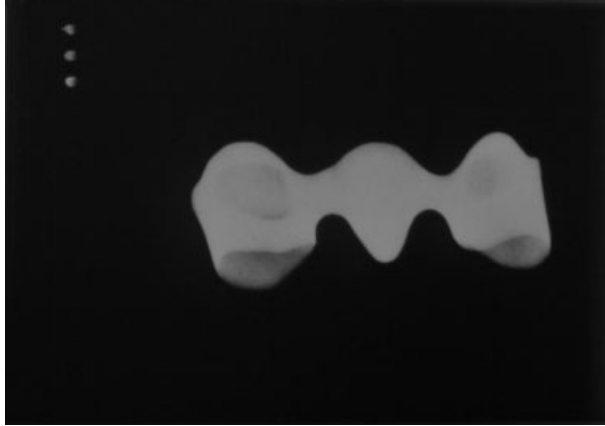
Fig. 17.3 Radiograph of a titanium bridge.

ple, this enables the diagnosis of secondary caries under a crowned tooth (Fig. 17.2). Cobalt- (atomic number 27) and gold-based alloys (atomic number 79) used in dentistry do not allow a crowned tooth to be X-rayed, at least not with a dose harmless to the patient. Beside use of X-rays by the dentist, radiotransparency of titanium is also a benefit for dental technology. For quality assurance within the dental laboratory, X-ray devices are used for detecting defects and documentation of perfect castings (Fig. 17.3). Full safeguard X-ray devices are being used, having an X-ray tube voltage of 70 kV, as shown in Fig. 17.4.

Fig. 17.4 X-ray device (full safeguard) for dental laboratories (X-Control, Dentaurum).

During X-ray diagnosis, radiation related to the patient is increased due to induced β-radiation. For pure titanium (cp-Ti1), the factor of increasing the effective dose is four times lower than for a gold alloy [26].

The low density of titanium (4.5 g cm^{-3}) compared to other metals (for example gold) provides feather-light restorations. The patient highly appreciates this, especially for more extensive restorations. Low density has also technical advantages during firing porcelain onto a titanium frame. Firing of appropriate ceramic masses is performed at nearly 800 °C. Due to its specific combination of low density and high melting point, titanium exhibits a high sag resistance. This enables firing of even large span restorations without any thermally induced dimensional changes and with no need for joining processes after firing [27].

17.3
Use of Titanium and Titanium Alloys in Dentistry

The fundamental work for using titanium in dental implantology was performed by Brånemark [3], who inserted the first dental titanium implant in 1965. For use of titanium in dental prosthetics, development of a melting and casting technology, adapted to the dental lab, was necessary as the commonly used casting systems based on resistance heating, induction, and torch melting couldn't be used. The same was required for investments because the phosphate-bonded types of investments, used for cobalt- and gold-alloys, were inadequate for casting titanium. In Germany, the first titanium casting machine for the dental lab was introduced in 1988 [4]. Basic research on this field of development was mainly done in Japan.

In spite of the large number of alloys in dentistry, there are only a few alloy systems beside titanium that are at the same time highly corrosion resistant, biocompatible, and suitable for a wide range of applications. Therefore, titanium-based materials are today used throughout dentistry in orthodontics, prosthetics, and implantology. Tab. 17.3 gives an overview of the materials used.

Tab. 17.3 Titanium and titanium alloys used in dentistry.

Alloy	Type of Phase	Used in		
		Orthodontics	Prosthetics	Implantology
cpTi1	α		×	
cpTi2	α	×	×	
cpTi3	α		×	
cpTi4	α	×		×
TiMo11Zr6Sn4	β	×		
TiAl6V4	α + β	×		×

17.3.1
Orthodontics

Orthodontics deals with correction of tooth misorientation with mechanical or functional aids and tools. For regulation of the misorientation, forces are required that are induced by different appliances. Removable appliances consist of splitted acrylic plates (PMMA), fixed at the patient's teeth with wire elements. Expansion screws (spindles with levorotatory and dextrorotatory threads) are used for applying forces to the teeth by spreading the plates apart (Fig. 17.5). For the fixed technique, forces are applied by wire elements to the teeth using fixations (Brackets and Bukkal tubes) (Fig. 17.6). Today pure titanium is used, in addition to stainless steels, for fixation and functional elements due to its lower weight and increased corrosion resistance.

For wire-spring elements, titanium alloys are also of particular importance because they exhibit a lower modulus of elasticity than stainless steel and higher strength than pure titanium. For β alloys, a tensile strength of up to 1300 MPa can be achieved by cold deformation. Due to better workability of β alloys, even thin wire diameters can be produced. Alternatively, cold worked pure titanium grade 4 can be chosen, exhibiting similar mechanical properties. Also, wires made from NiTi, shape-memory alloys, are used due to their pseudo-elastic behavior, which is based on stress induced formation of martensite.

a)   b)
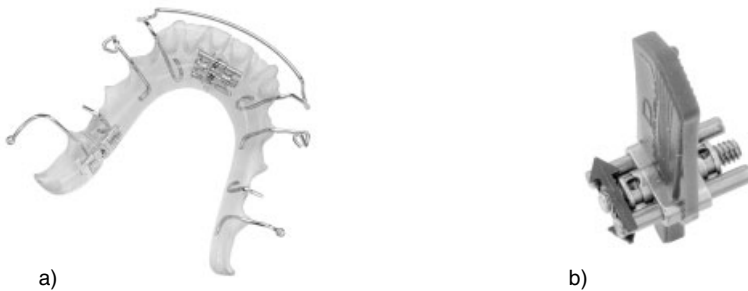
Fig. 17.5   a) Removable orthodontic appliance, b) titanium-expansion screw (cp Ti1).

a)   b)
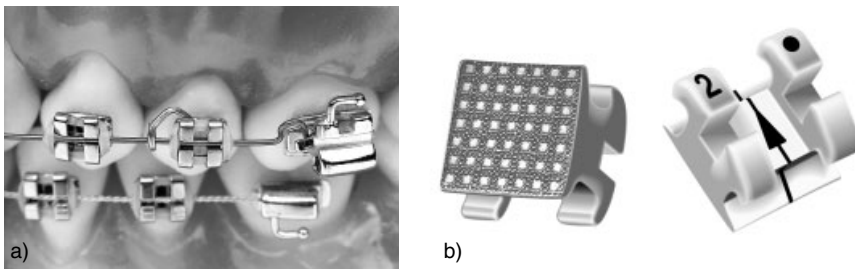
Fig. 17.6   a) Brackets and buccal tubes (cpTi1), b) bracket, detail.

17.3.2
Prosthetics

Dental prosthetics is the reconstruction of mastication, aesthetics, and phonetics by replacement of missing teeth or parts of them with prostheses. Since initial problems of processing titanium as a new and quite unfamiliar material in the dental lab have been solved, its use for dental restorations has increasingly succeeded.

Titanium has been used for cast partials (Fig. 17.7) as well as for crowns and bridges veneered with ceramics (Figures 17.8 and 17.9) and combined dentures (Fig. 17.10). Processing of titanium is most frequently by dental precision casting. For implant retained suprastructures (Fig. 17.11) (see paragraph 17.3.3), cast titanium is equivalent to industrially produced endosteal implants for its electrochemical properties and reduces the potential danger of electrochemical phenomena and corrosion effects. Titanium's wide range of application for prosthetic use is shown in Tab. 17.4 [28] compared to CoCr-based and precious metal alloys, the latter being dominant for many years.

In addition, titanium exhibits outstanding financial advantages compared to gold alloys. Therefore, it is designated the ideal material for combined, fixed, and remov-

Fig. 17.7 Cast partials, cpTi1 (raw castings).
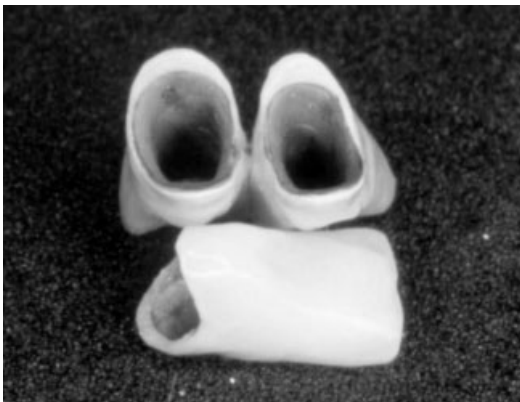
Fig. 17.8 Single crowns, cpTi1, veneered with Triceram® titanium ceramics.

Fig. 17.9 3-Unit-bridge, cast cpTi 1, veneered with Triceram® titanium ceramics.

Fig. 17.10 a), b) Combined denture, fixed/removable, cp Ti1.

Fig. 17.11 a), b) Implant retained suprastructure, cast cp Ti1.

able restorations [28]. To the patient, the financial benefit for a 4-unit bridge (veneered with ceramics) is 225 € from lower material costs alone, as compared to a high gold restoration. Compared to other pfc (porcelain fused to metal) alloys, titanium has an extremely low coefficient of thermal expansion ($\alpha_{25\,°C–500\,°C}=9.6\times10^{-6}$ K^{-1}). The use of adapted ceramics for veneering is therefore required. Titanium is known for its increasing oxidation at elevated temperatures and an increase of grain size and coarsening of microstructure nearby and passing through the β-transus at 882 °C. Therefore, the firing temperature for fusing porcelain to titanium is restricted to a maximum of 800 °C.

Tab. 17.4 Aptitude of titanium, Au-based, and Co-based alloys for dental prosthetic indications [28].

Indication	Titanium	Au-based	Co-based
Inlays	+	++	−
Full metal crowns	++	++	+
Veneered crowns	++	++	++
Bridges	++	++	++
Adhesive bridges	+	−	++
r.p.d. with clasps	++	−	++
Proth. with attachments/bars	++	+	++
Proth. with telescopic crowns	++	+	++
Implant-retained suprastructures	++	+	+
Endodontic pins	++	++	+

17.3.3
Implantology

Dental implantology is the reconstruction of mastication, aesthetics, and phonetics by subperiostal or endosteal implantation of (artificial) posts into the jaw for fixatation of prosthesis. In today's dental surgery, the use of endosteal implants, as shown in Fig. 17.12, is a particularly recognized treatment to replace single teeth, to create posts for fixed dentures, or to stabilize removable dentures. Dental implants, made from titanium or titanium alloys, have been used for over 30 years (Brånemark [3]) and are established for this indication. Usually the implant surface is roughened by blasting with aluminum oxide or by titanium plasma flame treatment for facilitating bone adhesion. A local resorbable layer of hydroxy-apatite in the upper (cortical) region also facilitates adhesion of the bone to the implant in a critical position.
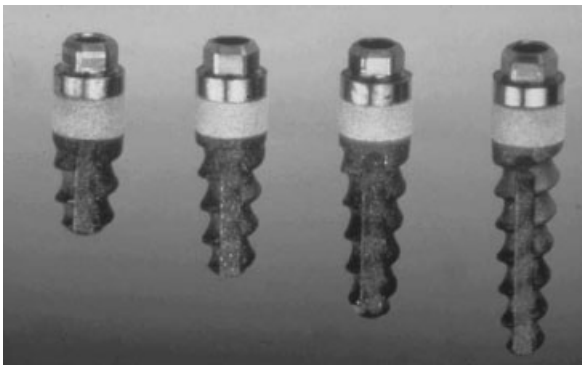
Fig. 17.12 Endosteal titanium-implants (Tiolox®).

17.4
Processing of Titanium in the Dental Laboratory

17.4.1
Dental Melting and Casting Technology

Titanium requires special melting and casting technology. The introduction of titanium casting to dental technology has required some modification of relevant working steps in the dental lab. Controlling this was the basis for making titanium available for applications in dental technology. Pure titanium is usually melted today by argon-arc melting using a copper crucible (scull-melting). Casting is done by a vacuum-pressure-casting-technique (Fig. 17.13). The maximum ingot size for the casting machine shown in Fig. 17.13 is 36 g. Due to differing densities, this equates to a melting capacity of approximately 70 g for a CoCrMo-based alloy, or 150 g for a gold-based alloy. The melting time for a 36 g titanium ingot is 46 s.

Due to requirements for precision, special investment materials based mainly on silica or silica-modifications are used in dental casting technology. Binders used for the investment powder are ethyl-silicates or phosphate/magnesium oxide systems. Since the reactivity of molten titanium with these types of investments is very high, they cannot be used for dental titanium castings due to formation of a large α case layer with micro-cracks and increased hardness that renders dental processing extremely difficult.

A significant reduction of the α case layer was attained by replacing the phosphate/magnesium oxide binder by an acetate-based system and eliminating any silica in the investment powder. As a result, the thickness of the α case layer was reduced to 10–30 μm [29]. This thin layer can be removed completely by usual dental surface treatments like grinding.
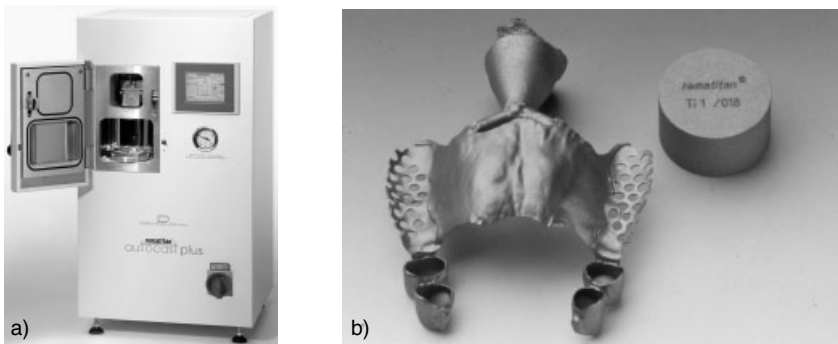
Fig. 17.13 a) Titanium melting and casting device, Autocast Plus, (Dentaurum), b) Titanium-casting ingots and raw casting.

17.4.2
CAD/CAM Technique

For a couple of years now, manufacturing of titanium crowns and bridges by cutting metal from a blank has been offered as an alternative to dental investment casting. Four and five axis machines are used with special dental CAD/CAM systems. An optical scanner conducts data generation from the master model. The design itself is accomplished by CAD software, adapted to the special demands of dental technology. Data generation of milling tracks and manufacturing are done automatically. Fig. 17.14 and 17.15 show parts manufactured by this technique. The process starts from rods (Fig. 17.14) or plates (Fig. 17.15), depending on the system used. The required investment for a dental CAD/CAM system is about 150 000 €. This is a very large burden to the financial resources of a dental lab. In addition, the range available for manufacturing dental restorations is limited for now and cannot be compared to the possibilities provided by dental casting technology. These are the likely reasons for the currently limited use of this technology.

Fig. 17.14 Titanium 3-unit bridge, milled from bar.

Fig. 17.15 Milled framework of a five-unit titanium bridge a) in the blank, b) on the master model (DCS AG, Allschwil, Switzerland).

17.5
Summary

Today titanium and titanium alloys have their fixed position in dentistry as biocompatible materials with a wide range of applications. The importance of titanium and titanium alloys will continue to increase in the future because they enable the manufacturing of esthetic prostheses not only due to their characteristics, but also because of their cost efficiency without any functional compromises.

17.6
Referenced Literature and Further Reading

1 DAS DENTALVADEMECUM, 7th Edition, Deutscher Ärzte-Verlag, Köln (2001)

2 "Legierungen in der zahnärztlichen Therapie, eine Informationsschrift des Bundesgesundheitsamtes", Berlin (1993)

3 P.-I. BRANEMARK, B.O. HANNSON, R. ADELL, U. BREINE, J. LINDSTRÖM, O. HALLEN, A. ÖHMAN: Osseointegrated implants in the treatment of the edentulous iaw. Scand. J. Plast. Reconstr. Surg. 111. Suppl. 16 (1977) 1–132

4 T. KITAMURA: Ohara-Reintitanium-Gußsystem, Quintessenz Zahntech 14 (1988) 590–604

5 ISO 10271:2001: Dental metallic materials – Corrosion test methods

6 R. STRIETZEL, P. GÖRLITZ, K.-U. BOCHDAM, I. BOROWSKI: In-vitro-Korosion von NEM-Legierungen und Titan, Dental-Labor XLV, Vol. 4/97, pp. 723–728

7 H.F. KAPPERT, H. SCHWICKERATH, ST. VEIEL, J. BREGAZZI: Zur Korrosionsfestigkeit aufbrennfähiger Edelmetallegierungen, Dtsch Zahnärztl Z 49 (1994) 716–721

8 W. BRÄMER: Biocompatibility of Dental Alloys, Advanced Engineering Materials 3, 10 (2001) 753–761

9 J. GEIS-GERSTTORFER: Untersuchung im Auftrag von Dentaurum J.P.Winkelstroeter KG (1998)

10 J. GEIS-GERSTTORFER, K.H. SAUER, H. WEBER: Untersuchungen zum Massenverlust von EM-, NEM- und Pd-Basis–Legierungen. Dentallabor XXXVII 11 (1989) 1605–1609

11 J. WIRZ, F. SCHMIDLI, M. MEDER: Materialprobleme in der Kieferorthopädie, Quintessenz 50, 4 (1999) 389–398

12 F. SERNETZ: Titan und Titanlegierungen in der Kieferorthopädie, Quintessenz Zahntech 21, 5 (1995) 615–626

13 Produktinformation Tikrutan, Deutsche Titan GmbH, Essen, Druckschrift Nr. 5 5 94 d3

14 STRIETZEL, ZWR 1994, Nr. 2, pp. 82–84

15 E. LENZ: Dtsch. Zahnärztl. Z. 52, 5 (1997) 351–354

16 A.J. PATYK, H. OHM: Dtsch. Zahnärztl. Z. 52, 5 (1997) 364–367

17 R. STRIETZEL: NEM & Titan-Symposium, Berlin, 22.5.96

18 D. WELKER: Zum toxikologischen und allergologischen Risiko von Dentalwerkstoffen für Zahntechniker und Patienten, Quintessenz Zahntech 27, 1 (2001) 57–62

19 R. SCHNEIDER: Metals used to Fabricate Removable Partial Denture Frameworks, Journal of Dental Technology 13, 2 (1996) 35–42

20 N. REULING: Biokompatibilität dentaler Legierungen, C. Hanser, München Wien (1992)

21 H. MEINERS, K.M. LEHMANN: Klinische Materialkunde für Zahnärzte, C. Hanser, München Wien (1998)

22 J. WIRZ: Titan – ein Werkstoff der modernen Prothetik, Quintessenz 45, 5 (1994) 731–739

23 H.F. KAPPERT: Titan als Werkstoff für die zahnärztliche Prothetik und Implantolo-

gie, Dtsch. Zahnärzt. Z. **498**, (1994) S. 1–12

24 F. Sernetz, in *Titan in der Zahnmedizin* (ed.: Wirz/Bischoff), Quintessenz-Verlags-GmbH, Berlin pp. (1997) 356–357

25 J. Wirz: Mundbeständigkeit von kieferorthopädischen Apparaturen und Geräten, Quintessenz **48**, 4 (1997) 545-554

26 M. Gente, A. P. Sommer: Zunahme der Strahlendosis im Nahfeld von Dentalle-

gierungen, Dtsch Zahnärztl Z **56**, 3 (2001) 181–183

27 J. Lindigkeit: Carmen – Aspekte einer Metallkeramik, Dentalspiegel 1, Vol.2, (1996) 25–27

28 E. Lenz: Titan als prothetischer Werkstoff, ZMK 6/99

29 M. Hopp, H. Krüger: Einbettmassen für den Titanguß, in: Titan in der Zahnmedizin (ed.: Wirz/Bischoff), Quintessenz-Verlags-GmbH, Berlin (1997) 87–105

18

Titanium in Automotive Production

O. Schauerte, *Volkswagen AG, Wolfsburg, Germany*

18.1
Introduction

The use of alternative materials in automotive production can lead to both significant weight reductions and oftentimes functional improvements as well. For this reason, manufacturers have long sought possibilities for using new materials. In the 1930s, these considerations in the field of metallic materials led to the first uses of aluminum and magnesium alloys. These materials have since established themselves in automotive production and their characteristics continue to be developed. Today, however, just as back then, steels are preferred for cost and strength reasons. Because of this, despite the large number of metals in the periodic table of the elements, only alloys based on iron, aluminum, and magnesium have come to be used as structural materials. Other metals can be found in automotive production only as functional materials because of their physical properties, such as copper (bearings and electrical wiring), lead (batteries), tin (bearings), precious metals (electronic components and catalysts), rare earth metals and cobalt (magnets) and chrome (decorative coatings). Other materials demonstrate a high level of suitability for structural applications, but will most likely not be used even in the long-term. Noteworthy examples would be nickel-based alloys, which despite very high stability, are only slightly superior to good steels in their specific properties, or beryllium materials, which are so extremely expensive, that they are hardly used in auto racing.

To attain weight and functional advantages in automotive production through the use of alternative materials in the future, only one element truly remains: titanium. Since the beginning of industrial production of titanium and titanium alloys in the 1950s, this material has been very attractive to car manufacturers because of its high specific strength, its highly elastic energy absorption capacity, and its excellent corrosion resistance. The greatest enthusiasm for the future of titanium in automotive manufacturing was shown by GM with its 1956 All Titanium GM Firebird. This prototype contained not only a range of titanium components, but also even a titanium body. Despite these high expectations and the numerous advantages of titanium materials, they have yet to establish themselves outside of motor racing in production automotive manufacturing. Their use has always failed just for a single reason: price.

Yet, because greater demands in safety and efficiency are being placed on coming generations of automobiles and as the aerodynamic and, with many components, the design options have been exhausted, the willingness to consider the use of more expensive materials is growing.

18.2
Possible Applications for Titanium in Automotive Production

18.2.1
Properties

Fig. 18.1 lists a number of automotive components that are well suited for the special properties of titanium. The specific properties of the most often used $\alpha + \beta$ titanium alloy Ti-6Al-4V are compared here to the higher-strength, heat-treated steel 34CrMo4 (SAE-(ASTM-) No. 4135, B.S. 708 A 37), the high strength AlZnMg-alloy Al7075, and the high strength magnesium forging alloy AZ80. The striped columns represent the specific Young's modulus. The dotted columns represent the fatigue strength scaled to density. Titanium alloys are clearly superior to other metallic materials when a structural component is designed for maximum strength or fatigue strength. If, however, a structural component must be designed for optimized stiffness, then titanium is less suited given its comparatively low Young's modulus, as is visible in the grey columns. In this case, lightweight construction is better realized with aluminum or magnesium. Because the body is designed for greatest possible torsional and bending stiffness, potential applications for titanium are primarily identified in the chassis and powertrain.
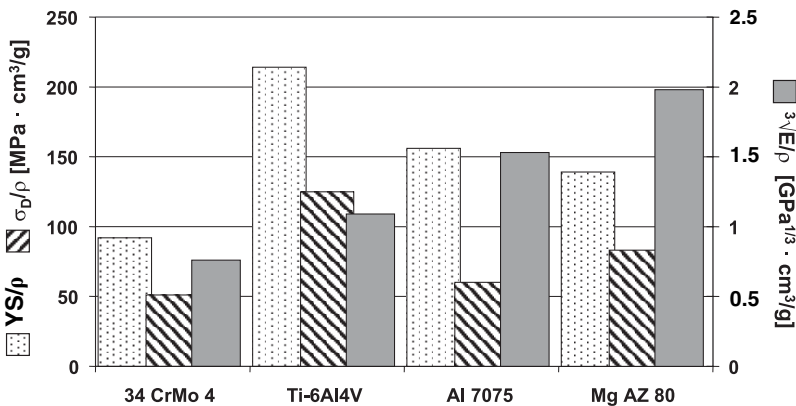
Fig. 18.1 Comparison of the specific properties (Yield Strength, Fatigue Strength, Young's Modulus) of a forging steel, an $\alpha + \beta$ titanium alloy, a high-strength aluminum alloy, and a high-strength magnesium forging alloy.
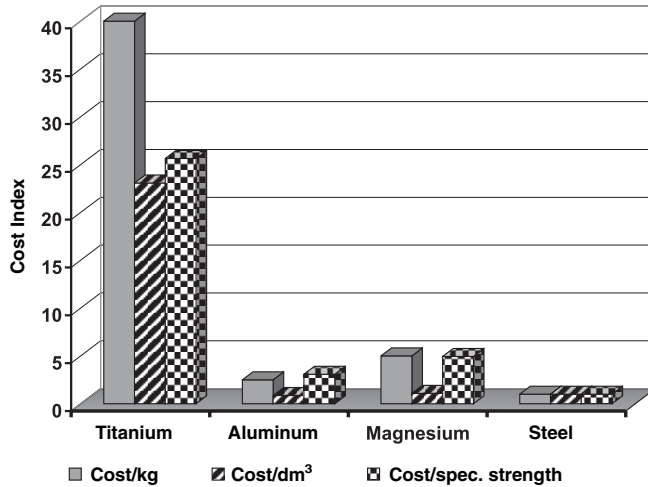
Fig. 18.2 Costs for titanium in comparison with aluminum, magnesium and steel (steel = 1).

Fig. 18.2 demonstrates that deciding to employ titanium is only feasible if the technical advantage is exceptional. Independent of the perspective, the costs for titanium today are much greater than for alternative materials [1].

Fig. 18.3 provides examples of a series of potential applications for titanium components in automotive production, Tab. 18.2 lists a number of potential titanium alloys. The majority of the listed components has already been developed, yet have practically never come to be used in production automobiles [2, 3]. The reasons for this, however, are not only the high material costs for titanium. Often it is the costs of component manufacturing that is the decisive factor. The production chain must also be taken into account in the development of titanium com-
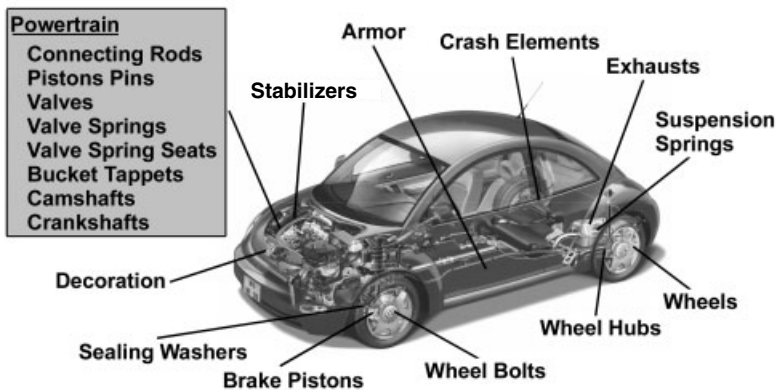
Fig. 18.3 Examples of possible automotive applications of titanium.

Tab. 18.1 Serial production components made from titanium.

Year	Component	Material	Manufacturer	Model	Annual consumption
1998	Brake guide pins	Grade 2	Mercedes-Benz	S-Class	~ 8 t/yr
1998	Sealing washer (brake)	Grade 1s	Volkswagen	all	~ 40 t/yr
1998	Gear shift knob	Grade 1 (?)	Honda	S2000 Roadster	n/a
1999	Connecting rods	Ti-6Al-4V	Porsche	GT 3	~ 1 t/yr
1999	Valves	Ti-6Al-4V & PM-Ti	Toyota	Altezza 6-cyl.	n/a
1999	Turbocharger rotors	Ti-6Al-4V	Mercedes-Benz	Diesel truck	n/a
2000	Suspension springs	LCB	Volkswagen	Lupo FSI	3-4 t/yr
2000	Valve cups	β titanium alloy	Mitsubishi	all 1.8l-4 cyl.	n/a
2000	Turbocharger rotors	γ TiAl	Mitsubishi	Lancer	n/a
2001	Exhaust system	Grade 2	General Motors	Corvette Z06	>150 t/yr
2002	Valves	Ti-6Al-4V & PM-Ti	Nissan	Infinity Q 45	n/a

ponents. As an example of this, axle springs and exhaust systems made from titanium will be discussed in further detail.

18.2.2
Potential Uses

18.2.2.1 **Applications in the Powertrain**
Manufacturers are ready to utilize more expensive materials in the engine if this contributes to reductions in rotating and, more importantly, oscillating masses.

The example that most often springs to mind is the *connecting rod*. In the market segment of super sports cars, titanium connecting rods have repeatedly been used or made available as replacement parts, such as with the Honda NSX or Ferrari. A current example is the Porsche 911 GT3 (Tab. 18.1). It is, however, often overlooked that only a third of the connecting rod's mass is counted in the oscillating mass. In addition, connecting rods are only partly designed for fatigue strength. Especially in the region of the large yoke eye (Fig. 18.4), stiffness is decisively important because its ovalising under the cyclic loading quickly leads to abrasion and eventually to the failure of the bearing shell. Titanium connecting rods are quite sensitive in this area since given their reduced thermal expansion compared to the crankshaft and piston pins, greater bearing clearance must be maintained. For these reasons, weight reductions can only reach about 20%, as compared to steel connecting rods, despite the fact that forging alloys such as Ti-6Al-4V can reach a much higher strength than connecting rod steels such as C45 or C70.

The manufacture of titanium connecting rods is associated with considerable additional costs because titanium, with its little wear resistance, must be coated in affected areas, for example with a PVD-CrN layer, as the Ducati connecting rod in

Tab. 18.2 Titanium materials for applications in automotive production.

Alloy	TS [MPa]	YS [MPa]	%El	Potential applications
CP-titanium Grade 1	∼ 300	∼ 250	30	Muffler, sealing washer
CP-titanium Grade 2	∼ 450	∼ 380	22	Exhaust systems, design elements
Ti-6Al-4V	∼ 1050	∼ 950	10	Connecting rods, intake valves, wheel hubs
Ti-6Al4Sn4Zr1Nb1Mo0.2Si [a]	n/a	1150	4	Exhaust valves
Ti-4.5Fe6.8Mo1.5Al [b]	1290	1380	10	Suspension springs, valve springs, bolts
γ Ti-46,8Al1Cr0,2Si (cast)	525	410	∼ 2	Valves, turbocharger rotors, piston pins

a) PM-alloy, reinforced with 5 Vol.% TiB, elastic modulus ∼ 150 GPa.
b) β Alloy, Low-Cost-Beta (LCB).

Fig. 18.4 demonstrates. In addition, metal-cutting of titanium is more difficult and its increased notch sensitivity necessitates structural optimizations and additional production steps, such as drilling out the thread runouts [5].

Other attractive powertrain applications for lightweight structural materials can be found in the valvetrain. Here, especially in the higher-revving gasoline engines, the oscillating masses determine the maximum engine speed.
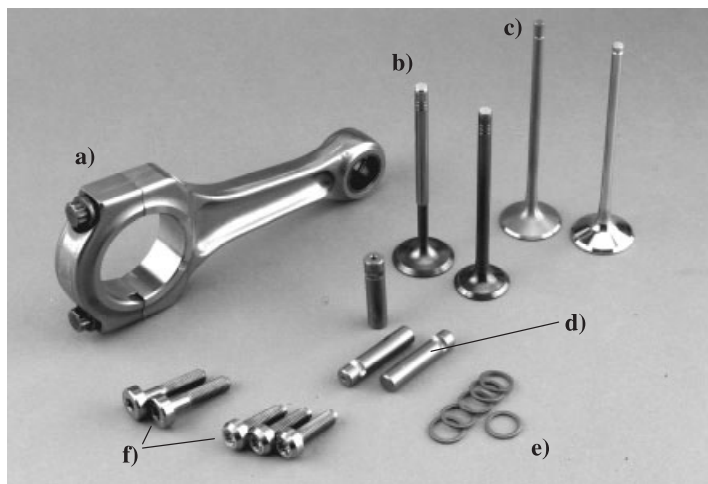
Fig. 18.4 Examples of titanium applications in car and motorcycle manufacturing: a) Connecting rod (Ti-6Al-4V, Ducati); b) intake valve (Ti-6Al-4V), outlet valve (near-α alloy reinforced with TiB-particles); c) γ TiAl valves uncoated/coated; d) brake pins (Grade 2, Mercedes-Benz); e) sealing rings for brake pressure tubes (Grade 1, Volkswagen); f) rim screws (Ronal and BBS, Ti-6Al-4V).

Lightweight valves enable reductions in mass, which positively affects consumption and engine performance, and enables secondary weight reductions such as lighter valve springs [6].

Extremely high demands are placed on the valve materials: beyond high thermal loading with exhaust temperatures of up to 900 °C, the valve plate is strained by the cyclic contact with the valve seat. The valve shaft can be subject to occasional bending loads. The sum of these loading conditions results in increased demands on the valve material's creep resistance, long-term stability, ductility, and resistance to oxidation. Conceivable alternatives to the steels currently in use are SiN ceramics, γ titanium aluminides, and high-temperature titanium alloys. All enable weight reduction of 40 to 50% [6–8]. SiN valves were successfully tested in the past, but couldn't find acceptance because of insufficient ductility and particularly the lack of effective quality control measures.

Currently two different lightweight candidates are in competition. Toyota has developed titanium valves (Fig. 18.4), whereby for the intake valve the characteristics of Ti-6Al-4V are sufficient. For the more thermally strained exhaust valve, the near-α alloy TIMETAL 834 (Ti-6Al-4Sn-4Zr-1Nb-1Mo-0.2Si-0.3O) is reinforced as a matrix material with TiB particles using a specially developed powder-metallurgical manufacturing process. The production of these valves uses the BE (blended element) process in which TiH_2 and TiB_2 powders are mixed with a master alloy powder and compacted. Afterwards a sintering step under vacuum conditions at 1300 °C takes place, in which in-situ TiB-particles are generated. Then, using a hot-extrusion process at 1200 °C, bar stock is generated from which valves can be forged. The valve blanks are heat-treated, finished and finally oxidized to improve resistance against abrasive wear. Through this production path, a volume fraction of 5% TiB is formed in a surrounding fine-grained duplex microstructure with grain sizes about 25 μm. The advantages of reinforcing with TiB particles are increased room and high temperature properties with a simultaneous increase in the Young's modulus to 150 GPa. These valves have been used in the production of the six-cylinder engines of the Toyota Altezza since 1999 [7, 9].

In the German automotive industry, for efficient production of lightweight valves, greater hope is being placed on the use of γ TiAl alloys (Fig. 18.4). The advantages of this material is a lower density, a very good strength at high temperatures, a good oxidation resistance, an excellent creep resistance, and a thermal coefficient of expansion of 11.5×10^{-6} m K^{-1}, which is better matched to connected steel components than titanium. The disadvantages are low room temperature ductility, difficult machining, and that valve production at justifiable costs is only possible by casting, which can cause shrinkage cavities in the shank. This problem is, however, now under control. Though valves made from extruded material are qualitatively better, for cost reasons they will in the long-term only be used in racing. For cast TiAl valves, several joint research projects, sponsored by the German government, have led to a production route enabling the manufacturing of these valves under production conditions by using the centrifugal casting method [8, 10].

It is currently impossible to conclusively judge, neither from an economic nor a technical perspective, whether particle-reinforced titanium valves or TiAl-valves

will succeed on the market. Nevertheless it can be emphasized that the technological advantage to the use of lightweight valves is the ability to ensure a mass reduction of 40–50% in comparison to conventional steel valves. This in turn enables an increase of 500 revolutions per minute and if the reduction in mass isn't completely converted into gained rpm, it enables improvements in fuel-consumption and a reduction in the valve spring mass of an additional 15–20%.

Valve springs can be easily produced from titanium and are widely used in racing. When combined with conventional steel valves, a weight reduction of around 40% can be attained. When combined with TiAl valves, a reduction of up to 70% of the spring mass can be attained. This reduction has the added benefit that half of the weight is counted in the oscillating masses. Because the use of β titanium alloys is necessary for this type of spring, and relatively thin wire with a diameter of 2–3 mm is very expensive, their use beyond racing is highly improbable.

Titanium valve cups are also used in car racing. Because of the low resistance to wear of titanium surfaces, however, they require a coating. In addition, aluminum cups have since also been successfully tested, on which the wear resistance has been optimized with ceramic inserts or coatings. The use of titanium cups in standard production is therefore not to be expected.

Since 2000, Mitsubishi has been using small amounts of precision cast turbocharger rotors made from γ TiAl on the exhaust side in the Lancer. This step depends in great part upon whether or not economic methods for production can be found. The thin-walled rotor blades could be especially problematic [11].

Other titanium applications in the powertrain are not to be expected. Its employment usually fails because of the low Young's modulus (crankshaft, piston pins), the low wear resistance (steering wheel, camshaft) or on the possibility of attaining the same or better weight reduction advantages at lower costs by using aluminum or magnesium (e.g. the valve cover).

18.2.2.2 Applications in the Chassis

The technologically most interesting application for titanium in the chassis might be the suspension spring, which is discussed in detail in section 18.3. The first production application of a titanium component in the chassis was therefore rather unspectacular: for reasons of corrosion protection, the *sealing washers* in the brake line's connecting flange in all Volkswagen automobiles with aluminum brake calipers have been made of titanium since 1998 (Fig. 18.4). CP-titanium Grade 1s was chosen in order to ensure that the washers deform sufficiently while tightening the nut so that the connection is optimally sealed. Also for reasons of corrosion resistance, Mercedes Benz introduced CP-titanium (Grade 2) *brake guiding pins* in the same year in the S-Class. This was done because in the design used, the pins are completely enclosed by the cast brake calipers so that they can never be removed again. Therefore, the component's operability must be guaranteed for the automobile's life span (Fig. 18.4). *Brake pad carrier plates* made from CP-titanium Grade 4 can also be recommended for corrosion resistance, weight reduction, and low thermal conductivity.

In the chassis as well, the use of lightweight materials becomes interesting when additional benefits beyond pure weight reduction are attainable. That is why special emphasis is placed on minimizing the "unsprung masses", such as wheels, brakes, wheel carriers, wheel bearings, axle springs, etc., because weight reduction in these directly effects driving comfort. Lighter masses can absorb unevenness in the road more easily. Many chassis components are well suited for titanium. The main barrier here is again the price. With minimal structural modifications, forged components such as *steering knuckles*, *wheel brackets*, *suspension links*, and *wheel hubs* can be simply substituted with $\alpha+\beta$ alloys such as Ti-64 or Ti-62222. Beyond the high material costs, as compared to the relatively inexpensive forged steels, another disadvantage is the great difficulty in forging, given the high degree of deformation in complex components such as steering knuckles with multiple arms. It is therefore unclear whether forging in the $\alpha+\beta$ field allows a sufficient deformation potential, or whether sufficient fatigue properties can be generated in a β-forging.

18.2.2.3 Further Applications

A few potential applications for titanium materials in automotive production can be found outside of the powertrain or chassis.

In the body, *crash elements* made from CP-Grade 4 or Ti-6Al-4V are conceivable, because titanium demonstrates a sufficiently uniform and therefore energy-absorbing deformation behavior. Newly developed, high-strength steels (e.g. TRIP-steels) currently offer a comparable weight savings at significantly lower costs.

The use of titanium can at least be partially considered for the *armoring* of security vehicles. Even if at the highest ballistic demands (7.62 mm full metal jacket armor-piercing bullets at 850 m s^{-1}) titanium's lightweight construction potential is low, good results can be expected with light armor and in anti-shrapnel protection, as demonstrated in the use of single-melted Ti-6Al-4V in the American M2A battle tanks for track chain protection and turret armor [12]. The ballistic behavior of combined armor forms (e.g. titanium or TiAl + Aramid) and fiber reinforced titanium alloys is unknown.

Further, *decorative elements* made from titanium both in the interior and for emblems is conceivable. Here, for example, thin-rolled CP-titanium Grade 1 could be used. For this application, titanium's sensitivity to finger prints must be considered. An appropriate surface treatment would therefore be needed to optimize the finish.

18.3
Suspension Springs made from Titanium

The mass m of an axle coil spring is described proportionally in the following equation:

$$m \approx \frac{\rho \cdot G}{\tau_f^2} \left(\frac{2 \cdot F_{max}^2}{C} \right) \qquad\qquad (eqn.\ 18.1)$$

As force, F, and spring rate, C, are fixed through the car's mass and tuning, the spring weight can only be influenced by material density, ρ, shear modulus, G, and the fatigue strength under torsional loading, τ_f. From this follows that effective weight reductions of 40–50% can only be attained through the use of high-strength β alloys, as only they can achieve the necessary torsional fatigue strength in the 800 MPa range. Because, however, the available spring steels have also been significantly improved in the last years, titanium remains in competition with steel to enable significant weight reductions justifying the use of the expensive material (Fig. 18.5).

Optimized mechanical properties, however, are not enough to justify using a titanium suspension spring in the cost framework of a production automobile.

To reach this goal, spring manufacturing must be oriented towards the demands of serial production. This means that the titanium spring wire must be able to be cold wound onto an automated coiling machine and then be aged and shot-peened at the spring manufacturer's facilities. In recognition of these demands, developments were pursued at Volkswagen that enabled the world's first production use of a titanium spring in the rear axle of the Lupo FSI in 1999 (Fig. 18.6).

The β alloy TIMETAL LCB® (Low-Cost Beta, Ti-4.5Fe6.8Mo-1.5Al) was chosen for this development project because it demonstrates a cost advantage compared to other β alloys. A reduced cost of raw material was achieved with this alloy, spe-
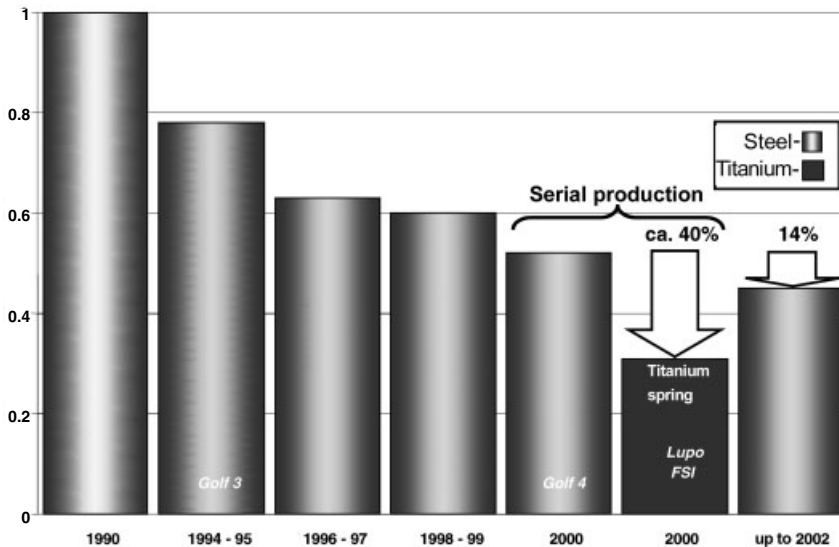
Fig. 18.5 Latest improvements in the weight of suspension springs (picture: Muhr & Bender).

cifically developed for non-aerospace applications, by stabilizing the β phase using an inexpensive FeMo master alloy widely used in the steel industry. With alternative β alloys (e.g. Beta-C, β-21s), however, the high percentage of relatively expensive alloying elements alone, such as Cr, Nb, Zr and Mo, is cause enough to expect little savings potential compared to LCB. Further, LCB distinguishes itself from other β alloys with an unusually high strength potential, which, with comparatively short ageing periods, enables tensile strengths of approximately 1350 MPa concurrent with a sufficient ultimate strain [13, 14].

Because of the need for use of existing production facilities in spring production, it was necessary, in cooperation with spring and titanium manufacturers, to optimize the microstructure in the as-delivered condition so that the wire could be cold-wound without damaging it. Further, the aging heat-treatment and the parameters of shot-peening needed to be coordinated with one another. The optimization of the properties led to an as-delivered condition having the microstructure pictured in Fig. 18.7. LCB's good ductility is the result of the very fine-grain deformation structure with a grain size about 3 μm. Primary α (α_p), which appears black when etched, forms when the wire temperature drops below the β-transus during wire rolling. The light areas consist of β phase, which is supersaturated. The β phase hardens by precipitating secondary α (α_s) during the thermal treatment that follows the coiling of the spring. These precipitates are needle-shaped, incoherent, and have a size of approximately 20×100 nm. The size and number of the precipitates is determined by the aging time and temperature, as well as the given degree of deformation. Because of the tendency for the majority of β alloys towards a non-uniform precipitation behavior, long aging times at lower aging temperatures are usually preferred. Efficient spring production, however, aims for a significant reduction in the usual aging times. Comprehensive investigations on the relationship between aging time and temperature have shown that LCB is quite tolerant in the range of two to four hours when compared to alloys such as Beta-C or Ti-15-333. This is most likely the result of the high diffusion rate of Fe as compared to elements such as Mo and V. The formation of ω phase was never observed.

Fig. 18.7 Microstructure of LCB, as-delivered condition for spring winding.

The aging temperature was selected in coordination with shot peening to follow, whereby the same facilities with the same steel shot are used as in steel spring production. It has been shown that higher fatigue life values after peening were attained when the springs were not peak-aged to the highest yield strength. In this way, the surface area is strengthened more and deeper through the induced internal stresses from shot peening and leads to improved fatigue lives around 1×10^6 LC (load cycles), which is relevant for the spring design. It was found, however, that the aging times did not affect the fatigue strength as much as it affected the yield strength. This is due to LCB's cyclic softening behavior, caused by the formation of preferred slip systems, that takes place preferably in the softer primary α and leads to early crack initiation [15]. So a weak point of this β alloy is that the primary α can't be age hardened since hardening can only take place in the β matrix by precipitating α_s lamellae.

With the introduction of production titanium suspension springs in the Lupo FSI, a manufacturing route for titanium springs under production conditions has been made available. However, research activities must be intensified to concentrate on both a performance increase in possible alloys and the optimization of production processes for wire and spring manufacturing.

18.4
Exhaust Systems

An additional and attractive potential application for titanium in automotive production is the exhaust system. This is because using comparatively inexpensive titanium semi-finished goods can save a remarkable amount of weight. In the Golf

class, for example, this accounts for 7 to 9 kg, depending on the engine. An additional benefit is the significant increase in life span achieved by using titanium. The first production use of an exhaust system was seen in early 2001 with the introduction of the new Corvette Z06 to the North American market.

High-quality exhaust systems are currently made from stainless steel 1.4301 (X5CrNi18-10, SAE-No. 304, B.S. 304 S 15). Titanium can only be an alternative for those sections of the exhaust system in which gas temperatures are not too high. With gas temperatures in the engine's exhaust region being over 900 °C, titanium can only be used behind the catalytic converter where exhaust temperatures for gasoline engines reach a maximum of 750 to 800 °C. In diesel-powered cars, the temperatures are significantly lower and reach a maximum of 600 °C in the mufflers.

Based on mechanical demands and costs, CP-titanium Grade 2 can be recommended since it has the best compromise between strength and cold formability. At room temperature, the yield strength of Grade 2 is nearly as twice that of stainless steel. If necessary, the more ductile Grade 1 can be used for more complex deep drawn components. In this context it has to be considered that the strength and cold formability of the CP-titanium grades is determined by the content of interstitial elements such as oxygen. And, because the influence of these elements decreases with increasing temperature, the difference in strength between the grades is reduced during use.

Oxidation experiments in air have shown that operation temperatures up to 500 °C merely lead to a discoloring caused by surface oxidation. The microstructure itself, however, is not affected. During long-term use at approximately 600 °C, a 20 μm thick TiO_2-layer and initial grain coarsening can be observed. During long-term use at approximately 700 °C, significant grain coarsening, the formation of a distinct α-case, and the initial peeling of oxide layers resulting in a reduction in thickness can finally be observed. Despite the loss of ductility accompanied with grain coarsening, the tensile strength and yield strength remain on the level of unexposed titanium.

In practical application, the effects of thermal loading are less pronounced since the titanium usually comes into contact with the exhaust gas from only one side, and increasing exhaust gas temperatures are related to a vehicle's increasing speed, which means more intense airflow cooling. Additionally, the exhaust from gasoline engines contains only about 1% of free oxygen. In diesel engines, the percentage of oxygen is much higher (around 10%), yet the gas temperatures are significantly lower. The components of the exhaust system that experience the highest temperatures are therefore the baffles and the interior muffler walls. If necessary, the use of single plates made of high temperature titanium alloys (e.g. β-21s) should be considered.

A requirement for the economic use of titanium exhaust systems in automotive production is to master a technology that is mostly oriented towards the mass production of steel components, i.e. using the existing tools and facilities. This pertains in particular to tube bending, wrapping and lock-seaming of wrapped mufflers, deep-drawing of half-shells for mufflers in shell construction, and final as-

sembly technology. In particular, deep-drawn half-shells must be strongly considered because the available space under the car's body is becoming increasingly limited, and increasing muffler volumes will be demanded in the future for acoustic reasons.

Today, tube bending and manufacturing of wrapped mufflers are well understood techniques, as demonstrated by the introduction of the production titanium exhaust system in the new Chevrolet Corvette Z06. But extensive research on the deep-drawing of titanium sheet has also been carried out [16, 17]. This and welding technology are the keys to the inexpensive production of titanium exhaust systems.

The disadvantages of titanium processing result from titanium's tendency to gall in contact with the tool material, and from its lower Young's modulus, which causes a more pronounced springback and a decreased dimensional stability of the drawn components.

Under pure tensile loading, CP-titanium sheet (both Grades 1 and 2) demonstrates surprisingly good deep drawing properties. Even Grade 2, with a maximum drawing ratio of $\beta = 2.5$, surpasses stainless steel's 1.4301. Unfortunately, its stretching behavior is significantly worse and, in the production of real components, strong localization of individual slip systems occurs quickly, leading to tearing. In combination with titanium's tendency for galling, this effect is even more pronounced because it causes an earlier hindrance to the material flow. From this, it follows that a greater demand for deep-drawing optimization must be made on the selection of both the lubricant properties and the tool materials.

Measurements of the coefficients of friction on CP-titanium sheet in contact with common tool steel 1.2379 (X155CrVMo12-1, SAE-No. D2, B.S. BD 2) demonstrated that only marginal differences could be determined between conventional lubricants, be they wax-based, soap-based or oil-based lubricants, graphitic oils or copper paste. Only drawing-lacquers containing MoS_2 or graphite create a significant improvement concerning the coefficient of friction. In practice, removal of the lacquer after drawing is very time-consuming and environmentally polluting work. The last remaining possibility is the use of drawing foil, which creates the best coefficients of friction and, as compared to drawing-lacquers, is seemingly the least time-consuming solution (Fig. 18.8).

Experiments on tool materials demonstrate that no significant improvement is attained through using alternative tool steels or coated steels. Dramatic improvements can be reached in using tools made of plastic or hardwood. Plastic demonstrates a self-lubricating behavior. The good results with wood are perhaps from its ability to absorb lubricants [16] (Fig. 18.8).

Both tool materials have the same disadvantage of increased tool wear. This is, however, balanced by the drastically reduced tool costs. It must also be considered that the production of titanium exhaust systems is more likely for smaller production runs where increased tool wear is therefore irrelevant.

Currently the most difficult technical production problem is, however, in joining technology. While cold joining methods, such as lock-seaming and flaring, are well under control, welding is still problematic. The problems are above all asso-
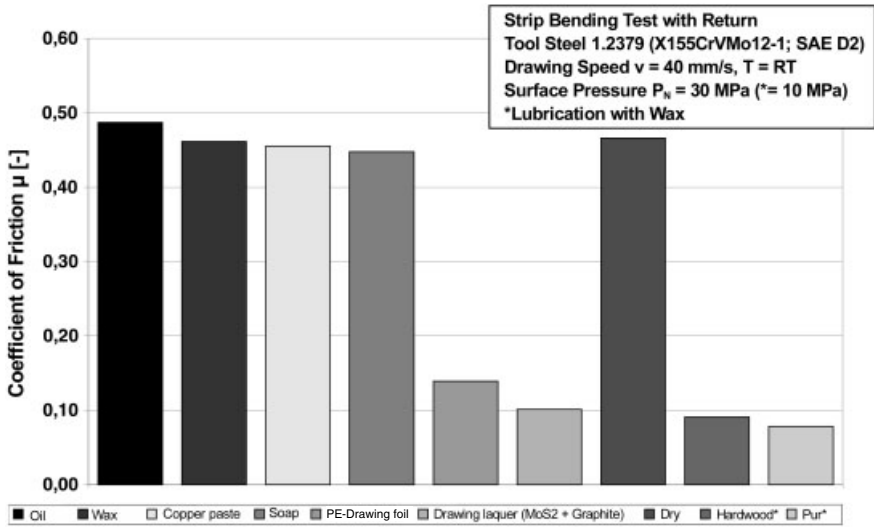
Fig. 18.8 Influence of different lubricants and tool materials on the deep drawing behavior of CP-titanium sheets, characterized by the coefficient of friction, µ.

ciated with the necessity to secure the reverse shielding of the weld seam with a sufficient gas cover of protective atmosphere (e. g. argon) as experienced, for example, in welding tubes onto the muffler. Because a thorough flushing of the entire system would lead to significant additional costs, especially with larger exhaust systems, a method must be found, e.g. fitting housings, with which the use of reverse shielding gas can be avoided. In general, the number of welds should be minimized, starting in the design phase of a titanium exhaust.

In summary, it can be seen that research efforts are still necessary. In principle, however, cost-efficient serial production of exhaust systems is possible in which the additional production costs should not significantly surpass those of comparable stainless steel systems.

18.5
Conclusion

In conclusion, the current perspective presented demonstrates that titanium has been able to make the leap to serial production in past years in a variety of applications, as shown in Tab. 18.1. This demonstration, however, should not hide the fact that the overall scope of application is very small and that given the potential components and automobiles, use ultimately pertains to quite small components and/or niche applications. Further, in only very few applications did the use of titanium result from weighing the technical and economic aspects. In order to be established even in small series production, significant cost-cutting is necessary

for semi-finished titanium products. This is true even though the automobile in-dustry must carry out more comprehensive development activities for many appli-cations.

New processes for titanium production are therefore urgently needed. Perhaps, in a few years, the process developed at Cambridge University for a direct, electro-chemical reduction of TiO_2 in molten $CaCl_2$ will have proven its functionality on a commercial scale and will open new perspectives [18].

Of course, it is not easy to predict the degree of cost reductions future research and development activities might achieve that could justify an increased use of ti-tanium in automotive production. But if one considers that the knowledge avail-able on the use of aluminum in automotive production has only now reached the level enjoyed by steel 20 to 30 years ago, and that magnesium's knowledge base is where aluminum's was perhaps 20 to 30 years ago, then it becomes clear that tita-nium is at the very beginning of its potential uses in automotive production. There is a good reason to believe that, with an interplay of the increased use of ti-tanium in automotive production and more intensive research and development activities, titanium will establish itself as the fourth structural metal in automotive series production.

18.6
Referenced Literature and Further Reading

1 S. EISENBERG (Volkswagen AG): "Titan-werkstoffe im Automobil"; EURO-FORUM, May 12–13, 1998

2 K. FALLER, F.H. FROES: "The Use of Tita-nium in Family Automobiles: Current Trends"; J. of Mat. Sci., **53**:4 (2001) 27–28

3 O. SCHAUERTE, S. EISENBERG, M. KRA-MER, K. FALLER: "Einsatzpotentiale für Ti-tan im Serienfahrzeug"; VDI/VW-Ge-meinschaftstagung 'Technologien um das 3l-Auto', Braunschweig, Nov 16–18, 1999

4 H. MEZGER, F. STREHLER (Porsche AG): "Erfahrungen mit Titan im Automobil-bau", Z. Automobil-Industrie, Vogel-Ver-lag **1** (1972)

5 T. MATSUBARA (translation from the Japa-nese): "Entwicklung einer Automaten-Ti-tanlegierung für Pleuelstangen"; Z. Chit-anium. Zirukoniumi **4** (1991) 39

6 U. HOYER, P. RAHNAVARDI (BMW AG): "Untersuchung mit Ventilen aus Leicht-bau-Werkstoffen"; MTZ Motortechnische Z. **60** (1999) 590–603

7 T. FURUTA, T. YAMAGUCHI, Y. SHIBATA, T. SAITO: "P/M Titanium Metal Matrix Composite for Exhaust Valve"; Proc. of the 9th World Conf. on Titanium, St. Pe-tersburg (1999)

8 S. KNIPPSCHEER, G. FROMMEYER: "Inter-metallische Leichtbaulegierungen für Motorkomponenten"; Ingenieur-Werk-stoffe **7**:3 (1998) 32–34

9 T. SAITO, T. FURUTA, T. YAMAGUCHI: "Development of Low Cost Titanium Metal"; in Recent Advances in Titanium Metal Matrix Composites', F. Froes and J. Storer (eds.), The Minerals, Metals & Mat. Soc. (1995)

10 N. N.: "Permanentkokillenguß für TiAl-Ventile"; BMBF-Project No. 03N3016

11 T. TETSUI: "Application of TiAl in a Tur-bocharger for Passenger Vehicles"; Ad-vanced Eng. Mat. **3**:5 (2001) 307–310

12 M. WELLS, M. BURKINS, B. POITHIER, J. FANNING, B. ROOPCHAND: "The Mechani-cal and Ballistic Properties of an Electron Beam Single Melt of Ti-6Al4V-Plate"; Proc. of the 9th World Conf. on Tita-nium, St. Petersburg (1999)

13 P. Allen, P. Bania, A. Hutt, Y. Combres: "A Low-Cost Beta Alloy for Automotive and Other Industrial Applications"; Proc. of the 8th World Conf. on Titanium, Birmingham (1995) 1680–1687

14 A. Sherman (Ford), S. Seagle: "Torsional Properties and Performance of Beta Titanium Alloy Automotive Suspension Springs"; in 'Beta Titanium Alloys in the 1980s', R. Boyer and H. Rosenberg (eds.), The Minerals, Met. & Mat. Soc. (1986)

15 O. Schauerte, D. Metzner, R. Krafzig, K. Bennewitz, A. Kleemann: "Fahrzeugfedern – Federleicht: Erster Serieneinsatz einer Achsschraubenfeder aus Titan"; ATZ -Automobiltechnische Zeitschrift **103** (2001) 7/8

16 E. Doege, S. Kulp, O. Schauerte: "CP-Ti sheet material and its application in deep drawing processes"; Proc. of the Int. Materials Solution Conf., Indianapolis (2001)

17 W. Beck, T. Hallfeldt: "Umformung von Titanblechwerkstoffen"; Z. Blech Rohre Profile **6** (1999) 38–42

18 G. Chen, D. Fray, T. Farthing: "Direct electrochemical reduction of titanium dioxide to titanium in molten calcium chloride"; Nature **407**:9 (2000) 361–364

19

Offshore Applications for Titanium Alloys

L. Lunde and M. Seiersten, *Institute for Energy Technology, Kjeller, Norway*

19.1
Introduction

Titanium and titanium alloys exhibit outstanding corrosion resistance to seawater and aqueous media. It is an attractive material for offshore use, especially in salt-water systems and other hostile environments; but despite its attractive properties it did not find large application in the offshore industry until the late 1980s. A major breakthrough occurred when Mobil decided in 1986 to use titanium as a replacement material for corroded and destroyed cement-lined carbon steel piping in the ballast water systems on the Statfjord platforms in the North Sea. The project demonstrated that the replacement costs by using titanium was only 5% higher than alternative stainless steel materials and that the titanium industry was able to deliver within a shorter time than steel companies. The installation was pioneering and it initiated a new direction of technology development for titanium.

In addition to corrosion resistance, the high strength to weight ratio makes titanium attractive for offshore applications. Weight is of great concern on both production platforms and vessels. Large quantities of titanium have been installed during the last ten years. The Njord platform in the North Sea has 110 tons of titanium seawater pipework installed, and the Troll platforms, built for a 70 year lifetime, have 500 tons of titanium installed. Development now moves towards sub-sea installations where it is anticipated that titanium will be used to a great extent because its high strength and corrosion resistance will improve the reliability and reduce lifecycle costs of such installations.

19.2
Materials and Materials Requirements

19.2.1
Titanium Materials for Offshore Applications

Tab. 19.1 lists the candidate grades for offshore environments. Grade 2 (commercially pure titanium) is by far the most used. It is corrosion resistant, readily

Tab. 19.1 Titanium alloys for offshore use.

ASTM Grade	UNS Design.	Nominal Composition	Min YS [MPa]	Crevice corrosion threshold [°C]	NACE Approved
2	R50400	Unalloyed (CP)	275	80	Yes
16	R52402	Ti-0.05Pd	275	>250	No
12	R53400	Ti-0.3Mo-0.8Ni	345	>200	Yes
9	R56320	Ti-3Al-2.5V	485	80	No
28	R56323	Ti-3Al-2.5V-0.1Ru	485	>250	Yes
23	R56407	Ti-6Al-4V-0.1O (ELI)	760	80	No
29	R56404	Ti-6Al-4V-0.1O-0.1Ru	760	>250	Yes
19	R58640	Ti-3Al-8V-6Cr-4Zr-4Mo	760	>200	Yes

formable, and easy to weld. This together with relatively low costs and good availability make it the preferred material for topside water management systems. Of the alloys, Grade 19 has found the widest application so far; mostly as high-pressure sampling bottles, downhole tubulars, logging and wireline equipment. Grade 23 is extensively used in taper stress joints. Grade 9, 28, 23 and 29 are of current interest for riser applications due to their high strength.

Palladium or ruthenium enhanced materials offer excellent crevice corrosion resistance in high temperature saltwater. The threshold temperature for crevice corrosion of these alloys is above 250 °C. The excellent corrosion properties of these alloys have been demonstrated in geothermal well service as well as in extensive testing for offshore applications.

19.2.2
Seawater Corrosion

Titanium is very corrosion resistant in seawater. Water, even heavily polluted brackish or deaerated water, is able to maintain the passive behavior of titanium. Titanium is also resistant to localized corrosion, which will not occur in commercially pure titanium or industrial alloys below 70 °C regardless of salinity or acidity of the solution. The critical crevice corrosion temperatures for some titanium alloys are listed in Tab. 19.1.

Temperature limits for pitting corrosion are considerably higher than for crevice corrosion. The unalloyed alloys can typically take at least 50 °C higher temperature under conditions without crevices.

Titanium alloys have demonstrated immunity to microbiologically influenced corrosion (MIC) in both laboratory and service exposures. The ability to resist biological activity in seawater is caused by titanium's high critical crevice corrosion temperature and high anodic pitting potential.

19.2.3
Corrosion in Oil and Gas Environments

The internal environment in risers is generally reducing, i.e. acidic without oxygen or other oxidizing agents and contains water with varying amounts of salts, CO_2, and H_2S. Temperature may be as high as $250\,^\circ C$. Titanium alloys are fully resistant in carbon dioxide, but may corrode in hydrogen sulphide-containing environments.

Crevice corrosion is normally not considered a problem for titanium under anaerobic conditions. The possible effect of H_2S as a crevice corrosion promoter under reducing conditions has been discussed, but no data for verification of this theory are available.

The behavior of titanium in contact with some process fluid constituents and dosing chemicals may lead to corrosive effects. This applies for some well workover fluids and for methanol, which is frequently used as hydrate preventer, see below.

Commercially pure titanium and all titanium alloys are rapidly attacked by hydrofluoric acid, even in very dilute concentrations and even in fluoride containing solutions below pH 7. Titanium can therefore not be specified in any applications where hydrofluoric acid may be used. Workover fluids for wells are of special concern since these normally consists of 12% HCl and 3% HF. Titanium also has limited resistance in hydrochloric acid and care should be taken if this acid is used. Inhibition by sodium molybdate or potassium pyroantimonate may be applied for hydrochloric acid, but not for fluoride.

19.2.4
Stress Corrosion Cracking (SCC)

Commercially pure titanium and the alloys listed in Tab. 19.1 are generally resistant to stress corrosion cracking (SCC) in chloride media. All but Grades 7 and 23 are approved for sour service under NACE MR-0175. There have not been any failures due to sulphide induced SCC during 20 years of service in offshore environments.

Titanium grades are susceptible to SCC in anhydrous methanol. Water is an effective inhibitor because it maintains the passivity of titanium. Commercially pure titanium grades require 2% water for immunity, but alloys require higher levels to stay passive. For sustained exposure, 10% water is specified for Grade 29. Tab. 19.2 lists the water levels in methanol recommended for the grades used in offshore applications.

Liquid metal embrittlement of titanium and its alloys has become an issue because of the presence of liquid mercury in production fluids, which could result in pools of mercury in contact with titanium. The concern is due to failures reported for aluminum under similar conditions. There have been no cases reported for titanium in the field, but in laboratory tests some titanium alloys have shown susceptibility to SCC in the presence of mercury.

Tab. 19.2 Recommended concentration of water in methanol to inhibit stress corrosion cracking.

Titanium Grade	Volume % water in methanol	
	Intermittent exposure [a]	Sustained exposure [b]
Grades 1, 2, 7, 11, 16, 17	1.5	2.0
Grades 9, 12	2.0	2.0
Grade 28	2.5	3.0
Grades 5, 23	3.0	3.0
Grade 29	5.0	10.0

a) Short-term exposure
b) Long-term continuous exposures

19.2.5
Galvanic Corrosion

Offshore applications require that a range of different metals have to perform together. Galvanic corrosion may occur when metals with different corrosion potentials are coupled together and there are both an electrical contact and an electrolytic path between the two. Seawater and produced waters have more than sufficient conductivity to promote galvanic corrosion. Titanium being more noble than most other metallic materials used offshore may induce corrosion of metals that are coupled to it. Fig. 19.1 shows the corrosion potentials for titanium and some of the materials it might be connected to. Corrosion resistant alloys with a potential close to that of titanium can be connected to titanium without problems, but care
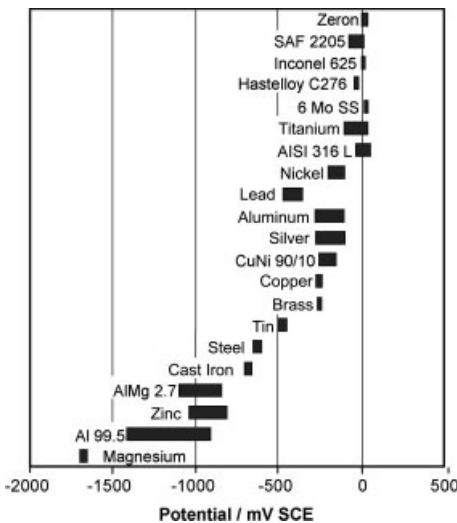
Fig. 19.1 The corrosion potentials for some materials in flowing seawater at 40 °C.

must be taken in systems that include alloys with a considerably lower crevice corrosion temperature than titanium. Steels are more susceptible to crevice corrosion than titanium at moderate and high temperatures.

A unique feature of titanium is its high pitting potential. Raising the potential of titanium into the passive region has only beneficial effects in most environments. The exception is strongly reducing acidic conditions where the oxide film cannot be maintained. Examples of such environments are concentrated hydrochloric and hydrofluoric acid.

Low alloy steel structures are normally cathodically protected in seawater. In many applications it is impossible to apply electrical insulation between the titanium component and the body structure and care must be taken as titanium may pick up some of the hydrogen that results from the reduction of water. Hydrogen evolution depends on the potential and will only take place when the potential is lower than –800 mV vs. SCE in seawater. Hydrogen uptake increases with lower potentials, and coupling titanium to magnesium electrodes, which have a potential of –1700 mV vs. SCE leads to unacceptable hydrogen levels. Zinc anodes with a potential of –1030 mV vs. SCE are most common in offshore applications. Although these will not have the same effect as magnesium, care should be taken and some protection may be necessary.

The solubility of hydrogen is very different in α and β titanium. While α titanium can dissolve a few hundred ppm, β can take up several thousand ppm without hydride precipitation. The diffusion constant is also much lower in the α than in the β phase. Hydrogen absorbed in α alloys will accumulate as hydride in the surface region, while hydrogen is distributed more evenly in β alloys. The hydrogen diffusion in β alloys is so high that concentration gradients are not expected, even in thick components at low temperature. In α+β alloys the phase ratio and the microstructure become important. A continuous β phase network will be able to distribute hydrogen, while accumulation in the surface area is expected for alloys with a low β volume fraction. Hydride formation in Grade 5 has only been demonstrated in a few cases, and then at α/β interfaces.

Some elements, especially nickel and iron, enhance hydrogen absorption. It has been seen that Grade 9, which contains 0.9% nickel, absorbs up to 20 times more hydrogen than nickel free alloys in acidified seawater. Palladium and ruthenium have a more moderate effect on hydrogen uptake, but up to 2–3 times more hydrogen has been measured in alloys containing these elements compared to other alloys. The fact that iron may enhance hydrogen absorption in titanium has led to the hypothesis that iron smeared on titanium's surface may accelerate hydrogen uptake. In a seawater environment any iron is readily converted to rust and rust stains on the surface of titanium do not cause problems.

Calcareous deposits are calcium carbonate precipitates that form on metals under cathodic protection in seawater. The reduction of water or hydrogen ions result in an alkalinization in the near surface region that lowers the solubility of calcium carbonate. Calcareous deposits are also formed on titanium, reducing the cathodic current and hydrogen evolution to a great extent. It is thus seen that hydrogen absorption in titanium decreases with time when calcareous deposits are

formed. The integrity of calcareous deposits is thus of great concern. The deposit may crack as a result of temperature or load fluctuations or mechanical impacts and the precipitation rate may decrease when the water stream is strong. For long-term exposure it might thus be necessary to coat loaded components if it is impossible to electrically insulate them from cathodic polarization.

19.2.6
Fatigue

Titanium alloys may suffer from fatigue in many offshore applications such as in various locations in catenary risers and stress joints. The fatigue strength is typically 50–60% of the tensile strength for unnotched specimens. The presence of notches or defects may lower this value considerably. Care must therefore be taken to avoid stress concentrators when cyclic stress is applied at high levels or at high frequency. A good practice for titanium is to remove cracks, tears, and other production defects. It is also necessary to remove thick oxide scales and α-case.

Even very small pores in welds can act as crack initiation sites in Grades 5, 23, or 29. The critical defect size is smaller than the detection limit for standard NDT tests of welds. Even if welded joints are stress relieved, a substantial reduction in fatigue life is seen for fusion welding. The fatigue design curves must therefore take into account the presence of micron-size pores. Alternative welding methods such as friction welding that might eliminate such crack initiating sites are thus evaluated in ongoing projects.

19.3
Fabrication

19.3.1
Welding

Titanium is easy to weld by most processes, but contamination with air or carbonaceous materials can lead to embrittlement. The materials to be welded must therefore be clean and protected by an inert shielding gas while hot. Commercially pure titanium is considered very easy to weld, while titanium alloys can be more difficult depending on phase composition. The β alloys are easier to weld than α + β alloys. Alloys generally show reduced weld metal ductility and toughness.

The offshore industry has high quality requirements and large efforts have been put into training and qualifying titanium welders. The result is reliable welding procedures and good quality welds.

19.3.2
Cold Forming

The development of cold forming has decreased the costs for fabricating thin-walled piping materials. In this way tees and knees can be produced without welding. An example is shown in Fig. 19.2. The technique can be utilized for various materials, but is particularly attractive for titanium from a technical as well as an economic point of view (see Fig. 19.3). For a 200 m long, 6-inch (15.2 cm) seawater pipe between two platforms on the Frigg field in the North Sea, cold bent titanium piping was installed at a lower cost than traditionally produced carbon steel. Titanium pipes in Grade 2 can be cold formed and flared in dimensions up to DN 200 (8 inches). Grade 5 and Grade 9 have been bent in dimensions up to 3 inches (7.6 cm). Flaring is so far limited to pipes with a maximum

Fig. 19.2 Cold forming of titanium pipes. Courtesy Aker Verdal AS.
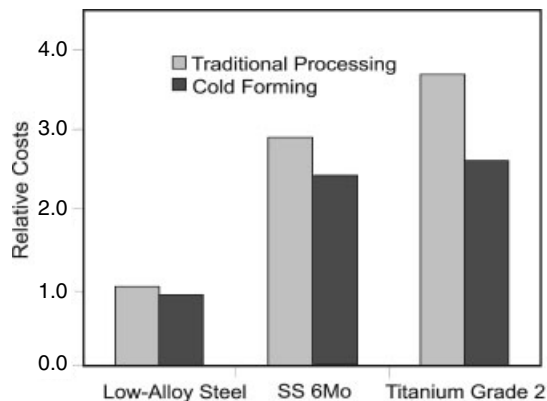
Fig. 19.3 Cost comparison for piping systems in different materials for the Njord Platform produced by traditional methods (knees and tees) compared to cold bending and flaring (1996).

wall thickness of 0.5 inch. Several thousand tons of titanium have been fabricated by cold forming and installed on platforms in the North Sea since 1990.

The pipes are sandblasted and pickled before forming. It is important to ensure that the pickling time is sufficient to remove all deformed material in order to avoid micro-cracks during the bending operation. In order to obtain satisfactory material properties after cold forming, good ductility is required with a minimum elongation of 25% normally required. The oxygen content is, however, more critical than elongation and should not exceed 0.16% in Grade 2 in order to avoid micro-cracks during cold forming.

For particular purposes that require thick walls or large bending radii, induction heat forming is an attractive alternative to conventional forming techniques.

19.3.3
Nitriding

Nitriding of titanium has been used as a surface hard facing method for titanium for many years. It improves the wear resistance and reduces the tendency for galling. The materials are nitrided in a vacuum furnace in the temperature range 770–870 °C for up to 16 hours while exposed to a flow of ultra pure nitrogen gas which dissociates thermally and diffuses into the material. Surface hardness can
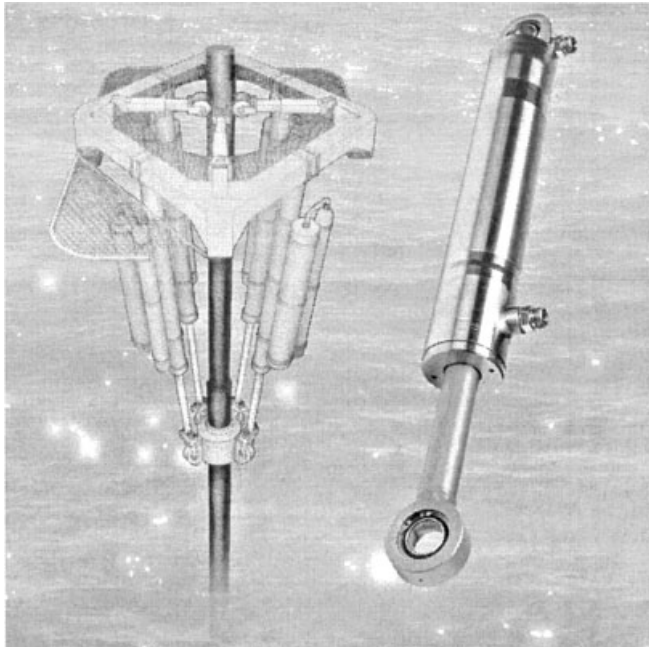
Fig. 19.4 Hydraulic cylinders for tension leg platforms with nitrided piston rods. Courtesy Permascand AB.

be increased from 240 to about 3000 HV for both commercially pure and alloyed titanium. An example of a nitriding application is the piston rods in hydraulic cylinders for tension leg platforms shown in Fig. 19.4. The piston rods are about 3300 mm long and 90 mm in diameter and have very strict tolerance limits for dimensions and straightness. The annealing procedure during nitriding requires very special precautions regarding underlay/support and temperature control in the furnace. Maximum temperature difference in the furnace is 2 °C. Nitrided titanium piston rods have now been in operation for about five years. They have replaced chromium coated duplex piston rods that became seriously corrosion/abrasion damaged after a few months.

19.4
Applications

There are an increasing number of offshore applications for titanium. Twenty years ago a few hundred kilograms had been used in chlorination systems and heat exchangers. Now total consumption is more than three thousand tons. The major applications are seawater and process fluid management systems and heat exchangers. Some selected applications are shown in Tab. 19.3.

19.4.1
Seawater Systems

Following the success with installations of titanium ballast water piping and manifolds, titanium has been used in other types of seawater systems such as fire water, cooling water, and sprinkler systems. In such systems titanium competes with stainless steel for moderate dimensions, and with graphite-reinforced plastic (GRP) and composites for larger dimensions. Investigations have shown that titanium is economically the best choice for diameters up to 8 inches, while composite materials are preferred for larger diameters.

Cold forming has reduced the costs for titanium piping. There are substantial amounts of piping on offshore platforms. Norsk Hydro's Njord platform, for instance, has 110 tons of piping and titanium was chosen because tees and knees can easily be formed by cold bending. The titanium pipework on deck consists of about 3500 cold-formed pieces. Flaring combined with loose flanges of AISI 316 were used for connections. This alternative gave a considerable reduction in cost compared to traditional production methods.

The increased use of titanium for seawater systems has been driven mainly by two factors – unexpected poor experience with 6 Mo-steel and introduction of cold bent titanium pipes. Poor crevice corrosion has been experienced with 6 Mo-steel on several platforms. The Norwegian offshore specification, NORSOK, therefore limits the use of 6 Mo and 25% Cr duplex for seawater applications to 15 °C, where crevices will appear.

Larger titanium components can be cast. Castings can be made from a few grams up to 2750 kg. Considerable numbers of control and deluge valves for fire-

Tab. 19.3 Selected offshore applications of titanium.

Applications	Companies	Projects	Titanium alloy grades
Taper Stress Joints	Placid Oil	Green Canyon	23 (Ti-6Al-4V ELI)
Taper Stress Joints	Ensearch	Garden Banks	23
Taper Stress Joints	Oryx Energy	Neptune	23
Fire Water Systems	Norsk Hydro	Troll B(Oil)	2 (CP)
Fire Water Systems	Elf Petroleum	Brage, Visund, Fry	2
Fire Water Systems	Statoil	Sleipner West, Siri, Norne	2
Seawater Lift Pipes	Statoil	Sleipner, Veslefrikk	2
Ballast Water Systems	Mobil	Statfjord A/B, Beryl	2
Ballast Water Systems	Mobil	Hibernia	2
Penetration Sleeves	Statoil	Sleipner West	2
Penetration Sleeves	Norsk Hydro	Oseberg	2
Freshwater Pipework	Elf	Frigg	2
Seawater Pipework	Esso	Jotun	2
Seawater Pipework	Norsk Hydro	Njord, Visund	2 (110 tons)
Seawater Systems, fire, ballast and produced water Pipework	Statoil	Åsgard B	2 (300 tons)
Seawater Systems, Gravity Based System	Statoil	Troll A (Gas)	2 (500 tons)
Drilling Riser	Statoil (Conoco)	Heidrun	23
Booster Lines	Statoil (Conoco)	Heidrun	9 (Ti-3Al-2.5V)
Anchor System Pipework	Statoil (Conoco)	Heidrun	2
Penetrations and Manholes	Statoil (Conoco)	Heidrun	2

water systems are produced and installed offshore. These are normally delivered in the proof machined condition with flanges and seats machined as shown in Fig. 19.5.

19.4.2
Heat Exchangers

Various types of heat exchangers are being used, from tube and shell heat exchangers to plate exchangers. The exceptional corrosion resistance of titanium makes it possible to produce thin-walled structures with high heat transfer density. Titanium also stays clean and free of scale and needs little maintenance. Conventional production techniques can be used preferentially with automated welding. Where space or weight is at a premium, compact heat exchangers offer a high heat transfer per unit volume. With the use of superplastic forming and diffusion bonding, compact heat exchangers can be designed for high-pressure applications.

Fig. 19.5 Cast titanium 30 inch valve body. Courtesy Alba AS.

19.4.3
Hypochlorite Systems

Titanium is a material frequently used in sodium hypochlorite systems on offshore platforms. Titanium is one of the few metallic materials to have high corrosion resistance in this strongly oxidizing environment. Serious problems have, nevertheless, been experienced with two installations on North Sea platforms. In both cases dramatic destruction of titanium Grade 2 components occurred, one case within a few days, while it took some weeks before any failure was observed in the other case. Investigations did not reveal any defects in the material or the welds. The possible explanation has been that titanium suffered anodic dissolution due to stray currents from the electrolytic cells producing hypochlorite.

19.4.4
Riser Pipes

Conoco decided in 1991 to use titanium for a drilling riser on the Heidrun platform, and this initiated a large activity on titanium risers. Norsk Hydro performed a large qualification program to qualify titanium Grade 29 (Ru) for production risers for the Visund field. The concept was technically qualified, but was unacceptable due to very high cost, mainly associated with installation. Titanium was also considered a strong candidate for the 700 m long, 28-inch gas export riser for the Åsgard B semisubmersible, but was turned down because a design could not be implemented in a short production time. Titanium is also being considered for rigid production and export risers, as well as for flexible risers of the

catenary type. Det Norske Veritas has finished a recommended practice for the design of titanium risers.

19.4.5
Riser Taper Stress Joint

Riser taper stress joints are cyclically loaded and may suffer from fatigue. Grade 23 titanium has shown excellent performance and is now probably the preferred material in this application. Titanium taper stress joints are typically one-third the length, one-quarter the weight, and less expensive than their steel counterparts.

19.4.6
Sub-Sea Systems

Many applications made of titanium are being used in sub-sea systems such as: flowline jumpers, manifold piping, sub-sea valves, umbilicals, coiled tubing, etc. Titanium is often selected to optimize weight, strength, buoyancy, and corrosion properties. One example is the Alcatel Capjet trenching tool which has its frame and hydraulic components in Grade 5. Some of the actuator rods are nitrided to enhance wear resistance.

19.5
Availability and Cost

19.5.1
Deliveries

One of the obstacles for the use of titanium for offshore applications had been long delivery times compared to competitive materials. Current experience shows that delivery times are similar to those expected for stainless steel, and deliveries are according to specifications.

There have been cases of wrong deliveries of titanium to offshore applications. In one case, a batch of material differed significantly from the corresponding certificate, which stated that it should be Grade 2 titanium. The material was highly brittle due to impurities and the whole batch was rejected. During investigation it was found that the material did not meet any American or Russian standard, and it turned out that the material was scrap material intended for titanium additions to steel production. For this reason most companies have introduced a more thorough follow up of manufacturing and documentation for titanium.

19.5.2
Cost

A 1996 cost comparison between various material alternatives for the seawater piping system for the Njord platform is given in Fig. 19.3. It is seen that titanium is cost competitive with 6 Mo-steel when cold forming is applied. In this project the valves, however, were not made of titanium due to unacceptably high prices. The cost of a large titanium valve was two to three times higher than a valve delivered in 6 Mo-steel.

A more recent cost comparison performed in January 1998 on a 8-inch piping system showed that titanium pipes and titanium fittings were price comparable to 6 Mo-steel, while duplex steel was more expensive, see Tab. 19.4. Titanium valves are still considerably more expensive than stainless steel valves, but titanium valves are used in many cases due to their higher reliability.

19.6
Standards

Norwegian oil and engineering companies have worked out a standard, NORSOK, for most materials to be used offshore. The aim is to limit the number of material qualities and dimensions to a minimum. Operation limits with respect to temperature and environment are given for most materials. Titanium Grade 2 is included in the following paragraphs:

- materials selection
- piping and valves
- welding and inspection for piping
- material data sheets for piping
- qualification of manufacturers of special materials.

Russia, as one of the major titanium producers in the world, can produce according to any given standard and exports large quantities of titanium. In Russia, aluminum is used instead of oxygen as a strengthening alloying element for commercially pure material. In a comparison of commercially pure Russian GOST

Tab. 19.4 Cost Comparison Piping system 8-inch 10S/Class 150.

	Relative cost [a]		
	Titanium Gr. 2	UNS S 31254	UNS S 32750
Pipes and fittings	1	1	1.37
Flanges	1	0.83	0.93
Valves	1	0.61	0.71

a) Averaged price from 4 suppliers January 1998.

standard titanium grade VT 1-0 with up to 0.7% Al with ASTM Grade 2, both materials turned out to have the same properties. The GOST material and the VT 1-0 have now been included in the most recent version of the NORSOK standard.

19.7
Conclusion

Several thousand tons of titanium have been installed on offshore platforms and vessels; and the use of titanium in sub-sea installation and in monitoring and sampling equipment is increasing. Most of this is installed in the North Sea, but titanium also finds its way to other offshore oil fields. Seawater systems are the dominant applications. Cold forming processes for pipes and fittings have been developed, leading to significant reductions in cost for these systems. The application of titanium in taper stress joints shows that titanium can outperform other materials in heavily loaded components. Titanium has also been qualified for several riser installations, but only one drilling riser in titanium exists. Better integration in the design process and more cost effective designs seem to be required if titanium is to find its way into this application. The increased use of sub-sea installation will require extensive use of titanium to ensure reliability and low lifecycle costs. Titanium will also be a preferred material due to its low impact on the marine environment. The ability to recycle used material and the high recovery value lead to favorable lifecycle costs for titanium.

19.8
Referenced Literature and Further Reading

*R. Boyer, G. Welsh, E.W. Collings, eds: Materials Properties Handbook: Titanium Alloys, The Materials Information Society (ASM), Materials Park, OH (1994)

*R. R. Boyer, D. Eylon, G. Lütjering, eds: Fatigue Behavior of Titanium Alloys, TMS, Warrendale, PA (1998)

E. Bardal, J. M. Drugli, P. O. Gartland, "The Behaviour of Corrosion-Resistant Steels in Seawater: A Review", Corrosion Science **35**(1–4) (1993) 257–267

C. F. Baxter, R. W. Schutz: Critical Design Aspects of Dynamic Titanium Alloy Risers, Paper No OMAE-96-731M, in 15th ASME Int. Conf. on Offshore Mechanics and Artic Engineering, ASME International, New York (1996)

S. Berge: Fatigue of Titanium Fusion Welds – Models for Assessment of Defect Sensitivity, eds R. Boyer, D. Eylon, G. Lütjering, TMS, Warrendale, PA (1998)

I. V. Gorynin, Titanium Alloys for Marine Application, Materials Science and Engineering **A263** (1999) 112–116

L. Lunde, H. B. Nordvik, M. Seiersten: A Comparison of Commercially Pure Titanium Produced According to the American Grade 2 and the Russian GOST VT 1-0 Standards, in Proc. 9th Intern. Conf. on Titanium, Central Research Institute of Structural Materials (CRISM) "PROMETEY", St. Petersburg (2000) 799–810

R. W. Schutz and J. Grauman: Fundamental Corrosion Characterization of High Strength Titanium Alloys, in Industrial Applications of Titanium and Zirconium; STP 917, Vol. 4, ASTM, Philadelphia, PA, (1986) 130–143

R.W. Schutz: Stress-Corrosion Cracking of Titanium Alloys, in Stress-Corrosion Cracking – Materials Performance and Evaluation, ed R.H. Jones, The Materials Information Society (ASM), Materials Park, OH (1992) 265–297

R.W. Schutz: Performance of Ruthenium-Enhanced Alpha-Beta Titanium Alloys in Aggressive Sour Gas and Geothermal Well Produced-Fluid Brine, Paper No. 32, COR-ROSION 97, NACE Houston, TX (1997)

Titanium for Offshore and Marine Applications – A Designer and Users Handbook, The Titanium Information Group and Institute for Energy Technology, Kidderminster/Kjeller (1999)

G. Venkataraman, A.D. Goolsby: Hydrogen Embrittlement in Titanium Alloys from Cathodic Polarization in Offshore Environments, and its Mitigation, Paper No. 554, CORROSION 96, NACE Houston, TX (1996)

* These are suited as overall recommended literature

Index

Dr.-Ing. Christoph Leyens
(1967) earned his Ph.D. from the RWTH Aachen, Germany. Having 1,5 years of research experience in the USA he is currently group leader light-metal composites at the German Aerospace Center (DLR). His current research interest is focused on the development of titanium matrix composites and on coatings for titanium- and nickel-base materials.

Titanium alloys are well known as materials for the aerospace industry already since the 1940s. Nowadays, due to their superior properties - high specific strength, excellent corrosion resistance - they find increasing applications in chemical engineering, for body implants like hip replacements or in the off-shore industry, energy or automotive industry. Not to forget the increasing demand of the sports and consumer goods industry, e.g. for golf clubs, bicycles or jewelry, that makes titanium a part of our everyday life already.

This handbook is an excellent reference for materials scientists and engineers that need to get more knowledge about the development, processing and application of titanium and titanium alloys. Following some introductory chapters about the fundamental materials properties of titanium the reader finds thorough descriptions of the developement, processing and properties of modern titanium alloys. Furthermore, applications of titanium and its alloys in aerospace, medicine, energy and automotive technology are discussed in detail.

Dr.-Ing. Manfred Peters
(1950) graduated from Ruhr-University of Bochum with a Ph.D. on structure and properties of titanium alloys. After 2 years at Carnegie-Mellon University, USA, he joined DLR in 1982 where he presently is Deputy Director of the Institute of Materials Research. He has more than 30 years of research experience on light metals and high temperature coatings.

Further titles:

ISBN 3-527-30534-3

9 783527 305346